DOE/ER-0313/16

Fusion Materials

Semiannual Progress Report for Period Ending March 31, 1994

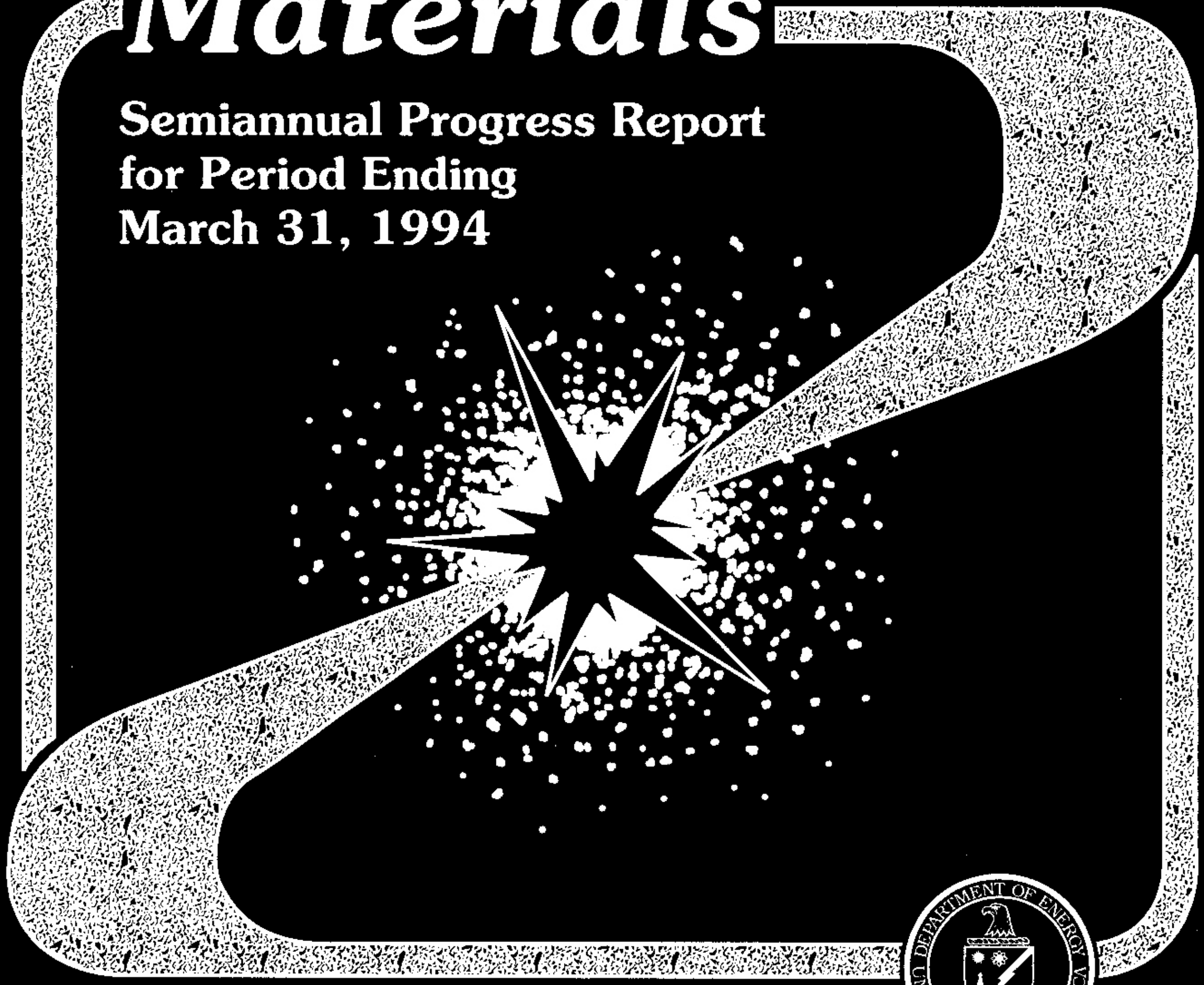

U. S. Department of Energy
Office of Fusion Energy

This report has been reproduced directly from the best available copy.

Available to DOE and DOE contractors from the Office of Scientific and Technical Information, P.O. Box 62, Oak Ridge. TN 37831; prices available from (615) 578-8401, FTS 626-8401.

Available to the public from the National Technical Information Service. U.S Department of Commerce. 5285 Port Royal Rd.. Springfield, VA 22161.

This report was prepared as an account of work sponsored by an agency of the United States Government. Neither the United States Government nor any agency thereof. nor any of their employees, makes any warranty. express or implied, or assumes any legal liability or responsibility for the accuracy, completeness, or usefulness of any information, apparatus, product, or process disclosed. or represents that its use would not infringe privately owned rights. Reference herein to any specific commercial product, process. or service by trade name. trademark. manufacturer, or otherwise, does not necessarily constitute or imply its endorsement, recommendation. or favoring by the United States Government or any agency thereof. The views and opinions of authors expressed herein do not necessarily state or reflect those of the United States Government or any agency thereof.

DOE/ER-0313/16
Distribution
Categories
UC-423, -424

FUSION MATERIALS
SEMIANNUAL PROGRESS REPORT
FOR THE PERIOD ENDING
MARCH 31, 1994

Prepared for
DOE Office of Fusion Energy
(AT 15 05 01 0)

DATE PUBLISHED: September 1994

Prepared for
OAK RIDGE NATIONAL LABORATORY
Oak Ridge, Tennessee 37831
Managed by
MARTIN MARIETTA ENERGY SYSTEMS, INC.
for the
U.S. DEPARTMENT OF ENERGY
under Contract DE-AC05-84OR21400

FOREWORD

This is the sixteenth in a series of semiannual technical progress reports on fusion reactor materials. This report combines research and development activities which were previously reported separately in the following progress reports:

Alloy Development for Irradiation Performance

Damage Analysis and Fundamental Studies

Special Purpose Materials

These activities are concerned principally with the effects of the neutronic and chemical environment on the properties and performance of reactor materials; together they form one element of the overall materials programs being conducted in support of the Magnetic Fusion Energy Program of the U.S. Department of Energy. The other major element of the program is concerned with the interactions between reactor materials and the plasma and is reported separately.

The Fusion Materials Program is a national effort involving several national laboratories, universities, and industries. The purpose of this series of reports is to provide a working technical record for the use of the program participants, and to provide a means of communicating the efforts of materials scientists to the rest of the fusion community, both nationally and worldwide.

This report has been compiled and edited under the guidance of A. F. Rowcliffe by G. L. Bum. Oak Ridge National Laboratory. Their efforts. and the efforts of the many persons who made technical contributions, are gratefully acknowledged.

F. W. Wiffen
Division of Advanced Physics
and Technology

Reports previously listed in this series are as follows:

DOEVER-0313/1	Period ending September 30.1986
DOE/ER-0313/2	Period ending March 31,1987
DOE/ER-0313/3	Period ending September 30,1987
DOE/ER-0313/4	Period ending March 31,1988
DOE/ER-0313/5	Period ending September 30.1988
DOE/ER-0313/6	Period ending March 31.1989
DOE/ER-0313/7	Period ending September 30,1989
DOEVER-0313/8	Periodending March 31, 1990
DOEVER-0313/9	Period ending September 30,1990
DOE/ER-0313/10	Period ending March 31,1991
DOE/ER-0313/11	Period ending September 30,1991
DOE/ER-0313/12	Period ending March 31.1992
DOE/ER-0313/13	Period ending September 30,1992
DOE/ER-0313/14	Period ending March 31,1993
DOE/ER-0313/15	Period ending September 30,1993
DOE/ER-0313/100	Technical Evaluation of the Technology of Vanadium Alloys for Use as Blanket Structural Materials in Fusion Power Systems

CONTENTS

1.0 IRRADIATION FACILITIES, TEST MATRICES, AND EXPERIMENTAL METHODS 1

1.1 STATUS OF U.S./JAPAN COLLABORATIVE PROGRAM PHASE II HFIR TARGET AND RB* CAPSULES - J. E. Pawel, R. L. Senn. and A. W. Longest (Oak Ridge National Laboratory) and K. Shiba (Japan Atomic Energy Research Institute). 3

Capsules HFIR-MFE-JP9 through **16** were installed in the High Flux Isotope Reactor (HFIR) target **July 20.1990** for irradiation beginning with ***HFIR*** fuel cycle **289.** Of these eight target capsules, JPIO, **11, 13, 16** accumulated 18 dpa and were removed from the reactor in September **1991. JP14** was removed from the reactor at the end of cycle 310 (September **1992) after** achieving a **peak** dose of **34** dpa Capsules **JP9, 12,** and **15** completed **35** cycles on April **1.1994** and were removed from the target region. Each capsule had accumulated a **peak** dose of approximately **57** dpa

Three new **capsules,** HFIR-MFE-JP20, 21, and 22, have been designed to complete the original experiment matrix of the **JP9 through JP16** series capsules. Irradiation began in December **1993** with the **start** of cycle 322. As of April **1, 1994** (end of cycle **324),** each capsule had achieved approximately **4.9** dpa.

The RB* experiments are the continuation of the ORR spectrally tailored experiments. **In** this stage, a hafnium liner is **used** to modify the spectrum to simulate fusion helium *to* displacements per atom (He/dpa) ratio in the austenitic steel specimens. Of the four capsules in **this set,** two **(60J-1** and **330J-1)** were disassembled during this reporting period **after** accumulating a peak dose in HFIR of 11 dpa Two capsules **(200J-1** and **400J-1) are** in the reactor and have achieved a dose of ***5.5*** dpa

1.2 THE COBRA-IB IRRADIATION EXPERIMENT IN EBR-II – H. Tsai, A. G. Hins, R. **V.** Strain, and D. L. Smith (Argonne National Laboratory). **8**

Design of the COBRA-IB irradiation experiment began in **this** reporting **period** and is in progress. The target reactor insertion dale. for COBRA-IB is September **1994.** Technical and programmatic feasibility approval for the experiment **has** been granted by EBR-II Operations.

2.0 DOSIMETRY, DAMAGE PARAMETERS, TRANSMUTATION, AND ACTIVATION CALCULATIONS.. .... **11**

2.1 **REVISED** NEUTRON **DOSIMETRY** RESULTS FOR THE MOTA-2A EXPERIMENT IN FFTF – L. R. Greenwood (Pacific Northwest Laboratory). **13**

Revised neumn fluence **and** damage **values are** reported for the MOTA-2A experiment in the Fast Flux Test Facility **(FFTF).** This revision corrects an **error** with processing of the **^{235}U(n,f)** reaction. Net corrections are on the order of ***5%.***

2.2 **REANALYSIS** OF NEUTRON **DOSIMETRY** FOR THE MOTA-1A/1B **EXPERIMENTS** IN **FFTF -** L. R. Greenwood (Pacific Northwest Laboratory). **15**

Neutron fluence and spectral measurements and radiation damage calculations have been revised for the MOTA-1A, 1B experiments in the Fast Flux Test Facility **(FFTF).** The **data** were revised in order to **correct** for nuclear **bumup** effects for several of the radiometric monitors, thereby increasing the fluence and damage up lo 20%, according to position the MOTA assembly. The MOTA-IA experiment **was** irradiated from January **18,1983,** *to* October **23,**

1983. for an exposure of 202.0 EFPD. MOTA-1B was irradiated from January 1.1984, to April 23, 1984, for an exposure of 109.4 EFPD. Neutron fluence and dpa values are. presented for both assemblies.

Neutron fluence and spectral measurements and radiation damage calculations are reported for the Materials Open Test Assembly (MOTA-)2B experiment in the Fast Flux Test Facility (FFTF). The irradiation was conducted from May 27.1991, to March 19,1992, for a total exposure of 203.3 EFPD (effective full-power days). The maximum fluence was about 9 x 10^{22} n/cm^2, 6 x 10^{22} above 0.1 MeV producing about 24 dpa in iron. Neutron fluence and radiation damage maps are presented for the entire MOTA assembly based on the analysis of ten neutron spectral measurements and fourteen additional flux gradient measurements.

Neutron fluence and spectral measurements and radiation damage calculations have been completed for the Materials Open Test Assembly (MOTA)-IC experiment in the Fast Flux Test Facility (FFTF). Although this irradiation was completed in 1985. the neutron dosimetry data were never analyzed. The MOTA-IC experiment was irradiated in cycles 5 and 6 from June 16, 1984, to June 24, 1985, for an exposure of 256.7 EFPD (effective full power days). The irradiation was conducted at 400 MW. Neutron fluence and dpa values are presented.

This study presents a comparison of nuclear transmutation rates for candidate fusion fust wall/blanket structural materials in available fusion test reactors with those produced in a typical fusion spectrum. The materials analyzed in this study include a vanadium alloy (V-4Cr-4Ti), a reduced activation martensitic steel (Fe-9Cr-2WVTa), a high conductivity copper alloy (Cu-Cr-Zr), and the SiC compound The fission irradiation facilities considered include the EBR-II (Experimental Breeder Reactor) fast reactor, and two high flux mixed spectrum reactors, HFIR (High Flux Irradiation Reactor) and SM-3 (Russian reactor). The uansmutation and dpa rates that occur in these test reactors are. compared with the calculated uansmutation and dpa rates characteristic of D-T fusion first wall spectrum. In general, past work has shown that the displacement damage produced in these fission reactors can be correlated to displacement damage in a fusion spectrum: however, the generation of helium and hydrogen through threshold reactions [(n,xα) and (N,xp)] are much higher in a fusion spectrum. As shown in this study, the compositional changes for several candidate structural materials exposed to a fast fission reactor spectrum are very low. similar to those for a characteristic fusion spectrum. However, the relatively high thermalized spectrum of a mixed spectrum reactor produces transmutation rates quite different from the ones predicted for a fusion reactor, resulting in substantial differences in the final composition of several candidate alloys after relatively short irradiation time. As examples, the transmutation rates of W, Ta, V, Cu, among others, differ considerably when the irradiation is performed under a mixed spectrum reactor's and fusion first wall's spectrum. The out-of-core positions in mixed spectrum reactors can be partially shielded against low energy neutrons, e.g., by hafnium. to reduce the transmutation rates but the displacement rates at these positions are much lower than those for the wre positions. Fast reactors (EBR-II) provide the only possibility for obtaining high damage rates without producing significant compositional effects in vanadium alloys, ferritic steels, and copper alloys.

A neutron transport calculation has been performed to determine the feasibility of **creating** a shielded facility in the Be reflector of the HFIR. It was found that the B_4C provides satisfactory **spectral** tailoring to reduce production of Cr below the tolerance limit for Cr in the original alloys. The shield would have to be replaced after eight cycles or 5 dpa but the operations schedule for the HFIR makes it easier to replace the shield after seven cycles. Three shields would then have to be used in order to reach 10 dpa. This facility would provide the equivalent of a low-temperature fast neutron position in the HFIR for development and preliminary qualification of vanadium alloys for fusion devices.

Brazing compounds containing silver ***or*** gold will transmute during irradiation, forming significant **amounts** of either cadmium or mercury, respectively, in all neutron **spectra** of current interest to the fusion materials program. The impact of **this** transmutation on braze performance and on development of fssion-fusion correlations has yet to be determined but will **he *addressed*** in an irradiation experiment that was recently completed in FFTF-MOTA. A lesser amount of transmutation will occur in brazes containing **tin,** but no specimens containing **brazes** with **tin** have yet **been** irradiited.

In December the ITER Joint **Central Team** authorized the creation of a Materials Properties Handbook. **This** Handbook is a cooperative activity between the four parties of ITER (Japan, the E.U., the R.F., and the U.S.). The U.S. Home Team **has** been **selected** to coordinate the documentation. while all four Parties will provide **data During** this **period** the effort focused on organizing this activity. developing a format for **use** by all of the parties, and demonstrating the ability to electronically transfer files between the four parties. First draft of the Handbook is scheduled for July.

No contributions.

Microstructural examinations have **been** performed on a **series** of **binary** Fe-Cr alloys irradiated in the FFTF/MOTA at 425°C to 200 dpa. The data represent the highest swelling levels reported in neutron irradiated femtic alloys. The alloy compositions ranged from 3 to 18%Cr in 3% Cr increments, and the irradiation temperature corresponded to the **peak** swelling condition for this alloy class. Density measurements showed swelling levels **as** high **as** 7.4% with the highest swelling found in the Fe9Cr and Fe6Cr alloys. Microstructural examinations revealed that the highest swelling conditions contained well-developed voids, often **as** large **as** 100 nm, and a dislocation network comprised of both $\frac{a}{2}$<111> and **a<100>** Burgers vectors. Swelling was lower in the other alloys, and the swelling reduction could be correlated with increased precipitation. These **results are** considered in light of the current theories for low swelling in ferritic alloys, but no theory is available to completely explain the **results.**

In evaluating fusion reactor **performance,** knowledge about permeation, diffusion, and concentration of hydrogen isotopes throughout the structure is of **critical** importance. The data **base** on hydrogen isotope permeation in relevant fusion reactor materials is reviewed in this report. Comparisons are made within alloys of the same ***type* as** well **as** with all the other classes of alloys. Both gasdriven permeation (GDP) and plasma-driven permeation (PDP) are included. Data on GDP behavior in Fe and Ni alloys are relatively consistent In metals that have a high solubility and/or are hydride formers, **e.g.,** V, **Nb.** Ti, there is much more variation in the data, and surface effects play a very dominant role. Permeation **under** plasma conditions is less well understood **as** more variables enter the relationship, e.g., reemission phenomena, internal concentration gradients, radiation effects, etc. The **data** show that **materials** do not necessarily rank in the same order under PDP conditions **as** under GDP conditions. A ***summary*** of the factors that influence permeation and the relative magnitude of their effect is given in the **report**

High-chromium (9-12% Cr) Cr-Mo and Cr-W ferritic steels are favored **as** candidates for fusion applications. In the early work to develop reduced-activation steels. an **Fe-2.25Cr-2W-0.25V-**0.1C steel (designated **2 1/4Cr-2WV) had better** strength than **an Fe-9Cr-2W-0.25V-0.07Ta-**0.1C (9Cr-2WVTa) steel (compositions are in weight percent). However, the 2 **1/4Cr-2WV bad** less-than-adequate impact toughness. **as** determined by the ductile-brittle transition temperature and upper-shelf energy of a Charpy impact test Because lowchromium **steels** have some advantages over high-chromium steels, a program to develop low-chromium steels is in **progress.** Microstructural analysis indicated that the reason for the inferior impact toughness of the 2 **1/4Cr-2WV** was the granular-bainite microstructure obtained when the steel was normalized. Properties can be improved by developing an acicular bainite structure by increasing the cooling rate after austenitization. Alternatively, acicular bainite can be promoted by increasing the hardenability. Hardenability was changed by adding *small* **amounts** of boron and chromium to the **2 1/4Cr-2WV** composition. A combination of B, Cr, and Ta additions resulted in low-chromium reduced-activation **steels** with mechanical **properties** comparable to those of 9Cr-2WVTa.

Tensile, Charpy, and transmission electron microscopy specimens of two conventional steels, modified 9Cr-1Mo (9Cr-1MoVNb) and Sandvik **HT9** (12Cr-1MoVW), and two reduced-activation steels, **Fe-9Cr-2W-0.25V-0.1C** (9Cr-2WV) and **Fe-9Cr-2W-0.25V-0.07Ta-0.1C (9Cr-2WVTa),** were irradiated in the Fast **Flux** Test Facility. Before irradiation, $M_{23}C_6$ was the primary precipitate in all four steels. which also contained some MC. Neutron irradiation did not substantially alter the $M_{23}C_6$ and MC. No new phases formed during irradiation of the 9Cr-2WV and 9Cr-2WVTa, but chi-phase precipitated in the 9Cr-1MoVNb and chi-phase and a' precipitated in the 12Cr-1MoVW. Irradiation-produced dislocation loops were observed in 9Cr-2WV, 9Cr-2WVTa, and 12Cr-1MoVW. The irradiation-produced microstructural changes caused the steels to harden, as measured by the change in yield stress. Hardening was correlated with a change in the Charpy impact properties of 9Cr-1MoVNb, 12Cr-1MoVW, and 9Cr-2WV. Although irradiation caused a yield stress increase of the 9Cr-2WVTa similar to that for 9Cr-2WV and 9Cr-1MoVNb, the change in Charpy properties was considerably less for 9Cr-2WVTa. This difference in Charpy behavior of the 9Cr-2WVTa with that of the 9Cr-2WV and 9Cr-1MoVNb was attributed to differences in the fracture stress-temperature relationship and/or the flow stress-temperature relationship between the 9Cr-2WVTa and the other two 9Cr steels.

Fracture toughness has been measured for two conditions of low activation martensitic steel F-82H, the first, a fully tempered condition and the second, completely untempered. In the fully tempered conditions. F-82H has a J_{IC} toughness of 284 kJ/m^2 (K_{IC} = 263.8 MPa$\sqrt{m}$), but in the untempered condition, the J_{IC} toughness is 18.4 kJ/m^2 (K_{IC} = 64 MPa$\sqrt{m}$). The consequences of not tempering are discussed in tight of these measurements.

Microstructures and density change measurements are reponed for martensitic commercial steels HT9 and modified 9Cr-1Mo (T9) and oxide dispersion strengthened ferritic alloys MA956 and MA957 following irradiation in the FFTF/MOTA at 420°C to 200 dpa Swelling as determined by density change remains below 2% for all conditions. Microstructures are found to be stable except in recrystallized grains of MA957, which are fabrication artifacts, with only minor swelling in the martensitic steels and a' precipitation in alloys with 12% or more chromium. These results further demonstrate the high swelling resistance and microstructural stability of the ferritic alloy class.

Effects of hydrogen (H) on the mixed-mode I/III critical J integrals (J_{MC}) and tearing moduli (T_M) were examined for a ferritic/martensitic stainless steel (F-82H) at ambient temperature. A determination of J_{MC} was made using modified compact-tension specimens. Different ratios of tension/shear stress were achieved by varying the principal axis of the crack plane between 0 and 55 degrees from the load tine. A specimen with 0 degree crack angle is the same as a standard mode I compact tension specimen. Specimens were heat-treated at 1000°C/20 h/air cooled (AC)-1100°C/7 min/AC-700°C/2 h/AC. The specimens were charged with H at a hydrogen gas pressure of 138 MPa at 300°C for two weeks, which resulted in a H content of 6 ppm(wt), as measured with the "inert gas fusion" technique. J_{MC} and T_M values were determined with the single specimen technique. Crack lengths were calculated by means of partial unloading compliances. The preliminary results from J integral tests showed that introducing H decreased J_{MC} and T_M values as compared to those without H. However. the presence of H did not change the dependence of J_{MC} and T_M values on the crack angles. Both mode I J and T values (J_{IC} and T_I) exhibited the highest values. Both the minimum J_{MC} and

T_M values occurred at a crack angle between 35 and 55 degrees, corresponding to the load ration (σ_{iii}/σ_i) of 0.7 to 1.4.

6.2 AUSTENITIC STAINLESS STEELS.... 171

6.2.1 FRACTURE TOUGHNESS OF IRRADIATED CANDIDATE MATERIALS FOR ITER FIRST WALL/BLANKET STRUCTURES – D. J. Alexander, J. E. Pawel. M. L. Grossbeck, A. F. Rowcliffe *(Oak* Ridge National Laboratory), and K. Shiba (Japan Atomic Energy Research Institute). 173

Candidate materials for first wall/blanket structures in ITER have been irradiated to damage levels of about 3 dpa at nominal irradiation temperatures of either 90 or 250°C. These specimens have been tested over a temperature range from 20 to 250°C. The results show that irradiation at these4 temperatures reduces the fracture toughness of austenitic stainless steels. but the toughness remains quite high. The toughness decreases as the test temperature increases. hdiation at 250°C is more damaging than at 90°C. causing larger decreases in the fracture toughness. Femtic steels are embrittled by the irradiation, and show their lowest toughness at room temperature.

6.2.2 LOW TEMPERATURE RADIATION-INDUCED SEGREGATION RELATIVE TO IASCC AND ITER – E. P. Simonen. R. H. Jones, L. A. Charlot. and S. M. Bruemmer (Pacific Nonhwest Laboratory). 194

Radiation induced segregation at grain boundaries in stainless steel has been evaluated as a function of temperature. Segregation caused by ion irradiation was measured and compared to temperature-dependent model predictions. The model was subsequently used to exuapolate predictions to ITER operating conditions. For ion irradiation, segregation was found to extend to temperatures below 400°C which implies that segregation is expected at temperatures less than 200°C for ITER irradiation damage rates. The model predictions were in accord with Cr depletion levels and profile widths as measured using FEG-STEM examination of ion irradiated grain boundaries. The model was further shown to be consistent with measured depletion levels at grain boundaries in 316 stainless steel irradiated in a light-water reactor at 288°C. The fmdings of this study suggest that chromium depletion and hence IASCC may be a concern for stainless steel structures irradiated in ITER high-temperature water environments.

6.3 REFRACTORY METAL ALLOYS.. 203

6.3.1 SWELLING AND STRUCTURE OF VANADIUM ALLOYS IRRADIATED IN THE DYNAMIC HELIUM CHARGING EXPERIMENT – H. M. Chung, B. A. Loomis, H. Tsai, L. Nowicki, J. Gazda, and D. L. Smith (Argonne National Laboratory). 204

Combined effects of dynamically charged He and neutron damage on density change, void distribution, and microstructural evolution of V-4Cr-4Ti have been determined *after* irradiation to 18-31 dpa at 425-600°C in the Dynamic Helium Charging Experiment (DHCE). FM specimens irradiated to –18 dpa at 600°C with an estimated He/dpa ratio of 3-9 appm He/dpa (a range similar to the fusion-relevant ratio of –5 appm He/dpa), only a few microvoids were observed at the interface of the grain matrix and some Ti(O,N,C) precipitates. No microvoids were observed either in the grain matrix or near grain boundaries. It seems that most of the dynamically produced He atoms are trapped in the grain matrix without significant void nucleation or growth. In this group of DHCE specimens. density changes were similar to those of non-DHCE (negligible He generation) specimens for a comparable fluence and irradiation temperature. Significant numbers of microvoids in the grain matrix and on localized *grain* boundaries were present only in specimens irradiated to ≈3 1 dpa at 425°C in high-tritium capsules, i which an excessive amount of helium was generated (estimated Hddpa ratio of 10-35 appm). Discontinuous regions of void segregation on *grain* boundaries were observed, and void number-density was significantly lower than in other alloys irradiated in tritium-trick experiments. The grain-boundary voids seem to have been produced by decay of tritium segregated to grain boundaries in the specimens at the onset of irradiation in high-tritium capsules (an artifact effect similar to tritium charging at 400°C in a tritium-trick experiment), rather than by segregation of He produced in the grain matrix. Density changes of the specimens were significantlyhigher than those from non-DHCE irradiations. Microstructuralevolution in V-4Cr-4Ti was similar for DHCE and non-DHCE irradiations, except for void number-density and distribution. As in non-DHCE specimens, irradiation-induced precipitation of ultrafine Ti_5Si_3 was observed for irradiation at 600°C but not at 425°C.

6.3.2 EFFECT OF DYNAMICALLY CHARGED HELIUM ON MECHANICAL PROPERTIES OF **V-4Cr-4Ti** – H. M. Cbung, B. A. **Loomis,** H. Tsai. L. Nowicki, D. E. Busch. and D. L. Smith (Argonne National Laboratory). 212

V-4Cr-4Ti has been reported to be virtually immune to irradiation embrittlement under conditions of negligible helium generation; DBTTs determined from one-third-size Charpy-impact specimens irradiated in a non-DHCE experiment were <-200°C. The effects of dynamically charged helium and tritium, and of neumn damage, on DBT of the alloy were determined after irradiation in the Dynamic Helium Charging Experiment (DHCE). TEM disks irradiated to 18-31 dpa at 425-600°C were fractured by repeated bending in a low-temperature bath. Miniature specimens were used because no Charpy-impact specimens were included in the DHCE experiment Ductile-brittle transition behavior was determined from quantitative SEM fractography. Bride fracture surface morphology was not observed at >-120°C regardless of the level of dpa damage or helium and tritium content in the alloy. Predominantly brittle-cleavage fracture morphologies were observed only at -196°C in some specimens irradiated to 31 dpa at 425°C and in which the estimated helium and tritium contents were highest. This indicates a DB'IT between -175 and -200°C in specimens containing the highest levels of dpa damage, helium. and tritium in the DHCE experiment. No intergranular fracture was observed.

6.3.3 STATUS OF THE DYNAMIC HELIUM CHARGING EXPERIMENT – H. Tsai, R. V. Strain. H. M. Chung, and D. L. Smith (Argonne National Laboratory). 220

Seven DHCE capsules containing vanadium-alloy specimens were irradiated in the MOTA-2B vehicle in FFTF to –20 to 29 dpa. In this and the previous reporting periods. equipment and procedures were developed at Argonne National Laboratory-East to disassemble these. capsules. Six of the seven capsules have been disassembled. (The seventh capsule was processed in April 1994, immediately following this reponing period.) Effluence of tritium into the cell exhaust was <2% of the total inventory. No contamination incidents occurred during the DHCE disassembly work. Initial testing of the retrieved Specimens is under way.

6.3.4 FABRICATION OF VANADIUM ALLOY FORMS FOR SPECIMEN PREPARATION – M. L. Grossbeck, T. K. Roche, W. S. Fatherly, F. F. Dyer. and N. H. Rouse (Oak Ridge National Laboratory). 225

The alloy V–5Cr–5Ti (Teledyne Wah Chang heat 832394) was received in the form of a 6.35 mm plate. and was rolled to 3.81 mm plate and 0.76 mm sheet The 3.81 mm plate was used for Charpy impact specimens and the 0.76 mm sheet was used for tensile specimens and welding experiments. Since interstitial impurities are important strengthening and embrittling agents in refractory metals, all anneals had to be done in ultra–high vacuum furnaces.

6.3.5 WELDING DEVELOPMENT FOR V-Cr-Ti ALLOYS – G. M. Goodwin and J. F. King (Oak Ridge National Laboratory). 235

Welds have been produced and characterized using the gas-tungsten arc (GTA) and electron beam (EB) welding processes. Thin sheet (0.75 mm) welds were made with three levels of interstitial contamination, and hardness and tensile properties were found to be strongly affected by oxygen pickup. Thick-section (6 mm) welds have been produced using both processes, and no embrittlement is experienced when high purity atmosphere is maintained. Metallographic examination shows a narrow. but coarse grained, heat affected zone for the GTA welds. Transition joint welding development between vanadium alloy and stainless steel has shown encouraging results.

6.3.6 CHEMICAL AND MECHANICAL INTERACTIONS OF INTERSTITIALS IN V-5%Cr-5%Ti – J. H. DeVan, J. R. DiStefano, and J. W. Hendricks (Oak Ridge National Laboratory). 240

Gas-metal reaction studies of V-5Cr-5Ti were conducted to determine the kinetics of reactions with H_2 and O_2, respectively. at 400-500°C. Reaction rates were determined through weight change measurements and chemical analyses, and effects on mechanical properties were evaluated by room temperature tensile tests. Exposure to hydrogen at pressures between 10'' to 10^{-2} torr lowered the tensile ductility in the case of coarse-grained specimens but had little effect on her-grained specimens. Similarly oxygen uptake at 500°C, at concentrations as low as *200* ppm (by weight), significantly lowered the ductility of the coarser-grained but not the finer-grained material.

6.3.7 THE RELATIONSHIP BETWEEN RECRYSTALLIZATION TEMPERATURE, GRAIN SIZE, AND THE CHARPY IMPACT PROPERTIES OF V-Cr-Ti ALLOYS – M. L. Grossbeck, D. J. Alexander, and A. F. Rowcliffe. 244

It is shown that the blunt notch Charpy impact properties of a V-5Cr-5Ti alloy are extremely sensitive to the grain size distribution developed during the final annealing treatment. Completely ductile behavior down to Liquid nitrogen temperatures *can* be induced, for example, by a treatment at 950°C, rather than annealing at 1125°C. It is proposed that the resistance to irradiation-induced shift in DB'IT reported by Argonne National Laboratory (ANL) researchers for the V-4Cr-4Ti alloy is related primarily to the exceptionally fme-grained microstructure developed during the low temperature processing route adopted for this alloy.

6.3.8 ROOM TEMPERATURE ELASTIC PROPERTIES OF V-5Cr-5Ti – W. A. Simpson (Oak Ridge National Laboratory). 258

Elastic moduli were measured for a specimen of the alloy V-5Cr-5Ti in the annealed condition using pulse-echo techniques. The value of Young's modulus was determined to be 125.6 GPa, the shear modulus was determined to be 45.9 GPa, and the Piosson's ratio to be 0.367.

6.3.9 THERMOPHYSICAL PROPERTIES OF V-5Cr-5Ti – W. D. Porter, R. B. Dinwiddie. and M. L. Grossbeck (Oak Ridge National Laboratory). 260

Measurements of thermal expansion of V-5Cr-5Ti have been made from room temperature to 600°C, and specific heat and thermal conductivity have teen measured over the range of 100 to 600°C. In each case, the results have been fitted to a polynomial expression to provide a convenient form for design studies.

The atom probe field ion microscope was used to examine two V-Cr-Ti alloys (V- 5Cr-5Ti and V-4Cr-4Ti) which have been shown to have very different fracture properties. The alloys were examined for clustering to detect the presence of small precipitates as well as to determine the distribution of solute elements in the matrix. The elements Ti, Cr, and Si were examined and no clustering of any of these three. elements was found.

A V-5Cr-5Ti specimen was fractured in-situ below its DBTT and the fracture surfaces analyzed by Auger Electron Spectroscopy (AES). About 70% of the fresh fracture surfaces were intergranular while the remainder were characteristic of cleavage fracture. Sub-micron-sized particles appeared to cover most of the grain boundary surfaces along with a few larger particles. Only one of these larger particles, probably a Ti-V sulfiddphosphide combination, contained Cl, at a level of only a few at.%. On the other hand, S, which is known to cause embrittlement in many alloy systems, was detected on virtually all of the grain boundary surfaces.

The critical mixed-mode I/III fracture toughness, J-integrals (J_{MC}), at mom temperature (RT) and 100°C were examined for a V-5Cr-5Ti alloy. Fracture toughness at 100°C was evaluated with a I-integral test and at RT with a K (the stress intensity factor) test. The determination of J_{MC} was made using modified compact-tension specimens. Different ratios of tension/shear stress were achieved by varying the principal axis of the crack plane between 0 and 45 degrees from the load line. Crack angles used in this study were 0, 15, and 45 degrees. A specimen with 0 degree crack angle is the same as a standard mode I compact tension specimen. In this limit, J_{MC} becomes J_{IC}. Specimens were annealed at 1125°C for 1 hour in a vacuum of 10^{-7} torr. J_{MC} and mixed-mode tearing moduli (T_M) were determined at 100°C with the single specimen technique. Crack lengths were calculated with partial unloading compliances. The J_{MC} values at RT were calculated from critical stress intensity factors (K_c). The results showed that at RT the V-5CR-5Ti alloy was brittle and experienced unstable crack growth with a mixture of intergranular, cleavage, and some microvoid coalescence (MVC) fracture while at 100°C it exhibited high fracture toughness and fractured with a mixture of MVC and intergranular failure. SEM investigation showed that some cleavage facets initiated at grain boundaries. The results suggest a low intergranular fracture strength and tendency towards cleavage fracture at room temperature. Preliminary data from Auger electron microscopy showed significant sulfur segregation on grain boundaries. The possible mechanism which might reduce intergranular fracture strength is discussed.

Addition of 1 at% nickel to vanadium and V-10Ti, followed by irradiation along with the nickel-free metals in HFIR to 2.3 x 10^{22} n cm^{-2}, E>1.0 MeV (corresponding to 17.7 dpa) at

400°C, has **been** used to study the influence of helium on microstructural evolution and embrittlement. Approximately 15.3% of the vanadium transmuted to chromium in these alloys The –50 appm helium generated from the ^{58}Ni(N,γ)^{59}Ni(n,α)^{56}Fe sequence was found to exert much less influence than either the nickel directly or the chromium formed by transmutation.

The V-IO-Ti and V-10Ti-1Ni alloys developed an extreme fragility and broke **into** smaller pieces in response to minor physical **insults** during density measurements. A similar behavior was not observed in pure V **or** V-1Ni. Helium's role in determination of mechanical properties and embrittlement of vanadium alloys in HFIR is overshadowed by the influence of alloying elements **such as** titanium and chromium. Both elements have **been** shown to **increase the** DB'IT rather rapidly in the region of 10% (CR + TI). Since Cr **is produced** by transmutatation of V, **this is** a possible mechanism for the embrittlement Large effects on the DBTT may have also **resulted** from uncontrolled accumulation of interstitial elements **such as** C. N, and O **during irradiation.**

The swelling of vanadium and its alloys is known to **be** sensitive t the level of chromium in the alloy. Chromium is also the major transmutation product during neutron irradiation. however, and the production rate of chromium is very sensitive to neutron spectra. **It** appears that an apparent dependence of void swelling in pure vanadium inadiated in FFTF may **arise** in part from the spectral difference that accompanies changes in displacement **rate.**

The density of vanadium alloys is strongly dependent on solute identity and concentration, especially for additions of chromium and titanium. One consequence of this dependence is that radiation-induced density changes **arise. from** segregation and precipitation. Transmutation of vanadium to chromium ***can*** also lead to significant increases in density and ***can*** therefore complicate somewhat the interpretation of swelling **data** derived **using** immersion density **techniques.**

The mechanical and physical properties of copper alloys are reviewed and compared with the requirements for high heat flux structural applications in fusion reactors. High heat flux structural materials must possess a combination of ***high*** thermal conductivity and high mechanical strength. The three most promising copper alloys **at** the present time are oxide dispersion-strengthened copper (Cu-Al$_2$O$_3$) and two precipitation-hardened copper alloys (Cu-Cr-Zr and **Cu-Ni-Be).** These three alloys **are** capable of room temperature yield strengths **>** 400 MPa and thermal conductivities up to 350 W/m-K. All of ***these*** alloys require extensive cold working to achieve their optimum strength. Precipitation-hardened copper alloys such **as** Cu-Cr-Zr **are** susceptible to softening due to precipitate overaging and **recrystallization** during **brazing,** whereas the dislocation structure in **Cu-Al$_2$O$_3$ remains** stabilized during typical high *temperature* **brazing** cycles. All three alloys exhibit good resistance to irradiation-induced softening and void swelling at temperatures below 300°C. The precipitation-strengthened alloys typically soften during neutron irradiation at temperatures above about 300°C and therefore should only be considered for applications operating at temperatures <300°C. Dispersion-strengthened copper may be used up to temperatures in excess of 500°C. Based on the available data, dispersion-strengthened copper ($Cu-Al_2O_3$) is considered to be the best candidate for high heat flux structural applications.

6.4.2 ROOM TEMPERATURE FATIGUE BEHAVIOR OF OFHC COPPER AND CuAl25 SPECIMENS OF TWO SIZES – A. Singhal and J. F. Stubbms (University of Illinois), B. N. Singh (Risø National Laboratory), and F. A. Gamer (Pacific Northwest Laboratory). . 342

Copper and its alloys are appealing for application in fusion reactor systems for high heat flux components where high thermal conductivities are critical, for instance, in divertor components. The thermal and mechanical loading of such components will be, at least in part, cyclic in nature, thus requiring an understanding of their fatigue behavior. This report describes the room temperature fatigue behavior of unirradiated OFHC (oxygen free high conductivity) copper and CuAl25 (copper strengthened with a 0.25% atom fraction dispersion of alumina). The response of two fatigue specimen sizes to strain controlled fatigue loading is examined, and differences in behavior are discussed. Specimens with the smaller size are not being irradiated in several reactors.

6.4.3 PREPARATION OF RUSSIAN COPPER ALLOY CREEP SPECIMENS – C. R. Eiholzer (Westinghouse Hanford Company), M. L. Hamilton (pacific Northwest Laboratory), and V. Barabash (D. V. Efremov Institute). 351

Eleven creep specimens of the Russian copper alloy MAGT-02 were pressurized and welded closed. The specimens were pressurized to levels ranging from 7.2 to 15.6 MPa (1052 to 2267 psia). These pressures will produce hoop stresses between 55 and 185 MPA (7.977 to 26,830 psia) when irradiated at 120°C.

6.4.4 VOID SWELLING OF PURE COPPER, CU-5NI AND CU-5MN ALLOYS IRRADIATED WITH FAST NEUTRONS – H. Watanabe (Kyushu University) and F. A. Gamer (Pacific Northwest Laboratory). 356

The effects of cold-work level and solute. addition (nickel or manganese) on pure copper under fast neutron irradiation have been investigated. Neutron irradiation was conducted in the Fast Flux Test Facility (FFTF) at temperatures from 638 to 873K to doses ranging from 8 to 98 dpa In pure copper, the void swelling behavior was investigated as a function of cold work level. At 638 and 703K, 10% cold-work reduced swelling somewhat with little influence at higher cold-work levels. In comparison with pure copper, void swelling was suppressed by 5% nickel addition at 648K but slightly increased at 696K. Cu-5Mn resisted swelling in both annealed and 40% cold-worked specimens in all temperatures examined. At 684K, void formation was not detected. Only stacking fault tetrahedra were observed in this specimen.

6.4.5 INFLUENCE OF NICKEL AND BERYLLIUM CONTENT ON SWELLING OF COPPER IRRADIATED IN COBRA-1A – F. A. Gamer (Pacific Northwest Laboratory) and B. N. Singh (Risø National Laboratory). 364

A series of annealed Cu-Ni dilute binary alloys were irradiated in COBRA-1A in EBR-II at temperatures of 373,420. and 500°C. Density measurements have been performed for specimens inadiated at 373°C to $1.78 \times 10^{22} n\ cm^{-2}$ (–11.3 dpa for pure copper). At this temperature and dose level nickel additions suppress swelling. There is a possible indication that some type of segregation-related phenomenon also occurs. yielding radiation-induced densification.

6.5 ENVIRONMENTAL EFFECTS IN STRUCTURAL MATERIALS.......... 369

6.5.1 FABRICATION OF ALUMINUM NITRIDE AND ITS STABILITY IN LIQUID ALKALI METALS – K. Natesan and D. L. Rink (Argonne National Laboratory)......... 371

AlN has been selected as a prime candidate for electrically insulating the V-alloy fist wall in the self-cooled ITER concept Several methods are being evaluated for fabricating coatings that have adequate thickness and desirable physical, electrical, chemical, and mechanical properties. Coatings developed thus far are being exposed to liquid Li at 350 and 400°C.

6.5.2 DEVELOPMENT OF ELECTRICAL INSULATOR COATINGS: IN-SITU ELECTRICAL RESISTANCE MEASUREMENTS ON CaO-COATED V-5%Cr-5%Ti IN LIQUID LITHIUM – J.-H. Park, G. Dragel, and R. W. Clark (Argonne National Laboratory)...... 376

The electrical resistance of CaO coatings produced on V-5%Cr-5%Ti by exposure of the alloy to liquid Li that contained 4 at% dissolved Ca was measured as a function of time at temperatures of 250 to 698°C. The solute element, Ca in liquid Li. reacted with the alloy substrate at 420°C to produce a CaO coating. The resistance of the coating layer was 4.4 and 35.7 Ω at 267 and 698°C, respectively. Thermal cycling between 267 and 698°C changed the resistance of the coating layer, which followed insulator behavior. These results and those reported previously suggest that thin homogeneous coatings can be produced on variously shaped surfaces by controlling the exposure time, temperature. and composition of the liquid metal. This coating method is applicable to reactor components of various shapes (e.g., inside/outside of tubes, complex geometrical shapes) because the coating is formed by liquid-phase reaction. The liquid metal can be used over and over because only the solutes are consumed within the liquid metal.

7.0 SOLID BREEDING MATERIALS AND BERYLLIUM.................. 383

7.1 PERFORMANCE OF CERAMIC BREEDER MATERIALS IN THE SIBELIUS EXPERIMENT – J. P. Kopasz and C. E. Johnson (Argonne National Laboratory) and D. L. Baldwin (Pacific Northwest Laboratories)............................... 385

Lithium containing ceramics are among the leading candidates for use as tritium breeding materials in a fusion reactor. An issue affecting both the safety and economics of the reactor is the tritium inventory. The SIBELIUS experiment was designed to examine material compatibility between different components of a breeder blanket and to examine the tritium inventory in the components of the blanket The tritium inventory in each of the ceramics was determined by measurements at end of life and were found to be quite low and in agreement with those determined in tests with no beryllium present The inventory increased in the order lithium zirconate < lithium oxide < lithium orthosilicate < lithium aluminate with the inventory in the zirconate less than 0.03 wppm at 550°C.

7.2 AB INITIO CALCULATIONS FOR HYDROGEN ADSORPTION ON LITHIUM OXIDE SURFACES – A. Sutjianto, S. W. Tam. L. Curtiss, and C. E. Johnson (Argonne National Laboratory) and R. Pandey (Michigan Technological University)............. 392

The study of hydrogen chemisorption on the (110) and (111) lithium oxide surfaces have been investigated by means of ab initio Hartree-Fock calculations. In general, for the n-layer slab (where n = 2 and 3) of the neutral (110) and for the three-layer slab of the neutral (111) surfaces, there is no hydrogen chemisorption. The oxygen *2p* band of the (110) surface is stabilized by the presence of more stacking sequences of layers which prevents charge transfer to the hydrogen. In the case of a neutral (110) layer due to low coordination of the anion, there is hydrogen chemisorption in the form of OH- and $Li^+H^-Li^+$ with the chemisorption energy of

0.93 eV. For the neutral (111) surface, there is no hydrogen chemisorption since the oxygen layer is screened by the cation layers hindering the charge transfer to the hydrogen.

7.3 IRRADIATION OF LITHIUM ZIRCONATE PEBBLE-BED IN BEATRIX-II. PHASE II – R. A. Verrall and J. D. Sullivan (AECL Research, Chalk River Laboratories), O. D. Slagle and G. W. Hollenberg pacific Northwest Laboratory), and T. Kurasawa (Japan Atomic Energy Research Institute). 406

BEATRIX-II was an in situ tritium recovery experiment that was designed to characterize the behavior of lithium ceramics irradiated to a high burnup, and to assess their suitability for use in a fusion reactor blanket This paper describes the results from a vented canister containing lithium enriched lithium zirconate spheres (85% ^{6}Li) that were irradiated to a burnup of 5.2% (total lithium) in a steep temperature profile–400°C edge, 1100°C center. The reference sweep gas was He-0.1%H_2, with systematic tests using alternate compositions: He-0.01%H_2 and pure He (maximum duration 8 days). Tritium recovery decreased slightly at lower H_2 concentrations. For example, the buildup of inventory during a 4-day test in pure He was 0.8 Ci which was approximately 6.5% of the tritium generated in the lithium zirconate during that period. The steadiness of the bed central temperature and the high tritium release rate. together with low moisture release rate, indicate good performance of the zirconate bed.

8.0 CERAMICS 417

8.1 FATIGUE CRACK GROWTH RATE (FCGR) BEHAVIOR OF NICALON/SiC COMPOSITES – N. Miriyala, P. K. Liaw. and C. J. McHargue (University of Tennessee), L. L. Snead *(Oak* Ridge National Laboratory), and D. K. Hsu and V. K. Saini (Iowa State University) 419

Ultrasonic measurements were carried out on the Nicalon/SiC composite specimens to correlate elastic moduli with percentage porosity in the in-plane as well as though-thickness directions. Compact type C(T) specimens were cyclically loaded to study the fatigue crack growth behavior. However, it was difficult to initiate the crack in the specimens.

8.2 TENSILE BEHAVIOR OF IRRADIATED SIC FIBERS – M. C. Osborne, Rensselaer Polytechnic Institute, L. L. Snead, Oak Ridge National Laboratory, and D. Steiner, Rensselaer Polytechnic Institute. 428

Tensile results are presented for low oxygen Nicalon fibers neutron irradiated at damage levels of 0.013 displacements per atom (dpa), 0.13 dpa and 0.32 dpa Single fibers were tensile tested and analyzed, using Weibull statistics, for mean strength and distribution. Tensile modulus was also determined. Using a diffractometer, the fiber grain size and percent crystallinity were determined. The mean strength and modulus decreased by 20% but then increased with the highest damage level tested. Both grain size and crystallinity decreased as dose increased. These initial results of low level neutron irradiation of low oxygen Nicalon fibers exhibit no substantial degradation of the properties investigated. Therefore. continued research at higher doses is recommended.

8.3 TEMPERATURE DEPENDENCE OF THE SUBCRITICAL CRACK GROWTH RATE OF A SiClSiC COMPOSITE – R. H. Jones and C. H. Henager, Jr. (Pacific Northwest Laboratory). 438

The long term stability of SiClSiC composites is an issue regarding their use for fusion structural applications only because there is insufficient data to determine if there is really a problem. Crack growth measurements have been made over the temperature range of 800 to 1100°C, in high-purity Ar, to help assess the long term stability of these materials. Stage II crack growth rates ranging from 2 x 10^{-9} m/s at 1100°C down to 3 x 10^{-11} m/s at 800°C were found for a **2-D** SiClSiC composite reinforced with 40% Nicalon fibers. The stage II velocities obeyed an Arrhenius relationship over this temperature range with an activation energy of **235** kJ/mol. At a fusion relevant temperature of **800°C,** the crack velocity will result in a crack growth of 1mm/yr. More creep resistant fibers are expected to reduce this crack growth amount to less than 1 x 10^{-2} mm/yr **at** 800°C. This is not an excessive amount of **crack** extension for a material with a fracture toughness of about **20** MPa $m^{1/2}$.

8.4 DEFECT ENERGETICS CALCULATIONS OF SiC USING THREE REPRESENTATIVE EMPIRICAL POTENTIALS – H. Huang, J. Wong. and N. Ghoniem (University of California), and **M.** Baskes (Sandia National Laboratory). **445**

Defect energetics is a critical issue not only for irradiation damage but also for semiconductor applications. Calculations of defect energetics rely mainly on using empirical potentials, which are developed based on information from equilibrium crystal configurations and which may not be suitable for investigating defected configurations. Therefore, not all potentials give accurate enough results. This paper first **calibrates MEAM** for silicon carbide. Calculations **are** then made for defect energetics of silicon carbide using the MEAM and *two* other representative empirical potentials. Results obtained with these potentials **are** compared with available fust principle calculations and experimental data. The results not only provide more information for defect formation and migration in silicon carbide, but also provide a critical assessment of the three empirical potentials. The results ***are*** analyzed in terms of construction and calibration of the empirical potentials

8.5 PHENOMENOLOGICAL INELASTIC CONSTITUTIVE EQUATIONS FOR SiC AND SiC **FIBERS** UNDER IRRADIATION – **A.** El-Azab and N. M. Gboniem (University of California-Los Angeles). 459

Experimental data on irradiation-induced dimensional changes and creep in β-SiC and SiC fibers is analyzed, with the objective of studying the constitutive behavior of these materials under high-temperature irradiation. The data analysis includes empirical representation of irradiation-induced dimensional changes in SiC matrix and **SiC** fibers as function of time and irradiation temperature. The analysis also includes formulation of simple scaling **laws** to extrapolate the existing **dala** to fusion conditions on the basis of the physical mechanisms of radiation effects on crystalline solids. Inelastic constitutive equations ***are*** then developed for SCS-6 SiC fibers, Nicalon fibers. and CVD SiC. The effects of applied stress, temperature, and irradiation fields on the deformation behavior of this class of materials **are** simultaneously represented. Numerical results are presented for the relevant **creep** functions under the conditions of the fusion reactor (ARIES IV) fust wall. The developed equations can be used in estimating the macro mechanical properties of Sic-Sic composite systems as well as in performing timedependent micro mechanical analysis that is relevant to slow ***crack*** growth and fiber pull-out under fusion conditions.

8.6 TRITIUM TRANSPORT AND **RETENTION** IN SILICON CARBIDE – S. W. Tam, J. Kopasz, and C. E. Johnson (Argonne National Laboratory). 485

A theoretical framework describing trapping, diffusion, and desorption of tritium from vapor-deposited β-silicon carbide **has** been proposed and an analytical version of **this** model was derived. This analytical model was used to extract trapping, diffusion, and desorption parameters from a limited **part** of the experimental data set The resulting parameter-free model was then used to test its predictive capability by calculating the time-dependent release behavior for the high temperature regimes. General agreement with the release data **was** found supporting the suitability of the present approach. Tritium trapping was found to be strong. Both bulk diffusion and surface desorption make comparable contributions to tritium release from the silicon carbide. Improvements beyond the present analytical model **lo** include dynamical detrapping *can* be achieved with the proposed framework

8.7 RADIATION-INDUCED CHANGES IN ELECTRIC, DIELECTRIC, AND OPTICAL PROPERTIES OF CERAMICS - S. J. Zinkle *(Oak* Ridge National Laboratory). 4Y3

The data base on radiation-induced changes in the electric and dielectric properties of ceramic insulators is reviewed Ionizing radiation causes a prompt increase in the electrical conductivity that is generally proportional to the ionizing dose rate. The precise magnitude of the radiation induced conductivity is sensitive to the detailed manufacturing process and impurity content. The conflicting evidence regarding the possibility of permanent radiation induced electrical degradation (RIED) is summarized. Further work is needed to define the physical mechanism and practical operating Limits of the RIED phenomenon. Displacement damage associated with neutron irradiation produces significant increases in the room temperature dielectric loss tangent of oxide ceramics for fast neutron fluences above 1×10^{22} n/m^2 (~0.001 dpa). A brief summary of the effects of irradiation on the optical properties of ceramics and silica optical fibers is also presented.

8.8 NEUTRON DAMAGE TO DIAGNOSTIC MIRRORS - E. H. Farnum and F. W. Clinard. Jr. (Los Alamos National Laboratory). S. P. Regan (Johns Hopkins University, Baltimore, MI)), and B. Schunke (JET Joint Undertaking, Abingdon, Ox. UK). 505

Diagnostic systems for fusion reactors will require mirrors capable of reflecting electromagnetic radiation in the soft x-ray, near uv, visible, and ir wavelengths. These components will be exposed to significant fluences of fast neutrons during use. Mirrors made from alternating layers of low-Z and high-Z materials were irradiated to a fluence of 1.1 x 10^{23} n/m^2 at 270-300°C, and subsequently evaluated for structural changes and in some cases changes in optical properties. Short-wavelength mirrors retained their structural integrity while exhibiting slight changes in reflectance; some long-wavelength mirrors showed structural degradation, while other did not. These results are discussed in terms of materials damage effects and possibilities for improvement of mirror performance under severe operating conditions.

8.9 ELECTRICAL PROPERTIES OF Al_2O_3 DURING IRRADIATION WITH SPALLATION NEUTRONS - E. H. Farnum and F. W. Clinard, Jr. (Los Alamo National Laboratory). 512

DC and AC conductivity of Al2O3 ceramics were measured at elevated temperatures during irradiation with neutrons and gamma rays at the Los Alamos Spallation Radiation Effects Facility. DC conductivity was increased at start of irradiation. bur was subsequently reduced as displacement damage was accumulated. AC conductivity appeared to increase at high levels of damage. The observed dc behavior is attributed to excitation of electrons into the conduction band by ionizing radiation, followed by charge napping and recombination at damage sites. The ac behavior, which resembles RIED, is attributed to conductivity in the residual gas surrounding the samples. Surface conductivity. while not the source of the apparent RIED, nevertheless is of sufficient magnitude to be of concern for fusion applications.

8.10 A COMPARISON OF THE EFFECT OF RADIATION ON THE THERMAL CONDUCTIVITY OF SAPPHIRE AT LOW AND HIGH TEMPERATURE - D. P. White (Oak Ridge National Laboratory). 517

It has been proposed that sapphire be used in insulating feedthroughs and windows in radiofrequency and microwave heating systems in fusion reactors. The degradation of the thermal conductivity of sapphire with irradiation is a concern in the design of these windows. It has been proposed to cool microwave windows to liquid nitrogen temperatures to lake advantage of the thermal conductivity *peak,* which occurs at approximately 30 K in unirradiated sapphire, and the lower dielectric loss tangent at these temperatures. In this paper the methods used to calculate the thermal conductivity and the changes which occur with changes in point defect concentration will be. reviewed and the results of the low temperature calculations will be. compared to the high temperature calculations.

It is found that vacancy scattering can significantly reduce the thermal conductivity over a wide temperature range; for example, a vacancy concentration of 0.01 per atom leads to a fractional change of about 90% at 77K versus 43% at 400 K. This reduction has significance for the design and placement of radio frequency and microwave windows in fusion reactors.

8.11 **NEUTRON-INDUCED** CHANGES IN OPTICAL PROPERTIES OF $MgAl_2O_4$ SPINEL - **A.** Ibarra (CIEMAT, Madrid, Spain) and F. **A.** Gamer (Pacific Northwest Laboratory) 523

High purity $MGAL_2O_4$ spinel specimens irradiated in FFTF-MOTA to very high exposure have been examined by three techniques to determine changes in their optical properties. Significant changes were observed in optical absorption, photoluminescence, and radioluminescence.

1.0 IRRADIATION FACILITIES, TEST MATRICES, AND EXPERIMENTAL METHODS

STATUS OF U.S./JAPAN COLLABORATIVE PROGRAM PHASE II HFIR TARGET AND RB* CAPSULES

– J. E. Pawel, R. L. Senn, A. W. Longest (Oak Ridge National Laboratory), and K. Shiba (Japan Atomic Energy Research Institute)

OBJECTIVE

The objective of the HFIR irradiations is to determine the response of the various U.S. and Japanese austenitic and ferritic steels with different pretreatments and alloy compositions to the combined effects of displacement damage and helium generation. Specimen temperatures during irradiation range from 60 to 600°C and fluences range up to 60 dpa. The RB* experiments are a continuation of the ORR spectrally tailored experiments in which the spectrum is modified with a hafnium shield to simulate the expected fusion helium to damage (He/dpa) ratio. In the HFIR target capsules, many specimens have been isotopically tailored in order to achieve fusion helium generation rates.

SUMMARY

Capsules HFIR-MFE-JP9 through 16 were installed in the High Flux Isotope. Reactor (HFIR) target July 20, 1990 for irradiation beginning with HFIR fuel cycle 289. Of these eight target capsules, JP10, 11, 13, 16 accumulated 18 dpa and were removed from the reactor in September 1991. JP14 was removed from the reactor at the end of cycle 310 (September 1992) after achieving a peak dose of 34 dpa. Capsules JP9, 12, and 15 completed 35 cycles on April 1,1994 and were removed from the target region. Each capsule had accumulated a peak dose of approximately 57 dpa.

Three new capsules, HFIR-MFE-JP20, 21, and 22, have been designed to complete the original experiment matrix of the JP9 through JP16 series capsules. Irradiation began in December 1993 with the start of cycle 322. As of April 1, 1994 (end of cycle 324), each capsule had achieved approximately 4.9 dpa.

The RB* experiments are the continuation of the ORR spectrally tailored experiments. In this stage, a hafnium liner is used to modify the spectrum to simulate fusion helium to displacements per atom (He/dpa) ratio in the austenitic steel specimens. Of the four capsules in this set, two (60J-1 and 330J-1) were disassembled during this reporting period after accumulating a peak dose in HFIR of 11 dpa. Two capsules (200J-1 and 400J-1) are in the reactor and have achieved a dose of 5.5 dpa.

PROGRESS AND STATUS

Target Capsules JP9 through JP16

Capsules HFIR-MFE-JP9 through 16 were installed in the High Flux Isotope Reactor (HFIR) target July 20, 1990 for irradiation beginning with HFIR fuel cycle 289. A complete description and details of the design, construction, and installation of capsules JP9 through JP16 have been previously reported [1,2,3]. The as-built specimen matrix can be found in a previous report [3]. These capsules contain primarily transmission electron microscopy disks (TEM) and SS-3 flat tensile specimens. A wide variety of alloys and thermomechanical conditions are included. Many of the TEM disks were made from isotopically tailored alloys to produce a range of He/dpa ratios (<0.1, 10, 20, 70 appm/dpa). Details of the irradiation history of these capsules are shown in Table 1. Capsules JPIO, 11, 13, and 16 were removed at the end of Cycle 300 (September 1991) after achieving a total of 18 dpa. Capsule JP14 was removed at the end of Cycle 310 (September 1992), after accumulating 34 dpa. Capsules JP9, 12, and 15 completed 35 cycles on April 1, 1994 and were removed from the reactor target region to the cooling pool. These capsules had accumulated 57 dpa and are scheduled to be disassembled during the next reporting period.

Many of the specimens from the JP10, 11, 13, 16 and 14 capsules have been tested in the Irradiated Materials Examination and Testing Facility hot cells. The initial set of tensile tests of JPCA and 316F stainless steels in solution annealed, cold worked, and welded conditions have been completed. Analyses include reduction-of-area measurements and fracture stress calculations. Details of the testing of JPCA are presented elsewhere [4]. Density measurements have been taken on specimens removed from nine (JP10 Position 6, JP11 Position 6, JP13 Position 6, and JP16 Position 6, JP10 Position 4, JP10 Position 8, JP14 Position 6, JP14 Position 4, JP14 Position 8) of the TEM tubes using the ORNL precision densitometer. These specimens include isotopically tailored alloys from both the ORNL and JAERI programs as well as other candidate fusion alloys.

Target Capsules JP20 through 22

Three new capsules, HFIR-MFE-JP20, 21, and 22. have been designed to complete the original experiment matrix of the JP9 through JP16 series capsules [5]. It is planned to irradiate the capsules in inner target positions for 5, 11, and 22 cycles, respectively, to achieve peak doses of approximately 8, 18, and 35 dpa Specimen temperatures in each capsule will be 300.400, 500, or 600°C. Irradiation began in December 1993 with the start of cycle 322. As of April 1, 1994 (end of cycle 324). each capsule bad achieved approximately 4.9 dpa. The complete test matrix is described in Reference 6.

RB* Capsules HFIR-MFE-60J-1, 200J-1, 330J-1 and 400J-1

The RB* capsules are irradiated in the removable beryllium positions of the HFIR. These experiments are a continuation of the ORR spectrally tailored experiments ORR-MFE-6J and 7J. At this stage in the experiment, a hafnium liner surrounds the capsules in order to harden the spectrum and achieve the expected fusion helium generation rate in the austenitic steel specimens. Capsule design, assembly and details of specimen loading have been previously described [7-10]. Capsules 60J-1 and 330J-1 were removed from the reactor in November 1992 after accumulating approximately 11 dpa in the HFIR. Details concerning the performance of these capsules can be found in Reference 11. Most of the specimens bad also been irradiated to approximately 7 dpa in the ORR (for a total of 18 dpa in these specimens). These capsules were disassembled in February 1994. Capsules 2001-1 and 400J-1 have completed 12 of the scheduled 20 irradiation cycles, as shown in Table 2. The capsules are performing as designed, with the temperatures holding within the expected ranges. Details of the capsule performances are described elsewhere [12].

REFERENCES

1. R. L. Senn, "Status of U.S./Japan Collaborative Program Phase II HFIR Target Capsules," Fusion Reactor Materials Semiannual Progress Report for the Period Ending September 30, 1987, DOE/ER-031313, U.S. DOE Office of Fusion Energy, 1988, p. 8.

2. R. L. Senn, "Status of U.S./Japan Collaborative Program Phase II HFIR Target Capsules," Fusion Reactor Materials Semiannual Progress Report for the Period Ending March 31, 1988, WEER-0313/4, U.S. DOE Office of Fusion Energy, 1988. p. 7.

3. R. L. Senn, "Status of U.S./Japan Collaborative Program Phase II HFIR Target Capsules," Fusion Reactor Materials Semiannual Progress Report for the Period Ending September 30, 1988, DOE/ER-0313/5, U.S. DOE Office of Fusion Energy, 1989, p. 6.

4. K. Sbiba, S. Jitsukawa, J. E. Pawel, and A. F. Rowcliffe. "Tensile Properties of Base and Weld Metal Specimens of Austenitic Stainless Steels Irradiated in the High Flux Isotope Reactor," Fusion Reactor Materials Semiannual Progress Report for the Period Ending September 30, 1993. DOE/ER-0313/15, U.S. DOE Office of Fusion Energy, p. 181.

5. J. E. Pawel and R. L. Senn. "Status of U.S./Japan Collaborative Program Phase II HFIR Target Capsules," Fusion Reactor Materials Semiannual Progress Report for Period Ending March 31, 1992, DOE/ER-0313/12, U.S. DOE Office of Fusion Energy, 1992, p. 15.

6. J. E. Pawel A. W. Longest, R. L. Senn, K. Shiba, D. W. Heatherly. and R. G. Sitterson, "Status of U.S./Japan Collaborative Program Phase II HFIR Target and RB* Capsules." Fusion Reactor Materials Semiannual Progress Report for Period Ending September 30, 1993, DOE/ER-0313/15, U.S. DOE Office of Fusion Energy. 1994, p. 3.

7. A. W. Longest, J. E. Corum, D. W. Heatherly, and K. R. Thoms, "Design and Fabrication of HFIR-MFE RB* Spectrally Tailored Irradiation Capsules." Fusion Reactor Materials Semiannual Progress Report for Period Ending September 30, 1987. DOE/ER-0313/3, U.S. DOE Office of Fusion Energy, 1988, p. 2.

8. A. W. Longest, J. E. Corum. and D. W. Heatherly, "Design and Fabrication of HFIR-MFE RB* Spectrally Tailored Irradiation Capsules." Fusion Reactor Materials Semiannual Progress Report for Period Ending March 31.1988. DOE/ER-0313/4, U.S. DOE Office of Fusion Energy, 1988, p. 2.

9. A. W. Longest J. E. Corum, and D. W. Heathefly, "Design and Fabrication of HFIR-MFE RB* Spectrally Tailored Irradiation Capsules," Fusion Reactor Materials Semiannual Progress Report for Period Ending September 30, 1988, DOE/ER-0313/5, U.S. DOE Office of Fusion Energy, 1989, p. 2.

10. A. W. Longest, J. E. Pawel, D. W. Heatherly. R. G. Sitterson. and R. L. Wallace, "Fabrication and Operation of HFIR-MFE RB* Spectrally Tailored Irradiation Capsules," Fusion Reactor Materials Semiannual Progress Report for Period Ending March 30.1993, DOE/ER-0313/14, U.S. DOE Office of Fusion Energy, 1993, p. 14.

11. A. W. Longest, D. W. Heatherly. E. D. Clemmer, and J. E. Corum. "Fahrication and Operation of HFIR-MFE RB* Spectrally Tailored Irradiation Capsules." Fusion Reactor Materials Semiannual Progress Report for Period Ending September 30, 1991, DOE/ER-0313/11, U.S. DOE Office of Fusion Energy. 1992, p. 17.

12. A. W. Longest, J. E. Pawel, D. W. Heatherly, R. G. Sitterson, and R. L. Wallace, "Fabrication and Operation of HFIR-MFE RB* Spectrally Tailored Irradiation Capsules," Fusion Reactor Materials Semiannual Progress Report for Period Ending September 30, 1993. DOE/ER-0313/15, US. DOE Office of Fusion Energy, 1992, p. 23.

Table 1. Irradiation History of **U.S./Japan** Phase **II** HFIR **Target Capsules**

HFIR OPERATION				JP-10,-11,-13,-16		JP-14		JP-9,-12,-15	
	START DATE	END DATE	Wd/ Cycle	MWd	dpa*			MWd	dpa*
	)7-20-90	9-07-90	879	1879	1.64	1879	1 64	1879	1 6 4
	)9-19-90	0-11-90	852	3731	3.26	3731	326	3731	3.28
	10-17-90	1-13-90	1838	5569	4 88	5569	4 8 8	5569	4.86
	11-25-90	2-10-90	1847	7416	6 4 7	7416	6 4 7	7416	8 4 7
293	12-27-90	)1-23-91							
294	32-01-91	12-25-91	1906						8.14
295	03-01-91	)3-24-91	1908	11230	9.80	11230	9.80	11230	9.80
296	04-06-91	)4-28-91	1874	13104	11.44	13104	11.44	13104	11.44
297	05-19-91	)6-15-91	1845	14949	13.05	14949	13.05	14949	13.05
298	06-20-91	)7-1 1-91	1747	16696	14.58	16696	14.58	16696	14.58
299	07-25-91	18-15-91	1741	18437	16.10	18437	16.10	18437	16.10
300	08-28-91		1724	20161	17.60	20161	17.60	20161	17.60
301	09-27-91	10-19-91	1851	REMOVED EOC 300		22012	19.22	22012	19.22
302	10-27-91	11-21-91	1829			23841	20.81	23841	20.81
303	12-01-91	12-22-91	1821			25662	22.40	25662	22.40
304	12-31-91	11-24-92	1826			27488	24.00	27488	24.00
305	01-30-92		1876			29364	25.63	29364	25.63
306	03-31-92	)4-27-92	1845			31209	27.25	31209	27.25
307	05-01-92	)5-28-92	1842			33051	28.85	33051	28.85
308	06-02-92	)6-30-92	1938			34989	30.55	34989	30.55
309	07-03-91	)8-01-92	1949			36938	32.25	36938	32.25
310	08-27-92	)9-18-92	1849			38787	33.86	38787	33.86
311	09-25-92	10-12-92	1856			REMOVED EOC 310		40643	35.48
312	10-22-92	11-14-92	1842					42485	37.09
313	11-21-9;	12-15-92	1850					44335	38.70
314	12-20-92	01-12-93	1866					46201	40.33
315	01-19-93		1861					48062	41.96
316	02-18-93	04-03-93	1807					49869	43.54
317	04-23-93	05-14-9:	1841					51710	45.14
318	05-20-9:	06-13-93	1878					53588	46.78
319	06-18-93	07-10-9:	1863					55451	48.41
320	07-15-93	08-07-9	1934					57385	50.10
321	08-12-93	09-04-9	1884					59269	51.74
322	12-16-93	01-07-9	1854					61123	53.36
323	01-23-9	02-14-9	1874					62997	55.00
324	03-04-9	04-01-9	1907					64904	56.66
325	04-10-9							REMOVED EOC 324	
32E									
327									

* **DPA levels** based on achieving 0.000873 dpa/MWd.

Table. 2. Irradiation History JP-9, -12, -15, 200J-1, 400J-1

CYCLE NO.	START DATE	END DATE	MWd/ Cycle	35 CYCLE IRR. MWd	35 CYCLE IRR. dpa [1]	INCREMENTAL MWd	INCREMENTAL dpa [1]
289	)7-20-90	09-07-90	1879	1879	1.64		
290	)9-19-90	10-11-90	1852	3731	3.26		
291	10-17-90	11-13-90	1636	5569	4.86		
292	11-25-90	12-10-90	1847	7416	6.47		
293	12-27-90	01-23-91	1965	OUT OF REACTOR			
294	32-01-91	02-25-91	1906		8.14		
295	33-01-91	03-24-91	1908	11230	9.80		
296	34-06-91	04-28-91	1874	13104	11.44		
297	05-19-91	06-15-91	1845	14949	13.05		
296	06-20-91	07-11-91	1747	16696	14.58		
299	07-25-91	08-15-91	1741	18437	16.10		
300	08-26-91	09-17-91	1724	20161	17.60		
301	09-27-91	10-19-91	1651	22012	19.22		
302	10-27-91	11-21-91	1829	23841	20.81		
303	12-01-91	12-22-91	1821	25662	22.40		
304	12-31-91	01-24-92	1826	27468	24.00		
305	01-30-92	02-27-92	1876	29364	25.63		
306	03-31-92	04-27-92	1845	31209	27.25		
307	05-01-92	05-28-92	1842	33051	28.85		
308	06-02-92	06-30-92	1938	34989	30.55		
309	07-03-92	06-01-92	1949	36938	32.25		
310	06-27-92	09-18-92	1846	38786	33.86		
311	09-25-92	10-12-92	1856	40642	35.48		
312	10-22-92	11-14-92	1834	42476	37.08	BEGIN CYCLE 313	
313	11-21-92	12-15-92	1858	44334	38.70	1858	0.46
314	12-20-92	01-12-93	1867	46201	40.33	3725	0.91
315	01-19-93	02-11-93	1861	48062	41.96	5586	1.37
316	02-17-93	04-03-93	1807	49669	43.54	7393	1.81
317	04-23-93	05-14-93	1841	51710	45.14	9234	2.26
316	05-20-93	06-13-93	1878	53588	46.78	11112	2.72
319	06-18-93	07-10-93	1863	55451	48.41	12975	3.18
320	07-15-93	08-07-93	1934	57365	50.10	14909	3.65
321	08-12-93	09-04-93	1884	59269	51.74	16793	4.11
322	12-16-93	01-07-94	1854	61123	53.36	18647	4.57
323	01-23-94	02-14-94	1874	62997	55.00	20521	5.03
324	03-05-94	04-01-94	1907	64904	56.66	22428	5.49
325	04-10-94			REMOVED EOC 324			
326							
327							
328							

[1] DPA levels based on achievinp 0.000873 dpa/MWd in the JP capsules and .000245 dpa/MWd in the MFE-RB* 200J-1 and 400J-1 capsules.

[2] JP-10,-11,-13,-16 removed at EOC 300. JP-14 removed at EOC 310.

THE COBRA-IB IRRADIATION EXPERIMENT IN EBR-11* H. Tsai, A. G. Hins, R. V. Strain, and D. L. Smith (Argonne National Laboratory)

OBJECTIVE

The objective of the forthcoming COBRA-1B experiment in EBR-II is to evaluate the effects of fast neutron irradiation on the physical and mechanical properties of candidate fusion structural materials. Of special interest in this experiment will be ITER-relevant temperature and exposure for the test specimens. Approximately 50% of the irradiation test volume will he devoted to vanadium-alloy specimens.

SUMMARY

Design of the COBRA-IB irradiation experiment began in this reporting period and is in progress. The target reactor insertion date for COBRA-1B is Septemher 1994. Technical and programmatic feasibility approval for the experiment has been granted by EBR-II Operations.

PROGRESS AND STATUS

Introduction

Vanadium-based alloys have heen identified as candidate structural materials for the first wallhlanket of **ITER.** Before any materials can qualify for such application, a data base on their irradiation performance **is** required. The purpose of the COBRA-1B experiment is to irradiate specimens of candidate alloys at ITER-relevant temperature and exposure (i.e., damage) in order to generate such data. Target temperature and exposure for the vanadium-alloy specimens in the COBRA-IB experiment are ≈370-425°C and ≈7-20 dpa, respectively. It is estimated that about 50% of the test volume in the COBRA-1B vehicle will he occupied by the vanadium-alloy specimens; the remaining volume will he used to test other candidate fusion materials. e.g., low-activation ferritic steels, copper alloys, and ceramics.

Experiment Description

The COBRA-1B experiment is a steady-state irradiation of specimens of candidate structural materials for fusion reactors. All specimens are previously nonirradiated. Except for the trace amount of ^{6}Li in the subcapsule lithium bond, there are no tritium-producing fusion-breeder materials in the experiment.

The suhassemhly will utilize a standard Mk-B7A vehicle. To maximize the rate of irradiation damage, the experiment will be irradiated in a high-flux, inner-row (row-2) position. Subassembly sodium flow rate will he ≈15 gal/min, which will allow specimen temperature of ≈370 to 425°C to be attained. (The lowest temperature currently attainable in EBR-II, 370°C. is within the ITER design range; 425°C is of importance because a large hody of data is available on vanadium alloys from previous irradiations at this temperature.)

The subassembly will contain seven capsules, all of them "weepers" (i.e., with perforated walls to allow reactor sodium to enter and exit the capsules) to minimize the specimen temperatures. Each capsule will contain ≈6-10 stacked subcapsules that hold the test specimens. Spacer tubes above the top subcapsule and below the bottom subcapsule will maintain the proper axial positions of the subcapsules. Standard top and bottom end plugs will he used for the capsules.

---

*Work supported by the Officc of Fusion Energy, U.S. Department of Energy, under Contract W-31-109-Eng-38.

All of the vanadium-alloy test specimens will be contained in sealed, lithium-handed subcapsules made of stainless steel. Depleted lithium (i.e., ^{7}Li) will be used to minimize tritium generation during irradiation. Other test specimens in the COBRA-1B experiment will be contained in sealed He-bonded subcapsules or weeper subcapsules, also made of stainless steel.

After ≈60-90 EFPDs of exposure (≈7-10 dpa in the vanadium specimens), the subassembly will be discharged from EBR-II and transferred to HFEF for disassembly. Four capsules will be removed and shipped to ANL-E and PNL for postirradiation processing. The remaining three capsules will be assembled at HFEF into a new Mk-B7A vehicle, together with four new capsules, for additional irradiation in EBR-II. Duration of the additional irradiation will be ≈60-90 EFPDs.

To assist postirradiation damage calculations, dosimetry materials contained in sealed tubes will be included in the test vehicle to provide data on the spatial distribution of neutrons.

FUTURE ACTIVITIES

The target reactor insertion date is September 1994. In the next reporting period, efforts will be devoted to complete the test matrix, fabricate the test specimens, complete the test vehicle assembly, and prepare all necessary documentation to support the reactor irradiation.

2.0 DOSIMETRY, DAMAGE PARAMETERS, AND ACTIVATION CALCULATIONS

REVISED NEUTRON DOSIMETRY RESULTS FOR THE MOTA-2A EXPERIMENT IN FFTF

L. R. Greenwood (Pacific Northwest Laboratory)"

OBJECTIVE

To provide dosimetry and damage analysis for fusion materials irradiation experiments.

SUMMARY

Revised neutron fluence and damage values are reported for the MOTA-2A experiment in the Fast Flux Test Facility (FFTF). This revision corrects an error with processing of the ^{235}U(n,f) reaction. Net corrections are on the order of 5%.

PROGRESS AND STATUS

Dosimetry results were published previously for the MOTA-2A experiment in FFTF.' Comparison with more recent experiments revealed a small error in the processing of the ^{235}U(n,f) reaction. Corrected values, as listed in Table 1, were used to readjust the neutron flux spectra which was in turn used to recalculate revised damage parameters, as listed in Table 2. The net corrections are on the order of 5%.

Table 1. Fission Measurements for MOTA-2A (atoms/atom-s)

Sample\ Level-Pin	Ht,cm	239Pu (xE-9)	237Np (xE-10)	235U (xE-9)
X14 8-BT	122.4	0.80	0.079	0.76
X13 6-BB	66.6	4.46	2.25	4.21
X12 5-FT	44.0	4.74	9.52	5.17
X11 5-FB	37.7	5.35	12.30	5.61
X10 4-AM	23.3	8.43	20.90	7.83
X08 3-AM	-1.0	10.20	25.00	9.54
X09 3-DM	-3.1	8.80	30.00	9.04
X07 2-EM	-25.0	7.68	18.70	7.76
X05 1-DM	-42.7	7.09	14.30	7.03
X06 1-FM	-42.9	6.89	13.70	7.08
X04 1-DB	-49.2	7.96		8.21
X02 BC-EM	-61.7	9.30		8.58
X01 BC-AM	-62.9	9.34		8.57

"Pacific Northwest Laboratory is operated for the U.S. Department of Energy by Battelle Memorial Institute under Contract DE-AC06-76RLO 1830.

Table 2. Neutron Fluence and Displacement Damage for MOTA-2A

Ht,cm	Fast Fluence (>0.1 MeV) xE+22 n/cm^2	Iron dpa	Ratio dpa/Fluence	Position	SS* dpa
-62.9	1.55	6.1	3.9	A	6.3
-61.7	1.57	6.2	3.9	E	6.5
-49.2	3.12	13.0	4.2	D	13.5
-42.9	5.29	22.8	4.3	F	23.6
-42.7	5.55	23.8	4.3	D	24.6
-25.0	7.12	31.9	4.5	E	33.0
-3.1	9.13	42.2	4.6	D	43.5
-1.0	9.52	41.3	4.3	A	42.7
23.3	7.97	34.7	4.4	A	35.9
37.7	4.67	20.9	4.5	F	21.6
41.0	3.71	16.3	4.4	F	16.9
66.6	1.19	4.6	3.9	B	4.8
122.4	0.061	0.24	3.9	B	0.25

* Stainless Steel Fe-18Cr-8Ni.

REFEKENCES

1. L. R. Greenwood and L. S. Kellogg, Neutron Dosimetry for the MOTA-2A Experiment in FFTF. Fusion Reactor Materials Semiannual Progress Report, DOE/ER-0313/12, 49-53, March 1992.

REANALYSIS OF NEUTRON DOSIMETRY FOR THE MOTA-1A/1B EXPERIMENTS IN FFTF - L. R. Greenwood (Pacific Northwest Laboratory)''

OBJECTIVE

To provide dosimetry and damage analysis for fusion materials irradiation experiments.

SUMMARY

Neutron fluence and spectral measurements and radiation damage calculations have been revised for the MOTA-1A,1B experiments in the Fast Flux Test Facility (FFTF). The data were revised in order to correct for nuclear burnup effects for several of the radiometric monitors, thereby increasing the fluence and damage up to 20%, according to position in the MOTA assembly. The MOTA-IA experiment was irradiated from January 18, 1983 to October 23, 1983 for an exposure of 202.0 EFPD. MOTA-IB was irradiated from January 1, 1984 to April 23, 1984 for an exposure of 109.5 EFPD. Neutron fluence and dpa values are presented for both assemblies.

PROGRESS AND STATUS

Neutron dosimetry results for the Materials Open Test Assembly (MOTA)-1A and 1B experiments in the Fast Flux Test Facility (FFTF) at Hanford were reported by R. L. Simons in 1984.[1] Recently, we have completed dosimetry measurements and fluence and damage calculations for several more recent irradiations including MOTA-1E, IF, 1G, 2A, and 2B.[2-6] The purpose of the present work was to reanalyze the previous MOTA-IA and IB data in order to include nuclear burnup effects for several of the radiometric monitors since these corrections were not included in the previous report. This reanalysis effort was deemed to be necessary since burnup calculations for more recent experiments indicated that these effects would be expected to increase the fast flux and damage by up to 20%. Using these new results further ensures that all neutron dosimetry for the MOTA experiments were performed on a consistent basis.

The MOTA-1A experiment included seven spectral sets of radiometric monitors at different axial locations in the MOTA assembly. MOTA-1B included two spectral sets in the below-core basket. The current effort focussed on nuclear burnup corrections to the ^{235}U, ^{237}Np, and ^{239}Pu fission monitors and the ^{59}Co monitor wire. None of the other reactions reported previously[1] require any burnup corrections. In principal, nuclear burnup corrections are easily understood as correcting for the depletion of either the target or the product isotope due to further neutron interactions. For example, in the case of the $^{59}Co(n,\gamma)^{60}Co$ reaction, both the initial ^{59}Co and the activated ^{60}Co atoms may be converted to other isotopes by interactions with the neutrons. In this case, the only significant reaction is the (n,γ) reaction of interest. Hence, the burnup correction can be performed in a simple iterative procedure. It can be shown that the first correction (assuming that the measured uncorrected reaction rate produces the burnup) is given by the relationship:

$$a\$,' = a\$, [(\lambda+\sigma\phi_2-\sigma\phi_1) / \lambda][1-\exp(-\lambda t)] / [\exp(-\sigma\phi_1 t)-\exp(-(\lambda+\sigma\phi_2)t)]$$

'Pacific Northwest Laboratory is operated for the U.S. Department of Energy by Battelle Memorial Institute under Contract DE-AC06-76RLO 1830.

where $\sigma\phi$ is the reaction rate, the subscripts 1 and 2 refer to the target and product isotopes, prime means the corrected value, λ is the decay constant of the product isotope, and t is the irradiation time. The term $[1-\exp(-\lambda t)]$ is the usual correction for decay during irradiation assuming no burnup effects are included. The iterative solution is obtained by substituting the value $\sigma\phi_1$' into the same equation in place of a$, and finding a new correction value. This process rapidly converges such that there is always a unique solution to the problem. In other words, there is only one value of $\sigma\phi_1$' that will produce the correct ratio when substituted into the rest of the equation. The only exception to this is for very high burnup when the value of the measured activity exceeds the saturation value for a given reaction. In this case the procedure will diverge and alternate means must be found to determine the proper burnup corrections.

One problem with the above procedure is that we rarely know the proper value to use for the reaction rate of the product isotope (eg - ^{60}Co in the above example). Often, the nuclear cross sections are simply not very well-known for many radioactive isotopes. Furthermore, this reaction rate should also be iterated. Often the best estimate we can make for these reaction rates is to take the ratio with the target isotope of either thermal neutron cross sections or resonance integrals. The iteration problem is then easily solved by rewriting it in terms of this ratio. This assumes that the ratio will remain constant regardless of the flux level. Although there may be considerable uncertainty in this part of the procedure, in most cases the correction for the product isotope is not very important relative to the correction for the target isotope. A sensitivity test quickly demonstrates that the net burnup correction is rather insensitive to the choice of the ratio of reaction rates for target and product isotope. In the present case, burnup corrections for the ^{59}Co(n,γ)^{60}Co reaction rates varied from 0.3 to 1.6%.

The most important burnup corrections are for the fission monitors. Basically, the same equation given above can also be used for these reactions with the following modifications. Since several different fission products are detected, a separate correction can be determined for each product. The separate results can then be averaged to determine the next correction and so on. Generally, sensitivity tests show that all of the fission products have very similar corrections.

The other problem with burnup corrections for fission monitors is that the fission reaction is only one part of the total burnup reaction cross section. The (n,γ) reaction also causes significant burnup and must also be included. In the case of the thermal fission monitors (^{235}U and ^{239}Pu), the (n,γ) reaction rate can be estimated from the known ratios of thermal neutron cross sections and resonance integrals. Fortunately, in both cases, the fission cross section is much larger than the gamma capture cross section. Hence, uncertainties in estimating the (n,γ) corrections do not have a very large impact on the net burnup correction. It is also easy to check that the result is self-consistent since both the initial and the final adjusted neutron flux spectra can be used to compute the reaction rates for both the fission and gamma capture cross sections. In fact, using the initial calculated flux spectrum provides the best estimate for the initial gamma-to-fission cross section ratios. The initial neutron flux spectra were taken from calculations by R. L. Simons.'

The largest uncertainty in the burnup corrections is for ^{237}Np. Since this is a threshold fission reaction, the epithermal gamma capture reaction rate may be much larger at out-of-core locations where the neutron spectrum has a much larger abundance of epithermal neutrons. In this case, the gamma-to-fission ratios for ^{237}Np were determined using the calculated neutron flux spectra.' The resultant ratios are shown in Figure 1. This figure actually shows the result of calculations based on the neutron spectral adjustments, as described in previous publications.[2-6]

For MOTA-IA, the burnup corrections varied from about 1.3 to 18% for U and Pu and from 1.2 to 11% for Np. For MOTA-1B, the two spectral sets in the below-core position required corrections

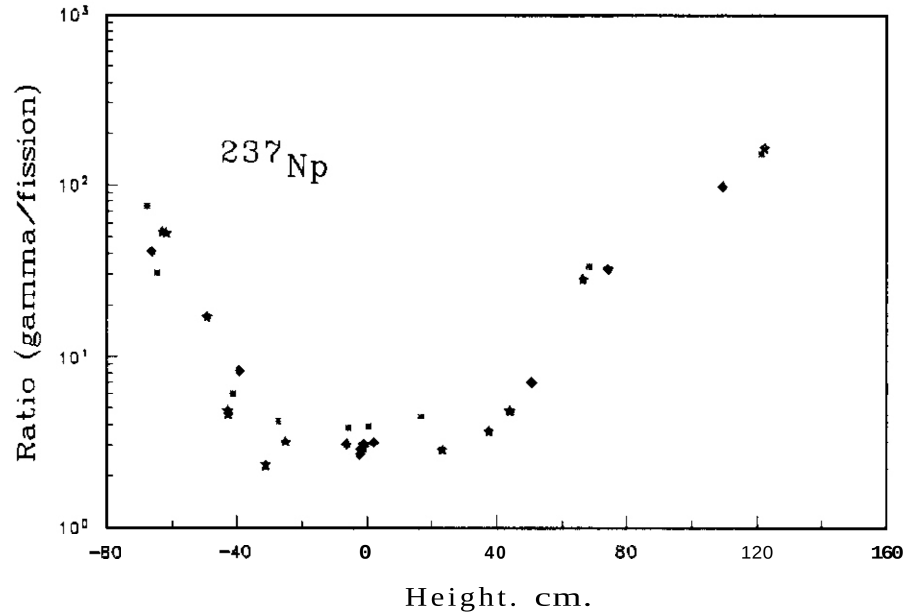

Figure 1 Calculated ratio of (n,γ)/(n,fission) for ^{237}Np in various MOTAs in FFTF.

of about 8 to 10% for U and Po and 8 to 11% for Np. At the below core locations, the Np fission reaction becomes unusable due to the ingrowth of ^{239}Pu which has a higher reaction rate and different fission yields than Np.

The corrected reaction rates are shown, along with the other reaction rates from reference 1, in Table 1. Data from both MOTAs are shown in the table. The MOTA-IB data are at the below core locations; all other results are from MOTA-IA. Additional gradient data from MOTA-IB are not shown in the table. These data are essentially unchanged, although the ^{59}Co(n,γ) results are up to 1% higher. The labels across the top of Table 1 indicate the position in the MOTA. For example, 2B3 means level 2, pin B, position 3. The mean heights to the center of the dosimeters is then listed.

The other monitors consisted of small wires of Fe, Cu, Ni, Ti, and 0.1% Co-Al alloy. According to reference 1, reaction rate uncertainties are on the order of 3%. The burnup corrections are estimated to increase the uncertainties in the fission reaction rates to about 5%. In comparisons with previously published work, it must be noted that MOTA-1A and 1B were irradiated at 400 MW power level rather than the 291 MW used for later irradiations.

The measured reaction rates were used as input to the STAY'SL computer code' to adjust the calculated neutron spectra determined for cycle 9A.[7] STAY'SL performs a generalized least-squares adjustment of all measured and calculated values including the measured activities, calculated neutron flux spectra, and neutron cross sections. Neutron cross sections and their Uncertainties were generally taken from ENDF/B-V, although new data were available from ENDF/B-VI for the ^{46}Ti(n,p) and ^{63}Cu(n,α) reactions.

Table 1 - Activation Rates Measured in MOTA-1A and 1B (atoms/atom-s)
(Only the Co and fission rates have been modified; all other values are from ref. 1)

MOTA Location Reaction\Height, cm:	BC[a] -65.3	BC[a] -60.1	1B3 -44.3	2B3 -22.8	3B2 -0.0	4B3 +20.3	5B2 +36.8	6B1 +71.1	8B2 +111.5
^{59}Co(n,γ)^{60}Co ($\times 10^{-10}$)	31.5	33.7	9.57	4.54	4.30	3.68	5.72	10.51	3.32
^{58}Fe(n,γ)^{59}Fe ($\times 10^{-11}$)	5.23	5.58	5.15	5.38	5.86	4.77	3.50	1.86	0.513
^{54}Fe(n,p)^{54}Mn ($\times 10^{-11}$)	0.246	0.470	2.42	4.21	4.54	3.80	2.14	0.0689	0.00318
^{63}Cu(n,α)^{60}Co ($\times 10^{-13}$)	0.247	0.356	1.39	2.43	2.58	2.17	1.23	0.0358	0.00239
^{58}Ni(n,p)^{58}Co ($\times 10^{-11}$)	0.352	0.666	3.63	6.03	6.49	5.53	3.08	0.104	0.00505
^{46}Ti(n,p)^{46}Sc ($\times 10^{-12}$)	0.281	0.563	3.05	5.39	5.86	4.88	2.78	0.0796	0.00243
^{237}Np(n,f) ($\times 10^{-09}$)	0.500	0.698	1.63	2.50	2.89	2.20	1.22	0.142	0.0141
^{239}Pu(n,f) ($\times 10^{-09}$)	10.64	11.89	9.19	10.95	11.56	9.77	6.56	3.26	0.928
^{235}U(n,f) ($\times 10^{-09}$)	11.24	11.65	9.44	11.03	11.85	9.74	6.78	3.42	0.991

[a] BC (below core) data from MOTA-1B; other positions are from MOTA-1A

The adjusted neutron flux values are listed in Table 2. The previous analysis of these data’ assumed that the flux and spectra for MOTA-1A and 1B were identical. Hence, Table 2 lists data for both MOTAs. In fact, there is no overlap between the two sets of spectral adjustments so we cannot directly compare them. However, the flux gradient data appear to be in good agreement. The MOTA-1B results are at the below core basket (-65 and -60 cm); all of the other results are from MOTA-1A. In all cases, the STAYS’L flux adjustments resulted in good agreement between the measured and calculated reaction rates. In comparisons with the calculated spectra, the agreement is reasonable (20-30%) for in-core positions. However, at out-of-core positions, the disagreement becomes progressively worse, as seen in earlier experiments. In order to obtain neutron fluence and dpa values for each individual irradiation, it is necessary to multiply the values in Table 2 by the net exposures of 202 EFPD for MOTA-1A and 109.5 EFPD for MOTA-IB.

Table 2 Corrected Neutron Flux and Displacement Rates for MOTA-1A and 1B

Capsule/ **Position**	**Ht,cm**	Total Flux xE+15 n/cm^2-s	Fast Flux (>.1 MeV) xE+15 n/cm^2-s	Iron dpals xE-6	Ratio“ **dpa/Flux (>0.1)**	**SS[b] dpa/s**
	-65.3	**2.46**	**1.11**	**0.408**	**3.7**	0.423
	-60.1	**2.71**	**1.38**	**0.517**	**3.7**	0.536
	-44.3	**4.29**	**2.70**	**1.13**	**4.2**	**1.17**
	-22.8	**5.91**	3.97	**1.70**	**4.3**	**1.77**
[illegible]	**-0.0**	6.28	4.27	**1.87**	**4.4**	**1.94**
4u3	20.3	5.26	3.54	**1.52**	**4.3**	1.57
5B2	36.8	3.20	2.04	**0.863**	**4.2**	0.895
6B1	**71.1**	0.849	**0.397**	**0.137**	**3.5**	0.142
[illegible]	111.5	0.149	**0.047**	**0.0165**	3.5	0.0171

‘Ratio of iron dpa to fast fluence **x10^{22}** nlcm’ above **0.1** MeV.

[b] **Stainless** steel: Fe-18Cr-8Ni

Damage calculations were performed at all spectral positions using the SPECTER computer code.’ Dpa rates for iron and 316 stainless steel are shown in Table 2 as well as the ratio of iron dpa per 10” nlcm’ fast flux above 0.1 MeV. Damage parameters for 40 other elements and several compounds have been calculated and will be made available on request.

Comparing the present results with reference 1 indicates that the peak flux and damage rates are increased by about 20% (midplane) with little effect at out-of-core locations.

FUTURE WORK

We plan to construct more detailed flux and damage maps for the entire MOTA-IA and 1B assemblies. Damage parameters will also be provided for a variety of elements and alloys **on** request. Work is in progress to complete analysis of radiometric dosimetry data obtained from MOTA-IC. This will then complete dosimetry for all fusion MOTA irradiations. Dosimetry work is in progress for a variety of US/Japanese experiments in the High Flux Isotopes Reactor at Oak Ridge National Laboratory.

ACKNOWLEDGEMENTS

This work was performed for the U. S. Department of Energy (DOE) under contract DE-AC06-76RLO 1830. Pacific Northwest Laboratory is operated for the DOE by Battelle Memorial Institute.

REFERENCES

1. R. L. Simons, *Analysis of Damage Exposure Rates in the MOTA of the FFTF*, Damage Analysis and Fundamental Studies Quarterly Progress Report, DOE/ER-0046/21, 10-14 May 1985.

2. L. R. Greenwood and L. S. Kellogg, *Neutron Dosimetry for the MOTA-2B Experiment in FFTF*, Fusion Reactor Materials Semiannual Progress Report, DOE/ER-0313/16 (elsewhere in this report).

3. L. R. Greenwood and L. S. Kellogg, *Neutron Dosimetry for the MOTA-2A Experiment in FFTF*, Fusion Reactor Materials Semiannual Progress Report, DOE/ER-0313/12, 49-53 March 1992.

4. L. R. Greenwood and L. S. Kellogg, *Neutron Dosimetry for the MOTA-IF Experiment in FFTF*, Fusion Reactor Materials Semiannual Progress Report, DOE/ER-0313/9, 31-36 September 1990.

5. L. R. Greenwood and L. S. Kellogg, *Neutron Dosimetry for the MOTA-1G Experiment in FFTF*, Fusion Reactor Materials Semiannual Progress Report, DOE/ER-0313/14, 51-54 March 1993.

6. L. R. Greenwood, *Reanalysis of the Neutron Dosimetry for the MOTA-IE Experiment in FFTF*, Fusion Reactor Materials Semiannual Progress Report, DOE/ER-0313/15, 53-59 September 1993.

7. R. L. Simons, *Damage Analysis and Fundamental Studies Quarterly Progress Report*, DOEIER-0046121, 10-14 May 1985.

8. F. G. Perey, *Least Squares Dosimetry Unfolding: The Program STAY'SL*, OHNLITM-6062, Oak Ridge National Laboratory, Oak Ridge, TN (1977).

9. L. R. Greenwood and R. K. Smither, *SPECTER: Neutron Damage Calculations for Materials Irradiations*, ANL/FPP-TM-197, January 1985.

PUBLICATIONS

L. R. Greenwood, F. A. Garner, and D. J. Edwards, *Calculation of Transmutation in Copper and Comparison with Measured Electrical Properties*, accepted for publication in ASTM-STP1228.

L. R. Greenwood. F. A. Garner, and B. M. Oliver, *An Assessment of the 59-Ni Isotopic Tailoring Technique to Study the Influence of Helium/DPA Ratio*, accepted for publication in Journal of Nuclear Material.

L. R. Greenwood and F. A. Garner, *Transmutation of Mo, Re, W, Hf, and V in Various Irradiation Test Facilities and STARFIRE*, accepted for publication in Journal of Nuclear Material.

NEUTRON DOSIMETRY FOR THE MOTA-ZB EXPERIMENT IN FFTF - L. R. Greenwood and L. S. Kellogg, (Pacific Northwest Laboratory).

OBJECTIVE

To provide dosimetry and damage analysis for irradiation experiments in fusion materials.

SUMMARY

Neutron fluence and spectral measurements and radiation damage calculations are reported for the (Materials Open Test Assembly) MOTA-ZB experiment in the Fast Flux Test Facility (FFTF). The irradiation was conducted from May 27,1991, to March 19,1992 for a total exposure of 203.3 EFPD (effective full-power days). The maximum fluence was about 9 x 10''nlcm', 6 x 10^{22} above **0.1** MeV producing about 24 dpa in iron. Neutron fluence and radiation damage maps are presented for the entire MOTA assembly based on the analysis of ten neutron spectral measurements and fourteen additional flux gradient measurements.

PROGRESS AND STATUS

Neutron dosimetry for the MOTA-2B experiment in the FFTF at Hanford provided comprehensive measurements over the entire assembly with a total of 25 capsules positioned at different axial locations in the assembly spanning a distance of **-68** to +121 cm. Dosimetry results have been reported previously for the MOTA-2A, 1F, 1G, and 1E experiments.'' Each stainless steel capsule measured about 2.5 **cm** long by 0.46 cm o.d. and contained dosimetry wires for either spectral or gradient measurements. The eleven spectral capsules contained small wires of Fe, Ti, Ni, Cu, Nh, 0.1% Co-AI alloy, 80.2% Mn-Cu alloy, 0.825% ^{235}**U** in V, and ^{237}**Np$_2$O** oxide wire, whereas the 14 gradient capsules contained Fe and 0.1% Co-AI alloy wires. One of the spectral capsules (located at level 7 of the MOTA) was not received. All dosimetry materials were separately encapsulated in vanadium. In addition, small amounts of Be, Fe, and Nb encapsulated in platinum were included in some of the spectral capsules for helium analyses. Altogether, there were a total of 118 radiometric monitor wires and 17 helium monitors.

Following irradiation, each dosimetry capsule was opened in a hot cell and each individual monitor was identified and mounted for gamma analysis. The measured activities were then converted to saturated activities by correcting for the sample weight, atomic weight, isotopic abundance, gamma absorption, reactor power history, and fission yield, as needed. Neutron self-shielding effects were not significant, since the Co and ^{235}**U** wires were dilute alloys and the FFTF neutron spectrum has few neutrons at lower neutron energies. For the U and Np fission monitors, the gamma measurements detected four fission products: namely, ^{95}Zr, ^{106}Ru, ^{137}Cs, and ^{144}**Ce.** The standard deviation from the mean fission rate was generally less than **5%** except for the ^{237}Np reactions at out-of-core locations, as discussed below.

Neutron burnup effects were found to be quite significant for the fission monitors, and a small correction was necessary for the ^{59}**Co(n,γ)** and fission reactions. In the case of ^{59}**Co** this correction can be applied using an iterative procedure since the reaction itself is the sole source of the burnup,

---

'Pacific Northwest Laboratory is operated for the U.S. Department of Energy by Battelle Memorial Institute under Contract DE-AC06-76RLO **1830.**

as described previously.' In the case of the ^{59}Co(n,γ) reaction, the burnup effect varied from 0.3% at midplane to 2.0% in the below-core basket. Burnup effects for the fission monitors were very similar to those determined for the MOTA-2A experiment.' In most cases the burnup corrections for the fission monitors were about 10-15% at midplane and decreased to only a few percent at out-of-core locations. For ^{237}Np, there appears to be a significant effect from the lower energy neutrons at the out-of-core positions due to inbreeding of ^{138}U and eventually ^{239}Pu, as evidenced by a larger scatter in the four measured fission products. Furthermore, the ^{144}Ce results for Np were lower than the other three fission products. Hence, the Np data were discarded at the below-core positions and not used in the spectral analyses.

The corrected reaction rates are listed in Tables 1-3. All values are normalized to 291-MW operation and the values have an estimated absolute uncertainty of about 5%, although there is an additional uncertainty of about 5% for the fission reactions due to problems in determining the burnup rates. The ^{58}Fe(n,γ) reaction rates also have a larger uncertainty (as noted in the tables) due to the long decay time prior to gamma counting. These rates appear to be in reasonable agreement with previous measurements.'.' Neither of the earlier experiments, MOTA-1A/1B, made any attempt to determine neutron burnup corrections for the fission reactions. Hence, values measured for MOTA-IF, 2A, 1G, and 2B are about 20-30% higher than these earlier measurements, when allowances are made for differences in reactor power (400 MW rather than 291 MW) and other core changes. Reanalysis of the MOTA-IA, 1B, and 1C experiments is currently in progress.

Table 1 - Activation Measurements in MOTA-2B (atoms/atom-s)

Sample/ Level-Pin	Ht, cm	^{54}Fe(n,p)^{54}Mn (xE-11)	^{58}Fe(n,γ)^{59}Fe (xE-11)	^{59}Co(n,γ)^{60}Co (xE-10)
			(±%)	
C22 BC-D5	-68.4	0.111	3.78 (3)	21.6
C02 BC-C5	-67.7	0.119	4.14 (3)	20.8
C37 BC-F4	-67.4	0.149	4.27 (3)	22.1
C16 BC-E4	-64.7	0.220	4.91 (8)	20.3
C21 BC-CI	-58.1			20.3
C04 I-C3	-41.2	1.63	3.51 (10)	6.78
C28 1-El	-39.0	1.97	3.13 (10)	5.18
C32 2-E5	-28.2	2.51		3.32
C18 2-84	-27.3	2.63	4.32 (15)	3.28
C30 2-D1	-18.9	3.46	4.59 (17)	
C29 2-A1	-17.8	3.22	4.81 (30)	2.88
C35 3-F4	-5.9	3.25	4.55 (14)	3.02
C05 3-D6	-5.8	3.07	3.69 (19)	2.71
C36 3-A4	-1.6	3.38	4.96 (18)	3.04
C19 3-B2	0.5	3.32	5.17 (9)	
C17 4-63	16.8	3.02	5.49 (13)	9.50
C33 4-F3	20.7	2.76	4.98 (8)	8.71
C31 4-C2	22.4	2.61	3.81 (9)	5.93
C25 5-F2	40.4	1.59	3.14 (10)	4.01
C24 5-D1	43.5	1.27	2.76 (9)	4.84
C03 5-82	44.3	1.46	3.09 (8)	4.84
C15 6-64	68.4	0.122	2.38 (4)	10.6
C20 8-B4	111.5	0.0039	0.614(4)	30.3
C01 8-B1	121.3	0.0022	0.399(13)	23.8

Table 2 - Activation Measurements in MOTA-26 (atoms/atom-s)

Sample/ Level-Pin	Ht, **cm**	**^{46}Ti(n,p)** (xE-12)	^{58}Ni(n,p) (xE-11)	**^{60}Ni(n,p)** (xE-13)	^{63}Cu(n,α) (xE-13)	**^{93}Nb(n,γ)** (xE-10)	**^{55}Mn(n,2n)** (xE-14)
		0.132	0.165	0.670	0.177	4.96	0.277
		0.231			0.107	5.78	0.618
C04 1C3			2.29		0.957	6.58	4.70
C18 264	-27.3		3.66			8.33	7.66
COS 3D6			4.25			8.86	8.67
C19 3B2			4.56	7.87	I.96	9.34	9.23
C17 4B3	16.8	3.86	4.16	7.54		9.49	8.71
C03 562	44.3	1.99	2.08		0.879	5.49	4.30
C15 6B4	68.4	0.129	0.162	0.290	0.0595	3.52	0.354
C01 8B1	121.3	0.00225	0.00342	0.0179	0.00124	0.566	0.0098

Table 3 - Fission Reaction Measurements in MOTA-26 (fission/atom-s)

Sample/ Level-Pin	Ht, cm	^{237}**Np** (n,f) (xE-10)	**^{235}U (n,f) (xE-9)**
COZ BC-C5	-67.7	2.80	7.42
C16 BC-E4	-64.1	4.39	8.26
C04 1C3	-41.2	9.16	6.77
C18 264	-27.3	14.90	8.23
C05 3D6	-5.8	16.60	8.42
C19 3B2	**0.5**	18.00	9.18
C17 4B3	16.8	18.00	10.8
C03 562	44.3	9.82	5.44
C15 664	68.4	1.80	4.16
C01 861	121.3	0.089	0.815

The measured reaction rates were used as input to the STAY'SL computer code[6] to adjust the calculated neutron spectra determined for cycle 9A.[7] STAY'SL performs a generalized least-squares adjustment of all measured and calculated values including the measured activities, calculated spectra, and neutron cross sections. Neutron cross sections and their uncertainties were generally taken from ENDF/B-V, although new data were available from ENDFIB-VI for the **^{46}Ti(n,p)** and **^{63}Cu(n,a)** reactions. The adjusted neutron fluence values are listed in Table 4. The neutron spectral adjustments for the 10 spectral positions are illustrated in Figure **1**, which shows neutron spectra results at midplane, the edge of the core, and the below-core basket. In comparisons with the calculated spectra, the agreement is reasonable (20-30%) for in-core positions. However, at out-of-core positions, the disagreement becomes progressively worse, as seen in earlier experiments.' At level 8 (+121 cm), the measured flux is about twice the calculated flux.

Damage calculations were performed at all spectral positions using the SPECTER computer code! Dpa rates for iron and 316 stainless steel are shown in Table 4 as well as the ratio of iron dpa per **10''** n/cm^2 fast flux above 0.1 MeV. Damage parameters for 40 other elements and several compounds have been calculated and will be made available on request.

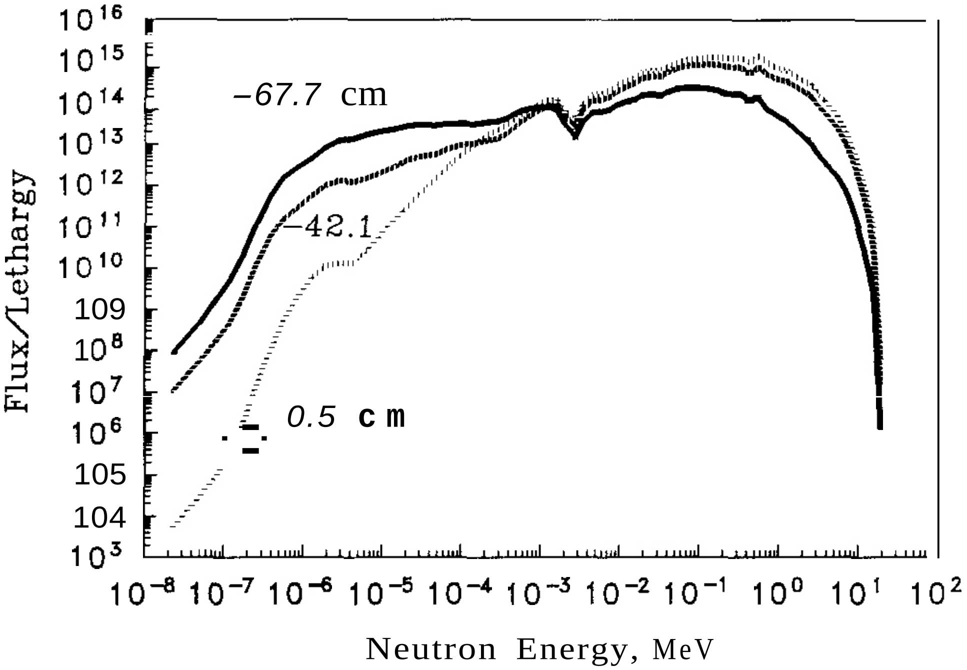

Figure 1 Adjusted neutron flux spectra are shown at axial locations of 0.5 cm (dotted line), -41.2 cm (dashed line), and -67.7 cm (solid line) for the MOTA-2B assembly. Note the drop in fast flux and increase in low-energy flux out-of-core.

Table 4 - Neutron Fluence and Displacement Damage for MOTA-ZB

Capsule/ Position	Ht, cm	Total Fluence xE+22 n/cm^2	Fast Fluence (>0.1 MeV) xE+22 n/cm^2	Iron dpa	Ratio dpa/Fluence (>0.1 MeV)	SS* dpa
C02 BC-C5	-67.7	1.88	0.67	2.49	3.6	2.60
C16 BC-E4	-64.7	3.15	1.53	5.63	3.1	5 85
C04 IC3	-41.2	5.63	3.28	13.5	4.1	14.0
C18 2B4	-27.3	7.91	4.91	20.1	4.1	20.9
C05 3D6	-5.8	8.11	5.22	21.8	4.2	22.6
C19 382	0.5	8.73	5.52	23.3	4.2	24.1
C17 4R3	16.8	9.76	6.24	24.7	4 0	25.6
C03 5B2	44.3	4.78	2.96	12.2	4.1	12.6
C15 684	68.4	1.64	0.73	2.71	3.7	2.82
C01 8R1	121.3	0.203	0.060	0.210	3.5	0.220

The flux and damage gradients at other positions can be found from the activity gradient data in Table 1, which are shown in Figure 2. Note that the ^{59}Co(n,γ) reaction peaks outside of the core because it is quite sensitive to the lower-energy neutrons. The unusual behavior of the Co reaction is due to neutron resonance effects. Fast fluence and dpa gradients from Table 4 are plotted in Figure 3. The apparent scatter in the data is caused by the radial flux gradients, as discussed below.

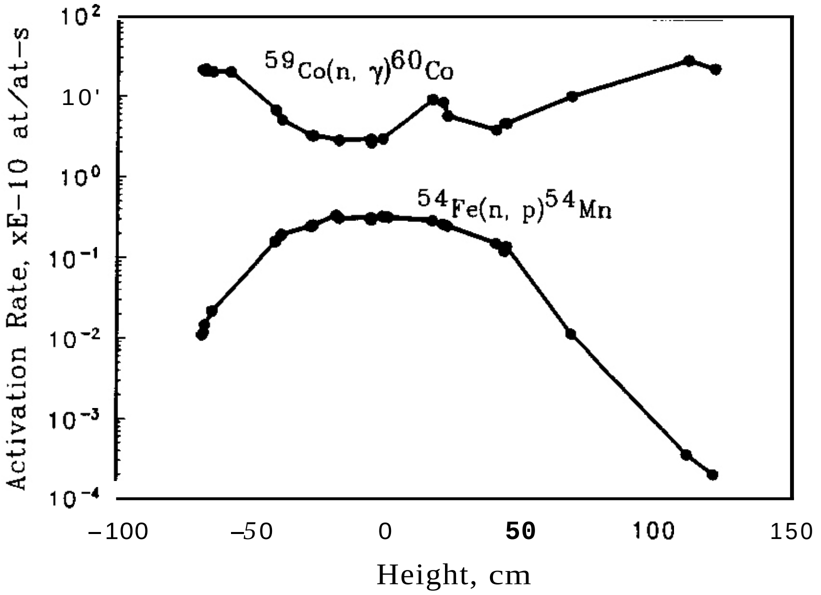

Figure 2 Activation rates are shown for the $^{54}Fe(n,p)^{54}Mn$ and $^{59}Co(n,\gamma)^{60}Co$ reactions as a function of height in the MOTA-2B assembly.

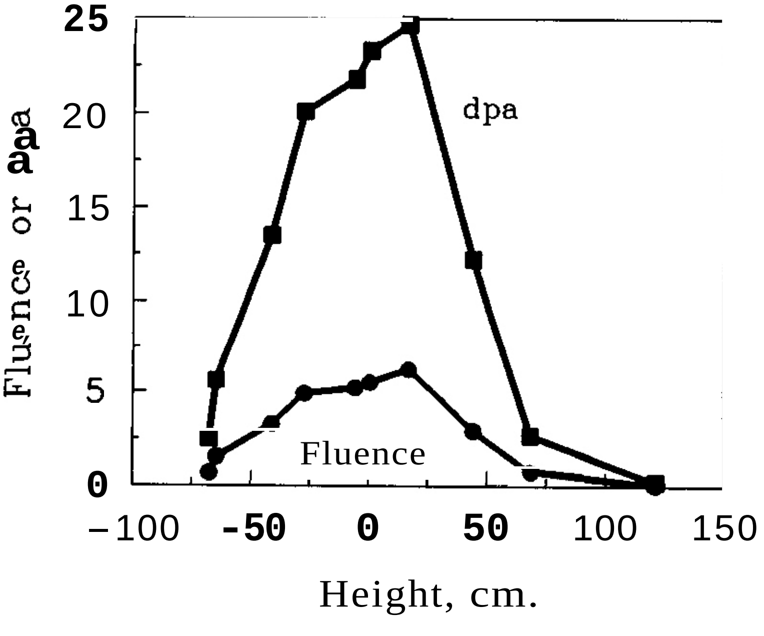

Figure 3 Fast neutron fluence ($x10^{22}$ n/cm^2 , >0.1 MeV) and dpa in iron are shown as a function of height in the MOTA-2B assembly.

Close examination of the activity data indicates the presence of radial and azimuthal flux and spectral gradients. The letters A to F under the position column in Table 4 refer to the radial position at the height indicated. The MOTA basket has six radial positions (A to F); hence, for example, A and D are the furthest apart while A and B or F are adjacent. The maximum radial flux differences are on the order of 10%; however, we also see some indications of spectral differences in the ratio of the fast flux to the ^{54}Fe(n,p) activity rate. Such differences are complex and we are now studying these effects in order to construct a more complete flux and damage map of the entire MOTA assembly.

FUTURE WORK

We plan to construct more detailed flux and damage maps for the entire MOTA-2B assembly. Damage parameters will also be provided for a variety of elements and alloys on request. Data from the MOTA-IG, 2A, and 2B irradiations are being used to help reanalyze previous data from MOTA-IA, 1B, and IC, especially to include burnup effects for the fission monitors. Dosimetry work is in progress for a variety of US/Japanese experiments in the High Flux Isotopes Reactor at Oak Ridge National Laboratory.

ACKNOWLEDGEMENTS

This work was performed for the U.S. Department of Energy (DOE) under Contract DE-AC06-76RLO 1830. Pacific Northwest Laboratory is operated for the DOE by Battelle Memorial Institute.

REFERENCES

1. L. R. Greenwood and L. S. Kellogg, Neutron Dosimetry for the MOTA-2A Experiment in FFTF. Fusion Reactor Materials Semiannual Progress Report, DOE/ER-0313/12, 49-53 March 1992.

2. L. R. Greenwood and L. S. Kellogg, Neutron Dosimetry for the MOTA-IF Experiment in FFTF, Fusion Reactor Materials Semiannual Progress Report, DOE/ER-0313/9, 31-36 September 1990.

3. L. R. Greenwood and L. S. Kellogg, Neutron Dosimetry for the MOTA-1G Experiment in FFTF, Fusion Reactor Materials Semiannual Progress Report, DOE/ER-0313/14, 51-54 March 1993.

4. L. R. Greenwood, Reanalysis of the Neutron Dosimetry for the MOTA-1E Experiment in FFTF, Fusion Reactor Materials Semiannual Progress Report, DOE/ER-0313/15, 53-59 September 1993.

5. R. L. Simons, Analysis of Damage Exposure Rates in the MOTA of the FFTF, Damage Analysis and Fundamental Studies Quarterly Progress Report, DOE/ER-0046/21, 10-14 May 1985.

6. F. G. Perey, Least Squares Dosimetry Unfolding: The Program STAY'SL, ORNL/TM-6062, Oak Ridge National Laboratory, Oak Ridge, TN (1977).

7. R. L. Simons, Damage Analysis and Fundamental Studies Quarterly Progress Report, DOEIER-0046/21, 10-14 May 1985.

8. L. R. Greenwood and R. K. Smither, SPECTER: Neutron Damage Calculations for Materials Irradiations, ANL/FPP-TM-197, January 1985.

PUBLICATIONS

L. R. Greenwood, F. A. Garner, and D. J. Edwards, Calculation of Transmutation in Copper and Comparison with Measured Electrical Properties, accepted for publication in ASTM-STP1228.

L. R. Greenwood, F. A. Garner, and B. M. Oliver, An Assessment of the 59-Ni Isotopic Tailoring Technique to Study the Influence of Helium/DPA Ratio, accepted for publication in Journal of Nuclear Materials.

L. R. Greenwood and F. A. Garner, Transmutation of Mo, Re, W, Hf, and V in Various Irradiation Test Facilities and STARFIRE, accepted for publication in Journal of Nuclear Materials.

NEUTRON DOSIMETRY FOR THE MOTA-IC EXPERIMENT IN FFTF - L. R. Greenwood (Pacific Northwest Laboratory)"

OBJECTIVE

To provide dosimetry and damage analysis for fusion materials irradiation experiments.

SUMMARY

Neutron fluence and spectral measurements and radiation damage calculations have been completed for the Materials Open Test Assembly (MOTA)-IC experiment in the Fast Flux Test Facility (FFTF). Although this irradiation was completed in 1985, the neutron dosimetry data were never analyzed. The MOTA-IC experiment was irradiated in cycles **5** and 6 from June 16, **1984** to June 24, 1985 for an exposure of 256.7 EFPD (effective full power days). The irradiation was conducted at 400 MW. Neutron fluence and dpa values are presented.

PROGRESS AND STATUS

The MOTA-IC irradiation was completed **in** 1985. At that time, the dosimetry capsules were retrieved and all dosimetry wires were gamma counted. The results were reported in a memo from W. Y. Matsumoto to A. M. Ermi, dated January 3, 1986. The present work has reexamined these activation data in order to complete neutron fluence measurements and radiation damage calculations.

Neutron dosimetry results and damage calculations have been reported for most of the other MOTA irradiations in FFTF, including MOTA-1A, IB, 1E, 1F, **1G**, 2A, and 2B.[1-6] With the addition of the present work, analyses are now complete for all MOTAs which contained fusion reactor material irradiation experiments. A decision was made not to analyze dosimetry materials from the MOTA-ID irradiation due to a temperature excursion for this experiment.

The MOTA-IC experiment included two spectral sets and nine gradient sets **of** radiometric monitors at various axial locations in the MOTA assembly. The spectral sets contained small wires of Fe, Ni, Cu, Ti, Sc_2O_3, **0.1%** Co-AI alloy, and encapsulated oxide wires of ^{237}**Np (87.4%)**, ^{235}U (0.825%), and ^{239}**Pu** (0.928%). The gradient sets contained only wires of Fe and **0.1%** Co-AI alloy. Following the irradiation, all of these wires were gamma counted and the disintegration rates per milligram (dpslmg) of material were reported, as mentioned previously.

The dpslmg values for each wire were converted to saturated reaction rates using the relationship:

$$\sigma\phi = (dps/mg)\ AW\ /\ [Gabs \times Ahn \times BCF \times N \times FYI$$

where AW = atomic weight, Gabs = gamma self-absorption, BCF = correction for decay during irradiation, N = Avogadro's number, and FY = fission yield (only for fission monitors). The saturated reaction rate is equal to the spectral-averaged activation cross section (σ) times the total

---

'Pacific Northwest Laboratory is operated for the **U.S.** Department of Energy by Battelle Memorial Institute under Contract DE-AC06-76RLO 1830.

neutron flux (ϕ). The resultant values are listed in Tables 1 and 2. The M values refer to our capsule numbers. The position of each capsule is denoted by the level, pin, and specific position, such as 3B3.

T: e 1 - Activatic 'atom-s)

Capsule	Ht.,cm	$^{54}Fe(n,p)^{54}Mn$ (x10^{-11})	$^{58}Fe(n,\gamma)^{59}Fe$ (x10^{-11})	$^{59}Co(n,\gamma)^{60}Co$ (x10^{-10})
M40 BC-D2	-62.7	0.278	**5.80**	35.6
M10 BC-B2	-61.4	0.359	6.25	32.9
M33 1E2	-42.9	2.07	4.71	10.9
M32 1B1	-39.4	2.81	4.89	7.92
M34 2B2	-20.3	3.75	5.56	4.30
M35 3E2	0.5	3.66	5.25	3.53
M36 4B4	16.9	2.81	5.24	3.67
M38 5E2	39.6	1.92	3.41	4.59
M37 582	45.0	1.56	3.84	7.49
M39 6B3	70.2	0.099	2.33	11.8

Table 2 - Activation Rates Measured in MOTA-IC (atoms/atom-s)

MOTA Location: Reaction/Height, cm:	BC-B2 -61.4	3B3 *-0.5*
$^{63}Cu(n,\alpha)^{60}Co$ (x10^{-13})	2.49	0.351
$^{58}Ni(n,p)^{58}Co$ (x10^{-11})	6.18	0.503
$^{46}Ti(n,p)^{46}Sc$ (x10^{-12})	5.39	0.415
$^{45}Sc(n,\gamma)^{46}Sc$ (x10^{-10})	2.14	2.05
$^{237}Np(n,f)$ **(x10^{-09})**	2.97	**1.63**[a]
$^{239}Pu(n,f)$ (x10^{-08})	1.19	1.31
$^{235}U(n,f)$ (x10^{-08})	1.28	1.24

"Large uncertainty (18%) due to ingrowth of ^{239}**Pu.**

Burnup corrections were performed for the ^{59}Co(n,γ) and fission reactions, as described previously.[1] Burnup corrections for the fission reactions varied from 20-35% at midplane and 30-67% below core. These corrections were larger than seen for previously reported irradiations since MOTA-IC was the longest irradiation at full reactor power (400 MW). The largest uncertainty in the burnup corrections is for ^{237}Np. Since this is a threshold fission reaction, the epithermal gamma capture reaction rate may he much larger at out-of-core locations where the neutron spectrum has a much larger abundance of epithermal neutrons. In this case, the gamma-to-fission ratios for ^{237}Np were determined using the calculated neutron flux spectra.'

The measured reaction rates were used as input to the STAY'SL computer code' to adjust the calculated neutron spectra determined for cycle 9A.[8] STAY'SL performs a generalized least-squares adjustment of all measured and calculated values including the measured activities, calculated neutron flux spectra, and neutron cross sections. Neutron cross sections and their uncertainties were generally taken from ENDF/B-V, although new data were available from ENDFIB-VI for the ^{46}Ti(n,p) and ^{63}Cu(n,α) reactions.

The adjusted neutron fluence values are listed in Table 3. Since we only have spectral data for two positions, neutron fluence and damage data for other positions must he determined from the gradient data and by comparison to other MOTA experiments. For this reason, the MOTA-IC neutron flux results are compared to data for the MOTA-IA and 1B irradiations in Figure I. As can be seen, all three experiments are in reasonably good agreement. Hence, the recommended procedure is to use these fluxes for all three irradiations, determining the neutron fluences and dpa values by multiplying times the respective irradiation times (eg - 256.7 EFPD for MOTA-IC).

Table 3 Neutron Fluence and Displacement Damage for MOTA-IC

Capsule/ Position	Ht,cm	Total Fluence x10^{23}n/cm^2	Fast Fluence (>.1 MeV) x10^{23} n/cm^2	Iron dpa	Ratio[a] dpa/Fluence (>0.1)	SS[b] dpa
3B3	-0.5	1.42	0.972	42.0	4.3	43.4
BC-B2	-61.4	0.425	0.187	6.7	3.6	6.9

Damage calculations were performed at all spectral positions using the SPECTER computer code? Dpa values for iron and 316 stainless steel are shown in Table 3 as well as the ratio of iron dpa per 10^{22} n/cm^2 fast flux above 0.1 MeV. Damage parameters for 40 other elements and several compounds have been calculated and will be made available on request.

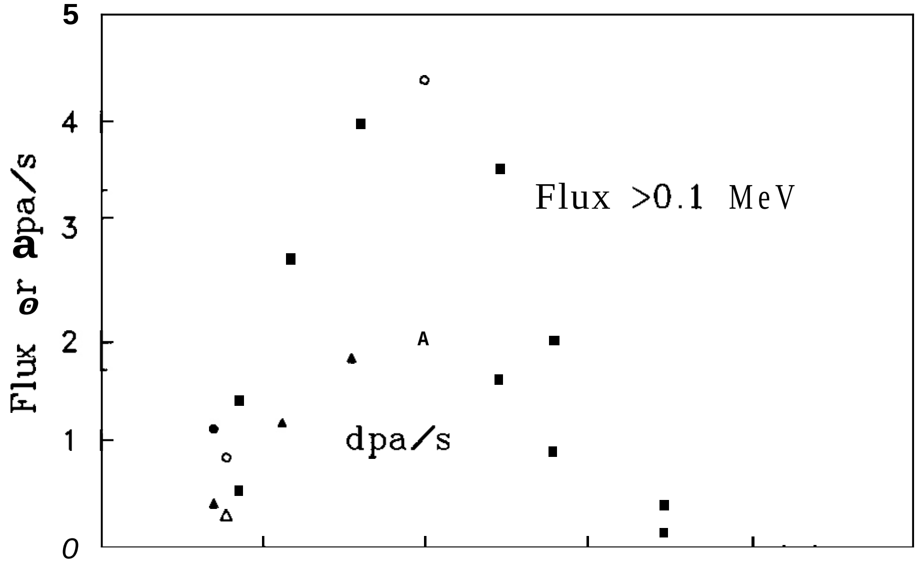

Figure 1 Fast neutron flux >0.1 MeV (circles) and dpa/s ($x10^{-6}$) (triangles) are shown for MOTA-1A and 1B (solid symbols), and 1C (open symbols).

FUTURE WORK

We plan to construct more detailed flux and damage maps for all of the MOTA irradiations. Dosimetry work is in progress for a variety of US/Japanese experiments in the High Flux Isotopes Reactor at Oak Ridge National Laboratory.

ACKNOWLEDGEMENTS

This work was performed for the U. S. Department of Energy (DOE) under contract DE-AC06-76RLO 1830. Pacific Northwest Laboratory is operated for the DOE by Battelle Memorial Institute.

REFERENCES

1. L. R. Greenwood, ***Reanalysis of Neutron Dosimetry for the MOTA-1A/1B Experiments in FFTF,*** Fusion Reactor Materials Semiannual Progress Report, DOE/ER-0313/16 (elsewhere io this report).

2. L. R. Greenwood and L. S. Kellogg, ***Neutron Dosimetry for the MOTA-ZB Experiment in FFTF,*** Fusion Reactor Materials Semiannual Progress Report, DOE/ER-0313/16 (elsewhere in this report).

3. L. R. Greenwood and L. S. Kellogg, *Neutron Dosimetry for the MOTA-2A Experiment in FFTF*, Fusion Reactor Materials Semiannual Progress Report, DOE/ER-0313/12, 49-53 March 1992.

4. L. R. Greenwood and L. S. Kellogg, *Neutron Dosimetry for the MOTA-IF Experiment in FFTF*, Fusion Reactor Materials Semiannual Progress Report, DOE/ER-0313/9, 31-36 September 1990.

5. L. R. Greenwood and L. S. Kellogg, *Neutron Dosimetry for the MOTA-IC Experiment in FFTF*. Fusion Reactor Materials Semiannual Progress Report, DOE/ER-0313/14, 51-54 March 1993.

6. L. R. Greenwood, Reanalysis of the *Neutron Dosimetry for the MOTA-IE Experiment in FFTF*, Fusion Reactor Materials Semiannual Progress Report, DOE/ER-0313/15, 53-59 September 1993.

7. F. C. Perey, *Least Squares Dosimetry Unfolding: The Program STAY'SL*, ORNL/TM-6062, Oak Ridge National Laboratory, Oak Ridge, TN (1977).

8. R. L. Simons, *Damage Analysis and Fundamental Studies Quarterly Progress Report*, DOE/ER-0046121, 10-14 May 1985.

9. L. R. Greenwood and R. K. Smither, *SPECTER: Neutron Damage Calculations for Materials Irradiations*, ANL/FPP-TM-197, January 1985.

TRANSMUTATIONS OF ELEMENTS UNDER IRRADIATION AND ITS IMPACT ON ALLOYS COMPOSITION - I. C. Gomes and D. L. Smith (Argonne National Laborataory)

OBJECTIVE

The objective of this study **is** to compare transmutation rates in available fission test reactors with those produced in a typical fusion reactor spectrum. The materials analyzed in this study are a vanadium alloy, a martensitic steel, a copper alloy and silicon carbide.

SUMMARY

This study presents a comparison of nuclear transmutation rates for candidate fusion first wallhlanket structural materials in available fission test reactors with those produced in a typical fusion spectrum. The materials analyzed in this study include a vanadium alloy **(V-4Cr-4Ti)**, a reduced activation martensitic steel **(Fe-9Cr-2WVTa)**, a high conductivity copper alloy (Cu-Cr-Zr), and the SiC compound. The fission irradiation facilities considered include the EBR-II (Experimental Breeder Reactor) fast reactor, and two high flux mixed spectrum reactors, HFIR (High Flux Irradiation Reactor) and SM-3 (Russian reactor). The transmutation and dpa rates that occur in these test reactors are compared with the calculated transmutation and dpa rates characteristic of a D-T fusion first wall spectrum. In general, past work has shown that the displacement damage produced in these fission reactors can be correlated to displacement damage in a fusion spectrum; however, the generation of helium and hydrogen through threshold reactions [$(n,x\alpha)$ and (n,xp)] are much higher in a fusion spectrum. As shown in this study, the compositional changes for several candidate structural materials exposed to a fast fission reactor spectrum are very low, similar to those for a characteristic fusion spectrum. However, the relatively high thermalized spectrum of a mixed spectrum reactor produces transmutation rates quite different from the ones predicted for a fusion reactor, resulting in substantial differences in the final composition of several candidate alloys after relatively short irradiation time. **As** examples, the transmutation rates of W, Ta, V, Cu, among others, differ considerably when the irradiation **is** performed under a mixed spectrum reactor's and fusion first wall's spectrum. The out-of-core positions in mixed spectrum reactors can be partially shielded against low energy neutrons. e.g., by hafnium, to reduce the transmutation rates but the displacement rates at these positions are much lower than those for the core positions. Fast reactors (EBR-II) provide the only possibility for obtaining high damage rates without producing significant compositional effects in vanadium alloys, ferritic steels and copper alloys.

PROGRESS AND STATUS

Introduction

Since a high flux source of 14 MeV neutrons does not exist, the effect of neutron irradiation on the properties and performance limits of candidate fusion first wallhlanket materials are currently being investigated with tests in fission reactors. Neutron irradiation produces atomic displacement damage that can affect the microstructure and properties of the material and nuclear transmutation that can alter the composition and hence the properties of the material. The dpa rate is basically a product of interactions with neutrons above 0.1 MeV. The high energy neutrons, characteristic of a fusion spectrum, produce more damage per neutron than the fission neutrons: however, the damage is qualitatively similar. The transmutation rates are quite sensitive to neutron energy since the nuclear cross setions vary significantly with the neutron energy. The transmutation of isotopes in other species has two main contributions, namely from the thermal neutrons through the (n,γ) reaction with the subsequent decay of the products and from the fast neutrons through threshold type of reactions [(n,p), (n,α), $(n,2n)$, etc.].

The neutron energy spectrum of mixed spectrum and fast fission are quite different, and hence, the effects of irradiation on materials in the two environments can differ substantially. The mixed spectrum

---

* Work supported by the U.S. Department of Energy, Office of Fusion Energy, under Contract Number W-31-109-Eng-38.

reactors have a neutron energy spectrum which tends to have a large number of low energy neutrons and a very small number of neutrons above 3 MeV. The fast reactors have a small number of low energy neutrons and a large number of neutrons with energy between 0.1 to 3 MeV. The fusion neutron energy spectrum. at positions close to the plasma, tends to have a relatively small number of low energy neutrons and a relatively large number of neutrons with energy above 10 MeV. These differences can be translated in terms of different nuclear reactions that will take place in these environments.

Calculations of the transmutation rate were performed using the REAC-3[1] code with 175 neutron energy groups

<u>Materials and Irradiation Facilities Analyzed</u>

The materials considered in this analysis are a ferritic steel (Fe9Cr2W0.2VTa), a vanadium alloy (V4Cr4Ti), a copper alloy (Cu0.5Cr0.3Zr), and silicon carbide (SiC). Table 1 present the atomic percentage of each major constituent of these alloys. The irradiation resistance of these materials has been the focus of an intense testing program[2,3,4] to select the best option for a structural material for ITER (International Thermonuclear Experimental Reactor).

The irradiation facilities selected for this analysis are presented in Table 2 along with total neutron flux at the mentioned irradiation positions and the number of displacement per atom per full power year (DPA/year) obtainable for each material considered and in each facility. Also, the STARFIRE fusion reactor first wall values is presented in Table 2 (despite not being included in the calculations). The fusion environment selected for this analysis is an ITER type of machine with liquid lithium as coolant and vanadium alloy (V4Cr4Ti) as the structural material (called ITER-LM hereafter). The responses presented for ITER-LM are related to the first wall neutron energy spectrum/flux. The inclusion of this ITEK design is for qualitative comparison and does not represent an absolute reference.

Table 1. Composition of the Alloys Considered in This Analysis

Alloy	Element	Atomic Percent
Fe9Cr2W.2VTa	Chromium	9.6
Nickel	0.0095	
Molybdenum	0.0006	
Manganese	0.45	
Silicon	0.311	
Iron	88.1967	
V4Cr4Ti	Vanadium	91.8406
Chromium	3.9111	
Titanium	4.2473	
Silicon	0.0911	
Cu0.5Cr0.3Zr	Copper	99.2311
Chromium	0.5738	
Zirconium	0.1323	
SiC Carbon	*50.0*	
Silicon	*50.0*	

The inclusion of the IFMIF (International Fusion Materials Irradiation Facility)[5] results is made in comparative basis and the results presented here should be seen as preliminary in nature. The beam **size** chosen in this analysis for IFMIF was 10x10 cm^2, the deuteron energy was 35 MeV, the deuteron current was 250 mA and the position of irradiation was at 0.5 cm from the back-plate inside the test cell in the direction of the beam.

Table 2. Irradiation Facilities Considered in This Analysis

Test Facility (Total Neutron Flux - n/cm^2sec)	DPA per Full Power Year of Operation			
	Fe9Cr2WVTa	V4Cr4Ti	Cu0.5Cr0.3Zr	SiC
ITER-LM-1stW (4.7e+14)	11.8	12.5	12.3	11.0
EBR-II 1A1 (2.9e+15)	41.3	51.9	41.6	74.9
IFMIF(0.5,0,0) (9.4e+14)	42.2	44.6	42.2	38.9
SM-3 (core) (3.8e+15)	42.0	53.4	41.2	64.4
HFIR (core) (5.8e+15)	25.3	32.2	24.6	32.2
HFIR (RB*) (2.3e+15)	6.1	9.0	6.8	11.0
HFIR (RBH) (1.0e+15)	6.3	x.3	6.	10.6
STARFIRE(1stW) (1.8e+15)	41.8	45.5	43.1	43.9

Figure 1 displays the normalized neutron energy spectra for the irradiation facilities and positions within the facilities considered in this analysis along with the **STARFIRE** first wall spectrum. **As one** can see the fusion and fast reactors exhibit a very low fraction of low energy neutrons, whereas the mixed spectrum fission reactors tend to have a large portion of the neutrons in the low energy end.

Results

Figures 2 through 11 display the variation of the concentration of selected elements as a function of the fluence, represented in dpa's, for the irradiation environments mentioned in the previous section. The irradiation time was assumed to be the same for all irradiation facilities, equal to 2 full power years or 730 days of continuous irradiation.

Figures 2 through 6 show the most important transmutations in ferritic steel (Fe9Cr2W0.2VTa). Tungsten is one of the components which will suffer large transmutation in a high thermal neutron energy spectrum. In HFIR at the core position. the depletion rate of tungsten is about 1.7% per dpa. The production of rhenium and osmium is a product of the transmutation chain of tungsten. Tantalum is another element which suffers a very large transmutation in the thermal and epitbermal neutron energy regions. The transmutation chain of tantalum shares part of the transmutation chain of tungsten and consequently ends up producing rhenium and osmium. Manganese in steels **is** interesting due to the different transmutation behavior under a fission and a fusion environment. Iron irradiated by high energy neutrons tends to produce manganese hut on the other hand, manganese irradiated by low energy neutriins tends to be depleted.

Figures 7 and 8 present the most important transmutation in V4Cr4Ti. It can be noticed that the transmutation rate of vanadium irradiated with high energy neutrons (fast and fusion reactors) is small hut vanadium irradiated by low energy neutrons produce transmutation rates as high as 0.8% per vanadium dpa. Chromium builds-up at the same atomic rate as vanadium is depleted.

Figures 9 and 10 present results for Cu0.5Cr0.3Zr. Copper irradiated by low energy neutrons transmutes to zinc and nickel (with about the same probability). The build-up of both, zinc and nickel, in Cu0.5Cr0.3Zr irradiated at the core position of HFIR occurs at a rate about 0.44% per dpa (relative tu the total number of atoms of the alloy).

Figure 11 displays the variation of the aluminum content in silicon carbide as a function of the fluence. The transmutation of silicon to aluminum occurs. in significant amount, only in a fusion environment (fusion and D-Li neutron source) due to the high threshold value for this nuclear reaction.

CONCLUSIONS

The main transmutations in the candidate alloys analyzed take place on the low energy end of the neutron energy spectrum. Significant variation on the composition of these alloys occur after even a short period of irradiation (several dpa) in a neutron spectrum with a large thermalized component. EBR-II being a fast reactor does not present either the high energy neutrons (above 10 MeV) nor the low energy neutrons in relatively large numbers. Therefore, the transmutation rates in EBR-II of the main alloying elements of the alloys analyzed are the lowest among the irradiation environments considered but similar tu those for the ITER-LM irradiation environment. Exception is made to the transmutation of silicon to aluminum which does not occur in either thermal or in fast fission reactors hut exhibits a high transmutation rate in the fusion spectrum. IFMIF (D-Li neutron source) also produces transmutation rates similar to the ITER-LM environment. Hnwever, the HFIR spectrum produces large transmutations rates in all alloys analyzed. which significantly affects the final composition of the alloy. The use of hafnium cover fur the RB position reduces the transmutation rates significantly for some of the elements of interest; however, the damage rate in this position is much lower than in the core.

REFERENCES

1. F.M. Mann. REAC-3 - A Computer Code Svstem for Activation and Transmutation, Hanford Engineering Development Laboratory Report, HEDL-TME-81-37(1993).

2. B.A. Loomis and D.L. Smith. J. Nucl. Mater. 191-194 (1992) 84-91

3. R.L. Klueh. K. Ehrlich and F. Abe. J. of Nucl. Materials 191-194 (1992) 116-124

4. V.V. Kyhin and D.L. Smith. J. of Nucl. Materials 191-194 (1992) 30-36.

5. I.C. Gomes and D.L. Smith, Neutronics of a D-Li Neutron Source - An Overview, Proceedings of the Third International Symposium on Fusion Nuclear Technology (to he published) June. 1994.

6. I.C. Gomes and D.L. Smith, Characterization of Nuclear Transmutations in Materials Irradiation Test Facilities, Proceedings of the Third International Symposium on Fusion Nuclear Technology (to he published) June. 1994.

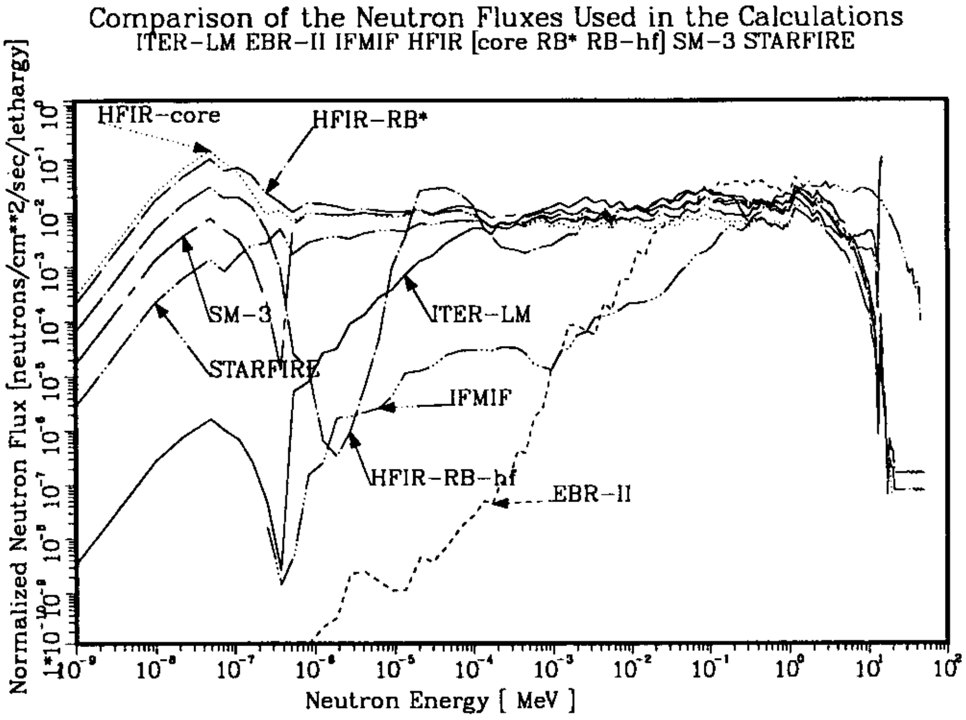

Figure 1. Normalized neutron energy spectra of several fission and fusion facilities.

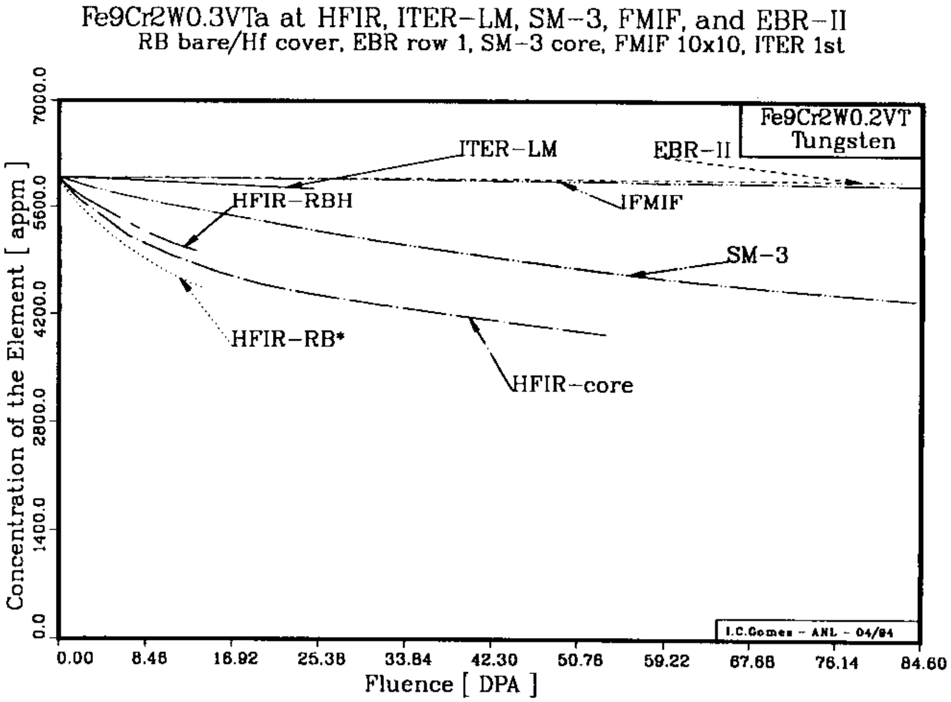

Figure 2. Variation of the tungsten concentration (appm) in Fe9Cr2W0.2VTa as a function of the fluence (DPA) for several facilities considering 2 FPY of operation.

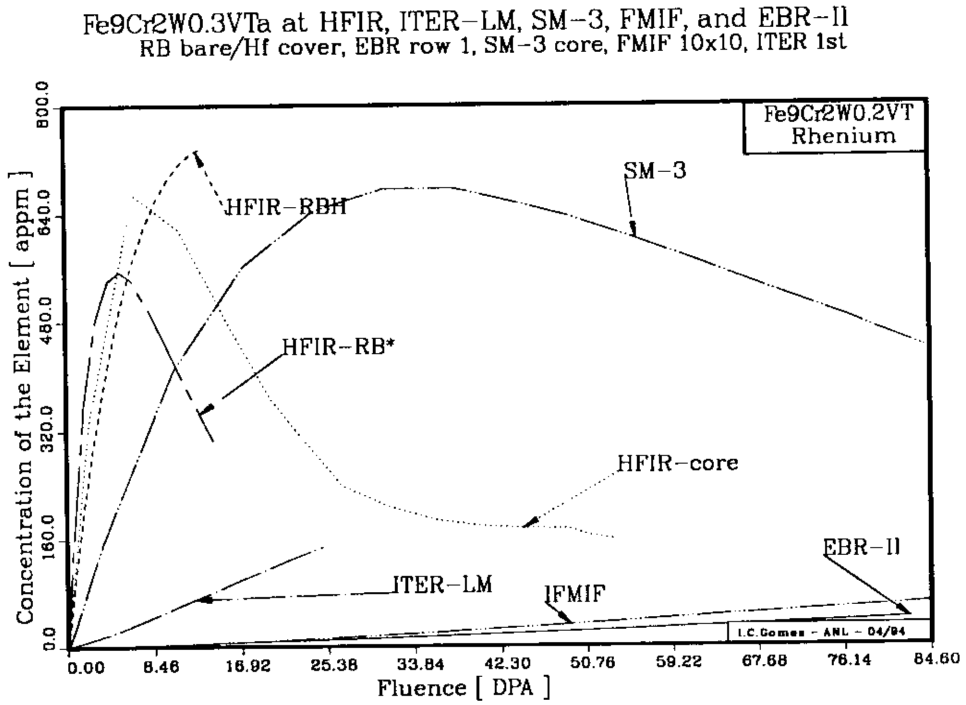

Figure 3. Variation of the rheniuim concentration (appm) in Fe9Cr2W0.2VTa as a function of the fluence (DPA) for several facilities considering 2 FPY of operation.

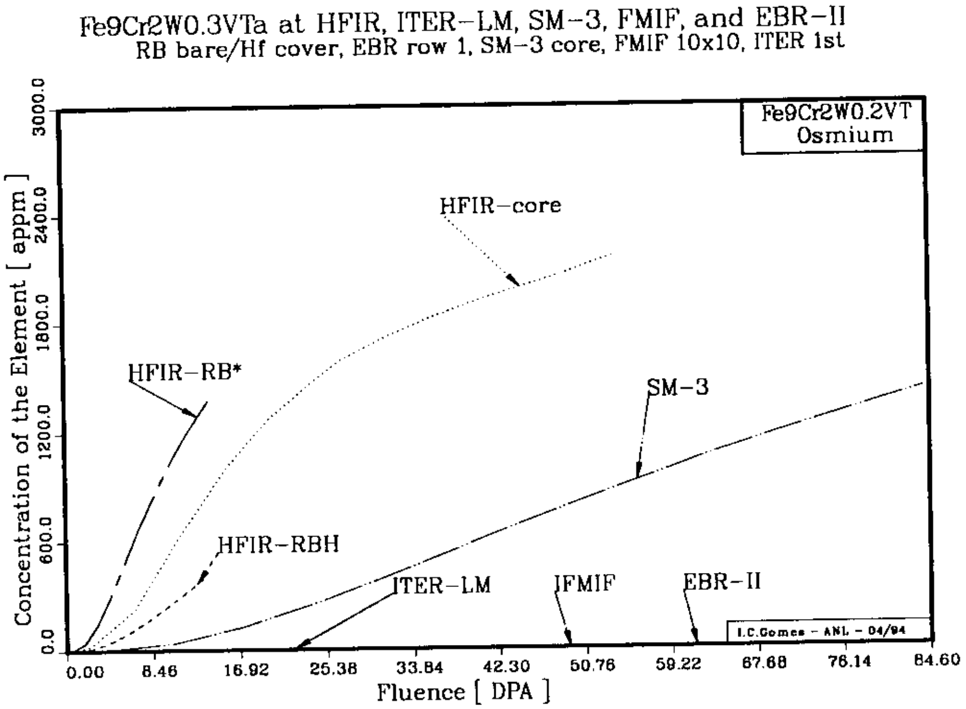

Figure 4. Variation of the osmium concentration (appm) in Fe9Cr2W0.2VTa as a function of the fluence (DPA) for several facilities considering 2 FPY of operation.

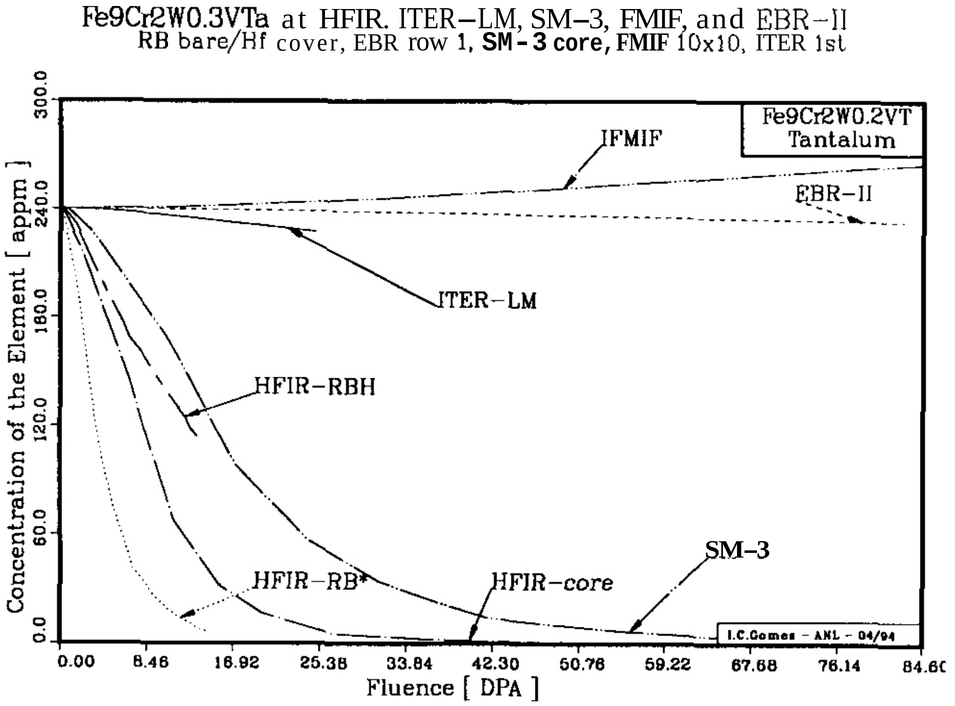

Figure 5. Variation of the tantalum concentration (appm) in Fe9Cr2W0.2VTa as a function of the fluence (DPA) for several facilities considering 2 *FPY* of operation.

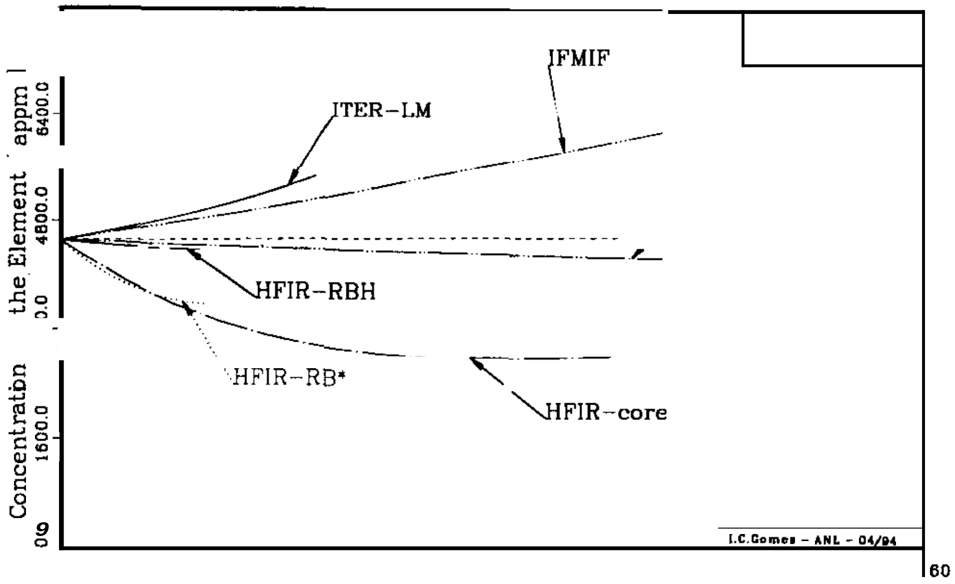

Figure 6. Variation of the manganese concentration (appm) in Fe9Cr2W0.2VTa as a function of the fluence (DPA) for several facilities considering 2 FPY of operation.

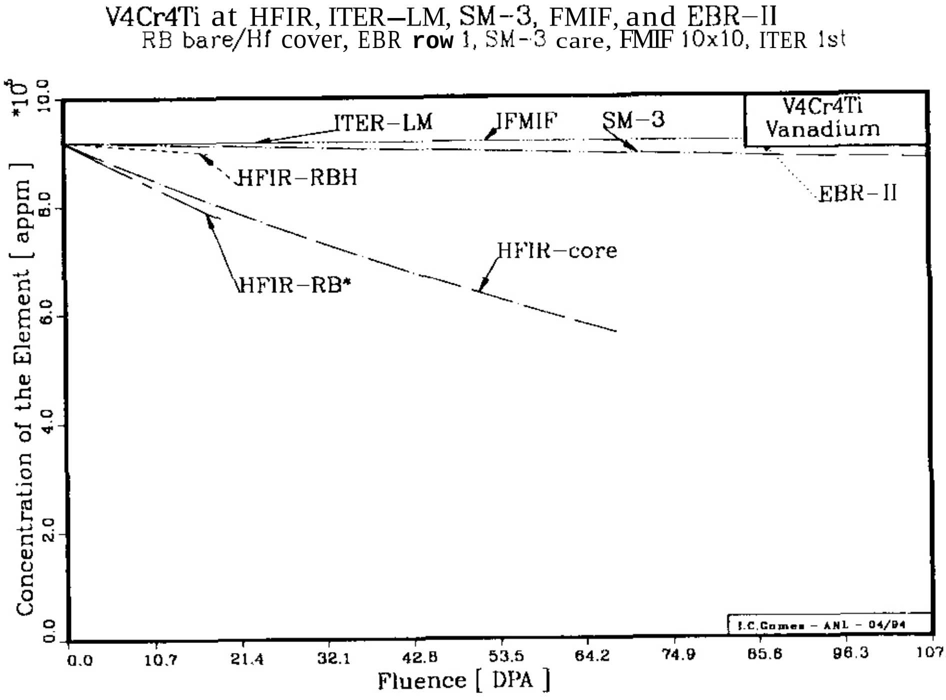

Figure 7. Variation of the vanadium concentration (appm) in V4Cr4Ti as a function of the fluence (DPA) for several facilities considering 2 FPY of operation.

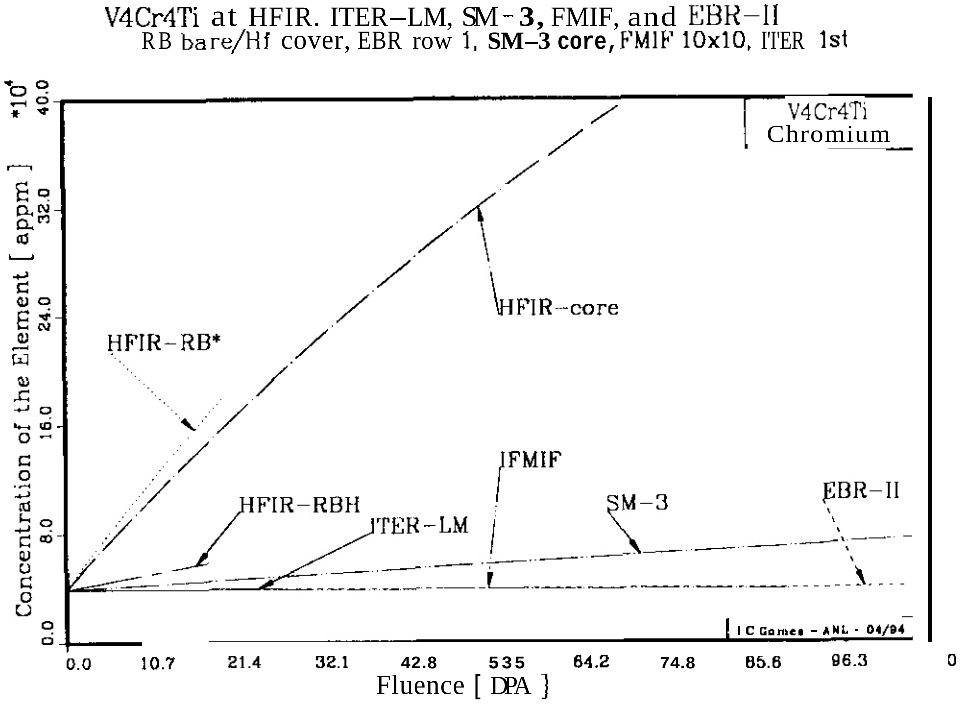

Figure 8. Variation of the chromium concentration (appm) in V4Cr4Ti as a function of the fluence (DPA) for several facilities considering 2 FPY of operation.

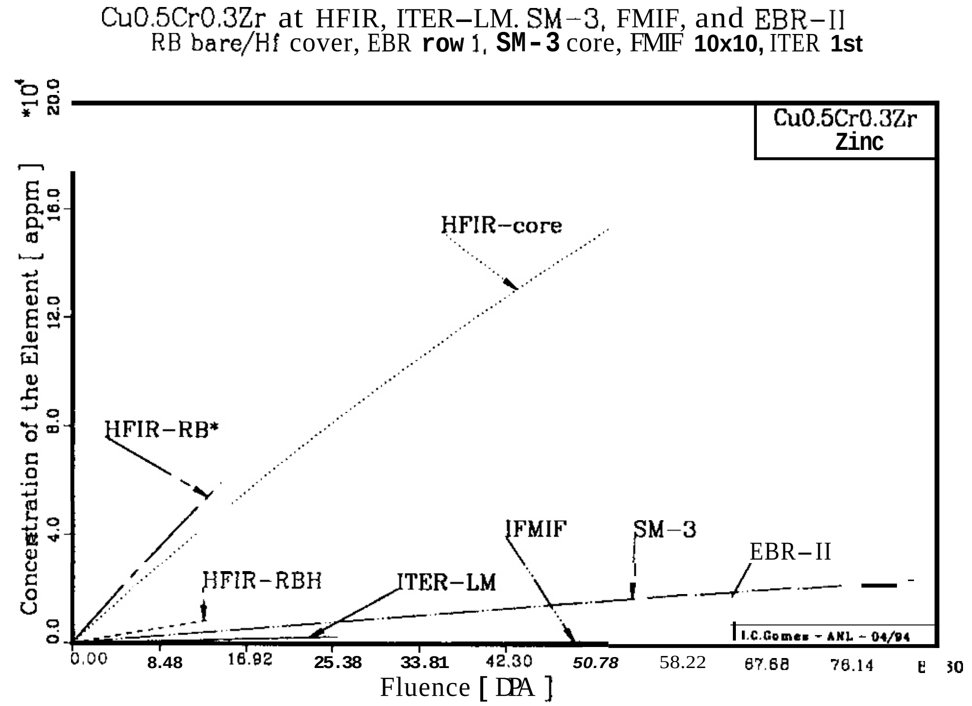

Figure 9. Variation of the zinc concentration (appm) in CuO.5Cr0.3Zr as a function of the fluence (DPA) for several facilities considering 2 **FPY** of operation.

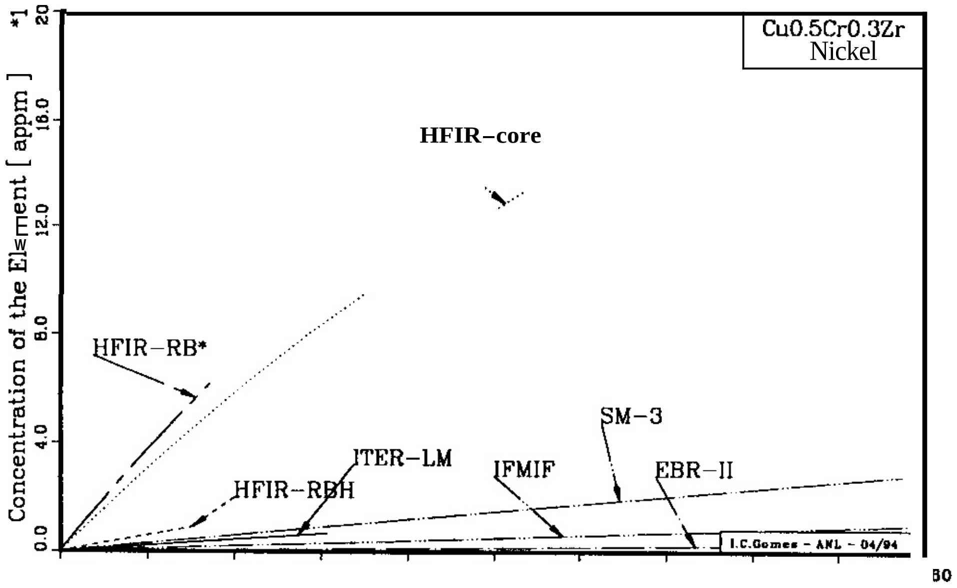

Figure 10. Variation of the nickel concentration (apprn) in CuO.5Cr0.3Zr as a function of the fluence (DPA) for several facilities considering **2 FPY** of operation.

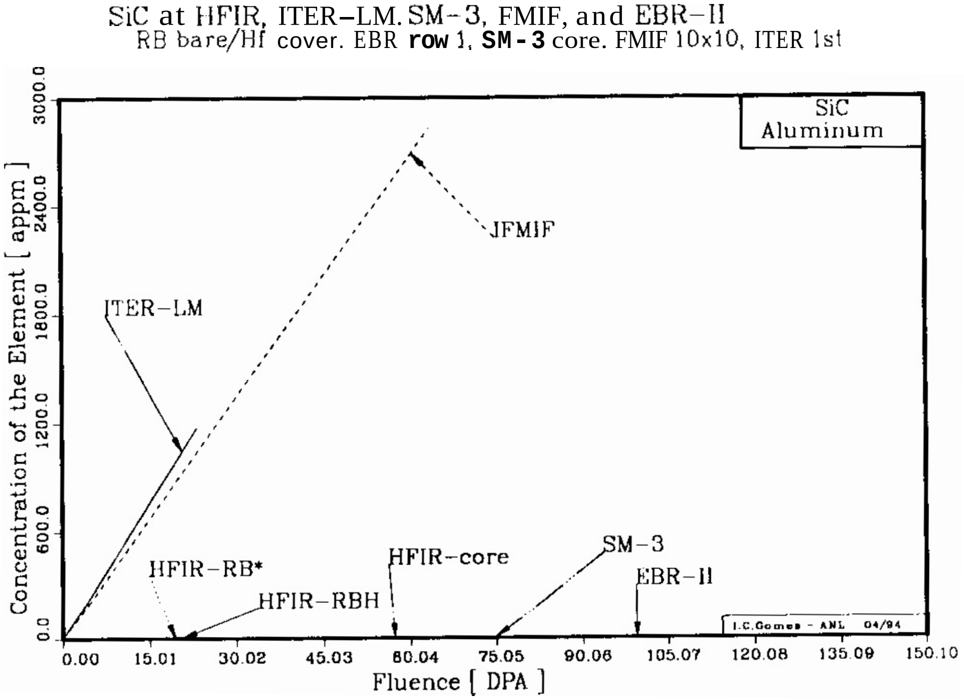

Figure 11. Variation of the aluminum concentration (appm) in SiC as a function of the fluence (DPA) for several facilities considering 2 FPY of operation.

CALCULATIONS TO DETERMINE THE FEASIBILITY OF USING A BORON CARBIDE SHIELD FOR SPECTRAL TAILORING IN THE HFIR FOR VANADIUM ALLOY IRRADIATION

R. A. Lillie (Oak Ridge National Laboratory)

OBJECTIVE

These calculations are part of an effort to design a low temperature irradiation facility in HFIR for vanadium alloys.

SUMMARY

A neutron transport calculation has been performed to determine the feasibility of creating a shielded facility in the Be reflector of the HFIR. It was found that the B_4C provides satisfactory spectral tailoring to reduce production of Cr below the tolerance limit for Cr in the original alloys. The shield would have to be replaced after eight cycles or 5 dpa, but the operations schedule for the HFIR makes it easier to replace the shield after seven cycles. Three shields would then have to be used in order to reach 10 dpa. This facility would provide the equivalent of a low-temperature fast neutron position in the HFIR for development and preliminary qualification of vanadium alloys for fusion devices.

PROGRESS AND STATUS

Introduction

The irradiation performance of vanadium alloys for first wall and blanket structural alloys has primarily been investigated using fast reactor irradiation facilities. However, liquid metal cooled fast reactors do not have coolant temperatures below 350-400°C. This creates a problem for evaluation of fracture and other mechanical properties for devices such as the ITER which will have first wall and blanket structures operating as low as perhaps 200°C. Research reactors operate with coolant temperatures below 100°C, but the thermal flux present in such reactors often produces undesirable transmutations. In the case of vanadium, the reaction $^{51}V(n,\gamma)^{52}V$ followed by a beta decay of the ^{52}V to ^{52}Cr with a 3.75 minute half life causes significant alteration of the original alloy composition.

To overcome this problem, experimental capsules containing V specimens must be surrounded with suitable thermal neutron shields. Previously performed simple hand calculations indicated that of the various materials which have large thermal neutron capture cross sections, only boron or boron compounds containing ^{10}B are satisfactory. Pure elemental cadmium (Cd), gadolinium (Gd), and europium (Eu) or compounds containing these elements can provide sufficient thermal neutron shielding, however at the required small thicknesses (one to five mm) these elements burn up much too fast to be of any practical use. Hafnium (Hf) has too small a thermal capture cross section to be of any use. Since the hand calculations only considered thermal neutron burnup, the current investigation was undertaken to verify the simple hand calculations for a 3 mm thick B_4C shield.

Description of calcu

The analysis of the B_4C shield was performed using the one-dimensional discrete ordinates radiation transport code ANISN.[1] A typical HFIR RB* (Instrumented Be reflector) position was modeled as an infinite 2.5 cm radius cylinder (≈2.97 inch diameter). The source term for all of the transport calculations was constructed by imposing the average of the beginning-of-cycle (BOC) and end-of-cycle (EOC) unperturbed fluxes at the HFIR core midplane at a RB* position on the outer boundary of the infinite cylinder. The unperturbed fluxes were obtained from previously completed two-dimensional calculations. These calculations were performed with the two-dimensional discrete ordinates code DORT[2] using 35 neutron energy group transport data taken from the ANSL-V cross section library[3] to determine the power shift within the HFIR core due to the presence of Hf shielded experiments in two of the RB* positions. The B_4C shield had an inner radius of 2.2 cm and an outer radius of 2.5 cm (3 mm thickness). The volume within the center of the cylinder was treated as void. The transport data for B_4C was taken from the 46 neutron energy group DABL69 cross section library.[4] The transmutation (V to Cr, V to Ti, and gas production) and dpa cross sections were taken from 105 neutron energy group data derived from the RECOIL data base.[5]

To determine the bumup of ^{10}B in the B_4C shield, one-dimensional ANISN calculations were performed for a large number of ^{10}B atom densities to determine the bumup rate as a function of ^{10}B atom density In addition, the fluences from these calculations (normalized to one HFIR full power day at 85 MW) werc folded with the various V transmutation and dpa cross sections to determine the transmutation and dpa rates as a function of ^{10}B atom density. The functional dependence of these quantities on ^{10}B atom density was then fitted and input to a small in-house bumup code to determine the time history of the ^{10}B in the B4C shield and the Cr production and dpa level in vanadium.

The results from these calculations are summarized in Table 1

Table 1. V to Cr Transmutation and Required Full Power Days at 10 dpa Level Assuming the B_4C Shield is Changed Out every 7 HFIR Core Cycles

Configuration	dpa Level	Required Full Power Days at 85 MW	Cr Production (% of V)
No shield	10	345	15.5
3 mm B_4C shield	10	365	<0.12

The fluence spectra per full power day in a HFIR RB* position with the 3 mm thick B_4C shield are presented for several irradiation times in Fig. 1. As expected, with increased ^{10}B bumup, i.e., increased irradiation time. the thermal fluence exhibits a rapid increase while the epithermal fluence exhibits a slower increase and essentially no change occurs in the fast flucnce.

The V to Cr uansmutation and dpa levels in the vanadium are given in Fig. 2 as a function of full power days (fpd). Even though the B4C shield is only needed for 154 fpd, i.e., seven cycles, it may be used for approximately 180 fpd to reach the 5.0 dpa level. At this dpa level, the produced Cr is still less than 0.2%. If this scenario is chosen, only two B_4C shields would be needed to reach the 10 dpa level and the produced Cr would still be less than 0.5 %.

In producing the data in Table 1 and Figs. 1 and 2, a number of conservative approximations were employed. First, in determining the ^{10}B bumup, the bumup rate at the beginning of a fpd was employed for the entire fpd resulting in a slight overestimate of the bumup. Second, the V to Cr transmutation rate at the end of each fpd was employed to overestimate the Cr production, and third. the dpa rate at the beginning of each fpd was employed to underestimate the dpa level. In addition to these conservative approximations, the one-dimensional model produces overestimates of the bumup rate since only the maximum or HFIR midplane fluence was employed. Thus, the performance of a 3 mm thick B4C shield should be slightly better than that indicated by the results presented here.

CONCLUSIONS

Irradiation of vanadium alloys at temperatures of 250°C or even below may be conducted in the HRR in instrumented positions. Displacement levels of 10 dpa can be reached in about one full power year with transmutation-produced Cr at levels well below the tolerance on the original alloy composition for this

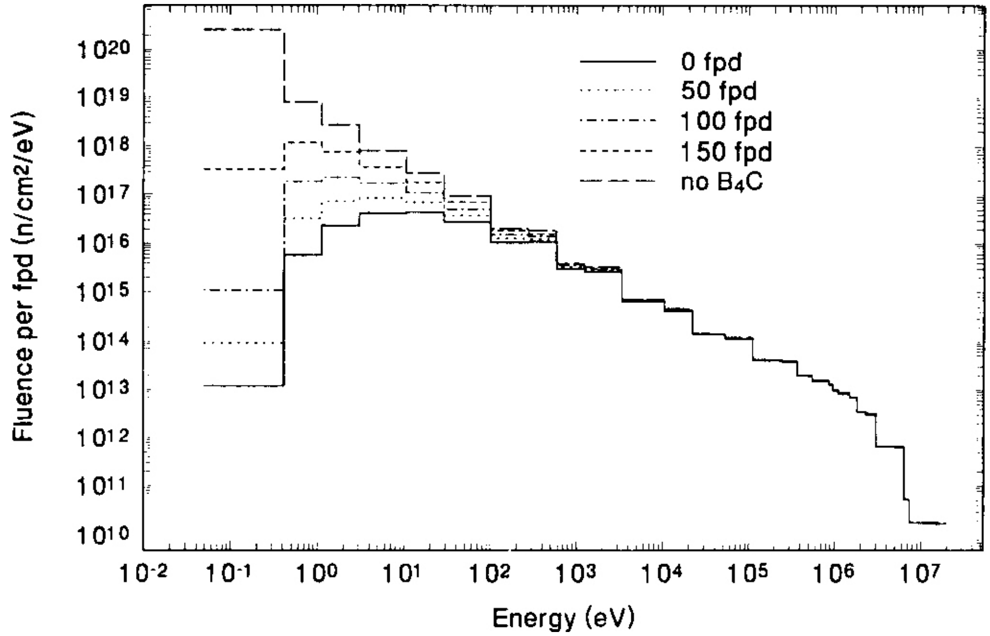

Fig. 1. Fluence spectra per full power day in HFIR RB* position iwth 3 mm B_4C shield around experimental capsule.

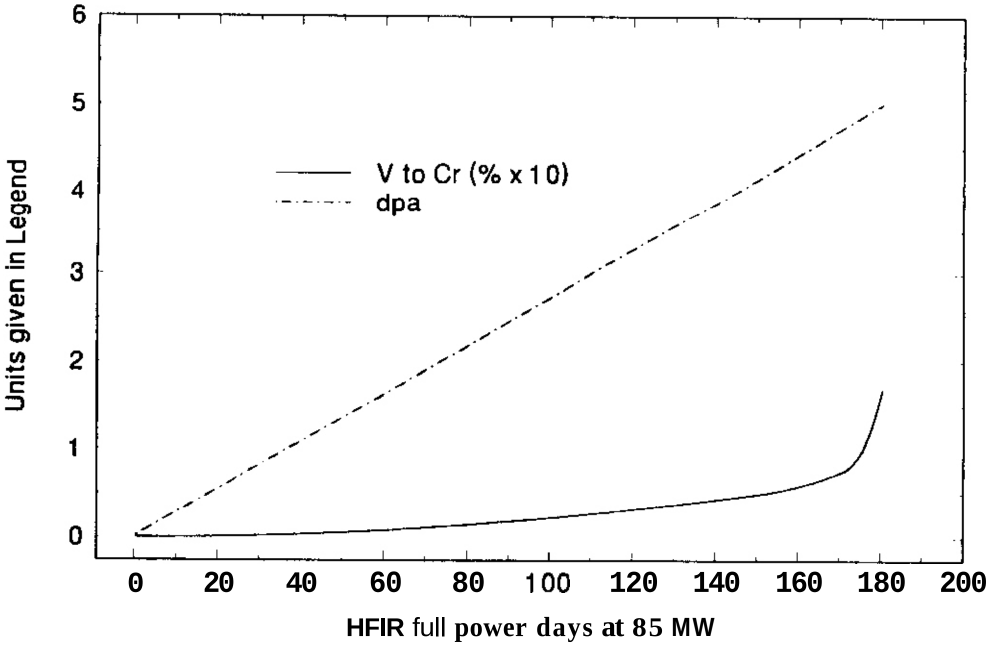

Fig. 2. Transumation and dpa in V with 3 mm B4C shield around experimental capsule in HFIR RB* position.

element. This irradiation facility effectively becomes a low-temperature fast reactor position in a research reactor.

FUTURE WORK

Design will begin on this concept to investigate the thermal performance of such an irradiation facility.

REFERENCES

1. W. W. Engle, Jr., "ANISN, A One-Dimensional Discrete Ordinates Code with Anisotropic Scattering," K-1693, *Oak* Ridge Gaseous Diffusion Plant (1967).
2. W. A. Rhoades and R. L. Childs, "The DORT Two-Dimensional Discrete Ordinates Transport Code," Nucl. Sci. & Engr. 99 88 (1988).
3. W. E. Ford, III, et al., "ANSL-V ENDF/B-V Based Multigroup Cross-section Libraries for Advanced Neutron Source *(ANS)* Reactor Studies," ORNL-6618, *Oak* Ridge National Library' (1990).
4. D. T. Ingersoll, et al., "DABL69: A Broad Group Neutron/Photon Cross Section Library for Defense Nuclear Applications, ORNL/TM-10568, *Oak* Ridge National Laboratory (1988).
5. T. A. Gabriel, et al., "Recoil Spectra, Damage Energy, and Displacement Cross Sections," Trans. Am. Nucl. Soc. 21 67 (1975).

TRANSMUTATION IN COPPER-BASE BRAZING MATERIALS - F. A. Garner, L. R. Greenwood and D. J. Edwards (Pacific Northwest Laboratory)"

OBJECTIVE

The objective of this effort is to determine the impact of transmutation on the performance of various brazes used to join copper alloys that are candidates for high heat flux service in fusion devices.

SUMMARY

Brazing compounds containing silver or gold will transmute during irradiation, forming significant amounts of either cadmium or mercury, respectively, in all neutron spectra of current interest to the fusion materials program. The impact of this transmutation on braze performance and on development of fission-fusion correlations has yet to be determined, but will be addressed in an irradiation experiment that was recently completed in FFTF-MOTA. A lesser amount of transmutation will occur in brazes containing tin, but no specimens containing brazes with tin have yet been irradiated.

PROGRESS AND STATUS

Introduction

In addition to the development and testing of materials for high heat flux applications in fusion devices, consideration must be directed toward the development and testing of joining methods for these materials. Brazing is a traditional method for joining of copper alloys, and a CuAgSn braze is being considered as a compliant layer for the ITER first wall. The impact of neutron irradiation on the stability and performance of brazes has not previously been explored, however.

An experiment that addresses the irradiation performance of brazes has just completed irradiation in FFTF/MOTA-2B. It involves the use of brazed TEM sandwiches and lapped minitensiles. The alloy employed was GlidCop CuAl25 and the brazes were CuAg, CuAu, TiCuAg and TiCuNi.[1]

As part of this study the radioactivation and transmutation aspects are being examined. Since the transmutation of copper bas been examined previously' and that of nickel is not very significant, this report examines the transmutation of Ag, Au, and Sn in FFTF, HFIR and STARFIRE.

Results of Calculations

Silver and gold will transmute strongly in almost all neutron spectrum of current interest. The main transmutation products in silver arise from (n,γ) reactions. Ag-107 forms Ag-108, with a 2.4m half-life, which decays 97.2% of the time to Cd-108 and 2.8% of the time to Pd-108. The Cd-108 isotope is stable but will transmute to Cd-109, with a half-life of 462d, decaying back to Ag-109. The Ag-109 isotope captures neutrons to produce Ag-110 (25s) and Ag-110m (250d). The latter

---

"Pacific Northwest Laboratory is operated for the U.S. Department of Energy by Battelle Memorial Institute under Contract DE-AC06-76RLO 1830.

isotope is the major source of radioactivity in irradiated silver. The 25s ground state is produced at a rate about twenty times larger than the isomer, but both decay almost completely to Cd-110, although some forms Pd-110. The cadmium formed is rather stable, with most subsequent neutron captures leading to other stable isotopes of cadmium. The predictions shown in figures 1-3 assume that the Ag-110m has already decayed to Cd-110. In the STARFIRE spectrum there will he some production of Pd-106 from Ag-107. Ag-109 will undergo a (n,2n) reaction, however, to form Ag-108. which then decays to Cd-108 and Pd-108. The net effect of these two reactions will be a slightly enhanced production of palladium.

The major transmutation in gold comes from the (n,γ) reaction of Au-197 to Au-198, which decays with a 2.7 day half-life to stable Hg-198. Further captures lead to other stable mercury isotopes. In the STARFIRE spectrum, the (n,2n) reaction leads to Au-196, which decays with a 6.2 day half-life, mainly to stable Pt-196 and weakly to Hg-196. Further reactions with Pt-196 always return to Au, and thus mercury is the main transmutant in all cases. Figures 1-3 also show the transmutation of gold.

The transmutation of tin is rather low in all three reactors (HFIR, FFTF, and STARFIRE) due to the predominantly low cross sections and the fact that most of the (n, γ) capture reactions lead only to other tin isotopes. For example, Sn 115-117 have the largest cross sections; however. the reactions simply move up the Sn chain until Sn-120. The main transmutation will be produced by Sn-112 to Sn-113 (115 d) which eventually decays to In-113, which in turn may transmute hack to Sn-114. However, Sn-112 is only 0.97% of natural tin; hence, the net transmutation production will only yield tenths of a percent transmutant per year.

There will also be some transmutation from Sn-120 and Sn-122 to Sb-121 and Sb-123, both of which are stable. These can in turn transmute somewhat to tellurium. Sn-124 will produce 125-Sb (2.8y), which is the biggest concern for activation considerations due to its long half-life. This will eventually decay to Te-125, which is stable. None of these isotopes of tin have significant thermal cross sections; hence, the transmutation rate will be low, reaching only tenths of a percent per year. with the largest transmutant rate occurring in HFIR. In STAKFIRE, the (n,2n) reactions at 14 MeV will produce similar amounts of In-113 and Cd-111, as well as Sb-121 and Sb-123.

Altogether. the net transmutation will be less than 1% per year, the highest rates being for HFIR. The major long-lived activation products of concern are Sb-125 (2.8y) and Sn-113 (I 15d). Sb-125 will be by far the biggest problem, due to its higher abundance and cross section, as well as its higher energy gamma rays and longer half-life.

Discussion

It is anticipated that significant formation of mercury or cadmium may degrade the performance of brazed joints in irradiated copper components. This possibility will soon be tested as examination proceeds on lapped minitensile specimens irradiated in FFTF. The lesser amount of transmutants formed in Sn-containing brazes may also impact the performance of brazed joints, but no irradiation tests are available on this type of braze.

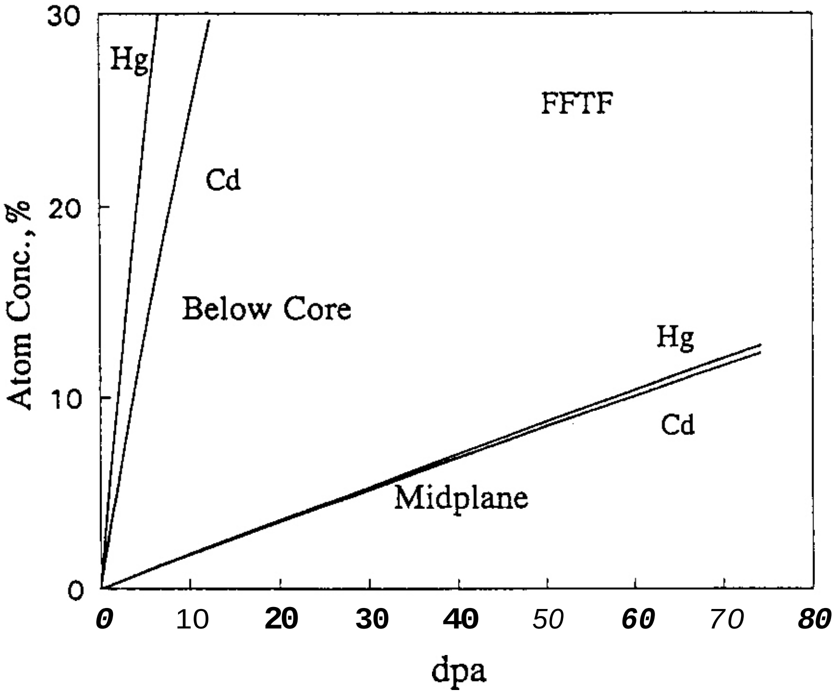

Figure 1. Production of mercury and cadmium from gold and silver in FFTF at the midplane and at -66cm, which is the middle of the below-core basket in MOTA.

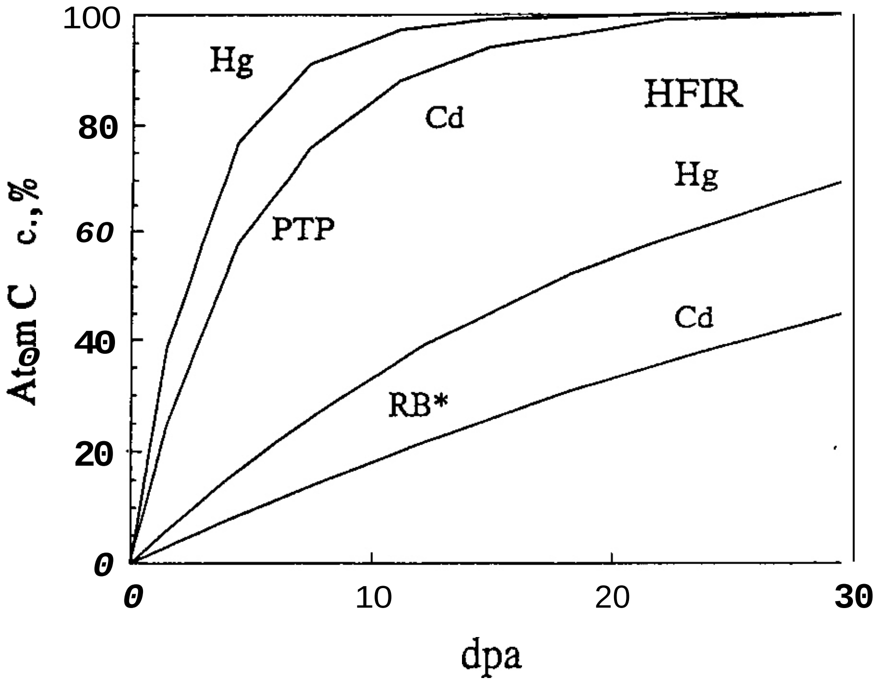

Figure 2. Production of mercury and cadmium from gold and silver in ITER.

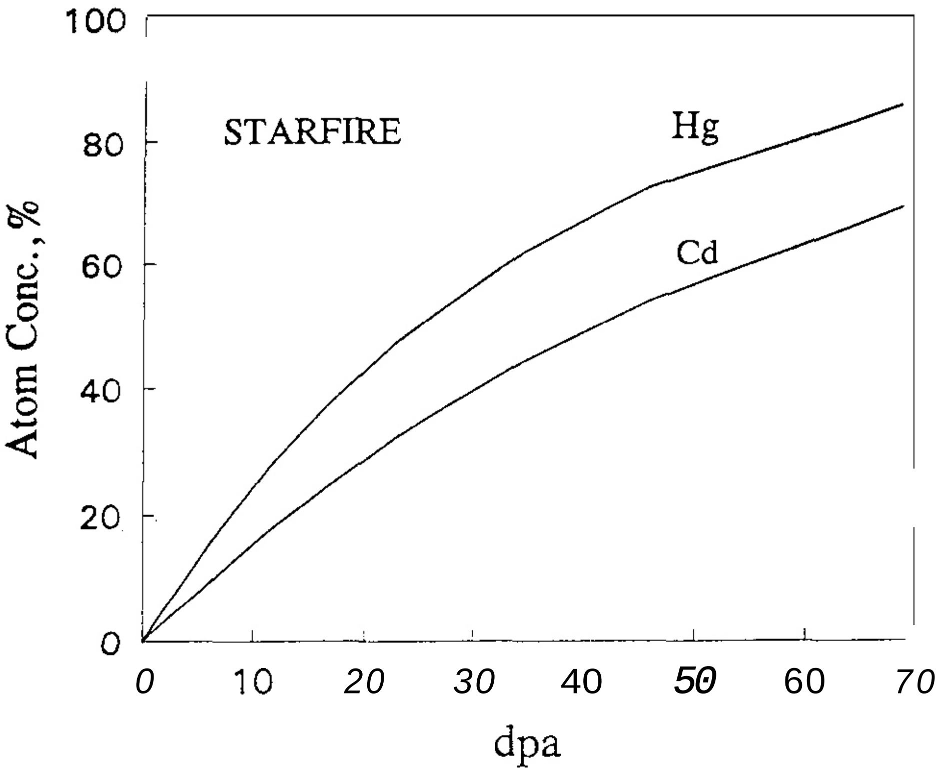

Figure 3. Production of mercury and cadmium from gold and silver in STARFIRE.

FUTURE WORK

Tensile testing and fractographic examination on irradiated lapped minitensile specimens will proceed.

REFERENCES

1. F. A. Garner, M. L. Hamilton, D. J. Ednards, B. N. Singh. J. F. Stubbins, T. Shikama. S. J. Zinkle and P. Samal, Fusion Reactor Materials Semiannual Progress Report DOE/ER-0313/10, 1991 pp. 186-191.

2. F. A. Garner, L. R. Greenwood and F. M. Mann, Fusion Reactor Materials Semiannual Progress Report DOE/ER-0313/13, 1993, pp. 43-47.

3.0 MATERIALS ENGINEERING AND DESIGN REQUIREMENTS

ITER MATERIAL PROPERTIES HANDBOOK - J. W. Davis (McDonnell Douglas Aerospace)

OBJECTIVE

The primary objective of this activity is to support the development of a Materials Properties Handbook for use during the Engineering Design Activity of ITER. A secondary objective is early identification of gaps in the material property database so that R&D to fill these gaps can be accomplished within the EDA time frame.

SUMMARY

In December the ITER Joint Central Team authorized the creation of a Materials Properties Handbook. This Handbook is a cooperative activity between the four parties of ITER (Japan, the E.U., the RF., and the U.S.). The U.S. Home Team has been selected to coordinate the documentation, while all four Parties will provide data. During this period the effort focused on organizing this activity. developing a format for use by all of the parties. and demonstrating the ability to electronically transfer files between the four parties. First draft of the Handbook is scheduled for July.

PROGRESS AND STATUS

Introduction

The performance requirements of many of the ITER components will put severe constraints on material selection. Large variations in material ppertie s caused by errors in interpreting the database could be the difference between these components working or not. Since material properties can come from a variety of sources, some developed from actual data, while others are extrapolations from similar materials, it is relatively easy to reach the wrong conclusions regarding a components life or operational capabilities with an incomplete or erroneous material database. To avoid this possibility it is important to design and analyze the ITER components using a uniform and verifiable database.

Currently there are a number of a number of data books and databases available which contain information on materials of interest to fusion. Some of these are: the U.S. Material Handbook for Fusion Energy Systems, the IEA Fusion Materials Handbook, the JAERI Material Performance Database (JMPD), the E.U.'s High Temperature Materials Data Bank (HTM-DB) at Petten, and the Russian Federation's PFC materials database which is a PC Windows based system. Many of these databases have restricted distribution and cannot be used by all of the ITER participants or do not contain all of the materials of interest to ITER. In addition. since these data books are not funded by the ITER program there is no guarantee. that additional property information, not currently contained in these books. could be developed in a time frame to meet the ITER schedules. It was for these reasons that ITER decided to develop its own Materials Properties Handbook. The ITER Material Properties Handbook was formally created on **13** December **1993** with the release of ITER Task Agreement **S72TD 04 93-11-23 FU.** The Handbook is the responsibility of the San Diego Joint Work Site of ITER. The U.S. is responsible for coordinating this activity along with equal participation among the four ITER partners (Japan, the E.U., the R.F. and the U.S.).in supplying information to the Handbook.

First Working Group Meeting

While the Handbook was officially chartered in December of **1993** actual work did not begin until after the First Working meeting which was held at the ITER Joint Work Site in San Diego on February **7-9, 1994.** The purpose of this meeting was to review the near term data needs for ITER and to identify which of the ITER partners would be responsible for the preparation of the data pages. In establishing priorities for preparing the data it was agreed that the materials used in the divertor, first wall and blanket, magnet, and automatically extract attached files such as the Eudora mail system. Eudora is the preferred mail system for the ITER JCT and as a result they would prefer to have participants sending files to them using this program. Japan is working on the connection. Because of the difficulty in transferring attached files to non-Joint Central Team sites that cannot convert BinHex files or retrieve electronic files, the Director of the Joint Central Team directed that all Home Teams insure that their participating organizations must have this capability. Once everyone gets to using Eudora, or an Eudora "like system" communications should be simpler. However, even with this capability, the biggest problem will still be to get people to read their e-mail more frequently than once once a week or once a mouth, particularily for those not used to working on e-mail.

Organization d Format

One of the goals of the Handbook program is to not only develop datapages for use on lTER but also to put this database in an electronic format for easy retrieval. A key in establishing an electronic database is to develop an outline or format for designating the materials. Because it is difficult to change the numbering sequence once it is established one needs to provide for growth in the original outline. Table 2 shows the organization of the Handbook. Since material specialists will be working on the ITER program it was decided to organize the Handbook by class of material (metals, ceramics. composites, gases, lubricants, etc.) and subdivide the headings by alloying element , phase, or common or commercial designation which would be familiar to material specialists. For future growth blanks or unassigned sections are identified as reserved. In the areas where a material system is identified but no material class is shown, such as femtic steels, indicates that a particular alloy within this class has not been identified by the ITER program at this time.

Future Work

The next Working Group is scheduled for the July 11-15, 1994 in Garching, Germany. Prior to that meeting all participants are scheduled to provide data so that a draft of the Handbook can be presented at that meeting. In preparation for the meeting a manual is being developed describing the organization of the Handbook and the format for presenting the data. Currently it is anticipated that the participants can supply the data either in a spread sheet type of format such as in "Excell" or as an equation that can be plotted in a graphics routing and inported into Microsoft word for distribution electronically. Work will also continue on verifying the ability of all of the participants to transfer the files electronically.

Materials code	Material Description
A	METALS
AA	Austenitic Steels
AA-01	316
AA-02	316L
AA-03	316 LN
AA-04	316 SPH (RCC MR1S)
AA-05	JN1
AA-06	RF-20Cr-16Ni-6Mn
AB	Femtic / Maninsitic Steels
AC	Other Steels
AD	Nickel Base Alloys
AD-01	Inconel 625
AD-02	Incoloy 901
AE	Titanium Base. Alloys
AE-01	Ti-6Al-4V
AF	Vanadium Based Alloys
AF-01	V-5 Cr-5Ti
	Reserved
AH	Reserved
AI	Reserved
AJ	Copper and Copper Alloys
	Pure Copper
AJ-02	Cu-Cr-Zr
AJ-03	Cu-Be-Ni
AJ-04	Dispersion Strengthened
AJ-05	Copper-Tin
	Beryllium
AK-01	Plasma Sprayed
AK-02	Sintered
AL	Reserved
	Reserved
	Reserved
AN	Reserved
AO [redacted]	Brazes
AP [redacted]	Liquid Metals
AP-01 [redacted]	Lithium
AP-02	Lithium-Lead
AP-03	Lead
AP-04	Potassium
AP-05	Sodium
AP-06	Sodium-Potassium (NaK)
B	CERAMIC MATERIALS
BA	Aluminium Based
BB	Lithium Based
BC	Spinels
C	COMPOSITE MATERIALS
CA	Resin based Composites
CB	Carbon Composites
CC	Metal Matrix Composites
D	Gases
DA-01	Helium
E	Lubricants

4.0 FUNDAMENTAL MECHANICAL BEHAVIOR

No contributions.

5.0 RADIATION EFFECTS, MECHANISTIC STUDIES, THEORY AND MODELING

VOID SWELLING IN BINARY FE-CR ALLOYS AT 200 DPA - D. S. Gelles, (Pacific Northwest Laboratory)"

OBJECTIVE

The objective of this work is to determine lifetime limits for reduced activation ferritic alloys by providing a better understanding of the inherent swelling resistance of ferritic alloys.

SUMMARY

Microstructural examinations have been performed on a series of binary Fe-Cr alloys irradiated in the FFTF/MOTA at 425°C to 200 dpa. The data represent the highest swelling levels reported in neutron irradiated ferritic alloys. The alloy compositions ranged from 3% to 18% Cr in 3% Cr increments, and the irradiation temperature corresponded to the peak swelling condition for this alloy class. Density measurements showed swelling levels as high as 7.4%, with the highest swelling found in the Fe-9Cr and Fe-6Cr alloys. Microstructural examinations revealed that the highest swelling conditions contained well-developed voids, often as large as 100 nm, and a dislocation network comprised of both $\frac{a}{2}$<111> and a<100> Burgers vectors. Swelling was lower in the other alloys, and the swelling reduction could he correlated with increased precipitation. These results are considered in light of the current theories for low swelling in ferritic alloys, but no theory is available to completely explain the results.

PROGRESS AND STATUS

Introduction

The present effort is one of a series that follows a set of simple Fe-Cr alloys ranging from 3% to 18% Cr in 3% Cr increments through a number of irradiation experiments.[1-4] Irradiations have been performed both in the Experimental Breeder Reactor (EBR) -II[1,2] and the Fast Flux Test Facility Materials Open Test Assembly (FFTF/MOTA),[3,4] and the present effort examines the alloys following irradiation in FFTFIMOTA to the highest dose attained, 200 dpa. The intent is to provide further understanding of the processes controlling void swelling in the ferritic alloy class.

Void swelling due to radiation damage is found to be significantly lower in ferritic alloys than in austenitic alloys.'. for example However, the cause of this difference in response is not yet clearly understood, Several theories have been proposed, but none have received completely general acceptance. Three recent papers summarize these theories, and may be referred to for details.'.' The most pertinent mechanisms are 1) the point defect bias to dislocations is inherently lower in the body centered cubic ferritic crystal structure,' 2) the presence of two competing dislocation Burgers reduces vacancy accumulation at voids,[1,9] 3) solute trapping of defects leads to increased recombination,'' and 4) the dislocation and void evolution produce populations that are not ideal for void swelling optimization in ferritic alloys.[11-12] However, it is important to differentiate between the two stages controlling swelling response: void nucleation (or swelling incubation) and void growth (or steady state swelling). Many of the mechanisms defined above only provide an

---

"Pacific Northwest Laboratory is operated for the U.S. Department of Energy by Battelle Memorial Institute under Contract DE-AC06-76RLO 1830.

explanation for the delayed onset of steady state swelling. For example, solute trapping would not be expected to control steady state swelling because the solute would eventually be segregated to point defect sinks. The present microstructural study is more pertinent to steady state swelling response.

Experimental Procedure

The International Nickel Company prepared alloys used for this and previous studies. Compositional impurities have previously been defined,' but it is worth emphasizing that the Fe-3Cr alloy has behaved anomalously because it contains significantly more impurity than was originally expected.'

For the present experiment, specimens were put into transmission electron microscopy (TEM) packet H4 and located in in-core weeper positions of the FFTF/MOTA from the beginning of cycle 4 and throughout the remaining operation of FFTF. The irradiation history for packet H4 was as follows:

MOTA 1B basket 2F-5 to 2.98×10^{22} n/cm' at an average temperature of 431°C.
MOTA 1C basket 2F-5 to 6.98×10^{22} n/cm' at 420°C.
MOTA 1D basket 2F-5 to 5.05×10^{22} n/cm' at 404°C.
MOTA 1E basket 2F-2 to 9.67×10^{22} n/cm^2 at 414°C.
MOTA 1F basket 2F-2 to 9.60×10^{22} n/cm^2 at 405°C.
MOTA 1G basket 2E-3 to 7.18×10^{22} n/cm^2 at 417°C.
MOTA 2B basket 3A-5 to 6.35×10^{22} n/cm^2 at 133°C.

Therefore, during that period, the specimens in packet H4 received a fluence of 4.78×10^{23} n/cm^2 at an average temperature of 418 + 11°C, hereafter reported as 420°C. The dose achieved, calculated from reference 13, which is based on dosimetry measurements from MOTA 1F, varies from 198 to 201 dpa, depending on alloy composition.

Microstructural examinations were performed on a JEOL JEM 1200EX scanning TEM operating at 120 kV and outfitted with a Tracor Northern energy dispersive x-ray fluorescence (EDX) detector and TN5500 computer and with a Gatan Electron energy loss spectrometer.

Results

Swelling

Results of density change measurements for simple ferritic alloy specimens irradiated at 420°C to 200 dpa are provided in Table I. Table 1 contains dose estimates for each alloy based on conversions from reference 13. Table I also includes density change results for specimens irradiated to lower dose in FFTF/MOTA experiments that were started later in the reactor history.' As shown from Table I, swelling values are 7.4% or less. The highest swelling value, 7.4%, is found in Fe-9Cr, and the next highest swelling, 7.0%, is in Fe-6Cr. In comparison, Fe-12 Cr swelled 2.8%. Fe-3Cr swelled 1.8%, and Fe-15Cr and Fe-18Cr swelled 1.3%. If these results are compared as a function of dose, assuming linear dependence between data points at two doses, the highest swelling rate is found for Fe-9Cr. 0.097%/dpa. This value is somewhat higher than the value previously estimated from EBR-II data of 0.06%/dpa,[2] where it was found that swelling levels in Fe-12Cr reached 4.72%, and swelling levels in Fe-9Cr reached 4.14%, at 1.9×10^{23} n/cm' or 91.2 dpa.

Microstructures

Microstructural examinations revealed that all specimen conditions had developed void swelling in the form of uniform arrays of voids. The amounts of void swelling and the relative void sizes were in proportion to the density changes measured. Voids were uniformly distributed, except in a few instances where denuded zones or reduced densities were found adjacent to grain boundaries, apparently associated with grain boundary migration. Also, examples were found in the Fe-18Cr alloy where larger voids were attached to needle shaped precipitates. Examples at low magnification are provided in Figure 1. Of particular note are the wide range of void sizes and the array of precipitates in the Fe-3Cr specimen shown in Figure 1a and the needle shaped precipitate with two large voids attached in the Fe-18Cr specimen in the lower right of Figure 1f. It may be noted that a broad void size distribution that includes small sizes is an indication that steady state swelling has not yet been achieved. The precipitates seen in Figure 1a are due to impurities in the Fe-3Cr alloy. Figures 1b, 1d and 1e display surface etching effects in the form of large pits; these are believed to be artifacts arising from preparation difficulties and were ignored.

Table 1. Swelling as measured by density change for simple ferritic alloy specimens examined in this study with comparison of specimens irradiated to lower dose.

CODE	Alloy	Dose (dpa)	Density Irradiated	Density Unirradiated	Swelling (%)
651A	Fe-3Cr	137.7	7.77042	7.8826	1.444
65H4	Fe-3Cr	197.6	7.74497	7.8826	1.777
661A	Fe-6Cr	138.2	7.65045	7.8185	2.197
66H4	Fe-6Cr	198.3	7.30779	7.8185	6.989
671A	Fe-9Cr	138.6	7.76389	7.7933	1.540
67H4	Fe-9Cr	199.0	7.2573	7.7933	7.386
6A1A	Fe-12Cr	139.1	7.71258	7.7596	0.610
6AH4	Fe-12Cr	199.6	7.54631	7.7596	2.826
6N1A	Fe-15Cr	139.6	7.73933	7.7461	0.087
6NH4	Fe-15Cr	200.4	7.64825	7.7461	1.279
6R1A	Fe-18Cr	140.1	7.68686	7.7233	0.474
6RH4	Fe-18Cr	201.1	7.62793	7.7233	1.250

Contrast experiments have been performed on each irradiated specimen condition to provide a detailed understanding of the dislocation and void structures. Examples are shown for each of the alloys in Figures 2 through 7. In each case, a stereo pair using $\vec{g} = 200$ is shown in parts a) and b), dislocation contrast using $\vec{g} = 0\bar{1}1$ is shown in part c) and void contrast is shown in part d) for a foil near (011) orientation that is tilted near (012) for part b). Void shape analysis in the following description is based on figures included in reference 14.

Figure 2 shows examples of the dislocation and void structures in Fe-3Cr following irradiation at 420°C to 200 dpa. Figure 2a displays horizonal features in strong contrast consisting of a[100] loops and dislocation line segments and more vertical features in lower contrast representing all the $\frac{a}{2}<111>$ dislocations present superimposed on an array of voids in poor contrast. Examination of the stereo model from Figures 2a and 2b reveals that the a[100] loops are steeply inclined, that the $\frac{a}{2}$<111> dislocation segments form a network that sometimes includes a[100] segments, and that the voids are uniformly distributed. Figure 2c shows a large number of loops that do not appear in Figure 2a that must therefore be of Burgers vector a[010] and a[001], distributed on planes approximately 45° to the plane of the micrograph. Therefore, from this sequence, it can be demonstrated that the dislocation structure in Fe-3Cr after 200 dpa at 420°C is predominantly a<100> in character, consisting primarily of loops, but a<100> and $\frac{a}{2}$<111> dislocation segments are present in the form of a dislocation network. Figure 2d can be used to demonstrate that voids vary widely in size, that void shape is equiaxed with the predominant shape equally truncated between cubes and dodecahedra (with a truncation factor between 0.4 and 0.5). Also, the precipitation due to an unexpectedly high impurity content is shown to be in the form of dark equiaxed particles, (approximately 20 nm in diameter) that are uniformly distributed.

Figure 3 provides examples of the dislocation and void structures in Fe-6Cr following irradiation at 420°C to 200 dpa. Figure 3a reveals that the density of a[001] dislocations is lower than that in Fe-3Cr, that most dislocations are line segments, and that $\frac{a}{2}$<111> dislocations are only line segments. The stereo model from Figures 3a and 3b shows a clear example of a dislocation node towards the upper left, but in most cases, the dislocation segments terminate at voids. Figure 3c shows a number of a[100] and a[010] loops and dislocation segments that cannot be seen in Figure 3a, but again segments tend to end at voids. Therefore, the dislocation structure is a mixture of a<100> and $\frac{a}{2}$<111> dislocations primarily in the form of a network with voids at the nodes. Figure 3d shows that voids in Fe-6Cr are larger than in Fe-3Cr and that voids are dodecahedral with {100} truncations (corresponding to a truncation factor between 0.6 and 0.8). However, larger voids are often elongated so that some of the facets are larger than others. Also, some of the smaller voids appear to be without significant truncation, but other small voids are clearly facetted. Therefore, considerable variation in void shape exists.

Figure 4 gives examples of the dislocation and void structures in Fe-9Cr following irradiation at 420°C to 200 dpa. Figure 4a again reveals the presence of both a[001] and $\frac{a}{2}$<111> Burgers vectors. The stereo model from Figures 4a and 4b shows that few a[001] loops are present, and most of those are connected to the dislocation network. Again, dislocation segments often terminate at voids. The images are confused by surface pits, and voids that are connected to the surface, often with a mottled appearance. Figure 4c shows a number of incomplete a[100] and a[010] loops and dislocation segments that cannot be seen in Figure 3a. Therefore, the dislocation structure is again a mixture of a<100> and $\frac{a}{2}$<111> dislocations in the form of a network but with several partial loops and with voids at some of the nodes. Figure 4d reveals that the truncation of the dodecahedral voids is even less than in Fe-6Cr (with a truncation factor of 0.8 to 1.0) with considerable variation in void aspect ratio and some variation in facet definition.

Figure 5 provides examples of the dislocation and void structures in Fe-12Cr following irradiation at 420°C to 200 dpa. Figure 5a shows a somewhat different dislocation structure, consisting of both small a[001] loops and large a[001] segments as well as large $\frac{a}{2}$<111> segments. The loops are as small as 15 nm in diameter with many features in strong contrast that are even smaller. The stereo model from Figures 5a and 5b verifies that the a[001] loops are steeply inclined, and that the density of small features is much higher than in alloys with lower chromium content. Figure 5c shows the a[100] and a[010] loops and line segments not visible in 5a and 5b, but also reveals that the small features remain in stronger contrast than the dislocation structure. Therefore, the strong contrast is due to precipitation, likely from chromium rich α' formation. Figure 4d reveals that void shapes are dodecahedral with slight cubic truncation (with a truncation factor 0.7 to 0.9), and larger voids are often elongated. A contrast due to precipitation can be identified, indicating that particles are on the order of 5 nm and larger in diameter.

vacuum vessel would be given equal priority. Emphasis was to be placed on developing data for the materials currently listed as reference in the EDA design. The priority in developing the data pages is shown in Table 1. Priority (1) indicates that the information is required by July 1994, while priority (2) indicated that information is needed in October 1994. In either case this does not mean that by these dates there has to be a completed data set for that material but rather some information must be contained in the Handbook on it To avoid duplication of effort it was agreed that for each material one Home Team would lead, shown in the table as (L) while the other Home teams could either support (S) or review the contributions (R).

TABLE 1. Priorities and Assignments for the Preparation of Data Pages

Priority	Material	E.U.	JPN	R.F.	U.S.
1	316L		L		R
1	316SPH	L			
1	Inconel 625	S	S	S	L
1	Beryllium, sintered and plasma sprayed		S	L	S
1	Cu-Cr-Zr, composition TBD	L	S	S	S
1	Cryogenic properties of 316 LN				L[1]
1	Incoloy 908				L[1]
2	316		S		L
2	316L	L	R		R
2	JN1		L[2]		
2	R.F. Alloy 20Cr-16Ni-6Mn			L[2]	
2	V-5Cr-5Ti	S	S	S	L
2	Titanium alloy Ti-6Al-4V		L	S	S
2	Dispersion Strengthened Copper, composition TBD			L	S
2	Lithium				L
2	Pure Copper				L[1]
2	Copper-Tin				L[1]

NOTES: (1) To be supplied by Task Agreement of Super conducting Coils and Structures
(2) Data to be for cryogenic temperature range of 4 K- 20 C

In addition to assigning responsibility for the preparation of data pages it was also agreed that data would be exchanged electronically so that the dam could be imported into the graphics routines and subsequently transmitted to the three ITER Working Sites (Garching, Naka, and San Diego). All of the parties indicated that they are on the Internet system and could easily transfer files.

Development of a Communications System

Subsequent to the First Working Meeting, the U.S. activity on the Handbook was concentrated on 3 areas, electronic file transfer. organization of the Handbook, and creation of a manual on data page preparation. The work on electronic file transfer has been the most challenging. A key part of data transmission is the ability to attach documents to the e-mail message. While it is relatively easy to send e-mail messages to organizations, it is not as easy to attach documents and then extract them from the body of the message. To determine the capabilities of each of the parties, e-mail messages were sent with a Microsoft Word attachment. a Rich Text Format (which can be read by any word program), and a graphics tile. The results were mixed. The U.S. could read all of the files and also send the files back, Russia could read the attached files but couldn't send attachments because they do not have a BinHex code. Europe is having difficulty retrieving attached files. Electronic mail files, without attachments, have been received from both the Ispra, Italy and the ECN, Netherlands sites. It appears that these sites, unlike Russia are unable to decode the BinHex format. We are able to place files in the microvax at Ispra using file transfer protocol (FTP) but this is essentially a temporary solution in comparison to having a computer program that can

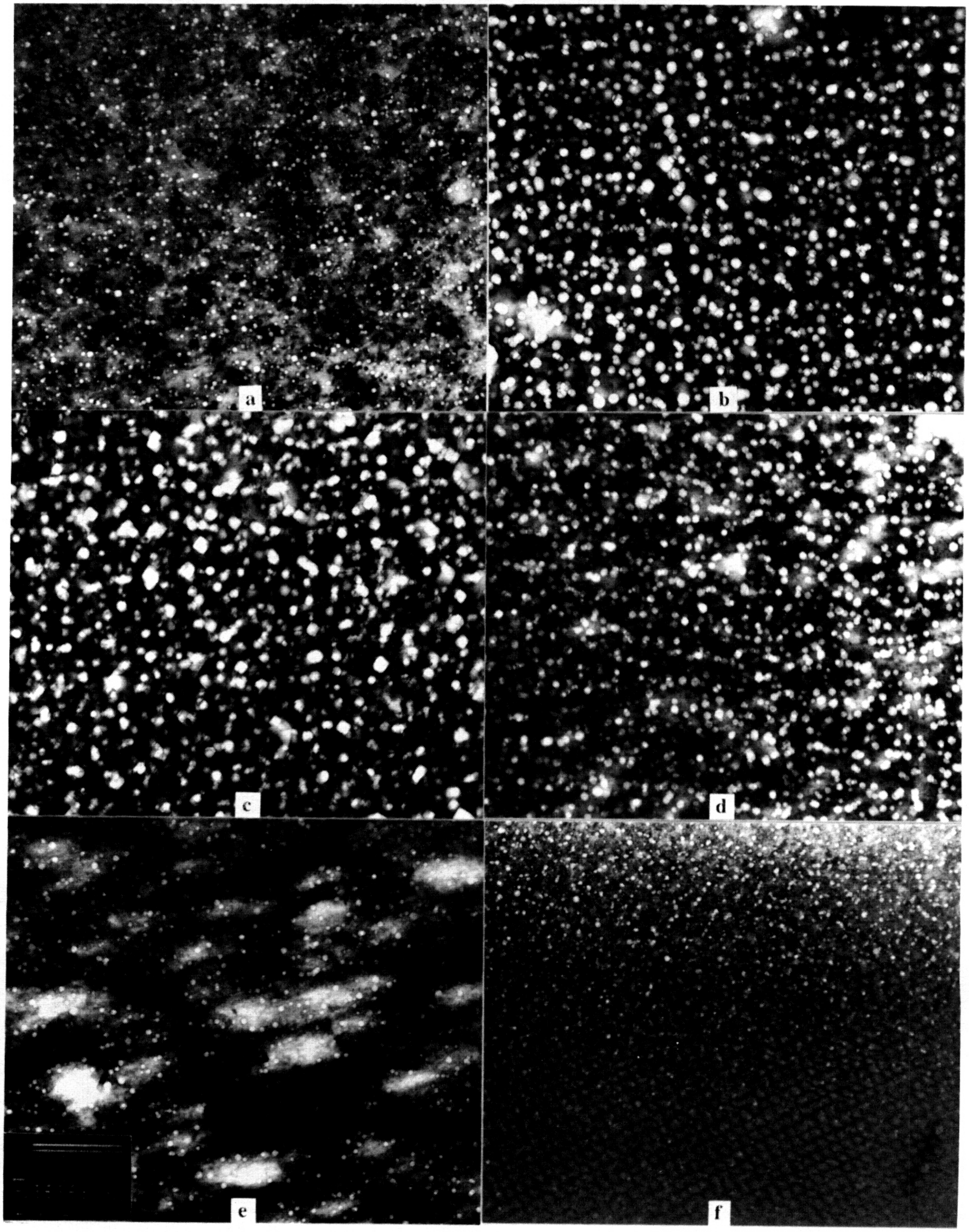

Figure 1. Void swelling at low magnification for a) Fe-3Cr, b) Fe-6Cr, c) Fe-9Cr, d) Fe-12Cr, *e)* Fe-15Cr, and f) Fe-3Cr following irradiation at 420°C to 200 dpa.

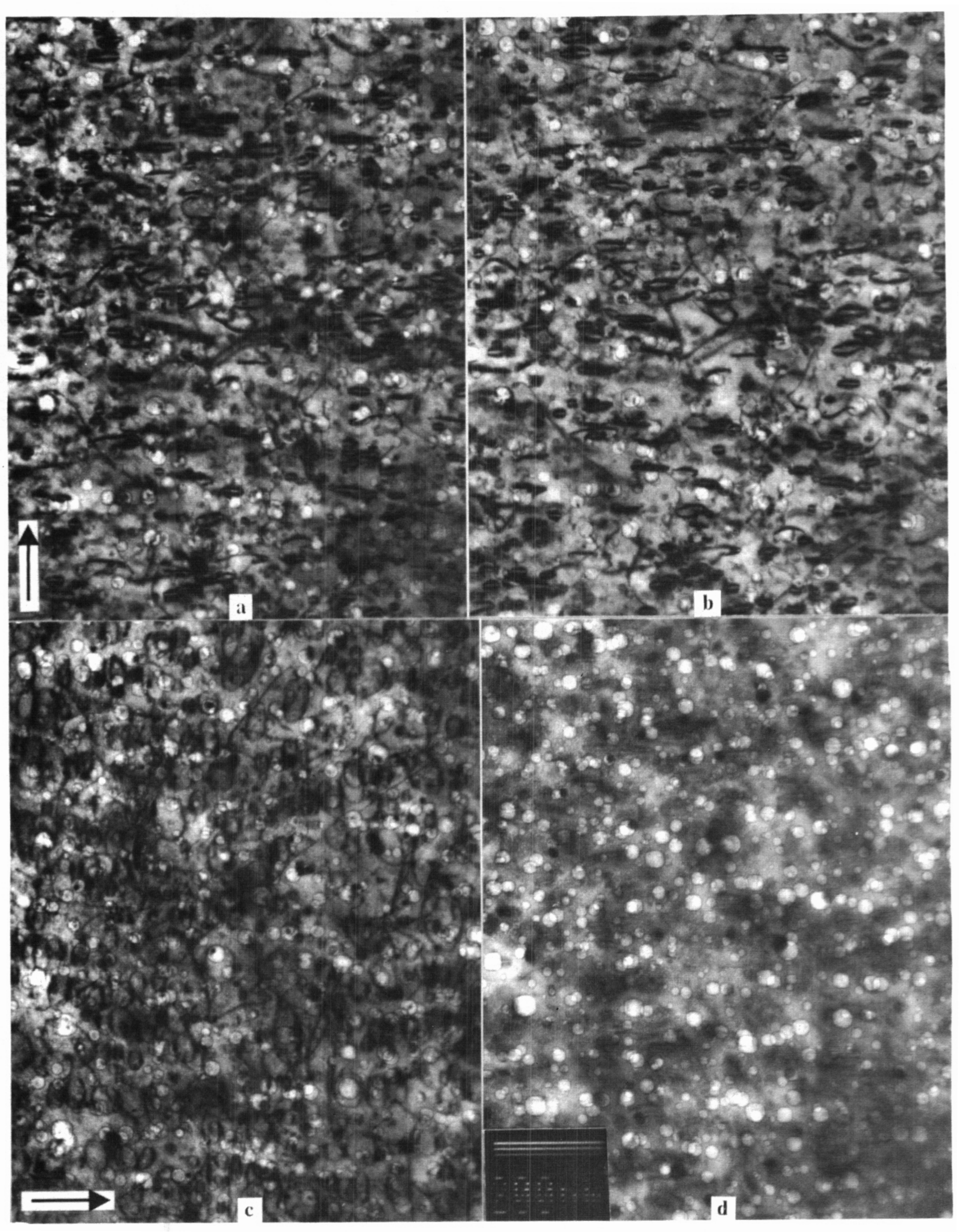

Figure 2. Microstructures in Fe-3Cr irradiated at 420°C to 200 dpa as a stereo pair using $\vec{g} = 200$ in a) and b), using $\vec{g} = 0\bar{1}1$ in c) and void contrast in d) for a foil near (011) orientation that is tilted near (012) for part b)

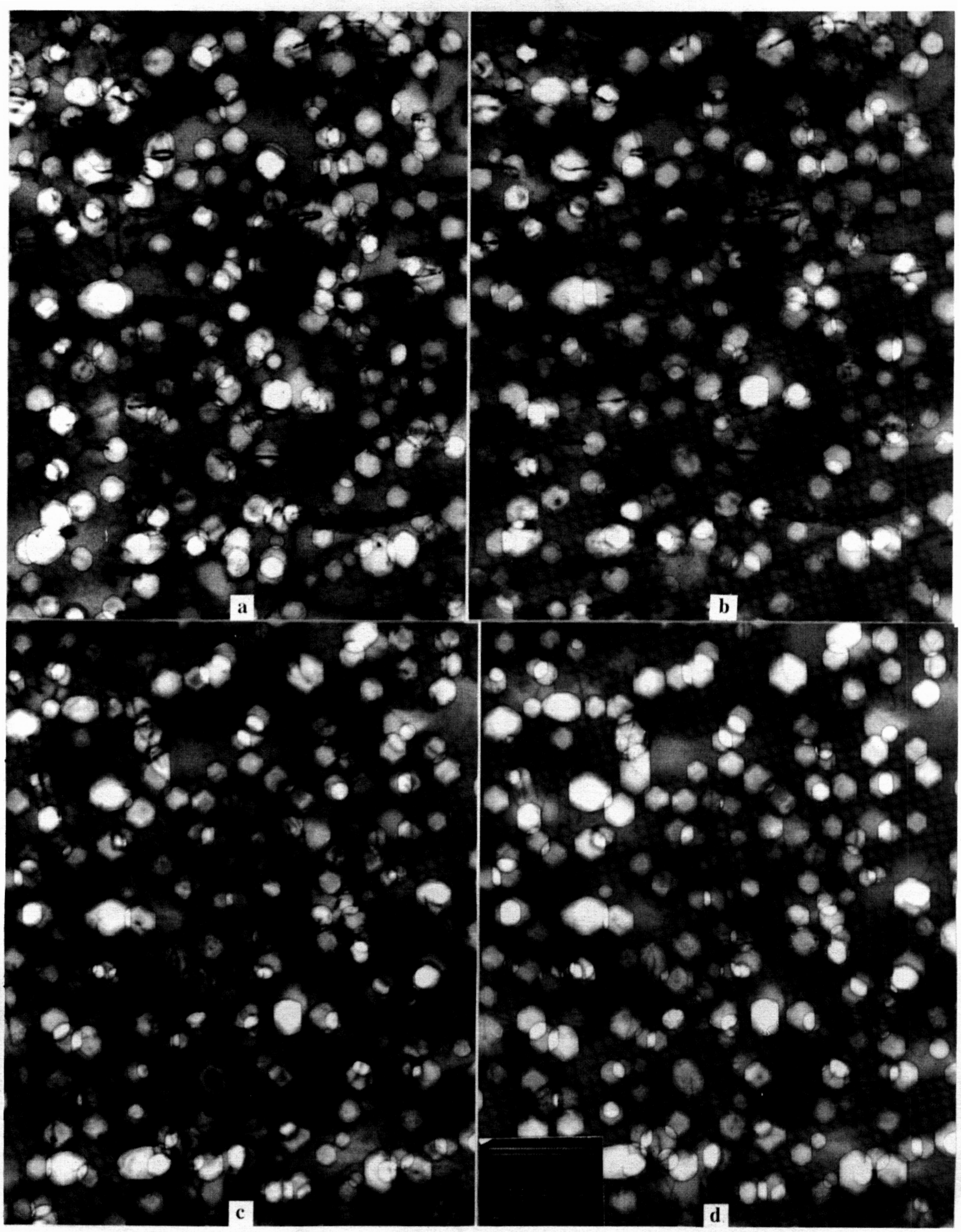

Figure 3. Microstructures in Fe-6Cr irradiated at 420°C to 200 dpa as a stereo pair using $\vec{g} = 200$ in a) and b), using $\vec{g} = 0\bar{1}1$ in c) and void contrast in d) for a foil near (011) orientation that is tilted near (012) for part b)

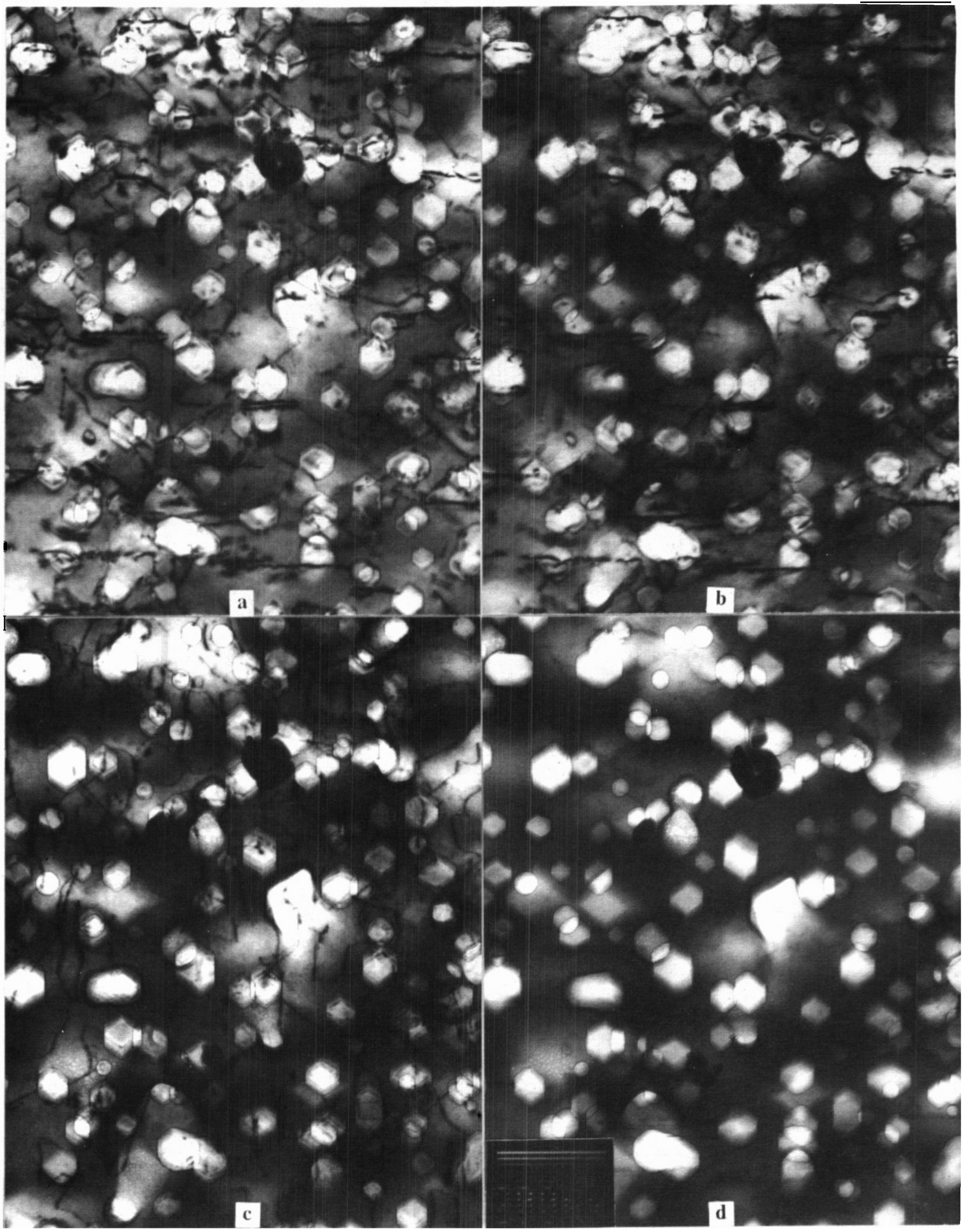

Figure 4. Microstructures in Fe-9Cr irradiated at 420°C to 200 dpa as a stereo pair using $\vec{g} = 200$ in a) and b), using $\vec{g} = 0\bar{1}1$ in c) and void contrast in d) for a foil near (011) orientation that is tilted near (012) for part b)

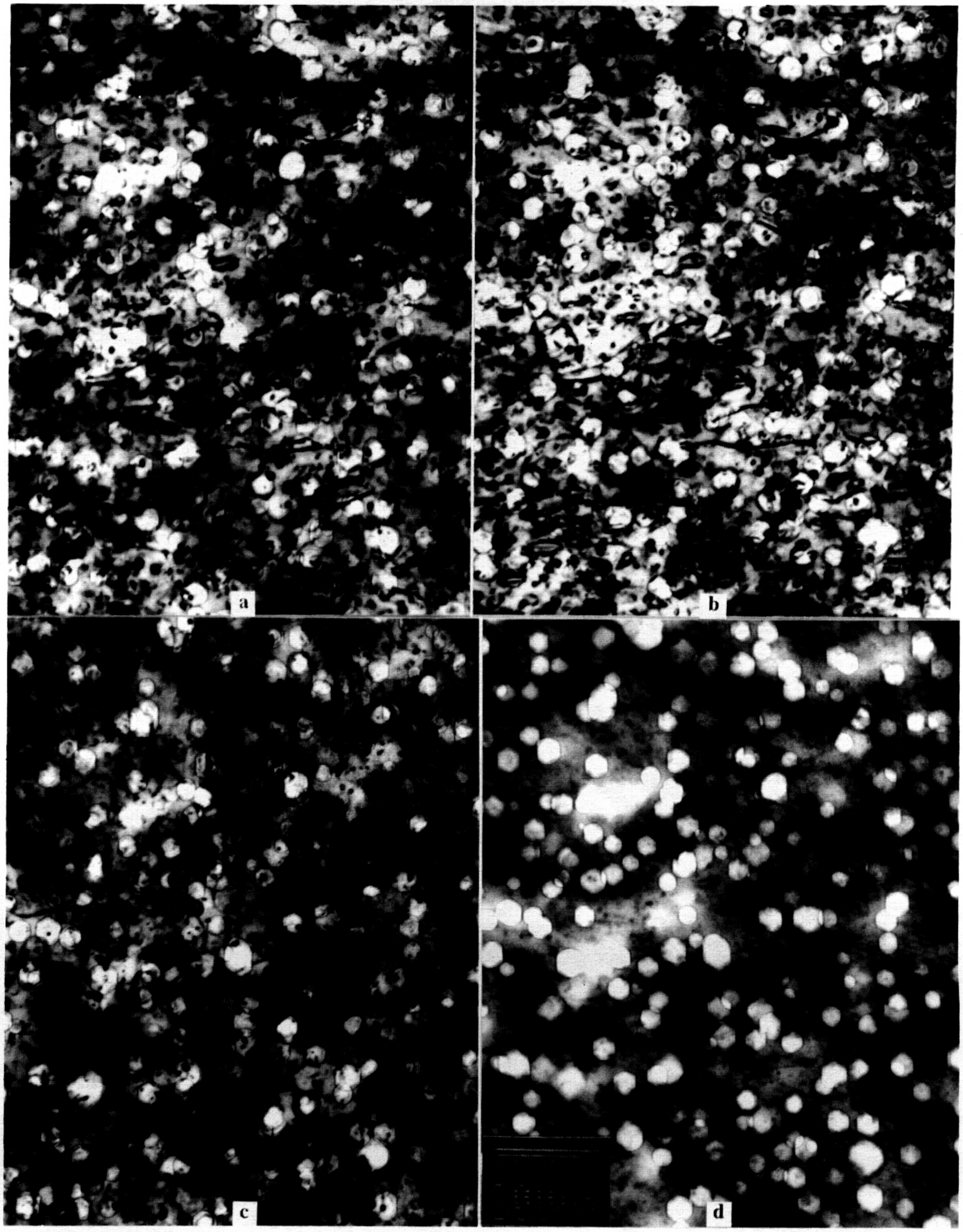

Figure 5. Microstructures in Fe-12Cr irradiated at 420°C to 200 dpa as a stereo pair using $\vec{g} = 200$ in a) and b), using $\vec{g} = 0\bar{1}1$ in c) and void contrast in d) for a foil near (011) orientation that is tilted near (012) for part b)

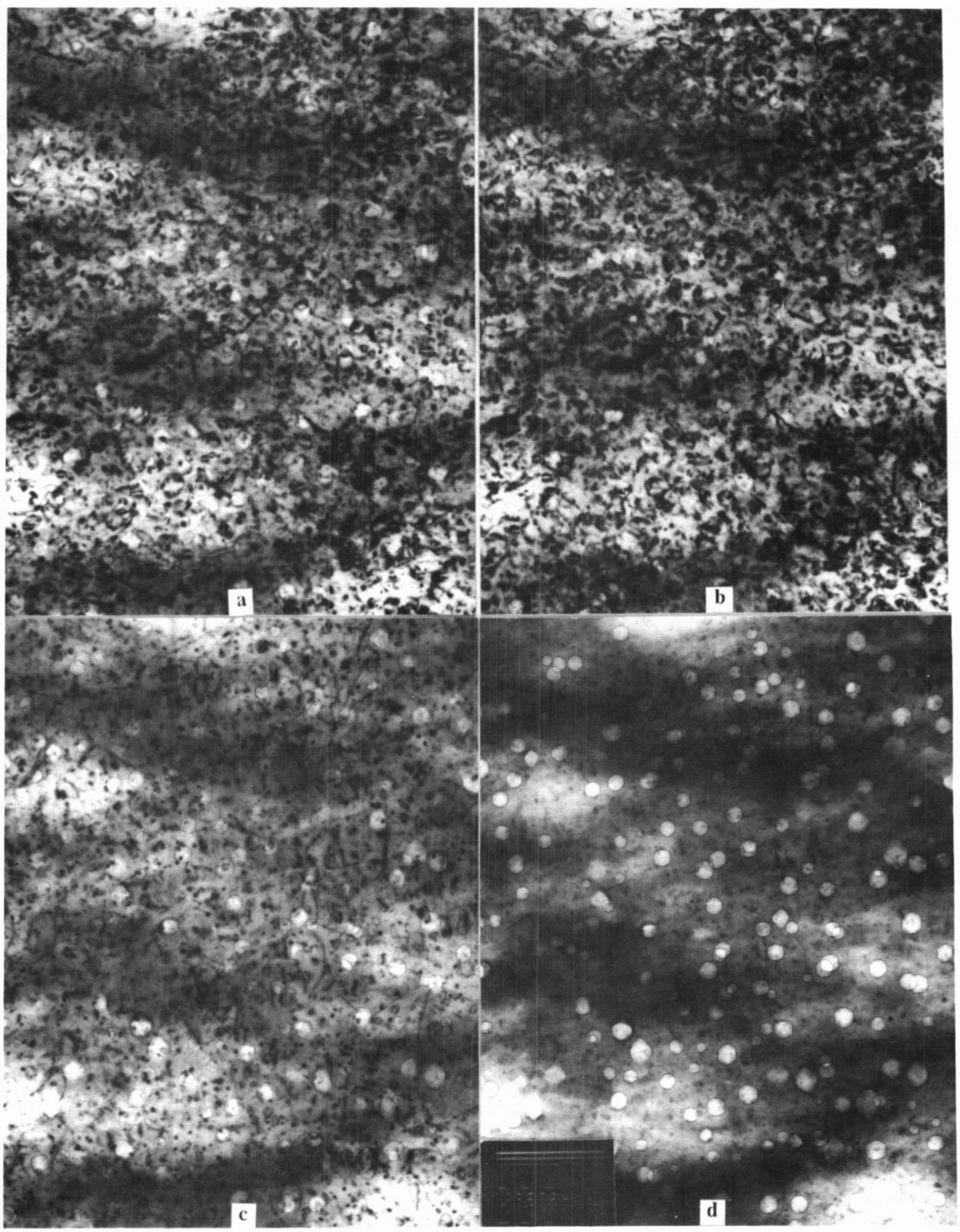

Figure 6. Microstructures in Fe-15Cr irradiated at 420°C to 200 dpa as a stereo pair using $\vec{g} = 200$ in a) and b), using $\vec{g} = 0\bar{1}1$ in c) and void contrast in d) for a foil near (011) orientation that is tilted near (012) for part b)

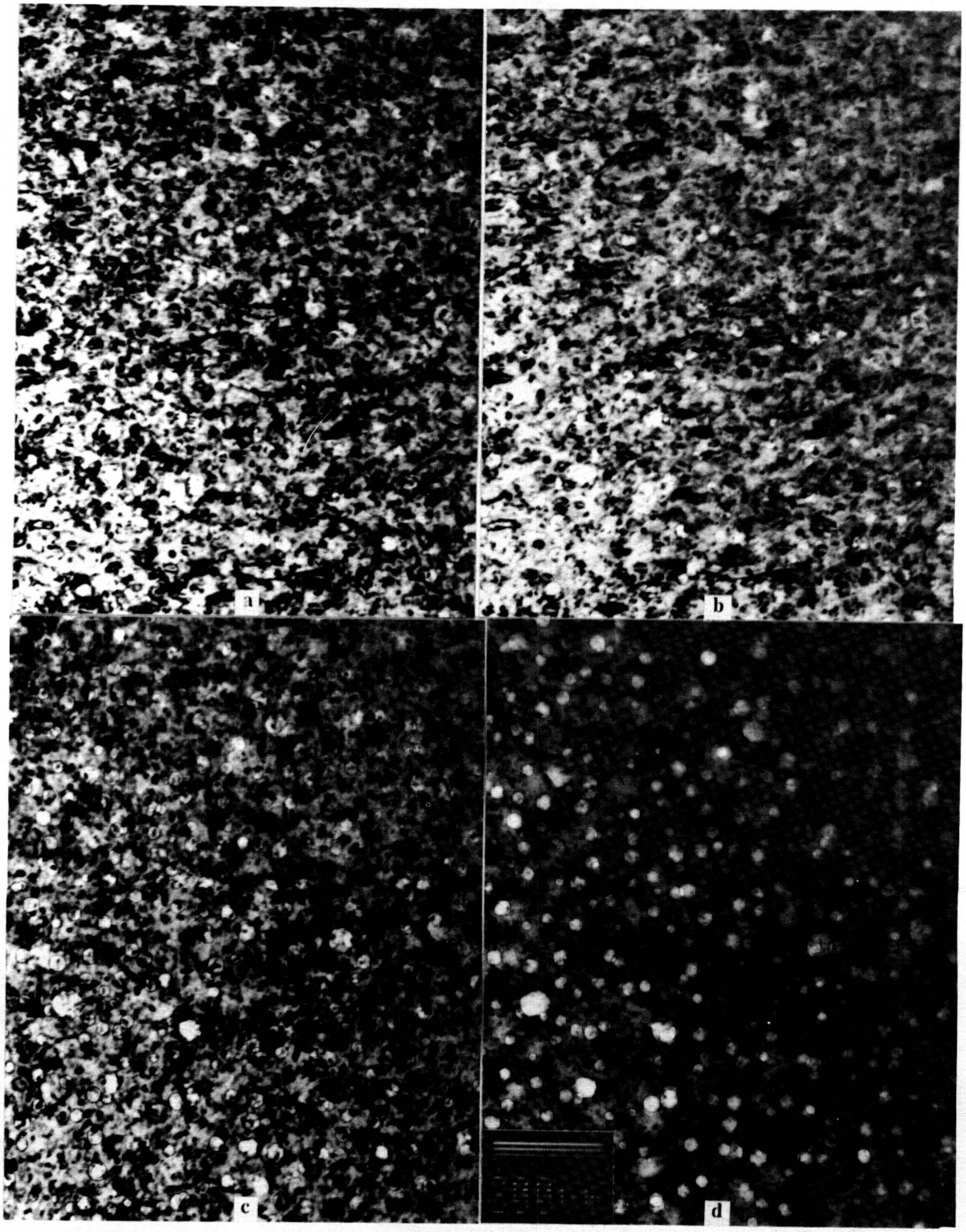

Figure 7. Microstructures in Fe-18Cr irradiated at 420°C to 200 dpa as a stereo pair using $\vec{g} = 200$ in a) and b), using $\vec{g} = 0\bar{1}1$ in c) and void contrast in d) for a foil near $(01\bar{1})$ orientation that is tilted near (012) for part b)

Figure **6** gives examples of the dislocation and void structures in Fe–15Cr following irradiation at 420°C to 200 dpa. Figure 6a shows again a somewhat different dislocation structure, consisting of small a[001] loops and large $\frac{a}{2}$<111> segments; large a[001] segments appear to be absent. The loops range in size from 7 to 20 nm in diameter, but again with many features in strong contrast that are even smaller. The stereo model from Figures 6a and 6b verifies that these features are evenly distributed through the thickness of the foil. Figure 6c reveals the dislocation line segments in better resolution, and several examples can be found of small loops at a different inclination than found previously, probably of type $\frac{a}{2}$<111>. Therefore, Fe-15Cr contains a higher fraction of $\frac{a}{2}$<111> dislocations, both as line segments and small loops, than was found in alloys with lower chromium contents. Figure 6d shows that voids are dodecahedra with moderate (100) truncation (corresponding to truncation factors from 0.4 to 0.7) and that precipitation appears to be more dense, as would be expected for chromium rich precipitates.

Figure 7 provides examples of the dislocation and void structures in Fe-18Cr following irradiation at 420°C to 200 dpa. This sequence is perhaps the most difficult to understand. However, Figure 7a again shows a dislocation structure, consisting of small a[001] loops and larger a[001] and $\frac{a}{2}$<111> segments. Many precipitates can also be seen. The stereo model from Figures 7a and 7b verifies that these features are evenly distributed through the thickness of the foil. Figure 6c shows configurations typical of a[100] and a[010] dislocations, but a few examples of small $\frac{a}{2}$<111> loops can also be seen. Therefore, the dislocation structure in Fe-18Cr appears to contain predominantly a<100> loops but with dislocation segments of both a<100> and $\frac{a}{2}$<111>. From Figure 7d, the void shape is found to contain greater cubic truncation than seen previously (with truncation factors between 0.3 and 0.6). Precipitation is more extensive, with particle sizes of about 8 nm.

Microstructural Analysis

The void and dislocation microstructures have been analyzed quantitatively to determine void swelling, void density, void size distribution, and dislocation density. Table 2 summarizes the information. Void swelling is measured based on the average truncated void shape with input consisting of measurements in a <110> direction as recommended in reference 14. Mean void sizes and void distributions are reported based on the equivalent sphere diameter for each truncated void.

Dislocation densities are based on the $\frac{a}{2}$<111> and a<100> dislocations visible using $\vec{g}$ = 200 contrast, but with the a<100> multiplied by a factor of three to correct for the invisibility of a[100] and a[010] Burgers vectors. Figure 8 presents the void size distributions (reported as equivalent sphere diameters). Based on Figure 8, it is apparent that the enhanced density change as reported in Table 1 is a consequence of enhanced void growth — the larger the largest voids, the higher the density change.

Discussion

The results obtained in this study can be used to provide the basis for discussions on two topics: 1) the reason for the high swelling resistance of ferritic alloys and 2) the cause of differences in swelling response from irradiation in EBR-II and FFTF/MOTA. First, the present microstructural results of importance will be summarized. Then, discussion will be provided relating those and previous results on the Fe-Cr alloy series to the available explanations for swelling resistance. Finally, differences in response in different reactors will be considered.

Table 2. Summary of quantitative microstructural observations.

Code	Alloy	Dose (dpa)	Swelling (%)	Mean Void Size (nm)	Void Density (#/cm3)	Truncation factor	Dislocation density (cm/cm3)
65H4	Fe-3Cr	197.6	1.20	19.1	$1.69x10^{15}$	0.4-0.5	$\frac{a}{2}$<111> $1.25x10^{10}$ a<100> $1.8x10^{10}$
66H4	Fe-6Cr	198.3	6.07	47.7	$6.8x10^{14}$	0.6-0.8	$\frac{a}{2}$<111> $7.2x10^{9}$ a<100> $2.8x10^{10}$
67H4	Fe-9Cr	1990	9 24	57 3	$6.1x10^{14}$	0.8-1.0	$\frac{a}{2}$<111> $1.84x10^{10}$ a<100> $9.8x10^{10}$
6AH4	Fe-12Cr	199.6	3 76	40 8	$7.0x10^{14}$	0.7-0.9	$\frac{a}{2}$<111> $8.3x10^{9}$ a<100> 4 $1x10^{10}$
6NH4	Fe-15Cr	2004	2 21	24 9	$1.85x10^{15}$	04-07	$\frac{a}{2}$<111> $8.6x10^{10}$ a<100 ,9 $0x10^{10}$
6RH4	Fe-18Cr	201 I	2 54	19.0	$4.0x10^{15}$	0.3-0.6	$\frac{a}{2}$<1 11 , $17x10^{10}$ a<100> 8 1x10'''

Explanation for low swelling in ferritic alloys

The present results provide confirmation from previous studies that void swelling develops in ferritic alloys in much the same ways as in other crystal structures. Voids can nucleate uniformly along with two types of dislocation loops, the voids can grow to sizes exceeding **200** nm, and the dislocation structure can evolve into a network. As had been shown in previous studies, two types of Burgers vectors developed, a<100> and $\frac{a}{2}$<111>. The balance between these two Burgers vectors varies with composition, but large changes in this balance do not appear to significantly reduce swelling, an observation also made in a companion study.[15] Also, it is shown that precipitation reduces swelling, for example in Fe-3Cr and in Fe-12Cr to Fe-18Cr. It may well be significant that dislocation populations in α' forming alloys include smaller loops along with a well developed dislocation network. For example, the enhanced dislocation densities that result from the small loop population may be responsible for reduced swelling.

Many of the models that have been developed to explain swelling resistance in ferritic alloys are really arguments concerning the incubation dose for swelling. It must be remembered that the modeling of swelling involves two stages, an incubation period followed by a steady state swelling period. The incubation period includes the void nucleation phase, and the steady state response only applies after the microstructure of voids and dislocations stabilizes. For the purposes of this discussion, those models that argue that ferritic alloys should have longer incubation periods, such as those controlled by solute segregation or those that keep the incubation period indefinitely long, will be ignored. This includes models by Little and Stow regarding segregation control,'' by Little, Bullough, and Wood based on point defect bias between the a<100> and $\frac{a}{2}$<111> Burgers vectors at the exclusion of a bias to voids,' and by Odette and others based on low helium production, which delays void nucleation.[5]

The models that remain under consideration are therefore 1) an inherent crystal structure effect: 2) a sink strength effect,''.'' 3) a microstructural effect due to precipitation or lath structure: 4) a bias effect on voids evidenced by changes in void shape due to segregation,' and 5) reduced dislocation mobility due to the presence of a<100> sessile dislocations.'

The present results have provided the highest swelling found in neutron irradiated ferritic alloys, producing 7.4% at 200 dpa with an estimated rate of 0.1%/dpa in a simple Fe-9Cr alloy, which is free of precipitation and subgrain lath structure. This swelling rate is still very low in comparison to 1%/dpa in austenitic alloys[16] and 2%/dpa in some vanadium alloys.” Considering the above models in reverse order, it can be noted that the present work has shown that the dislocation network eventually evolves to one where nodes between dislocations with different Burgers vectors become the voids themselves. In other words, such nodes do not actually exist because individual dislocation segments terminate at void surfaces. Therefore, the junction of a<100> and $\frac{a}{2}$<111> Burgers vectors, although sessile, cannot reduce the climb of the dislocation network, and ferritic alloys behave just like other systems where the voids eventually provide the sites for dislocation network junctions. The present work also shows moderate variation in void shape from one alloy to another with dodecahedral shapes dominating, whereas, at low dose, the void shapes were found to be octahedra, with (111) facets dominating: so that a large change in void shape has developed with increasing dose. Therefore, large changes in shape have occurred with increasing dose, but at high dose, the void shape is relatively constant. It is true that for the highest swelling rate condition, **Fe-9Cr,** the highest truncation factor is found, corresponding to voids of almost perfect dodecahedral shape. However, the variations in shape do not seem to correlate directly with a reduction in swelling response, and it appears unreasonable to expect that the flux of vacancies to a void surface will be significantly reduced by a segregated layer. (Instead, the consequence would be to increase recombination, in effect shifting the peak swelling temperature.) A model based on precipitation or lath dislocation substructure cannot apply to the present simple alloys with large grain size and negligible substructure before irradiation.

The sink strength ratio model is worthy of more careful consideration. Table 3 has been prepared to summarize the sink strength ratio information that is available for Fe-Cr binary alloys in the present series of irradiations. Table 3 includes estimates for swelling rate based on density change measurements when they are available, but including TEM measurements, where the rate is defined assuming zero swelling at 0 dpa. Microstructural information for mean void diameter, void density, and total dislocation density (the sum of the a<100> and $\frac{a}{2}$<111> dislocation populations) is also given. Finally, the sink strength ratio, Q, is calculated based on the expression from reference 12:

$$Q = L/4\pi \frac{d}{2} N$$

where L is the total dislocation density, $\bar{d}$ is the mean void diameter, and N is the void density. The values for sink strength in Table 3 are found to vary from 0.4 to 10, but the majority fall in the range 0.8 to 6. Therefore, most of these microstructures correspond to sink strength ratios close to 1. It may be noted that the first four values for Q in Table 3 do not quite agree with those calculated in reference 12 where the values reported were between 1.5 and 5.4.

The argument has been made that swelling resistance in ferritic alloys is a consequence of the fact that the maximum cavity growth rate occurs when $Q \approx 1$, and that most microstructural measurements on ferritic alloys indicated that the cavity number density is low, leading to a high value for Q.[11,12] The results shown in Table 3 indicate that at least for the simple Fe-Cr alloys in the present experiment, Q values are indeed ≈ 1, and yet, swelling rates remain an order of magnitude below those of the higher swelling alloy classes. Therefore, ferritic alloys are indeed able to generate microstructural conditions conducive for high swelling response, but swelling rates remain low.

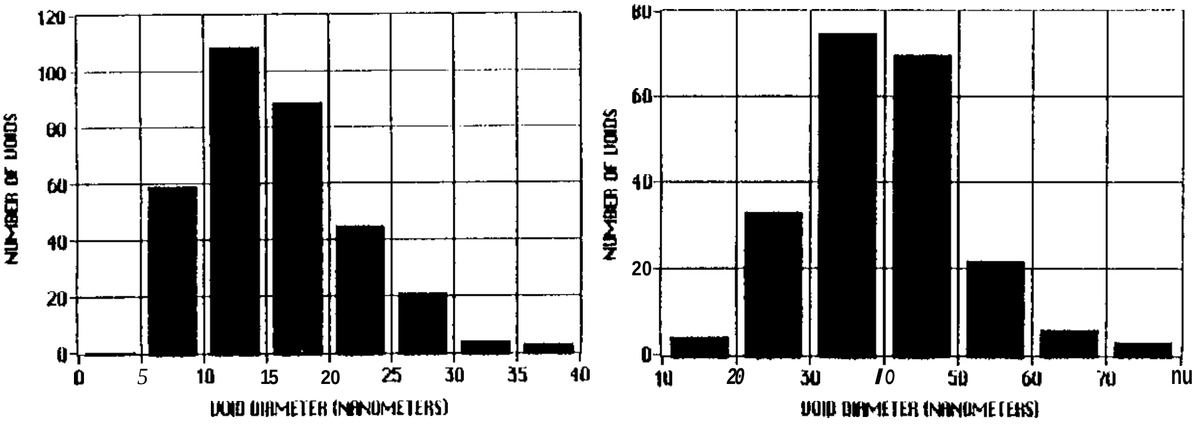

(a) Fe-3Cr

(b) Fe-6Cr

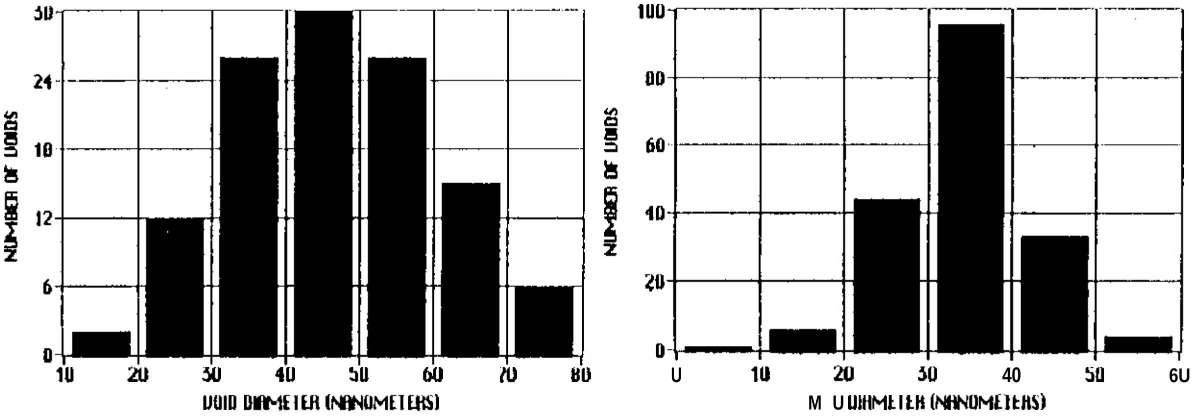

(c) Fe-9Cr

(d) Fe-12Cr

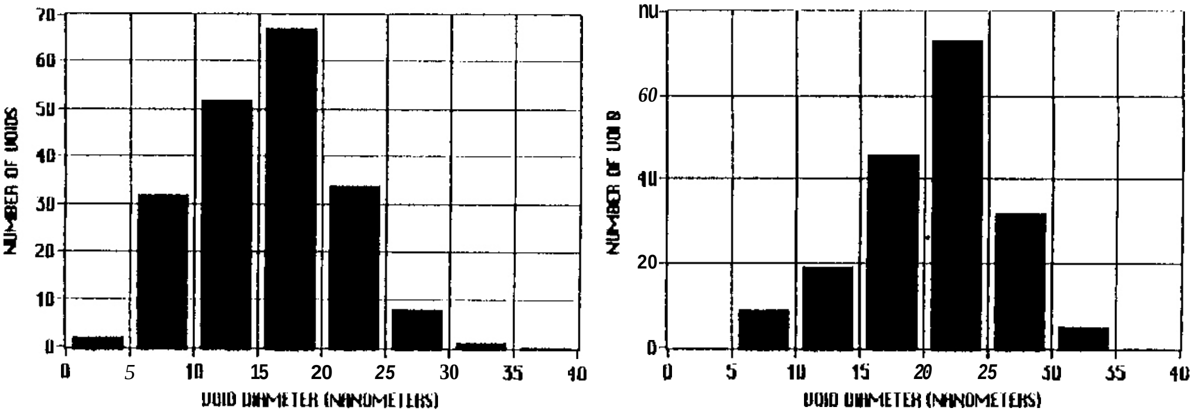

(e) Fe-15Cr

(f) Fe-18Cr

Figure 8. Void size distributions for Fe-Cr specimens irradiate at 420°C to 200 dpa.

Table 3. Evaluation of Sink Strength Ratio Values for Fe-Cr alloys for which steady state swelling rates can be estimated.

Code	Alloy	Dose (dpa)	Swelling Rate (%/dpa)	Mean Void Size (nm)	Void Density, N (#/m3)	Total Dislocation Density, L (m/m3)	Sink Strength Ratio, Q
6507[1]	Fe-3Cr	21	0.02	26.1	$8.0x10^{19}$	$1.0x10^{13}$	0.8
66O7[1]	Fe-6Cr	21	0.04	33.8	$2.8x10^{20}$	$2.1x10^{13}$	0.4
6707[1]	Fe-9Cr	21	0.05	33.9	$2.2x10^{20}$	$7.0x10^{13}$	1.5
6A07[1]	Fe-12Cr	21	0.06	30.3	$4.2x10^{20}$	$6.8x10^{13}$	0.9
65FT[3]	Fe-3Cr	15	0.0004	8.6	$2.0x10^{20}$	$1.1x10^{14}$	10.3
66FT[3]	Fe-6Cr	15	0.01	12.2	$1.7x10^{20}$	$1.2x10^{14}$	0.9
67FT[3]	Fe-9Cr	15	0.02	16.9	$1.2x10^{21}$	$2.0x10^{14}$	1.5
6AFT[3]	Fe-12Cr	15	0.01	10.8	$1.8x10^{21}$	$4.7x10^{14}$	3.8
6NFT[3]	Fe-15Cr	15	0.004	8.7	$2.3x10^{21}$	$2.2x10^{14}$	1.7
6RFT[3]	Fe-18Cr	15	0.006	8.9	$3.1x10^{21}$	$2.8x10^{14}$	1.6
65H4	Fe-3Cr	197.6	0.006	20.1	$3.1x10^{21}$	$3.1x10^{14}$	0.8
66H4	Fe-6Cr	198.3	0.080	47.7	$6.8x10^{20}$	$3.5x10^{14}$	1.7
67H4	Fe-9Cr	199.0	0.097	57.3	$6.1x10^{20}$	$1.08x10^{15}$	6.0
6AH4	Fe-12Cr	199.6	0.037	40.8	$7.0x10^{20}$	$4.9x10^{14}$	2.7
6NH4	Fe-15Cr	200.4	0.020	24.9	$1.9x10^{21}$	$1.76x10^{15}$	6.0
6RH4	Fe-18Cr	201.1	0.013	19.0	$4.0x10^{21}$	$9.8x10^{14}$	2.1

Finally, a model based on the inherent atomic packing of the body centered cubic lattice is appealing. The model predicts that the bias for vacancies to accumulate at voids is due to the difference in bias factors for dislocations and voids, and that difference is greater in austenitic than ferritic alloys.' The present results provide the argument that swelling appears to develop normally in simple ferritic alloys, but the swelling rates obtained remain low, in agreement with model predictions. However, the model comes into question when trying to explain why alloys of V-5Fe, which are also body centered cubic, can develop swelling rates in excess of 2%/dpa.[17]

Therefore, it must be concluded that it is not yet clear why swelling rates in ferritic alloys are low.

Different response in different reactors

When the swelling results for Fe-Cr simple binary are compared following irradiation in different reactors, significant differences in response can be identified. Following irradiation in EBR-II to 19 dpa at 425°C, swelling as high as 0.68% was found in Fe-9Cr and 0.63% in Fe-12Cr based on void measurements.' Following irradiation in EBR-II to 90 dpa at 425°C, swelling as high as 4.14% was found in Fe–9Cr and 4.72% in Fe-12Cr based on density change measurements.' In comparison, following irradiation in FFTF/MOTA to 139 dpa at 420°C, swelling of only 1.54% was found in Fe-9Cr and 0.61% in Fe-12Cr based on density change measurements, as noted in Table 1.

Also, further irradiation in FFTF/MOTA to 199 dpa resulted in a swelling rate for Fe-9Cr that was similar to that found in EBR-II, but with continued lower swelling in Fe-12Cr compared to Fe-9Cr, 2.83% versus 7.39%, based on density change measurements. Therefore, irradiation in FFTF/MOTA at 420°C produces swelling response with a higher incubation and produces significantly less swelling in Fe-12Cr than Fe-9Cr.

Comparison of the microstructures for Fe-12Cr in EBR-II and FFTF/MOTA shows further differences. The a' development is much more extensive, and the dislocation structures are more complicated, for the FFTF/MOTA case. The present results indicated that precipitation produces the more complex dislocation evolution and leads to reduced swelling. Therefore, at least part of the difference is likely due to enhanced precipitation of a' io FFTF/MOTA.

As FFTF and EBR-II are similar reactors with very similar neutron energy spectrums, it is unlikely that differences are a consequence of different dose or transmutation responses. A more likely explanation is an Uncertainty in irradiation temperature or differences in reactor temperature cycling history. The a' precipitation process is temperature dependent such that more precipitation is produced at lower temperatures. Therefore, the differences in response between Fe-9Cr and Fe-12Cr could be explained by assuming that the EBR-II temperature was underestimated, by 30°C or more. Note that temperatures io FFTF/MOTA were monitored by thermocouples. However, the EBR-II irradiation employed a weeper design at 425°C without thermocouples, and temperatures were usually estimated based on reactor sodium temperature measurements well away from the irradiation test assemblies. Nonetheless, an error as large as 30°C is unexpected.

Although the difference in response as a function of composition can he explained by temperature uncertainty, the difference in swelling incubation cannot. Swelling incubation is a measure of how rapidly a steady state microstructure can develop. That microstructure is generated by nucleation of dislocation loops and voids and then growth and evolution of those features into steady state configurations. The nucleation process will govern that evolution, and nucleation is favored at lower temperatures. Therefore, any operation helow the irradiation temperature could promote nucleation and accelerate the approach to steady state swelling. It can be anticipated that the temperatures were maintained more constant during operation in FFTF/MOTA than in EBR-II. However, startup and shutdown operations were more rapid in EBR-II due to required intermediate power levels holds in FFTF. Such intermediate power level holds would provide slightly reduced weeper temperatures, but the differences are not expected to cause significant nucleation of new microstructure. Therefore, it is not yet clear that specific differences in reactor operations can be identified to explain the differences found in swelling incubation response in the different reactors. The irradiation of Fe-Cr simple ferritic alloys is being rerun in the most recent EBR-II irradiation. Those specimens will be examined to check for similar response.

CONCLUSIONS

Density change measurements and microstructural examinations have been performed on a series of Fe-Cr alloys following irradiation in the FFTF/MOTA at 420°C to 200 dpa, and the results have been compared with results on specimens irradiated to lower dose and on similar specimens irradiated in EBR-II. The highest swelling of 7.4%, corresponding to a swelling rate of 0.097%/dpa, is found in Fe-9Cr, but swelling representative of steady state swelling is found in all alloys except Fe-3Cr. The microstructures in all conditions have been quantitatively analyzed, and estimates for the sink density ratios have been shown to he approximately 1. Comparison with previous experiments reveals that response is different in different reactors such that swelling is relatively lower in Fe-12Cr and swelling incubation is larger for irradiation in FFTFIMOTA. Explanations are proposed that suggest that EBR-II weeper temperatures were higher than expected, but no explanation is available to explain swelling incubation response. Comparison of microstructural features with those found at lower doses provided the unexpected result that void shapes shift from octahedra to dodecahedra as dose increases. Examination of proposed theories for the low swelling rates found in ferritic alloys provided no completely acceptable explanation.

FUTURE WORK

This work will be continued when appropriate specimens become available.

REFERENCES

1. D. S. Gelles. J. Nucl. Matl. **108-9** (1982) 515.

2. D. S. Gelles and R. M. Meinecke-Ermi, "Swelling in Simple Ferritic Alloy Irradiated to High Fluence," in Alloy Development for Irradiation Performance Progress Report for Period Ending September 1983, DOE/ER-0045/11, p. 103, 1984.

3. D. S. Gelles, in Effects of Radiation on Materials: 14th International Symposium, Volume 1, ASTM STP 1046, N. H. Packan, R. E. Stoller and A. S. Kumar, Eds., ASTM, Philadelphia, 1989, 13.

4. Y. Katoh, A. Kohyama, and D. S. Gelles, "Swelling and Dislocation Evolution in Simple Ferritic Alloys Irradiated to High Fluence in FFTF/MOTA" to be presented at the 17th ASTM Symposium on Effects of Radiation on Materials to be held in Sun Valley, ID, June 20-23, 1994.

5. G. R. Odette, J. Nucl. Matl. **155-7** (1988) 921.

6. P. J. Maziasz and R. L. Klueh, in Effects of Radiation on Materials: 14th International Symposium, Volume I, ASTM STP 1046, N. H. Packan, R. E. Stoller, and A. S. Kumar, Eds., ASTM, Philadelphia, 1989, 35.

7. E. A. Little, J. Nucl. Matl. **206** (1993) 324.

8. J. J. Sniegowski and W. C. Wolfer, "On the Physical Basis for the Swelling Resistance of Ferritic Steels," in Proc. of Topical Conf. on Ferritic Alloys for Use in Nuclear Energy Technologies, Eds. J. W. Davis and D. J. Michel (AIME Warrendale, PA, 1984).

9. E. A. Little, R. Bullough, and M. H. Wood, "On the Swelling Resistance of Ferritic Steel," Proc. R. Soc. Lond. A372, p. 565, 1980.

10. E. A. Little and D. A. Stow, "Void Swelling in Irons and Ferritic Steels, Part II," J. Nucl. Matl. 87, p. 25, 1979.

11. L. K. Mansur and E. H. Lee, J. Nucl. Matl. **179-81** (1991) 105.

12. E. H. Lee and L. K. Mansur, Met. Trans. 21A (1990) 1021

13. F. A. Garner and L. R. Greenwood, "Calculation of Displacement Levels for Pure Elements and Most Multicomponent Alloys Irradiated in FFTF MOTA-1F," Fusion Reactor Materials Semiannual Progress Report for the Period Ending March 31,1992, DOE/ER-0313/12 (July 1992) 54.

14. D. S. Gelles, R. M. Claudson, and L. **E.** Thomas, in Electron Microscopy 1990, V. 4, (San Francisco Press, Inc., San Francisco, 1990) 844-845. Also **see** DOE/ER-0313/3 131 for figures at higher magnification.

15. D. S. Gelles, "Microstructural Examination of Commercial Ferritic Alloys at 200 dpa," in DOE/ER-0313/16, this report.

16. F. A. Garner, **J.** Nucl. Matl., 122-3 (1984) 459.

17. D. S. Gelles and **J.** F. Stubbins, "Microstructural development in Irradiated Vanadium Alloys," Fusion Reactor Materials Semiannual Progress Report for the Period Ending September 30, 1993, DOE/ER-0313/15 (February 1994) **115.**

DATA BASE ON PERMEATION, DIFFUSION, AND CONCENTRATION OF HYDROGEN ISOTOPES IN FUSION REACTOR MATERIALS - J. L. Brimhall, E. P. Simonen and R. H. Jones, (Pacific Northwest Laboratory)*

OBJECTIVE

To assess the current status of the data base on permeation, diffusion and solubility of hydrogen isotopes in selected fusion reactor materials. Both gas-driven and plasma-driven permeation are considered.

SUMMARY

In evaluating fusion reactor performance, knowledge about permeation, diffusion and concentration of hydrogen isotopes throughout the structure is of critical importance. The data base on hydrogen isotope permeation in relevant fusion reactor materials is reviewed in this report. Comparisons are made within alloys of the same type as well as with all the other classes of alloys. Both gas-driven permeation (GDP) and plasma-driven permeation (PDP) are included. Data on GDP behavior in Fe and Ni alloys are relatively consistent. In metals that have a high solubility and/or are hydride formers, **e.g.,** V, Nb, Ti, there is much more variation in the data, and surface effects play a very dominant role. Permeation under plasma conditions is less well understood as more variables enter the relationship, e.g., re-emission phenomena, internal concentration gradients, radiation effects, etc. The data show that materials do not necessarily rank in the same order under PDP conditions as under GDP conditions. A summary of the factors that influence permeation and the relative magnitude of their effect is given in the report.

TECHNICAL PROGRESS

Compilation of Hydrogen Isotope Permeation Data

The basic relationship for gas permeation in metals is $P = S \times D$. S is the solubility given by $S_0\exp(-E_s/kT)$ where $S_0=K_0\sqrt{p}$ for a diatomic gas and D is the diffusivity given by $D_0\exp(-E_d/kT)$. The permeation rate is then given by $P=P_0\exp(-E_p/kT)$ where $\mathbf{P_0=(S_0)(D_0)}$ and $E_p=E_s+E_d$. Data on the activation energies and pre-exponential terms for permeation, diffusion and solubility of hydrogen isotopes in relevant fusion reactor materials are compiled in Table **1.** Diffusion, solubility and permeation data are listed separately as most experiments determine one of the components in permeation but generally not all three. All possible data are not listed but only a sufficient representation to indicate the range of values. In general, the more recent data are represented. The temperature and pressure ranges under which the data were obtained are also given where available. Some specific comments regarding the experiments or data are given in the table under remarks. The data in Table 1 primarily represent GDP. Those instances where activation

---

[a] Pacific Northwest Laboratory is operated for the U.S. Department of Energy by Battelle Memorial Institute under Contract DE-AC06-76RLO 1830

Table 1. Representative Sampling of Permeation, Diffusion, and Solubility Data for Hydrogen Isotopes in Relevant Fusion Materials

Metal	P_o	E_p	D_o	E_d	S_o	E_s	Temp	Press	Ref	Remarks
Aus. Steel	.023	.688	-*	-	-	-	-	-	1	Average of much data
"	-	-	5x10^{-4}	.67	-	-	20-300	-	2	T; Surface layer
"	.032	.666	.007	.51	4.2	.15	300-800	10^3-10^5	3	Ultra high pure hydrog
304	.33	.844	.0032	.53	-	-	400-500	10-2x10^4	4	H; Oxide affects transi
304LN	-	-	.025	.6	-	-	-	5x10-7	8	Implanted deuterium
316	.034	.699	.017	.60	1.96	.085	300-600	10^2-10^5	5	D;
316L	.01	.666	6x10^{-4}	.46	7.0	.21	250-600	10^2-10^5	7	H; $P_D = P_H/\sqrt{2}$
PCA	-	-	.46	.71	2.2	.11	400-700	10^5	6	T; E_s increases with C
18-10	.012	.71	.0084	.58	-	-	380-800	<7x10^5	9	H; In-reactor tests, Ru
" *(Irr)*	*.0017*	*.51*	7x10^{-4}	.27	-	-	380-800	"	9	"
16-11-Mo	.019	.68	-	-	-	-	400-800	"	9	"
" (Irr)	.025	.63	-	-	-	-	500-800	"	9	"
Pure Fe	.003	.36	-	-	-	-	-	-	1	Average of much data
Pure Fe	-	.13	-	-	-	-	35-380	0.4	10	H, RG discharge, H_2+
HT-9	.0027	.48	-	-	-	-	-	-	11	T;
C Steel	-	-	8x10^{-4}	.08	7.4	.28	50-40	-	12	H;
C Steel	-	-	.001	≈.15	0.5-3	.3	100-600	-	13	T;
Ferritic St.	.006	.511	-	-	-	-	400-700	1	14	T; ppM T_2 in H_2 at 1
Mart. Steel	.0023	.455	8x10^{-4}	.15	8.3	.29	250-699	10^2-10^5	7	H;
"	-	-	.015	.28	-	-	20-100	10^5	15	H, Electrochem metho
Pure Ni	-	-	-	-	3.0	.15	100-400	10^5	13	T;
"	.03	.533	-	-	-	-	600-1000	10^5	16	H;
"	-	.144	-	-	-	-	200-600	2x10^{-6}	17	Implanted Deuterium
"	.012	.555	.004	.40	-	-	400-800	1	18	T;
"	.05	.577	.0074	.46	6.7	.11	350-800	10^3-10^5	3	Ultra high pure hydrog

Table 1. (continued)

Metal	P_o	E_p	D_o	E_d	S_o	E_s	Temp	Press	Ref	Remarks
Ni Base	.06	.68	-	-	-	-	600-1000	10^5-10^6	16	H; Flowing gas in He
"	.02	.69	-	-	-	-	-	1	15	T; ppM T_2 in H_2 at 1 atm
IN 600	.067	.69	.0014	.39	14	.3	350-800	10^3-10^5	3	Ultra high pure hydrogen
IN X	.0017	.56	5x10-4	.38	3.6	.18	350-800	10^3-10^5	3	"
Vanadium	.003	.34	-	-	-	-	400-800	10^2-10^4	19	H; Lower E_p at high pressure
	.9	.65	-	-	-	-	400-800	$<10^2$	19	H; E_p function of surface
"	«1	2.3	-	-	-	-	<400	10-100	19	H; Surface effect suspected
"	.008	.91	-	-	-	-	500-800	10^3-10^5	20	H; Surface oxide
"	P = 6.7x10^{-5} cm^3/		s @ 40	and 39 Pa		-	-	-	21	H; Concurrent sputtering
"	≈10	.61	-	-	-	-	450-550	10^5	22	H;
"	-	-	-	.062	-	-	35-175	-	23	D;Thermal transport
"	-	-	-	-	≈1	-0.3	-	-	24	D;
"	.088	.25	-	-	-	-0.31	>150	67-2600	25	H; In-situ sputter etching,$T^{1/4}$ dep
"	-	-	4x10-4	.08	-	-	< 300	-	26	D; Surface independent method
V-Cr-Ti	-	-	1x10-4	.11	-	-	450-500	10^{-6}	27	Implanted deuterium
	956	.23	-	-		-	950-1000	10^5	28	H;
	[illegible]	.2-.3	-	-		-	> 600	-	29	H;
	-	.47	-	-		-	< 600	-	29	H
	.43	.44	-	-		-	400-700	1-100	30	H; Sputter cleaned surface
			5x10-4	.3	.001	-0.37	>100	-	13	H; For H/Nb $<10^{-3}$
			2x10-4	.8		-	200-300	-	13	D; For high D_2 Conc.
"			-	.12	-	-	0 -200	-	31	D; D_2 Absorption
"	-	-	-	.17	-	-	35-175	-	23	D;Thermal transport
a-Titanium	-	-	.018	.54	-	-	-	-	32	H;
"	.35	.65	.009	.6	-	-	400-800	.5-300	33	H; Linear P dep., not same units
b-Ti Alloy	-	-	.002	.23	-	-	20-500	-	34	H; Vac extraction
a-Ti	-	-	-	-	1.0	-0.54	500-800	.01-1	35	D;
b-Ti	-	-	-	-	2.0	-0.61	900-1150	.01-1	35	D;

Table 1. (continued)

Metal	P_o	E_p	D_o	E_d	S_o	E_s	Temp	Press	Ref	Remarks
Molybdenum	.01	.62	4x10^{-4}	.23	24.0	.39	450-800	10^{5}	36	H; High purity H_2
"	.007	.74	6x10^{-4}	.17	11.0	.57	<800	10^{5}	37	H;
"	-	-	10^{-2}-10^{-6}	.36-1.2	.001	.29-.4	> 600	-	13	H;
TZM	.03	.76	0.5	.88	.005	-0.12	650-900	-	38	H; Sol. reaction is exothermic,
"	-	-	2.0	.99	.003	-0.17	650-900	-	38	D; outgassing experiments
Beryllium	-	-	3x10^{-7}	.19	.014	≈0	400-900	-	39	T; Gas release
"	-	-	-	-	.07	1.0	400-1000	~1	40	D+T plasma; T release
"	-	-	.1-.001	≈1.0	-	-	100-400	-	41	Implant D, Trapping effects
"	-	-	7x10^{-5}	.29	-	-	340-500	10^{4}	42	D; E_d = .36 for lower purity
Tungsten	.054	1.37	-	-	-	-	850-2100	.1-10^{4}	43	
	-	-	.0041	.39	11.0	1.0	850-2100	10^{5}	44	
"	.005	1.1	6.0	1.07	-	-	750-1050	10^{2}-10^{4}	45	

* No entry means parameter was not determined in the experiments

P_o Units: $cm^3H_2(STP)/cm\cdot s\cdot atm^{1/2}$

D_o Units: cm^2/s

So Units: $cm^3H_2(STP)/cm^3\cdot atm^{1/2}$

$E_p.E_d,E_s$ Units: eV

Temp Units: °C

Pressure Units: Pa

1 cm^3H_2@STP = 5.38 x10^{19} atoms H

energy was determined under **PDP** are noted in the table. Reviews of tritium technology related to fusion, which have included permeability values, have been published[41,46]. This current review includes more recent data and presents a range of data for particular metals and alloys.

Discussion of Permeation in Unirradiated Materials

The following section discusses **GDP** permeation data **for** materials of interest. The extent of the data, expected reliability and/or uncertainties and the need for additional data are discussed.

Austenitic stainless steel

An extensive data base exists on hydrogen isotope permeation and diffusion in stainless steel. Le Claire[1] compiled all the data up to 1982 and determined a consensus value given by:

$$P = 2.33 \times 10^{-2} \exp(-.68/kT) \mathrm{cc\text{-}H_2/cm \cdot s \cdot atm^{1/2}}. \qquad (1)$$

Approximately 75% of the data agreed with this relationship within *a* factor of 50%. Differences in composition of the various austenitic stainless steels had little systematic effect on the permeation value. The data represent permeation through stainless steel with *a* "clean" surface. Results that tended to show significantly lower permeation values were almost certainly due to an inhibiting surface oxide. Much of these data were from earlier experiments where good surface control was not practiced. A few data sets fall significantly above the values given **by** equation **1** and these are more difficult to rationalize. The isotope effect in which the permeation is inversely proportional to the square root of the mass has been confirmed through comparison of the various data sets.

The temperature dependence *of* permeation is shown graphically in Figure **1**. One curve represents the consensus activation energy of 0.68 eV as determined by Le Claire' and the other represents the maximum activation energy reported of 0.84 eV[4]. Because there is generally a compensating effect of a low P_0 term with a lower activation energy, the absolute values are not too different except near very low temperatures.

More recent measurements of hydrogen permeation in stainless steels have confirmed the expression of Le Claire. For example, the permeation of deuterium in 316 stainless steel was found to obey the relations:

$$P = 3.4 \times 10^{-2} \exp(-.69)/kT, \qquad (2)$$

which is very close to the equation given by Le Claire. The units for **P** in all equations are those given in equation 1.

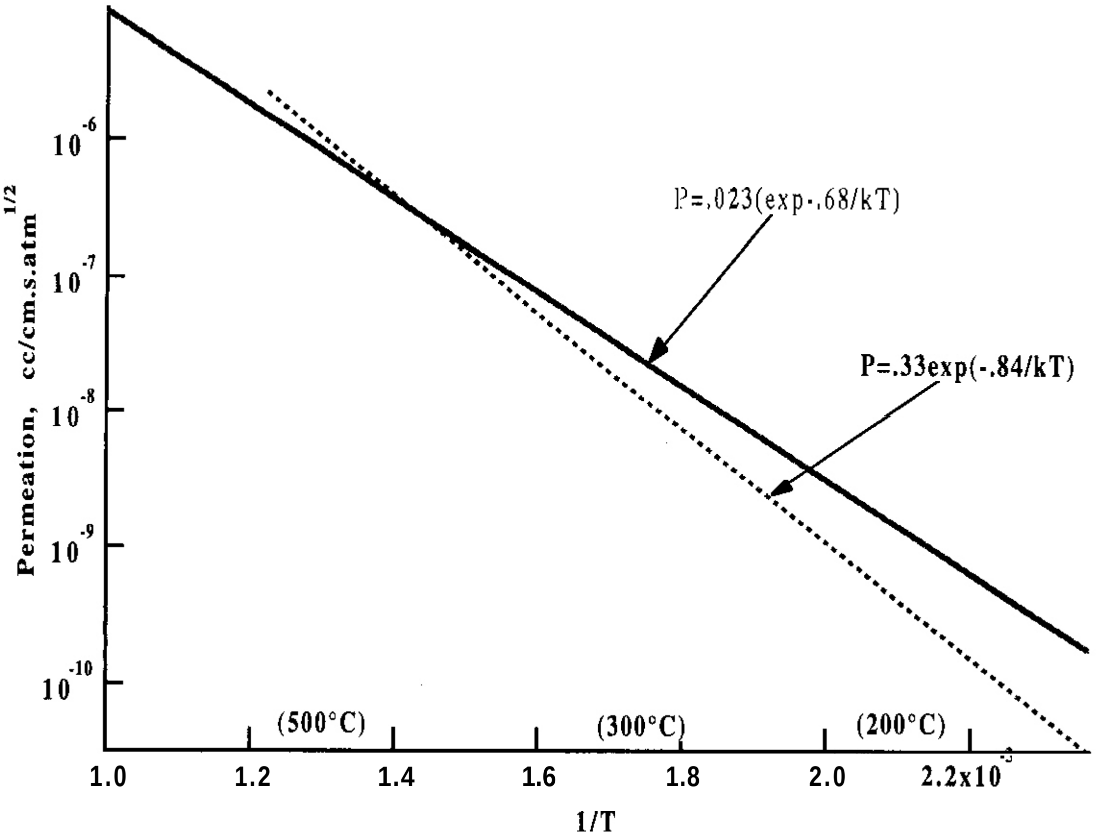

Figure 1. Hydrogen permeation in austenitic stainless steel based on the average and maximum activation energies.

Ferritic allovs

Permeation in ferritic alloys has also been reviewed and compiled by Le Claire[1]. For pure a-iron, a consensus of the hydrogen permeation data produces the relation:

$$P = 2.9 \times 10^{-3} \exp(-.36/kT) \qquad (3)$$

Permeation in ferritic steel alloys falls between the values for pure iron and the austenitic stainless steels. Researchers at ANL[11] have determined the following equation for tritium permeation in HT-9:

$$P = 4.66 \times 10^{-3}(1/\sqrt{3}) \exp(-.48/kT) \qquad (4)$$

The $\sqrt{3}$ factor accounts for the atomic mass of tritium. It was stated that the expression is for a "clean" surface and that the permeation should be reduced by a factor of 20 to 100 for an oxidized surface.

Tritium permeation specifically was measured in several ferritic alloys and the activation energy was in the range of 0.49 to 0.53 eV[14]. In the experiments, a small amount of tritium was mixed with hydrogen at 1 atm pressure at the upstream side. The partial pressure of tritium at the downstream side was essentially zero. The temperature range extended from 200 to 750°C. A high pressure of hydrogen was used as a sweep gas at the downstream side, so the tritium flux was counter current to the hydrogen flux. The effect of this on the final results was not evaluated.

The temperature dependence is shown in Figure 2 for permeation in pure Fe and in HT-9. The alloy shows about an order of magnitude lower permeation rate than pure Fe with the difference increasing toward lower temperatures. As the data in Figure 2 and in Table 1 indicate, the ferritics have a much lower activation energy for hydrogen diffusion, ≈0.1 eV, compared to the austenitics, 0.5 to 0.6 eV. This is somewhat compensated by a higher energy of solution of 0.3 eV compared to that in austenitics of 0.1 eV. The result is that the activation energy for permeation is only slightly less. One study that used atomic hydrogen from a glow discharge gave a much lower permeation activation energy, 0.13 eV[10]. This is more properly the activation energy for PDP.

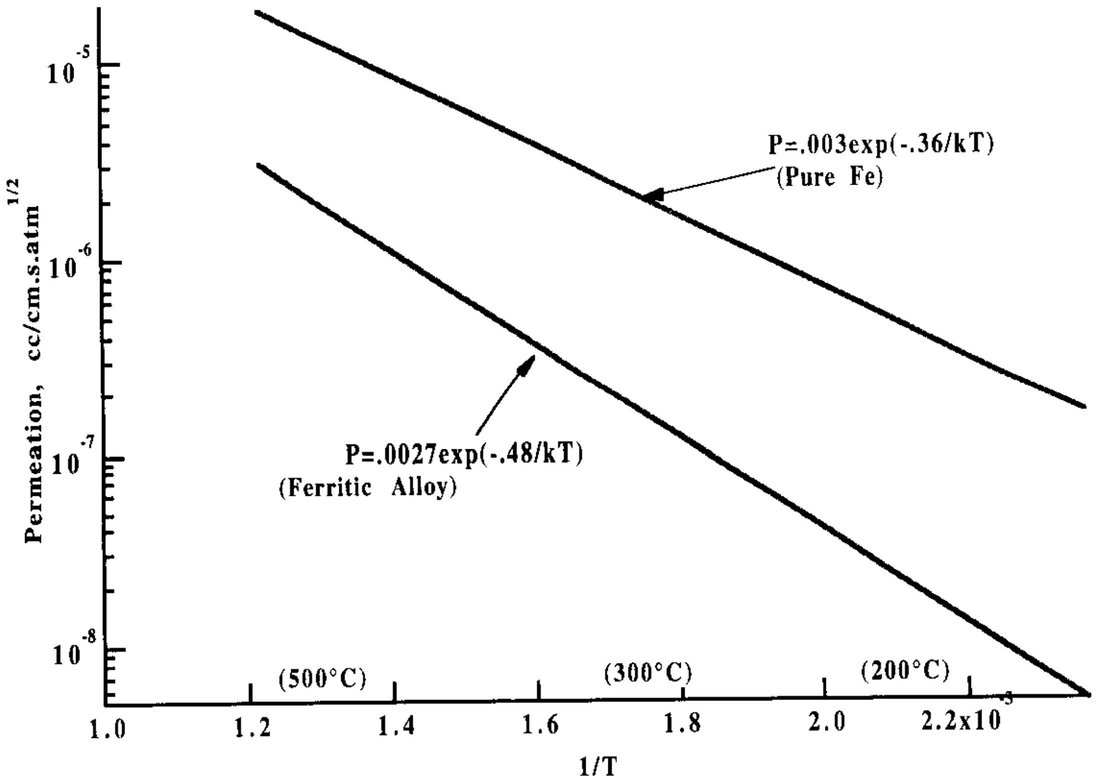

Figure 2. Comparison of hydrogen permeation in pure Fe with a ferritic alloy.

Nickel-base allovs

Permeation rates of hydrogen in nickel-base alloys are very close to those in austenitic stainless steels although the activation energies for diffusion are somewhat lower than in stainless steel. The permeation rate is, however, lower than that in pure nickel. In one study of hydrogen effects in Inconel alloys[3], the activation energy for permeation was 0.69 eV for Inconel 600 and 0.56 eV for Inconel X, close to that of pure Ni.. The temperature dependence is plotted in Figure 3 comparing pure nickel and Ni-base alloys. In this case, the difference in the absolute rate is also about an order of magnitude.

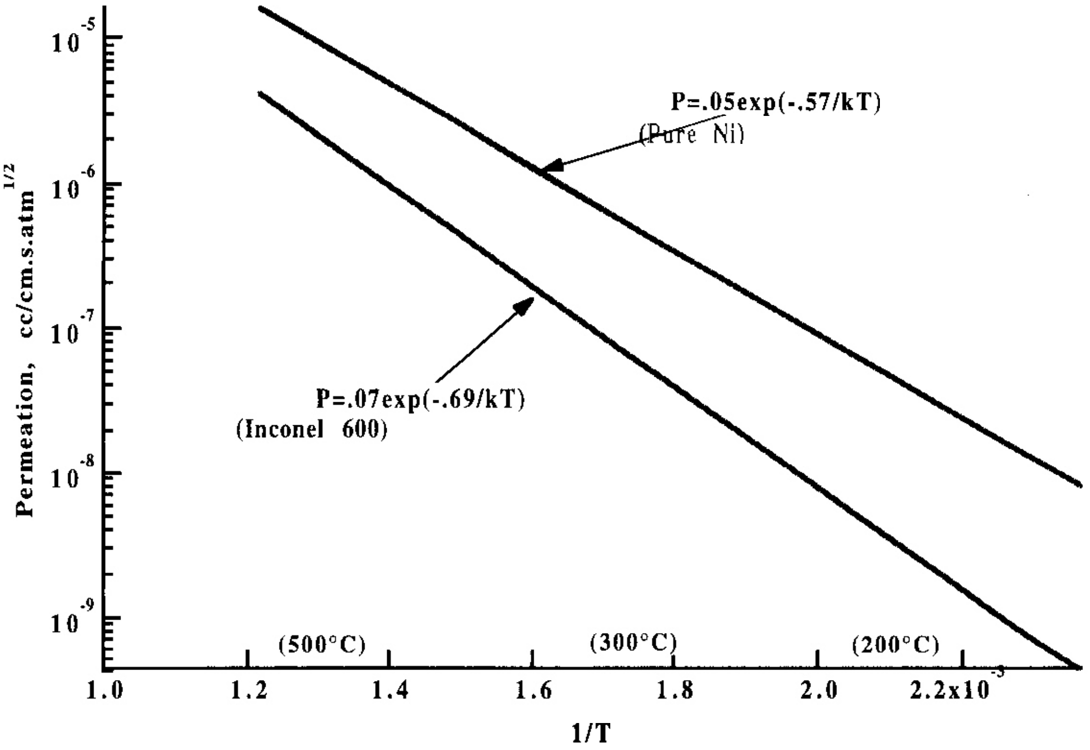

Figure 3. Comparison of hydrogen permeation in pure Ni and in a Ni-base alloy, Inconel 600.

Refractorv metals: Vanadium. Niobium and Titanium

Permeation in vanadium is strongly influenced by surface films. Van Deventer et al.[20] determined hydrogen permeation in vanadium at relatively high pressures (0.01-0.3 atm) and observed the permeation to decrease significantly with time. Permeation rates remain relatively high if the vanadium is flashed periodically at high temperatures in hydrogen. This presumably reduces the oxide film. For clean surfaces, the permeability was approximately 10^{-4} cc-H_2/cm.s.atm$^{1/2}$ at 300°C. Allowing for oxide film build-up reduces the permeability by about five orders of magnitude.

In a study of the effect of surface barriers on permeability in vanadium, the permeability did not truly follow a $p^{1/2}$ dependence[19] for all pressures. The permeability was linearly dependent on pressure at low pressure and square root dependent on pressure at high pressures. The activation energy varied from 0.3 to **0.73** eV with the activation energy increasing with decreasing pressure as shown in Figure **4.** The data indicated a sharp decrease in permeability at temperatures below

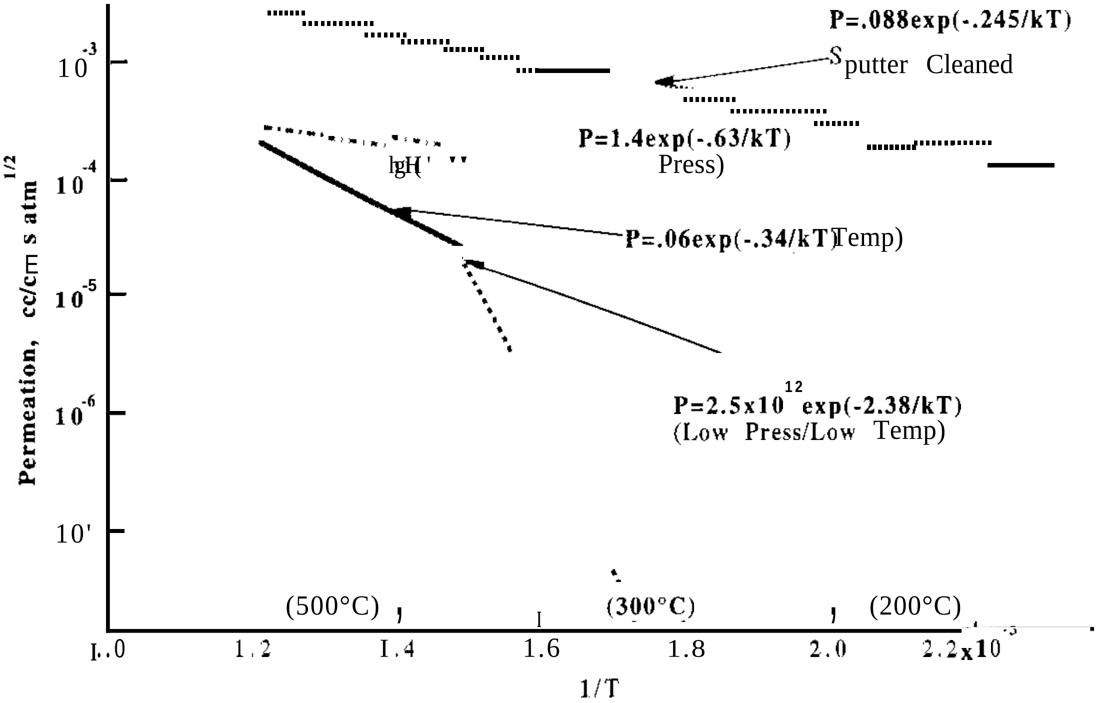

Figure **4.** Hydrogen permeation in vanadium determined under low and high pressure conditions. Also shown is hydrogen permeation after sputter cleaning of the surface.

400°C. E„ is computed to he 2.38 eV **in** this low temperature range which seems unrealistic. The permeation at low pressure in Figure **4** is hypothetical in that a $p^{1/2}$ dependence was assumed in order to compare the data. The activation energy varied from specimen to specimen in this study, which was attributed to variation in surface contamination Additional studies showed sulfur to also have an inhibiting effect on hydrogen permeation in vanadium[45].

The most recent investigation of hydrogen diffusion in vanadium gives an activation energy for permeation of **0.245 eV**[25]. This result is also plotted in Figure **4.** In the experiment, the surface was sputter-etched prior to permeation, which can account for the low activation energy and subsequent high permeation. There was little inhibiting effect from a surface film. In this same experiment, the energy of solution was determined to be -0.31 eV, which indicates an exothermic reaction. However, the overall permeation still showed a positive activation energy.

As is apparent from Table 1, there is considerable variation in the activation energies for permeation in vanadium. Steward[24], in a review of hydrogen permeability in pure metals, proposed the following equation for vanadium:

$$P = 2.7 \times 10^{-4} \exp(.26/kT) \qquad (5)$$

Use of this relationship is questionable as it was derived from the product of the diffusivity and solubility which were determined in completely separate investigations.

According to equation 5, the permeability should decrease as the temperature increases, which is contrary to behavior observed in most experiments.

The effect of a surface oxide on the permeability in vanadium is shown graphically in Figure 5. The curve for the oxide is taken from Van Deventer et al.[20]. At lower temperatures, permeability of hydrogen can he reduced by more than seven orders of magnitude when oxide films are present.

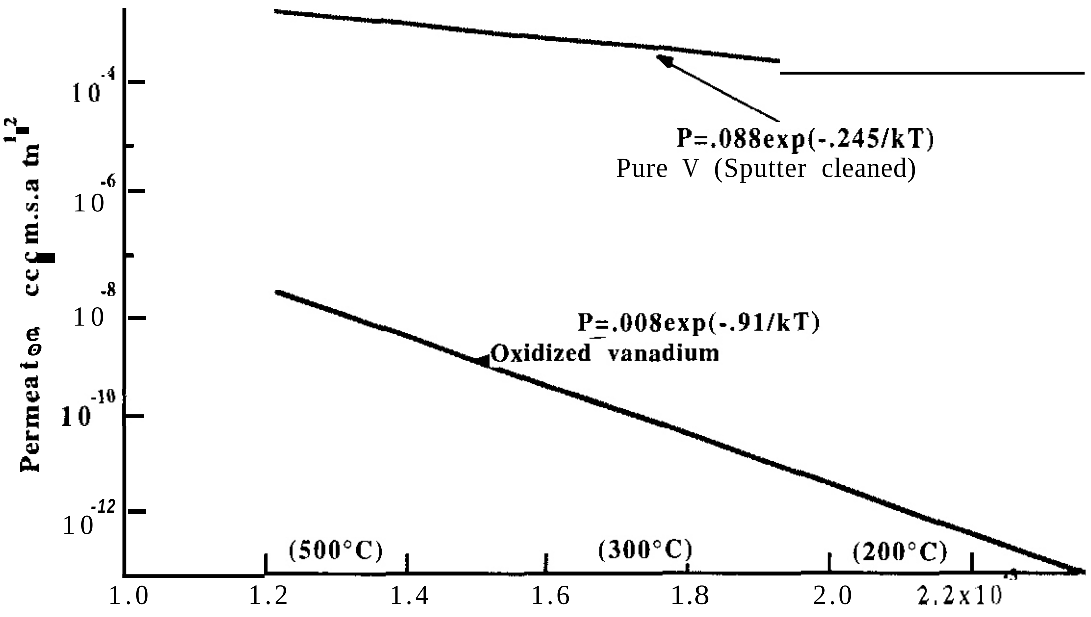

Figure 5. Hydrogen permeation in vanadium comparing an oxidized surface with an ion-sputtered surface

Vanadium does show an apparent anomaly in the permeation through the oxide layer. A fresh oxide layer is relatively porous to hydrogen and it takes a certain amount of time for the oxide layer to heal and become impervious. Such surface behavior is not observed in similar metals like niobium and tantalum.

Burger and Morgan[13] have reviewed the permeability of hydrogen isotopes in niobium, a metal chemically similar to vanadium. The temperature dependence of the permeation rate was considerably different at low temperatures compared to high temperatures. Results could not be interpreted as a simple diffusion-controlled process. Surface oxide films were observed to have a dominant effect.

Sputter cleaning of the surface was used in more recent permeation experiments from which the temperature dependencies shown in Figure **6** were derived. Also shown is

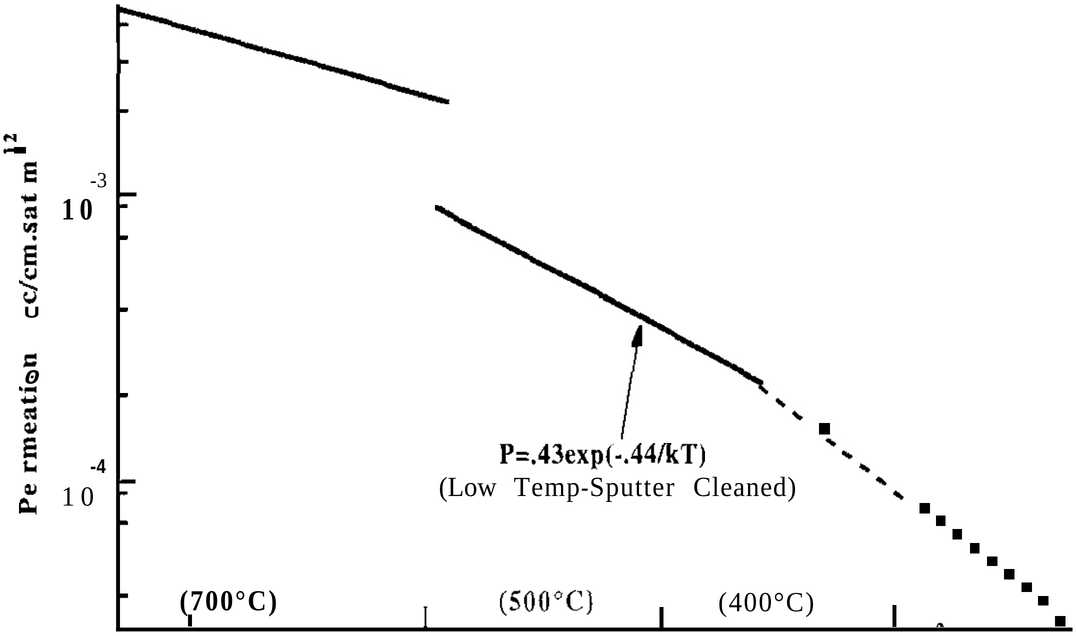

Figure *6.* Hydrogen permeation in niobium illustrating the different activation energies in different temperature regimes.

the curve based on high temperature permeation experiments. Sputter cleaning was much more effective in increasing the permeation rate than vacuum annealing of the surface. Sputter cleaning was also more effective at higher temperatures. The permeability decreased at a faster rate below **400°C** as indicated **by** the dotted line in Figure 6, but there was no attempt **by** the authors to establish an activation energy below 400° C. This behavior is similar to that observed in vanadium. In these particular experiments, the authors concluded that both adsorption/desorption and bulk diffusion processes controlled permeation but that the former were dominant.

The equations for permeation show the expected negative temperature dependence (positive activation energy). Steward, however, gives an expression for niobium which shows a positive temperature dependence for hydrogen permeability similar to that for vanadium[24]. However, it was also calculated from independent measurements of solubility and diffusion and must he suspect.

There are extensive studies of the behavior of hydrogen in titanium, most of which deal with solubility effects. Under most conditions, permeation is essentially surface controlled except at very high temperatures. Because of the surface effects, a square root dependence is not observed. An expression of the type:

$$P = 4.7 \times 10^{-4} \times p \times \exp(.65/kT) \ \mathrm{cc\text{-}H_2.atm/cm^2 \cdot s} \qquad (8)$$

has been proposed for hydrogen permeation in titanium[33]. This equation was determined for data obtained over the temperature range 400-800°C and a pressure range of 5×10^{-6} to 2×10^{-3} atm(0.5-200 Pa). Titanium also shows a negative activation energy for solution of hydrogen similar to vanadium and niobium. Tritium and deuterium have been observed to segregate near the surface regions in titanium[48]. The permeation of tritium in elements such as titanium is further complicated by the fact that hydrides (tritides) are stable.

Molybdenum, Beryllium and Tungsten

The most recent data for pure molybdenum show a permeation rate similar to that of stainless steel although the solubility of hydrogen is greater in molybdenum[36]. TZM, which is molybdenum alloyed with titanium and zirconium, showed a higher permeation activation energy than pure molybdenum[38]. Even though the amount of Ti and Zr in TZM is small, it is sufficient to cause the solution reaction to be exothermic. This study also indicated that the diffusion activation energy was significantly greater for deuterium than for hydrogen. It is generally believed that the isotope effect is only important in the pre-exponential term. Figure 7 shows the temperature dependence for several reported activation energies. Permeation in the TZM alloy *is* not appreciably different from pure Mo.

Hydrogen isotope behavior in beryllium appears to be poorly understood at the present time. No direct measurement of permeation has been made but reported values of activation energy for diffusion range from 0.19 to 1.0 eV [39,41,42,49]. Activation energies for solution ranged from zero to 1.0 eV[39, 40]. A recent study of diffusion in beryllium concludes that the diffusion behavior is very dependent on the purity of the material being tested••. The activation energy of 0.29 eV for extra high purity was somewhat lower than the 0.36 eV for commercial purity. Temperature dependence of permeation has been calculated from the available diffusivity and solubility data and is shown in Figure 8. These curves are drawn merely to show the wide disparity in results. Definitive experiments have yet to be done on permeation behavior in beryllium.

Only high temperature permeation experiments have been carried out on tungsten. Permeation curves representing the range of reported activation energies are shown in Figure 9. Although the reported permeation activation energies are close, there is a large difference in the reported diffusion and solution activation energies as noted in

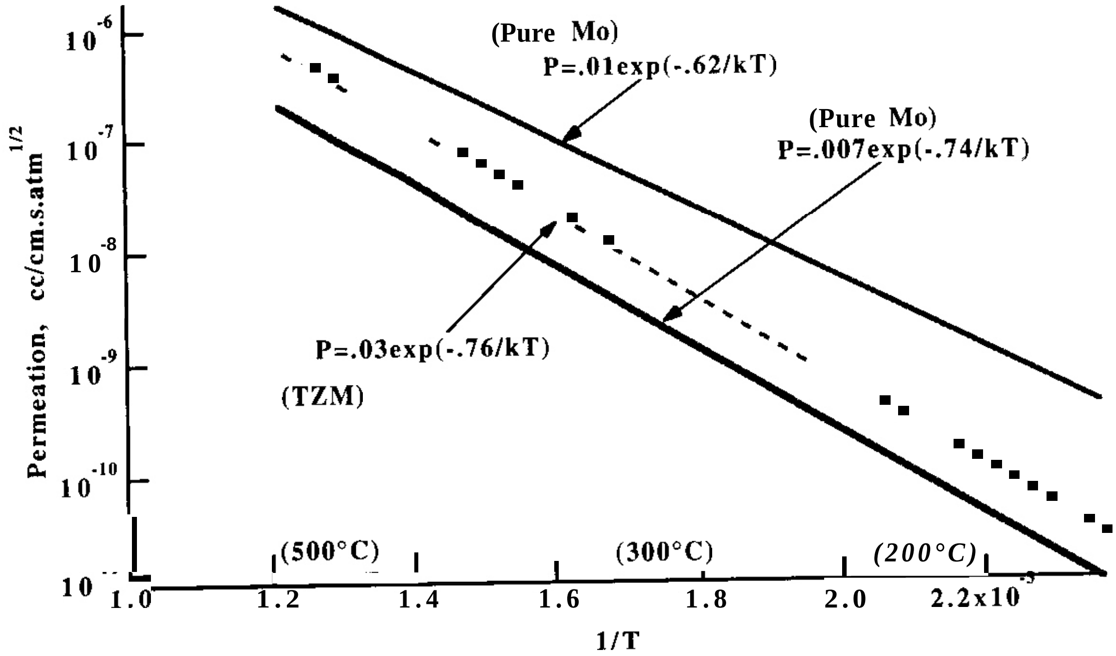

Figure 7. Hydrogen permeation in molybdenum showing variations between different pure molybdenum material and a molybdenum alloy, TZM.

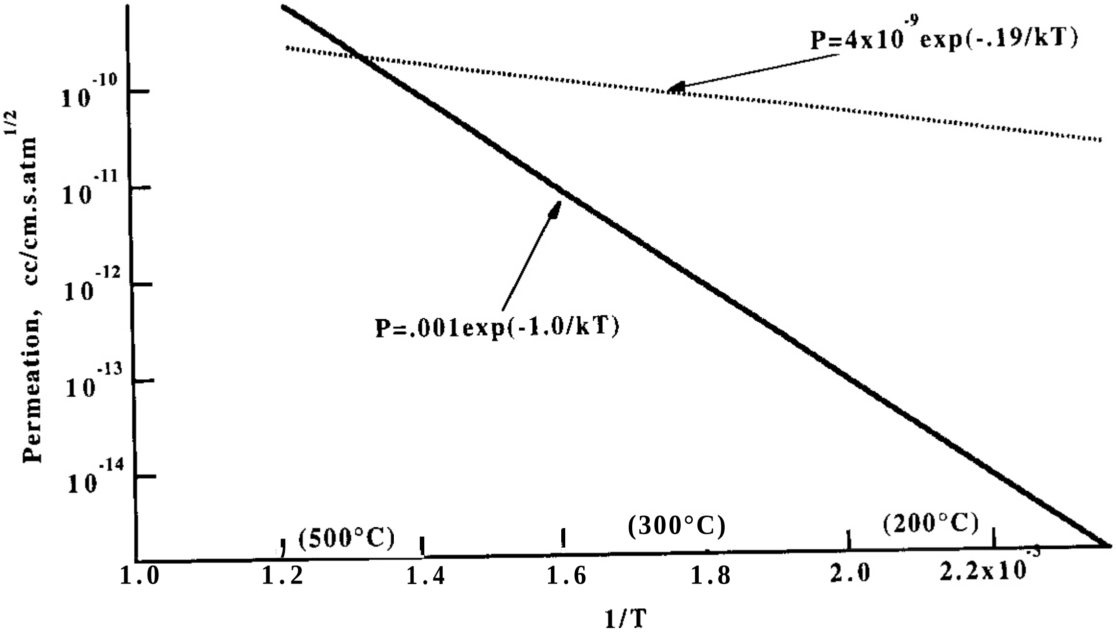

Figure 8. Calculated hydrogen permeation curves for Be based on diffusion and solubility data in Table 1.

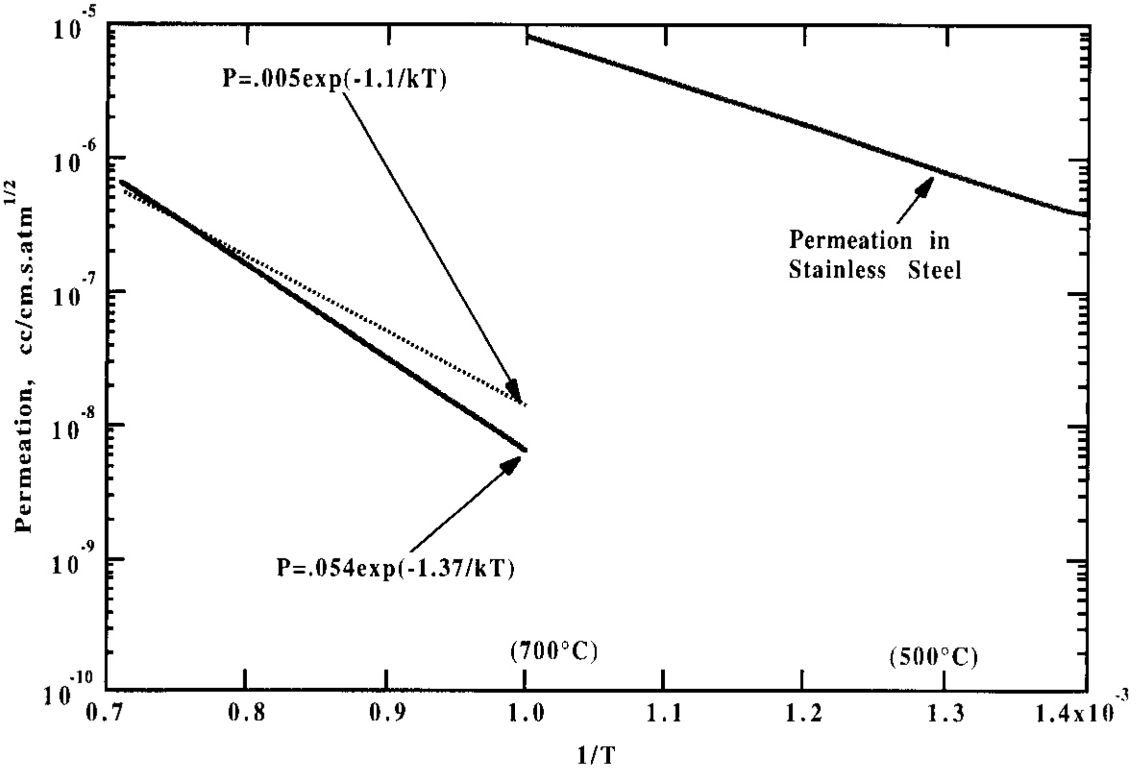

Figure 9. Hydrogen permeation in tungsten showing the range of reported activation energies. Permeation in stainless steel is shown to illustrate the much lower permeation in tungsten

Table 1. Extrapolating the curve with the lowest activation energy in Figure 9 to lower temperatures indicates extremely low permeabilities at temperatures less than 400°C.

Overall Comoarison of Materials

The temperature dependence of permeation for all the selected materials is compared in Figure 10 using the relationships shown in the preceding figures. Beryllium is not shown as interpretation of the data is still quite uncertain. Since titanium did not show the square-root pressure dependence, the permeation is plotted for a particular pressure, 1 atm. The temperature dependence can he compared in this case but the units of permeation can not he compared directly with the other materials. All of the curves shown are based on GDP experiments. The iron base, nickel base and molybdenum alloys show similar permeation behavior, although at low temperatures, permeation in the ferritic alloys is more than an order of magnitude greater than in stainless steel. Permeation in niobium and vanadium is more than three orders of magnitude greater than in stainless steel.

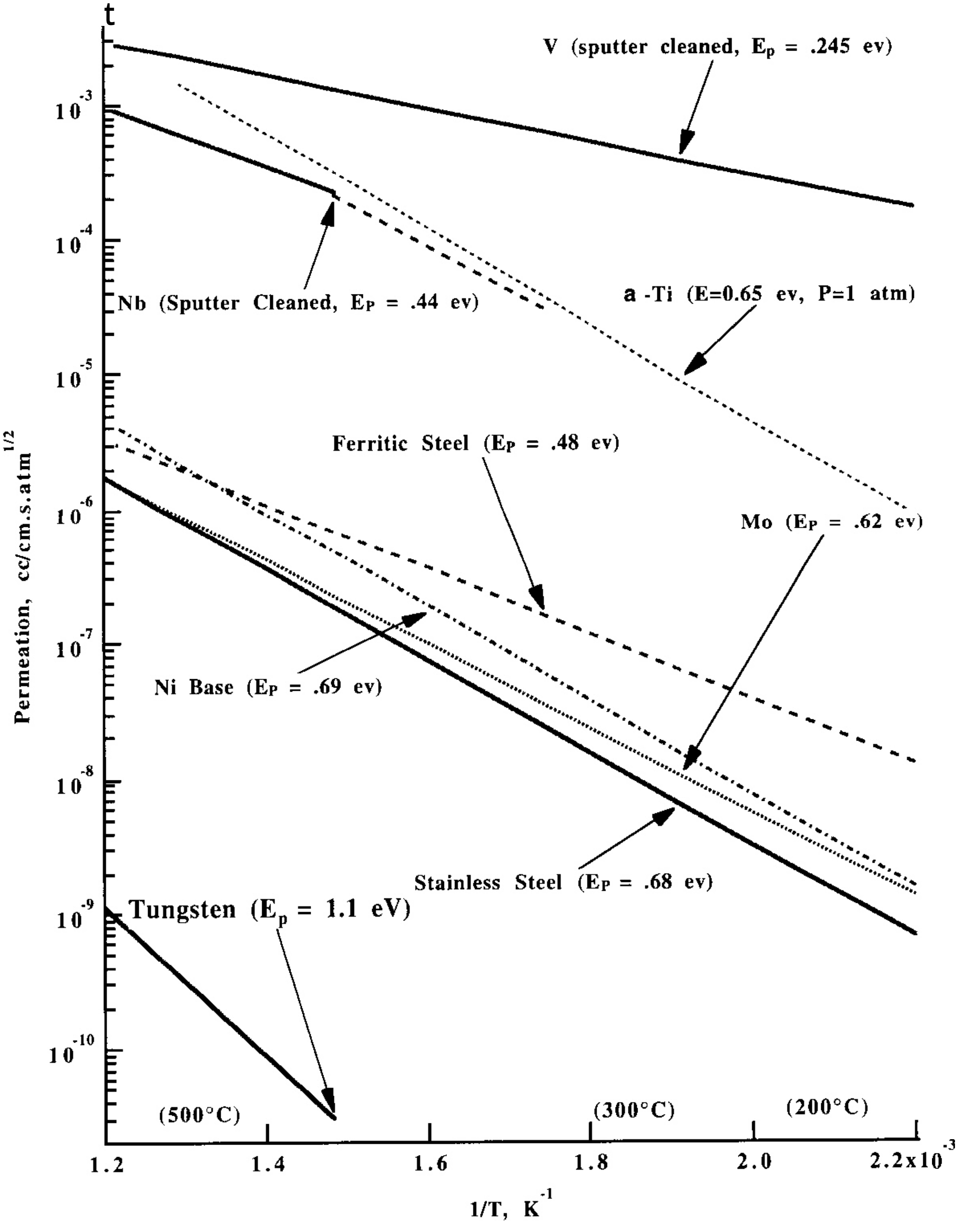

Figure 10. Comparison of hydrogen permeation for selected fusion reactor materials.

Permeation behavior in elements of the class vanadium, niobium, titanium shows the most scatter in the data. To represent these alloys, conditions most applicable to fusion were used to construct the curves. Surface behavior has such a dominant effect that it is apparently difficult in these materials to evaluate the inherent solutionldiffusion behavior that constitutes permeation. Most studies related to fusion have been on vanadium and show that if no surface film is present, permeation will he very high.

Effect of Radiation on Permeation

Particle irradiation

Only a few reports have been found that have measured permeation during irradiation. Polosuhin et al.[9] have measured hydrogen permeability in stainless steel during reactor irradiation. The temperature ranged from 200-800°C in a pressure of 0.7 MPa. The neutron flux was 1.6 x 10^{14} n/cm^2·s. Permeation increased during neutron irradiation and the effect of the irradiation was greater at lower temperatures. The data of Polosuhin et al. are shown in Figure 11 relative to the consensus permeation curve compiled by Le Claire'. Polosuhiu et al. also claimed that hydrogen diffusion in stainless steel was greater in the presence of neutron irradiation and in fact the enhancement due to radiation was greater for diffusion than for permeation.

In an apparent contrary result, Dobrozemsky and Schwarsinger[50] observed that hydrogen diffusion in stainless steel during irradiation in-reactor was slower than without irradiation by about 10%. In some earlier experiments, these same authors had claimed an enhancement of permeation and diffusion due to irradiations'. They postulate that any radiation enhanced permeation is related to a surface effect rather than hulk effect. Earlier work by the same authors indicated irradiation-induced desorption of hydrogen from the surface of stainless steel.

Enhanced diffusion of deuterium through a stainless steel membrane was observed when bombarding with carbon ions [52]. The enhancement was very small, however, amounting to only several percent.

Some post-irradiation studies have also been done. The diffusivity of hydrogen in stainless steel after neutron irradiation to 1 x 10^{17} n/cm^2 at 100°C was about 113 that of unirradiated steel[53]. The difference was in the pre-exponential term as the activation energy was the same. Solubility of hydrogen, however, was lower by two orders of magnitude in the irradiated material. Repulsion of the atomic hydrogen by the radiation defects such as self-interstitials was proposed as a mechanism.

Pre-irradiation of molybdenum with neutrons decreased subsequent hydrogen permeability by about 20% with about a 10% increase in the activation energy[37]. The dose was low, 3 x 10^{15} to 1 x 10^{17} n/cm^2, and a very low hydrogen content was used. No plausible explanation of the results was given. Neutron irradiation was found to have no effect on tritium diffusion in zirconium; however, the dose of 10^{14} n/cm^2 was extremely low[54].

Absorption and desorption rates of hydrogen from titanium were greater after irradiation to 6 x 10^{21} n/cm^2 at 450-600°C, although the activation energies

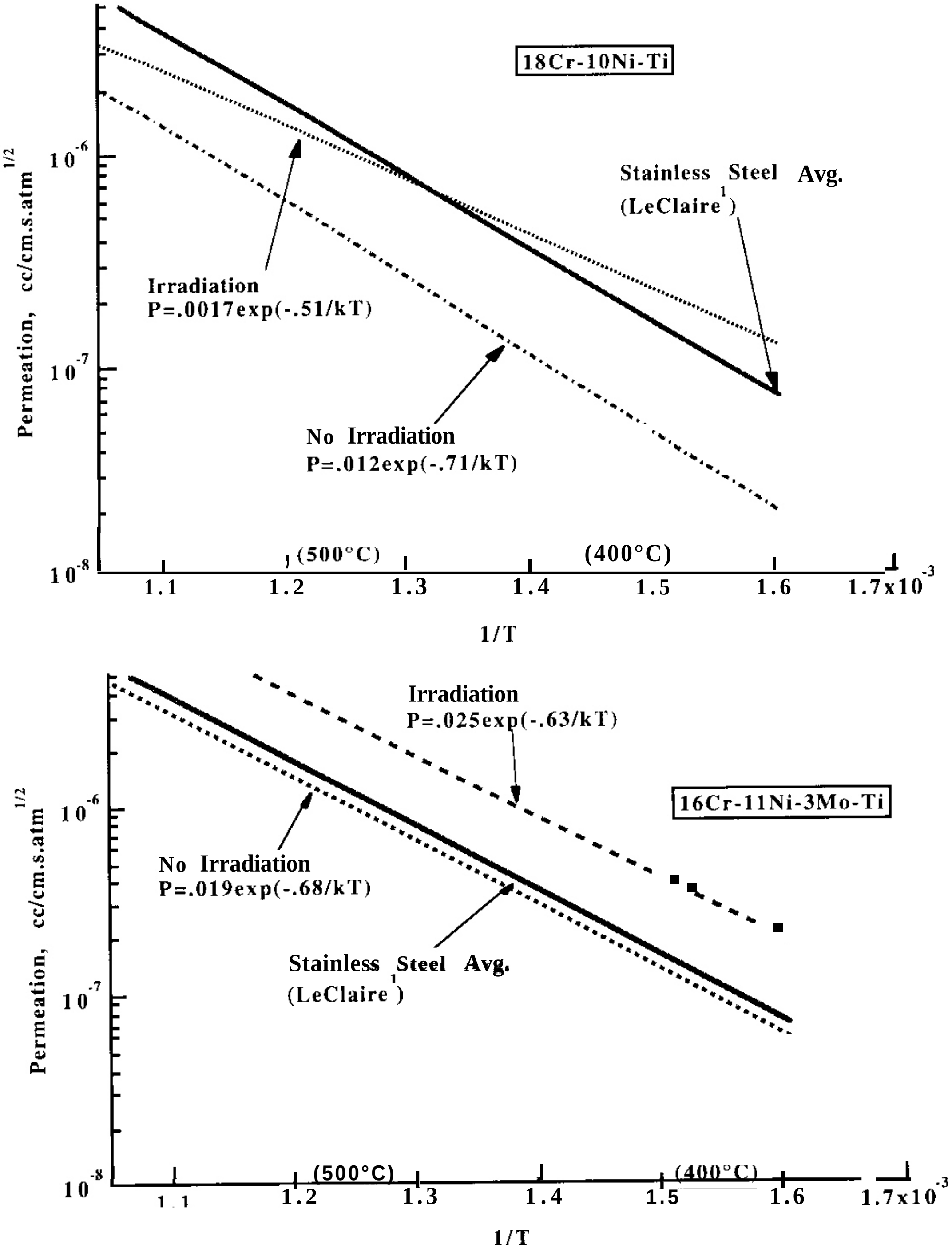

Figure 11. Hydrogen permeation in stainless steel under concurrent neutron irradiation.

were similar to unirradiated titanium[55]. This was believed to he due to an excess solubility of hydrogen in irradiated titanium. It was claimed that up to 100 hydrogen atoms per defect could exist in the irradiated material

Gamma irradiation

The evidence is sparse, but several studies indicate that gamma radiation has a very small or no effect on hydrogen isotope permeation in metals. One study by Causey et al.[56] shows no effect at all from gamma radiation. Another study by Longhurst[57] shows a slight increase in the permeation rate during gamma irradiation. If the surfaces are highly oxidized, the data become very scattered and any effect is difficult to detect. This indicates that gamma irradiation primarily affects surface-related phenomena.

Plasma Driven Permeation (PDP)

In this phenomenon, the hydrogen isotope is ionized and implanted into the material to a depth dependent on the energy and mass of the ion. It is a process which has direct application to fusion energy. Once the isotope is implanted in the material it can diffuse out through either surface. Diffusion out through the implantation surface is more often referred to as re-emission. Permeation is specifically reserved for migration and release from the opposite or downstream surface. A number of reports have addressed the issue of plasma effects in tritium permeation in fusion reactors[12, 41, 58-60].

PDP is different than GDP in that no surface reaction process is required at the upstream surface to dissolve the hydrogen isotope. In typical gas-driven permeation experiments, the gas molecules must dissociate at the surface, dissolve into the metal structure as an atomic species and subsequently diffuse through the material. At the other surface, the process must he reversed with the atoms recombining and escaping from the surface. Although the gas is driven into the matrix in PDP, recombination to the molecular form at the exit surface can still he important in controlling the overall permeability. PDP is also complex, in that there is an internal concentration gradient and radiation damage is occurring simultaneously with the implantation of the hydrogen isotope.

As mentioned above, the recombination rate at an exit surface can he significant in PDP. Baskes[12] has calculated the surface recombination rate constants and predicted the regime over which recombination or diffusion will he rate controlling. In general, for endothermic metals (Fe, Ni, Mo) diffusion is rate controlling at low temperatures and in exothermic metals (Ti, Nh, V) recombination is rate controlling. The concepts have been further developed and estimates of tritium inventory and release through the first wall have been made[41, 58]. One of the results of the analyses is that E_p under PDP for endothermic metals should he closer to $1/2(E_d+E_s)$ rather than equal to E_d+E_s as is the case for GDP. However, an attempted fit of the data available at that time to verify this relationship was not good[41].

As the hydrogen or tritium ion is driven into the metal, the solubility term, S, in the permeability relationship, $P = S \times D$, should he less of a factor and the activation energy should be closer to that for diffusion. The hydrogen diffusivities of the selected materials have been plotted in Figure **12** using data from Table 1. The relative values can be compared to the permeabilities in Figure **10.** **An** average was used when more than one value of activation energy was available. Some distinct differences are observed when rating materials on diffusivities compared to permeabilities. The diffusivities of hydrogen in niobium and vanadium are much higher than those in stainless steel or nickel base similar to that observed for permeabilities. However, the diffusivity in ferritic alloys is much higher than in stainless steel and comparable to vanadium. Molybdenum also shows a significantly higher diffusivity relative to stainless steel. Two curves are shown for diffusivity in titanium. The higher diffusivity (smaller E_D) is for β-Ti and is comparable to vanadium and niobium. a-Ti apparently has a significantly lower diffusivity.

A Russian study directly compared hydrogen permeation under both GDP and PDP conditions[61]. Permeation was always greater under PDP conditions but the magnitude of the effect depended on the material. Permeation under glow discharge conditions with energies up to **500** eV (PDP) was more than two orders of magnitude greater than GDP in molybdenum at temperatures <450°C. However, in nickel, PDP was only a factor of two greater than GDP. These results are shown graphically in Figure 13. This trend is similar to that observed when comparing diffusion rates with permeation rates in that the diffusion rate relative to the permeation rate was greater in molybdenum than in nickel. These studies demonstrate that comparisons of permeabilities in materials based on CDP experiments can be quite different than those based on PDP experiments.

More recent data seem to show that the activation energy for PDP is closer to that for diffusivity alone. In pure iron, an activation energy of 0.13 eV was reported for a PDP experiment[10], which is close to that of 0.15 reported for the diffusion activation energy[13]. Some specific experiments were done on molybdenum which showed the temperature dependence of diffusivity using atomic hydrogen was the same as that for the permeability using gaseous hydrogen[62]. However, in pure nickel, the activation energy for permeation was **0.14** eV[17] in an implantation experiment, whereas the activation energy for diffusion was reported to be **20.4** eV[3,18]. There was no apparent explanation for the very low value in the implantation experiment. More definitive experiments on other materials need to be done.

In PDP, a permeation spike is generally observed in which there is a rapid initial increase to a maximum followed **by** a slower decrease to steady state [41,63,64]. The initial increase is attributed to normal diffusion through the specimen. The decrease occurs when re-emission becomes significant. **As** more hydrogen is re-emitted, there is less that permeates through the specimen. This re-emission increases as the surface is cleaned **by** the implanting ion. Such an explanation is consistent with the observation that the permeation decreases with increase in ion energy up to several hundred **eV**[65]. Higher energy ions become more efficient as sputter cleaning of the surface occurs. In one experiment, the plasma was doped with CH_4 which increased the permeation rate[65]. The explanation was that the carbon collects at the bombardment surface, thereby retarding re-emission, and hence permeation through the specimen is increased.

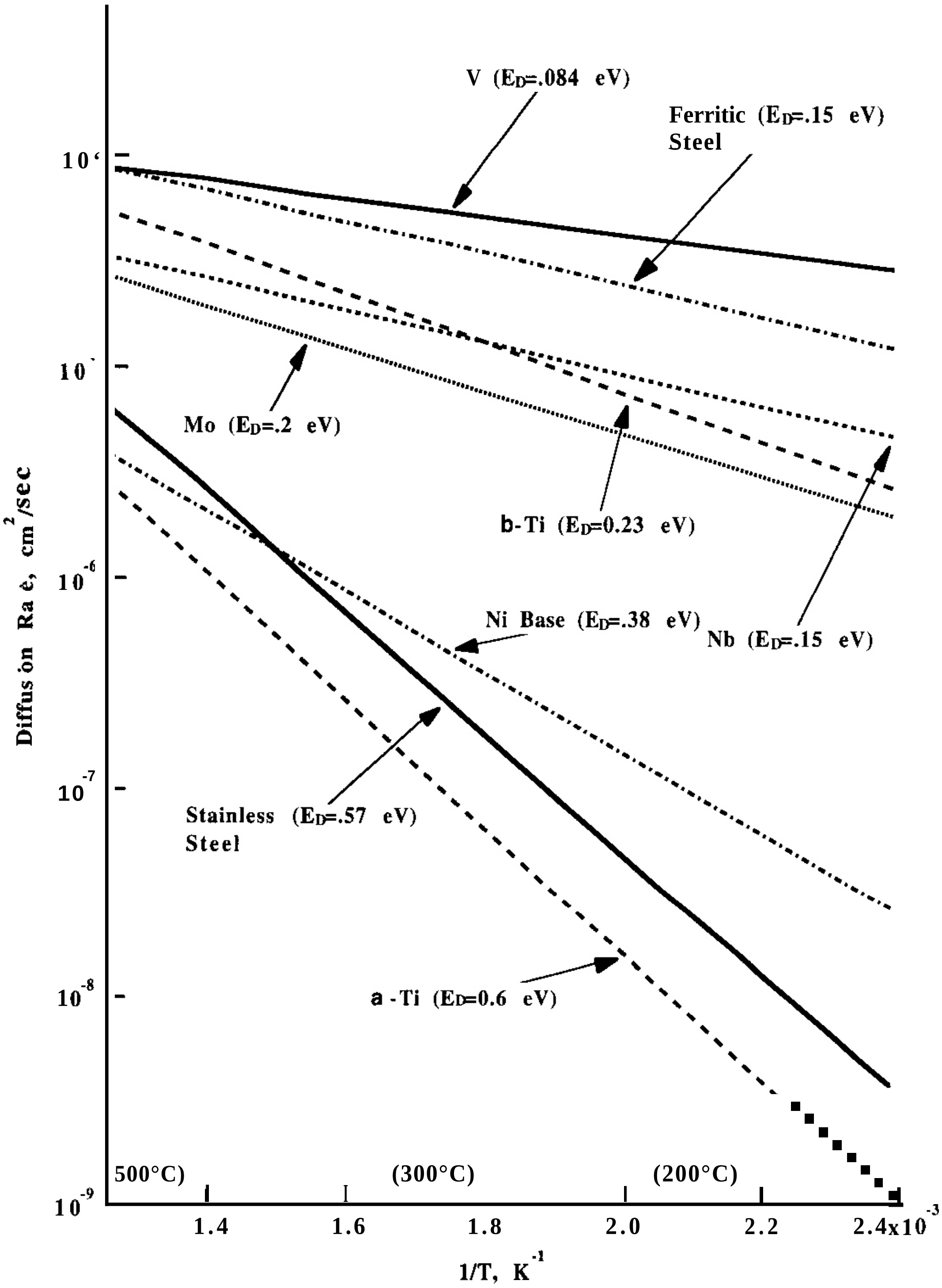

Figure 12. Comparison of hydrogen diffusivities for selected fusion reactor materials

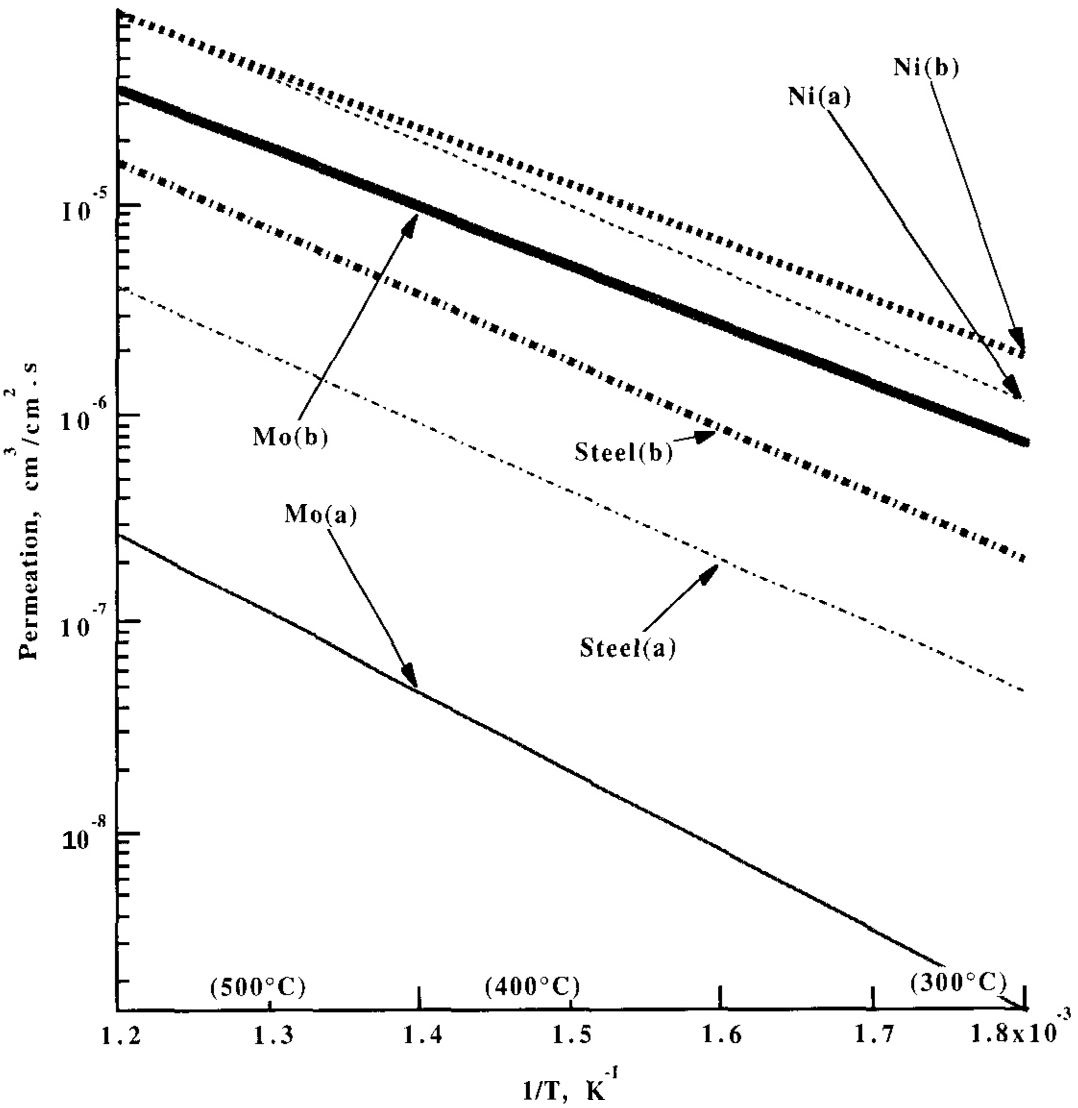

Figure **13.** Hydrogen permeation in Mo, steel and Ni under (a)-GDP and (b)-PDP conditions. Glow discharge **(500** eV) used in PDP experiments.

This spike phenomenon is temperature dependent. In experiments using 20 keV D ions, the spike effect was most pronounced in the temperature range 200-420°C[66]. It was less at 100" C and not observed at all at 700" C. The reasoning is that at low temperature, diffusion is limiting permeation and at very high temperatures, the thermally-induced surface desorption is comparable to radiation-induced desorption.

PDP studies on different alloys have shown variation in behavior. The permeation spikes have been observed in stainless steel, hcc ferritic alloys, vanadium and molybdenum[67]. At steady state, approximately .02% of the implanted deuterium was permeating through stainless steel and about .09% permeating through HT-9. In vanadium, however, about **15%** of the implanted deuterium permeated through the material. This reflects the much higher diffusivity of hydrogen isotopes in vanadium. The diffnsivity did appear to slow down with time in vanadium which was attributed to hydride formation. It was estimated that there was about 2000 ppm of deuterium in vanadium at steady state.

A complicating factor with **PDP** is the simultaneous radiation damage that can be introduced if the energy of the ionized atoms is high enough. Most of the effort has been centered around the role of trapping by the radiation-induced defects. It is believed by some that radiation-induced traps have no effect on the eventual steady state permeation rate but do control the time to reach steady state[41]. This is **an** important issue as the time to reach steady state could exceed the life of the reactor. The Russian study[61] attributed the greater effect of **PDP** in molybdeuum to differences in the type of radiation damage and the way hydrogen interacts with radiation defects.

In a study of **PDP** of deuterium in stainless steel, pre-bombardment with He ions retarded subsequent deuterium permeation[68]. The effect saturated after a certain He concentration level was reached. Simultaneous He ion bombardment also reduced the permeation rate. The rate decreased rapidly initially and then slowly decreased. When the He beam was cut off, the permeation increased although it did not reach the pre-irradiation values. The reasoning was as follows. The initial decrease is due to trapping at vacancies and He-vacancy complexes. The slow decrease is due to trapping at loops, bubbles, clusters, etc. The increase in permeation when the He beam is cut off results from the removal of the vacancy traps. It could not he definitely resolved whether the reduction in permeation due to pre-implantation of He was due solely to implanted He or to the residual radiation damage.

Strong binding of deuterium atoms to He bubbles in stainless steel has been proposed based **on** another study[69]. The experiments were done at low temperature (200" C) and the trap strength was estimated at 0.22 eV. The binding was similar to free surface absorption although the bubbles were only of 1 nm in size. There was also a suggestion of deuterium-vacancy binding.

In the Russian study mentioned earlier[61], additional radiation damage was introduced **by** simultaneous bombardment with inert gas ions during the **PDP** experiments. Simultaneous bombardment with inert gas ions increased the permeation rate in molybdeuum but actually decreased the rate in nickel. It was postulated that the high sputtering rate of nickel due to the inert ions caused a high re-emission rate of hydrogen. A high re-emission rate results in a low permeation rate. Molybdenum has a low sputtering rate so re-emission was less and the enhancement of the permeation due to irradiation more than compensated for the low re-emission.

CONCLUSIONS

There are many factors that will influence permeability in actual operation of a fusion reactor. Factors will he more or less important depending on the particular material. Table 2 lists the important factors in the permeation of hydrogen isotopes along with a brief explanation of how these factors affect permeation and the relative magnitude of the effect.

For the common iron and nickel-based alloys as well as for some refractory metals such as molybdenum and tungsten, permeabilities and permeation behavior are fairly well established. Metals such as vanadium, titanium and niobium have a high inherent permeability, but the permeation rate is generally dominated by the surface film. For this reason, these materials can show a wide divergence in the reported permeability values. The permeation data on beryllium also show much variation for reasons not well understood. More studies need to be done on beryllium to get reliable data. The data base on **PDP** is limited and fragmented, primarily because many different types of experiments have been done. The proper choice of activation energy for **PDP** is not well established. Based on available data, rankings of materials based on **GDP** experiments may be misleading for fusion application, particularly for materials in which the solubility is the dominant effect in permeation. For some materials such as vanadium, permeability is very high under both **GDP** and **PDP** conditions.

FUTURE WORK

This review of the data on permeation of hydrogen isotopes in fusion materials is considered to be complete with this report.

Table 2 Factors Influencing Permeation

Surface Condition	Influence
Finite surface film	Retards permeation, particularly strong in materials with high inherent permeability
Surface Composition/Structure	Affects recombination rate, k. Strong influence in PDP
Surface roughness	Effect not well studied, probably affects k
Radiation	
Trapping by defects	Transient influence, retards permeation by increasing time to reach steady state
Radiation enhanced diffusion	Apparently not a strong effect except possibly at low temperatures and for stainless steel
Sputtering	Has strong effect by removing surface film
Isotope Uptake	
Solution from gas phase	Dependent on gas pressure
Ion implantation	Independent of pressure, reduces or eliminates solubility term
Alloy Chemistry	
Overall Composition	Not strong as long as there is no phase change
Hydride formation	May be strong, eventually decreases permeability
Impurity Trapping	Not well known, effects may be neutral over long time
Environmental Effects	
Pressure effects	Solubility dependent on pressure, not important in PDP
Temperature	Arrenhins temperature dependence, mechanism can change in different temperature regimes
Isotope Composition	Competition effects between isotopes not well studied but may be important. Mass effect is well known

REFERENCES

1. A. D. Le Claire, "Permeation of Gases Through Solids - II", AERE-R **10598, 1982.**

2. R. A. Langley, J. Nucl. Mat., **128&129 , 622-628 (1984).**

3. T. Tanahe, Y. Yamanishi, K. Sawada and **S.** Imoto, J. Nucl. Mat.. **122&123, 1568, (1984).**

4. T. Namha, M. Yamawaki and M. Kanno, J. Nucl. Mat. **128&129, 646 (1984).**

5. F. Reiter, J. Camposilvan. M. Caorlin, *G.* Saibene and R. Sartori, Fus. Tech.. **8, 2344 (1985).**

6. R. A. Causey, L. M. Steck and R. van Namen, Fus. Tech., 8, **2384 (1985).**

7. K. **S.** Forcey, D. K. Ross, J. C. B. Simpson and D. S. Evans, J. Nucl. Mat., **160, 117 (1988).**

8. J. Bohdansky, K. L. Wilson, A. E. Pontau, L.G. Haggmark and M. I. Baskes, J. Nucl. Mat., **93&94, 594 (1980).**

9. B. **G.** Polosuhin, E. P. Baskakov, E. M. Sulimov, A. P. Zyryanov, Yu. S. Shestakov, G. M. Kalinin, Yu. S. Strebkov and A. G. Dobrynskih, J. Nucl. Mat.. **191-194, (1992).**

10. **J.** Winter, F. Waelbroeck, P. Weinhold and T. Schelske, J. Nucl. Mat., **, 111&112, (1982).**

11. A. Hassanein and D. K. Sze, "Blanket Comparison and Selection Study", ANL Report, ANl/FPP/84-1, **p.6.6-9 (1984).**

12. M. **I.** Baskes, J. Nucl. Mat., **92, 318 (1980).**

13. L. L. Burger and L. G. Morgan, "Tritium Safety in Fusion Reactor Design, Task 2-Tritium Properties", **1980.**

14. **J.** T. Bell, J. D. Redman and H. F. Bittner, J. Mat. for Energv Svst.. **1, 55 (1979).**

15. **G.** Benamati, A Donato, S. Aolina and **S.** Lanza, Proc. of 6th Intl. Conf on Fusion Reactor Materials, **1993,** to be published.

16. N. Kishimoto, T. Tanabe, H. Araki, H. Yoshida and R. Watanahe, Nucl Tech., **66, 578 (1984).**

17. T. Tanabe, Y. Furuyama, H. Hirano and S. Imoto, J. Nucl. Mat., **128&129, 641 (1984).**

18. **J. T.** Bell and J. D. Redman, The J. Phvs. Chem., **82, 2834 (1978).**

19. T. Namha, H. Miyaguchi, M. Yamawaki and M. Kanno, J. Nucl. Mat., 105, 318 (1982).

20. E. H. Van Deventer, T. A. Renner, R. H. Pelto and V. A Maroni, J. Nucl. Mat., 64, 241 (1977).

21. T. Namba, M. Yamawaki and M. Kanno, J. Nucl. Sci Tech., 20, 752 (1983).

22. R. R. Heinrich, C. E. Johnson and C. E. Crouthamel, J. Electro. Chem. Soc., 112, 1071 (1965).

23. D. T. Petersen and M. F. Smith, Met. Trans., 13A, 821 (1982).

24. S. A. Steward, “Review of Hydrogen Isotope Permeability Through Materials, UCRL-53441, 1983.

25. K. Takata and T. Suzuki, Mat. Sci. and Engr., A163, 91 (1993).

26. J. Vokl and G. Alefeld, in “Diffusion in Solids; Recent Developments”, eds. A. S. Nowick and J. J. Burton, Academic Press, London, pp. 232-295 (1975).

27. R. A. Anderl, G. R. Longhurst and D. A. Struttman, J. Nucl. Mat., 145-147, 344 (1987).

28. D. W. Rudd, D. W. Vose and S. Johnson, J. Phys.Chem., 66, 351 (1962).

29. M. Kanno, M. Yamawaki and T. Namba, “Hydrogen Permeation Through Niobium” in Proc. of Symp. on Hydrogen in Metals, Japan, Nov. 1979.

30. M Yamawaki, T. Namba, T. Kiyoshi and M. Kanno, J. Nucl. Mat., 122&123, 1573 (1984).

31. H. Wipf and G. Alefeld, Phys. Stat. Sol., 23, 175 (1974).

32. R. J. Wasilewsky and G. L. Kehl, Metallureia, 50, 225 (1954).

33. D. L. Johnson and H. G. Nelson, Met. Trans., 4A, 569 (1973).

34. W. R. Holman and R. W. Crawford, Trans. Met., 233, 286 (1965).

35. M. Nagasaka and T. Yamashina, J. Less Com. Met., 45, (1976).

36. T. Tanahe, T. Yamanishi and S. Imoto, J. Nucl. Mat., 191-194, 439 (1992).

37. H. Katsuta, T. Iwai and H. Ohno, J. Nucl. Mat., 115, 206 (1983).

38. S. Tominetti, M. Caorlin, J. Camposilvan, A. Perujo and F. Reiter, J. Nucl. Mat., 176&177, 672 (1990).

39. P. M. S. Jones and R. Gibson, J. Nucl. Mat., 21, 353 (1967).

40. R. A. Causey, W. L. Hsu, B. E. Mills, J. Ehrenherg and V. Phillips, J. Nucl. Mat., 176&177, 654 (1990).

41. R. A. Kerst and W. A. Swansiger, J. Nucl. Mat., 123, 1499 (1984).

42. E Ahramov, M. P. Riehm, D. A. Thompson and W. W. Smeltzer, J. Nucl. Mat., 175, 90 (1990).

43. R. Frauenfelder, J. Chem. Phvs., 45, 3955 (1968).

44. R. Frauemfelder, J. Vac Sci. and Tech., 6, 388 (1969).

45 A. P. Zakharov, V. M. Sharapov, and E. I. Evko, Soviet Mater. Sci., 9, 149 (1973).

46. P. A. Finn and D.K. Sze, Fusion Tech., 8, 693 (1985).

47. M. Yamawaki, T. Namha, T. Kiyoshi, T. Yoneoka and M. Kanno, J. Nucl. Mat., 133&134, 292 (1985).

48. P. N. Adler, R. L. Schulte and R. Margolin, Met. Trans. **21A,** 2003 (1987).

49. W. R. Wampler, J. Nucl. Mat., 122&123, 1598 (1985).

50. G. W. Schwarzinger and R. Dohrozemsky, J. Nncl. Mat., 122&123, 1560 (1984).

51. R. Dohrozemsky and G. W. Schwarzinger, "Radiation Enhanced Permeation of Hydrogen through Austenitic Steel Tnhes, Proc. 8th Intl. Vac Congress, Paris, September 1980.

52. B. L. Boyle and D. K. Brice, J. Nucl. Mat., 145-147, 288 (1988).

53. N. Quick, "Gas Phase Hydrogen Permeation through Ferritic Iron, Austenitic Stainless Steel and Neutron Irradiated Austenitic Stainless Steel from Near 300 K to 873 K", COO-3166-18 (1976).

54. W. Kunz, H. Miinzel and U. Helfrich, J. Nucl. Mat., **105,** 178 (1982).

55. H. Miyake, Y. Hirooka, H. Shinmura, S. Yamanaka, T. Sano and Y. Higashignchi, **J. Nucl. Mat.,** 103&104, 477 (1981).

56. R. M. Causey and L. M. Steck, J. Nucl. Mat., 122&123, 1518 (1984).

57. G. R. Longhurst, G. A. Deis, P. Y. Hsu and L. G. Miller, Nucl. Tech. Fusion, **4,** 681 (1983).

58. M. I. Baskes, W. Bauer, and K. L. Wilson, J. Nucl. Mat., 111&112, 663 (1982).

59. B. L. Doyle, J. Nucl. Mat., **111&112, 628 (1982).**

60. B. L. Doyle and D. K. Brice, J. Nucl. Mat., **122&123, 1523 (1984).**

61. V. M. Sharapov, A. I. Pavlov and A. P. Zakharov, Russian J. Phys. Chem., **56, 730 (1982).**

62. T. Tanabe, J. Nucl. Mat., **191-194, 444 (1992).**

63. H. K. Perkins and T. Noda. J. Nucl. Mat., **71, 349 (1978).**

64. T. Tanabe, Y. Furuyama and S. Imoto, J. Nucl. Mat, **122&123, 1563 (1984).**

65. R. A. Causey, R. A. Kerst and B. E. Mills, J. Nucl. Mat., **122&123, 1547 (1984).**

66. T. Tanabe, N. Saito, Y. Etoh and S. Imoto, J. Nucl. Mat., **103&104, 483 (1982).**

67. G. R. Longhurst, R. A. Anderl and D. A. Struttman, J. Nucl. Mat., **141-143, 229 (1986).**

68. K. Fukushima, K. Ebisawa, S. Nakahigashi, M. Imura and M. Terasawa, J. Nucl. Mat., **133&134, 284 (1985).**

69. S. M. Myers and W. R. Wampler, J. Nucl. Mat., **111&112, 579 (1982).**

6.0 DEVELOPMENT OF STRUCTURAL ALLOYS

6.1 Ferritic Martensitic and Bainitic Steels

DEVELOPMENT OF LOW-CHROMIUM, CHROMIUM-TUNGSTEN STEELS FOR FUSION --

R. L. Klueh and D. J. Alexander *(Oak* Ridge National Laboratory)

OBJECTIVE

The goal of this study is the development of reduced-activation ferritic steels.

SUMMARY

High-chromium (9-12% Cr) Cr-Mo and Cr-W ferritic steels are favored as candidates for fusion applications. In the early work to develop reduced-activation steels, an Fe-2.25Cr-2W-0.25V-0.1C steel (designated 2 1/4Cr-2WV) had better strength than an Fe-9Cr-2W-0.25V-0.07Ta-0.1C (9Cr-2WVTa) steel (compositions are in weight percent). However, the 2 1/4Cr-2WV had less-than-adeqnate impact toughness, as determined by the ductile-brittle transition temperature and upper-shelf energy of a Charpy impact test. Because low-chromium steels have some advantages over high-chromium steels, a program to develop low-chromium steels is in progress. Microstructural analysis indicated that the reason for the inferior impact toughness of the 2 1/4Cr-2WV was the granular-bainite microstructure obtained when the steel was normalized. Properties can be improved by developing an acicular bainite structure by increasing the cooling rate after austenitization. Alternatively, acicular hainite can be promoted by increasing the hardenability. Hardenability was changed by adding small amounts of boron and chromium to the 2 1/4Cr-2WV composition. A combination of B, Cr, and Ta additions resulted in low-chromium reduced-activation steels with mechanical properties comparable to those of 9Cr-2WVTa.

PROGRESS AND STATUS

Introduction

Ferritic steels have been candidate structural materials for first wall and blanket structures of fusion power plants since the late 1970s when fast-reactor irradiation showed them to be more swelling resistant than austenitic stainless steels. They also have higher thermal conductivity and lower thermal expansion coefficients than austenitic steels, thus providing improved resistance to thermal stresses for a fusion power plant operating in a pulsed mode. The first femtic steels considered in the U.S. program were Sandvik HT9 (nominally 12Cr-1Mo-0.25V-0.5W-0.5Ni-0.2C, here designated 12Cr-1MoVW) [1] and modified 9Cr-1Mo steel (9Cr-1Mo-0.2V-0.06Nb-0.1C, designated 9Cr-1MoVNb) [2]. To a lesser extent, *2* 1/4Cr-1Mo (2.25Cr-1Mo-0.1C) was also considered [3]. All compositions are in weight percent.

During the mid 1980s, fusion programs throughout the world began to emphasize the development of "low-activation" or "reduced-activation" femtic steels [4-6]. The difference between these steels and conventional steels is how rapidly the induced radioactivity in the reduced-activation steels decays. For that reason, the steels have also been referred to as fast induced radioactivity decay (FIRD) steels [4]. In FIRD or reduced-activation steels, alloying elements that produce long-lived radioactive isotopes during neutron irradiation are eliminated or replaced. Elements that must be eliminated or minimized include Mo. Ni, Nb, Cu. and N. In the FIRD steels, tungsten replaced molybdenum to produce Cr-W steels as alternatives to the Cr-Mo steels; small amounts of tantalum replaced the niobium.

Just as work on conventional steels emphasized high-chromium Cr-Mo steels, development of reduced-activation steels has concentrated on chromium levels between 7 and 10 wt.% [4-6]. Initial studies at *Oak* Ridge National Laboratory (ORNL) were on steels with 2.25 to 12% Cr [7-91. Of the original eight ORNL steels studied (Table 1), a 2 1/4Cr-2WV steel had the highest strength [7]. However, the impact toughness of 2 1/4Cr-2WV, as measured in a Charpy test, was inferior to that of a 9Cr-2WVTa steel [9]. The 9Cr-2WVTa had comparable tensile properties [4] and superior Charpy impact properties [9] to those of 9Cr-1MoVNb and 12Cr-1MoVW.

Table 1. Nominal Compositions for Fast Induced-Radioactivity Decay Steel Development Program

Steel	Nominal Chemical Composition^a				(wt %)
	Cr	W	V	Ta	C
2 1/4CrV	2.25		0.25		0.1
2 1/4Cr - 1WV	2.25	1	0.25		0.1
2 1/4Cr - 2W	2.25	2			0.1
2 1/4Cr - 2WV	2.25	2	0.25		0.1
5Cr - 2WV	5	2	0.25		0.1
9Cr - 2WV	9	2	0.25		0.1
9Cr - 2WVTa	9	2	0.25	0.07	0.1
12Cr - 2WV	12	2	0.25		0.1

^{a} Balance iron

An important property for ferritic steels is the effect of irradiation on impact toughness. Charpy specimens of the 9Cr-1MoVNb and 12Cr-1MoVW steels irradiated to 13 dpa at 400°C in the Experimental Breeder Reactor (EBR-II), a fast reactor, showed increases in the ductile-brittle-transition temperature (DBTT) of 52 and 124°C, respectively [10]. The 9Cr-2WVTa irradiated to 13 dpa in the Fast Flux Test Facility (FFTF), also a fast reactor, developed an increase in DBTT of only 15°C [11].

Despite the excellent behavior of the 9Cr-2WVTa, there are advantages for low-chromium steels [12]. It might be possible to use a low-chromium steel without a post-weld heat treatment, an important consideration for a complicated structure, such as a fusion power plant. A bainitic steel might also be used without tempering. an economic advantage. Finally, a low-chromium steel would conserve chromium, a strategic material.

Although relatively modest shifts in DBTT occurred for 9Cr-1MoVNb and 12Cr-1MoVW after irradiation in the fast reactors EBR-II and FFTF, much larger shifts (>200°C) were observed when irradiated in the High Flux Isotope Reactor (HFIR), where displacement damage is accompanied by transmutation helium formation in the steels [13]. Helium is produced by an (n,a) reaction of nickel with the thermal neutrons in the mixed-spectrum of HFIR. By irradiating nickel-doped and undoped steels in HFIR and EBR-II, the difference in behavior in the two reactors was attributed to the larger amount of helium produced during irradiation in HFIR. Helium was concluded to promote intergranular fracture [13]. This result is important, because the high-energy neutrons from the fusion reaction will produce large amounts of transmutation helium in the first wall of a fusion power plant.

To minimize the effect of helium in austenitic stainless steels, microstructures were developed with a high number density of fine precipitates [14]. For such a microstructure, the transmutation helium formed during irradiation is trapped at the matrix/precipitate interface of the fine precipitates. Because of the large number of precipitates, the helium is widely distributed, and the high number density of small bubbles that form suppresses swelling. Elevated temperature helium embrittlement is also inhibited because the precipitates prevent helium from migrating to grain boundaries [15]. A similar process might be effective in the ferritic steels to minimize the effect of helium on the shift in DBTT.

The 9Cr-2WVTa has a fairly low number density of precipitates, which are mainly relatively large $M_{23}C_6$, with a lesser number of smaller MC particles [Fig. 1(a)] [8]. Figure 1(b) compares the high number density of fine precipitates in the 2 1/4Cr-2WV to the precipitates in 9Cr-2WVTa. The high density of fine precipitates in the 2 1/4Cr-2WV are vanadium-rich MC precipitates [8]. The precipitate number density and type of precipitates in 9Cr-2WVTa are similar to those in 9Cr-1MoVNb and 12Cr-1MoVW, which showed the effect of helium on properties when irradiated in HFIR [13,16]. The $M_{23}C_6$ precipitates are generally large and of low number density. MC particles are present in the high-chromium steels. but in much lesser amounts than the $M_{23}C_6$. The number of precipitates in these steels is probably too small to be effective in trapping the helium during irradiation. Figure 1(b) indicates that it may be possible to develop a high density of precipitates in a low-chromium steel. Of course, to be successful it will also be

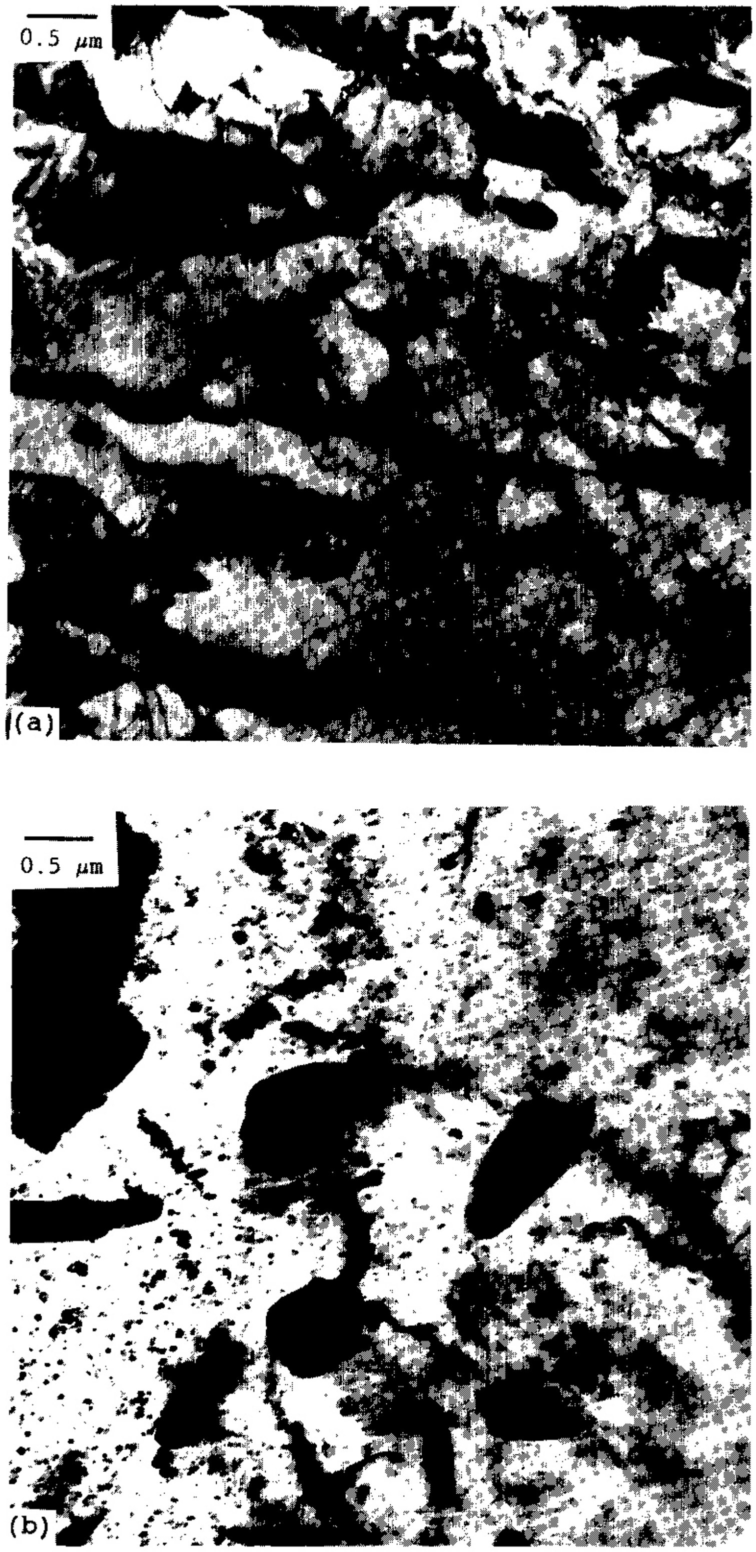

Fig. 1. A comparison of the precipitate microstructures of (a) 9Cr-2WVTa and (b) 2 1/4C4-2WV steels after a normalizing and tempering heat treatment

necessary to develop a steel with improved impact toughness in the unirradiated condition over that for 2 1/4Cr-2WV.

Experimental Procedure

Eight electroslag-remelted heats of FIRD steel with the nominal compositions in Table 1 were prepared by Combustion Engineering, Inc., Chattanooga, Tennessee. These steels were used in the original ORNL studies on reduced-activation steels [7-9], and the results from those previous studies are the basis for the work discussed in this paper. The tensile and Charpy tests on those steels were primarily on specimens taken from 0.76-mm-thick sheet [8] and 15.9-mm-thick plate [9], respectively.

For the present study, 450-g vacuum arc-melted button heats were made. Table 2 lists melt compositions and designations of the steels. which were variations of 2 1/4Cr-2WV. Material from the 2 1/4Cr-2WV heat was used as starting stock, and Ta, B. and Cr were added, with desired additions being 0.07% Ta, 0.005% B, and 0.25% Cr. Table 2 also includes melt compositions for 2 1/4Cr-2W, 2 1/4Cr-2WV, and 9Cr-2WVTa from the original study [7], since these will be used for comparison. Although the original heats were designated as 2 1/4Cr steels (they were. patterned after 2 1/4Cr-1Mo steel), the actual chromium compositions of 2 1/4Cr-2W and 2 1/4Cr-2WV were ≈2.4 wt. % (Table 2).

Table 2. Chemical Composition of Steels

Steel	C	Si	Mn	P	S	Cr	V	W	Ta	B
2 1/4Cr-2WVTa	0.10	0.12	0.40	0.016	0.006	2.41	0.24	2.03	0.05	
2 1/4Cr-2WVB	0.090	0.12	0.38	0.015	0.007	2.37	0.24	2.04		0.005
2 1/4Cr-2WVTaB	0.092	0.12	0.38	0.015	0.008	2.36	0.24	2.04	0.05	0.005
2.6Cr-2WVTa	0.11	0.11	0.39	0.014	0.009	2.59	0.25	2.02	0.05	
2.6Cr-2WVTaB	0.11	0.11	0.39	0.014	0.008	2.60	0.25	2.07	0.05	0.004
2 1/4Cr-2W	0.11	0.15	0.39	0.016	0.006	2.48		1.99		
2 1/4Cr-2WV	0.11	0.20	0.42	0.016	0.006	2.41	0.24	1.98		
9Cr-2WVTa	0.10	0.23	0.43	0.015	0.005	8.72	0.23	2.09	0.07	

Half of each 12.1 x 25.4 x 127 mm ingot was hot rolled to 6.4 mm and half to 0.76 mm. Tensile specimens 44.5-mm long with a reduced gage section of 20.3 x 1.52 x 0.76 mm were machined from the 0.76-mm sheet; gage lengths were parallel to the rolling direction. One-third size Charpy specimens 3.3 x 3.3 x 25.4 mm with a 0.51-mm-deep 30' V-notch and a 0.05- to 0.08-mm-root radius were machined from the 6.4-mm plate. Specimens were taken along the rolling direction with the notch transverse to the rolling direction.

Normalized-and-tempered specimens were tested. The 0.76-mm sheet tensile specimens were heat treated directly, and the Charpy specimens were taken from the heat treated 6.4-mm plate. All of the new heats, as well as the 2 1/4Cr-2WV and the 9Cr-2WVTa were normalized by austenitizing 0.5 h at 1050°C, followed by a rapid cool in flowing helium. The 2 1/4Cr-2W was austenitized 0.5 h at 900°C. A higher austenitizing temperature was used for the steels with vanadium and tantalum to ensure dissolution of V- and Ta-rich carbides. Material for the Charpy specimens of 2 1/4Cr-2W, 2 1/4Cr-2WV, and 9Cr-2WVTa were heat treated in two different forms: as 15.9-mm plate [9] and as 113-size Charpy specimens. Specimens heat treated in the latter geometry will be used for comparison with the new steels heat treated in the 6.4-mm plate. All steels were tested after tempering 1 h at 700°C and 1 h at 750°C.

Room temperature tensile tests were conducted in vacuum on a 44-kN-capacity Instron universal testing machine at a nominal strain rate of 4.2 x 10^{-4}/s. Charpy tests were carried out in a pendulum-type impact machine specially modified to accommodate subsize specimens [17]. The absorbed energy values were fit with a hyperbolic tangent function to permit the upper-shelf energy (USE) and ductile-brittle transition temperature (DBTT) to be evaluated at the energy midway between the upper- and lower-shelf energies.

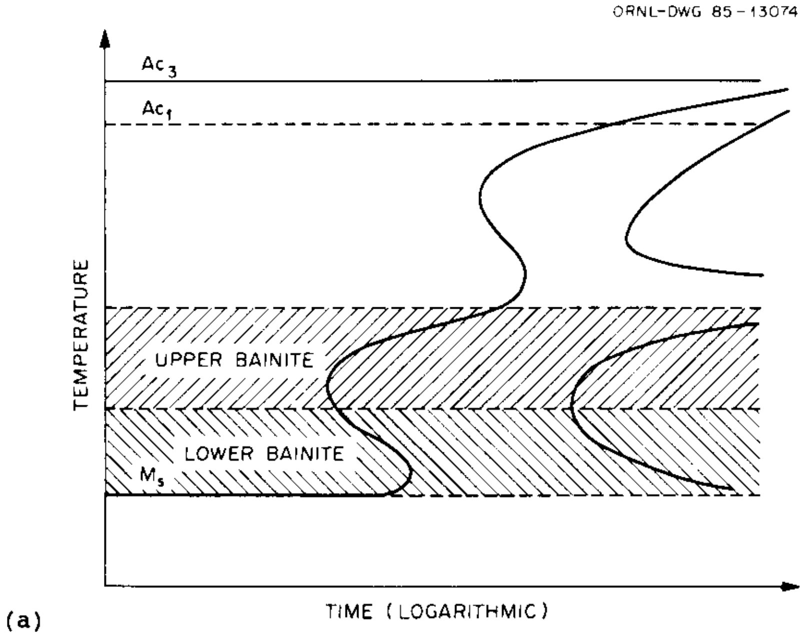

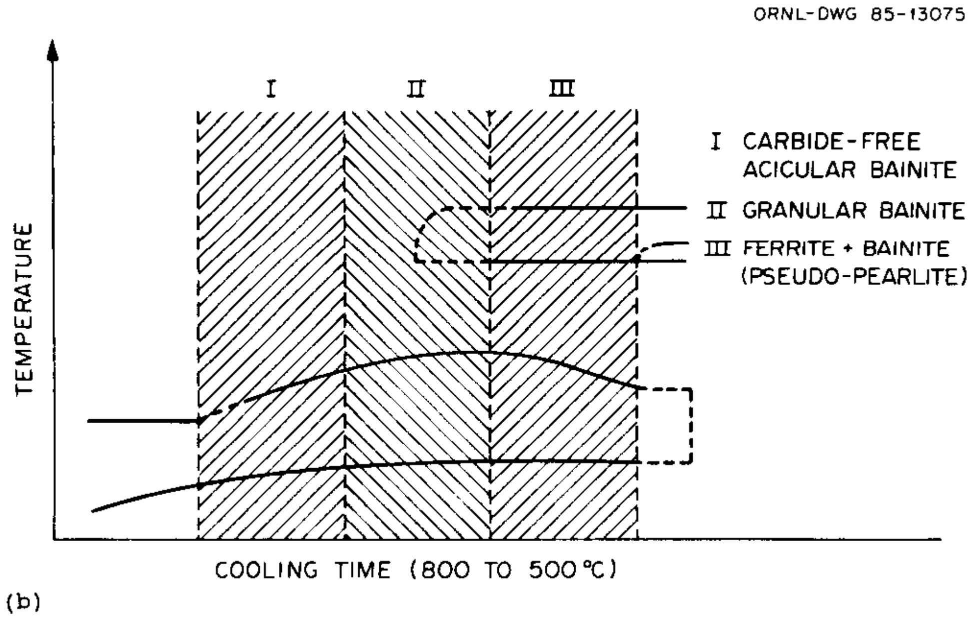

Fig. 4. Schematic representation of (a) isothermal transformation diagram that shows upper-and lower-bainite transformation zones and (b) continuous-cooling transformation diagram that shows zones for the formation of three morphological variations of bainite.

RESULTS AND DISCUSSION

Summary of properties of original heats

Charpy properties of the 2 1/4Cr-2W, 2 1/4Cr-2WV, and 9Cr-2WVTa **steels** from the original eight ORNL **heats** of **steel** were determined on specimens taken from normalized-and-tempered 15.9-mm plate. After **this** heat treatment, the 2 1/4Cr-2WV contained ≈20% polygonal ferrite and 80% hainite, **the** 2 1/4Cr-2W contained 100% bainite, and the 9Cr-2WVTa contained 100% martensite [7]. Microstructures of the normalized-and-tempered 0.76-mm-thick tensile specimens were 100% bainite for the 2 1/4Cr steels and 100% martensite **for** the 9Cr-2WVTa steel [7]. **Properties** for these steels in these heat-mated condition *are* given in Table 3.

Table 3. Tensile and Charpy Impact Properties of Three of the Original **Steels and** a Ta-Modified Low-chromium Steel

		Room Temperature Tensile Strength (MPA)				
Steel^a	Tempering Temperature (°C)	YS	UTS	Elongation (%)	DBTT (°C)	Use (J)
		Charpy Specimens of Original Heats Heat Treated as 15.9 mm Plate				
2 1/4Cr-2W	700	594	677	9.5	-48	9.6
2 1/4Cr-2WV	750	684	758	9.8	0	9.7
9Cr-2WVTa	750	645	784	1.9	-78	9.7
		Charpy Specimens of Original Heats Heat Treated as 3.3 mm Bar				
2 1/4Cr-2W	700	594	677	9.5	-56	11.5
	750	554	626	13.2	-71	10.1
2 1/4Cr-2WV	700	889	978	7.5	-9	7.0
	750	684	758	9.8	-52	11.0
9Cr-2WVTa	700	823	955	6.6	-43	7.5
	750	645	784	7.9	-80	10.1
		Mechanical Property Data for Tantalum-Modified 2 1/4Cr-2WV Steel				
2 1/4Cr-2WVTa	700	908	979	7.9	-10	9.2
	750	621	716	10.6	-65	13.8

^{a}Nominal compositions: Cr, Mo, and W as indicated in designation: V=0.25%; Ta=0.07%

It **was** concluded that the inferior impact toughness of the 2 1/4Cr-2WV (Table 3), **as** measured by the ductile-brittle transition temperature (DBTT), was caused by the ferrite in the microstructure [18]. Table 3 also gives the Charpy properties after the three steels were heat treated in the 1/3-size Charpy geometry (3.3-mm-square bars) to produce 100% bainite in the 2 1/4Cr-2WV. **The** 2 1/4Cr-2W and 9Cr-2WVTa were again 100% bainite and 100% martensite, respectively. Although the Charpy properties of **2** 1/4Cr-2WV improved after this heat treatment, the properties were *still* not equivalent *to* those of **2 1/4Cr-2W and** 9Cr-2WVTa, which showed little change after being heat treated in the smaller geometry (compare the properties after similar tempering **treatments--700°C** for 2 1/4Cr-2W and 750°C for 2 1/4Cr-2WV and 9Cr-2WVTa).

Tantalum effect

It was originally concluded that the 9Cr-2WVTa had better Charpy properties than 9Cr-2WV (tensile properties were similar) because the grain-refining effect of the tantalum [7-9]. Therefore, a 2 1/4Cr-

2WVTa heat with ≈0.05% Ta was produced. The Charpy properties of the 2 1/4Cr-2WVTa were an improvement over those for 2 1/4Cr-2WV, but the strength was not as good after the 750°C temper (Table 3). Tensile and Charpy impact properties were also not as good as those for 9Cr-2WVTa.

Microstructure of 2 1/4Cr-2W and 2 1/4Cr-2WV

In addition to adding tantalum to try to improve the toughness of the 2 1/4Cr-2WV, the difference in the microstructures of the 2 1/4Cr-2WV and 2 1/4Cr-2W steels were investigated to determine the source of the Charpy property differences. Transmission electron microscopy (TEM) examination indicated a difference in the bainitic microstructures of the normalized-and-tempered 2 1/4Cr-2W and 2 1/4Cr-2WV after the heat treament in 15.9-mm plate (Fig. 2) [18]. Although both microstructures were tempered bainite. the microstructures, especially the precipitates, appeared different. Indications of an elongated substructure and precipitates appeared in the 2 1/4Cr-2W [Fig. 2(a)], giving evidence of a lath-like microstructure prior to tempering. Precipitates in the 2 1/4Cr-2WV were globular and often appeared to form in patches [Fig. 2 (b)]. The reason for these differences was attributed to the different kind of bainite that formed in the two steels when they were normalized [18], a difference associated with how rapidly the steels were cooled from the austenitizing temperature [19,20].

To demonstrate the effect of cooling rate, pieces of tested standard-size Charpy specimens (10 x 10 mm bar) and pieces of 1/3-size Charpy specimens (3.3 x 3.3 mm bar) were austenitized in a helium atmosphere of a tube furnace and cooled by pulling into the cold zone of the furnace. An austenitization treatment of 0.5 h at 900°C was used for the 2 1/4Cr-2W and 0.5 h at 1050°C for the 2 1/4Cr-2WV. To speed the cooling of the small specimens, they were cooled in flowing helium. The large specimens were cooled in static helium to further slow the cooling rate relative to the small specimen.

Optical metallography indicated both steels were 100% bainite after both the fast and slow cools, although there were differences in appearance. as shown in Fig. 3 for 2 1/4Cr-2WV. The specimen given the fast cool appeared more acicular. Similar observations were made for 2 1/4Cr-2W.

Bainite, which is generally defined microstructurally as carbides in a ferrite matrix that transformed in the temperature range ≈250-550°C, was originally thought to consist of only two morphological variations, upper and lower bainite. These bainites were defined according to the temperature of formation and can be differentiated by the appearance of the carbide particles relative to the axis of the bainitic ferrite plate or needle. Upper bainite forms as a collection of ferrite plates or laths with carbide particles parallel to the plates. Lower bainite consists of ferrite plates or needles with carbides forming within the ferrite at about a 60° angle to the axis of the plate or needle.

Important variations from these classical bainites exist as first pointed out by Habraken [19]. He found morphological variations in the bainite transformation products that differed from upper and lower bainite, although they formed in the bainite transformation temperature regime. Such "nonclassical" bainites formed more easily during continuous cooling than during an isothermal transformation [19,20], where classical bainites generally formed.

Habraken and Economopoulos [20] contrasted the morphologies of the nonclassical bainite structures formed during continuous cooling with classical bainites obtained during isothermal transformation. Classical upper and lower bainite form when transformed in different temperature regimes of the bainite transformation temperature region, as defined on an isothermal-transformation (IT) diagram [Fig. 4(a)] [20]. This means that the bainite transformation region of an IT diagram can be divided into two temperature regimes by a horizontal line, above which upper bainite forms and below which lower bainite forms. For the nonclassical bainites. Habraken and Economopoulos [20] showed that a continuous cooling transformation (CCT) diagram could be divided into three vertical regimes [Fig. 4(b)]. Three different nonclassical bainite microstructures form when cooling rates are such as to pass through these different zones. A steel cooled rapidly enough to pass through zone I produces a "carbide-free acicular" structure, which consists of side-by-side plates or laths [20]. When cooled through zone II, a carbide-free "massive or granular" structure results, generally referred to as granular bainite [20]. It has been determined that granular bainite

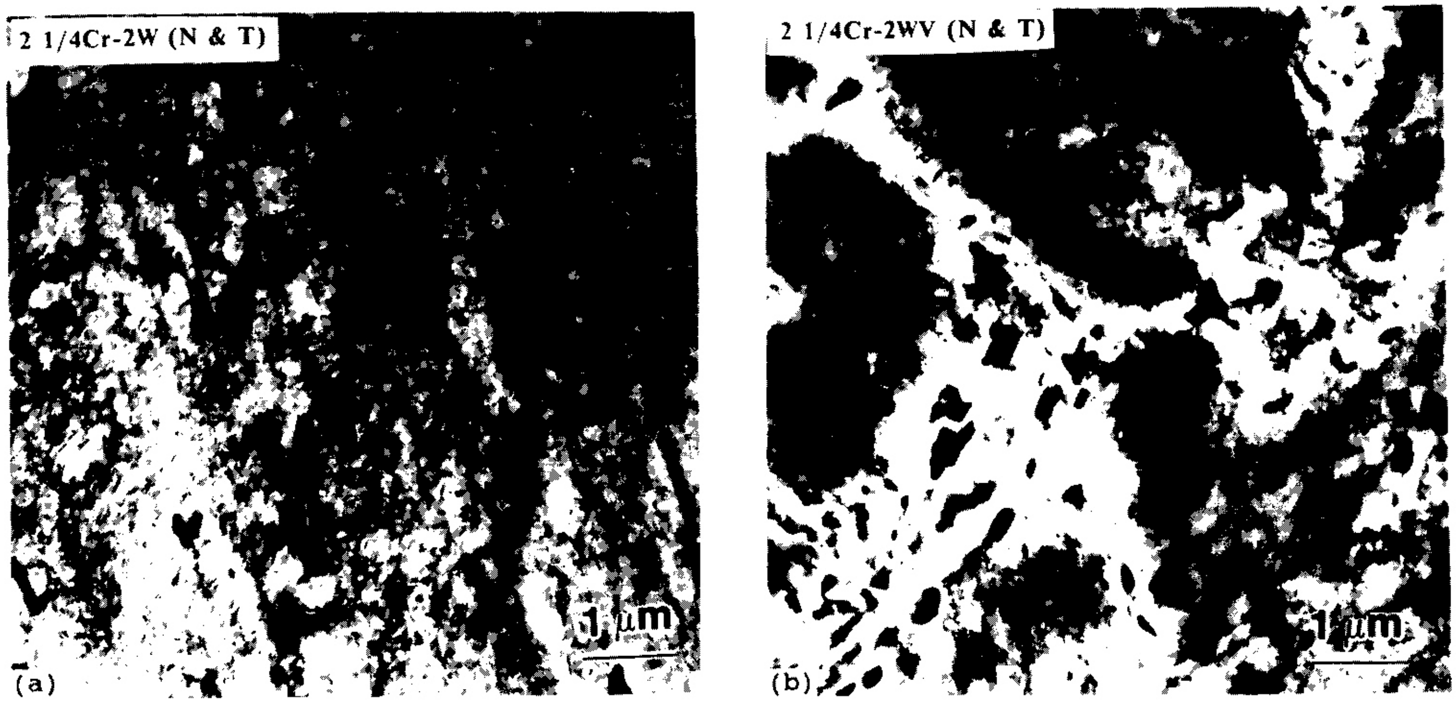

Fig. 2. Transmission electron microscopy photomicrographs of the bainitic microstructures of normalized-and-tempered (a) 2 1/4Cr-2W and (b) 2 1/4Cr-2WV steels.

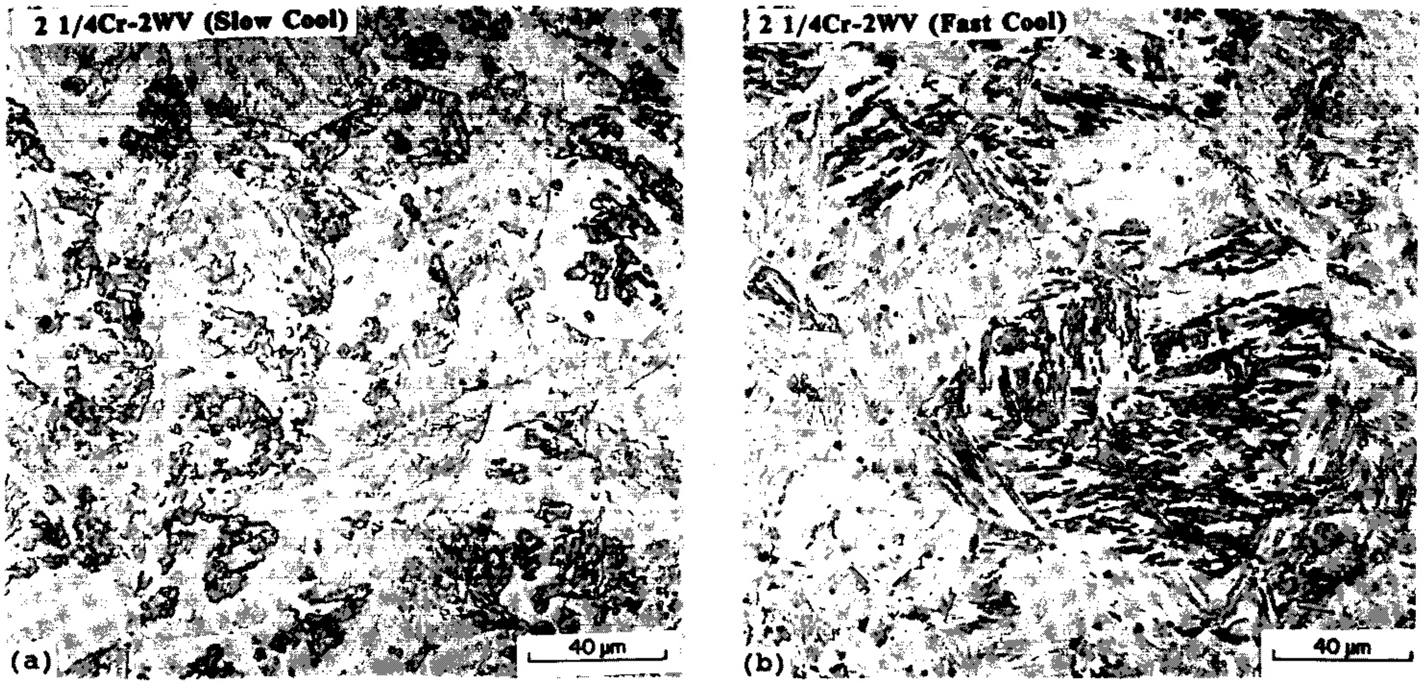

Fig. 3. Optical microstructures of 2 1/4Cr-2WV steel given a (a) slow cool and (b) a fast cool from the 1050°C austenitizing temperature.

consists of a ferrite matrix with a high dislocation density that contains martensite-austenite (M-A) "islands" [20]. Since Habraken's "pseudo bainite" microstructures developed by cooling through zone III were not observed in this study, they will not be discussed.

To visualize the formation of granular bainite, Habraken and Economopoulos [19] concluded there was a dehomogenization during cooling from the austenitizing temperature. Dehomogenization was supposed to have occurred above the B_S temperature, the bainite start temperature, giving carbon-enriched and carbon-depleted regions. (The possibility of dehomogenization above the B_S temperature for the formation of carbon-depleted and carbon-enriched regions has since been challenged [21], although there is no doubt that the regions exist after cooling from the austenitization temperature [19]). In the bainite-transformation temperature regime, the carbon-depleted zones transform to carbide-free bainitic ferrite with a high dislocation density. The high-carbon regions do not transform to bainite. hut some of the retained austenite transforms to martensite if the steel is cooled below the Ms temperature. Thus, the high-carbon regions give rise to the M-A islands within the bainitic ferrite.

Microstructures observed by TEM on the different-sized specimens of normalized 2 1/4Cr-2W and 2 1/4Cr-2WV are shown in Figs. 5 and 6, respectively. The slowly cooled specimens are shown in Figs. 5(a) and 6(a) and are characteristic of granular bainite [19,20]; the dark areas are the M-A islands. Micrographs of the specimens cooled rapidly Figs. 5(b) and 6(b)] are characteristic of carbide-free acicular bainite [19,20]. When granular bainite is tempered, large globular carbides form in the high-carbon M-A islands, whereas elongated carbides form on lath boundaries of acicular bainite [22], just the types of morphology observed when 2 1/4Cr-2W Fig. 2(a)] and 2 1/4Cr-2WV Fig. 2(b)] were tempered.

Experimental work on a 3Cr-1.5Mo-0.25V steel indicated that tempered carbide-free acicular bainite has a higher impact toughness (low DBTT and high USE) than granular bainite after a low-temperature or short-time (constant temperature) tempering treatment [22]. Further, optimum strength and toughness were obtained for the carbide-free acicular bainite under modest tempering conditions, after which further tempering had little effect on toughness. Considerably more tempering (longer time or higher temperature) was required for the granular bainite. which meant optimum properties were achieved at a lower strength. This could explain the difference in the effect of tempering on the DB'IT of 2 1/4Cr-2W (carbide-free acicular) and 2 1/4Cr-2WV (granular bainite) when tempered at 700 and 750°C. Only a small difference in DB'IT was observed for the 2 1/4Cr-2W when tempered 1 h at 700°C and 1 h at 750°C, compared to a relatively large difference for the 2 1/4Cr-2WV (Table 3).

Improvement of properties of low-chromium steels

No CCT diagrams are available for the reduced-activation steels under discussion. Figure 4 is schematic, but even when CCT diagrams are available, details on the three cooling zones must be determined experimentally. The reason for the large amount of proeutectoid ferrite in 2 1/4Cr-2WV and not in 2 1/4Cr-2W of the 15.9-mm plates was attributed to the difference in cooling rates caused by the different austenitization temperatures [7]. (A temperature of 1050°C was used for the 2 1/4Cr-2WV to assure dissolution of the vanadium carbide; 900°C was used for the 2 1/4Cr-2W). If the interpretation of the effect of microstructure is correct, it would appear that the toughness of the 2 1/4Cr-2WV could be improved if the steel was cooled more. rapidly, perhaps by quenching instead of normalization (air cooling).

Another possibility to promote carbide-free acicular bainite is by improving the hardenability. Hardenability is defined as the relative ability of a steel to avoid forming the soft ferrite phase when cooled from the austenitizing temperature. Increasing hardenability has the same effect as increasing the cooling rate: it moves the transformation of ferrite to longer times so the steel can be cooled more slowly and still obtain a bainite microstructure.

Hardenability can be changed by changing chemical composition. For example, more carbon could be added, although carbon generally has a negative effect on DB'IT. Small amounts of boron (0.003-0.005%) also improve hardenability [23,24]. Data at the top of Table 4 can be used to compare properties of 2 1/4Cr-2WVTa with a 2 1/4Cr-2WVB steel containing ~0.005%B. Properties for the 2 1/4Cr-2WV and

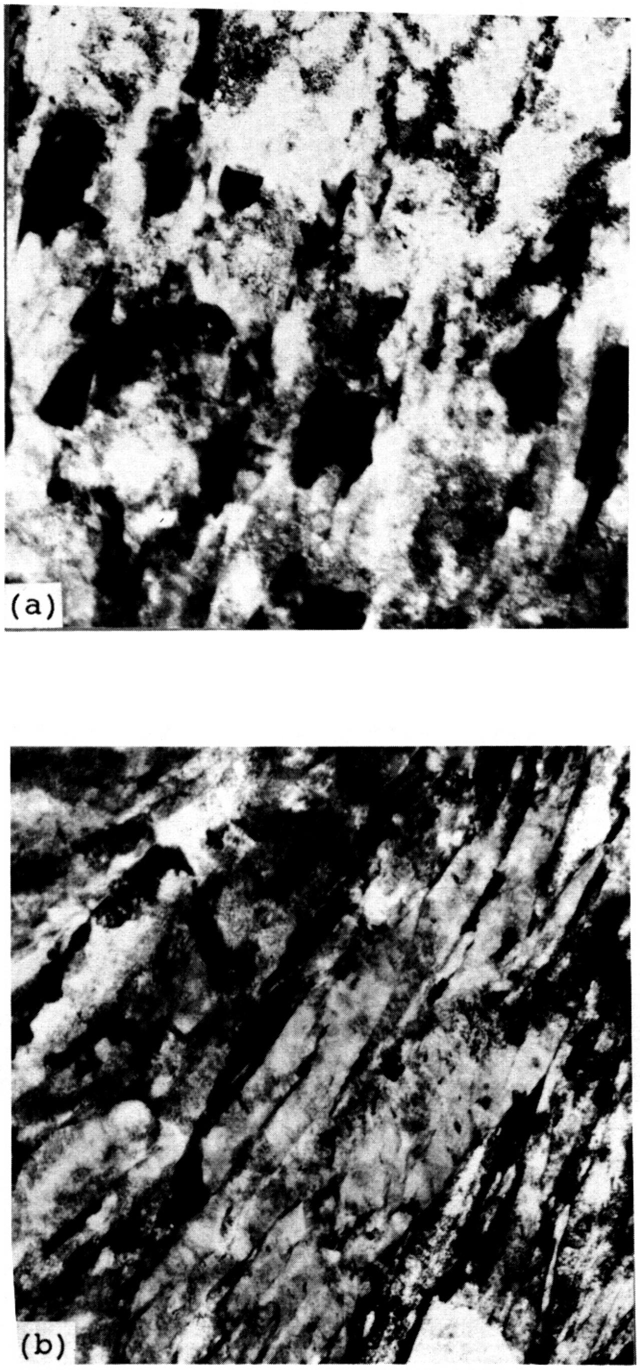

Fig. 6. Photomicrographs of bainitic microstructures of normalized **2 1/4Cr-2WV steel** after **(a) slow** cool **and (b)** fast cool **from 1050°C.**

Table 4. Tensile and Charpy Impact Properties of Ferritic Steels Modified to Increase Hardenability Compared to Original Heats

Steel[a]	Tempering[b] Temperature (°C)	Room Temperature Tensile Strength (MPA)			DBTT (°C)	Use (J)
		YS	UTS	Elongation (%)		
			New Reduced-Activation Chromium-Tungsten Heats			
2 1/4Cr-2WVTa	700	908	979	7.9	-10	9.2
	750	621	716	10.6	-65	13.6
2 1/4Cr-2WVB	700	804	889	8.6	-21	8.1
	750	598	691	10.7	-90	11.5
2 1/4Cr-2WVTaB	700	876	951	7.6	-30	7.7
	750	664	739	9.6	-78	11.7
2.6Cr-2WVTa	700	826	897	8.6	-54	7.7
	750	636	700	7.8	-103	10.9
2.6Cr-2WVTaB	700	823	904	8.4	-60	8.0
	750	623	702	9.1	-94	11.1
			Original Reduced-Activation Chromium-Tungsten Heats			
2 1/4Cr-2W	700	594	677	9.5	-56	11.5
	750	554	626	13.2	-77	10.2
2 1/4Cr-2WV	700	889	978	7.5	10	8.4
	750	684	758	9.8	-78	12.7
9Cr-2WVTa	700	823	955	6.6	-43	7.5
	750	645	784	7.9	-80	10.1
			Chromium-Molybdenum Steels			
9Cr-1MoVNb	700	670	815	7.8	22	7.9
	750	541	656	9.6	-22	8.7
	760				-57	8.8
12Cr-1MoVW						
	700				2	5.2
	750	653	806	10.4	-36	6.5
	780	549	716	9.9	-46	6.0

[a] Nominal compositions: Cr, Mo. and W as indicated in designation: V=0.25%; Ta=0.07%, Nb=0.06%, B-0.005%; nominal composition of W in 12C4-1MoVW is 0.5%.

[b] All tempering times were 1 h except for 2.5 h at 780°C for the 12Cr-1MoVW.

9Cr-2WVTa steels are also shown. The properties of 2 1/4Cr-2WVB showed an improvement in Charpy behavior over the 2 1/4Cr-2WV and 2 1/4Cr-2WVTa--the steels without boron. Also shown in Table 4 are results for 2 1/4Cr-2WVTaB, a steel containing a combination of 0.005% B and 0.05% Ta. This combination produced a steel with impact properties comparable to those of the 2 1/4Cr-2WVB, but with greater strength. Therefore, increasing hardenability gave the steels improved impact properties over those for 2 1/4Cr-2WV (also shown in Table 4), and the 2 1/4Cr-2WVTaB has comparable tensile properties. After the 750°C temper, the tensile and impact properties of the 2 1/4Cr-2WVB and 2 1/4Cr-2WVTaB steels were similar to those for 9Cr-2WVTa (shown in Table 4).

The optical microstructures showed the effect of boron on hardenahility (Fig. 7). The 2 1/4Cr-2WVTa steel contained a finer prior-austenite grain size than the 2 1/4Cr-2WVB steel. However, much more acicularity is evident in the microstructure of the 2 1/4Cr-2WVB steel Fig. 7(b)], indicating the effect of boron on promoting tbe formation of carbide-free acicular bainite and thus, hardenability. From Fig. 7(a) it is not possible to determine whether the light-etching constituent is tempered granular bainite or whether this is polygonal ferrite. The former is felt to be the case (note the light-etching material in Fig. 3 in a steel that TEM showed to be essentially 100% granular bainite). TEM is required to verify this; TEM results will be reported separately.

Adding more chromium can also improve hardenability. An addition of 0.25% Cr, 0.07% Ta. and 0.005% B was attempted to the 2 1/4Cr-2WV composition. The final composition indicated that about 0.2% Cr, 0.05% Ta, and 0.004% B was present to produce 2.6Cr-2WVTa and 2.6Cr-2WVTaB steels. Optical microstructures of these two steels are shown in Fig. 8. An increase in acicularity for these steels is obvious (compare Figs. 7 and 8). The acicularity in the boron-containing steel Fig. 8(a)] also appears greater than the steel without boron [Fig. 8(b)]. These changes are taken as evidence that the improved hardenability promoted carhide-free acicular hainite formation during the normalizing heat treatment.

The strengths of the new 2.6Cr steels are slightly below those for 9Cr-2WVTa and 2 1/4Cr-2WV (Table 4). Both 2.6Cr steels showed an improvement in Charpy properties over the 9Cr-2WVTa (Table 4). If a further improvement could be achieved at the 700°C tempering temperature, it would result in a steel with both increased strength and toughness compared to 9Cr-2WVTa, which is tempered at 750°C.

Table 4 also shows data for the 9Cr-1MoVNb and 12Cr-1MoVW, the conventional Cr-Mo steels considered for fusion. Even after a 750°C temper, the Charpy data for 9Cr-1MoVNb and 12Cr-1MoVW are not as good as those for the 2.6Cr steels after a 700°C temper. Tempering temperatures of 760 and 780°C are used for the 9Cr-1MoVNb and 12Cr-1MoVW steels, respectively [2]; the tensile and Charpy data after such a standard temper are shown in Table 4. Even when these higher tempering temperatures are used, however, the Charpy properties of the 2.6Cr steels are better than those for 12Cr-1MoVW tempered at 780°C, and equivalent to those for the 9Cr-1MoVNb tempered at 760°C. Under these tempering conditions, the 2.6Cr steels tempered at 700°C have a substantially higher strength than the two high-chromium Cr-Mo steels.

The above results verified that changing hardenability by varying composition can improve the Charpy impact properties of the 2 1/4Cr-2WV steel. Only minor changes were attempted in the composition. Further changes in composition should be possible to optimize the properties. Such optimization studies are in progress.

SUMMARY AND CONCLUSIONS

A program to develop low-chromium, reduced-activation steels is underway. This program is based on observations on the mechanical properties of a 2 1/4Cr-2WV steel in the original reduced-activation steels tested at ORNL. Although this steel had the best strength properties of the steels tested, Charpy impact properties were inferior to those of 9Cr-2WVTa and 2 1/4Cr-2W steels. Microstructural studies indicated that the inferior impact properties of the 2 1/4Cr-2WV relative to the 2 1/4Cr-2W were due to the type of bainite formed in the two steels. The 2 1/4Cr-2WV contained granular bainite, and the 2 1/4Cr-2W contained acicular hainite. Acicular bainite formation can be enhanced by increasing the cooling rate during the normalizing heat treatment or by increasing the hardenability. Additions of boron and chromium were made to the 2 1/4Cr-2WV composition to increase hardenability. The resulting steels had improved impact toughness compared to the 2 1/4Cr-2WV, and the mechanical properties were equivalent to those of the 9Cr-2WVTa. These preliminary studies indicate that further improvement in the mechanical properties should be possible.

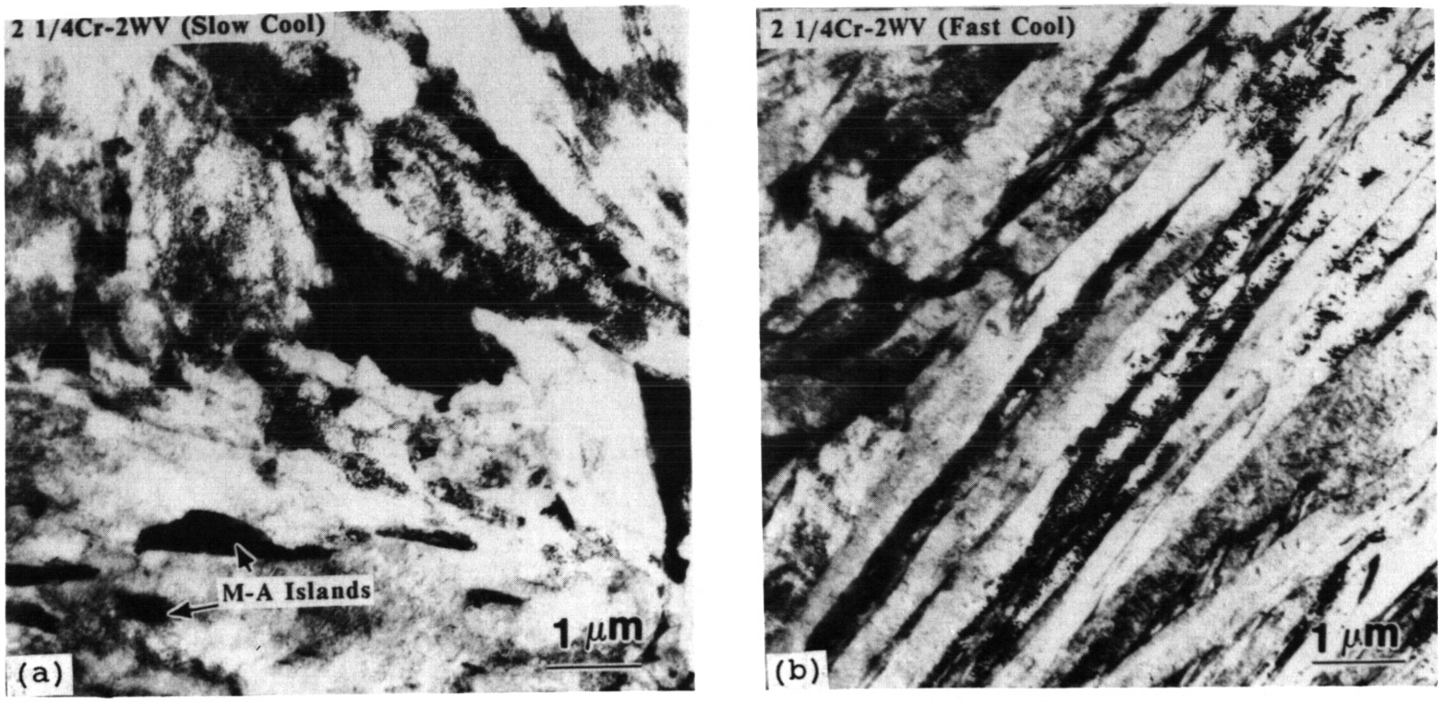

Fig. 5. Photomicrographs of bainitic microstructures of normalized 2 1/4Cr-2W steel after (a) slow cool and (b) fast cool from 1050°C.

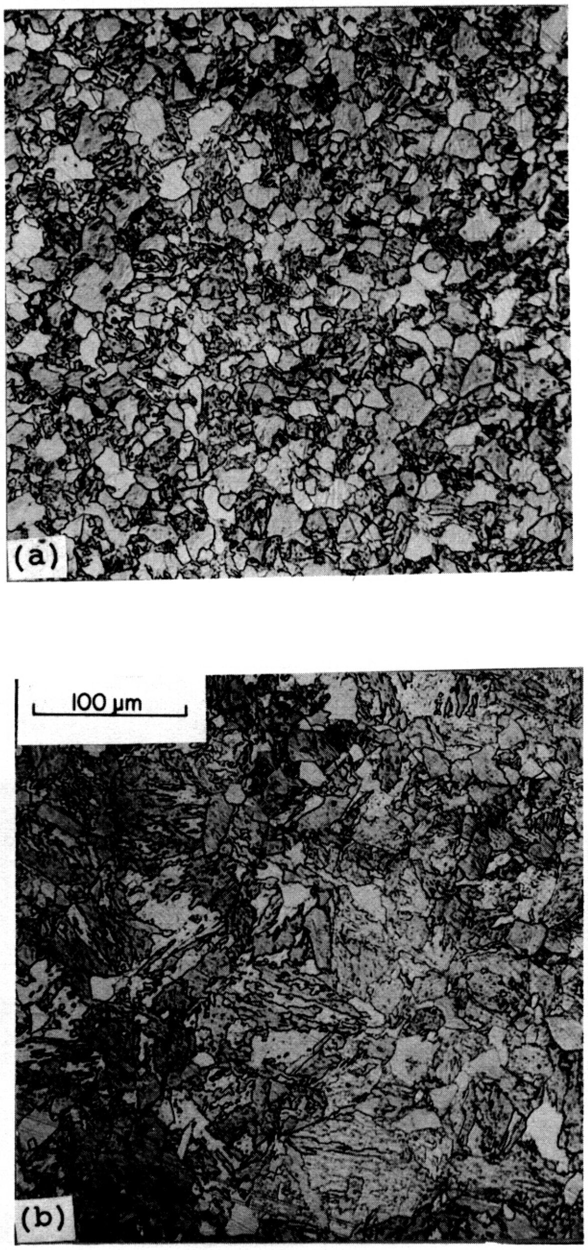

Fig. 7. Optical microstructures of normalized-and-tempered (a) 2 1/4Cr-2WVTa and (b) 2 1/4Cr-2WVB steels.

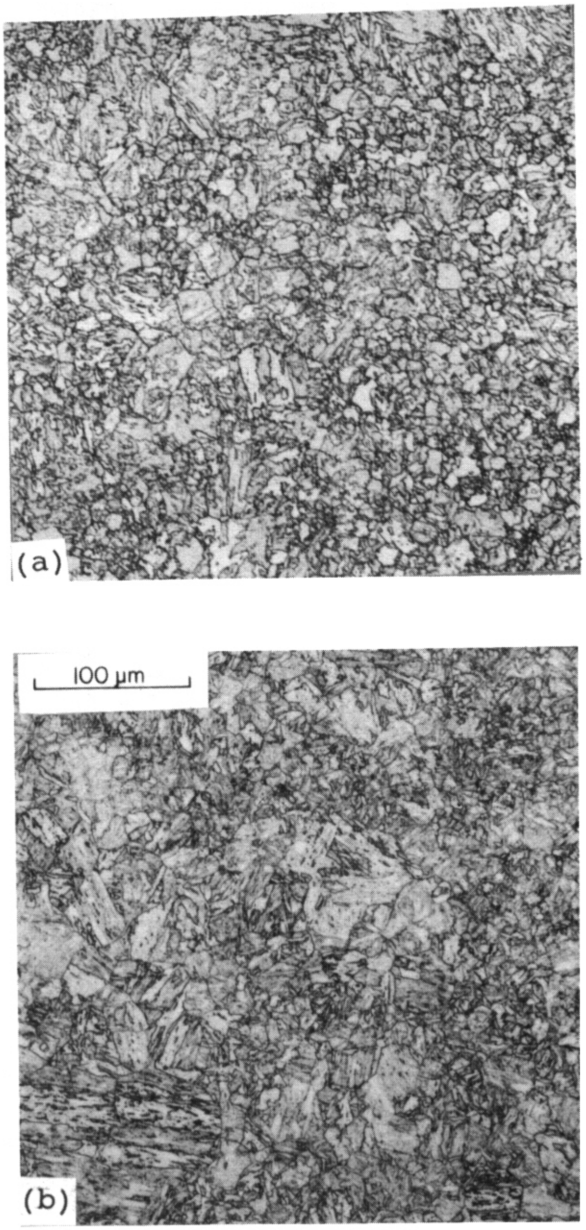

Fig. 8. Optical microstructures of normalized-and-tempered (a) 2.6Cr-2WVTa and (b) 2.6Cr2WVTaB steels.

REFBRENCES

1. **S.** N. Rosenwasser et al., **J**. Nucl. Mater. **85 & 86 (1979) 177.**

2. R. **L.** Klueh, J. M. Vitek, and M. L. Grossbeck, Effects **of** Irradiation on Materials: Eleventh Conference, ASTM **STP 782,** H. **R.** Brager and **J.** S. Perrin, **Eds**. (American Society for Testing Materials, Philadelphia, **1982)** p. **648.**

3. **R.** L. Klueh and J. M. Vitek, Ferritic Alloys for **use** in Nuclear Energy Technologies, **J.** W. Davis and D. J. Michel. Eds. (The Metallurgical Society of AIME. Warrendale, PA, **1984)** p. **615.**

4. R. L. Klueh, D. S. Gelles, and T. A. Lechtenberg, J. Nucl. Mater., **141-143 (1986) 1081**

5. **D.** Dulieu, K. W. Tupholme, and G. J. Butterworth. **J**. Nucl. Mater., **141-143 (1986) 1097**

6. M. Tamura, H. Hayakawa, M. Tanimura. A. Hishinuma, and T. Konda **J.** Nucl. Mater., **141-143 (1986) 1067.**

7. R. **L.** Klueh and P. J. Maziasz, Met. Trans. **20A (1989) 373.**

8. R. L. Klueh, Met. Trans, **20A (1989) 463.**

9. R. **L.** Klueh and W. R. Corwin, J. Eng. Mater.. **11 (1989) 169.**

10. W. L. Hu and D. S. Gelles, Influence of Radiation on Material Properties: **13th** International Symposium (Part 11), **ASTM** STP **956,** F. **A.** Gamer, C. H. Henager, Jr., and N. Igata, Eds. (American Society for Testing Materials, Philadelphia, **1987)** p. **83.**

11. R. **L.** Klueh and D. J. Alexander, J. Nucl. Mater., to be published.

12. R. L. Klueh, Nucl. Eng. Design, **72 (1982) 329.**

13. R. **L.** Klueh and D. J. Alexander, J. Nucl. Mater., **187 (1992)** 60.

14. P. J. Maziasz, J. Nucl. Mater., **122 & 123 (1984) 472.**

15. **P.** J. **Maziasz** and D. N. Braski, **J. Nucl.** Mater., **141-143 (1986) 973.**

16. P. J. Maziasz, R. L. Klueh, and J. M. Vitek, **J.** Nucl. Mater., **141-143, 929 (1986).**

17. **D.** J. Alexander, R. **K.** Nanstad, W. R. Corwin, and J. T. Hutton, Applications of Automation Technology to Fatigue and Fracture Testing, ASTM **STP 1092, eds.** A. A. Braun, N. **E.** Ashhaugh, and F. M. Smith **(*Am*** Soc. for Testing and Mater., Philadelphia, **1990)** p. **83.**

18. R. L. Klueh, P. J. Maziasz, and D. J. Alexander, J. Nucl. Mater., **179-181 (1991) 679.**

19. L. **J.** Habraken. Proc. **4th** Int. Conf. Electron Microscopy, Vol. **1** (Springer-Verlag, Berlin, **1960)** p. **621.**

20. L. J. Habraken and M. Economopoulos, Transformation and Hardenability in Steels (Climax-Molybdenum Company, Ann Arbor, MI, **1967) p. 69.**

21. H. K. **D.** H. Bhadeshia, Bainite in **Steels** (The Institute **of** Materials, London, **1992)** p. **285.**

22. R. **L.** Klueh and A. M. Nasreldin, Met. Trans., **18A, 1279 (1987).**

MICROSTRUCTURE-MECHANICAL PROPERTIES CORRELATION OF IRRADIATED CONVENTIONAL AND REDUCED-ACTIVATION MARTENSITIC STEELS

– R. L. Klueh (Oak Ridge National Laboratory), Ji-Jung Kai (National Tsing Hua University, Taiwan), and D. J. Alexander (Oak Ridge National Laboratory)

OBJECTIVE

The goal of this study is the development of reduced-activation ferritic steels

SUMMARY

Tensile, Charpy, and transmission electron microscopy specimens of two conventional steels, modified 9Cr-1Mo (9Cr-1MoVNb) and Sandvik HT9 (12Cr-1MoVW), and two reduced-activation steels, Fe-9Cr-2W-0.25V-0.1C (9Cr-2WV) and Fe-9Cr-2W-0.25V-0.07Ta-0.1C (9Cr-2WVTa), were irradiated in the Fast Flux Test Facility. Before irradiation, $M_{23}C_6$ was the primary precipitate in all four steels, which also contained some MC. Neutron irradiation did not substantially alter the $M_{23}C_6$ and MC. No new phases formed during irradiation of the 9Cr-2WV and 9Cr-2WVTa, but chi-phase precipitated in the 9Cr-1MoVNb and chi-phase and α' precipitated in the 12Cr-1MoVW. Irradiation-produced dislocation loops were observed in 9Cr-2WV, 9Cr-2WVTa, and 12Cr-1MoVW. The irradiation-produced microstructural changes caused the steels to harden, as measured by the change in yield stress. Hardening was correlated with a change in the Charpy impact properties of 9Cr-1MoVNb, 12Cr-1MoVW, and 9Cr-2WV. Although irradiation caused a yield stress increase of the 9Cr-2WVTa similar to that for 9Cr-2WV and 9Cr-1MoVNb, the change in Charpy properties was considerably less for 9Cr-2WVTa. This difference in Charpy behavior of the 9Cr-2WVTa with that of the 9Cr-2WV and 9Cr-1MoVNb was attributed to differences in the fracture stress-temperature relationship and/or the flow stress-temperature relationship between the 9Cr-2WVTa and the other two 9Cr steels.

PROGRESS AND STATUS

Introduction

Ferritic and martensitic steels are being developed for service in future fusion power plants [1]. Originally, the primary candidates for fusion applications in the U. S. Department of Energy Fusion Materials Program included the conventional Cr-Mo steels 2 1/4Cr-1Mo, 9Cr-1MoVNb (modified 9Cr-1Mo), and 12Cr-1MoVW (Sandvik HT9). In recent years, a program to develop reduced-activation ferritic/martensitic steels has been in progress.

All steels in the first wall and blanket structure of a fusion power plant will become highly radioactive from transmutation reactions that are caused by high-energy neutrons from the fusion reaction interacting with elements in the steel. Reduced-activation or fast induced-radioactivity decay (FIRD) ferritic steels are steels in which the induced radioactivity decays quickly to low levels. Such steels can be more readily disposed of or recycled after the reactor service lifetime than conventional alloys [2]. A FIRD alloy cannot contain molybdenum and niobium, important constituents in the conventional Cr-Mo steels. Experimental FIRD steels have been developed based on chromium compositions of conventional Cr-Mo steels with molybdenum replaced by tungsten and niobium replaced by tantalum [1].

Eight FIRD steels were examined in the Oak Ridge National Laboratory (ORNL) reduced-activation steel development program (Table 1)[3-5]. These included steels with 2.25, 5, 9, and 12 wt% Cr. The four 2.25Cr steels were bainitic, the 5 and 9Cr steels were martensitic, and the 12Cr steel was 25% δ-ferrite, with the balance martensite [4]. The 2 1/4Cr-2WV steel was the strongest, followed by 9Cr-2WVTa and the 9Cr-2WV [3]. Based on the ductile-brittle transition temperature (DBTT) and the upper-shelf energy **(USE)** determined in a Charpy impact test. the impact toughness of the **2 1/4Cr-2WV** steel was inferior to that of the two **9Cr** steels [5]. The 9Cr-2WVTa steel had the best impact **toughness** in the unirradiated condition.

Table 1 Nominal **compositions** for **ORNL fast induced-radioactivity decay** steels

steel	Nominal Chemical Composition[a] (wt %)				
	Cr	W	V	Ta	C
2 **1/4CrV**	2.25		0.25		0.1
2 **1/4Cr-1WV**	2.25	1	0.25		0.1
2 **1/4Cr-2W**	**2.25**	2			0.1
2 **1/4Cr-2WV**	**2.25**	2	0.25		0.1
5Cr-2WV	5	2	0.25		0.1
9Cr-2WV	*9*	2	**0.25**		0.1
9Cr-2WVTa	9	2	0.25	0.07	0.1
12Cr-2WV	12	2	0.25		0 1

[a] **Balance iron.**

Neutron irradiation of ferritic steels causes an increase in strength, an increase in the DBTT, and a decrease in the **USE.** All eight steels were irradiated in the Fast Flux Test Facility **(FFTF)**, and **data** on the tensile and **Charpy** impact properties after irradiation to 7 and 13-14 dpa at 365°C have been reported [6-8]. For the eight FIRD steels in Table 1, the 9Cr-2WVTa was superior to the other seven. The **small** shift in DBTT in the 9Cr-2WVTa of only 4 and 15°C after irradiation to 7 and 13 dpa, respectively, was the smallest shift ever observed for any conventional or reduced-activation ferritic/martensitic steels irradiited to these conditions [7,8].

Irradiated specimens of 9Cr-2WV and 9Cr-2WVTa have now been examined by transmission electron microscopy (TEM). For comparison, irradiated specimens of 9Cr-1MoVNb and 12Cr-1MoVW were also examined. **A** detailed analysis of the TEM observations is to be presented separately [9]. In this report, **an** attempt will be made *to* correlate TEM observations with mechanical properties for the 9Cr-2WV and 9Cr-2WVTa reduced-activation steels and the 9Cr-1MoVNb and 12Cr-1MoVW conventional **steels.**

Experimental Procedure

Melt compositions of the **9Cr-2WV,** 9Cr-2WVTa, **9Cr-1MoVNb,** and 12Cr-1MoVW are given in Table **2.** Normalized-and-tempered steels were irradiated with normalization carried out **by** austenitizing in a helium atmosphere, followed by a rapid cool in flowing helium. The **9Cr-2WV, 9Cr-2WVTa,** and 12Cr-1MoVW were austenitized **at** 1050°C for 0.5 h and the 9Cr-1MoVNb at 1040°C for 0.5 b. Tempering of the 9Cr-2WV and 9Cr-2WVTa was for 1 h at 750°C. the **9Cr-1MoVNb** for **1** h at 760°C, and the 12Cr-1MoVW for ***2.5*** h at 780°C. The 750°C tempering temperatures for the reduced-activation steels were determined in previous studies [4], and the tempering temperatures for the 9Cr-1MoVNb and 12Cr-1MoVW are the standard temperatures for these steels.

Tabla *2* Chemical **composition of steels tested**

Steel	C	Si	Mn	P	S	Cr	Mo	Ni	V	W	Nb	N
9Cr-2WV	0 12	0.25	0.51	0.014	0.005	8.73			0.25	2.09		
9Cr-2WVTa	0.10	0.23	0.43	0.015	0.005	8.72			0.23	2.09		
9Cr-1MoVNb	0 092	0.15	0.48	0.012	0.004	8.32	0.86	0.09	0.20		0.06	0.054
12Cr-1MoVW	0.20	0.17	0.57	0.016	0.003	12.1	1.04	0 51	0.29	0.61		0.027

Standard 3-mm-diameter disks punched from 0.25-mm-thick sheet stock were irradiated in FFTF at ≈420°C to ≈7.8 x 10^{26} n/m^2, –36 dpa More details on the TEM studies have been published [9].

Sheet tensile specimens (44.5-mm long with a reduced gage section of 20.3 x 1.52 x 0.76 mm) and miniature 1/3-size Charpy specimens (3.3 x 3.3 x 25.4 mm with a 0.51-mm-deep 30" V-notch and a 0.05- to 0.08-m-root radius) were irradiated. Details on the tensile and Charpy specimens have been published [6,7].

There were some differences in irradiation conditions for the mechanical properties specimens and the TEM specimens, and irradiation conditions for all specimens are summarized in Table 3. Tensile and Charpy specimens of the 9Cr-2WV and 9Cr-2WVTa steels were irradiated to –7 and 13-14 dpa at 365°C. Tensile specimens of the 9Cr-1MoVNb and 12Cr-1MoVW steels were irradiated to –7 dpa at 365°C. Charpy specimens of 9Cr-1MoVNb and 12Cr-1MoVW were irradiated as follows: (1) both steels to 4-5 dpa at 365°C, *(2)* 12Cr-1MoVW to 10 dpa at 365°C, and (3) both steels to 35-36 dpa at 420°C.

Table 3. Irradiation conditions for martensitic steels irradiated in FFTF

TEM Specimens	
9Cr-2WV	35 dpa at 420°C
9Cr-2WVTa	35 dpa at 420°C
9Cr-1MoVNb	35 dpa at 420°C
12Cr-1MoVW	35 dpa at 420°C
Tensile Specimens	
9Cr-2WV	7 and 14 dpa at 365°C
9Cr-2WVTa	7 and 14 dpa at 365°C
9Cr-1MoVNb	7 dpa at 365°C
12Cr-1MoVW	7 dpa at 365°C
Charpy Specimens:	
9Cr-2WV	14 dpa at 365°C
9Cr-2WVTa	13 dpa at 365°C
9Cr-1MoVNb	5 dpa at 365°C and 36 dpa at 420°C
12Cr-1MoVW	4 and 10 dpa at 365°C and =35 dpa at 420°C

RESULTS

Summary of Mechanical Properties Observations

Details on the effect of irradiation on tensile and Charpy behavior have been published [6-8,10,11]. To aid the discussion of the correlation of properties with microstructure, a brief *summary* of the mechanical properties observations will be presented. **Results** are given in Table 4.

Figure 1 **shows** the yield stress for the four **steels** before and after irradiation to ≈7 dpa at 365°C. **Results** for 7 dpa are shown **because** no data are available **for** 9Cr-1MoVNb and **12Cr-1MoVW** at 14 dpa Data *are* available for 9Cr-2WV and 9Cr-2WVTa after 14 dpa (Table 4); based on the observed variations, these results indicate that hardening saturates with fluence by 7 dpa. Figure 1 shows that the increase in yield stress $(\Delta\sigma_y)$ for 9Cr-2WVTa after 7 dpa was slightly less than for the other two 9Cr steels. However, after irradiation **to 14** dpa, there was little difference between $(\Delta\sigma_y)$ for 9Cr-2WV **and** 9Cr-2WVTa (Table 4). Therefore, it appears that the yield stress in the unirradiated condition and the change in yield **stress** after irradiation for the **9Cr-2WV**, 9Cr-2WVTa, and 9Cr-1MoVNb steels were similar. The 12Cr-1MoVW steel showed the largest increase, being over twice that of the 9Cr steels.

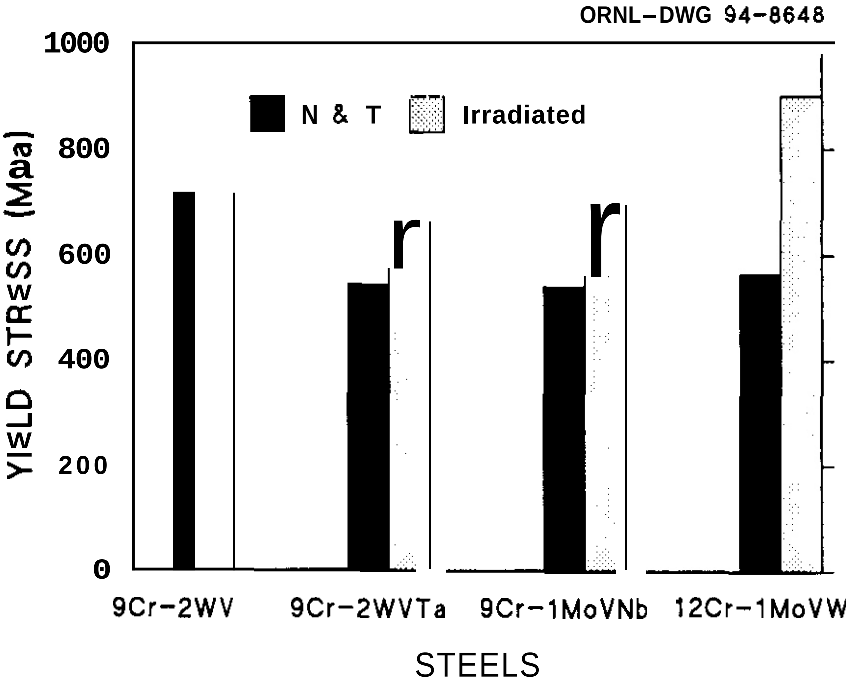

Fig. 1. Yield stress of 9Cr-2WV, 9Cr-2WVTa, 9Cr-1MoVNb, and 12Cr-1MoVW steels as normalized and tempered and alter irradiation in FFTF at 365°C.

Table 4. Irradiation effects on impact properties of martensitic steels[a]

Steel Designation	specimen Condition'	DBTT[c] (°C)	ADBX (°C)	Upper-Shelf Energy (J)	ΔUSE (%)	$\Delta\sigma_y$ (MPa)
		Irradiated at 365°C				
9Cr-2WV	N&T	-60		8.4		
	I (7)	8	68	6.4	-24	161
	I (14)	-31	29	6.3	-25	141
9Cr-2WVTa	N&T	-88		11.2		
	I (7)	-84	4	8.6	-23	125
	I (13)	-73	15	8.5	-24	147
9Cr-1MoVNb	N&T	-64		10.5		
	I (5)	-19	45	1.6	-38	153
12Cr-1MoVW	N&T	-35		7.6		
	I (4)	95	130	3.4	-55	364
	I (10)	105	140	3.2	-58	
		Irradiated at 420°C				
9Cr-1MoVNb	N&T	-64		10.5		
	I(36)	-25	39	8.2	-22	133
12Cr-M O W	N&T	-35		7.6		
	I(35)	72	107	4.1	-46	199

[a] One-third size Charpy specimens were tested.

[b] N&T -- Normalized and tempered: I -- Irradiated: dpa in parentheses.

[c] Evaluated at an energy level halfway between the upper and lover shelves.

Charpy specimens **of** the 9Cr-2WV and 9Cr-2WVTa steels were irradiated at 365°C to ≈7 and 13-14 dpa [7,8]. Specimens of the 9Cr-1MoVNb steel were irradiated to 5 dpa [10], and specimens of the 12Cr-1MoVW steel to 4 and 10 dpa (Table 4) [10,11] . There was little change in the shift in DB1T **(ADB'IT)** in going from 7 to 13-14 dpa for the reduced activation **steels,** and little difference in going from 4 to 10 dpa for the 12Cr-1MoVW, indicating that ADB'IT probably saturated with fluence by ≈4 dpa.

Charpy specimens of the 9Cr-1MoVNb and 12Cr-1MoVW steels were also irradiated in FFTF at 420°C to 35-36 dpa [10], similar to the irradiation conditions of the TEM specimens (Table 4). Hardening occurred at this higher temperature just **as** it did at 365°C, and there was an increase in DB'IT. Although the ΔDBTT was smaller **after** irradiation at 420°C, the difference was small.

TEM Observations

Detailed discussion of microstructural changes, swelling. experimental verification of precipitates, etc., will be presented in a future report [9]. This paper will concentrate on TEM observations that affect mechanical properties. The important mechanical properties observations were that irradiation caused an increase in strength, **as** measured in a tensile test, and a decrease in impact toughness. **as** observed by an increase in DBTT and a decrease in USE measured in a Charpy test. Microstructural features that cause such changes will be emphasized

The normalized-and-tempered microstructures of the four steels were 100% tempered martensite. Prior-austenite grain sizes determined by metallography indicated that 9Cr-1MoVNb and 9Cr-2WVTa steels had the smallest grain sizes (estimated average grain diameters of *22* and 32 µm, respectively), followed by the **12Cr-1MoVW** (45 µm), and the 9Cr-2WV (65 µm). There was little difference in the average lath sizes estimated by TEM.

Figures 2-5 are TEM micrographs that show the lath and precipitate structure in the unirradiated Figs. 2(a), 3(a), 4(a), and 5(a)] and irradiated [Figs 2(b), 3(b), 4(b), and 5(b)] conditions. Most of the precipitate in the microstructure of all four steels before irradiation was $M_{23}C_6$. The 12Cr-1MoVW contained about twice **as** much $M_{23}C_6$ **as** the other steels [9], because it contained twice **as** much carbon (0.2% vs. 0.1% for the three 9Cr steels). The 9Cr-1MoVNb, 9Cr-2WV, and 9Cr-2WVTa contained comparable amounts of $M_{23}C_6$ precipitate.

The only other precipitate observed in the unirradiated condition was MC. Negligible amounts were detected in the **12Cr-1MoVW,** and although present in larger quantities in the other steels, it was much **less** abundant than $M_{23}C_6$. In **9Cr-2WV,** the MC was vanadium rich, and in the 9Cr-2WVTa it contained both V-rich and Ta-rich particles. The 9Cr-1MoVNb contained V-rich and Nb-rich MC. The average size and number density of the MC particles in the 9Cr-1MoVNb and 9Cr-2WVTa were similar, but the 9Cr-2WV steel contained somewhat **less** MC than the 9Cr-2WVTa. **A** comparison of the number of small MC particles relative to the larger number of large $M_{23}C_6$ precipitates is evident in the photomicrographs of Figure 6 for **9Cr-2WVTa.**

Irradiation affected the microstructure in several ways, depending on the steel. Figures 2(b), 3(b), 4(b), 5(b), and 6(b) show photomicrographs of the irradiated structure for comparison with the unirradiated microstructure Figs. 2(a), 3(a), 4(a), 5(a), and 6(a)].

The simplest changes caused by irradiation occurred in the tungsten-containing steels. Lath size grew from about 0.3 to 0.4 µm in the 9Cr-2WV and from 0.3 to 0.45 µm in the 9Cr-2WVTa. Irradiation had only a minor effect on the $M_{23}C_6$ and MC in these two steels. The number density of $M_{23}C_6$ particles in the **9Cr-2WV** was estimated at ≈2.9 x $10^{13}/cm^3$ (average diameter 0.16 µm) and that in the 9Cr-2WVTa at –3.9 x $10^{13}/cm^3$ (0.15 **p)** The MC particles grew slightly and the number density decreased slightly during irradiation to about 1 x $10^{12}/cm^3$ (60 nm) for the 9Cr-2WV and 5.6 x $10^{12}/cm^3$ (36 nm) for the 9Cr-2WVTa.

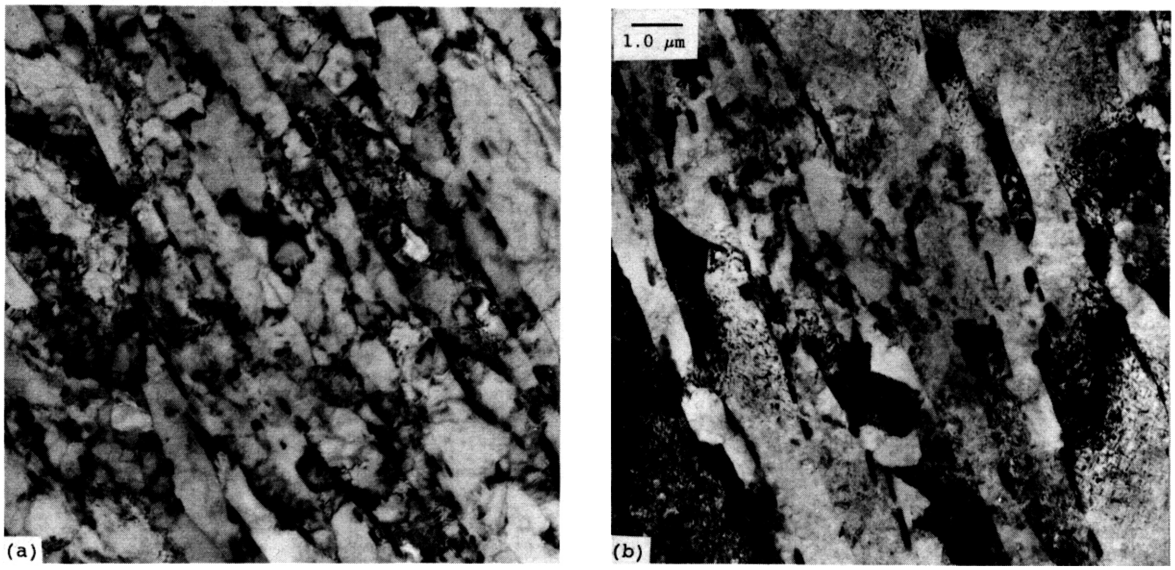

Fig. 2. Electron micrograph of 9Cr-2WV (a) in the normalized-and-tempered condition and (b) after irradiation at 420°C to –36 dpa.

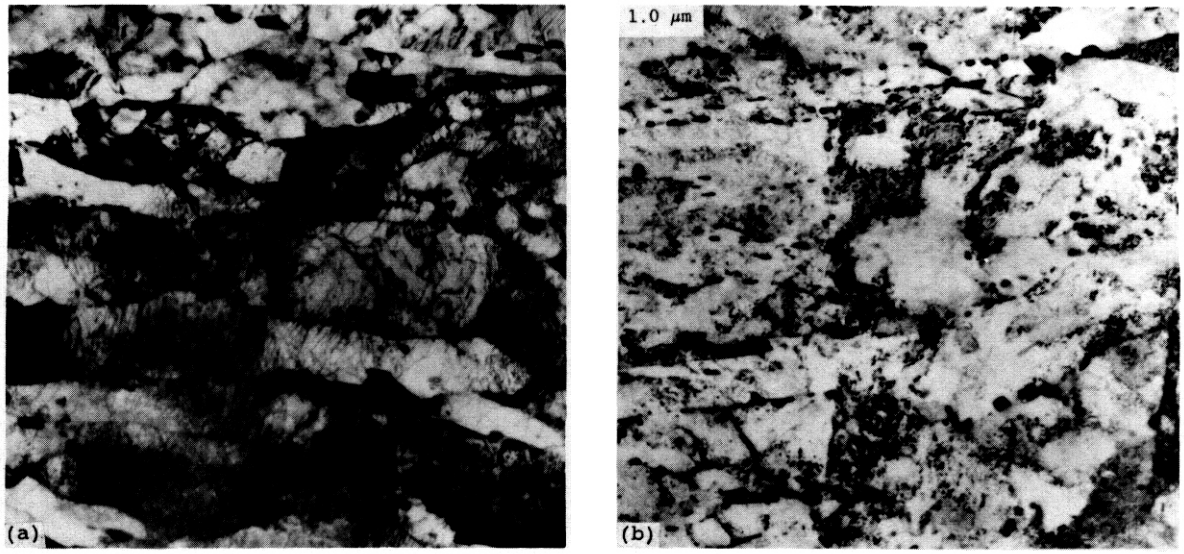

Fig. 3. Electron micrograph of 9Cr-2WVTa (a) in the normalized-and-tempered condition and (b) after irradiation at 420°C to –36 dpa.

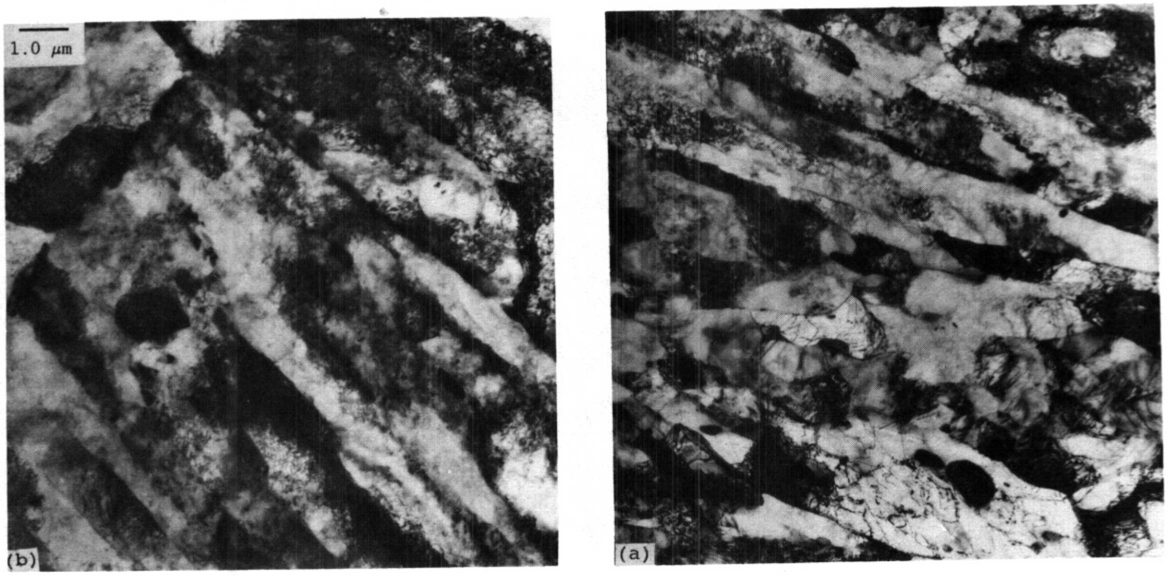

Fig. 4. Electron micrograph of 9Cr-1MoVNb (a) in the normalized-and-tempered condition and (b) after irradiation at 420°C to –36 dpa.

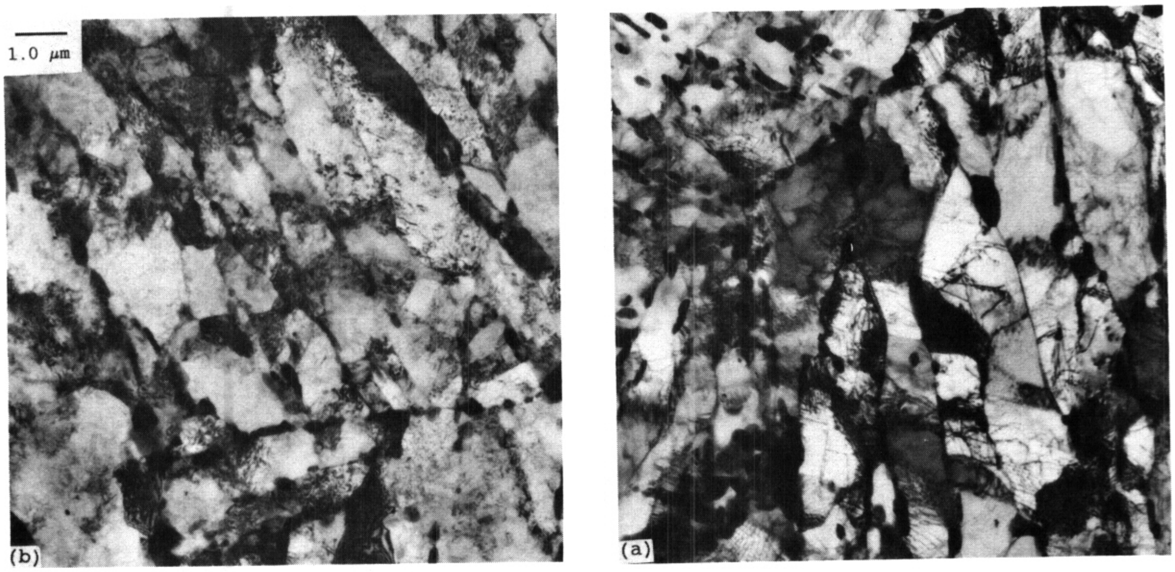

Fig. 5. Electron micrograph of 12Cr-1MoVW (a) in the normalized-and-tempered condition and (b) after irradiation at 420°C to –36 dpa.

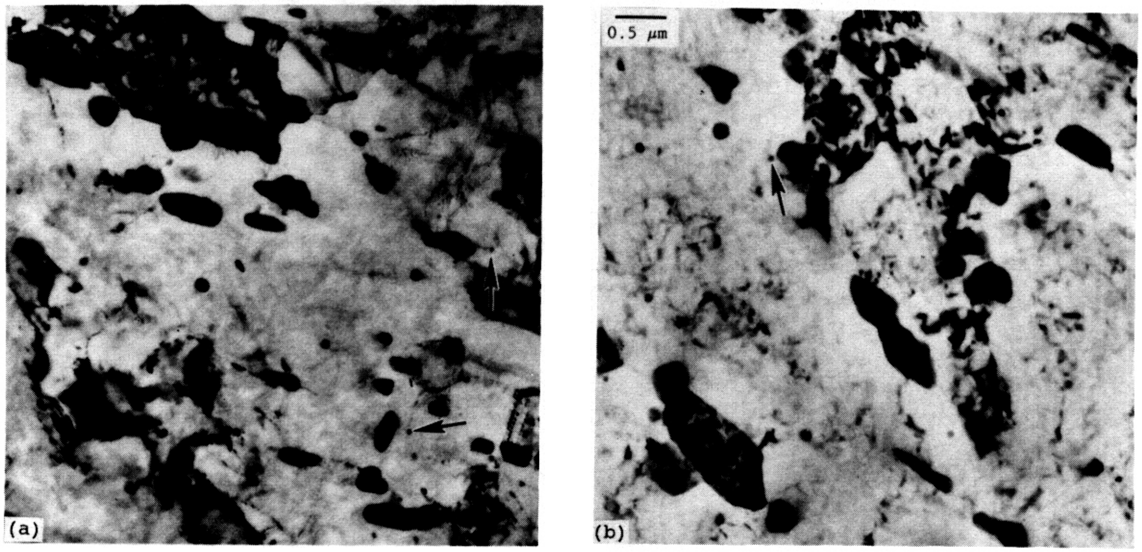

Fig. 6. High-magnification electron micrographs of 9Cr-2WVTa that indicates the relative abundance of $M_{23}C_6$ (large panicles) and MC precipitates (a) as normalized and tempered and (b) after irradiation at 420°C to –36 dpa Arrows indicate examples of the small MC particles and the smaller number density of these panicles relative to the larger $M_{23}C_6$.

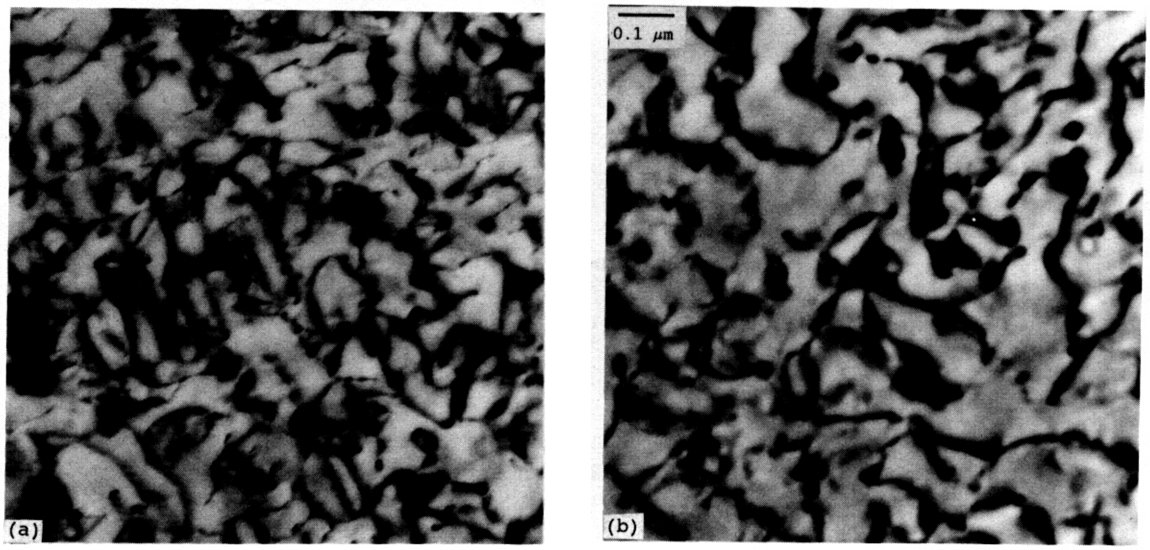

Fig. 7. Electron micrographs of dislocation loops observed in (a) 9Cr-2WV and (b) 9Cr-2WVTa irradiated to –36 dpa at 420°C.

Fig. 7 shows the dislocation loops in 9Cr-2WV and 9Cr-2WVTa that formed during irradiation. Average loop size was estimated to be 40-100 nm at a density of –3 x $10^{15}/cm^3$ for both steels. The only other observation was void formation: 25 nm voids formed at densities of 0.5 x $10^{13}/cm^3$ and 3 x $10^{13}/cm^3$ in the 9Cr-2WV and 9Cr-2WVTa, respectively [9].

No noticeable change in lath size occurred in the two molybdenum-containing steels: the lath size of the 9Cr-1MoVNb remained at 0.45 µm and the 12Cr-1MoVW remained at 0.5 µm. For the 9Cr-1MoVNb, the number density of MC particles was relatively unchanged at –7.3 x $10^{13}/cm^3$, but the size increased from ≈40 to 50-100 nm. Essentially no MC was found in the 12Cr-1MoVW, similar to the unirradiated condition.

The major difference between the Cr-Mo and Cr-W steels was the irradiation-induced precipitates that formed in 9Cr-1MoVNb and 12Cr-1MoVW, but not in 9Cr-2WV and 9Cr-2WVTa. Two new phases precipitated in the 12Cr-1MoVW: a high number density (1.5 x $10^{16}/cm^3$) of 4-8 nm particles formed within the laths and were tentatively identified as chromium-rich *a'* (Fig. 8). and particles –15 nm in diameter at a number density of ≈6 x $10^{14}/cm^3$ formed mainly on lath boundaries and were identified as chi-phase [9]. For the 9Cr-1MoVNb, only the chi-phase was observed, and it formed primarily in the matrix. These chi-phase particles were 10-15 nm in diameter at a number density of ≈9 x $10^{14}/cm^3$ (Fig. 9).

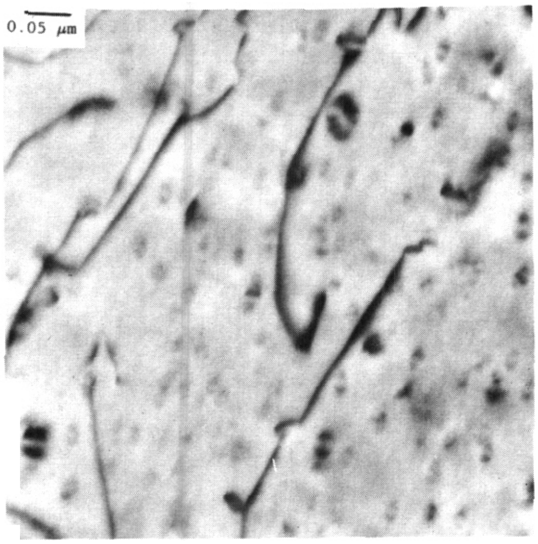

Fig. 8. Electron micrograph of the fine precipitates observed in the irradiated 12Cr-1MoVW that were tentatively identified as *a'*.

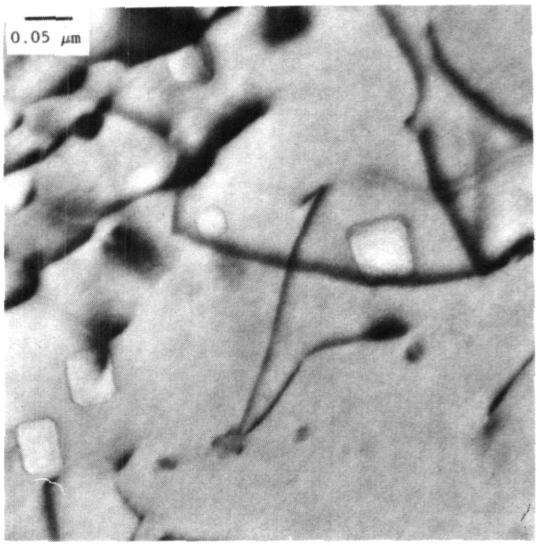

Fig. 9. Electron micrograph showing the voids, chi-phase precipitates, and low dislocation density (no loops) in irradiated 9Cr-1MoVNb.

An estimated 5 x $10^{14}/cm^3$ (≈100nm diameter) dislocation loops were observed in 12Cr-1MoVW, which is almost an order of magnitude less than in the tungsten-containing steels. The loop density in 9Cr-1MoVNb steel was negligible, with only a few dislocation lines present (Fig. 9). On the other hand, the 12Cr-1MoVW steel contained very few voids (≈5 x $10^{12}/cm^3$) compared to the 9Cr-1MoVNb (≈6 x $10^{14}/cm^3$) [9]. Examples of the voids in 9Cr-1MoVNb are visible in Fig 9.

Discussion

Although most of the mechanical property test specimens were irradiated at 365°C and the TEM disks were irradiated at 420°C, similar irradiation-produced microstructural changes are expected at the two temperatures [12]. Furthermore, as indicated by a comparison of the Charpy properties for the 9Cr-1MoVNb and 12Cr-1MoVW steels irradiated at 365 and 420°C (Table 4), the relative Charpy behavior is similar at the two temperatures. Tensile specimens of 9Cr-1MoVNb and 12Cr-1MoVW irradiated at 420°C [10] also show relative hardening changes similar to those observed after irradiation at 365°C. At the 365°C irradiation temperature, the precipitate particles, dislocation loops, and voids will be finer and form at a higher number density [12], leading to the higher hardening and larger changes in Charpy properties observed at the lower temperature. Thus, because similar irradiation processes are expected at 365 and 420°C, the comparison between microstructure and properties made in this paper should be valid.

A comparison between the mechanical properties and microstructure of 12Cr-1MoVW and the three 9Cr steels will be made first, followed by an examination of the differences among the 9Cr steels. In the unirradiated condition, there was little difference in the yield stresses of the four steels (Fig. 1). However, there were differences in the Charpy behavior: the DBTT of the 12Cr-1MoVW was considerably higher and the USE considerably lower *than* for the three 9Cr steels.

The difference in the unirradiated Charpy properties of the 9Cr-1MoVNb and 12Cr-1MoVW steels was previously attributed to the difference in carbon concentration (0.1% in the 9Cr-1MoVNb and 0.2% in the 12Cr-1MoVW) [10]. Twice as much carbon resulted in twice as much carbide in the 12Cr-1MoVW when the steels were tempered [9], in agreement with previous observations when 9Cr-1MoVNb and 12Cr-1MoVW were compared [13]. The larger amount of carbide can enhance crack formation in 12Cr-1MoVW, thus leading to the inferior fracture behavior [10]. The same argument applies to the 12Cr-1MoVW relative to the 9Cr-2WV and 9Cr-2WVTa, since both contain 0.1% C and half as much carbide as the 12Cr-1MoVW [9].

Irradiation had a much larger effect on the tensile and impact behavior of the 12Cr-1MoVW than on the three 9Cr steels. To examine this difference, consider again the difference between the 9Cr-1MoVNb and 12Cr-1MoVW steels. Relative changes in the tensile and impact properties of these two steels after irradiation were similar at both 365 and 420°C (the temperature at which the TEM disks were irradiated) [10]. Both steels contained similar amounts of chi-phase after irradiation. The primary irradiation-produced microstructural differences were the high number density of *a'* precipitates and the presence dislocation loops in 12Cr-1MoVW that were not present in 9Cr-1MoVNb. The hardening caused by these two constituents in the 12Cr-1MoVW could produce the larger increase in yield stress in the 12Cr-1MoVW, which could then produce the larger ΔDBTT for 12Cr-1MoVW over that of the 9Cr-1MoVNb. Similarly, the *a'* and chi-phase can account for the difference in the irradiated properties of the 12Cr-1MoVW and the 9Cr-2WV and 9Cr-2WVTa steels, All three of these steels contain dislocation loops, with the density greater in the 9Cr-2WV and 9Cr-2WVTa.

To understand the differences among the three 9Cr steels, consider first the differences between the 9Cr-2WV and 9Cr-2WVTa, which in the unirradiated condition had similar yield stresses but different Charpy properties. Irradiation caused comparable hardening, but a smaller ΔDBTT and a smaller decrease in the USE for the 9Cr-2WVTa than the 9Cr-2WV. Since the only differences between the two steels is the tantalum in the 9Cr-2WVTa, this difference must cause the difference in Charpy behavior before irradiation. Tantalum refines the austenite grain size [7], which can affect the DBTT. The only other difference in the two steels to account for the difference in Charpy properties is the tantalum in solid solution. (The tantalum-containing steel had about twice as much MC, but the small amounts of MC did not appear to affect the strength before irradiation. and the MC would not be expected to lower the DBTT). Based on the amount of tantalum-rich MC carbides present, it was calculated that well over 50% of the tantalum remained in solid solution.

The ADBTT of the 9Cr-2WVTa (4°C) after ≈7 dpa at 365°C was much smaller than the shifts for 9Cr-2WV (68°C) and 9Cr-1MoVNb (45°C), given that the difference in $\Delta\sigma_y$ was minimal (Table 4). This means that the ADB'IT for the 9Cr-2WVTa was not as affected by hardening as the other two 9Cr steels, because a much larger ΔDBTT would be expected if it was due to the change in yield stress alone.

Figures 10 and 11 offer a possible explanation for this behavior. A schematic diagram of flow curves as a function of temperature are shown in Fig. 10 for two steels before and after irradiation. Fracture stress, assumed to be the same for both steels, is also shown, and the DB'IT is taken as the intersection of the fracture stress curve with the flow stress curve. In the unirradiated condition. Fig. 10 shows two steels with flow stresses (yield stresses) that approach each other at elevated temperatures (the irradiation temperature), but diverge at low temperatures. thus giving Steel 1 a lower DB'IT (T_1^0) than Steel 2 (T_2^0). The curves after irradiation are drawn for a yield stress change that is the *same* for both steels, $\Delta\sigma_y^1 = \Delta\sigma_y^2$. Also shown is the ADB'IT for the two steels, and although the same change in yield stress occurred for both steels. Steel 1, with the lowest DB'IT before irradiation, had a smaller ADBTT than Steel 2. This follows from the *shape* of the flow curves.

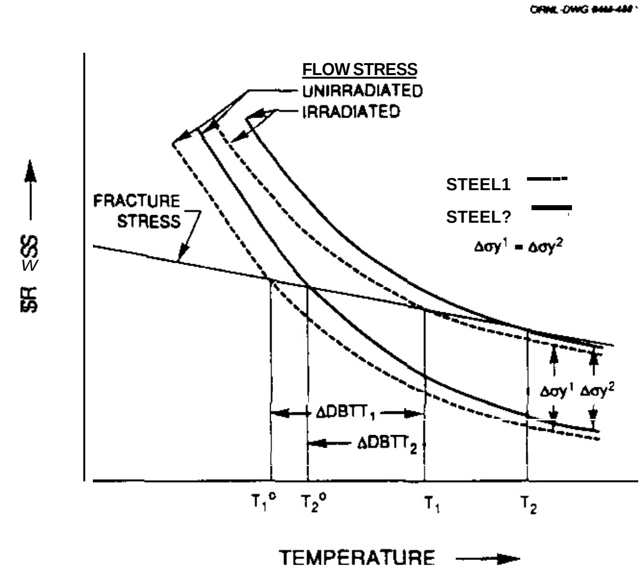

Fig. 10. Schematic diagram that illustrates how two steels with the same fracture stress and a similar yield stress at an elevated temperature (the irradiation temperature) can show the same increase in yield stress due to irradiation and still have different shifts in DBTT due to the irradiation.

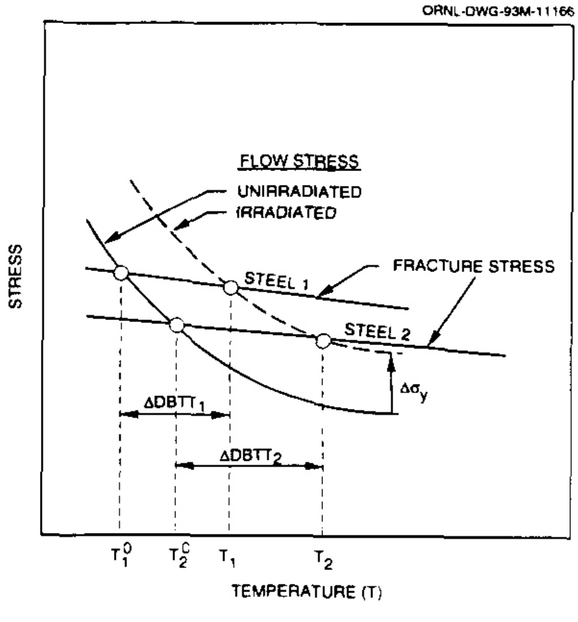

Fig. 11. Schematic diagram that illustrates how two steels with the same yield stress-temperature relationship and show the same increase in yield stress due to irradiation but have different fracture stresses can have different shifts in DB'IT due to the irradiation.

Alternatively, if the flow curves for the two steels were the same, but the fracture stresses were different, the same conclusion follows (Fig. 11). In this case, the steel with the highest fracture stress develops the smallest ΔDBTT, which in Fig. 11 is again Steel 1.

A comparison of the yield stress behavior from room temperature to 600°C for 9Cr-2WV and 9Cr-2WVTa gives no indication that the flow stress of the two steels would be substantially different at low temperatures. or that the flow stress of the 9Cr-2WVTa would be less than that of the 9Cr-2WV (the opposite is indicated by the low-temperature data [4]). Therefore, it appears that the effect depicted in Fig. 11 offers the most likely explanation for the superior DBTT of the 9Cr-2WVTa prior to irradiation and the smaller ΔDBTT after irradiation. This, despite the two steels having similar yield stresses before and after irradiation. Data on the effect of tantalum on fracture stress are required to verify this possibility.

Before irradiation, the yield stresses of 9Cr-1MoVNb, 9Cr-2WV, and 9Cr-2WVTa were similar. The Charpy properties of 9Cr-1MoVNb and 9Cr-2WV were similar before and after irradiation. Irradiation hardening in the 9Cr-1MoVNb was attributed to chi-phase (an Fe-Mo intermetallic compound), while hardening in the 9Cr-2WV and 9Cr-2WVTa was due to the dislocation loops. These must have produced equivalent increases in yield stress. From the microstructural observations, no obvious reason for the difference in the Charpy behavior of 9Cr-1MoVNb and 9Cr-2WVTa could be detected. Therefore, the difference must involve the one steel containing molybdenum and niobium and the other tungsten and tantalum. This difference in chemical composition also manifests itself by the higher tempering temperature (760°C) required for the 9Cr-1MoVNb to obtain a satisfactory strength-toughness balance compared to that of the steels containing tungsten (750°C).

Although the above discussion involved considerable speculation, some interesting inferences follow from the observations. First the major difference in irradiation hardening between the 12Cr-1MoVW and the 9Cr steels involves the formation of *d* in 12Cr-1MoVW. The *d* is a high-chromium phase that does not form in the 9Cr steels. A similar observation on *d* in 12Cr steels was made by Dubuisson et al. [14]. Thus, even if the carbon concentration of a 12Cr steel was lowered to improve the unirradiated Charpy behavior, post-irradiation properties would probably remain worse in the 12Cr steel.

A second observation involves the difference between molybdenum and tungsten in the 9Cr steels. Molybdenum-rich chi-phase formed in irradiated 9Cr-1MoVNb, whereas no new phases formed in 9Cr-2WV and 9Cr-2WVTa. This new phase and the lack of significant dislocation-loop formation in 9Cr-1MoVNb constituted the major difference in the steel with molybdenum and those with tungsten. The absence of significant loop formation in the 9Cr-1MoVNb may mean that the faster-diffusing molybdenum allowed loops to grow rapidly and anneal out, but the loops remained in the 9Cr-2WV and 9Cr-2WVTa because of the slower-diffusing tungsten. The diffusion coefficient of molybdenum in ferritic steels is ≈1000 times greater than that of tungsten at 400°C under nonirradiation conditions (irradiation will enhance diffusion) [15]. A somewhat similar observation applies to a comparison of the loops in the 12Cr-1MoVW and the two tungsten-containing steels. There were about an order of magnitude less loops in the 12Cr-1MoVW and they were larger than those in the two tungsten-containing steels. The difference in loop concentrations between the 12Cr-1MoVW and the 9Cr-1MoVNb may have been that loop evolution in the 12Cr-1MoVW had to compete with *d* formation, and this could delay loop growth in this molybdenum-containing steel. Chi-phase is not postulated to play a role, since it is also present in the 9Cr-1MoVNb steel, where no loops were observed.

In the final analysis, the excellent resistance to irradiation-produced changes in impact behavior of 9Cr-2WVTa compared to the other two 9Cr steels is caused by quite minor differences in microstructure. The better impact properties of the 9Cr-2WVTa are caused by a slightly different fracture stress-temperature relationship or flow stress-temperature relationship for this steel before irradiation, which must somehow be caused by the small tantalum addition.

SUMMARY AND CONCLUSIONS

The microstructures of 9Cr-2WV, 9Cr-2WVTa, 9Cr-1MoVNb, and 12Cr-1MoVW in the nodi-and-tempered and irradiated conditions were correlated with changes in tensile and Charpy impact behavior caused by neutron irradiation. Irradiation caused an increase in strength, an increase in DBTT, and a decrease in USE. TEM specimens were examined after irradiation in the FFTF to =36 dpa at 420°C. Irradiation of mechanical property specimens was in FFTF to –14 dpa at 365°C. A major objective was to determine the source of the excellent post-irradiation properties of the 9Cr-2WVTa.

The following summarizes the observations and conclusions:

1. Before irradiation, the microstructures of the four steels were tempered martensite containing $M_{23}C_6$ and MC precipitates. The steels bad similar yield stresses, but the Charpy properties of the 12Cr-1MoVW steel were inferior to those for the 9Cr steels, because of the higher carbon concentration of the 12Cr-1MoVW. The 9Cr-2WVTa steel had a lower DBTT and higher USE than the other two 9Cr steels. No microstructural explanation is available for why tantalum affected the steel in this way.

2. During irradiation of the 12Cr-1MoVW steel. small dislocation loops formed. along with precipitates identified as *d* and chi-phase. These irradiation-induced precipitates and dislocation loops caused the 12Cr-1MoVW steel to develop the largest increase in yield stress and the largest change in impact properties of the four steels.

3. The only irradiation-induced microstructural change in the 9Cr-1MoVNb steel was the formation chi-phase. Therefore, mechanical properties changes for the 9Cr-1MoVNb were significantly less than for the 12Cr-1MoVW.

4. Irradiation caused no new precipitate phases to form in the 9Cr-2WV and 9Cr-2WVTa steels, although a relatively high density of dislocation loops formed. A similar density of loops in the two steels caused comparable hardening, as measured by yield stress. However. the 9Cr-2WV developed a larger change in Charpy impact properties than the 9Cr-2WVTa. No microstructural changes were detected to quantitatively account for this difference. The change in yield stress and impact properties of the irradiated 9Cr-2WV were similar to those for irradiated 9Cr-1MoVNb.

5. In the absence of microstructural differences to account for the superior impact properties of 9Cr-2WVTa over 9Cr-2WV and 9Cr-1MoVNb, the differences were attributed to a different fracture stress-temperature relationship or flow stress-temperature relationship for the 9Cr-2WVTa and the other two 9Cr steels.

REFERENCES

1. Klueh, R. L., Ehrlich, K., and Abe, F., "Ferritic/Martensitic Steels: Promises and Problems." J. Nucl. Mater., 191-194 (1992) 116.

2. Conn, R. W., Bloom, E. E., Davis. J. W., Gold, R. E.. Little, R., Schultz. K. R., Smith. D. L., and Wiffen, F. W., "Panel Report on Low Activation Materials for Fusion Applications," UCLA Report PPG-728, University of California at Los Angeles, June 1983.

3. Klueh, R. L. and Maziasz, P. J., "Microstructure of Cr-W Steels," Met. Trans. 20A (1989) 373.

4. Klueh, R. L. "Heat Treatment Behavior and Tensile Behavior of Cr-W Steels," Met. Trans, 20A (1989) 463.

5. Klueh. R. L. and Corwin, W. R., "Impact Behavior of Cr-W Steels," J. Eng. Mater., 11 (1989) 169.

6. Klueh. R. L.. "Irradiation Hardening of Ferritic Steels: Effect of Composition," J. Nucl. Mater., 179-181 (1991) 728.

7. Klueh, R. L., Alexander, D. J., and Maziasz, P. J.. "Impact Behavior of Reduced-Activation Ferritic Steels Irradiated in the Fast Flux Test Facility," J. Nucl. Mater., 186 (1992) 185.

8. Klueh R. L., and Alexander, D. J., "Impact Toughness of Irradiated Reduced-Activation Ferritic Steels," J. Nucl. Mater., to be published.

9. Kai, J. J. and Klueh, R. L., "Microstructural Analysis of Neutron-Irradiated Martensitic Steels." Fusion Reactor Materials Semiannual Progress Report. to be published.

10. Klueh, R. L. and Alexander, D. J., "Charpy Impact Toughness of Martensitic Steels Irradiated in FFTF: Effect of Heat Treatment" p. 591 in: Effects of Radiation on Materials: 16th International Symposium. ASTM STP 1175. Arvind S. Kumar, David S. Gelles, and Randy K. Nanstad, Eds., American Society for Testing and Materials, Philadelphia 1994.

11. Klueh, R. L. and Alexander, D. J.. "Irradiation Effects on the Impact Behavior of 12Cr-1MoVW and 2 1/4Cr-1Mo Steels," p. 1256 in: Effects of Radiation on Materials: 15th International Symposium, ASTM STP 1125, R. E. Stoller, A. S. Kumar, and D. S. Gelles. Eds.. American Society for Testing and Materials, Philadelphia, 1992.

12. Maziasz, P. J., Klueh, R. L.. and Vitek, J. M., "Helium Effects on Void Formation in 9Cr-1MoVNb and 12Cr-1MoVW Irradiated in HFIR," J. Nucl Mater.: 141-143, 929 (1986).

13. Vitek, J. M. and Klueh, R. L., "Precipitation Reactions during the Heat Treatment of Ferritic Steels," Met. Trans. 14A (1983) 1047.

14. Dubuisson, P, Gilbon, D., and Seran, J. L., "Microstructural Evolution of Ferritic-Martensitic Steels Irradiated in the Fast Breeder Reactor Phenix," J. Nucl Mater.: 205 (1993) 178.

15. Honeycombe, R. W. K., Structure and Strength of Alloy Steels, Climax Molybdenum Co. Ltd, London, 1974.

CONSEQUENCES OF NO POSTWELD HEAT TREATMENT ON THE FRACTURE TOUGHNESS OF LOW ACTIVATION MARTENSITIC STEELS - Huaxin Li (Associated Western Universities, Northwest Division), D. S. Gelles and R. H. Jones (Pacific Northwest Laboratory)[a]

OBJECTIVE

The objective of this work is to provide guidance on the design of components using martensitic steels.

SUMMARY

Fracture toughness has been measured for two conditions of low activation martensitic steel **F-82H**, the first, a fully tempered condition and the second, completely untempered. In the fully tempered condition, F-82H has a J_{IC} toughness of 284 kJ/m^2 (K_{IC} = 263.8 MPa$\sqrt{m}$), but in the untempered condition, the J_{IC} toughness is 18.4 kJ/m^2 (K_{IC} = 64 MPa$\sqrt{m}$). The consequences of not tempering are discussed in light of these measurements.

PROGRESS AND STATUS

Introduction

Designers using martensitic steels are often tempted to avoid tempering welds to simplify fabrication. Tempering requires complex postweld heat treatments. Metallurgists usually recommend that welds be tempered to reduce embrittlement. Untempered martensitic steels are known to be extremely brittle. However, the issue has not been quantified in terms of usable design parameters.

The present effort is based on efforts to determine fracture toughness in the low activation ferritic alloy F-82H as a function of loading mode.[1] That work showed that F-82H has very high toughness, as high as 500 kJ/m^2 for mode I J-integral toughness (J_{IC}) and a tearing modulus of (360 kJ/m^2}/mm. However, it is difficult using the J-integral approach to measure fracture toughness in very brittle materials. Instead, a stress intensity factor (K_{IC}) approach must be used, and fatigue precracking is preferred. Therefore, it was necessary to alter procedures to provide specimens with sharp cracks, and for the tempered condition, a thicker specimen geometry was employed in comparison with previous work to ensure a plane strain condition and therefore valid data.

Experimental Procedure

The F-82H plate used in this study, as well as in previous fracture toughness studies,[1] was supplied by Nippon Kokan Steel Company (NKK) of Japan. The chemical composition of the plate (as provided by NKK in wt%) is: **7.71Cr-2.1W-0.18V-0.04Ta-0.096C-0.003P-0.003S.** Specimens used in this study were machined in a T-L orientation as specified in American Society for Testing and Materials (ASTM) standard E399-90. The fully heat treated condition used 1000°C/20 h/air cooling

---

[a] Pacific Northwest Laboratory is operated for the U.S. Department of Energy by Battelle Memorial Institute under Contract DE-AC06-76RLO 1830.

(AC), 1100°C/7 min/AC, and **700°C/2 h/AC** in order to provide homogenization, normalization and tempering. The untempered condition added a further treatment of 1100°C/7 min/AC.

Specimen geometries are shown in Figure **1**, with the fully tempered specimen shown in Figure 1a at a thickness of 14 mm and the untempered condition specimen shown in Figure 1b at a thickness of 15 mm. Side grooves were included in the J specimen but not shown in Figure 1a with a resultant thickness reduction of **10%** on each side, for a total of 20%. Fatigue precracking followed heat treatment and produced cracks of approximately **1.5 mm.** For the fully tempered condition, J,, was determined using the single specimen technique following ASTM procedure **E813-89.** and **K,** testing for the untempered condition followed ASTM procedure **E399-90.**

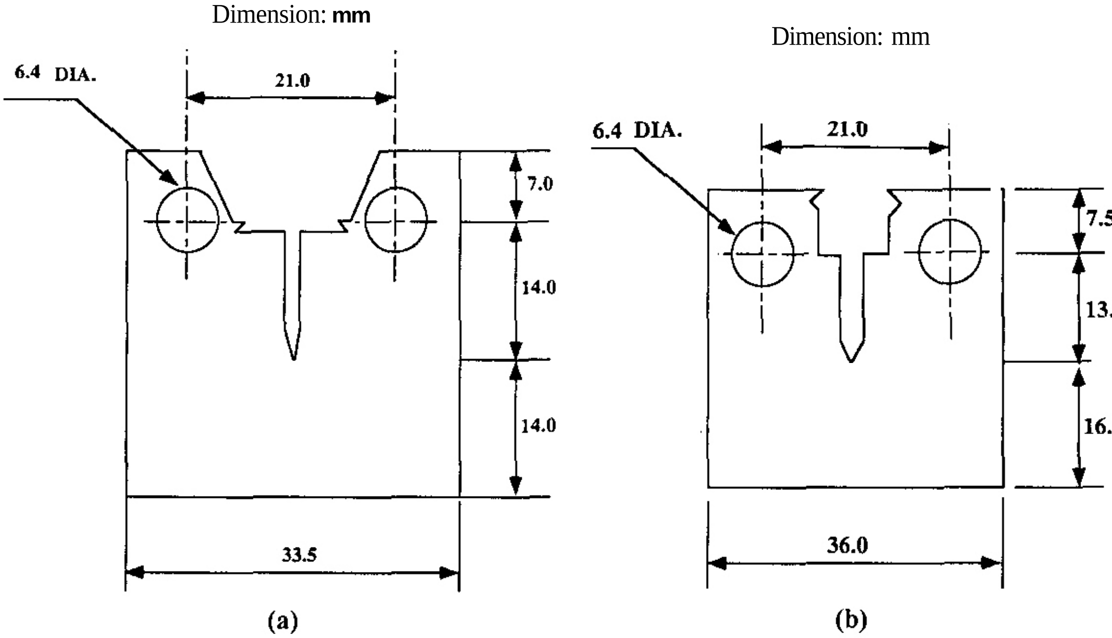

Figure 1. Specimen geometries for fracture toughness testing, **a)** J_{IC} in fully tempered F-82H with a thickness of **14 mm** and b) **K,** in untempered F-82H with a thickness of **15** mm. Side grooves for the J,, specimen geometry are not shown.

Results

The results of fracture toughness testing are provided in Table **1**, which contains values for J,, and **K,** for each condition with conversion based on the expression:

$$J_{IC}=\frac{K_{IC}^{2}}{E}\quad(1-\nu^{2}) \qquad (1)$$

where J,, is the critical J integral expression for fracture toughness, K,, is the critical stress intensity factor and v is Poisson's ratio. The tearing modulus for the fully tempered condition was {270 kJ/m^2}/mm. Table **1** also provides hardness values for comparison.

Table **1.** Fracture Toughness Measurements **on** F-82H as a Function of Heat Treatment Condition.

Specimen Condition	K_{IC} (MPadm)	J_{IC} (KJ/m^2)	Hardness
Fully tempered*	(263.8)	284	R_B = **83**
Untempered^B	64.3	**(18.4)**	R_C = **35**

HEAT TREATMENTS (with AC = air cooled, RT = room temperature)

A = 1000°C/20 hr/AC to RT + 1100/7 min/AC to RT + 700/2 hr/AC

B = *A* + 1100°C/7 min/AC to RT

( ) indicates conversion to value given was made using equation **(1)**

From Table **1,** it is apparent that J_{IC} is reduced by as much as **an** order of magnitude when comparing the untempered with the fully tempered condition. However, it may be noted that the level of fracture toughness measured for the untempered condition is comparable to values obtained for lower shelf response of fully tempered material (details to be provided in the next semiannual report).

Discussion

The fracture toughness value obtained for fully heat treated F-82H in the present work is lower than the value that was previously obtained.' The two experiments had two differences in specimen condition: thickness and notch acuity. The specimen thickness was increased from 7.6 to 14 **mm** in the current study, and the notch was changed from an electric discharge machining (EDM) notch of radius **0.051** mm to a fatigue precracked notch that is much sharper. It is appropriate to identify which factor may have been responsible for the reduction in toughness values. Because F-82H was found **to** be much tougher than expected, the data given in reference 1 for the 0 degree crack angle did not satisfy the thickness requirements for standard J,, determination, necessitating the use of a thicker specimen in the current work.

The earlier tests gave a J,, value **of** 430 kJ/m^2 and a tearing modulus of (360 kJ/m^2}/mm using a 7.6 **mm** thick specimen.' This is a factor of two higher than the toughness obtained in the present test. However, subsequent testing of a 14 **mm** thick J,, specimen with only an EDM notch gave 395 kJ/m^2 for J_{IC} and (348 kJ/m^2}/mm for the tearing modulus. Therefore, the reduction in toughness is a result of the change in notch acuity. Also, although earlier tests did not satisfy ASTM standards, the earlier data provide a reasonable estimate for fracture toughness in F-82H.

The finding that notch acuity affects the determination of J_{IC} emphasizes that specimens should be precracked whenever possible to provide the most conservative estimate of toughness. This is similar to recent results showing that ductile to brittle transition temperature (DBTT) based **on** absorbed energy in Charpy specimens is a function of the ratio of notch depth to notch root radius that is independent of specimen size.'

The results of this work can be used to estimate the consequences of not tempering F-82H welds in a different way. The critical crack length a, for failure in a component is related to K,, by the expression:

$$a_c = \frac{K_{IC}^2}{\sigma^2 \pi} \qquad (2)$$

where a is the stress applied to the Component. Since the fracture toughness, K_{IC}, is reduced by a factor of 4 when welds are untempered, the critical crack length is reduced by a factor of **16.** Therefore, flaw discrimination procedures must be improved by a factor of **16** to maintain safety margins in welded components if the components are untempered. However, it may be noted that, after a welded component has been put into service, diffusion is sufficient to relax internal stresses and promote carbide precipitation, and the fracture toughness of the weldments can be expected to improve dramatically.

CONCLUSIONS

The fracture toughness (K_{IC}) of an untempered weld of **F-82H** is **64** MPa√m (J_{IC} = **18.4** kJ/m^2) corresponding to a reduction in toughness of a factor of **4 in** comparison with the fully heat treated condition. This equates to a requirement for improvement in flaw discrimination by a factor of **16** if no postweld heat treatment is used.

FUTURE WORK

F-82H fracture toughness results for low temperature tests will be provided in the next semiannual report.

REFERENCES

1. Huaxin Li, R H. Jones, J. P. Hirth and D. S. Gelles, “Effect of Loading on the Fracture Toughness of a Ferritic/Martensitic Stainless Steel,” DOE/ER-0313/15 (1993) 134.

2. H. Kurishita, H. Kayano, M. Narui, **M.** Yamazaki, Y. Kano and I. Shibahara, ***Mater. Trans., JIM,*** **34** (1993) **1042.**

MICROSTRUCTURAL EXAMINATION OF COMMERCIAL FERRITIC ALLOYS AT 200 DPA •

D. S. Gelles, (Pacific Northwest Laboratory)”

OBJECTIVE

The objective of this work is to determine lifetime limits for ferritic/Martensitic alloys.

SUMMARY

Microstructures and density change measurements are reported for Martensitic commercial steels HT-9 and Modified 9Cr-1Mo (T9) and oxide dispersion strengthened ferritic alloys MA956 and MA957 following irradiation in the FFTF/MOTA at 420°C to 200 DPA. Swelling as determined by density change remains below 2% for all conditions. Microstructures are found to be stable except in recrystallized grains of MA957, which are fabrication artifacts, with only minor swelling in the Martensitic steels and ***a'*** precipitation in alloys with 12% or more chromium. These results further demonstrate the high swelling resistance and microstructural stability of the ferritic alloy class.

PROGRESS AND STATUS

Introduction

Reduced activation ferritic alloys appear to be promising first wall and structural materials far commercial fusion reactors. This expectation is based in part on limited experiments using reduced activation alloys, hut also on a large number of experiments using commercial ferritic/Martensitic alloys. The present effort investigates the high dose limit of the commercial steels by examining the effect of irradiation in a fast reactor at the peak swelling temperature to a very high dose, not likely to be exceeded for many years.

The materials being examined include two classes, Martensitic stainless steels in the 9 to 12% Cr range and oxide dispersion strengthened (ODS) alloys made by the mechanical alloying process. The Martensitic steels are HT-9 and Modified 9Cr-1Mo (now designated as T9), and the ODS alloys are MA956 and MA957. The original candidate ferritic alloy for fusion structural materials applications was HT-9, an Fe-12Cr-1Mo-0.2C-WV steel. Due to better irradiation embrittlement expectations, T9, an Fe-9Cr-1Mo-0.1C-VNb steel, was considered an alternative to HT-9. Mechanical alloying, a process using high energy hall milling procedures, is expected to provide a ferritic alloy option with applications to significantly higher temperatures,’.’ albeit with worst ductile to brittle transition temperature response. The first ferritic alloy to he manufactured commercially using mechanical alloying was MA956, an **$Fe\text{-}20Cr\text{-}4Al\text{-}0.5Ti\text{-}0.5Y_2O_3$**. A similar alloy with lower chromium, MA957, was invented for radiation damage resistance.’ It may be noted that results of microstructural examination have been reported previously for identical specimens of HT-9 to the lower dose of 110 dpa,[4] and the density measurements for HT-9 and T9 at 200 dpa have already been reported? The International Nickel Company kindly provided the two experimental batches of MA957 for irradiation before commercial production was available.

‘Pacific Northwest Laboratory is operated for the **U.S.** Department of Energy by Battelle Memorial Institute under Contract DE-AC06-76RLO 1830.

The present experiment is based on specimens included in early Fast Flux Test Facility/Materials Open Test Assembly (FFTF/MOTA) irradiation tests. The tests were continued until the shutdown of the reactor. Specimens were in weeper positions operating at temperatures **on** the order of 420°C, the temperature range found to result in peak swelling for the ferritic alloy class. As a result, examination of these specimens allows the opportunity to evaluate the ferritic alloy class at extremely high dose, in order to assess life limiting conditions for Martensitic and ODS steels.

Experimental Procedure

The alloy compositions and heat treatments are provided in Table 1. As indicated in the identification (ID) codes, specimens of HT-9 and T9 were included in transmission electron microscopy (TEM) packet FL whereas specimens of MA956 and MA957 were in TEM packet H4. TEM packets FL and H4 were located in in-core weeper positions of the FFTF/MOTA from the beginning of cycle 4 and throughout the operation of FFTF. The irradiation history for packet FL was as follows:

MOTA 1B basket 1E-4 to $\mathbf{2.21x10^{22}}$ nlcm’ (all tluences are given as E > 0.1 MeV) at an average temperature of 407°C.
MOTA 1C basket 2C-4 to $7.25x10^{22}$ n/cm^2 at 425°C.
MOTA 1D basket 2C-2 to $5.46x10^{22}$ nlcm’ at 406°C.
MOTA 1E basket 2C-2 to $9.59x10^{22}$ nlcm’ at 403°C.
MOTA IF basket 2C-1 to $9.58x10^{22}$ nlcm’ at 406°C.
MOTA 1G basket 3A-1 to $7.96x10^{22}$ n/cm^2 at 431°C.
MOTA 2B basket 3A-4 to $6.38x10^{22}$ nlcm’ at 433°C.

Table **1.** Compositions of commercial ferritic/Martensitic alloys

ID Code	Alloy	Heat No.	Composition (w/o)										HT*
			Cr	C	Mo	V	Mn	Si	Ni	P	S	Other	
PTFL	T9	30176	8 43	09	.89	.24	.37	.16	.11	.011	.004	Nb: .08 Cu: .04	A
RFFL RHFL	HT-9	9607R2	12 1	20	1.04	0.28	0.57	.17	51	.016	.003	N: 027 W .45	B C
RLH4	MA956	ABB0042	19.1 0	019	na	na	0 09	.10	19	009	.004	Y_2O_3: .48 Al: 4.20 Ti. .34	D
RMH4	MA957	T88793	13.8	na	0.26	na	na	na	na	na	na	Y_2O_3: .26 Ti .90 O(total): .32 N .031	E
RNH4	MA957	T88794	13.1	na	0.27	na	na	na	na	na	na	Y_2O_3: .25 Ti: .95 O(total): .28 N: 036	E

* HEAT TREATMENTS with AC = air cooled, RT = room temperature
A = 1040°C/1 hr/AC to RT + 760/1 hr/AC
B = 1000°C/20 hr/AC to RT + **110015** min/AC to RT + 700/2 hr/AC
C = 1050/5 min/AC to RT + 760/0.5 hr/AC
D = 1330°C/1 hr/AC
E = 1100°C/1 hr/AC

Therefore, during that period, the specimens in packet FL received a fluence of $4.84x10^{23}$ nicm' at an average temperature of 416 ± 13°C, hereafter reported as 420°C. The irradiation history for packet H4 was as follows:

MOTA IB basket 2F-5 to $2.98x10^{22}$ n/cm² at an average temperature of 431°C.
MOTA IC basket 2F-5 to $6.98x10^{22}$ nicm' at 420°C.
MOTA ID basket 2F-5 to $5.05x10^{22}$ nicm' at 404°C.
MOTA IE basket 2F-2 to $9.67x10^{22}$ n/cm² at 414°C.
MOTA IF basket 2F-2 to $9.60x10^{22}$ n/cm² at 405°C.
MOTA 1G basket 2E-3 to $7.18x10^{22}$ nicm' at 417°C.
MOTA 2 6 basket 3A-5 to $6.35x10^{22}$ nlcm' at 433°C.

Therefore, during that period, the specimens in packet H4 received a fluence of $4.78x10^{23}$ n/cm² at an average temperature of 418 ± 11°C, hereafter reported as 420°C. The dose achieved, calculated from reference[6] which is based on dosimetry measurements from MOTA 1F, varies from 200 to 202 dpa, depending on alloy composition.

Microstructural examinations were performed on a JEOL JEM 1200EX scanning TEM operating at 120 kV and outfitted with a Tracor Northern energy dispersive x-ray fluorescence (EDX) detector and TN5500 computer and with a Gatan Electron energy loss spectrometer. Determination of precipitate compositions from extraction replicas involved computer analysis of EDX spectra which included analysis for tungsten.

Results

Swelling

Results of density change measurements for commercial alloy specimens irradiated at 420°C to 200 dpa are provided in Table 2. Table 2 contains dose estimates for each alloy based on conversions from reference! As shown from Table 2, swelling values are in the range 0.09 to 1.76%. The highest swelling values are for T9 and one of the heats of MA957. All others are at about 1% or less. Therefore, commercial ferritic steels are extremely resistant to radiation induced void swelling.

Table 2. Swelling as measured by density change for commercial ferritic/Martensitic alloy specimens.

CODE	Alloy	Heat Treatment	Dose (dpa)	Density Irradiated	Density Unirradiated	Swelling (%)
PTFL	T9	760/1 hr/AC	201.4	7.65245	7.7869	1.76
RFFL	HT-9	700/2 hr/AC	201.6	7.78535	7.7924	0.09
RHFL	HT-9	760/0.5 hr/AC	201.6	7.76079	7.84079	1.02
RLH4	MA956	1330°C/1 hr/AC	201.3	7.27343	7.35823	1.17
RMH4	MA957	1100°C/1 hr/AC	200.0	7.61565	7.74904	1.75
RNH4	MA957	1100°C/1 hr/AC	199.9	7.64425	7.66355	0.25

However, significant variation can exist between different heats or different heat treatments of the same steel. Both in the case of MA957 where two different batches of materials are compared, and

HT-9 where the same steel in two different heat treatments is compared, swelling varies between less than 0.25% and over 1%.

Microstructural examination

Microstructural examinations revealed that following irradiation at 420°C to 200 dpa, all specimens contained cavities, typical of void swelling. However, large regions in each of the MA957 specimens contained negligible cavitation, and the cavitation present in those regions is expected to be a remnant of the mechanical alloying process. In contrast, there were regions in the MA957 specimens where significant void swelling and dislocation evolution had developed. The T9 and HT-9 conditions developed void structures typical of martensitic steels. These void structures consisted of void arrays between lath boundaries and void free regions on, and adjacent to, the boundaries.

Low magnification examples are provided in Figure 1. Figure 1 shows Martensite lath boundary structures in irradiated T9 and HT-9, and subgrain structures selected to show the most typical regions for irradiated MA956 and MA957. The example for T9 in Figure 1a is found to contain a fairly uniform array of voids within laths and a moderate density of blocky carbide precipitate decorating subgrain boundaries. Figures 1h and **1c** for HT-9 show structures with significantly more blocky precipitation decorating boundaries and a lower density of sightly larger voids. It may also be noted that the foil shown in Figure **1c** was attacked non-uniformly **by** the electropolishing electrolyte, indicating that some large scale compositional variation may develop at high dose. Figure 1d provides an example of MA956 that shows a uniform structure, containing voids but with several very large precipitate particles and a typical wavy grain boundary. **No** evidence of subgrain structure was found in this material. Figures 1e and 1f provide examples of the fine subgrain structure retained in MA957. Cavitation in these subgrains is very limited. However, precipitation can be noted throughout. The precipitation is expected to include both yttria and ***a'***, a body centered cubic phase rich in chromium. Many examples can be found where subgrain boundaries are denuded of precipitation. The denuded regions are typically about 15 nm wide. Also, it should be noted that Figure 1f has been selected to show a region at the lower right containing a well developed array of voids. Further discussion of these features will follow.

Figure 2 provides examples (at higher magnification) of the microstructure found in T9 following irradiation at 420°C to 200 dpa. Figures 2a, 2b, and 2c provide different imaging conditions for the same region to define the dislocation structures. Figures 2a and 2b use $\vec{g} = 200$ and $1\bar{1}0$ respectively for an **(001)** foil orientation, and Figure 2c provides a view of the voids in absorption contrast. By comparing Figures 2a and 2b, it can be shown that the dislocation structure is comprised of **a<100>** loops and **a** network **of** $\frac{a}{2}\langle 111\rangle$ dislocation segments. Figure 2d gives another example of $\vec{g} = 1\bar{1}0$ contrast for a foil near (001) with similar dislocation development. However, Figures 2e and 2f show a third region in $\vec{g} = 200$ and $01\bar{1}$ contrast for an (011) foil. In this case, the dislocation structure is predominantly of Burgers vector $\frac{a}{2}\langle 111\rangle$. This difference may be a result of the nearby subgrain boundaries, which provided dislocation sources. However, the void structure appears similar in all three areas, indicating that Burgers vector variations have only small effects on void evolution.

Figure 3 provides examples at higher magnification of the microstructures found in irradiated HT-9 following a 700°C temper. The microstructures are typical of HT-9 irradiated at 420°C, and show well developed precipitate arrays decorating subgrain lath boundaries, non-uniform void arrays within laths and a fine precipitate on boundaries and within laths. An area is shown in dislocation, void and precipitate contrast, Figures 3a and 3h in $\vec{g} = 200$ and $01\bar{1}$ contrast, Figure 3c in void contrast, and Figure 3d in $\vec{g} = ⅓[333]$ for a foil near 011. From these figures, it can be shown that

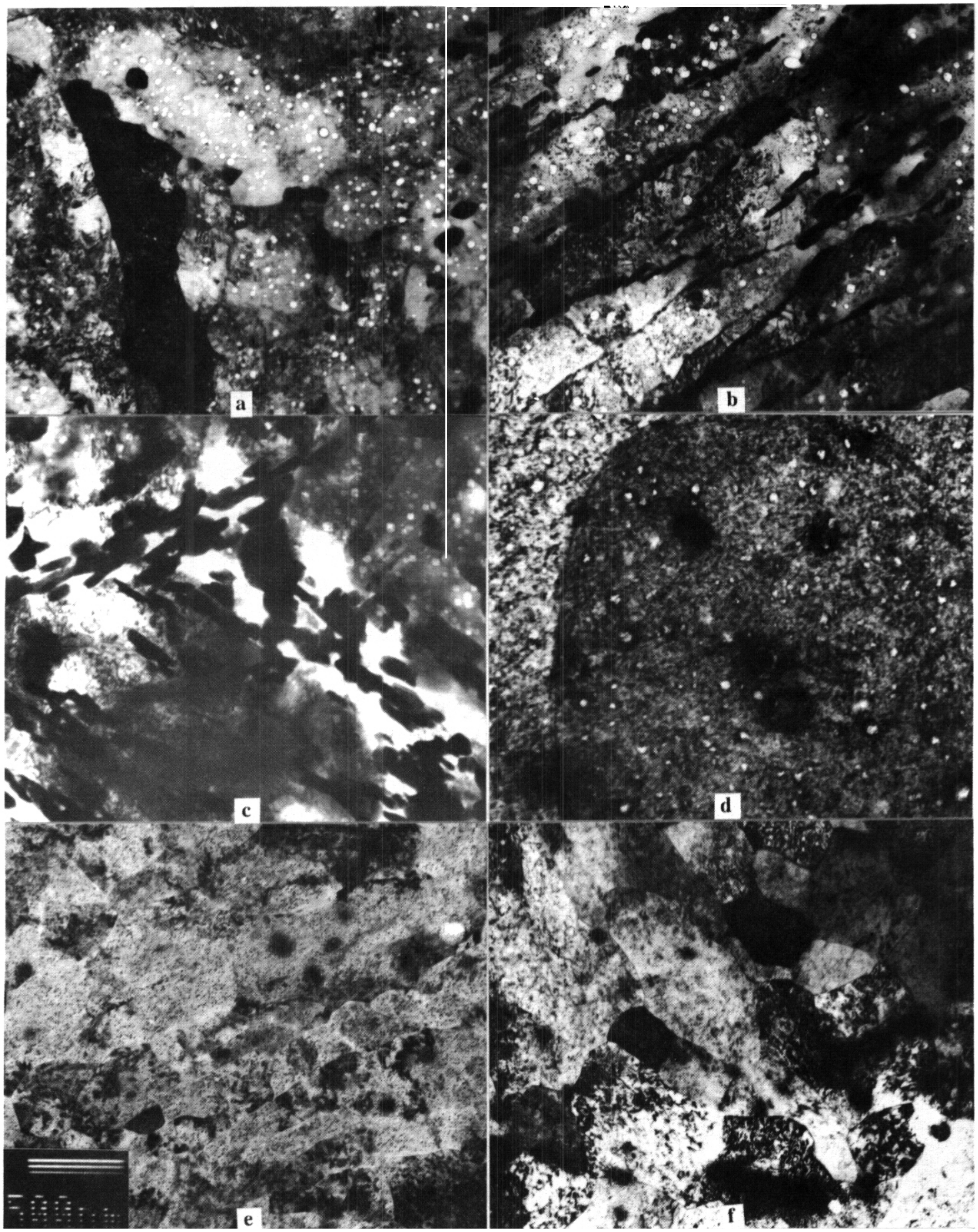

Figure 1. Microstructures at low magnification of Commercial Ferritic Alloys Following Irradiation at 420°C to 200 dpa (a) T9, (b) HT-9 heat treated at 700°C, (c) HT-9 heat treated at 760°C, (d) MA956, *(e)* MA957 heat T88793 and (f) MA957 heat T88794.

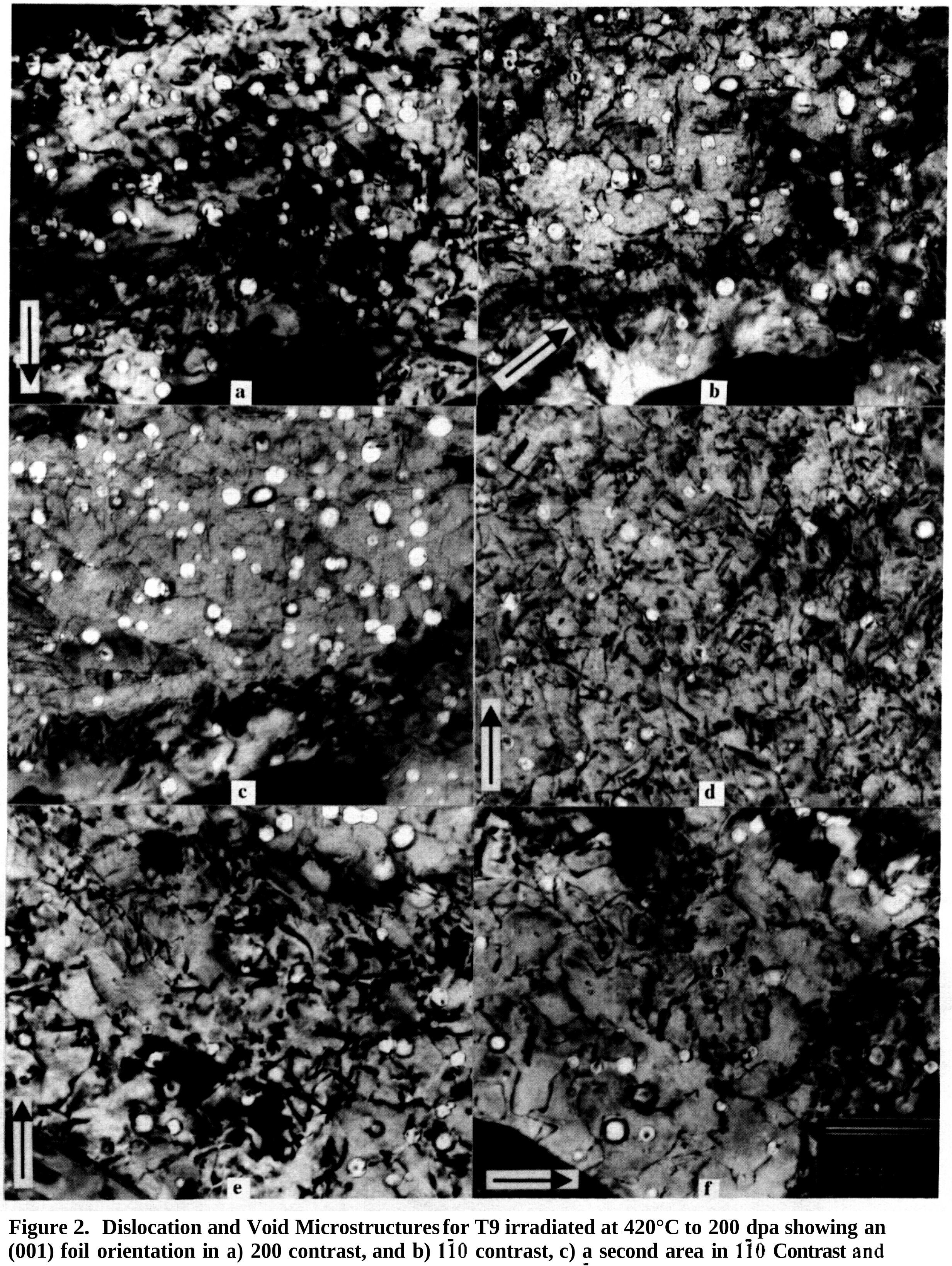

Figure 2. Dislocation and Void Microstructures for T9 irradiated at 420°C to 200 dpa showing an (001) foil orientation in a) 200 contrast, and b) $1\bar{1}0$ contrast, c) a second area in $1\bar{1}0$ Contrast and a third area in an (011) foil orientation io d) 200 contrast, e) $01\bar{1}$ contrast and f) void contrast.

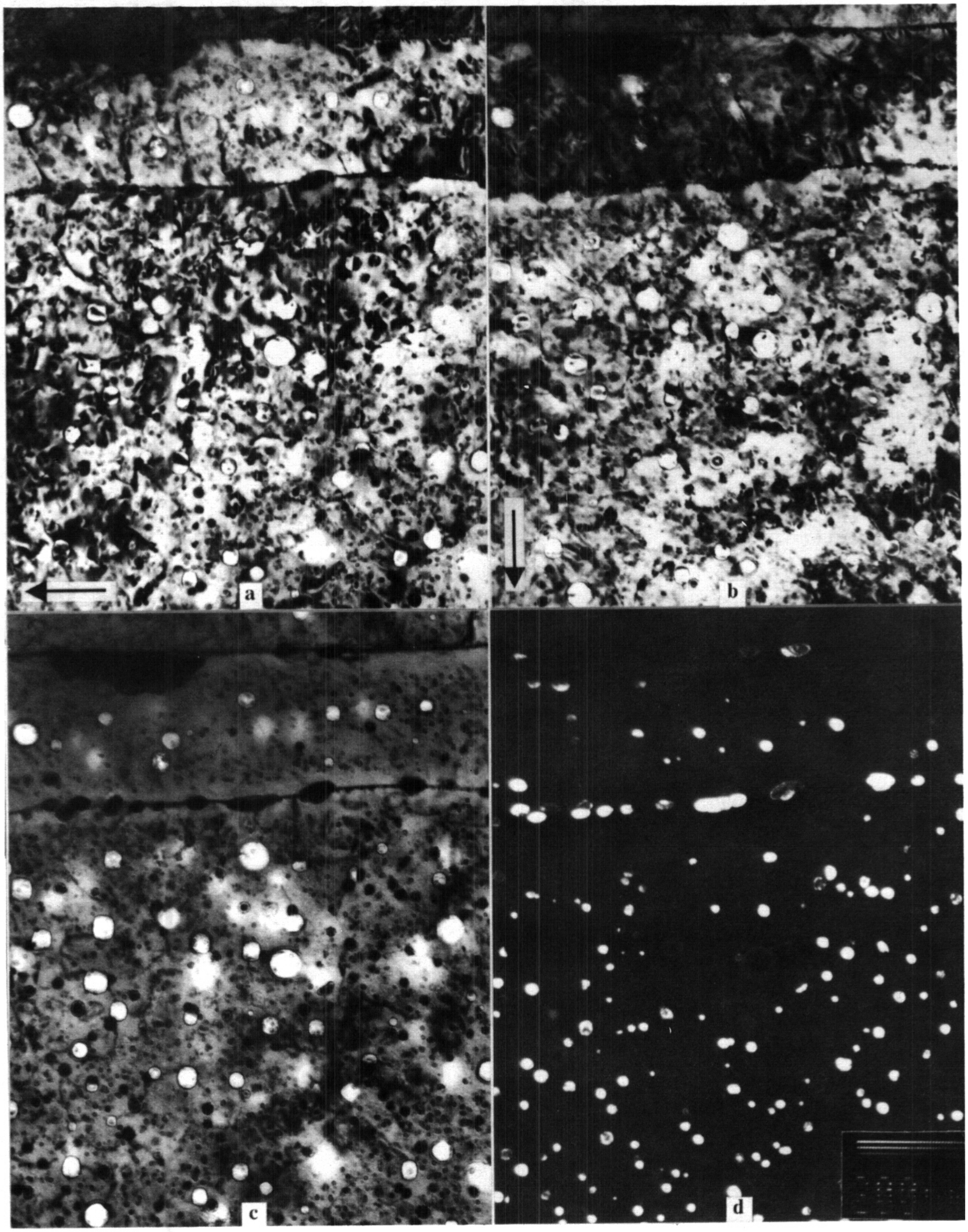

Figure 3. Microstructures of HT-9 tempered at 700°C and irradiated at 420°C to 200 dpa showing an (011) foil orientation in a) 200 contrast, b) $01\bar{1}$ contrast, c) void contrast and d) dark field precipitate contrast.

the dislocation structure is predominantly of type $\frac{a}{2}\langle 111\rangle$, but with a low density of $a\langle 100\rangle$ loops, and that voids vary in shape between cubes with $\{011\}$ truncation and even truncation between cubes and dodecahedra. Figure 3d is intended to show the precipitation that is found in irradiated HT-9 and has previously been called G-phase by the author. The precipitate is 10 nm in diameter within laths, but somewhat larger on subgrain boundaries. Irradiation hardening found in HT-9 can be attributed to this phase. However, comparison of Figures 3c and 3d reveals that not all precipitates are imaged in Figure 3d; the smaller ones do not appear. These smaller precipitates are expected to be a'.

Figure 4 provides similar examples for irradiated HT-9 following a temper at 760°C. Two areas are shown in dislocation and void contrast, Figures 4a and 4e in $\vec{g} = 200$ contrast, Figures 4h and 4f in $01\bar{1}$ contrast, and Figures 4c and 4d in void contrast for foils near (001) and (011) orientations, respectively. From these figures, it can be shown that dislocation structures contain both $a\langle 100\rangle$ loops and $\frac{a}{2}\langle 111\rangle$ network segments, but where subgrain boundaries are present, the $a\langle 100\rangle$ dislocation density is significantly reduced. Also, voids vary in shape, but are generally evenly truncated between cubes and dodecahedra. Evidence for the fine precipitate noted in Figure 3 can be found.

Figure 5 provides an example of the microstructures found in MA956 following irradiation at 420°C to 200 dpa. The same region is imaged in $\vec{g} = 200$, $01\bar{1}$, and absorption contrast (to show voids) for a foil near an (011) orientation. The dislocation images are difficult to interpret, but the presence of both $a\langle 100\rangle$ loops and $\frac{a}{2}\langle 111\rangle$ network segments can be identified. The voids in Figure 5c are found to vary in shape, but the dominant configuration is cuboidal with (111) octahedral facets. Comparison with other void images in this report will confirm that the voids in MA956 are different, showing clear (111) facets. Figure 5c also reveals the presence of precipitation, typical of a', as expected for an alloy with 19% Cr. The complex dislocation imaging and variability in void shape are likely due to the *a'* formation. However, it is noteworthy that again, no evidence of subgrain structure can be identified.

Figures 6 and 7 give examples of the microstructures found in the experimental batches of MA957 following irradiation at 420°C to 200 dpa. Figure 6 shows three areas in batch T88793 with varying levels of void swelling. Figure 6a gives an example where no voids are present; only a mottled background due to precipitation can be seen. The precipitation is expected to include both a' and yttria (Y_2O_3), and based on experience imaging the yttria in unirradiated MA957 where particle diameters are about 2 nm, the precipitation apparent in Figure 6a is expected to be *a'*. Figure 6b shows an area containing two subgrains that have developed voids on the order of 40 nm in diameter. One of the void arrays is linear, indicating that void nucleation was heterogeneous. Figures 6c and 6d show an area in an (011) orientation using 200 and $01\bar{1}$ contrast, respectively. Comparing these images indicates that a few $a\langle 100\rangle$ loops are present, but the dislocation structure is comprised mainly of $\frac{a}{2}\langle 111\rangle$ dislocation segments (and *a'* precipitates complicate the analysis). Voids are generally evenly truncated between cubic and dodahedral shapes. Figure 7 provides a similar comparison for a large grain near (011) orientation, with adjacent subgrains that contain no voids. Figures 7a and 7b show dislocation imaging in the large grain using $\vec{g} = 200$ and $01\bar{1}$, respectively, and Figure 7c provides void contrast. From this sequence, similar observations can be made: the dislocation structure consists predominantly of $\frac{a}{2}\langle 111\rangle$ dislocation segments, and voids are evenly truncated between cubic and dodecahedral geometries.

A summary of microstructural observations is tabulated in Table 3. From Table 3, it can be shown that the swelling was measured as high as 5% in isolated regions, that the dislocation structure

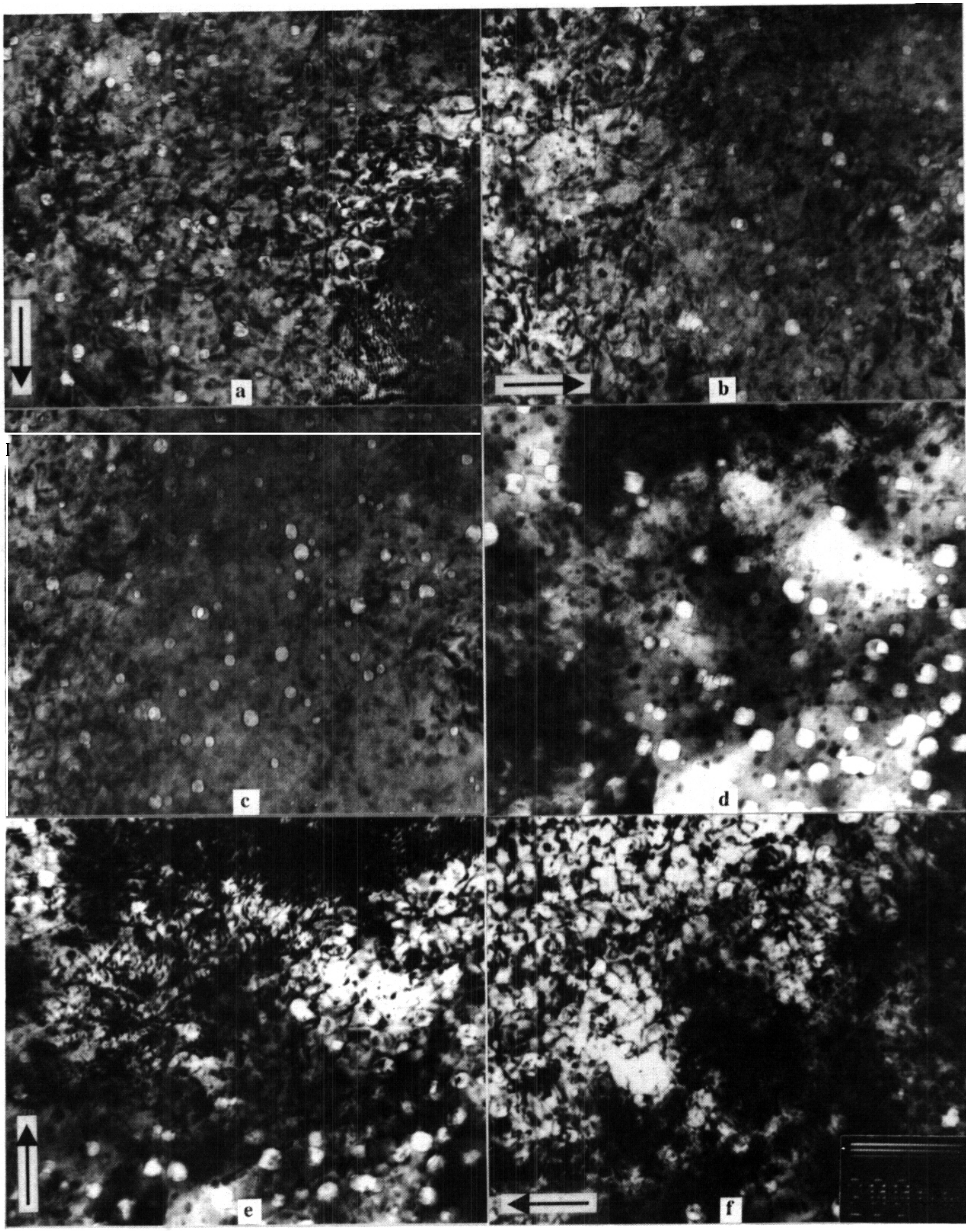

Figure 4. Dislocation and Void Microstructures for HT-9 tempered at 760°C and irradiated at 420°C to 200 dpa showing (011) foil orientations for two areas in a) and e) 200 contrast, b) and f) $01\bar{1}$ contrast and c) and d) void contrast, respectively.

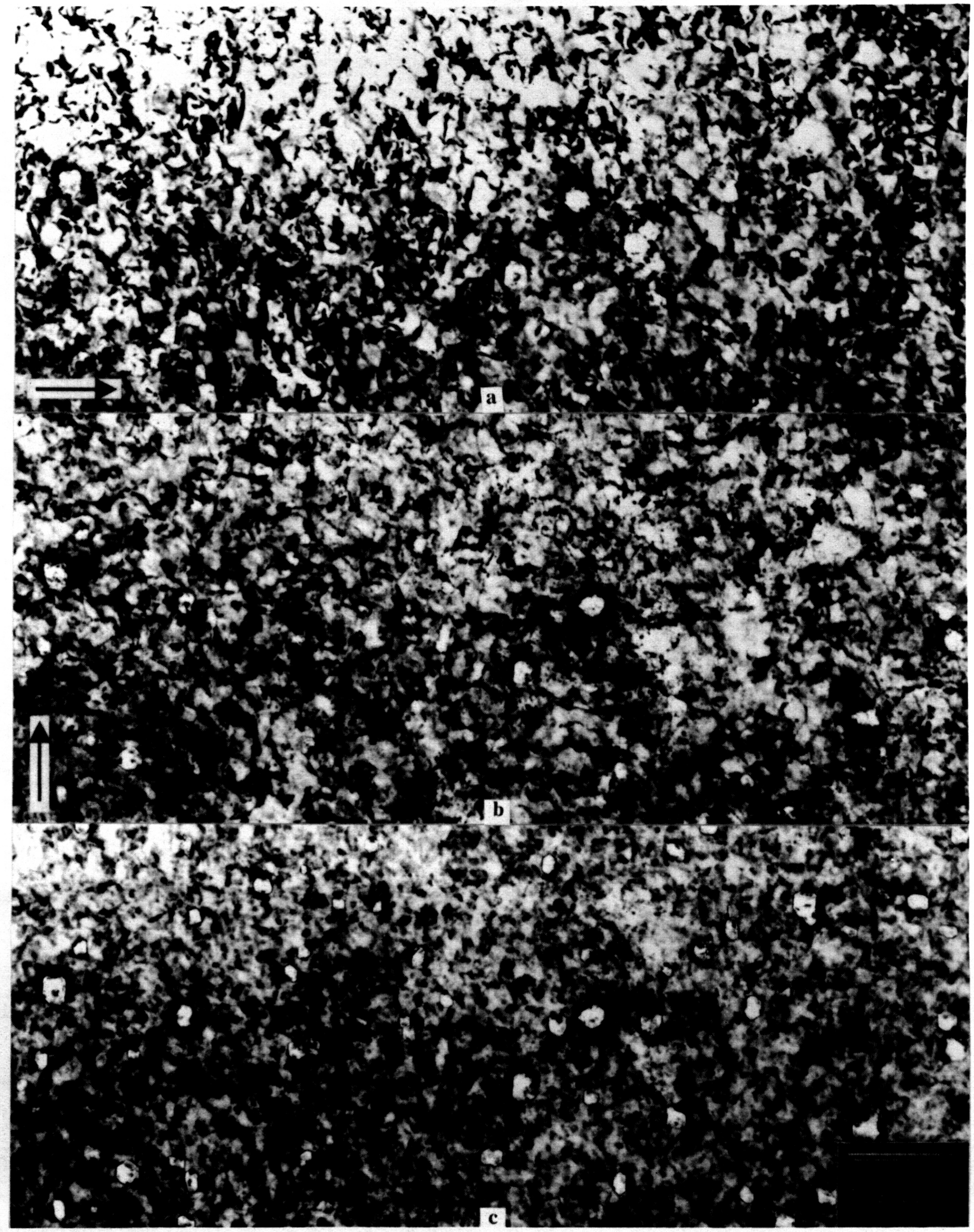

Figure 5. Example of the Microstructures found in MA956 following irradiation at 420°C to 200 dpa showing a region with foil orientation (011) in a) 200 contrast, b) in $01\bar{1}$ contrast, and c) in void contrast.

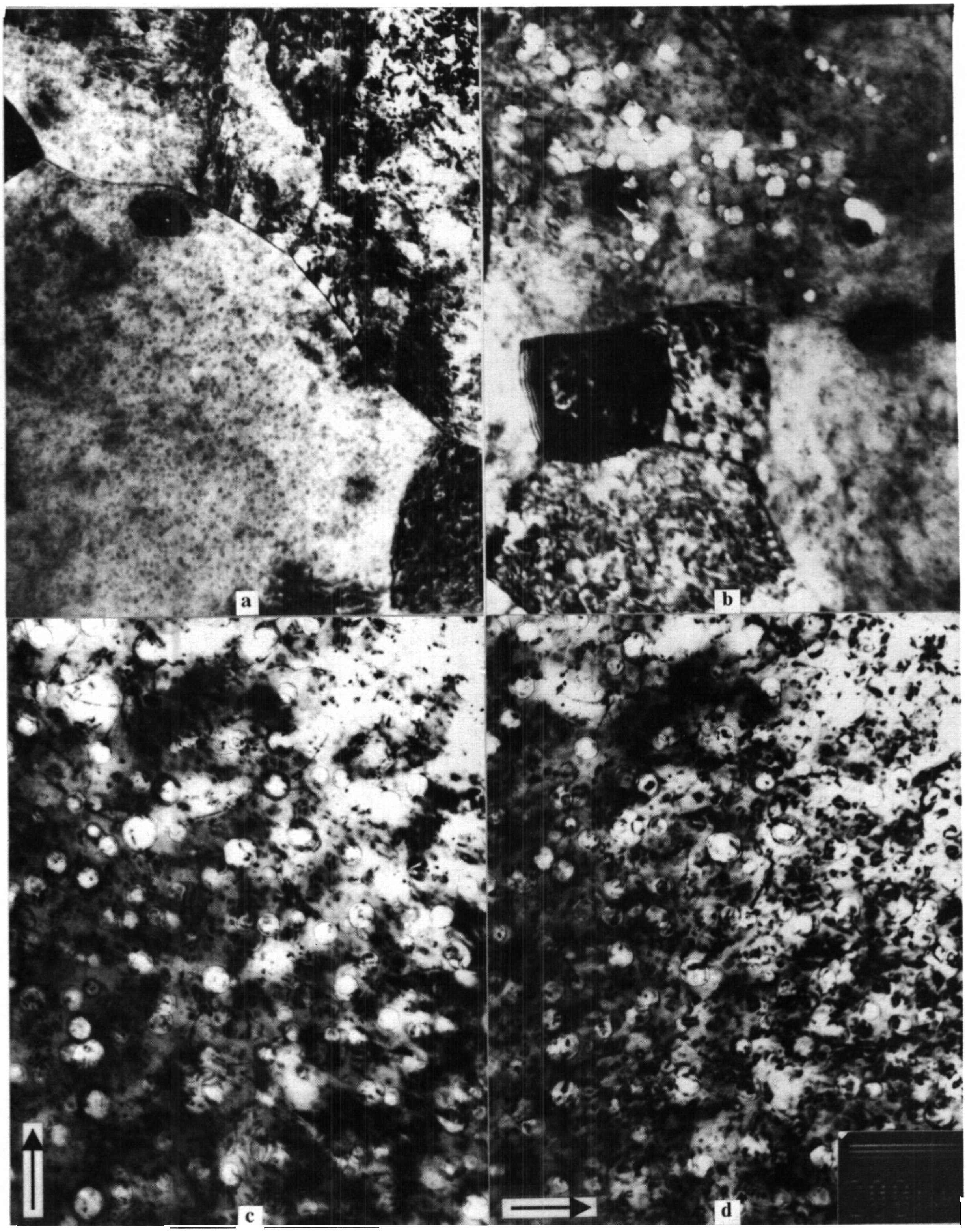

Figure 6. Precipitate, void and dislocation microstructures in MA957 heat T88793 following irradiation at 420°C to 200 dpa for a) a region containing no voids, b) a region containing a moderate void density and for a region in (011) orientation containing a well developed void array in c) 200 contrast and d) $01\bar{1}$ contrast.

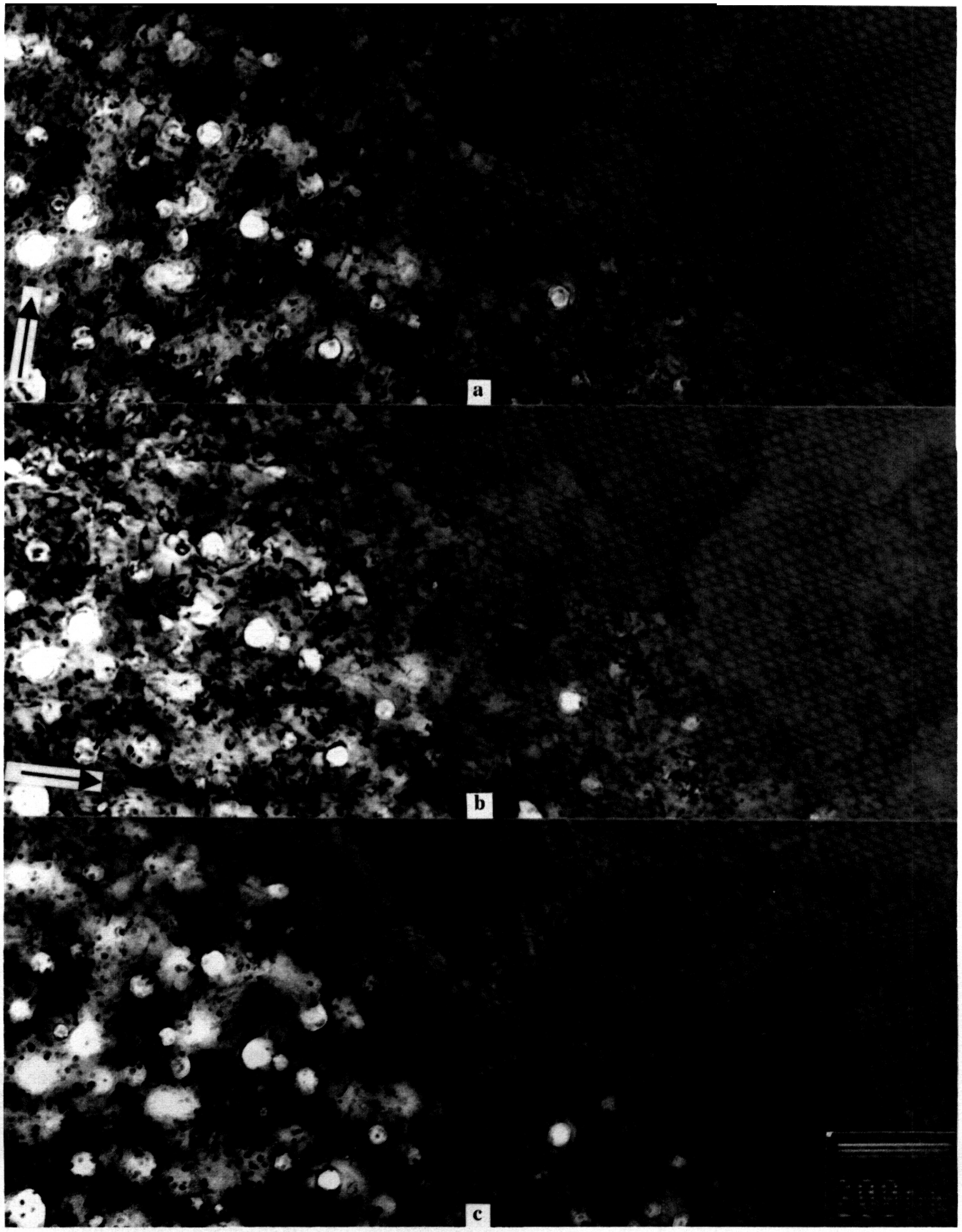

Figure 7. Microstructures in MA957 heat T88794 following irradiation at 420°C to 200 dpa for a grain containing voids in (011) orientation in a) 200 contrast, b) $01\bar{1}$ contrast and c) void contrast.

contains both $\frac{a}{2}$<111> and a<100> Burgers vectors, and voids are generally truncated between dodecahedra and cubes. The void truncation notation is intended to mean that the **(100)** and **(110)** facets are about equal in size.

Discussion

The results of this work are highly encouraging. Commercial ferritic/Martensitic alloys are demonstrated to have the high dose swelling resistance and microstructural stability that had been predicted.' Although precipitate identification is incomplete, the phases present seem to match those found at lower dose. The Martensite lath structure is also retained. Swelling is found in both Martensitic stainless steels, but the levels of swelling are very modest, and the swelling is not expected to alter mechanical properties significantly. Blocky precipitation on prior austenite and subgrain boundaries is enhanced compared to the preirradiation condition, and some degradation of properties can be envisioned, such as Charpy impact. Also, in a fusion environment, transmutation of iron to manganese will encourage further FeCrMn chi phase development. Therefore, intermetallic precipitation is expected to be the metallurgical process controlling properties and life limits at high dose.

Table 3. Summary of microstructural observations.

CODE	Alloy	Dose (dpa)	Highest Swelling (%)	Mean Void Size (nm)	Void Density (#/cm^3)	Void Shape	Dislocation Structure
PTFL	T9	203.2	5.0	21.4	4.8×10^{15}	truncated between dodecahedra and cubes	examples of both primarily $\frac{a}{2}$<111> network and primarily a<100> network
RFFL	HT-9	203.5	3.2	21.2	3.1×10^{15}	truncated dodecahedra	a<100> loops and primarily $\frac{a}{2}$<111> network
RHFL	HT-9	204.0	1.7	32.2	5.6×10^{14}	truncated between cubes and dodecahedra	a<100> loops and primarily $\frac{a}{2}$<111> network
RLH4	MA956	204.8	0.21	26.7	1.9×10^{14}	truncated between cubes and octahedra	a<100> loops and primarily $\frac{a}{2}$<111> network
RMH4	MA957	205.7	3.7	36.1	9.2×10^{14}	truncated between dodecahedra and cubes	original ODS structure retained, a<100> & $\frac{a}{2}$<111> loops and $\frac{a}{2}$<111> network in recrystallized regions
R"4	MA957	206.0	3.5	35.4	8.6×10^{14}	truncated between dodecahedra and cubes	original ODS structure retained, a<100> & $\frac{a}{2}$<111> loops and $\frac{a}{2}$<111> network in recrystallized regions

Results of radiation damage resistance of ODS ferritic alloys are even more encouraging. Evidence was apparent in both MA956 and MA957 for *a'* precipitation, and in regions where recrystallization had occurred before irradiation in MA957, void development was extensive. But both these problems can be overcome by suitable alloy design. The ODS alloy microstructures, when properly manufactured to provide a uniform oxide dispersoid in a subgrain structure, appear to be completely radiation damage resistant to doses as high as 200 dpa.

Other observations are worthy of further emphasis. Regions were found in both Martensitic alloys where comparable void development had occurred, but the dislocation structures were quite different. Apparently, void swelling is unaffected by whether the dislocation structure contains a significant a<100> component. Possible explanations for low swelling in ferritic alloys were based on the presence of two different Burgers vectors so that either a net bias was developed between the two components, or, as one of the components was sessile, point defect absorption would be limited. The present results indicate that either the Burgers vector distribution has little effect on swelling, or the magnitude of swelling is independent of differences in dislocation response in isolated regions.

Two instances were found where either heat-to-heat variations or heat treatment variations led to differences in density change. It is possible to provide an explanation for both situations. In the case of MA957, swelling was generally restricted to large recrystallized regions. Therefore, it is likely that the differences in density change in the two batches of MA957 were a result of different volume fractions of recrystallized regions, with batch T88793 containing more recrystallization. No attempt has been made to verify this. However, the differences in HT-9 are due to heat treatment, such that the lower tempering temperature resulted in lower swelling. Lower tempering temperatures result in finer distributions of carbide precipitation and less complete relaxation of the dislocation structures generated from the Martensite transformation. Both of these differences can be expected to delay the onset of swelling. Also, precipitation will be less complete at the lower tempering temperature so that during subsequent irradiation, further precipitation can occur that would create densification, offsetting the swelling due to void growth and producing a lower total density change measurement. The lower swelling found in HT-9 following the lower tempering temperature is likely a combination of these factors.

CONCLUSIONS

Alloys HT-9 in two heat treatment conditions, T9, MA956, and two experimental batches of MA957 have been irradiated in the FFTF/MOTA at 420°C to 200 dpa and then measured for density change and examined by transmission electron microscopy. All alloys are found to be highly radiation resistant.

1. Swelling as measured by density change was less than 2%.

2. All specimens contained cavities, but in the ODS alloys, large regions were found with negligible cavitation, probably a remnant from mechanical alloying. Voids in the Martensitic steels were non-uniformly distributed within laths. Recrystallized regions, manufacturing defects in the MA957 specimens, contained the greatest swelling.

3. Dislocation evolution included both $\frac{a}{2}$<111> and a<100> Burgers vectors, and similar swelling response was found in regions with different Burgers vector distributions.

4. Voids were generally truncated between dodecahedra and cubes. Some variation in shape was found as a function of size.

5. Variations in swelling were found from heat-to-heat variation in MA957 and from heat treatment variation in HT-9.

6. Microstructural changes from irradiation to high dose are not expected to significantly change mechanical properties. The life limits are expected to arise due to embrittlement from phase separation (a') and intermetallic phase precipitation (chi and Laves) governed to some extent by the transmutation of iron to manganese.

FUTURE WORK

This work is a continuing effort.

REFERENCES

1. A. N. Niemi, M. G. McKimpson and D. S. Gelles, "Processing of Two Iron-Chromium Oxide Dispersion Strengthened Steels by Mechanical Alloying," DOE/ER-0313/6 (1989) 187.

2. A. N. Niemi, M. G. McKimpson and D. S. Gelles, "Improved Processing for Two Ferritic Low Activation Oxide Dispersion Strengthened Steels" DOE/ER-0313/8, (1990) 177.

3. J. J. Fischer, US Patent 4,075,010, February 21, 1978.

4. D. S. Gelles and A. Kohyama, "Microstructural Examination of HT-9 Irradiated in the FFTF/MOTA to 110 dpa," Fusion Reactor Materials Semiannual Progress Report for the Period Ending March 31. 1989, DOE/ER-0313/6 (March 1989) 193.

5. D. S. Gelles, "Microstructural Development in Reduced Activation Ferritic Alloys Irradiated to 200 DPA at 420°C," J. Nucl. Mater., (1994), also included in DOE/ER-0313/15.

6. F. A. Garner and L. R. Greenwood, "Calculation of Displacement Levels for Pure Elements and Most Multicomponent Alloys Irradiated in FFTF MOTA-IF," Fusion Reactor Materials Semiannual Progress Report for the Period Ending March 31, 1992, DOE/ER-0313/12 (July 1992) 54.

7. D. S. Gelles and R. L. Meinecke-Ermi. "Swelling in Simple Ferritic Alloys Irradiated to High Fluence," Alloy Development for Irradiation Performance Semiannual Progress Report for the Period Ending September 30, 1983, DOE/ER-0045/11 (March 1984) 103.

EFFECT OF HYDROGEN ON THE FRACTURE TOUGHNESS OF A FERRITIC/MARTENSITIC STAINLESS STEEL

- Huaxin Li (Associated Western Universities--Northwest Division), R. H. Jones (Pacific Northwest Laboratories). J. P. Hirth (Washington State University--Pullman) and D. **S.** Gelles (Pacific Northwest Laboratories)'

OBJECTIVE

The purpose of this research is to investigate the effect of hydrogen on mixed-mode fracture toughness of a reduced activation ferriticlmartensitic stainless steel (F-82H).

SUMMARY

Effects of hydrogen (H) on the mixed-mode I/III critical J integrals **(J_{MC})** and tearing moduli (T,) were examined for a ferritic/martensitic stainless steel (F-82H) at ambient temperature. A determination of J_{MC} was made using modified compact-tension specimens. Different ratios of tensionlshear stress were achieved by varying the principal axis of the crack plane between 0 and **55** degrees from the load line. A specimen with 0 degree crack angle is the same as a standard mode I compact tension specimen. Specimens were heat-treated at **1000°C/20** h/air cooled (AC)-**1100°C/7** min/AC-700°C/2 h/AC. The specimens were charged with H at a hydrogen gas pressure of 138 MPa at 300°C for two weeks, which resulted in a H content of 6 ppm(wt), as measured with the "inert gas fusion" technique. J_{MC} and T, values were determined with the single specimen technique. Crack lengths were calculated **by** means of partial unloading compliances. The preliminary results from J integral tests showed that introducing H decreased J_{MC} and T , values as compared to those without H. However, the presence of H did not change the dependence of J, and T , values on the crack angles. Both mode I J and T values **(J_{IC}** and T,) exhibited the highest values. Both the minimum J_{MC} and T, values occurred at a crack angle between **35** and **55** degrees, corresponding to the load ratio **(σ_{iii}/σ_i)** of 0.7 to 1.4.

PROGRESS AND STATUS

Introduction

Traditionally, mode I fracture has been used to study elastic-plastic fracture mechanics. However, in recent years, mixed-mode fracture has become **a** focus of many studies because many observed failures included shear components [1-9]. Fracture characteristics have been found to differ from one another when subjected to mixed-mode I/III loading, depending on the microstructure, strength, and toughness level of materials. In low-toughness high-strength alloys, such as 0.29C-0.83Cu steel, and 1.25C bainitic steel [7-10], mode **111** contributions to mode I loading had little or no effect on the overall value of J_{iC}, the mode I component of the J integral for mixed-mode crack initiation, and tended to increase J_{MC}, the total J integral for mixed-mode crack initiation. In tougher materials (such as a high-purity rotor steel **(HPRS)** **[5,6],** which failed primarily by a microvoid nucleation and growth mechanism) mode III contributions lowered the J, values considerably from their mode I values. The J_{MC} values passed through a minimum at a position between mode I and mode III on a plot of **J_{MC}** vs crack inclination angle. More generally, materials can be divided into three

---

'Pacific Northwest Laboratory is operated for the US. Department of Energy **by** Battelle Memorial Institute under Contract DE-AC06-76RLO 1830.

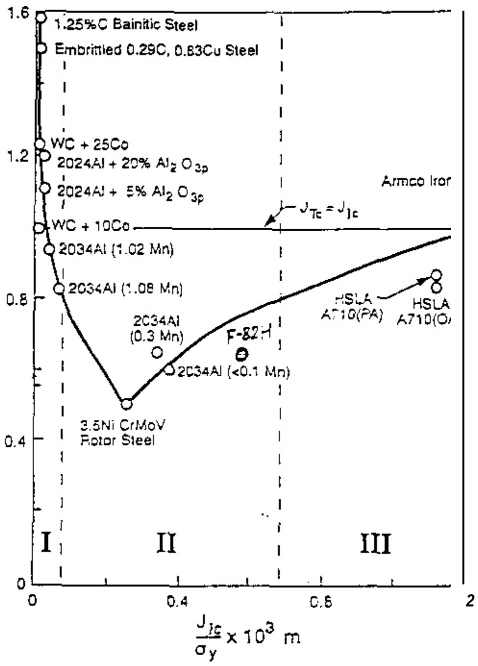

Fig. 1. J_{TC}/J_{IC} versus J_{IC}/σ_Y for different materials; where J_{TC} is the mixed-mode I/III J integral at a crack angle of 45 degrees; J_{IC} is mode I J integral; σ_Y is yield strength. The materials in Region I, II and III are brittle, tough and ductile materials, respectively.

categories according to their process zone size (presented by J_{IC}/σ_Y) and the ratio of J_{MC} (at crack angle of 45 degrees) to J_{IC}, as shown in Fig. 1 [11]. According to Ref. 11, the materials in Region I are brittle and sensitive to mode I loading and, consequently, mode I fracture toughness is the lowest one as comparing with mixed-mode I/III fracture toughness, therefore, mode I fracture toughness should be used for design; Those in Region II are tough and sensitive to mixed-mode I/III loading, mode I fracture roughness is the highest one, the minimum J_{TC} is recommended as a design criterion; For the materials in Region III, mode I fracture toughness can be used for designing. Our results [12] on the fracture toughness of F-82H steel showed that the steel is a tough material and is classified in Region II in Fig. 1 so that the presence of mode III stress component lowers its fracture toughness significantly. However, the minimum upper shelf fracture toughness is still higher than those for most tough materials.

Structural materials in fusion reactors will be exposed to hydrogen from the plasma and (n, σ) reactions. For a tough material, the introduction of hydrogen (H) was found to decrease the overall mixed-mode fracture toughness [6,13]. Hence, an investigation of the combined effects of mixed mode loading and hydrogen on fracture toughness of F-82H steel is necessary to determine its suitability for fusion applications.

Material and Experimental Methods

1. Material and Hydrogen-Charging

The F-82H plate used in this study was supplied by Nippon Kokan Steel Company (NKK) in Japan. The chemical composition of the plate (as provided by NKK) is (by wt%): 0.096C-7.71Cr-2.1W-0.18V-0.04Ta-0.003P-0.003S. Specimens used in this study were cut in the orientation of T-L as specified in ASTM E399-90 and were given a heat-treatment of 1000°C/20 h/air cooling (AC),

1100°C/7 min/AC, and **700°C/2 h/AC**. The resulting microstructure was tempered martensite. The mean intercept grain size was **25 μm** (ASTM **#7.5**). The heat-treatment resulted in a yield strength (σ_y) of 648 **MPa**, ultimate tensile strength (σ_{uts}) of **735 MPa**, elongation of **16.7%**, and reduction of area of **70%.**

H-charging was done at Sandia National Laboratories, Livermore, CA. The specimens were charged with H at a hydrogen gas pressure of **138 MPa** at **300°C** for two weeks, which resulted in a **H** content of *6* ppm(wt). H contents were measured with the "inert gas fusion" technique. A copper (Cu) coating was applied immediately after H-charging. The specimens with Cu coating were stored at **-60°C.** Before performing **J** testing, a specimen was warmed up **to 24 C. J** testing took about 60 minutes. H-loss during **J** testing was negligible because of a low H diffusivity in ferriticlmartensitic stainless steel at **24°C** [**14**] and the added barrier of the Cu coating.

2. Experimental Methods

The details of the experimental methods were reported in Ref. 13. Only the important portions of experimental methods are summarized here.

The geometry of modified compact-tension (MCT) specimens used for mixed-mode I/III testing is schematically shown in Fig. **2.** The magnitude of the mode III components can be varied by a change of crack slant angle Φ. An angle of 0 degree represents mode 1 loading and the geometry of a 0-degree specimen becomes the standard compact-tension (CT) specimen as specified in ASTM standard **E813-89.** As Φ increases, the contribution of mode **III** components increases. The crack-inclination angles used in this study were 0, IS, **25, 35, 45,** and 55 degrees. Side grooves of **20%** reduction of total thickness were incorporated in all specimens. These side grooves can increase the triaxiality at the edges of a growing crack and constrain the advancing crack in the original crack plane. The calculation of the J integrals in mixed-mode I/III requires a measurement both of the vertical displacement (6,) and the horizontal displacement (δ_h) of the load points. A pair of knife edges was secured **to** the front face of a specimen. A standard crack opening distance (COD) clip gage was positioned on the knife edges. The load-line **6,s** were calculated from the front face δ_v**s** with the method proposed **by** Saxena and Hudak, Jr. [**16**]. We found that the 6, increased with δ_v in a linear mode [**1,3**]. Hence **6,s** were calculated approximately from the relation 6, $= a \times \delta_v$, where $a = \delta_{hmax} / \delta_{vmax}$.

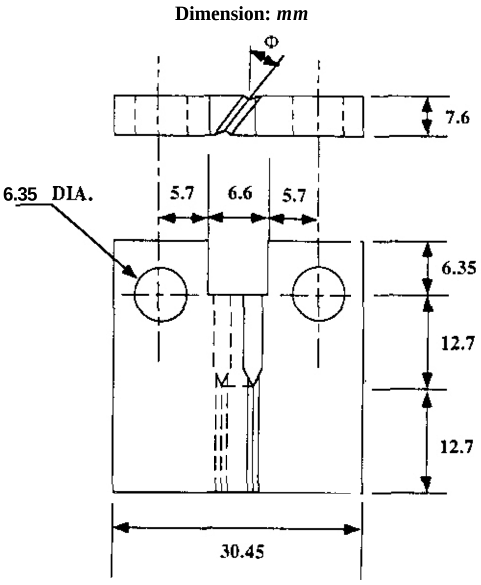

Fig. **2.** The geometry of a modified compact tension specimen.

An electric discharge machine (EDM) was used **to** make thin cuts with a small radius (radius = 0.051 mm) and approximately 1.3 mm **long.** The cuts were used as a substitute for a pre-fatigued-crack (PFC) because a PFC tends **to** grow out of the original crack plane **in** mixed-mode specimens. The EDM cuts were made after final heat-treatment. The single-specimen technique was used in this study, which allows a J-R curve (**J** vs crack extension Aa) **to** be generated with one specimen. During testing, the specimen was frequently and partially unloaded, and the partial unloading compliances were used to calculate the corresponding crack lengths following the procedure described in E813-89 and Ref. **15.** Values of J matching those crack lengths were also calculated by means of Eq. (1) in the next section. At least 20 pairs of J-Aa data were used to construct a J-R curve.

Data Analysis

The mode I integral J, and mixed mode I/III integral J, were calculated from the area under the load vs load-line-displacement curve by means of Eq. **(1)** |17|:

$$J = \frac{2}{B_{net}\, b_o} \int_0^{\delta_v} P\, dV \qquad (1)$$

where

B_{net} = 0.8B/cosΦ (the net crack front width excluding the **10%** side grooves on each side)
B = the overall specimen thickness Φ = the crack-inclination angle
b_o = W - *a,* (the initial unbroken ligament) W = the specimen width
a, = the initial physical crack length.

To construct J-R curves and determine critical J values (J_{IC} and J,,), ASTM E813-89 was used. The slope of the blunting line for mixed mode 11111 was calculated using Eq. (2):

$$m_{i/iii} = \frac{m_i \cos\Phi + m_{iii} \sin\Phi}{\sin\Phi + \cos\Phi} \qquad (2)$$

where $m_i = (\sigma_y + \sigma_{uts})$ and $m_{iii} = (\sigma_y + \sigma_{uts})/2$, which are the blunting line slopes for pure mode I and mode *III*, respectively. When Φ equals **0** and 90, $m_{i/iii}$ is equal to m_i and m_{iii}, respectively. A best straight line was also constructed from the J-Aa data between the upper and lower exclusion lines, and the slope of the straight line was taken as the unnormalized tearing modulus (T_I or T_M) for each specimen. The critical mode I and mode **111** J components (J_{iC} and J_{iiiC}) in mixed-mode specimens could also be calculated in terms of the corresponding resolved loads and displacements. The calculations of the resolved mode I and mode III load and displacement and the determinations of J_{iC} and J_{iiiC} have been reported in detail in Ref. **6,** 7, and **15.**

Results

I. The Critical J Values

The preliminary results for the effect of H on J,, (the total critical mixed-mode J values) are shown in Fig. 3. In the limit of Φ = **0** , J_{MC} is equal **to** J_{IC}, while for 0< Φ <90 degrees J_{MC} represents the total critical J values under mixed-mode loading. Crack angles reported here are 0, **15, 45,** and **55** degrees. Each of the data points presented in Fig. 3 were obtained from a single specimen. The results from specimens without H are also included for comparison. From Fig. 3, one can see that the introduction of H into F-82H steel decreased its overall fracture toughness considerably, independent of crack angle. However, the presence of H seemed not to change the trend of the J-Φ curve. J,, is still the highest J value, and the minimum J,, occurs at a crack angle between 35 to

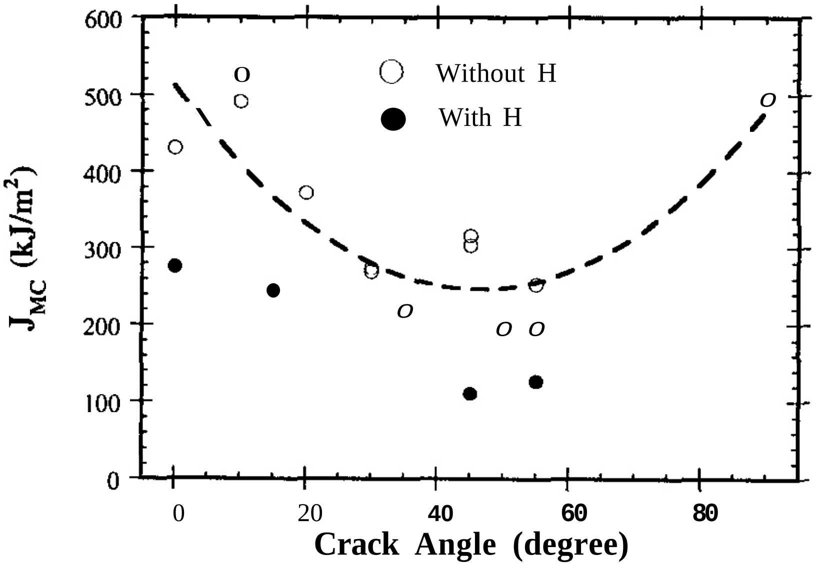

Fig. **3.** The dependence of critical total J integrals of F-82H on crack inclination angles and the effect of hydrogen on J integrals.

55 degrees, where the ratio of σ_{iii}/σ_i is between 0.7 and **1.4.** The change of $J_{„}$ with Φ is similar to that for the specimens without H, which follow a polynomial function of order 2. The effect of H on J_{MC} of F-82H is similar to that for another tough steel, HPRS **[6,13],** where the addition of H also lowered the overall J_{MC}. However, the minimum $J_{„}$ for H charged F-82H steel is around **100** kJ/m², higher than the value of **64 kJ/m²** reported for the HPRS **[6,13].**

2. The Tearing Modulus (T,)

The introduction of H also reduced the resistance to crack growth, i.e. lowered the overall mixed-mode tearing moduli (T,) from relative tests performed without H. The unnormalized tearing moduli corresponded different crack angles are shown in Fig. **4.** From Fig. **4,** one can see once again that H does not change the dependence of T, on crack inclination angles. The variation of T_M with Φ is also found to obey a polynomial function of order **2,** similar to the curve of the steel without H (see Fig. **4).**

3. Fractography

The crack fronts of all specimens remained in their initial orientation during J testing. Preliminary results from two fracture surfaces showed that internal H in F-82H steel did not induce intergranular or cleavage facets. While the two specimens exhibited **a** microvoid-coalescence type of fracture, qualitatively, it appears that the size of microvoids might be smaller than those without H. A smaller microvoid size usually corresponds to lower $J_{„}$ and $T_{,}$. A more detailed and quantitative study on fracture surfaces is underway.

Discussion

Addition a of a mode III component to mode I loading has been found to increase, decrease, or have little or no effect on the J_{MC}, depending on the toughness of the materials. For brittle materials,

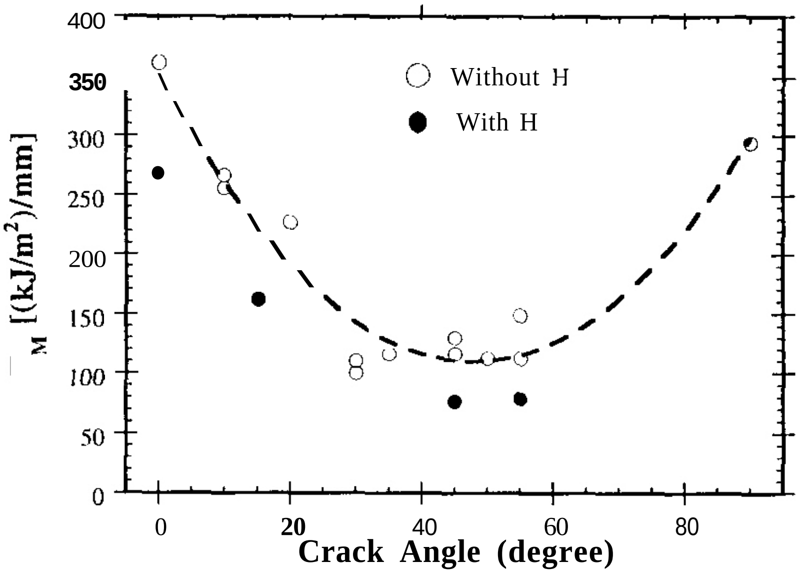

Fig. **4.** The dependence of total tearing moduli **on** crack inclination angles and the effect of hydrogen of tearing moduli.

such as glass [18], 0.29C-0.83Cu steel and 1.25C bainitic steels [4,8-10], where fracture was controlled by tensile stress and the local crack-opening displacements, the addition of mode III components had little or **no** effect on the J_{iC} (mode I J component of J_{MC}), but tended to increase J_{MC}. For tough steels, such as HPRS, which failed primarily by microvoid coalescence, the presence of shear strain in the crack plane associated with mode III loading produced incompatibility stresses at the particle interfaces in the trajectory of the crack, causing decohesion or particle fracture (shear damage). This process led to enhanced void formation that limited the mode I plastic flow field and caused premature separation of voids by mode I stress. Accordingly, tough materials exhibited a lower fracture toughness for a mixed-mode crack than for mode I crack. For those materials with intermediate toughnesses, such as **AISI** 1090 steel, the addition of a mode III component decreased J,, moderately, and had little effect on J_{MC}.

As was discussed in Ref. 12, F-82H steel is a very tough steel and very sensitive to incompatibility stresses at particle interfaces caused by the mode **111** component. Under mixed lode loading, J_{MC} decreased as the mode III load component increased, reaching a minimum at a crack angle between **40** and 50 degrees.

The issue remains of the mechanism for the degrading effect of H in steel of the type of F-82H where H degrades the properties but leaves the ductile fracture mechanism unchanged. A variety of studies of such steels in plain strain tension [17-28] have shown that H promotes the onset of plastic instability in the form of shear localization. **In** relatively pure, single phase materials, this may be the consequence of a lowered flow stress for dislocation glide [29-31] nr a tendency for increased coplanarity of slip [32]. **In** multiphase engineering materials, the effect instead is associated with localized damage in the form of enhanced void formation by particle decohesion and cracking [31-36] and of enhanced void growth and agglomeration [33-35]. Voids also enhance shear localization [36-38]. Thus, the H enhances void formation, which enhanced shear localization, which in turn enhances further void formation because of incompatibility effects. This autocatalytic phenomenon leads to failure at loner strains in the presence of H.

Preliminary fractographic analysis indicates that H plays a similar role in reducing J„ in H-charged F-82H. The in-plane shear formed by mode III loading causes damage in the form of void initiation. In the presence of H, the initiation of damage ensues at a lower strain. Even under mode I loading, the presence of J reduced the mode I stress level at which particle decohesion and void nucleation occurs. Hence, both J„ and T, for F-82H are decreased at all crack angles.

CONCLUSION

The presence of H reduced both J„ and T, for F-82H, independent of crack slant angles. But H did not change the dependence of J„ and T, on crack angles. Both J,, and T, exhibited the highest values and the minimum J„ and T, were attained at a crack angle between 35 and **55** degrees, where the ratio of σ_{iii}/σ_i is between 0.7 and 1.4. The J_{min} remained high, about **100** kJ/m^2.

FUTURE WORK

Further research is in progress to evaluate the remaining specimens charged with H, the effect of mixed-mode loading on the ductile-brittle-transition temperature, and effects of irradiation on J_{min}.

ACKNOWLEDGEMENTS

We are grateful to Dr. N. R. Moody of Sandia National Laboratories, Livermore, CA for hydrogen-charging. The assistance of Dr. A. Kumar at Washington State University, Pullman and Mr. J. L. Humason at Pacific Northwest Laboratory in developing the test methods is gratefully acknowledged. This research was supported by the Office of Fusion Energy of the U. S. Department of Energy under Contract DE-AC06-76RLO 1830 with Battelle Memorial Institute.

REFERENCES

1. M. T. Miglin, I.-H. Lin, J. P. Hirth, and A. R. Rosenfield, in Fracture Mechanics: 14th Symp. --Vol. II: Testing and Applications, ASTM STP **791,** J. *C.* Lewis and G. Sines, Eds., ASTM, Philadelphia, 1983, pp. II-353-II-369.

2. M. T. Miglin, J. P. Hirth and A. R. Rosenfield, Res. Mech., **11** (1984), pp. 85-95.

3. J. G. Schroth, J. P. Hirth, R. G. Hoagland, and A. R. Rosenfield, Met. Trans. A, 18A (1987), pp. 1061-1072.

4. M. Manoharan, J. P. Hirth, and A. R. Rosenfield, J. of Test. and Eval., **18** (1990), No.2, pp. 106-114.

5. S. Raghavachary, A. R. Rosenfield, and J. P. Hirth, Met. Trans. A, 21A (1990), pp. 2539-45.

6. J. A. Gordon, J. P. Hirth, A. M. Kumar, and N. R. Moody, Jr., Met. Trans. A, 23A (1991), pp. 1013-1020.

7. M. Manoharan, S. Raghavachary, J. P. Hirth, and A. R. Rosenfield, J. Eng. Mater. Technol., 111 (1989), October, pp. 440-442.

8. A. M. Kumar and J. P. Hirth, Scripta Metall. Mater., **25** (1991), pp. 985-90.

9. M. Manoharan, Scripta Metall. Mater., 26 (1992), pp. 1187-1192.

10. M. Manoharan, J. P. Hirth and A. R. Rosenfield, Scripta Metall. Mater., 23 (1989), pp. 763-166 and pp. 1647-1648.

11. S. V. Kamat and J. P. Hirth, Scripta Metall. Mater., 30 (1994), pp. 145-48.

12. H. Li, R. H. Jones, P. J. Hirth and D. S. Gelles, in Fusion Reactor Materials Semiannual Proeress Report DOE/ER-0313/7, Oak Ridge National Lab., Oak Ridge, TN (October, 1993).

13. A. M. Kumar, N. R. Moody, Jr., J. P. Hirth, and J. A. Gordon, Met. Trans. A, **24A** (1993), pp. 1450-1451.

14. J. Xu, X. Z. Yuan, X. K. Sun and B. M. Wei, Scripta Metall. Mater., 29 (1993), pp. 925-30.

15. H. Li, R. H. Jones, P. J. Hirth and D. S. Gelles, in Fusion Reactor Materials Semiannual Progress Report DOE/ER-0313/7, Oak Ridge National Lab., Oak Ridge, TN (March, 1993).

16. Ashok Saxena and S. J. Hudak, Jr, Int. J. Fract., 14 (1978), pp. 453-468.

17. J. R. Rice, P. C. Paris, and J. G. Merkle, in ASTM STP 536, ASTM, Philadelphia, 1973, pp. 231-235.

18. A. R. Rosenfield and W. H. Duckworth, Int. J. Fract., 32, (1987), p. R59.

19. A. W. Thompson and I. M. Bernstein, in Proc. Hvdroeen in Metal Coneress, Paris, France, Pergamon Press, Oxford, 1977, vol. 3, pp. 1-8.

20. T. D. Lee, T. Goldenhemg and J. P. Hirth, Metall. Trans. A, **10A** (1979), pp. 199-208.

21. T. D. Lee, T. Goldenhemg and J. P. Hirth, Metall. Trans. A, **10A** (1979), pp. 439-48.

22. O. A. Onyewuenyi and J. P. Hirth, Metall. Trans. A, **14A** (1983), pp. 259-69.

23. S. C. Chang and J. P. Hirth, Metall. Trans. A, 17A (1986). pp. 1485-7.

24. A. Chatterjee, R. C. Hoagland and J. P. Hirth, Mater. Sci. and Engin., **A142** (1991), pp. 235-43.

25. I. G. Park and A. W. Thompson, Metall. Trans. A, 21A (1990), pp. 465-77.

26. I. G. Park and A. W. Thompson, Metall. Trans. A, 22A (1991), pp. 1615-26.

27. C. Hwang and I. M. Berstein, Acta Metall., 34 (1986), pp. 1001-10, pp. 1011-20.

28. T. D. Le, I. M. Bernstein and S. Mahajan, Acta Metall. Mater., 41 (1993), pp. 3363-80.

29. C. D. Beachem, Met. Trans. 3 (1972), pp. 437-451.

30. T. Tabata and H. K. Birnbanm, Scripta Metall. **17 (1983),** pp. **947-950.**

31. **I.** M. Robertson and H. K. Birnbanrn, Acta Metall. **34 (1986),** pp. **353-366.**

32. **H.** Matsni, A. Kimnra and H. Kimnra: in Streneth of Metals and Allovs, P. Haasen, **V.** Gerold and G. Kostorz, eds., vol. **2,** MP **977-87,** Pergamon, Oxford, **1979.**

33. R. Garber, I. **M.** Bernstein and A. W. Thompson, Metall. Trans. A, **12A (1981),** pp. **225-34.**

34. H. Cialone and R. J. Asaro, Metall. Trans. A, 10A **(1979),** pp. **376-75.**

3s. **R.** A. Oriani and P. H. Josephic, Acta Metall. **22 (1974),** pp. **1065-1074.**

36. **J.** W. Hutchinson and **V.** Tvergarrd, Int. J. Mech. Sci., **22 (1980),** pp. **339-54.**

37. J. W. Hutchinson and V. Tvergaard, Int. J. Solids Structures, **17 (1981),** pp. **451-70.**

38. **L.** Anand and W. A. Spitzig, J. Mech. Phvs. Solids, **28 (1980),** pp. 113-28.

6.2 Austenitic Stainless Steels

FRACTURE TOUGHNESS OF IRRADIATED CANDIDATE MATERIALS FOR ITER FIRST WALL/BLANKET STRUCTURES - D. J. Alexander, J. E. Pawel, M. L. Grossbeck, A. F. Rowcliffe *(Oak* Ridge National Laboratory), and K. Shiba (Japan Atomic Energy Research Institute)

OBJECTIVE

The purpose of this work is to determine the effect of irradiation at low temperature (less than 300°C) and to damage levels of about 3 dpa on the mechanical properties, in particular the fracture toughness, of candidate materials for ITER first wall/blanket structures.

SUMMARY

Candidate materials for first wallhlanket structures in ITER have been irradiated to damage levels of about 3 dpa at nominal irradiation temperatures of either 90 or 250°C. These specimens have been tested over a temperature range from 20 to 250°C. The results show that irradiation at these temperatures reduces the fracture toughness of austenitic stainless steels, but the toughness remains quite high. The toughness decreases as the test temperature increases. Irradiation at 250°C is more damaging than at 90°C, causing larger decreases in the fracture toughness. Ferritic steels are embrittled by the irradiation, and show their lowest toughness at room temperature.

PROGRESS AND STATUS

Introduction

Work is under way at Oak Ridge National Laboratory (ORNL) to evaluate the fracture toughness of candidate materials for first wallhlanket structure applications in the International Thermonuclear Experimental Reactor (ITER). A variety of austenitic stainless steels are being examined, as well as several additional materials. Specimens were fabricated from material in several different conditions, including annealed or cold worked, as well as weldments. These specimens have been irradiated in the High Flux Isotope Reactor (HFIR) at ORNL. To date, three capsules have been designed, fabricated, and irradiated to dose levels of approximately 3 dpa; this approaches the expected accumulated dose at the end of the physics or basic phase of operation of ITER. The helium concentration generated as a result of transmutation of nickel was about 50 appm; this is in the range expected for the ITER first wall blanket and shield structure after a neutron exposure of about 3 dpa. These capsules were designed for irradiation temperatures of either 60 to 125°C (capsules HFIR-JP-18 and -19) or 250 to 300°C (HFIR-JP-17) [1-3]. All of the capsules have been successfully irradiated and disassembled. Some of the results of earlier testing have already been presented [4,5]. This report presents the final results for all of the fracture toughness tests.

Experimental Procedure

Four major alloy types were included in this experiment: American and Japanese type 316 steels (designated US316 and J316, respectively), a European type 316L steel (EC316L), and the JPCA alloy. The compositions of the alloys are given in Table 1. Specimens of the alloys were tested in solution annealed (SA) or cold-worked (CW) conditions. The J316 material was also tested after a thermomechanical treatment in which it was strained, aged, and recrystallized (J316 SAR). There were a total of 12 variants of the austenitic materials in composition and thermomechanical treatment, including several weldments. The EC316L was welded using 16-8-2 filler metal (see Table 1) and gas tungsten arc (GTA) welding with argon cover gas. Both the plate and the filler wire were provided by Joint Research Centre-lspra from the European Fusion Stockpile. The JPCA and 1316 plate material were supplied by the Japan Atomic Energy Research Institute. The JPCA specimens were welded with filler wire with a composition similar to the base metal (see Table 1) for both the case of GTA welding and electron beam (EB) welding. The US316 material was from the U. S. fusion program standard heat. Two ferritic steels were also included in this experiment, HT-9 and F82H.

Table 1. Specimen alloy composition

Alloy	Composition (wt %)								
	Fe	Ni	Cr	Ti	Mo	Mn	Si	C	N
JPCA	Bal	15.95	14.3	0.21	2.4	1.6	0.54	0.064	0.003
US316	Bal	12.4	17.3	--	2.1	1.7	0.67	0.061	--
EC316L	Bal	12.3	17.4	--	2.3	1.8	0.46	0.024	0.06
J316	Bal	13.95	16.77	--	2.31	0.23	0.04	0.038	0.011
16-8-2 weld wire	Bal	8.98	16.28	--	2.16	1.82	0.060	0.036	0.029
JPCA weld wire	Bal	16.06	14.39	0.23	2.44	1.77	0.35	0.057	0.0095

In order to utilize the HFIR target region for the irradiations, the specimen size was severely limited. Therefore, a small disk compact specimen 12.5 mm in diameter was selected for the fracture toughness experiments. Techniques were developed for generating the J-integral-resistance (J-R) curve using either unloading compliance (UC) or potential drop (PD) to monitor crack extension [6,7]. Initial trials showed that either method could be used to develop useful fracture toughness data from these small specimens [6-8]. As a result of the success of the laboratory trials, it was decided to use the unloading compliance technique for testing the irradiated specimens.

The disk compact specimens [designated DC(T)] were 12.5 mm in diameter by 4.63 mm thick. All specimens were fabricated from the middle of the thickness of the parent plate of material, with the notch oriented so that crack growth would occur parallel to the rolling direction (T-L orientation). The specimens were fatigue precracked at room temperature and side grooved 10% of their thickness on each side, prior to irradiation. Filler pieces were inserted in the loading holes and in the notches to reduce disturbances in the flow of cooling water over the specimens in the capsules and to improve the uniformity of heat transfer across the specimens.

Capsules JP-18 and -19 completed their irradiations in October 1991, and capsule JP-17 completed its irradiation in February 1992 [3]. After disassembly of the capsules, the inserts in the individual specimens were pushed out of the loading holes using an arbor press and punch. The filler in the notch was removed with the aid of a hammer and a thinned screwdriver blade.

Tests were conducted in general accordance with American Society for Testing and Materials standards E 813-89, Standard Test Method for J,,, A Measure of Fracture Toughness, and E 1152-87, Standard Test Method for Determining J-R Curves. The equations in E 1152-87 were used for the J calculations. The specimens were tested with a computer-controlled testing and data acquisition system [9]. Tests in the laboratory used an 89-kN capacity servohydraulic test machine. In the hot cell, a 445-kN capacity servohydraulic testing machine with an 22-kN load cell was used. All tests were run in strain control. The displacements were measured with an "outboard" clip gage that seated in grooves machined on the outer edge of the specimen along the load line [6,7]. This arrangement provided very good load-displacement and UC results. Test temperatures from 90 to 250°C were maintained within ±2°C of the desired temperature with a split-box furnace that enclosed the specimen and the grips during the test. Temperature was monitored throughout the testing with a thermocouple that was held in contact with the specimen by a spring-loaded clip. Tensile data from specimens included in the capsules were used for calculations in the J-R analyses [IO]. Estimated values were taken from literature data when necessary.

After testing, the specimens were heat tinted by placing them on a hot plate and beating them until a noticeable color change had occurred. The specimens were cooled to room temperature and then broken open. The initial and final crack lengths for the unirradiated specimens were measured with an optical measuring microscope. For the irradiated specimens, photographs of the fracture surfaces were fastened to a digitizing tablet to measure the crack lengths.

Materials with very high toughness and low yield strength, such as the annealed austenitic stainless steels, proved to be more difficult to test than materials with lower toughness such as HT-9. The soft, tough materials showed enormous crack-tip blunting before stable crack growth began. This resulted in gross changes in the specimen geometry, and so the crack length predictions were not very accurate. The J-R curve was much steeper than the calculated blunting line. In these cases, the data were used to calculate a blunting line. A straight line was fit by eye through the initial portion of the data points, and a second line was drawn parallel to the first but offset by an amount corresponding to a crack extension of 0.2 mm. The candidate toughness value J_Q value was then determined from the intersection of the data with this offset line. In cases where the data rose very steeply, the test was terminated before there was enough crack growth to cross the second exclusion line (drawn corresponding to a crack extension of 1.5 mm as defined in the ASTM standards). As a result, no tearing modulus value could be calculated. Materials with lower toughness, such as the cold-worked austenitic stainless steels, behaved in a much more conventional manner. For these materials, the data followed the calculated blunting line quite closely, so no additional construction was required. These specimens also showed very good agreement between the measured and predicted final crack lengths.

Results and Discussion

The results of the testing are given in Tables **2** to **6. These** tables also include the tensile values used in the analyses. The critical stress intensities calculated from the candidate J values for the various alloys are summarized in Figs. 1 to **12 as** a function of test temperature. These **figures** show that the toughness of the austenitic steels is very high. In general, the toughness decreases **as** the test temperature increases, but remains very high.

Both before and after irradiation, the fracture toughnesses of the solution annealed materials, **as** shown in Figs. 1, **3,** and **6,** are generally very high ($K_J >$ **150 MPdm)** in **the** test temperature range. The toughness decreases slightly **as** the temperature increases, but remains very high, even after irradiation and testing at **250°C.** The **EC316L** and **J316** annealed steels show only a slight decrease in toughness (about **50 MPdm)** after irradiation. **The JPCA** annealed material undergoes a larger decrease in toughness (about **100 MPdm)** after irradiation (Fig. **6).** Even in this case, the toughness is still high, with a K, value of 150 **MPdm** (Table **4). The** range of fracture toughness values of these materials is in the upper range of previously reported data from a variety of steels, reactor environments, and test methods [11-13]. The **US316** material has the lowest toughness both before and after irradiation (Fig. 10). This heat of material was air melted and contains an unusually high volume fraction of nonmetallic inclusions which are likely to promote rapid microvoid growth and coalescence.

The fracture toughness of the cold-worked material is generally lower than that of the annealed material **by** about 75 **MPdm,** both before and after irradiation. Even so, the fracture toughnesses of the cold-worked **JPCA** and **J316** materials remain high. It is important to note that the uniform elongations of these materials, tested at 90°C, are less than 1% [10], while the fracture toughness and tearing modulus values are still high. The toughness of the cold-worked **US316** material, which had the lowest toughness of the austenitic steels in the solution annealed condition, was by far the lowest toughness values of the set, about **65 MPdm.** This material also bad very low values of tearing modulus (Table ***5).***

Electron beam welds of **JPCA** and GTA welds of **JPCA** and **EC316L** proved to be very tough, both before and after irradiation. The **JPCA GTA** welded material had approximately the same toughness **as** the **JPCA SA** material ($K_J \cong$ 240 **MPdm)** after irradiation and testing at **90°C,** while the **IPCA** EB-welded material had an even higher toughness.

As pointed out above, the unirradiated **EC316L** material contained ferrite stringers running along the rolling direction of the plate. However, it was found that specimens with the crack propagation direction parallel to the direction of the delta ferrite stringers had essentially the same toughness **as** specimens with the crack propagation perpendicular to the stringer direction.

The austenitic steels in the annealed condition can be ranked from best to worst **as** follows: **J316** annealed; **EC316L** annealed; **JPCA** annealed; **J316 SAR; US316** annealed. **The JPCA** annealed and the **J316 SAR** are very similar. For the cold-worked alloys, the ranking from best to worst

Table 2. Fracture toughness of EC316L

Material	Specimen	Irradiation temperature (°C)	Test temperature (°C)	J (kJ/m^2)	K_J (MPa$\sqrt{m}$)	T	σ_y (MPa)	σ_u (MPa)	E (GPa)
EC316L Ann	FA14	Unirradiated	22	769	385	NA	276	579	193
	FA22	Unirradiated	100	889	407	NA	228	503	186
	FA5	Unirradiated	200	696	353	NA	186	441	179
EC316L Ann	FA16	90	25	775	387	109	621	689	193
	FA3	90	25	799	393	95	621	689	193
	FA21	90	25	751	381	150	621	689	193
	FA6	90	100	658	350	130	607	676	186
	FA11	90	100	575	327	92	607	676	186
	FA17	90	100	498	299	168	600	676	179
EC316L Ann	FA2	250	25	430	288	43	779	786	193
	FA10	250	100	390	269	39	772	779	186
	FA9	250	250	254	213	45	758	765	179
	FA18	250	250	351	251	62	600	648	179
EC316L Per	FS4	Unirradiated	90	834	394	NA	228	510	186
EC316L Per	FS1	90	90	697	360	169	607	676	186
EC316L Weld	FB3	Unirradiated	22	316	397	NA	276	579	193
	FB14	Unirradiated	90	576	355	NA	186	469	186
	FB17	Unirradiated	250	513	332	NA	241	448	179
EC316L Weld	FB4	90	90	340	252	19	607	575	186
EC316L Weld	FB5	250	250	159	169	28	758	765	179
	FB13	250	250	152	165	22	758	765	179

Table 3. Fracture toughness of J316

Material	Specimen	Irradiation temperature (°C)	Test temperature (°C)	J (kJ/m²)	K_J (MPa√m)	T	σ_y (MPa)	σ_u (MPa)	E (GPa)
J316 Ann	FC8	Unirradiated	22	798	[illegible]	NA	[illegible]	[illegible]	[illegible]
	FC24	Unirradiated	90	958	[illegible]	NA	221	[illegible]	186
	FC21	Unirradiated	250	843	[illegible]	[illegible]	62	[illegible]	179
J316 Ann	FC12	90	90	[illegible]	[illegible]	[illegible]	[illegible]	[illegible]	[illegible]
	FC16	90	250	640	369	110	552	593	179
J316 Ann	FC10	250	90	77	298	72	689	758	186
	FC2	250	250	32	244	[illegible]	758	765	179
J316 SAR	FM5	Unirradiated	22	687	364	141	276	572	193
	FM8	Unirradiated	90	602	335	99	221	552	186
	FM9	Unirradiated	250	391	265	107	455	559	179
J316 SAR	FM11	90	90	259	220	32	724	758	186
	[illegible]	[illegible]	[illegible]	[illegible]	174	28	758	765	179
J316 CW	FD7	Unirradiated	22	870	410	[illegible]	696	800	193
	FD5	Unirradiated	90	538	317	[illegible]	676	772	186
	FD1	Unirradiated	250	333	244	[illegible]	572	607	179
J316 CW	FD12	[illegible]	90	[illegible]	[illegible]	[illegible]	793	827	179
	FD8	90	250	300	232	[illegible]			
J316 CW	FD10	250	90	272	225	39	889	938	186
	FD11	250	250	136	156	18	800	827	179

Table 4. Fracture toughness of JPCA

Material	Specimen	Irradiation temperature (°C)	Test temperature (°C)	J (kJ/m^2)	K_J (MPa$\sqrt{m}$)	T	σ_y (MPa)	σ_u (MPa)	E (GPa)
JPCA Ann	FF10	Unirradiated	22	672	360	NA	248	579	193
	FF13	Unirradiated	100	705	362	NA	228	517	186
	FF20	Unirradiated	200	439	299	NA	207	462	179
JPCA Ann	FF6	90	25	348	259	23	758	793	193
	FF5	90	25	360	264	41	724	752	193
	FF16	90	100	306	239	34	710	738	186
	FF15	90	100	311	241	31	710	738	186
	FF2	90	200	220	198	38	683	703	179
JPCA Ann	FF3	250	25	269	228	19	827	848	193
	FF11	250	100	131	156	15	806	841	186
	FF18	250	250	123	148	21	621	669	179
JPCA EBW	FR7	Unirradiated	250	621	334	NA	214	490	179
JPCA EBW	FR11	90	90	882	405	102	710	738	186
JPCA EBW	FR12	250	250	314	237	52	779	827	179
JPCA CW	FE6	Unirradiated	22	356	262	43	669	710	193
	FE3	Unirradiated	90	296	234	48	655	703	186
	FE1	Unirradiated	250	181	180	82	524	572	179
JPCA CW	FE8	90	90	168	177	25	924	945	186
JPCA CW	FE7	250	250	124	149	8	868	896	179
JPCA Weld	FG10	Unirradiated	22	738	378	NA	248	579	193
	FG13	Unirradiated	90	1026	437	NA	248	531	186
	FG1	Unirradiated	250	960	415	NA	214	490	179
JPCA Weld	FG8	90	90	317	242	46	710	738	186
JPCA Weld	FG12	250	250	237	206	42	621	660	179

Table 5. Fracture toughness of US316

Material	Specimen	Irradiation temperature (°C)	Test temperature (°C)	J (kJ/m²)	K_J (MPa√m)	T	σ_y (MPa)	σ_u (MPa)	E (GPa)
US316 Ann	FK16	Unirradiated	22	240	215	80	248	[illegible]	[illegible]
	FK6	Unirradiated	90	233	208	70	221	510	186
	FK8	Unirradiated	250	214	196	89	152	462	179
[illegible]	[illegible]	[illegible]	[illegible]	155	170	15	503	648	186
[illegible]	FK10	250	250	33	77	4	758	765	179
US316 CW	FL13	Unirradiated	22	37	83	5	724	780	195
	FL8	Unirradiated	90	39	85	0	717	772	186
	FL9	Unirradiated	250	25	67	-	572	648	179
US316 CW	FL15	90	90	21	62	0	848	862	180
US316 CW	FL5	250	250	17	95	0	827	862	[illegible]

Table 6. Fracture toughness of ferritic alloys

Material	Specimen	Irradiation temperature (°C)	Test temperature (°C)	J (kJ/m^2)	K_J (MPa$\sqrt{m}$)	T	σ_y (MPa)	σ_u (MPa)	E (GPa)
HT-9	[illegible] FH3 FH4	Unirradiated Unirradiated Unirradiated	22 90 250	447 419 408	304 294 281	76 64 131	648 641 427	[illegible]00 [illegible]93 [illegible]27	207 207 193
HT-9	FH1	90	90	278	236	42	896	910	200
HT-9	FH5 FH6	250	25 250	5 136	33 162	- 17	931 889	965 903	207 193
F82H	FI3	Unirradiated	250	330	252	[illegible]	[illegible]	[illegible]	[illegible]
F82H	FI4 FI1	250	25 250	114 193	153 193	- 23	758 855	862 862	207 193

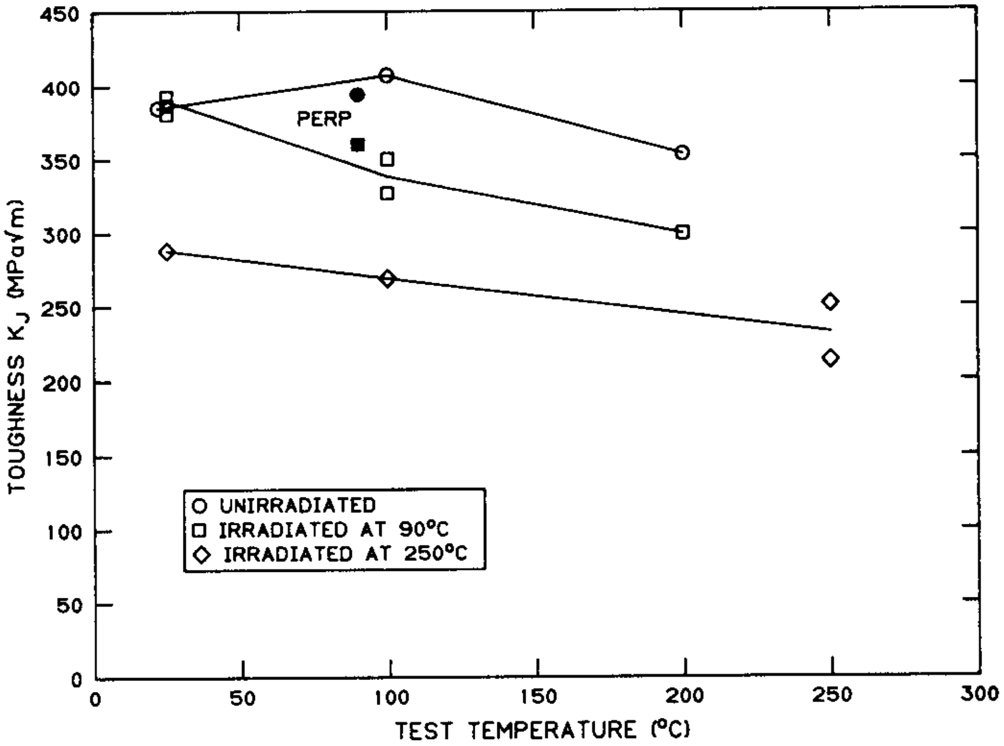

Fig. 1. Fracture toughness values for annealed EC316L. Also shown are two specimens oriented perpendicular to the rolling direction (PERP).

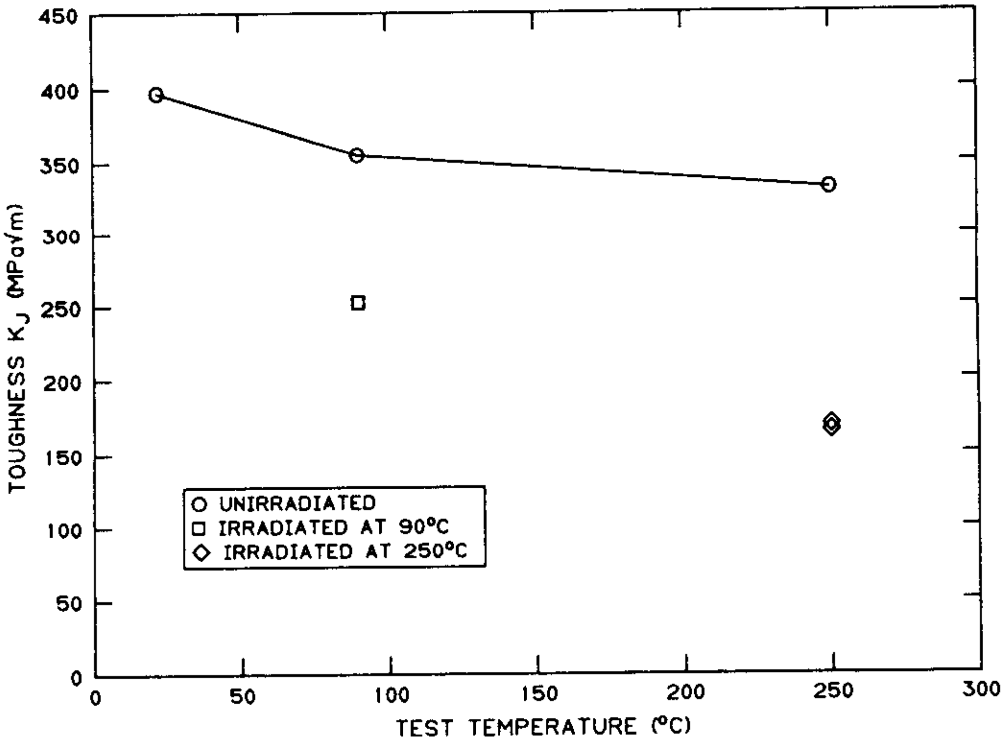

Fig. 2. Fracture toughness values for the weldment in EC316L base metal.

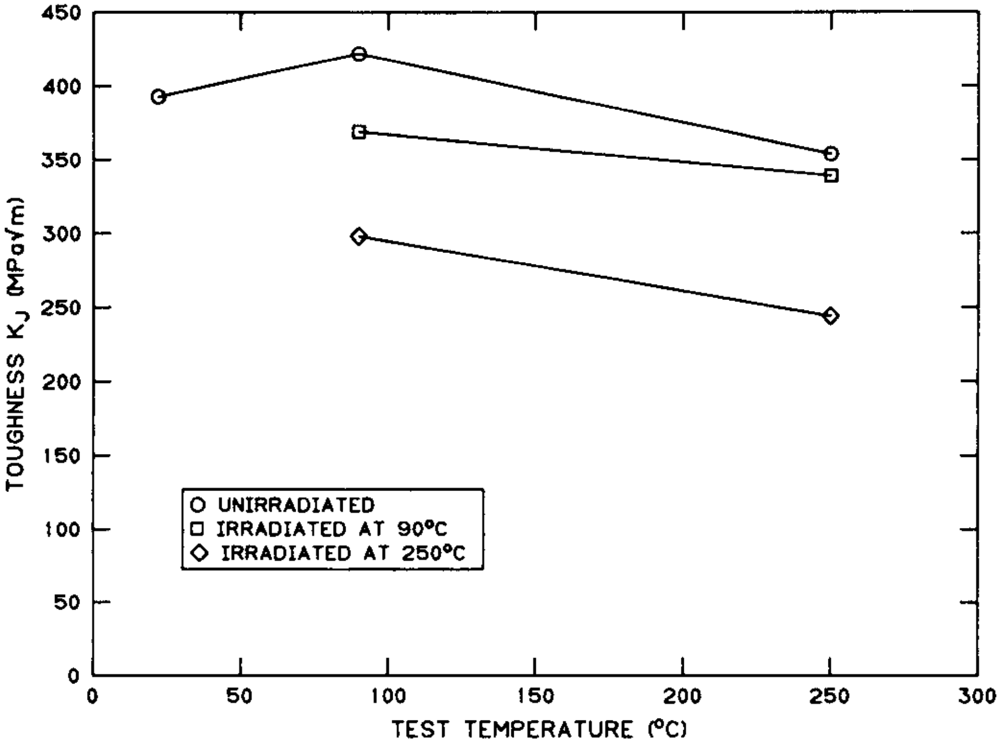

Fig. 3. Fracture toughness values for annealed J316.

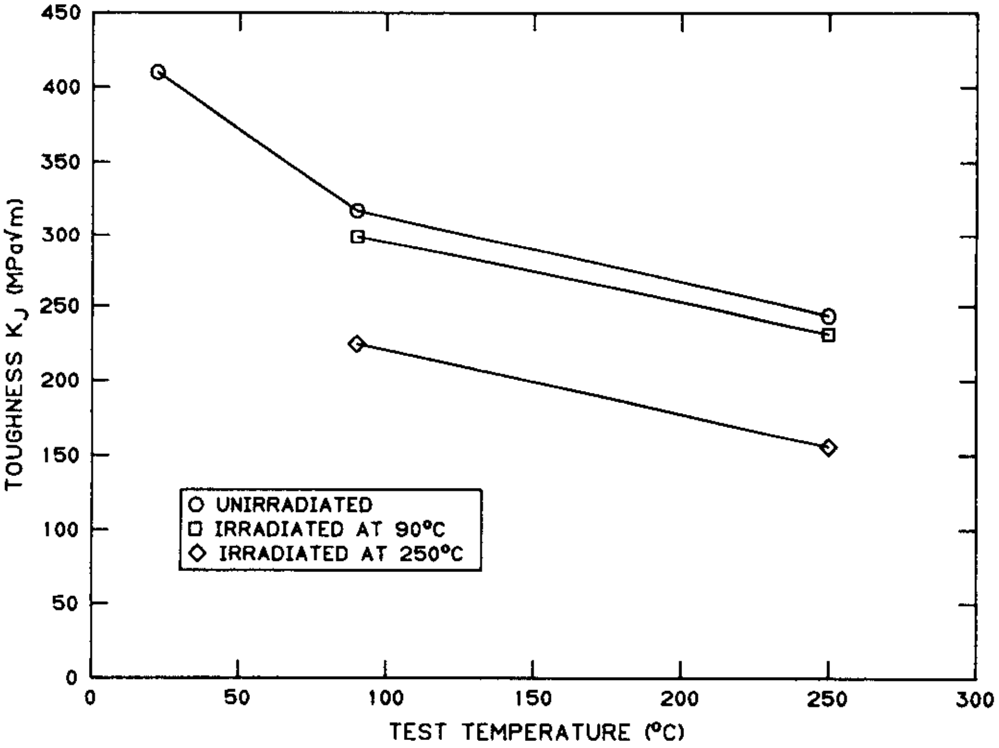

Fig. 4. Fracture toughness values for cold-worked J316.

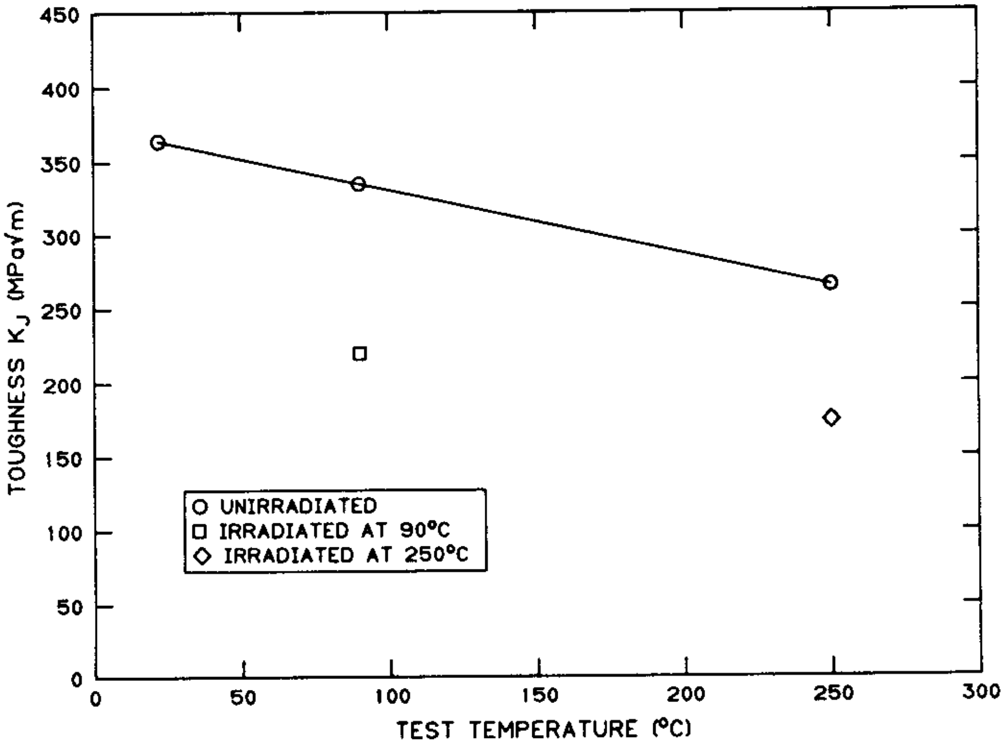

Fig. 5. Fracture toughness values for strain aged and recrystallized (SAR) J316.

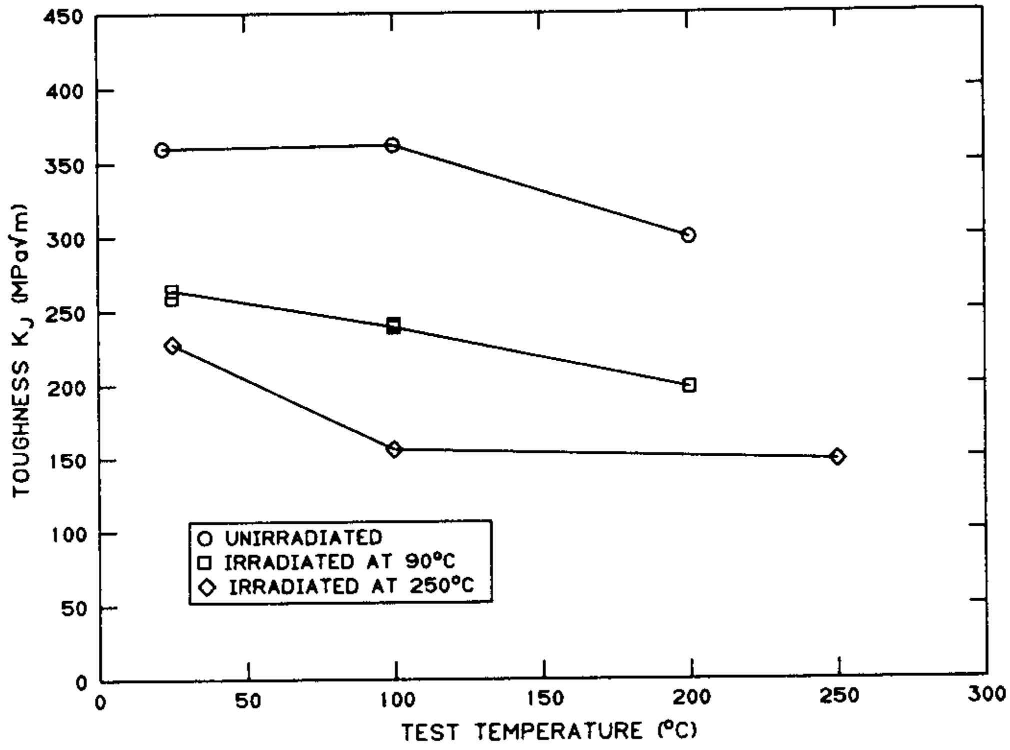

Fig. 6. Fracture toughness values for annealed JPCA.

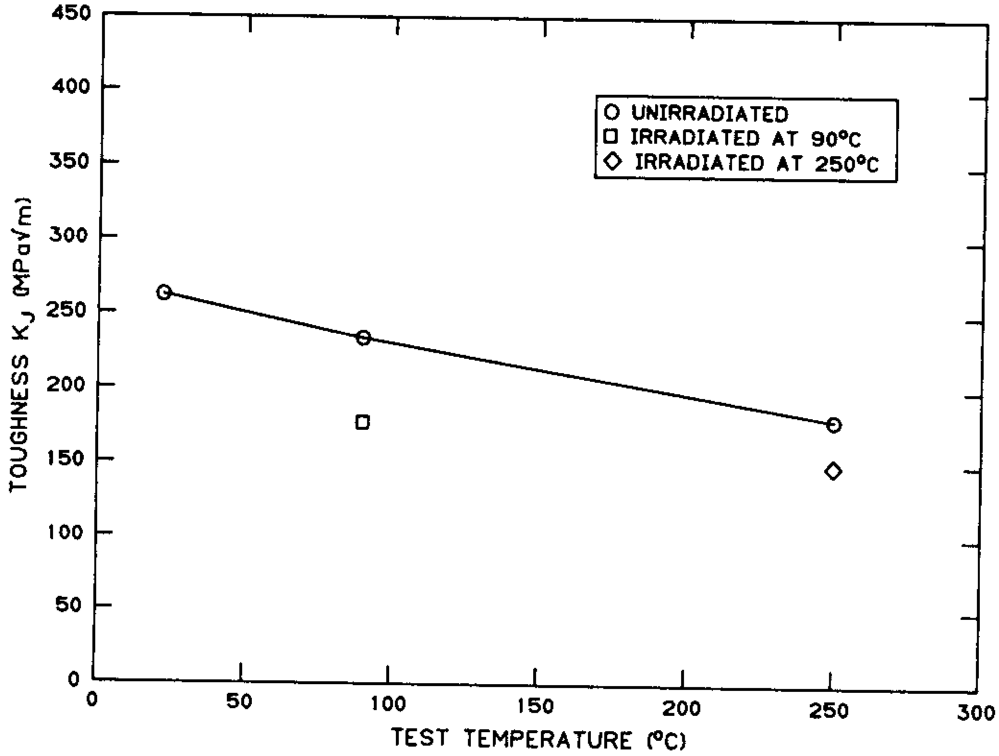

Fig. 7. Fracture toughness for cold-worked JPCA.

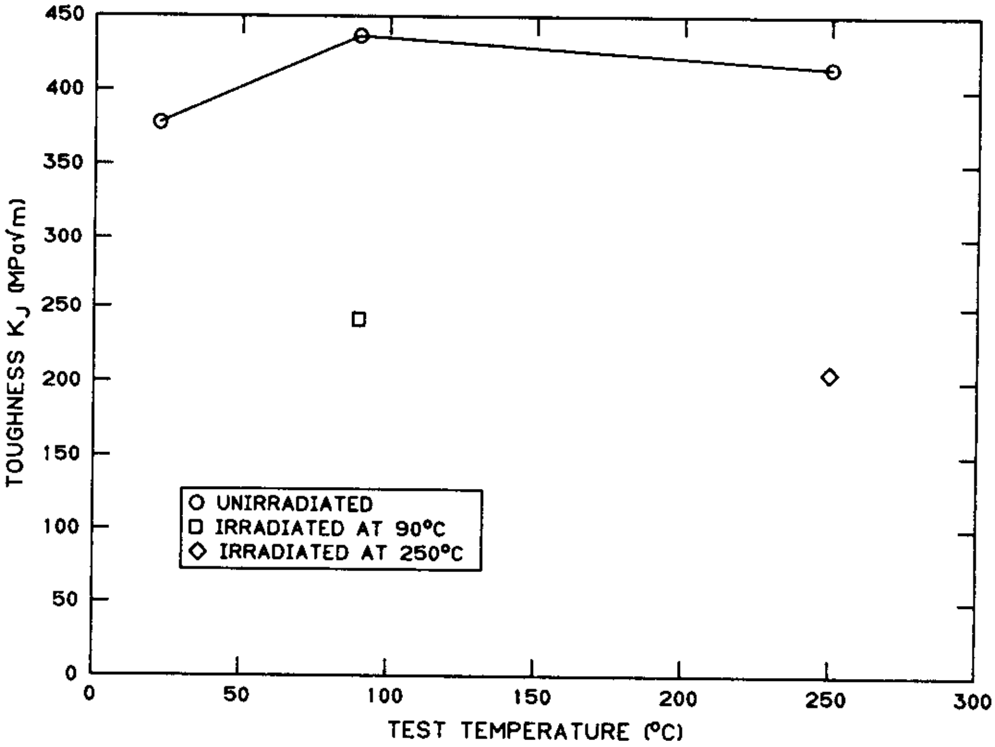

Fig. 8. Fracture toughness for weldment in JPCA.

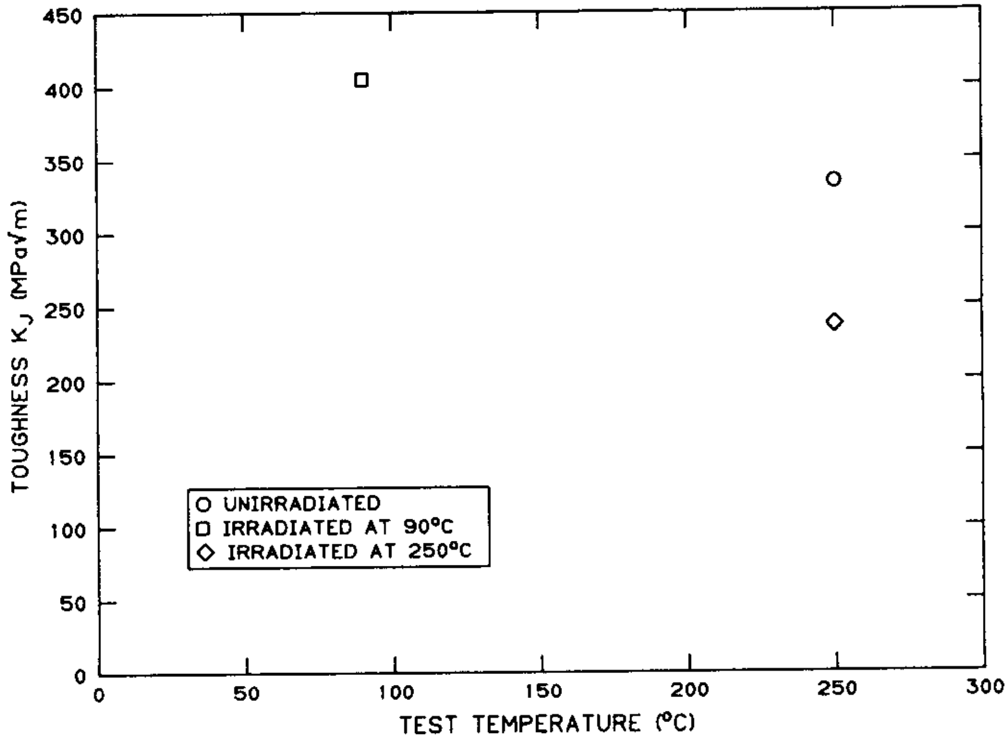

Fig. 9. Fracture toughness for electron beam (EB) weldment in JPCA.

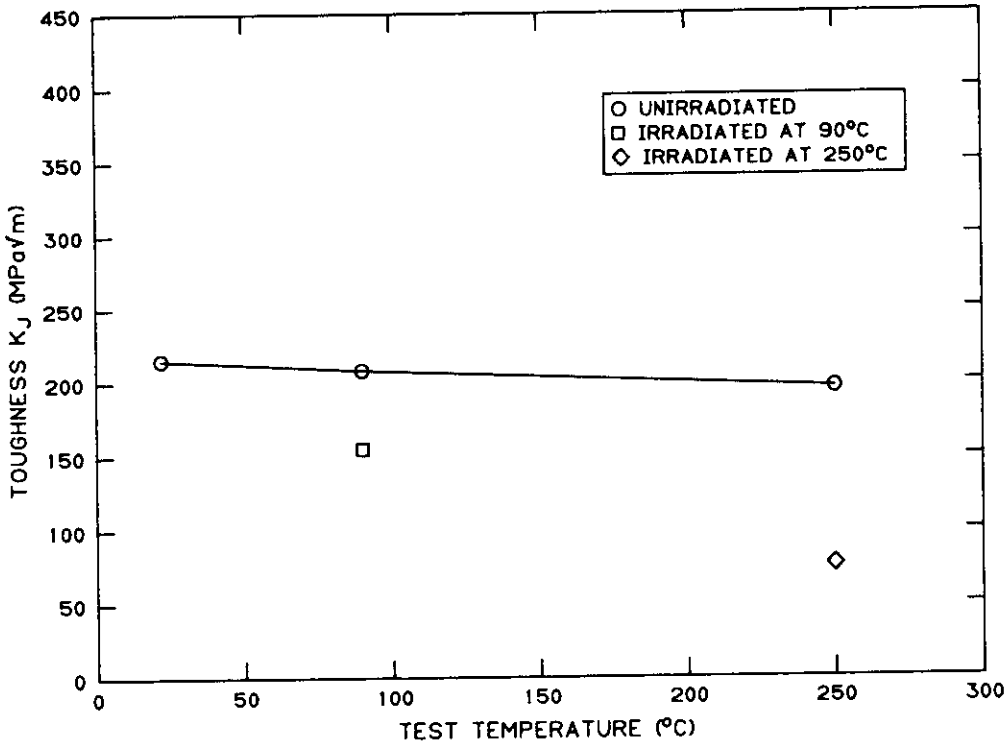

Fig. 10. Fracture toughness in annealed US316.

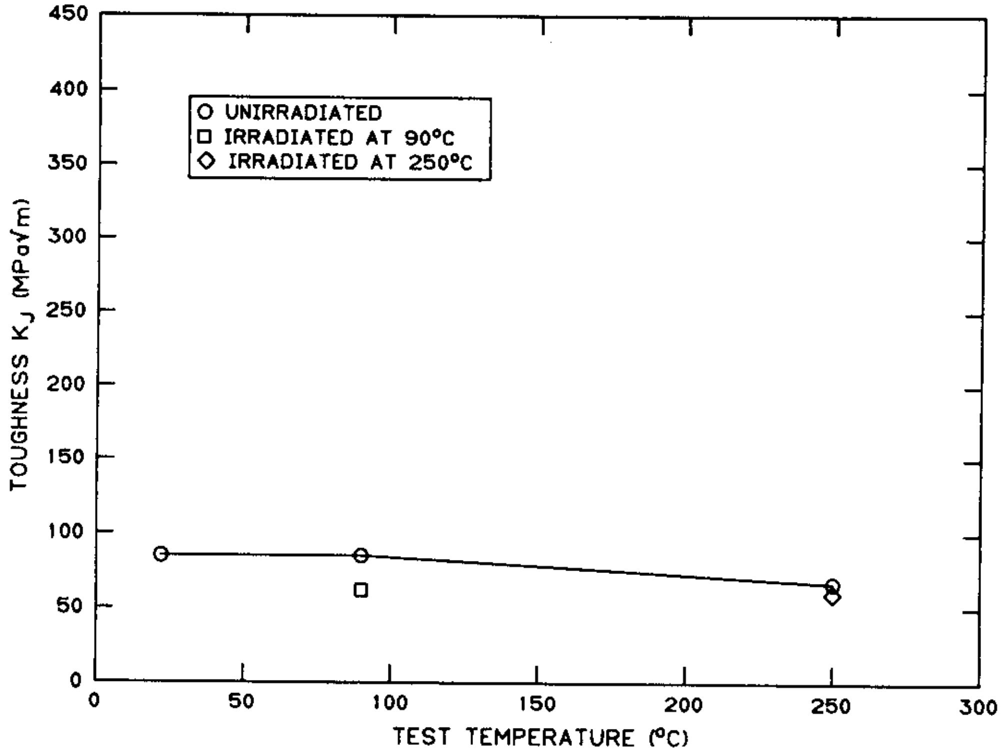

Fig. 11. Fracture toughness in cold-worked US316.

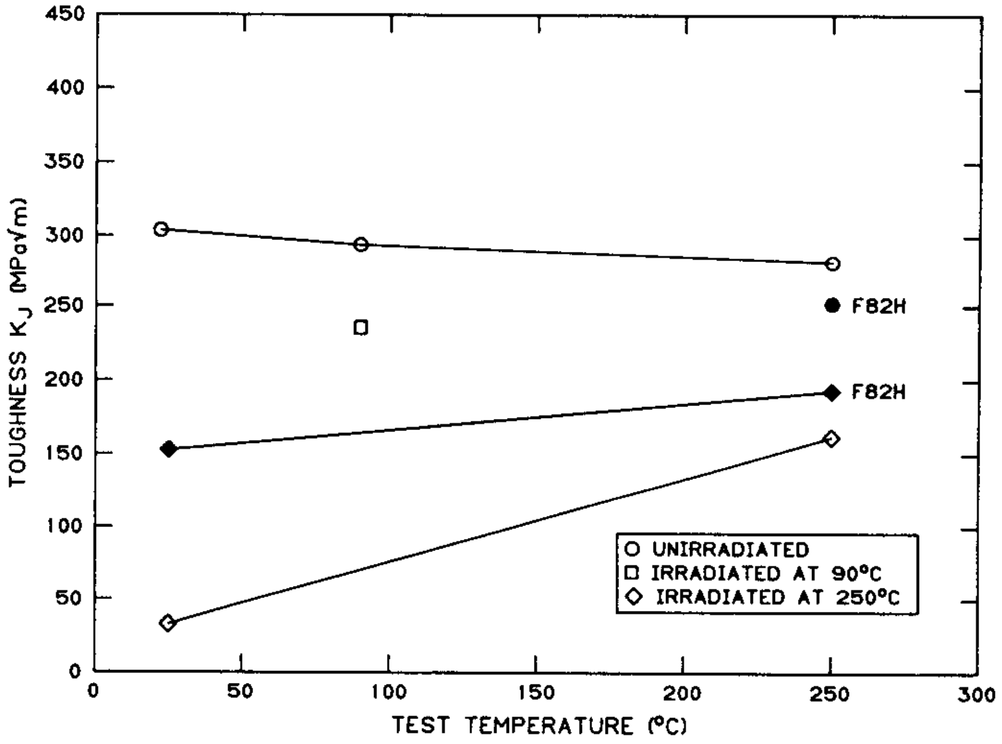

Fig. 12. Fracture toughness in ferritic materials HT-9 and F82H.

is: **J316 CW; IPCA CW; US316 CW. For** the weldments, the ranking is: **JPCA** EB weld; **JPCA** weld: **EC316L** weld. These rankings hold for both unirradiated and irradiated material.

The J-R curves for specimens of **EC316L, J316,** and **JPCA,** all in the annealed condition, are shown in Figs. **13** to 15. The **J316** material shows the smallest degradation in toughness and the **IPCA** alloy shows the greatest decrease. After irradiation, the J-R curves have a lower slope, which reflects the lower values of tearing moduli given in Tables **2** to **4. The** toughness level decreases with increasing test temperature.

The fracture toughness of the ferritic materials is also reduced by these irradiations. The **F82H** alloy is more resistant to damage than the HT-9 material. Both of these alloys show high toughness at high test temperatures **(250°C)** with lower toughness at **25°C** (Fig. **12). The HT-9** specimen irradiated at **250°C** fractured in a brittle manner when tested at room temperature. The loaddisplacement trace was linear, and the value of the fracture toughness **(33** MPa$\sqrt{m}$) is **so** low that it satisfies the specimen thickness validity criteria for plane strain fracture toughness, despite the very small specimen size. The **F82H** specimen irradiated at **250°C** and tested at **25°C** also shows a lower toughness than when tested at **250°C,** but the loaddisplacement curve shows considerable non-linearity and the final fracture, although unstable, occurs at a high toughness level of **153 MPadm.**

CONCLUSIONS

Specimens of several austenitic stainless steels have been irradiated in **HFIR** to about **3** dpa at nominal irradiation temperatures of 90 or **250°C.** Irradiation reduces the fracture toughness. Irradiation at **250°C** is more damaging than at **90°C.** The fracture toughness decreases with increasing test temperature, for all the austenitic materials. The annealed materials have higher toughnesses than the cold-worked materials. The toughness of the cold-worked materials is still high, with the exception of the **US316** material. The welds also have high toughnesses. For the ferritic materials, the specimens irradiated at **250°C** and tested at room temperature fail in an unstable manner. The **F82H** has a much higher toughness than the **HT-9** alloy.

FUTURE WORK

No further fracture toughness testing is planned at this time, although there are many additional specimens that could be tested. Some specimens will be selected for fractographic examination.

ACKNOWLEDGMENTS

The fracture toughness testing was performed by R. L. Swain. The manuscript was prepared by J. **L.** Bishop.

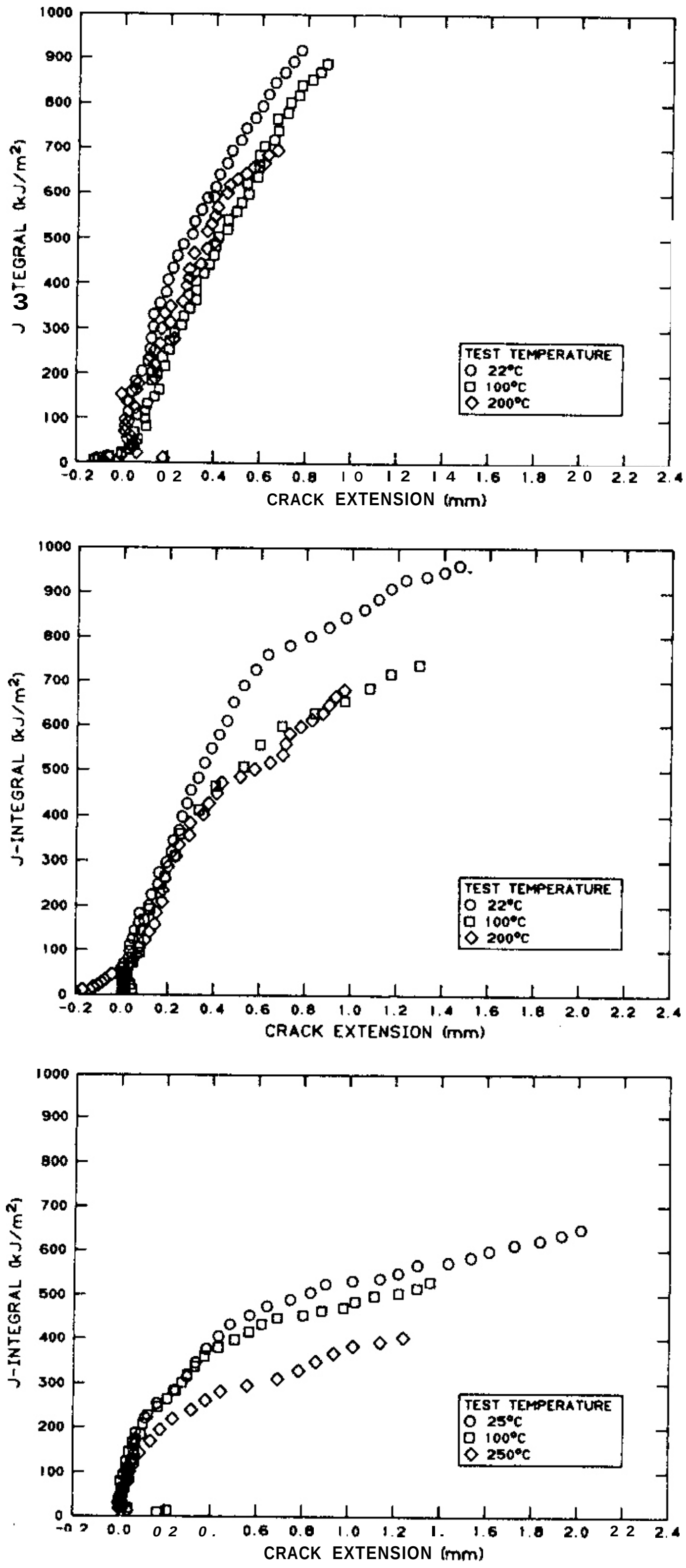

Fig. 13. J-R curves for annealed EC316L material in the unirradiated condition (top), and after irradiation at 90°C (middle) and 250°C (bottom).

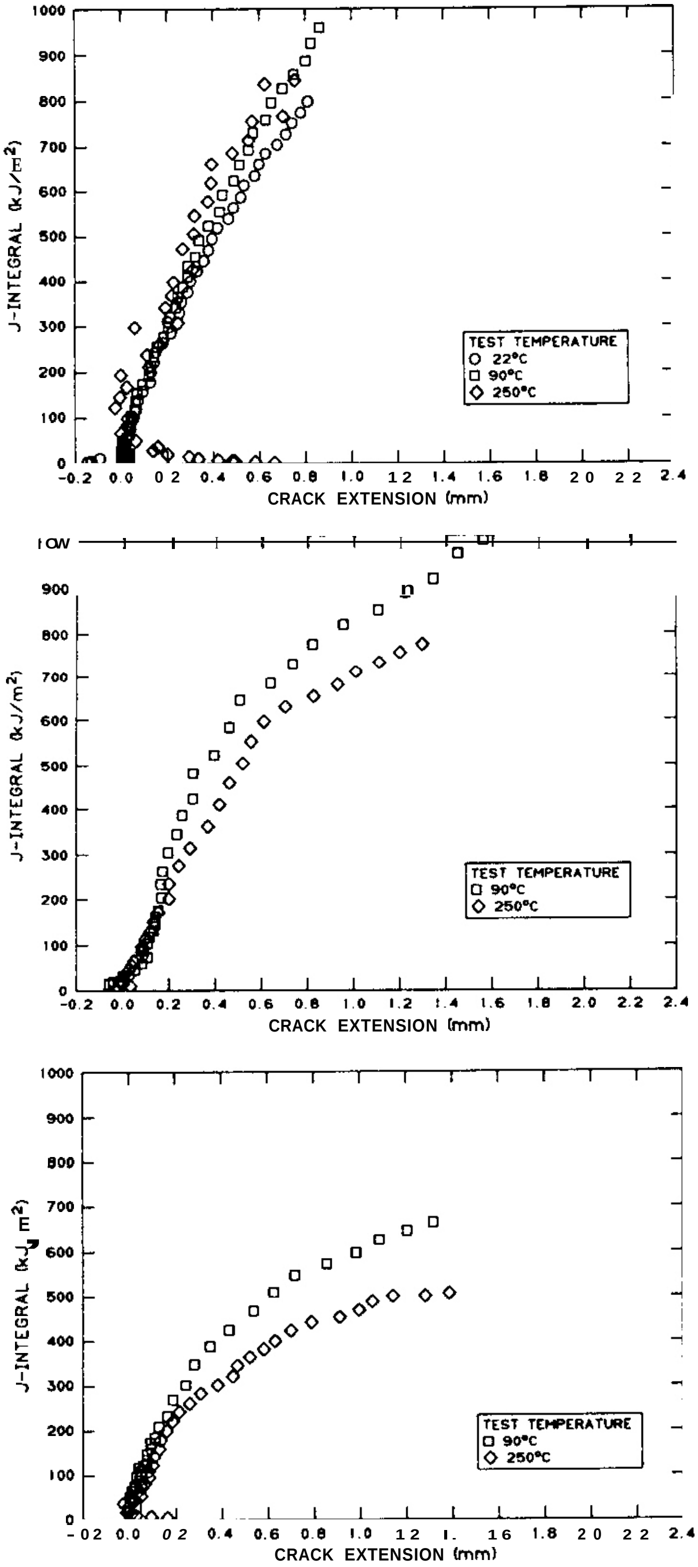

Fig. 14. J-R curves for **annealed** J316 **material in the unirradiated condition (topj. and** after **irradiation at** 90°C (middle) **and** ***250°C*** **(bottom).**

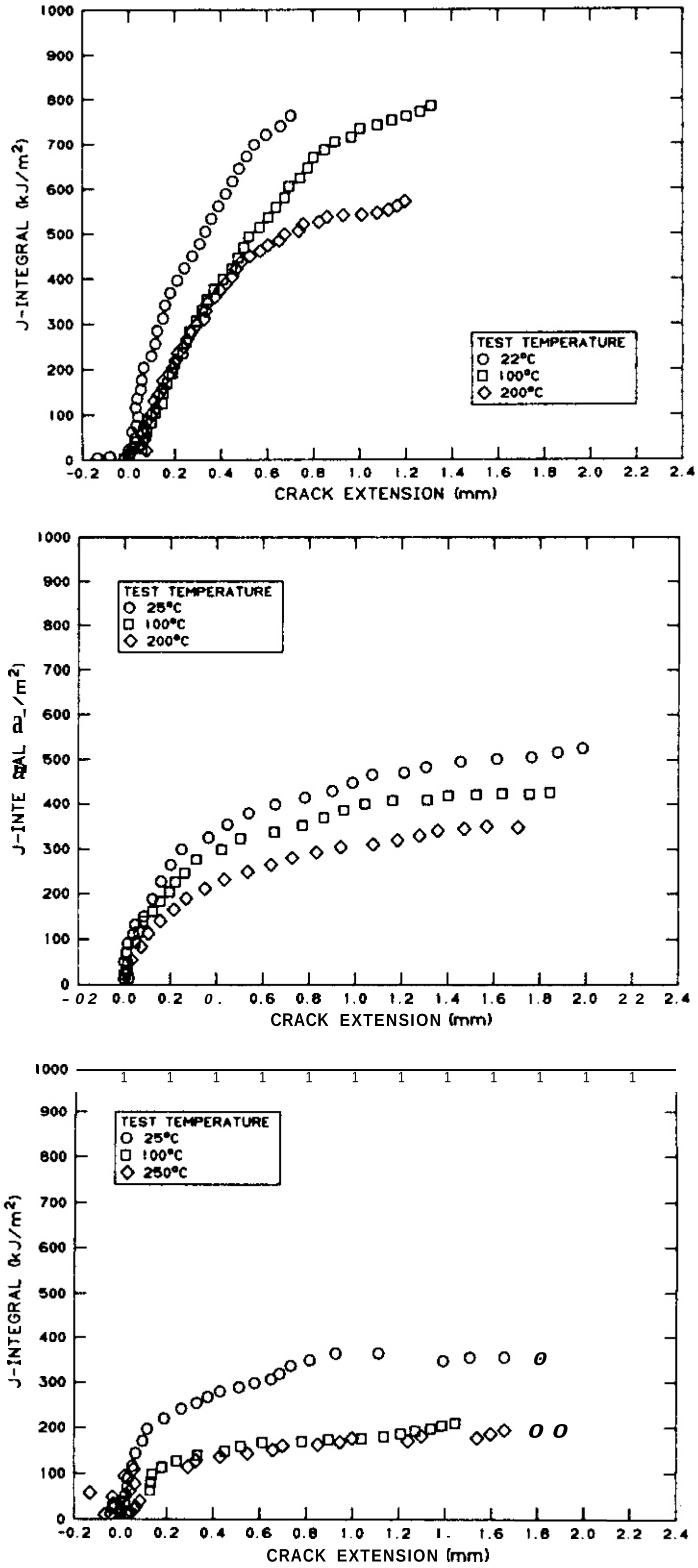

Fig. 15. J-R curves for annealed JPCA material in the unirradiated condition (top), and after irradiation at 90°C (middle) and 250°C (bottom).

REFERENCES

1. A. W. Longest, D. W. Heatherly, K. R. Thorns, and J. E. Corum, "Design and Fabrication of HFIR-MFE-IP Target Irradiation Capsules," Fusion Reactor Materials Semiannual Progress Report for Period Ending March 31, 1991, DOE/ER-0313/10, 1991, p. 3.

2. A. W. Longest, D. W. Heatherly, J. E. Wolfe, K. R. Thorns, and J. E. Corum, "Fabrication and Irradiation of HFIR-MFE-JP-17, -18, and -19 Target Irradiation Capsules," Fusion Reactor Materials Semiannual Progress Report for Period Ending September 30, 1991, DOE/ER-0313/11, 1992, p. 30.

3. A. W. Longest, D. W. Heatherly, K. R. Thoms, and J. E. Corum, "Fabrication and Irradiation of HFIR-MFE-JP-17, -18, and -19 Target Irradiation Capsules," Fusion Reactor Materials Semiannual Progress Report for Period Ending March 31, 1992, DOE/ER-0313/12, 1992, p. 24.

4. D. J. Alexander, J. E. Pawel, M. L. Grossbeck, and A. F. Rowcliffe, "Fracture Toughness of Irradiated Candidate Materials for ITER First Wall/Blanket Structures: Preliminary Results", Fusion Reactor Materials Semiannual Progress Report for Period Ending March 31, 1992, DOE/ER-0313/14, 1993, p. 271.

5. J. E. Pawel, D. J. Alexander, M. L. Grossbeck, A. W. Longest, A. F. Rowcliffe, G. E. Lucas, S. Jitsukawa, A. Hishinuma, and K. Shiba, "Fracture Toughness of Candidate Materials for ITER First Wall, Blanket, and Shield Structures," Fusion Reactor Materials Semiannual Progress Report for Period Ending September 30, 1993, DOE/ER-0313/15, 1992, p. 173.

6. D. J. Alexander, "Fracture Toughness Measurements with Subsize Disk Compact Specimens," Fusion Reactor Materials Semiannual Progress Report for Period Ending March 31, 1992, DOE/ER-0313/12, 1992, p. 35.

7. D. J. Alexander, "Fracture Toughness Measurements with Subsize Disk Compact Specimens," in Small Specimen Test Techniques Applied to Nuclear Reactor Vessel Thermal Annealing and Plant Life Extension, ASTM STP 1204, W. R. Corwin, F. M. Haggag, and W. L. Server, eds., American Society for Testing and Materials, Philadelphia, 1993, p. 130.

8. C. Elliot, M. Enmark, G. E. Lucas, and G. R. Odette, "Development of Disc Compact Specimens and Test Techniques for HFIR Irradiations," Fusion Reactor Materials Semiannual Progress Report for Period Ending September 30, 1990, DOE/ER-0313/9, 1991, p. 7.

9. R. K. Nanstad, D. J. Alexander, R. L Swain, J. T. Hutton, and D. L. Thomas, "A Computer-Controlled Automated Test System for Fatigue and Fracture Testing," in Applications of Automation Technology to Fatigue and Fracture Testing, ASTM STP 1092, A. A. Braun, N. E. Ashhaugh, and F. M. Smith, eds., American Society for Testing and Materials, Philadelphia, PA, 1990, p. 7.

10. J. E. Pawel, unpublished research, Oak Ridge National Laboratory, 1994

11. G. E. Lucas, J. Nucl. Mater., Vol. 206, 1993, p. 287

12. G. R. Odette and G. E. Lucas, J. Nucl. Mater., Vol. 179-181, 1991, p. 572.

13. G. R. Odette and G. E. Lucas, J. Nucl. Mater., Vol. 191-194, 1992, p. 50.

LOW TEMPERATURE RADIATION-INDUCED SEGREGATION RELATIVE TO IASCC AND ITER - E. P. Simonen, R. H. Jones, L. A. Charlot and S. M. Bruemmer (Pacific Northwest Laboratory)

OBJECTIVE

To evaluate low temperature segregation implications for ITER and irradiation assisted stress corrosion cracking (IASCC).

SUMMARY

Radiation induced segregation at grain boundaries in stainless steel has been evaluated as a function of temperature. Segregation caused by ion irradiation was measured and compared to temperature-dependent model predictions. The model was subsequently used to extrapolate predictions to ITER operating conditions. For ion irradiation, segregation was found to extend to temperatures below 400°C which implies that segregation is expected at temperatures less than 200°C for ITER irradiation damage rates. The model predictions were in accord with Cr depletion levels and profile widths as measured using FEG-STEM examination of ion irradiated grain boundaries. The model was further shown to be consistent with measured depletion levels at grain boundaries in 316 stainless steel irradiated in a light-water reactor at 288°C. The findings of this study suggest that chromium depletion and hence IASCC may be a concern for stainless steel structures irradiated in ITER high-temperature water environments.

TECHNICAL PROGRESS

Background

Radiation-induced Cr depletion at grain boundaries in stainless steel has been implicated as contributing to IASCC in high temperature water[1,2]. Radiation causes changes in grain boundary composition as compared to bulk composition because of flow of point defects to grain boundaries. **In** addition to Cr depletion, depletion of Fe and Mo and enrichment in Ni and Si have been measured. Cracking susceptibility has been reported for austenitic stainless steels irradiated at 288°C to doses above **1** dpa. The cracking can be induced either by post-irradiation, slow-strain-rate tests or by in-situ straining during irradiation. Because Cr depletion is a well known cause for thermal sensitization of stainless steels, the observation of Cr depletion in IASCC susceptible alloys has suggested an IASCC mechanism similar to thermal sensitization. Although Cr depletion correlates with cracking susceptibility, other irradiation-induced processes may also contribute to cracking such as irradiation hardening and change in deformation modes.

Radiation-induced segregation at grain boundaries in austenitic steels for ITER may be a concern for water cooled structures.3 Segregation behavior at temperatures below 288°C, and at high damage levels above 10 dpa, has not been characterized. The aim of the present study is to examine the temperature dependence of segregation using Ni^{++} irradiation and field-emission-gun, scanning transmission electron microscopy (FEG-STEM). Measured ion and neutron responses are compared to inverse-Kirkendall segregation predictions. The rate theory model is then used to project behavior for ITER irradiation temperatures, dose rates, and doses.

Descrintion of Segregation Model

Perks et al.[4] have developed a model for radiation-induced segregation based on the production, migration and interaction of point defects with major solute elements. Radiation produces vacancies and interstitials in the matrix and a fraction of these defects migrate to grain boundaries. The flow of defects and the differential interaction of major alloying elements with the defects results **in** nonequilibrium solute profiles at grain boundaries. In particular, slow diffusing Ni enriches and fast diffusing Cr depletes at grain boundaries. Inverse Kirkendall diffusion accounts for a flow of solute induced by defect diffusion to grain boundaries in contrast with conventional Kirkendall diffusion which accounts for a flow of defects induced by solute diffusion down a concentration gradient. Perks et al. were successful at predicting solute composition profiles at irradiated grain boundaries using differential diffusion rates measured during annealing and hence concluded that the segregation coupling was related to the vacancy defect flow.

The flow of defects and solutes can be described by a set of coupled reaction rate equations for Fe, Cr, Ni, vacancies and interstitials. Continuity equations account for solute diffusion during irradiation and are described by

$$\frac{dC_k}{dt} = -\frac{d}{dx}\left[D_k\alpha\frac{dC_k}{dx} + C_k\left(d_{kv}\frac{dC_v}{dx} - d_{ki}\frac{dC_i}{dx}\right)\right]. \qquad (1)$$

Similarly, production, migration and annihilation of vacancies and interstitials are described by

$$\frac{dC_v}{dt} = -\frac{d}{dx}\left[C_v\sum_k\left(d_{kv}\alpha\frac{dC_k}{dx}\right) - D_v\frac{dC_v}{dx}\right] + K + K' - R_r - R_v \qquad (2)$$

and

$$\frac{dC_i}{dt} = -\frac{d}{dx}\left[C_i\sum_k\left(d_{ki}\alpha\frac{dC_k}{dx}\right) - D_i\frac{dC_i}{dx}\right] + K - R_r - R_i \qquad (3)$$

Solute species are indicated by the index, k, and vacancies and interstitials are represented by v and i, respectively. Of main interest are the coupling parameters, $d_{k,v \text{ or } i}$. Other parameters shown are the diffusivities, D, the production rates, K (displacement) and K' (thermal), and the loss rates by mutual recombination R_r and by annihilation at sinks, $R_{v \text{ or } i}$. The thermodynamic factor, ***a,*** is assumed to be unity. The coupling parameters assumed in the present calculations were the same as those proposed by Perks et al. The product of the relative jump rate and vacancy correlation factor for Fe, Cr and Ni were **1.46,** 2.22 and **0.872,** respectively.

The effect of irradiation on grain boundary microchemistry in a microcrystalline stainless steel was characterized as a function of temperature using Ni++ ion irradiation and FEG-STEM analysis. Irradiations were conducted to **10** dpa at temperatures ranging from **250** to **550°C.** The displacement rate was 5 x 10^{-3} dpa/s. The irradiation procedure and sample descriptions have been described previously[5]. Specimens were analyzed using a Vacuum Generator **HB501** dedicated STEM and an energy dispersive X-ray spectrometer with a through thickness resolution of **3** nm. The microcrystalline stainless steel samples were prepared **by** sputter deposition and had grain sizes of about 700 nm. The matrix Fe, Cr and Ni concentrations were **56, 19** and **23** wt%. A single **304SS** specimen was ion irradiated at 250°C to a dose of **10** dpa.

Model Predictions and Experimental Results

Model predictions were based on reference parameters recommended by Perks et al.[4] and for a damage efficiency for producing freely migrating defects of 0.03 for ions. The measured temperature dependence of the ion-induced Cr depletion profile was used **to** calibrate the temperature dependent aspect of the model. A comparison of predicted grain boundary Cr concentrations with measured Cr concentrations is shown in Figure **1.** Similarly, predictions of full width of the Cr depletion profile are shown compared to measured widths in Figure 2. The predictions based on the reference choice of parameters overpredicted the grain boundary Cr concentration and underpredicted the width of the Cr depletion profile, particularly at and below a temperature of 400°C. Alternatively, a reduction in the assumed vacancy migration energy from **1.29** eV to **1.15** eV was found to improve the model fit to the measured grain boundary Cr concentration and depletion profile width as shown in Figures **1** and **2.**

The predicted grain boundary concentrations have been convoluted to take into account the FEG-STEM beam profile. The through thickness beam profile was assumed to have a normal distribution with **85%** of the beam intensity within a 3 nm diameter. Predicted depletion widths were based **on** the distance from the boundary at which the concentration achieved a level of **1** wt% below the matrix concentration.

The adjusted model was also used to compare predicted and measured Cr depletion magnitudes for conditions appropriate for light-water-reactor irradiation of **316SS** at 288°C. Jacobs et al.6 reported a total of **26** measurements of grain boundary Cr concentration in a variety of **316 SSs.** The alloys were all irradiated at 288°C to a dose of about 3 dpa in a boiling-water-reactor. A histogram of measured grain boundary Cr concentration is shown in Figure 3. An example profile, noted in Figure 3, is shown in Figure **4** and is compared to the model prediction assuming a vacancy migration energy of **1.15** eV and a damage efficiency for producing freely migrating defects of **0.01.** The damage efficiency was selected to reasonably fit the example profile.

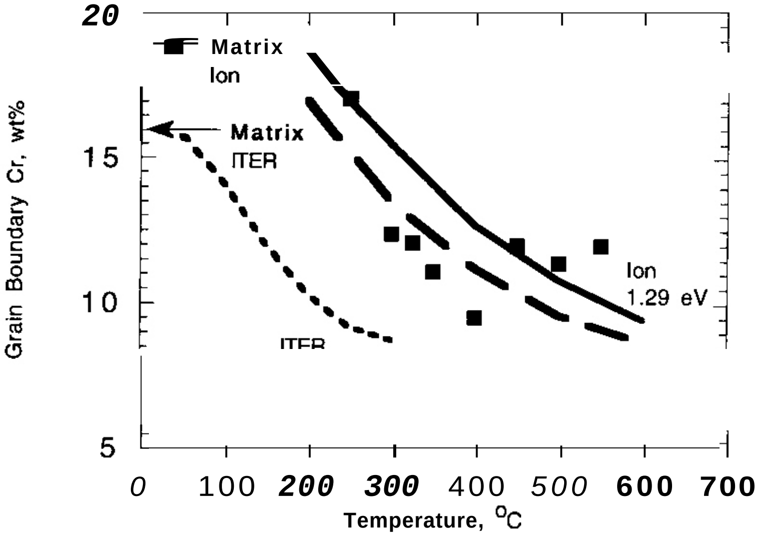

Figure 1. Grain boundary Cr concentrations at 10 dpa are shown as a function of temperature. Inverse Kirkendall mechanism predictions are compared to measurements using Ni^{++} irradiation and FEG-STEM grain boundary analysis. Microcrystalline stainless steel was used except at 250°C for which a conventional wrought 304SS specimen was used.

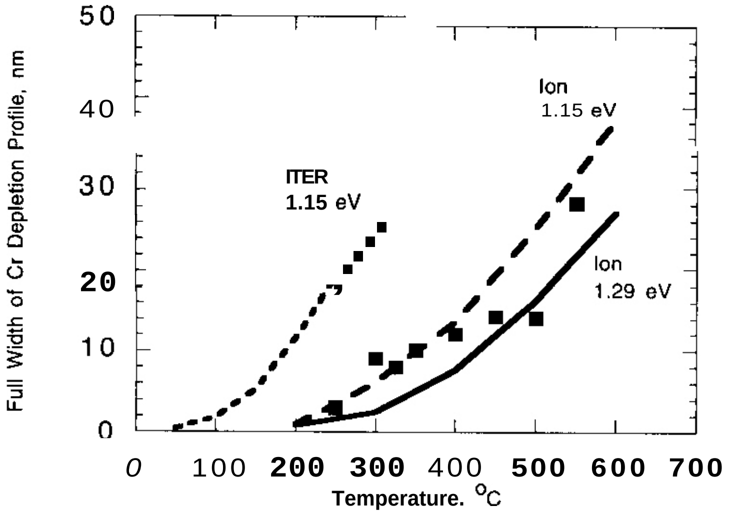

Figure 2. Calculated full width of the Cr depletion profile (defined as 1 wt% less than bulk Cr) is compared to measured values for ion irradiation to 10 dpa as a function of temperature for the adjusted assumption of vacancy migration energy.

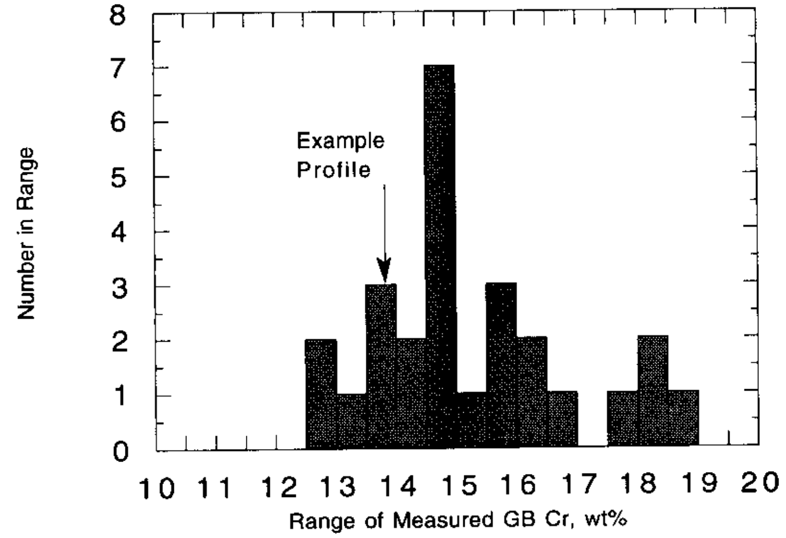

Figure 3. Measured Cr grain boundary concentration histogram for light-water-eactor irradiation of 316SS. The composition for the example profile used in Figure 4 is shown by the arrow.

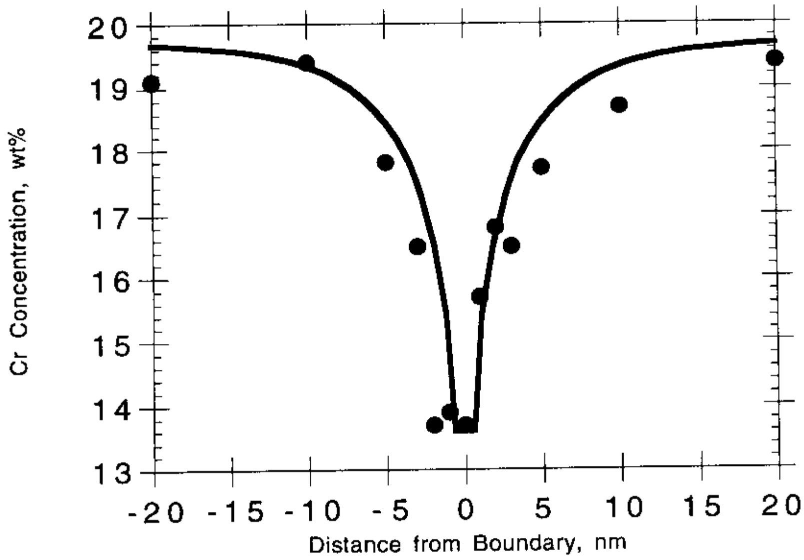

Figure 4. Comparison of the predicted Cr profile with an example measured Cr concentration profile for 316SS irradiated in a boiling-water-reactor at 288°C to about 3 dpa.

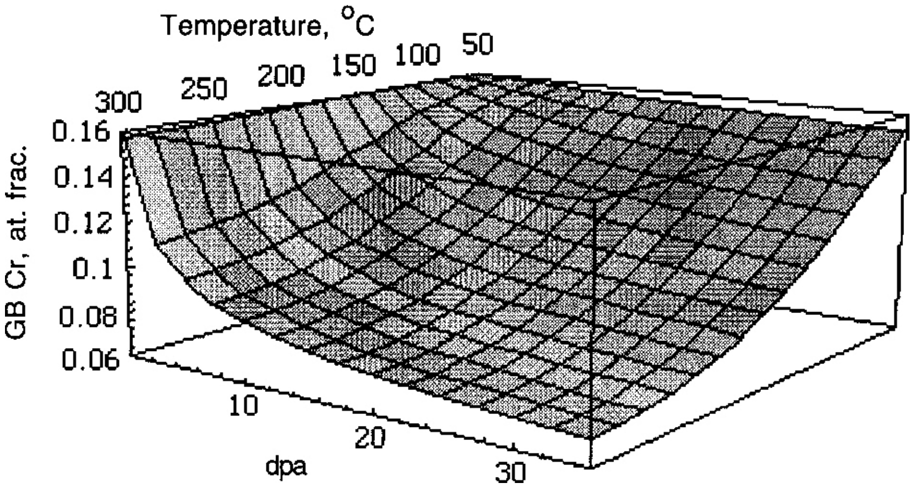

Figure **5.** Predicted temperature and dose dependence of grain boundary Cr concentration for ITER irradiation dose rates. A vacancy migration energy of **1.15** eV and a damage efficiency of **0.01** were assumed.

The predicted low-temperature behavior for ITER conditions is also shown in Figure **1** and in Figure **5.** A vacancy migration energy of 1.15 eV was assumed based on the model calibration to the temperature dependent ion data and a damage efficiency of **0.01** was assumed based on the model calibration to neutron data at 288°C. The difference **in** dose rate between ions, **5** x 10^{-3} dpa/s, and ITER, 3 x 10^{-7} dpa/s,[7] causes an expected downward temperature shift of about 200°C in the Cr depletion predictions for ITER compared to ion irradiation. For the ITER predictions, the assumed alloy compositions were 71, **16,** and **13** wt% for Fe, Cr, and Ni, respectively.

Discussion of Low Temperature Effects

Measured Cr grain boundary concentration as a function of temperature indicates that significant segregation occurs at temperatures from **300** to 400°C for the case of high-rate ion irradiation. When these temperature dependent observations are projected to the case of low-rate neutron irradiation, segregation is predicted to occur at neutron temperatures below 300°C as shown in Figures **1** and **5.** When the reference parameters were assumed, the predicted Cr grain boundary concentrations were overestimated compared to measured ion values. Changing the assumed vacancy migration energy from **1.29** to **1.15** eV improved the comparison of model and measured grain boundary Cr concentrations as well as for depletion profile widths. The lesser activation energy resulted in increased vacancy mobility such that vacancy loss by mutual recombination is reduced. A larger fraction of vacancies survive recombination and succeed in migrating to grain boundaries. Migration of a large number of vacancies to grain boundaries is a necessary condition for radiation-induced Cr depletion.

Measured grain boundary Cr concentrations for ion irradiations greater than 400°C were higher than expected from the kinetic model. Model predictions indicate that the grain boundary Cr concentrations should not increase with increasing temperature until temperatures are above 600°C. The irradiated grain boundaries at and above 500°C may have experienced some migration during irradiation. Detailed examination of profiles indicate a degree of asymmetry suggesting some grain boundary migration. A moving boundary is expected to disturb steep concentration gradients, although this effect has not been quantified.

Observed Cr depletion at 288°C and at 3 dpa is predicted to occur at lower temperatures and at higher dpa as shown in Figure 5. The calculations suggest that the depletion may occur even to temperatures less than 100°C. The model predictions indicate the need to evaluate grain boundary concentrations after high-dose, low-temperature irradiation to establish the magnitude of irradiation effect on grain boundary microchemistry.

Conclusiong

Significant depletion measured at temperatures below 400°C for ion irradiation strongly suggests that significant segregation measured at 288°C for neutron irradiation should persist at temperatures below 288°C. A rate theory model has been used to account for temperature and dose rate differences between ion irradiation measurements and ITER irradiation predictions. Ion irradiation clearly shows that radiation-induced Cr depletion does not vanish at reduced temperatures as low as **50°C.** The model was shown to be consistent with the temperature dependence for ion-induced segregation profiles and to be consistent with neutron-induced segregation at 288°C. Therefore, grain boundary compositions are expected to be affected by irradiation below 200°C and should be evaluated to assess possible concerns for IASCC in water-cooled ITER designs.

FUTURE WORK

Temperature dependencies for ion-induced segregation and neutron-induced segregation will be further evaluated using rate theory models for segregation. Mechanisms for temperature dependent defect processes on low-temperature irradiation response will be related ***to*** potential ITER irradiation and structural material requirements.

ACKNOWLEDGEMENTS

This work was supported by the U.S. Department of Energy Office of Fusion Energy and the Office of Basic Energy Sciences under contract DE-AC06-76RLO 1830.

REFERENCES

1. P. L. Andresen, F. P. Ford, S. M. Murphy, and J. M. Perks, "State of Knowledge of Radiation Effects on Environmental Cracking in Light Water Reactor

Core Materials," Proc. 4th Int. Symp. on Environmental Degradation of Materials in Nuclear Power Systems - Water Reactors, ed. D. Cubiciotti, Jekyll Island, GA, August 1989, NACE, Houston, 1990, p. 1-83.

2. P. L. Andresen, "Irradiation-Assisted Stress Corrosion Cracking," Stress Corrosion Cracking, ed. R. H. Jones, ASM International, Metals Park, OH, 1992.

3. E. P. Simonen, R. H. Jones and S. M. Bruemmer, J. Nucl. Mat., 191-194, 1002 (1992).

4. J. M. Perks and S. M. Murphy, "Modeling the Major Element Radiation-Induced Segregation in Concentrated Fe-Cr-Ni Alloys, "Proc. Materials for Nuclear Reactor Core Applications, Vol. 1, BNES, London, 1987, p. 199.

5. S. M. Bruemmer, M. D. Merz and L. A. Charlot, J. Nucl. Mater., 186, 13 (1991).

6. A. J. Jacobs, G. P. Wozadlo, K. Nakata, S. Kasahara, T. Okada, S. Kawano and S. Suzuki, "The Correlation of Grain Boundary Composition in Irradiated Stainless Steel with IASCC Resistance," Proc. 6th Int. Symp. on Environmental Degradation of Materials in Nuclear Power Systems - Water Reactors, eds. R. E. Gold and E. P. Simonen, San Diego, CA, August The Minerals, Metals and Materials Society, Warrendale, PA 1994, p. 587-604.

7. G. Viedler, A. Cardella, M. Akiba, R. Matera and R. Watson, **Fusion Engineering and Desien**, **16,** 23 (1991).

63 Refractory Metal Alloys

SWELLING AND STRUCTURE OF VANADIUM ALLOYS IRRADIATED IN THE DYNAMIC HELIUM CHARGING EXPERIMENT.

H. M. Chung, B. A. Loomis, H. Tsai, L. Nowicki, J. Gazda, and D. L. Smith (Argonne National Laboratory)

OBJECTIVE

The objective of this work is to determine the effects of dynamically charged He on density change, void distribution, and microstructural evolution of V–4Cr–4Ti irradiated in the Dynamic Helium Charging Experiment (DHCE).

SUMMARY

Combined effects of dynamically charged He and neutron damage on density change, void distribution, and microstructural evolution of V–4Cr–4Ti have been determined after irradiation to 18–31 dpa at 425–600°C in the Dynamic Helium Charging Experiment (DHCE). For specimens irradiated to ≈18 dpa at 600°C with an estimated He/dpa ratio of 3–9 appm He/dpa (a range similar to the fusion–relevant ratio of ≈5 appm He/dpa), only a few microvoids were observed at the interface of the grain matrix and some Ti(O,N,C) precipitates. No microvoids were observed either in the grain matrix or near grain boundaries. It seems that most of the dynamically produced He atoms are trapped in the grain matrix without significant void nucleation or growth. In this group of DHCE specimens, density changes were similar to those of non–DHCE (negligible He generation) specimens for a comparable fluence and irradiation temperature. Significant numbers of microvoids in the grain matrix and on localized grain boundaries were present only in specimens irradiated to ≈31 dpa at 425°C in high–tritium capsules, in which an excessive amount of helium was generated (estimated He/dpa ratio of 10–35 appm). Discontinuous regions of void segregation on grain boundaries were observed, and void number–density was significantly lower than in other alloys irradiated in tritium–trick experiments. The grain–boundary voids seem to have heen produced by decay of tritium segregated to grain boundaries in the specimens at the onset of irradiation in high–tritium capsules (an artifact effect similar to tritium charging at 400°C in a tritium–trick experiment), rather than by segregation of He produced in the grain matrix. Density changes of the specimens were significantly higher than those from non–DHCE irradiations. Microstructural evolution in V–4Cr–4Ti was similar for DHCE and non–DHCE irradiations, except for void number-density and distribution. As in non–DHCE specimens, irradiation–induced precipitation of ultrafine Ti_5Si_3 was observed for irradiation at 600°C but not at 425°C.

INTRODUCTION

Recent attention in the development of vanadium–base alloys for application in fusion reactor structural components has focused on V-4Cr-4Ti, an alloy reported to exhibit an excellent combination of mechanical and physical properties before and after irradiation.[1–6] An unresolved issue in the performance of the alloy, however, has been the effects of fusion–relevant simultaneous generation of He and neutron–displacement damage (at a ratio of ≈5 appm He/dpa) on density change and void swelling behavior. Helium effects determined for other vanadium–base alloys by means of less fusion–relevant simulation approaches such as tritium–trick,[7–13] cyclotron–injection,[14–18] and boron–doping[18–21] techniques have been inconsistent with regard to concentration of He voids on grain boundaries and the concomitant propensity for intergranular fracture. In the unique Dynamic Helium Charging Experiment (DHCE),[22–24] a fusion–relevant He–to–dpa damage ratio is closely simulated by utilizing transmutation of controlled amounts of ^6Li and a tritium–doped mother alloy immersed in $^6Li + {}^7Li$. This report describes initial results of microstructural characterization and density measurements of V–4Cr–4Ti specimens irradiated to 18–31 dpa at 425400°C in the DHCE.

---

* Work supported by the Office of Fusion Energy, U.S. Department of Energy, under Contract **W-31-109-Eng-38.**

MATERIALS AND PROCEDURES

V–4Cr–4Ti specimens (ANL ID BL–47) were retrieved from DHCE capsules after irradiation to 18–31 dpa at 425400°C in the Fast Test Flux Facility (FFTF).[24] Elemental composition of the V–4Cr–4Ti alloy before irradiation is given in Table 1. Table 2 provides a summary of the irradiation parameters, tritium inventories, and estimated He/dpa ratios; the data are based on calculations by Greenwood[Z5] for the present time, i.e., ≈2 yr after the end of irradiation. The retrieved TEM specimens, containing He, tritium, and hydrogen and exhibiting neutron displacement damage, were cleaned ultrasonically in alcohol prior to density measurements and microstructural analysis. Most of the TEM disks were not annealed at 400°C for 1 h, a customary degassing procedure to expel tritium and hydrogen from Charpy–impact and tensile specimens. A limited number of TEM disks were examined after degassing but none indicated any appreciable difference in void distribution and microstructural characteristics from nondegassed specimens that should contain tritium and hydrogen in addition to He. The irradiated specimens were jet-thinned for TEM in a solution of 15% sulfuric acid–72% methanol–13% butyl cellosolve maintained at –5°C. TEM was conducted with a JEOL 100CX-II scanning transmission electron microscope operating at 100 keV, or with a Philips CM-30 transmission electron microscope operating at 200 keV. Density change was determined from specimen weights measured in air and in research–grade CCl_4.

Table I. Preirradiation elemental composition of V–4Cr–4Ti (ANL ID BL–47) irradiated in DHCE

	Nominal Composition	Impurity Composition (wppm)							
Alloy ID	(wt.%)	O	N	C	Si	S	P	Nh	Mo
BL-47	V–4.1Cr–4.3Ti	350	220	200	870	20	<40	<100	<100

MICROSTRUCTURE AND VOID DISTRIBUTION

Microstructural characteristics of the DHCE specimens irradiated to ≈18 dpa at 600°C in a low–tritium capsule (Capsule 5C1, 16 Ci of tritium charged, estimated He of 60–200 appm at this time) are shown in Fig. 1. These specimens contained few voids, except at interfaces between the grain matrix and a limited number of Ti(O,N,C) precipitates (Fig. 1A). In Fig. 1A, a total of 10 voids =30 nm in size are visible near four Ti(O,N,C) precipitates of a total of 25 precipitates present. In the bright–field image in Fig. 1B are visible dense dislocation loops, line dislocations, ultrafine Ti_5Si_3 precipitates, and large blocky Ti(O,N,C) precipitates. No microvoids are visible near the grain boundary shown in Fig. 1B. These microstructural characteristics are similar to those observed in non–DHCE specimens irradiated under similar conditions (≈28 dpa, 600°C, Fig. ID). Morphologies of Ti_5Si_3 precipitates obtained from specimens irradiated in DHCE (≈18 dpa, 600°C) and non–DHCE (≈28 dpa, 600°C) experiments shown in dark–field images of Figs. 1C and 1E, respectively, are also similar.

For DHCE specimens irradiated to 31 dpa at 425°C in high–tritium Capsule 4D2 (70 Ci of tritium charged), the numberdensity of He microvoids (size ≈5 nm) in the grain matrix was significantly higher than that for the specimens irradiated in low–tritium Capsule 5C1. Number–density near some grain boundaries in specimens irradiated in Capsule 4D2 was higher than in the grain matrix, although it was still significantly lower than those observed in other alloys irradiated in tritium–trick experiments.[7–12] This is shown in Fig. 2A. However, the void density near most grain boundaries was similar to that in the grain matrix. Specimens irradiated in Capsule 4D2 were also characterized by extremely thin (≈5 nm) shells of voids that surround some Ti(O,N,C) precipitates (Fig. 2B). For specimens irradiated to 31 dpa at 425°C in the high–tritium Capsules 4D1 (99 Ci of tritium charged), number–densities of He microvoids (size ≈5 nm) in the grain matrix and near grain boundaries were similar, except for very limited portions of some grain boundaries.

Table 2 Summary of Irradiation Parameters of Dynamic Helium Charging Experiment (DHCE)

	Irradiation	Fluence	Total	Ratio[d] at EOI[e] (Assumed k_a or k_w)[f]			Tritium Inventory with Leakage (Ci)				Total Tritium Activity during	(appm)/dpa Ratio for PIE, 3/94[i]	
Capsule ID No.	Temp. (°C)	(E >0.1 MeV) (10^{22} n·cm^{-2}	Damage[c] (dpa)	k_a=0.073 (k_w=0.01)	0.220 (0.03)	0.734 (0.10)	BOI[e] 5/91	EOI[g] 3/92	EOHS[h] 1/92	PIE 3/94	Processing (Ci)	kw 0.01	kw 0.03
4D1	425	6.4[a]	31	3.8	–	23.2	99	105	101	93	46.0	13.5	35
4D2	425	6.4[a]	31	2.8	7.3	17.4	70	77	74	68	38.1	9.9	26
5E2	425	3.7[b]	18	2.1	–	12.5	26	26	25	23	3.2	7.1	18
5D1	500	3.7[b]	18	4.4	–	29	73.5	76	73	68	–	15.2	39
5E1	500	3.7[b]	18	3.1	–	20.2	57	52	50	46	24.0	–	–
5C1	600	3.7[b]	18	1.1	2.9	6.7	16.4	15.9	15	14	7.2	3.6	9

[a] FFTF Level 4, fast neutron flux ≈3.64 x 10^{15} n·cm^{-2}s^{-1} (E >0.1 MeV).

[b] Level 5, fast neutron flux ≈2.08 x 10^{15} n·cm^{-2}s^{-1} (E >0.1 MeV).

[c] Calculated for V–4Cr–4Ti.

[d] L. R. Greenwood "Revised Calculations for the DHCE Experiment," April 30, 1993.

[e] Beginning of irradiation (BOI) May 27, 1991; end of irradiation (EOI) March 19, 1992; 203.3 effective–full–power days (EFPD).

[f] Equilibrium ratio (k_a by atom, k_w by weight) of tritium in vanadium alloy to that in the surrounding liquid Li.

[g] Letter from L. R. Greenwood to H. Matsui, "Tritium Calculations for the DHCE Experiment," November 20, 1993.

[h] End of hot standby at ≈220°C, November 1992.

[i] Based on letter from L. R. Greenwood to H. M. Chung, "DHCE Calculations for Actual Run Conditions," May 4, 1994.

This is shown in Fig. 2C. The number-density in the grain matrix was similar to that **in** specimens irradiated in Capsule 4D2. Because charged tritium **and** calculated He contents were similar for specimens irradiated in Capsules **4D1** (99 Ci and 400–1000 appm) and **4D2** (70 Ci and 300–800 appm), similar void–swelling behavior is expected

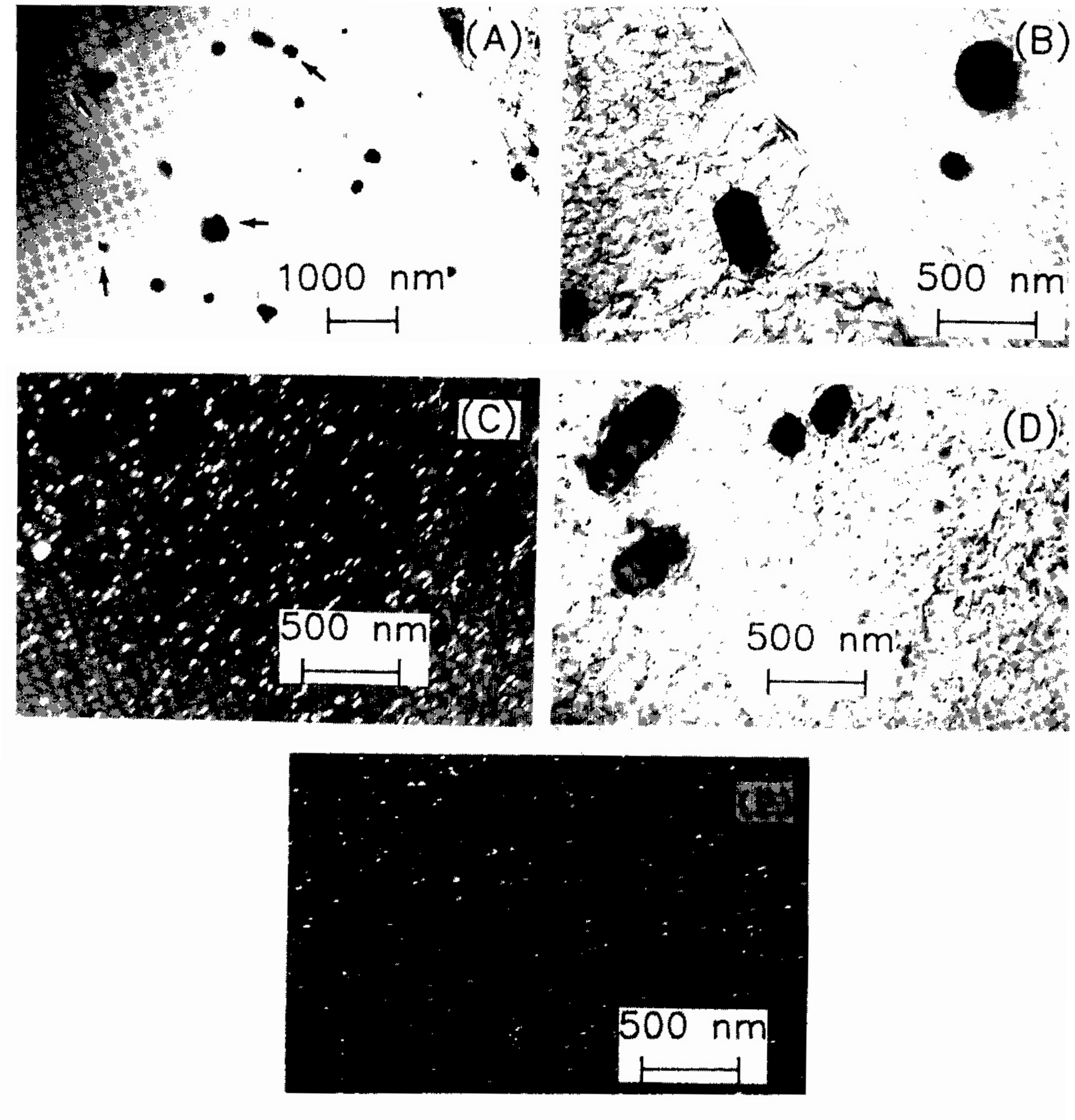

Figure 1.** **Microstructure** of V-4Cr-4Ti **irradiated at** 600°C to≈18 **dpa in DHCE (Capsule** 5C1): **(A) voids near** Ti(O,N,C); (B) **dislocations, dislocation loops, and** Ti_5Si_3; (C) **dark–field image of** Ti_5Si_3. (D) **and (E) are similar** to (B) **and** (C), respectively, **but from non–DHCE specimens irradiated at 600% ***to*** =28 ***dpa.***

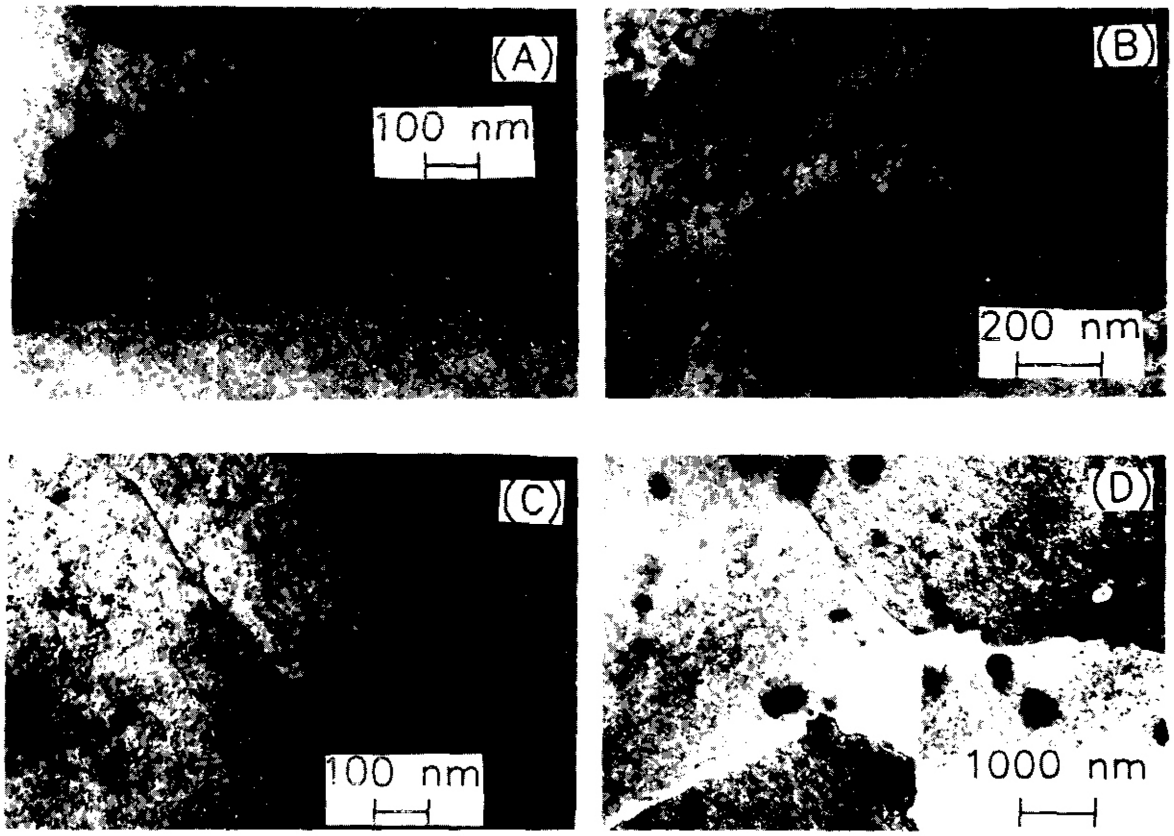

Figure 2. Microstructure of V-4Cr-4Ti irradiated at 425°C io ≈31 dpa in DHCE (Capsules 402 and 4D1): (Ai voids neur grain boundary, 402: (B) void shells surrounding Ti(O,N,C), 402; (C) similar void distributions in grain matrix and near grain boundaries, 401; and (O) low-magnification of grains und Ti(O,N,C), 4D1

As in non–DHCE specimens? Ti_5Si_3 did not precipitate during irradiation at 425°C in the DHCE. If Ti_5Si_3 precipitation wds indeed significant for 425°C irradiation, void swelling at this temperature would have been suppressed significantly as in non–DHCE specimens of V–18Ti and V–20Ti irradiated at 420°C.^{26}

Because of the high level of initial tritium charged in Capsules 4DI and 4D2, a significant amount of tritium should have transferred from the mother alloy to liquid Li at 425°C and to the V–4Cr–4Ti specimens soon after startup of irradiation. High diffusivity of tritium at 425°C should result in an equilibrium partitioning among the mother alloy, Li, and the specimens at a relatively early period before accumulation of appreciable dpa and He in the specimens. Initial tritium contents in V–4Cr–4Ti specimens are estimated to he as high as several thousand appm in Capsules 4D1 and 4D2 at the beginning of irradiation (i.e., 425°C, ≈0 dpa). During tritium–trick charging at high concentration in vanadium alloys at ≈400°C, tritium is suspected to segregate preferentially near grain boundaries even before irradiation.$^{7-12}$ A similar situation seems to have occurred in DHCE specimens irradiated at 425°C in high–tritium Capsules 4D1 and 4D2. Thus, for specimens irradiated in these capsules, which were designed to produce an intentionally high He appm/dpa ratio of ≈10 instead of a fusion–relevant ratio of 5 He appm/dpa, an unintended artifact effect seems to have been introduced. However, grain–boundary accumulation of He voids was limited to local regions and was not as pronounced as in tritium–trick specimens. Because of these limitations, no intergranular separation was observed in specimens fractured at low temperatures.^{27}

DENSITY CHANGE

Results of density measurements for specimens irradiated at 600°C (18 dpa in Capsule 5C1) and at 425°C (18 dpa in Capsule 5E2, and 31 dpa in Capsules 4D1 and 4D2) are given in Figs. 3A and 3B, respectively. Ranges of He contents in the DHCE specimens, calculated by Greenwood for the approximate time of these measurements,[25] are also given in the figure (also see Table 2). The calculated values are strongly dependent on the assumed equilibrium ratio of tritium in Li and the vanadium alloy, and must be considered approximate until results of He analyses are available. For comparison, density changes in non–DHCE specimens for similar irradiation conditions[3] are also shown in the figures.

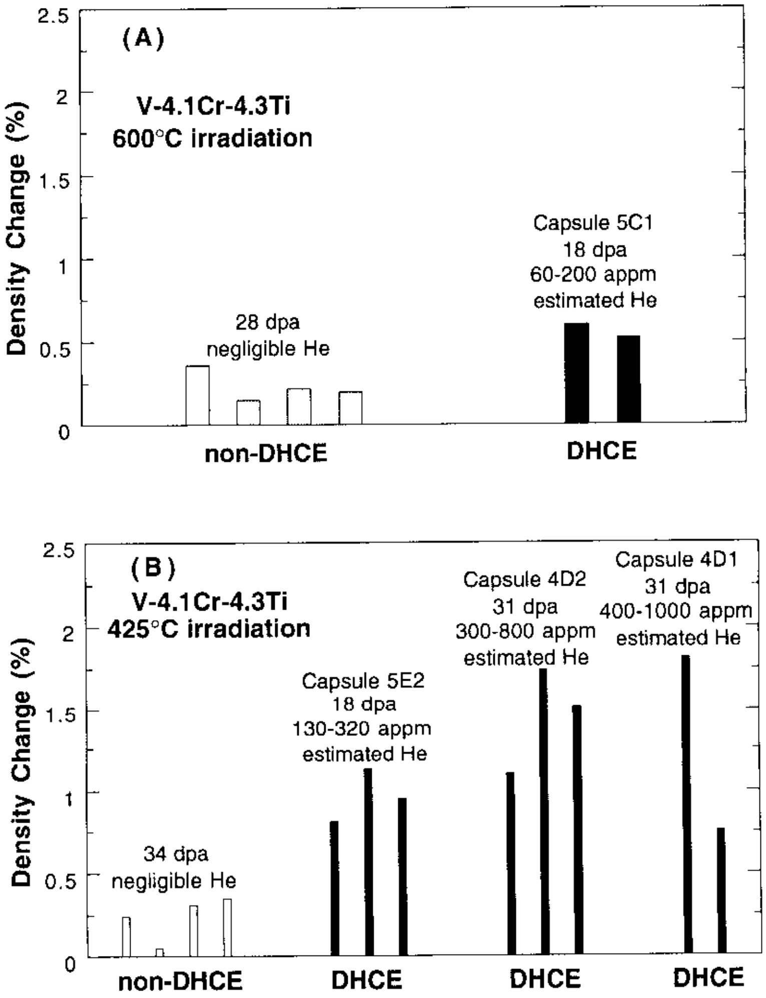

Figure 3. Density changes of V–4Cr–4Ti from DHCE and non–DHCE specimens: (A) 600°C and (B) 425°C

Density changes measured for non–DHCE and DHCE specimens irradiated at 600°C in the low–tritium capsule (5C1) are low (<0.6 %). The estimated ratio of He generation to displacement damage is ≈3.6–9 appm He/dpa (Table 2), a value close to a fusion–relevant ratio of ≈5 He appm/dpa. The small density change seems to be consistent with the negligible number–density of voids shown in Fig. 1.

However, density changes measured for DHCE specimens irradiated at 425°C in high–tritium capsules (4D1 and 4D2) are significantly higher than those of non–DHCE specimens. The estimated ratio of He generation to displacement damage for specimens irradiated in these capsules is ≈10–35 appm He/dpa, a value significantly higher than the fusion–relevant ratio. The relatively large density change for these specimens seems to be consistent with the high number-density of He voids visible in Figs. 2A–2C.

CONCLUSIONS

1. For specimens irradiated to ≈18 dpa at 600°C with an estimated ratio of He generation to displacement damage of ≈3–9 appm He/dpa, similar to a fusion–relevant ratio of ≈5 appm He/dpa, only a limited number of microvoids were observed at the interface between the grain matrix and some Ti(O,N,C) precipitates. No microvoids were observed either in the grain matrix or near grain boundaries. Most of the dynamically produced He atoms seem to be trapped in the grain matrix without significant void nucleation or growth. Density changes in DHCE and non–DHCE (negligible He generation) specimens of V–4Cr–4Ti were similar (<0.6%).

2. Moderate number–densities of microvoids were observed in the grain matrix and on localized regions of grain boundaries in DHCE specimens irradiated to ≈31 dpa at 425°C in high–tritium capsules, in which an excessive amount of He was generated (estimated He/dpa ratio of 10–35 appm). Discontinuous regions of void segregation on grain boundaries were observed, and void number–density was significantly lower than in other alloys irradiated in tritium–trick experiments. The grain–boundary voids seem to have been produced from decay of tritium that segregated to grain boundaries in the specimens at the onset of irradiation in the high–tritium capsules (an artifact effect similar to the tritium charging at 400°C in a tritium–trick experiment). rather than by segregation of He produced in the grain matrix. Density changes of these specimens were significantly higher than those from non–DHCE irradiations.

3. Microstructural evolution in V–4Cr–4Ti was similar for DHCE and non–DHCE irradiations except for void number-density and distribution. As in non–DHCE specimens, irradiation–induced precipitation of ultrafine Ti_5Si_3 was observed at 600 but not at 425°C.

FUTURE WORK

Microstructural characteristics, void–swelling behavior, and density change of V-4Cr-4Ti specimens irradiated in three other DHCE capsules will be determined. Similar analyses will be conducted for V, V–5Ti, V–7Cr–5Ti, and V–3Ti–1Si alloys irradiated in the DHCE.

ACKNOWLEDGMENT

The authors are grateful to L. R. Greenwood for providing updated calculations of He contents in the DHCE specimens.

REFERENCES

1. B. A. Loomis, L. Nowicki, and D. L. Smith, "Effect of Neutron Irradiation on Tensile Properties of V–Cr–Ti Alloys," in Fusion Reactor Materials. Semiannual. Proe. Report, DOE/ER-0313/15, **Oak** Ridge National Laboratory, **Oak** Ridge, TN (1994), pp. 219–222.
2. B. A. Loomis, H. M. Chung, L. Nowicki, and D. L. Smith, "Effects of Neutron Irradiation and Hydrogen on Ductile-Brittle Transition Temperatures of V–Cr–Ti Alloys," ibid., pp. 253–257.
3. H. M. Chung, B. A. Loomis. L. Nowicki, J. Gazda. and D. L. Smith, "Irradiation-Induced Density Change and Microstructural Evolution of Vanadium-Base Alloys," ibid., pp. 223–231.

4. H. Matsui, M. Tanno, J. Garda, and H. M. Chung, “Microstructural Stability of V-4Cr-4Ti During Neutron Irradiation,” ibid., **pp.** 240–246.
5. H. M. Chung, J. Garda, L. Nowicki, J. E. Sanecki, and D. L. Smith, “Effects of Fabrication Variables on Impact Properties and Microstructure of V–Cr–Ti Alloys,” ihid., pp. 207–218.
6. H. M. Chung, B. A. Loomis, and D. L. Smith, “Thermal Creep Behavior of V–5Cr–5Ti and V–10Cr–5Ti Alloys,” in Fusion Reactor Materials. Semiannual. Proe. Report, DOEIER-0313/14, Oak Ridge National Laboratory, Oak Ridge, TN (1993), pp. 309-317.
7. D. N. Braski and D. W. Ramey, in Effects of Radiation on Material Pronerties, ASTM-STP 870, F. A. Garner and J. S. Perrin, eds., American Society for Testing and Materials, Philadelphia. 1985, pp. 1211–1224.
8. D. N. Braski, in Influence of Radiation on Material Properties, ASTM-STP 956, F. A. Garner, C. H. Henagcr, and N. Igata, cds., American Society for Testing and Materials, Philadelphia, 1987. pp. 271-290.
9. D. N. Braski, J. Nucl. Mater. **141-143** (1986) 1125.
10. D. N. Braski, in Reduced Activation Materials for Fusion Reactors, ASTM-STP 1047 (1988) **pp.** 161-178.
11. H. Matsui, M. Tanaka, M. Yamamoto, and M. Tada, J. Nucl. Meter. **191-194** (1992) 919.
12. M. Satou, K. Abe, and H. Matsui, J. Nucl. Mater. **191-194** (1992) 938
13. M. Tanaka and H. Matsui, Mater. Trans., JIM, **34** (1993) 1083.
14. W. van Witzcnburg, A. Mastenhroek, and J. D. Ellen, J. Nucl. Matcr. **103-104** (1981) 1187.
15. M. P. Tanaka, E. E. Bloom, and J. A. Horak, J. Nucl. Mater. **114** (1981) 895.
16. M. L. Grossheck and J. A. Horak, in Influence of Radiation on Material Properties, ASTM-STP 956 (1986) 291.
17. J. M. Vitck, D. N. Braski, and J. **A.** Hordk, J. Nucl. Mater. **141-143** (1986) 982.
18. W. van Witzenburg and E. de Vries, in Effects of Radiation on Materials. ASTM-STP 1125 (1990).
19. L. L. Horton and K. Farrell, J. Nucl. Matcr. **122-123** (1984) 687.
20. H. Kawanishi and S. Ishino, in Reduced Activation Materials for Fusion Reactors, ASTM-STP 1047 (1988), **pp.** 179-189.
21. H. Kawanishi, Y. Arai. and S. Ishino, J. Nucl. Mater. **191-194** (1992) 933
22. D. L. Smith, H. Matsui, L. R. Grccnwood, and B. A. Loomis, J. Nucl. Mater. **155-157** (1988) 1359
23. D. L. Smith, B. A. Loomis, H. Matsui, M. L. Hamilton, K. L. Pcarce. J. P. Kopasr, C. E. Johnson, R. ***G.*** Clemmer. and L. R. Greenwood, in Fusion Reactor Materials. Semiannual. Proe. Rep. DOEIER-0313/10, Oak Ridge National Laboratory, Oak Ridge, TN (1991), p. 159.
24. H. Tsai, R. V. Strain, H. M. Chung, and D. L. Smith. “Status of Dynamic Helium Charging Experiment (DHCE),” in this report.
25. Letter from L. R. Greenwood to H. M. Chung, “DHCE Calculations for Actual Run Conditions,” May 4, 1994.
26. H. M. Chung, B. A. Loomis, and D. L. Smith, in Effccts **of** Radiation on Materials, ASTM-STP 1175, A. S. Kumar, D. S. **Gelles,** R. K. Nanstad, and T. **A.** Little, eds., American Society for Testing and Materials, Philadelphia, 1993, **pp.** 1185–1200.
27. H. M. Chung, B. A. Loomis, H.-C. Tsai, L. Nowicki, D. Busch, and D. L. Smith, “Effect of Dynamically Charged Helium on Mechanical Properties of V–4Cr–4Ti,” in this report.

EFFECT OF DYNAMICALLY CHARGED HELIUM ON MECHANICAL PROPERTIES OF V–4Cr–4Ti[*]

H. M. Chung, B. A. Loomis. H. Tsai, L. Nowicki, D. E. Busch, and D. L. Smith (Argonne National Laboratory)

OBJECTIVE

The objective of this work is to determine the effect of dynamically charged helium on ductile–brittle transition temperature (DBTT) of V–4Cr–4Ti alloy, based on miniature specimens irradiated to 18–31 dpa at 425–600°C in the Dynamic Helium Charging Experiment (DHCE).

SUMMARY

V-4Cr-4Ti has been reported to be virtually immune to irradiation embrittlement under conditions of negligible helium generation; DBTTs determined from one–third–size Charpy–impact specimens irradiated in a non–DHCE experiment were <–200°C. The effects of dynamically charged helium and tritium, and of neutron damage, on DB'M of the alloy were determined after irradiation in the Dynamic Helium Charging Experiment (DHCE). TEM disks irradiated to 18–31 dpa at 425–600°C were fractured by repeated bending in a low–temperature bath. Miniature specimens were used because no Charpy–impact specimens were included in the DHCE experiment. Ductile–brittle transition behavior was determined from quantitative SEM fractography. Brittle fracture surface morphology was not observed at >–120°C regardless of the level of dpa damage or helium and tritium content in the alloy. Predominantly brittle–cleavage fracture morphologies were observed only at –196°C in some specimens irradiated to 31 dpa at 425°C and in which the estimated helium and tritium contents were highest. This indicates a DBTT between –175 and –200°C in specimens containing the highest levels of dpa damage, helium, and tritium in the DHCE experiment. No intergranular fracture was observed.

INTRODUCTION

Recent attention has focused on V-4Cr-4Ti for fusion reactor structural components because of its excellent combination of mechanical and physical properties before and after irradiation.[1–6] However, no data have been reported on effects of simultaneous generation of helium and neutron displacement damage under fusion–relevant conditions (i.e., ≈5 appm He/dpa ratio), although helium effects on other vanadium–base alloys have been investigated by simulation techniques such as tritium-trick,[7–11] cyclotron-injection,[12–16] and boron-doping.[16–19] In the Dynamic Helium Charging Experiment (DHCE),[20–22] the fusion–relevant helium–to–dpa damage ratio is closely simulated by utilizing slow transmutation of controlled amounts of ^{6}Li and a tritium–doped mother alloy immersed in ^{6}Li + ^{7}Li.

MATERIALS AND PROCEDURES

Vanadium–alloy specimens were retrieved from DHCE capsules after irradiation to 18–31 dpa at 425–600°C in the Fast Test Flux Facility (FFTF).[22] Summaries of DHCE capsule loading and irradiation parameters are given in Tables 1 and 2. respectively. The specimens contain helium, tritium, and hydrogen and have undergone neutron displacement damage. Concentrations of the elements are being measured as a part of the postirradiation examination (PIE); estimated He contents and He/dpa ratios are given in Table 2, based on extensive calculations by Greenwood.[23–25]

---

[*] Work supported by the Office of Fusion Energy, U.S. Department of Energy, under Contract W–31–109–Eng–38

TEM disks of the V–4Cr–4Ti alloy retrieved from the DHCE capsules were sorted, identified, and cleaned ultrasonically in a bath of alcohol prior to PIE (i.e., density measurement, TEM microstructural analysis, bend test, and quantitative **SEM** fractography). Chemical composition of the alloy is given in Table 3. Some disks were annealed at 400°C for 1 h in vacuo at 2 x 10^{-6} Pa to expel tritium and hydrogen before bend testing. However, most specimens were tested without degassing, and hence should contain considerable tritium and helium.

Table I. Summary of Capsule-Loading Parameters of the Dynamic Helium Charging Experiment (DHCE)

Capsule ID No.	Irradiation Temp. (°C)	Total Weight (g)			Fraction of ^{6}Li (%)	Initial Tritium Charged[a]		He (appm) to dpa ratio at EOI[c] (for assumed k_W)[d]		
		Vanadium[a]	Specimen[b]	Lithium		(Ci)	(mmol)	0.01	0.03	0.10
4D1	425	1.5468	5.86	0.765	5.0	99	1.70	3.8	–	23.2
4D2	425	1.5536	5.38	0.765	4.5	70	1.20	2.8	7.3	17.4
5E2	425	1.5657	5.38	0.670	1.0	26	0.45	2.1	–	12.5
5D1	500	1.5727	5.77	0.938	6.5	73.5	1.26	4.4	–	**29**
5E1	500	1.5651	5.82	0.952	1.0	57	0.98	3.1	–	20.2
5C1	600	1.5656	5.82	0.808	8.0	16.4	0.28	1.1	2.9	6.7
5C2	600	1.5466	5.95	0.955	8.0	18	0.31	1.1	–	6.8

[a] Letter from C. E. Johnson to K. Pearce, April 23, 1991, 1 mmol = 58.3 Ci.

[b] Excluding tritium-charged mother alloy.

[c] Beginning of irradiation May 27, 1991; end of irradiation **(EOI)** March 19, 1992; 203.3 effective–full–power days.

[d] Equilibrium ratio (by weight) **of** tritium in vanadium alloy to that in the surrounding liquid Li. "Revised Calculations for the DHCE Experiment," L. R. Greenwood, April 30, 1993.

Fracture behavior of TEM disks was determined by repeated bending in low–temperature baths of liquid nitrogen or mixtures of dry ice and acetone. Temperature of the surrounding liquid was measured with a calibrated thermocouple. Approximately one–third of each side of a disk specimen was firmly held by two grips in the test bath and the middle portion of the disk was bent repeatedly until fracture. Thus, the specimen constraint was similar to that in a four–point bend test. Depending **on** irradiation conditions and test temperature, 2 to 62 bends were required to produce fracture in the specimens at –196 to 50°C. **At** a given test temperature, cold–work accumulated in the specimen with the number of bends. After fracture, morphology of the fracture surface was examined quantitatively by **SEM.** A few dozen SEM fractographs were taken at ≈300 **X,** and a composite of the whole fracture surface was made. Four types of fracture morphology were observed: cleavage, quasicleavage, ductile-dimple, and fibrous ductile fracture. From the fracture surface composite, the percentage of ductile-fracture morphology was measured for each specimen with a planimeter.

RESULTS AND DISCUSSION

As reported **previously,**[2,5] brittle fracture of V–4Cr–4Ti did not occur at temperatures >–196°C in impact tests on one–third–sire Charpy specimens in the nonirradiated condition or after irradiation to 24–34 dpa at 425–600°C in the non–DHCE experiment (i.e., negligible He/dpa ratio). Consistent with this behavior, only ductile fracture was observed from the present multiple–bend tests on nonirradiated TEM disks of the alloy in a similar temperature range. This is shown in Fig. 1.

ble 2. *Summary of Irradiation Parameters of the Dynamic Helium Charging Experiment (DHCE)*

Capsule ID No.	Irradiation Temperature (°C)	Fluence (E >0.1 MeV) (10^{22} n·cm^{-2})	Total Damage[c] (dpa)	He (appm) to dpa Ratio[d] at EOI[e] (Assumed k_a or k_w)[f] k_a=0.073 (k_w=0.01)	0.220 (0.03)	0.734 (0.10)	Tritium Inventory with Leakage (Ci) BOI[e] 5/91	EOI[g] 3/92	EOHS [h]11/92	PIE 3/94	Total Tritium Activity during Processing (Ci)	Estimated He (appm) to dpa Ratio (for k_w = 0.03)[i] EOI 3/92	4/93	PIE 3/94
4D1	425	6.4[a]	31	3.8	–	23.2	99	105	101	93	46.0	9.9	23.7	35
4D2	425	6.4[a]	31	2.8	7.3	17.4	70	77	74	68	38.1	7.3	17.6	26
5E2	425	3.7[b]	18				26	26	25	23	3.2	5.5	12.8	18
5D1	500	3.7[b]	18	4.0		29	3.5	76	73	[illegible]	–	11.5	26.8	–
5E1	500	3.7[b]	.3	[illegible]		20.2	7	52	50	4[illegible]		8.1	17.7	–
5C1	600	3.7[b]	18	1.1	2.9	6.7	16.4	15.9	15	14	7.2	2.9	6.5	17
5C2	600	3.7[b]	18	1.1	–	6.8	18	18	17	16	12.2	2.9	6.5	–

[a] FFTF Level 4, fast neutron flux ≈3.64 x 10^{15} n cm^{-2}s^{-1} (E > 0.1 MeV).

[b] Level 5, fast neutron flux ≈2.08 x 10^{15} n cm^{-2}s^{-1} (E > 0.1 MeV).

[c] Calculated for V–4Cr–4Ti.

[d] L. R. Greenwood "Revised Calculations for the DHCE Experiment," April 30, 1993.

[e] Beginning of irradiation (BOI) May 27, 1991; end of irradiation (EOI) March 19, 1992; 203.3 effective full power days (EFPD).

[f] Equilibrium ratio (k_a by atom, k_w by weight) of tritium in vanadium alloy to that in the surrounding liquid Li.

[g] Letter from L. R. Greenwood to H. Matsui, "Tritium Calculations for the DHCE Experiment," November 20, 1993.

[h] End of hot standby at ≈220°C, November 1992.

"DHCE Calculations for Actual Run Conditions," May 4, 1994.

Table 3. Composition of V–4Cr–4Ti alloy (ANLID BL–47) irradiated in DHCE experiment

	Nominal Composition	Impurity Composition (wppm)							
Alloy ID	(wt.%)	O	N	C	Si	S	P	Nb	Mo
BL-47	V–4.1Cr–4.3Ti	350	220	200	870	20	<40	<100	<100

The percentage of fracture surface of DHCE–irradiated TEM–disk specimens at 600°C and 425°C with ductile–fracture morphology is plotted as a function of test temperature in Figs. 2 and 3, respectively. For comparison, similar results obtained for nonirradiated and irradiated non–DHCE specimens (containing negligible amounts of He, T, and H) are also shown in the figures. As indicated, the percentage of brittle–cleavage morphology in specimens from Capsule 5C1 (600°C, 18 dpa, and 16.4 Ci of tritium charged) was higher for tests at –196°C than for specimens from Capsule 5E2 (425°C, 18 dpa, and 26 Ci of tritium charged) despite the higher irradiation temperature and the lower level of tritium charged in the former capsule. However, actual tritium release during processing of the two capsules[Zh] was higher for Capsule 5C1 than for 5E2. This is shown in Fig. 4.

The results in Figs. 2 and 3 show that the percentage of brittle cleavage measured from fracture surfaces produced at –196°C generally was more pronounced in specimens retrieved from high–tritium capsules (e.g., 4DI and 4D2) than in specimens retrieved from low–tritium capsules (e.g., 5E2 and 5C1). However, at >–125°C, all specimens exhibited only ductile fracture. The results in Figs. 2 and 3 indicate that the DBTTs for specimens irradiated at 600 and 425°C are between –225 and –200°C, and –200 and –175°C, respectively.

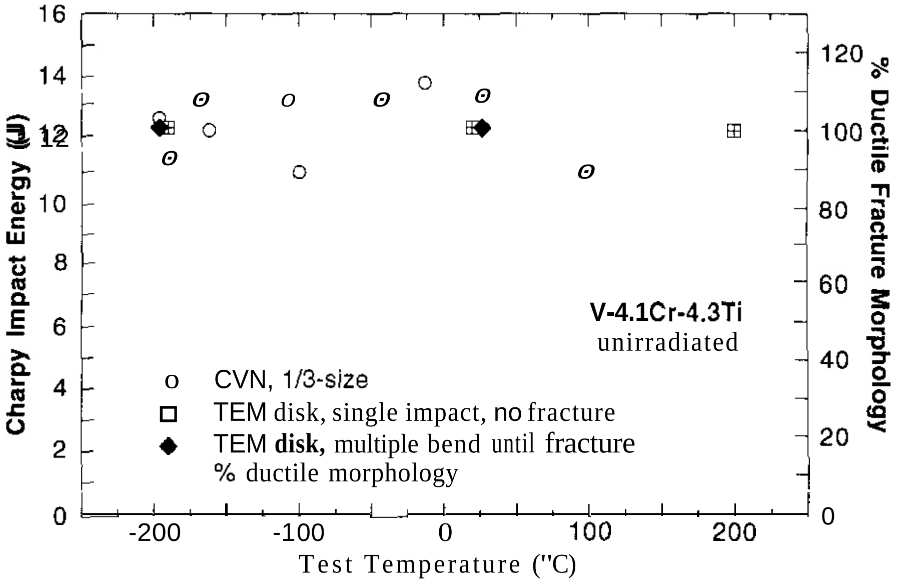

Figure 1. Ductile behavior of nonirradiated V–4Cr–4Ti from impact tests of one–third–size Charpy specimens (CVN) and multiple–bend tests of TEM disks

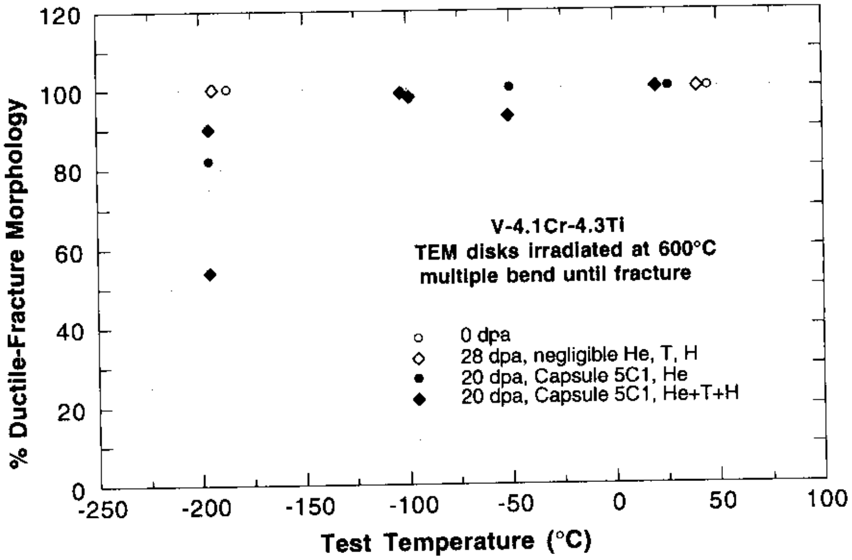

Figure 2. Percent ductile-fracture morphology of DHCE specimens irradiated at 600°C vs. test temperature. Results from nonirradiated and non-DHCE specimens are shown for comparison.

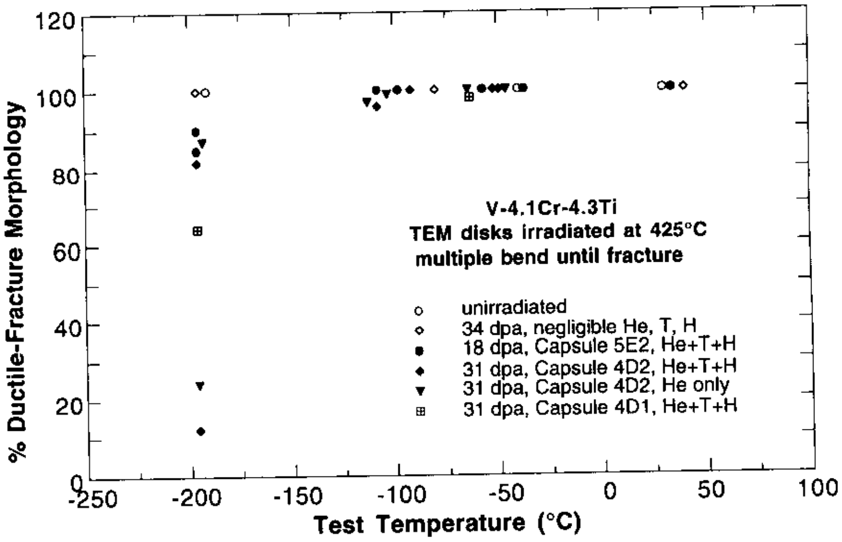

Figure 3. Percent ductile-fracture morphology of DHCE specimens irradiated at 425°C vs. test temperature. Results from nonirradiated and non-DHCE specimens are shown for comparison.

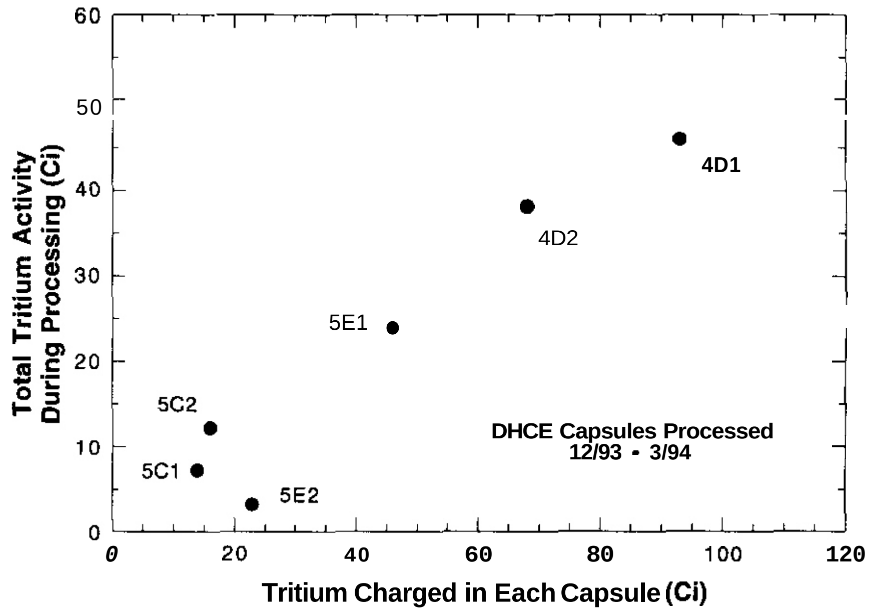

Figure 4. Comparison of tritium release measured during processing, and amount of tritium charged in each DHCE capsule before irradiation

Helium microvoids were negligible in specimens retrieved from Capsule 5C1 (16.4-Ci tritium charged and irradiated to 18 dpa at 600°C), and only a few He bubbles were observed at the interface between the grain matrix and some Ti(O,N,C) precipitates that are normally present in V–Ti and V–Cr–Ti alloys.[27] For specimens irradiated to **31** dpa at 425°C (retrieved from Capsules 4D1, 99 Ci tritium charged and 4D2, 70 Ci tritium charged), the number-density of He microvoids in the grain matrix was higher than that for specimens from Capsule 5C1. The numberdensity near grain boundaries was somewhat higher than in the grain matrix,[27] although it was still significantly lower than those observed in other V–base alloys irradiated in tritium–trick experiments.[7–11] Because of the high level of initial tritium charged in Capsules 4D1 and 4D2, significant tritium should have transferred from the mother alloy to liquid Li at 425°C, and to the specimens soon after the startup of irradiation hut before accumulation of appreciable dpa and helium. Initial tritium contents in V–4Cr–4Ti specimens loaded in Capsules 4D1 and 4D2 in this situation (425°C, ≈0 dpa) are estimated to be as high as several thousand appm. At such high levels, tritium has been known to segregate preferentially near grain boundaries during tritium–trick charging of V alloys at ≈400°C.[7–11] A similar situation seems to have occurred in specimens irradiated at 425°C in Capsules 4D1 and 4D2 containing high tritium levels (70–99 Ci). These capsules were designed to produce an intentionally high He appm/dpa ratio of ≈10 instead of the fusion–relevant ratio of **5** He appm/dpa. However, an unintended side effect of tritium accumulation at specimen grain–boundaries seems to have occurred. Despite this, intergranular fracture was not observed in any of the irradiated specimens shown in Figs. 2 and 3. An example of mixed ductile and cleavage–fracture–surface morphologies, observed for specimens irradiated at 425°C to 31 dpa (Capsule 4D2), is shown in Fig. **5**.

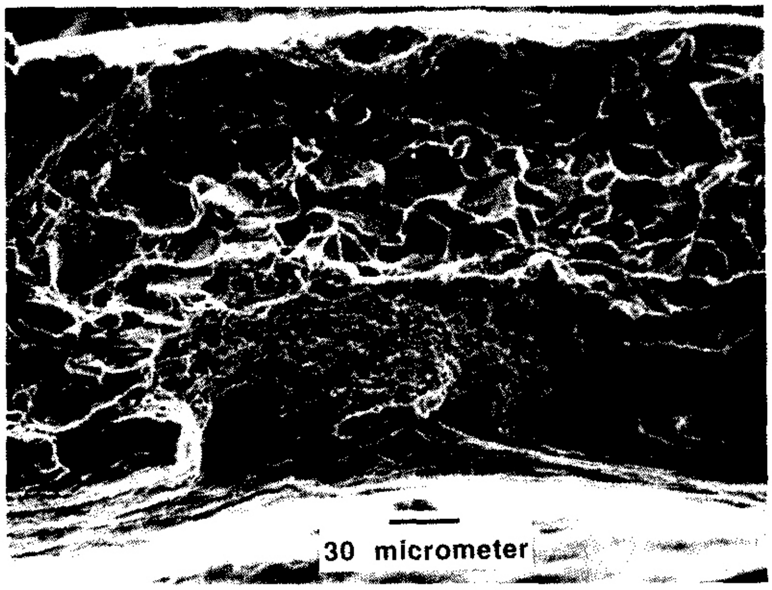

Figure 5. Example of mixed ductile and cleavage fracture surface morphologies observed in specimens irradiated at 425°C to 31 dpa and testedut -196°C

CONCLUSIONS

1 Effects of dynamically charged helium, neutron damage, and retained tritium on DBTT of V-4.1Cr-4.3Ti alloy were determined after irradiation in the Dynamic Helium Charging Experiment (DHCE). TEM disks irradiated at 425-600°C to 18-31 dpa, which contain 100-900 appm helium (estimated) and an unknown amount of tritium, were fractured by repeated bending while submerged in low-temperature baths. Ductile-brittle transition temperature. based on quantitative SEM fractography of ductile and brittle fracture surface morphologies, was between -175 and -200°C in specimens irradiated at 425°C to 31 dpa and <-200°C in specimens irradiated at 600°C to 18 dpa.

2 Neither partial nor predominantly intergranular fracture was observed in any of the specimens irradiated under the most severe conditions of the experiment. Predominantly cleavage fracture was observed at -196°C in some specimens irradiated at 425°C to 31 dpa in which the levels of helium (estimated to he 400-900 appm) and tritium were highest.

FUTURE WORK

Similar bend tests will he conducted on broken tensile specimens (0.76 mm thick) after tensile tests at room temperature and at the irradiation temperatures (425-600°C).

REFERENCES

1. B. A. Loomis, L. Nowicki. and D. L. Smith, "Effect of Neutron Irradiation on Tensile Properties of V-Cr-Ti Alloys," in Fusion Reactor Materials, Semiannual. Prog. Report, DOE/ER-0313/15, Oak Ridge National Laboratory, Oak Ridge, TN (1994), pp. 219-222.

2. B. A. Loomis, H. M. Chung, L. Nowicki, and D. L. Smith, "Effects of Neutron Irradiation and Hydrogen on Ductile-Brittle Transition Temperatures of V-Cr-Ti Alloys," ibid.. pp. 253-257.

3. H. M. Chung, B. A. Loomis, L. Nowicki, J. Gazda, and D. L. Smith, "Irradiation-Induced Density Change and Microstructural Evolution of Vanadium-Base Alloys," ihid.. pp. 223–231.
4. H. Matsui, M. Tanno, J. Gazda, and H. M. Chung, "Microstructural Stability of V-4Cr-4Ti During Neutron Irradiation," ihid., pp. 240–246.
5. H. M. Chung, J. Gazda, L. Nowicki, J. E. Sanecki, and D. L. Smith, "Effccts of Fabrication Variables on Impact Properties and Microstructure of V–Cr–Ti Alloys," ihid., pp. 207–218.
6. H. M. Chung, B. A. Loomis, and D. L. Smith, "Thermal Creep Behavior of V–5Cr–5Ti and V–10Cr–5Ti Alloys," in <u>Fusion Reactor Materials. Semiannual. Prog. Report</u>, DOE/ER-0313/14, Oak Ridge National Laboratory, Oak Ridge, TN (1993), pp. 309-317.
7. D. N. Braski, in <u>Influence of Radiation on Material Properties</u>, ASTM-STP 956 (1986), pp. 271-290.
8. D. N. Braski, J. Nucl. Mater. 141-143 (1986) 112.5.
9. D. N. Braski, in <u>Reduced Activation Materials for Fusion Reactors</u>, ASTM-STP 1047 (1988), pp. 161-178.
10. H. Matsui, M. Tanaka, M. Yamamoto, and M. Tada, J. Nucl. Mater. 191-194 (1992) 919.
11. M. Satou, K. Abe, and H. Matsui, J. Nucl. Mater. **191-194** (1992) 938.
12. W. van Witzenburg, **A.** Mastenhroek, and J. D. Ellen, J. Nucl. Mater. **103-104** (1981) 1187.
13. M. P. Tanaka, E. E. Bloom, and J. A. Horak, J. Nucl. Mater. 114 (1981) 895.
14. M. L. Grossheck and J. **A.** Horak, in <u>Influence of Radiation on Material Prooerties</u>, ASTM-STP 956 (1986), p. 291.
15. J. M. Vitek, D. N. Braski, and J. A. Horak, J. Nucl. Mater. 141-143 (1986) 982.
16. W. van Witzenburg and E. de Vries, in <u>Effects of Radiation on Materials.</u> ASTM-STP 1125 (1990).
17. **L.** L. Horton and K. Farrell, J. Nucl. Mater. 122-123 (1984) 687.
18. H. Kawanishi and S. Ishino, in <u>Reduced Activation Materials for Fusion Reactors</u>, ASTM-STP 1047 (1988), pp. 179-189.
19. H. Kawanishi, **Y.** Arai, and **S.** Ishino, J. Nucl. Mater. 191-194 (1992) 933.
20. D. L. Smith, H. Matsui, L. R. Greenwood, and B. A. Loomis, J. Nucl. Mater. **155-157** (1988) 1359.
21. D. L. Smith, B. A. Loomis, H. Matsui, M. L. Hamilton, **K.** L. Pearce, J. P. Kopasz, ***C.*** E. Johnson, **R.** G. Clemmcr, and L. R. Greenwood, in <u>Fusion Reactor Materials. Semiannual. Proe. Rep</u>. DOE/ER-0313/10, Oak Ridge National Laboratory, Oak Ridge, TN (1991), p. 159.
22. H. Tsai, H. M. Chung, **B.** A. Loomis, and D. L. Smith, "Status of Dynamic Helium Charging Experiment (DHCE)," in <u>Fusion Reactor Materials. Semiannual. Prog. Reoort</u>, DOE/ER-03 13/15, Oak Ridge National Laboratory. Oak Ridge, TN (1994), pp. 247–252.
23. L. R. Greenwood "Revised Calculations for the DHCE Experiment," Pacific Northwest Laboratories, April 30, 1993.
24. Letter from L. R. Greenwood to H. Matsui, "Tritium Calculations for the DHCE Experiment," Novemher 20, 1993.
25. Letter from L. R. Greenwood to H. M. Chung, "DHCE Calculations with Range of Tritium Equilibrium Constants," May 4, 1994.
26. H. Tsai. R. V. Strain, H. M. Chung, and D. L. Smith, "Status of Dynamic Helium Charging Experiment (DHCE)," in this report.
27. H. M. Chung, H.-C. Tsai, L. Nowicki, J. Gazda, and D. L. Smith, "Swelling and Structure of Vanadium **Alloys** lrradiated in the Dynamic Helium Charging Experiment," in this report.

STATUS OF THE DYNAMIC HELIUM CHARGING EXPERIMENT*

H. Tsai, R. V. Strain, H. M. Chung, and D. L. Smith (Argonne National Laboratory)

OBJECTIVE

The objective of the dynamic helium charging experiment (DHCE) **is** to investigate the effects of concurrent helium production and fast-neutron irradiation on the physical and mechanical properties of vanadium-based alloys for fusion blanket applications. A major task in this reporting period was to disassemble the tritium-hearing DHCE capsules to retrieve irradiated specimens for examination and testing.

SUMMARY

Seven DHCE capsules containing vanadium-alloy specimens were irradiated in the MOTA-2B vehicle in FFTF to −20-29 dpa. In this and the previous reporting periods, equipment and procedures were developed at Argonne National Laboratory-East to disassemble these capsules. Six of the seven capsules have been disassembled. (The seventh capsule was processed **in** April 1994, immediately following this reporting period.) Effluence *of* tritium into the cell exhaust was <2% of the total inventory. No contamination incidents occurred during the DHCE disassembly work. Initial testing of the retrieved specimens is under way.

PROGRESS AND STATUS

Introduction

Because helium generated in vanadium-based structural materials from (n,α) reactions may affect the physical and mechanical properties of these materials for fusion reactor applications, the potential effects ***of*** enhanced helium generation to levels comparable in fusion reactors must he studied. This was achieved in the DHCE in the FFTF MOTA-2B by doping the lithium bond in the capsules with tritium, which diffused into the specimens and subsequently decayed in-situ into helium. Tritium doping was performed by placing a piece of tritiated vanadium foil in the capsule during assembly. Additional tritium generation from the (n,T) reactions with ^{6}Li in the lithium bond replenished the tritium lost to diffusion leakage through the capsule wall. **A** detailed description of the DHCE capsules is provided in Refs. 1–3.

In processing the irradiated DHCE capsules to retrieve the specimens, the main challenge was to contain the tritium, which ranged between 17 and 99 Ci per capsule, in the capsules. Because of the induced radioactivity in the capsule material (molybdenum-based TZM alloy), capsule disassembly was performed remotely in a hot cell.

System Description

The basic approach adopted for capsule disassembly was to use liquid ammonia (-33°C bp) to dissolve the lithium bond, alcohol to rinse the retrieved specimens, and chemical getters (containing a reactive metal alloy) to trap the released tritium gas. The system, built specifically for these tasks, consisted of a capsule–puncture jig, **a** chamber for ammonia dissolution and alcohol rinsing, two stages of cold traps at liquid-nitrogen temperature to remove (by condensation) the ammonia and alcohol vapors from the process gas stream, and two or three chemical getters in series. The capsules were processed one at a time. Except during capsule loading and unloading, the entire system was isolated from the cell atmosphere and maintained under **a** purge of high-purity (99.999%) nitrogen gas. Nitrogen was selected mainly for its compatibility with the tritium detectors because, unexpectedly, helium gas. the first choice, caused the ionization chambers in the tritium detectors to

---

*Work supported by the Office **of** Fusion Energy. **U.S.** Department **of** Energy. under Contract W–31–109–Eng–38

arc. The puncture jig and the dissolution chamber were located inside the hot cell; the remainder of the system was out-of-cell in a nearby vented cabinet. Flow meters, pressure gauges, thermometers, and tritium monitors were deployed at various locations in the system to provide operational data. A schematic representation of the system, showing two getters, is shown in Fig. 1.

The equipment most critical to successful operation was the remotely operated dissolution chamber. The final design incorporated a counterbalanced top cover capable of maintaining hermeticity up to $\approx 3 \times 10^4$ Pa (5 psi) positive pressure, a translucent (for viewing purposes) chamber body that could be slid back and forth to facilitate removal/replacement of used ammonia and alcohol beakers, a feed line that permitted the loading of liquid ammonia directly from a supply cylinder without breaking the hermeticity, a heater in the base to evaporate excess liquid ammonia, and all necessary purge lines.

Procedures

The major steps used for the disassembly of the capsules were as follows:

1. Puncture the capsule in the puncture jig and sweep the released gas to the tritium getters before venting.
2. Open the capsule with a tubing cutter to expose the contents inside.
3. Load the opened capsule into a wire-mesh specimen basket and attach the specimen basket to a support rod in the dissolution chamber.
4. After thoroughly purging the chamber, load liquid ammonia directly from a supply cylinder into a beaker in the chamber. Lower the specimen basket into the ammonia to dissolve the lithium bond that encased the specimens. Condense all evaporated ammonia in the gas stream with the cold traps and send the swept gas to the tritium getters.
5. When lithium dissolution is complete, raise the specimen basket above the ammonia and evaporate the residual ammonia in the beaker. Condense the ammonia vapor and trap the tritium gas as in Step 4.
6. Open the dissolution chamber and remove the used ammonia beaker with the reaction residues (a thin crust possibly containing azide, amide, and hydroxide).
7. In the same enclosed chamber but with a new beaker, load alcohol into the beaker and use alcohol to remove the surface residues on the specimens. Condense the evaporated alcohol as in Step 4 and send the swept gas to the tritium getters.
8. Repeat the rinsing of specimens in clean alcohol in the open atmosphere of the cell
9. Completely evaporate the residual alcohol remaining in the beakers from Steps 7 and 8.
10. Allow the cold traps to return to room temperature and vent the contents (condensed ammonia and alcohol) in preparation for the next capsule.

Steps 2, 3, 6, 8, and 9 involved operations in the open atmosphere of the cell. Tritium releases during these operations were monitored with a monitor located in the cell exhaust duct (T5, see Fig. 1). The releases were found to he small and well within the allowable limits. Step 10 was also performed under fully monitored conditions, with monitors T2 and T4, shown in Fig. 1. Because tritiation of ammonia or alcohol was minimal, the releases werc also small and well within allowable exhaust limits. The total tritium release from these operations to the cell exhaust was <2% of the tritium content of the capsules.

Prior to the processing of the DHCE capsules, two dry runs, with low-tritium capsules (COBRA-IA capsules V575 and V680 for the first and MOTA capsule V673 for the second) were completed. In the first dry run, the second-stage tritium getter overheated, evidently because the portable tritium monitor was deployed between the

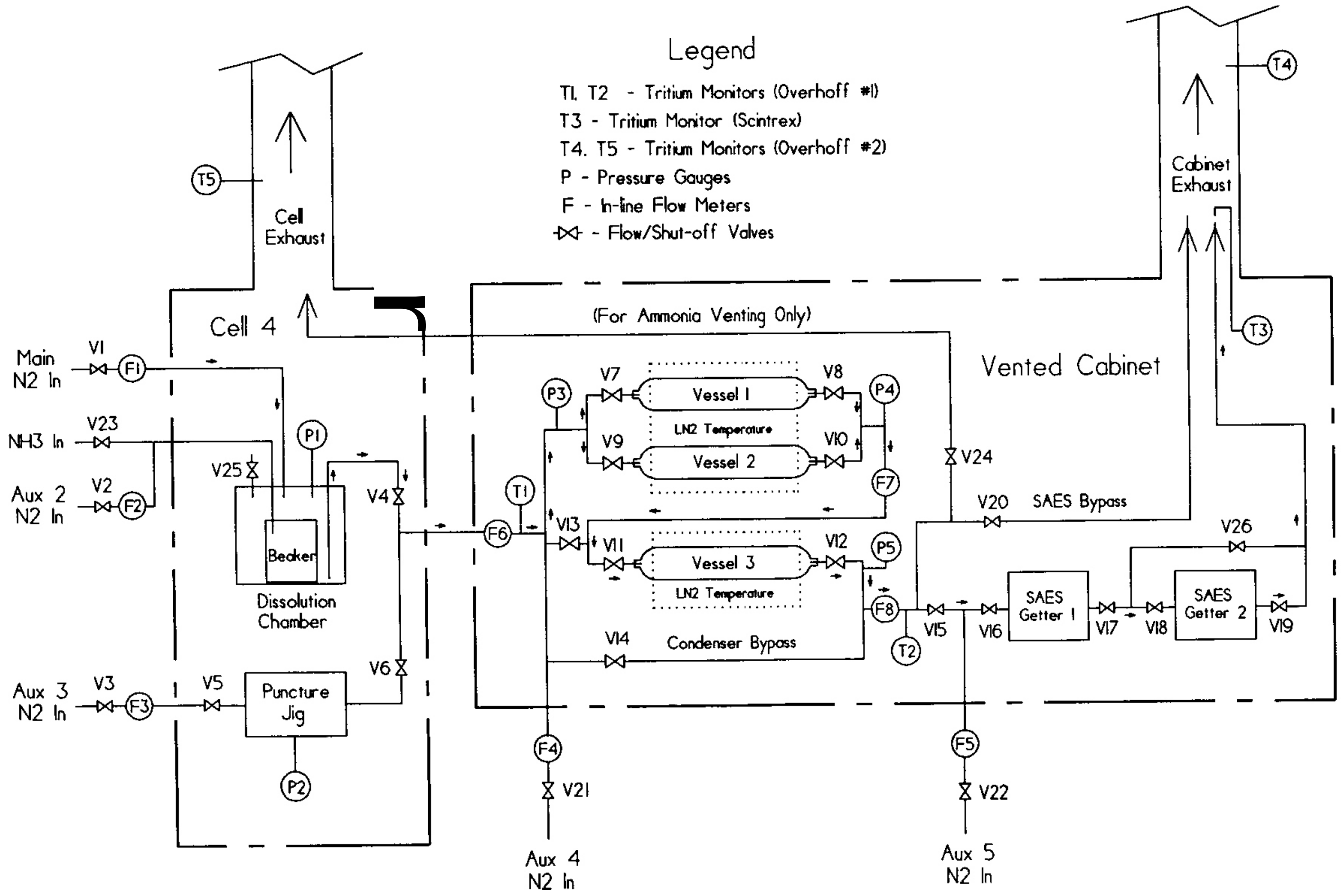

Figure 1. Schematic representation of DHCE capsule disassembly system.

two tritium getters to monitor the performance of the first getter. The monitor had a built-in recirculating pump to sample the process gas in the line. Apparently, the recirculating system contained an unforeseen air leak, which introduced oxygen to the line and caused **an** excessive reaction with the getter alloy. This situation was rectified by relocating the tritium monitor downstream of all getters, and the affected getter was replaced before the second dry run. The relocated monitor is shown **as** T3 in Fig. 1. After this modification, no further overheating occurred. The overheating did not cause a tritium release hecause the structural integrity of the affected getter was not breached. Any tritium release would have been small hecause of the insignificant tritium content of V575 and V680 capsules.

RESULTS AND CONCLUSIONS

Six of the seven DHCE capsules were processed in this reporting period. The seventh, i.e., capsule 4D1, was processed immediately after this reporting period, on April **4,** 1994. The sequence of processing was generally in ascending order of tritium content of the capsules to gain experience and avoid a large inadvertent tritium release should an error develop in either the hardware or the procedures during the processing of the first capsules.

Tritium removal for the first DHCE capsule, 5C1, was substantially more difficult than the dry runs. The cause of the difficulty was apparently an insufficient opening of the capsule for the ammonia to dissolve the lithium. **In** the interest of protecting the test specimens to the maximum extent possible, only two cuts, one at each end of the capsule, were made. The elongated capsule geometry (120 mm long x 9 mm ID) and the tightness of specimen packing in the capsule were such that prolonged and repeated rinsing was necessary to remove the lithium bond. Although all specimens were eventually successfully retrieved, the strain on the equipment and operators was substantial. After the 5C1 operation, the procedure was modified to include a third cut, near the middle of the capsule, where the specimens were still protected by the coiled vanadium mother **alloy.** A further advantage of this third cut was that the brittle TZM capsule would invariably split longitudinally and create more contact surfaces for dissolution. With this modification, **all** remaining capsules were processed with minimal difficulties.

It was necessary to replace the reactive metal cartridges in the tritium getters twice during the experiment. The apparent lack **of** capacity of the cartridges was possibly the result of contamination of the reactive metal by ammonia and alcohol vapors that escaped the cold traps upstream of the getters. **In** any future work, a third-stage cold trap will be added to improve condensation efficiency. Replacement of the tritium-bearing reactive-metal getter cartridges in a fume hood was straightforward and caused no contamination.

Tritium concentrations in the process gas were measured by tritium monitors in the system. The recorded data were integrated to yield the estimated quantities of gaseous tritium released during each of the major steps of the operation. The results are summarized in Table 1. In all cases, most of the tritium release (up **to** ≈50-60% of the total inventory in the capsule) occurred during the ammonia dissolution process (Step 4). **All** other releases, such as those from plenum gas venting, alcohol rinsing, or venting of the condensers, were substantially smaller. Much of the unaccounted-for tritium activity **is** apparently contained in the reaction residues formed at the bottom of the ammonia beaker after evaporation. These heakers will be carefully disposed of by approved procedures in the near future.

Radiographs of the assembled capsules before irradiation show that some of the tensile specimens in the DHCE capsules were not fully immersed in the lithium bond, apparently because of interference with the tritiated mother alloy coil, and jam-packing of the specimens. During capsule disassembly, the elevated positions of these specimens were generally confirmed visually. For future in-reactor experiments, both specimen packing density and internal capsule design should be reviewed to ensure proper lithium bonding of **all** specimens.

Table 1. Integrated tritium activity measured during the processing of DHCE capsules

			Tritium Activity (Ci)					
Capsule No.[1]	Irrad. Temp. (°C)	Tritium Content	Capsule Puncture	Ammonia Dissolved	Ammonia Evaporated	Alcohol Rinse	Ammonia Venting	Total
5C1	600	16	<0.001	2.0	1.1	1.4	0.03	4.5
5E2	425	26	<0.001	1.7	0.4	1.2	0.06	3.4
5C2	600	18	<0.001	11.4	0.6	0.2	0.1	12.3
5E1	500	57	<0.001	≈19.5	1.1	3.4	0.1	≈24.1
4D2	425	70	<0.001	33.0	2.8	2.3	0.3	38.4
5D1	500	74	<0.001	ND[2]	ND	ND	ND	ND
4D1	425	99	<0.001	37.3	5.9	2.8	0.3	46.3

[1] The order of the processing sequence.

[2] ND: No data, due to malfunctioning of the tritium detector.

REFERENCES

1. D. L. Smith, et al., ***Status of the Dynamic Helium Charging Experiment (DHCE) in FFTF/MOTA,*** Fusion Reactor Materials Semiannual Progress Report DOE/ER-0313/10, March 31, 1991, pp. 159-163.

2. L. R. Greenwood, ***Revised Calculations for the Dynamic Helium Charging Experiment in FFTF/MOTA 2B,*** Fusion Reactor Materials Semiannual Progress Report DOE/ER-0313/10, March 31, 1991, pp. 156-158.

3. H. Tsai, et al., ***Status of the Dynamic Helium Charging Experiment** (DHCE),* Fusion Reactor Materials Semiannual Progress Report DOE/ER-0313/15, September 30, 1993, pp. 247-252.

Fabrication of Vanadium Alloy product Forms for Specimen Preparation – M. L. Grossbeck, T. K. Roche, W. S. Eatherly, F. F. Dyer. and N. H. Rouse (Oak Ridge National Laboratory)

OBJECTIVE

This project was undertaken to determine the proper methods of working and heat treating vanadium alloys and to prepare the proper thicknesses of sheet and plate of vanadium alloys in order to machine test specimens.

SUMMARY

The alloy V–5Cr–5Ti (Teledyne Wah Chang heat 832394) was received in the form of a 6.35 mm plate and was rolled to 3.81 mm plate and 0.76 mm sheet. The 3.81 mm plate was used for Charpy impact specimens and the 0.76 mm sheet was used for tensile specimens and welding experiments. Since interstitial impurities are important strengthening and embrittling agents in refractory metals, all anneals had to be done in ultra–high vacuum furnaces.

PROGRESS AND STATUS

Introduction

Vanadium alloys have received renewed attention for application to the International Thermonuclear Experimental Reactor (ITER). The high thermal conductivity and low coefficient of thermal expansion of vanadium result in low thermal stresses as opposed to those of stainless steels which lead to high thermal *stresses* and resultant thermal fatigue. Vanadium alloys (V–Cr–Ti) have low neutron activation properties and do not form long–lived radionuclides. Both of these properties make vanadium alloys attractive for fusion reactor application.

In order to perform Phase I design, the physical and mechanical properties of the particular vanadium alloys to be used must be available. It has been proposed to use a V–4Cr–4Ti alloy for fust wall and blanket structures of the ITER.' The work described here was carried out using a V-5Cr-5Ti alloy (Wah Chang heat number 832394). This material is also referred to as alloy BL63 by researchers at Argonne National Laboratory (ANL). Previous studies at ANL showed that the V-5Cr-5Ti alloy (BL63) had inferior Charpy impact properties compared to a V-4Cr-4Ti alloy (BL47). It was suggested that these inferior properties could be related to the presence of Cl contamination arising from the Ti sponge material used in the production of alloy BL63.[2]

This work was undertaken to provide material for a variety of physical and mechanical property measurements. The physical properties that were investigated were Poisson's ratio, Young's modulus, Lame constants, thermal conductivity. thermal expansion, and specific heat. The mechanical properties were fatigue and Charpy impact. The results of these tests and measurements are reported in this volume.[3,4]

Considerations for Processing Refractory Metals

The following discussion applies to the group Vb metals, V, Nb, and Ta. This group of metals is characterized by very high melting points, 1890°C for vanadium up to 2996°C for tantalum. However, despite their otherwise excellent high temperature properties, these metals form stable oxides which are volatile at temperatures where the metals would otherwise be useful. It is the oxidation properties of these metals which precludes their use at high temperatures in an air environment. The oxide V_2O_5 has the additional but fascinating property that it has a melting point of 675°C so that the surface of vanadium becomes wet and drips oxide when heated in air above this temperature5 Not only is surface oxidation important, but dissolved oxygen as well as other interstitials are potent hardeners in these metals. The effect of small concentrations of interstitials is shown in Fig. 1 where the embrittling effect of interstitials is illustrated for vanadium6

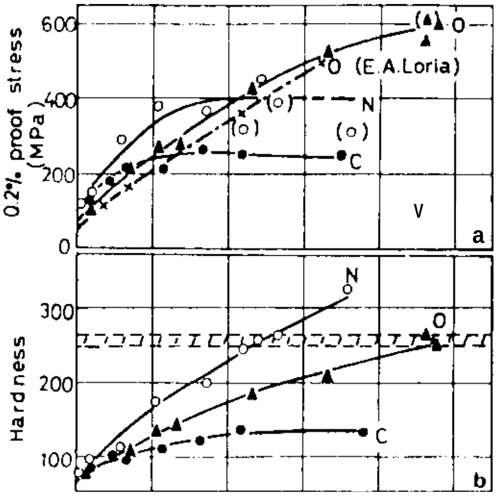

Fig. 1. Effect of O, N, and C on the total elongation of vanadium at room temperature (from Kainuma et al.. J. Nucl. Mater 80 (1979), 339.

In a fusion reactor, vanadium alloys would be in contact with liquid lithium which forms more stable oxides than vanadium, and oxygen would partition almost entirely in the Li. Nitrogen is still a consideration. In fabrication of vanadium alloys, ultra–high vacuum must be used for all high–temperature heat treatments. However, such precautions only slow the dissolution of oxygen and nitrogen. This is illustrated in Fig. 2 where the oxygen concentration in solution in vanadium in equilibrium with external oxygen is plotted.[7] As can be seen from the prohibitively high vacuums, and resulting high concentrations in solution, it is not possible to eliminate oxygen absorption during processing and application of the metal in high–temperahue systems. It is only possible to slow the process by reducing the rate at which atoms impinge on the surface and by keeping the time at high temperatures to a minimum.

Since the concentration of interstitials in solid solution determines the hardness of the matrix and often leads to embrittlement, getters can be used in design of refractory metal alloys. In the present alloy, V–5Cr–5Ti, titanium serves this purpose. Previous studies have shown that the primary precipitates identified in vanadium alloys are Ti(O,N,C), titanium oxycarbonitrides.[8] In this case, more relevant than the interstitial concentration in equilibrium with an external gas is the concentration in equilibrium with an internal phase. This depends on the temperature as well as the particular precipitate. Therefore, the temperature of the last heat treatment received by the alloy determines the interstitial concentration quenched into the matrix. Of course, a slow cool would result in a different concentration than a rapid quench. This is one reason that the properties of refractory metal alloys are very sensitive to heat treatment.

Hydrogen is also important in determining properties. In particular, hydrogen severely embrittles vanadium alloys under the proper conditions. The relative effects of interstitial embrittlement are illustrated in Fig. 3 where a tensile ductile–brittle transition temperature is plotted as a function of concentration of H, O, N, and C g The embrittling effect of hydrogen can be clearly seen from the data presented. Information on the

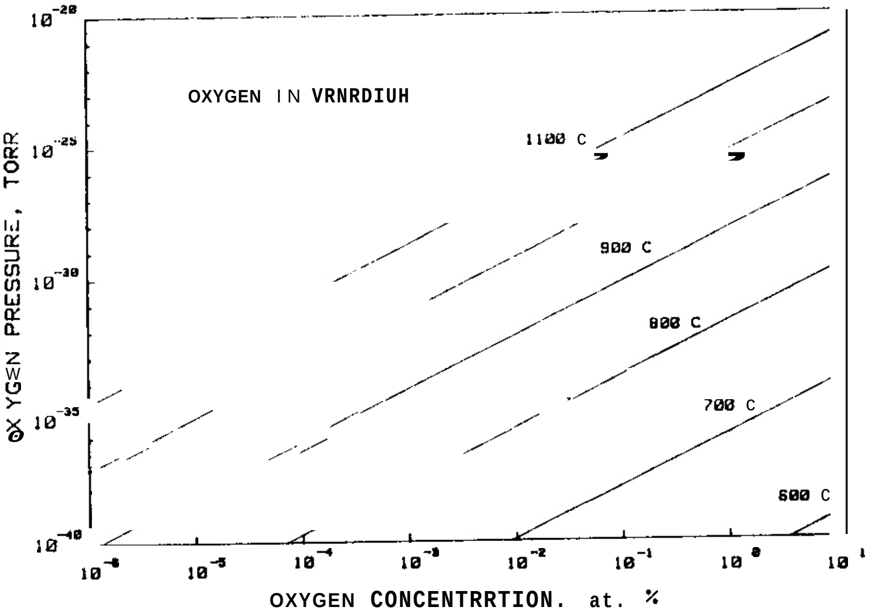

Fig. 2. Relationship between equilibrium O concentration and the external O partial pressure in vanadium (after Fromm and Gebhardt. Gase und Kohlenstoff in Metallen, Berlin, Springer-Verlag (1976), 221.

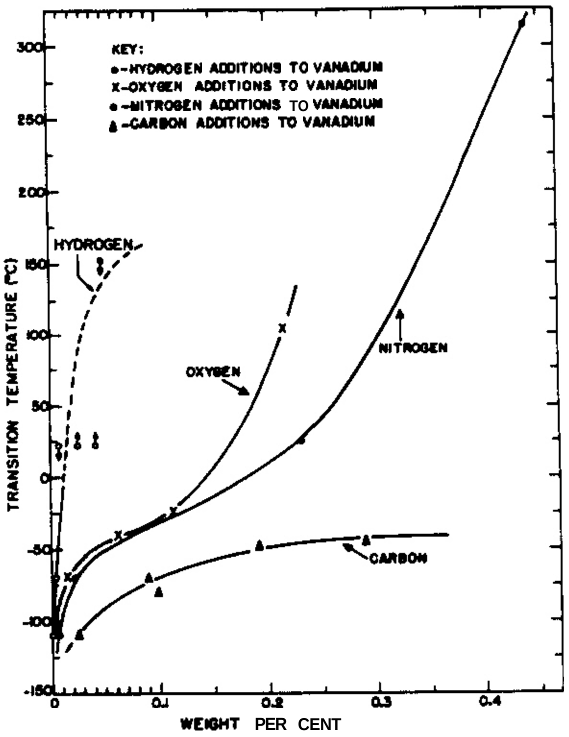

Fig. 3. Effect of nonmetallic elements on the brittle-ductile transition in vanadium (from Loomis and Carlson in Reactive Metals: Proceedings of the Third Annual Conference, New York, Interscience Publishers (1959), 227.

nature of hydrogen embrittlement can be obtained from Fig. 4 where the temperature and concentration dependence is shown.[10] The relationship between the brittle transition temperature and the appearance of hydride can be seen. It is clear at the lower concentrations of hydrogen that embrittlement occurs at a temperature above that of hydride formation. The transition temperature can be compared with the hydride solvus measured by resistivity shown in Fig. 5.[11] It can be seen that the ductile–brittle transition temperature is slightly above the hydride solvus temperature. This can be understood in terms of stress–induced hydride formation at the tip of a moving crack. This phenomenon was studied in niobium where the formation of stress–induced hydride was confirmed.[12]

The ease with which hydrogen can be introduced into refractory metal alloys is remarkable. A method used routinely at Argonne National Laboratory to introduce hydrogen is polishing in water followed by a homogenization heat treatment.[13] The surface oxide appears to function as a barrier to hydrogen, but if it is removed by polishing, scratching, or chemical etching, hydrogen may be introduced from an aqueous medium, moisture in air, or an acid. Whenever possible, a high temperature outgassing heat treatment should be employed prior to testing or use of vanadium alloys. In the present evaluation program, grinding and electro–discharge machining (EDM) were not used so as not to introduce locally high concentrations of hydrogen sufficient to nucleate cracks which would remain even after an outgassing treatment. The tolerance of vanadium alloys to normal machining operations remains to be investigated further.

Experimental Procedure

From the above considerations it is apparent that extreme precautions must be taken in handling vanadium alloys. All high temperature anneals must be conducted in UHV furnaces, and hot rolling operations must be followed by pickling to remove oxide. The process began with 6.35 mm thick plate of V–5Cr–5Ti of Teledyne Wah Chang Albany Corp. heat 832394. Two strips were sheared 63.5 mm x 305 mm. This plate was received in the annealed condition: however, it was labeled as 50% worked when received. As a result, the processing began with annealing. The steps are shown in Fig. 6. Annealing was done at 1125°C for one hour in a resistance heated furnace. The base pressure was in the low 10^{-5} Pa range prior to heating. During the anneal, the pressure rose into the low to mid 10^{-4} Pa range. All plates and sheets were wrapped in Ta foil. Analysis for interstitial impurities was conducted following all annealing and some rolling steps. The results of the analyses are also shown in Fig. 6. It is clear that no significant interstitial contamination resulted from the processing.

Rolling was done at 250–300°C with a maximum reduction of 5% per pass. As can be seen from Fig. 6, deformation did not exceed 50% prior to annealing. Before each anneal, the material was pickled in 30% HNO_3 – 10%HF – 60%H_2O for five minutes to remove oxide and ferrous metal contamination from the rolls. The major product forms produced were 3.56 mm plate for Charpy impact specimens and 0.76 mm sheet for tensile specimens. All products were fluorescent dye checked for surface cracks prior to fabrication of specimens.

Chemical Analysis

Chemical analyses were of three types. The first was analysis for the interstitial elements: inert gas fusion analysis for O, N, and H, and high temperature combustion analysis for C. These analyses were conducted by Leco Corp., St. Joseph, MI. The second analysis was glow discharge mass spectrometry used for the major elements and substitutional impurities. The third was neutron activation analysis which was focused primarily on the element chlorine. The results are provided in Fig. 6 and Tables 1–2.

Table 1. Chemical Analysis for V-5Cr-5Ti (Heat 832394) Excluding Gaseous Impurities

	Glow Discharge Mass Spectrometry		Ingot Analysis by Vendor			
			Position 1		Position 2	
	%	ppm	%	ppm	%	ppm
Al		<300		190		210
B				<5		<5
Cr	4.2		4.3		4.6	
Fe		<450				
Hf		13				
Mo		360				
Nb		<75		<50		<50
Ni		13				
P		<25		<30		<30
S		8*		30		20
Si		<310		300		310
Ti	5.4		5.1		5.1	
U				<1		<1
V	bal		bal		bal	
W		26				
Zr		<100				

*High temperature combustion analysis

Table 2. Chemical Composition Determined by Neutron Activation Analysis (wt ppm)

	Fit Irradiation		Second Irradiation	
Element	Conc	Err	Conc	Err
Na	1.8	0.04	0.06	0.02
K	1.7	1		
	38000			
		0.001		0.002
Zr	170	60		
Ga	1.7	0.03	1.5	0.04
As	0.6	0.04		
Mo	330	40	350	80
W	29	0.1	27	0.1
Au	<0.005		<.007	
Hf	20	2		
Ta	10	1		

Table 1 shows the result of glow discharge mass analysis for major elements and substitutional impurities. Since standards were not used, the results are accurate to about ±30%. Also included in the table are the results of the ingot analysis provided by the vendor. Considering the limits of error, close agreement is apparent for elements that appear in both analyses.

Results of analyses for gaseous interstitials appear in Fig. 6. Carbon was monitored during processing in order to guard against contamination from the rolling process. Oxygen was monitored carefully to control contamination during the high temperature anneals. As can be seen from Fig. 6, the oxygen concentration slowly increased during the processing by about 10%. Contamination of this magnitude is almost unavoidable during processing on this scale. Nitrogen, a slower diffuser, did not increase significantly during the processing. Hydrogen was very low following all high temperature anneals as expected because of its very high diffusivity and low partial pressure in the vacuum systems.

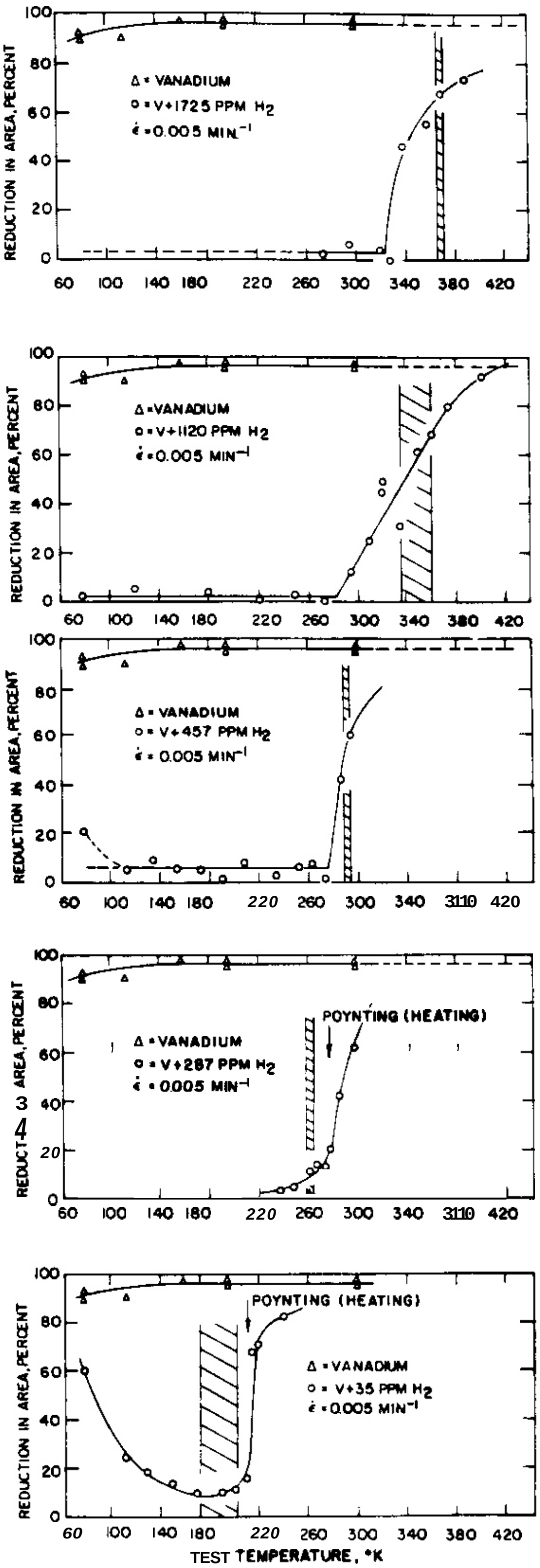

Fig. 4. Ductility of vanadium containing hydrogen as a function of test temperature. Cross-hatched vertical band indicates the temperature range of visual observation of hydride (from Owen and Scott, Met. **Trans.** 3 (1972) 1715.

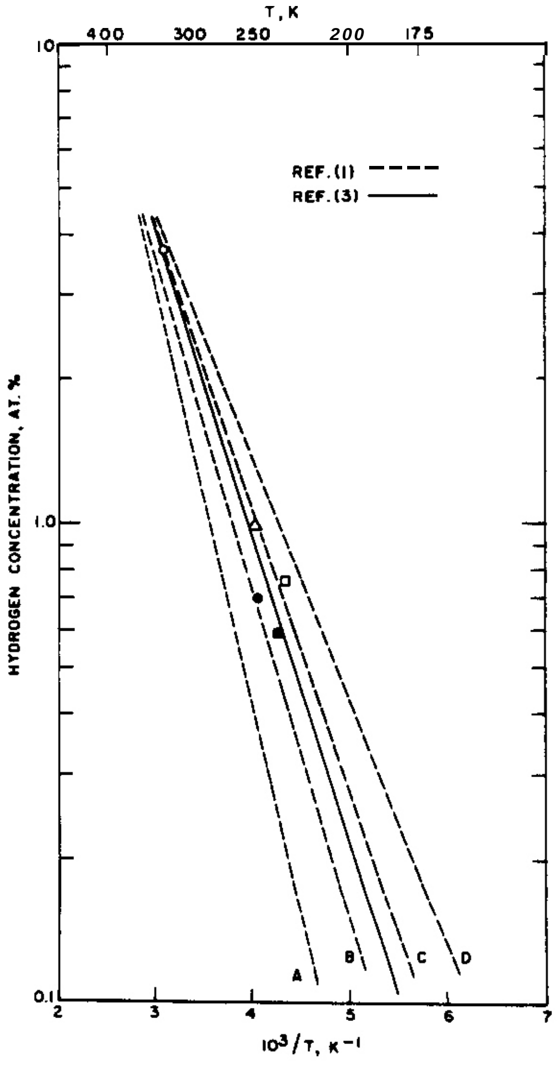

Fig. 5. Effect of oxygen on the solubility limit **of** hydrogen in vanadium. ● Wire, hydrogen charged electrolytically after UHV treatment. **O** Hydrogen charged electrolytically after oxygen addition (–1300 at. ppm). ■ Sheet, charged with hyrodrogen gas. ☐ Sheet, charged with hydrogen gas after oxygen addition (–3200 **at.** ppm), **A** Sheet, charged with hydrogen gas after oxygen addition (–3200 at. ppm), 17h wait for equilibrium at each temperature. (a) "Pure" vanadium, (b) 2000 at. ppm additional oxygen, (c) 4000 at. ppm additional oxygen, (e) 6000 at. ppm additional oxygen (from Westlake and Ockers, Met. Trans. 6a (1975), **399.**

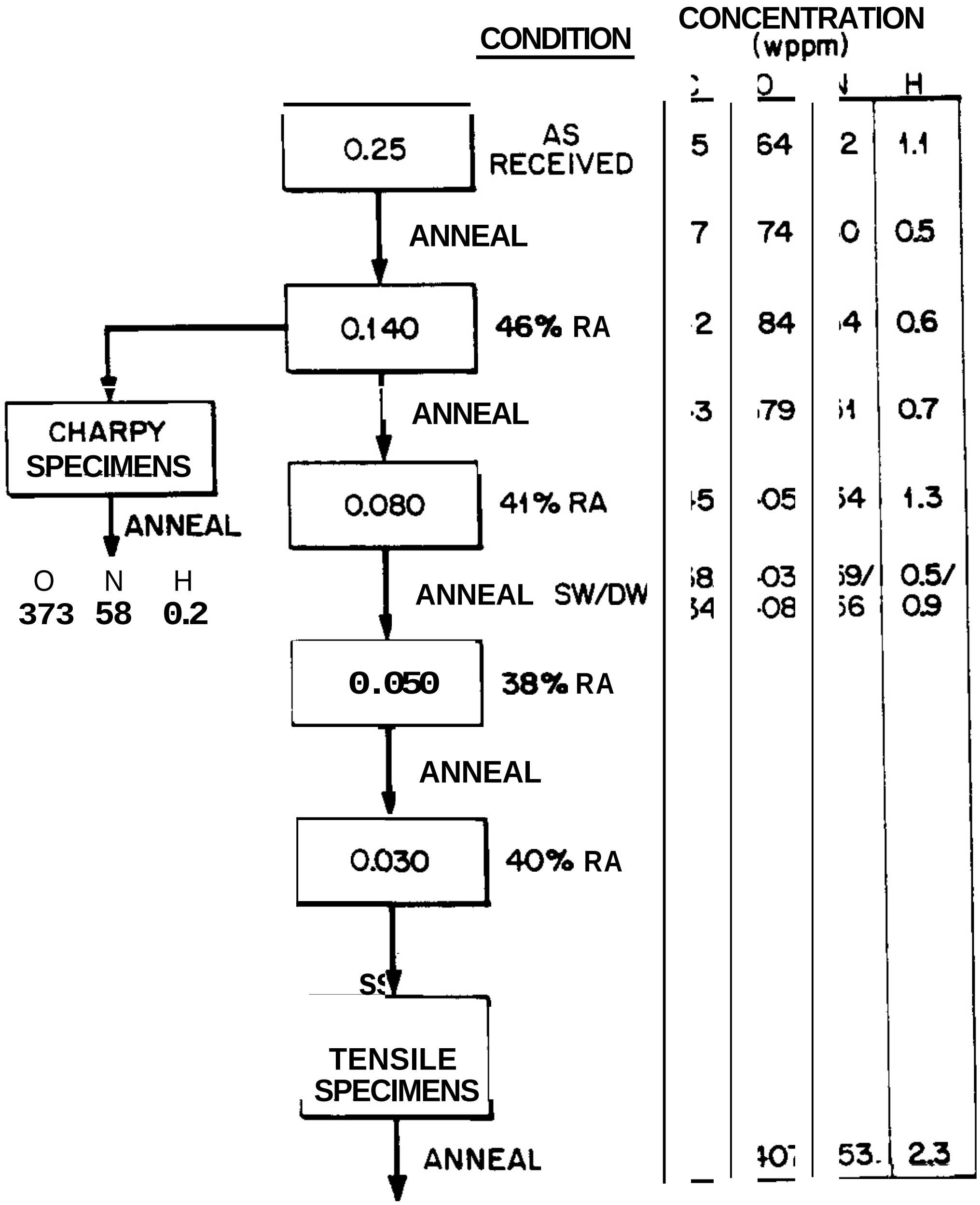
ORNL-DWG 94–9367

PROCESSING STEPS SHOWING INTERSTITIAL CONCENTRATIONS AS DETERMINED BY VACUUM FUSION ANALYSIS (wt. ppm)

Fig. 6. Processing history of V-5Cr-5Ti. Condition refers to the reduction during rolling. Interstitial concentrations correspond to the step in the flow sheet where they are positioned. SW and DW refer to single and double Ta wrap.

Chlorine Analysis

The analysis for chlorine requires some introduction. Inferior impact properties of V–5Cr–5Ti (Wah Chang Heat 832394) have been attributed to contamination by chlorine introduced through the Ti sponge used in its production.[2] To further investigate this mechanism, Auger electron spectrometry was used to search for chlorine–containing precipitates on fracture surfaces.[14] In addition, neutron activation analysis was used to determine the concentration of chlorine in the alloys.

In neutron activation analysis, the experimenter must select irradiation and decay times to favor detection of the desired elements. In this research. the analysis was optimized for chlorine although other elements were accurately measured and reported, as shown in Table 2. Two irradiations were ma& the fust was made using a conventional acetone wash prior to irradiation. As can be seen in Table 2, Na and Cl were present in nearly equal concentrations. This raises the suspicion that the elements are from NaCl from finger prints on the surface. The samples were subsequently washed with both acetone and high–purity water and re–irradiated. The fust irradiation was made for 300 s and the second for 60 s. Gamma spectra were acquired for about 90 minutes after each irradiation.

Vanadium forms ^{52}V by the reaction ^{51}V(n,γ)^{52}V with a half–life of 3.7 minutes. The cross section is 4.9 barns, and the gamma energy is 1434 keV. Chlorine forms ^{38}Cl by the reaction ^{37}Cl(n,γ)^{38}Cl. The half–life is 37.2 minutes, thus there is only a short window of time when the ^{52}V has cooled enough and before the ^{38}Cl has decayed too much. when the ^{38}Cl can be measured. The decay time was refined following the fust irradiation, but Cl could be measured at concentrations below 1 ppm in both cases. The errors listed in Table 2 are exclusively counting errors expressed approximately at the 95% confidence limit. Experience has shown that elements with stable isotopes that activate with "1/v or near 1/v" cross sections can be measured by absolute neutron activation analysis using the ORNL system with uncertainties of only a few percent. Overall errors due to factors other than counting statistics (i.e. sample–to–sample flux differences, counting geometries. etc.) are no larger than 5–10 %. This conclusion has been reached after the analysis of numerous standard reference materials from NIST having certified trace element concentration. Elements such as Cr, Zn, Hf, and Ta that yield long–lived radionuclides were not measured after the second irradiation because the induced activities were already present in larger amounts from the first irradiation.

As can be seen from Table 2, the Cl concentration dropped by a factor of 5 to 10 following the cleaning and second irradiation. In addition, the Cl concentration no longer correlates with the Na concentration. The bulk Cl concentration was measured to be about 0.2 ppm. For comparison, V–4Cr–4Ti (BL–47), V–5Ti (BL–46), and commercial Ti sponge were also analyzed. The Cl concentrations were determined to be <0.8, 0.35, and 34 ppm, respectively. The analyses show that Ti sponge is indeed high in Cl, but the vanadium alloys under study have nearly the same trace concentrations of Cl.

CONCLUSIONS

1. Plate of 3.6 mm thickness for Charpy specimens and sheet of 0.76 mm thickness were prepared from 6.35 mm plate of V–5Cr–5Ti.
2. The oxygen concentration in the alloy was increased by only about 10% during the processing, and the carbon and nitrogen were not measurably altered.
3. It was determined that chlorine concentrations did not differ significantly among the vanadium alloys studied and were below ppm concentrations in all cases.

FUTURE WORK

Techniques have now been worked out to fabricate vanadium plate and sheet on a laboratory scale. With satisfactory control of interstitial impurities; these techniques will be used to fabricate specimens for irradiation environments.

REFERENCES

1. B. A. Lwmis and D. L. Smith, "Vanadium Alloys for Structural Applications in Fusion Systems: A Review of Vanadium Alloy Mechanical and Physical Properties." J. Nucl. Mater. 191-194 (1992) 84.
2. H. M. Chung, J. Gazda. L. J. Nowicki, J. E. Sanecki, and D. L. Smith," Effects of Fabrication Variables on Impact Properties and Microstructure of V-Cr-Ti Alloys," Fusion Reactor Materials Semiannual Progress Report for Period Ending September 30,1993 (DOE/ER-0313/15), p. 207.
3. W. A. Simpson, "Room Temperature Elastic Properties of V-5Cr-5Ti," this document.
4. M. L. Grossbeck, A. F. Rowcliffe, and D. J. Alexander, "The Relationship Between Recrystallization Temperature, Grain Size, and the Charpy Impact Properties of V-Cr-Ti Alloys," this document.
5. W. Rostoker, The Metallurgy of Vanadium, New York, John Wiley & Sons (1958), p. 122.
6. T. Kainuma, N. lwao, T. Suzuki, and R. Watanabe, "Effects of Oxygen, Nitrogen. and Carbon Additions on the Mechanical Properties of Vanadium and V/Mo Alloys," J. Nucl. Mater. 80 (1979). 339.
7. E. Fromm and E. Gebhardt. "Gase und Kohlenstoff in Metallen." Berlin. Springer-Verlag (1976) p. 446.
8. T. Schober and D. N. Braski, 'The Microstructure of Selected Annealed Vanadium-Base Alloys," Met. Trans. 20A (1989), 1927.
9. B. A. Loomis and O. N. Carlson, "Investigation of the Brittle-Ductile Transition in Vanadium," Reactive Metals: Proceedings of the Third Annual Conference, New York, Interscience Publishers (1959), p. 227.
10. C. V. Owen and T. E. Scott, "Relation Between Hydrogen Embrittlement and the Formation of Hydride in the Group V Transition Metals," Met. Trans. 3 (1972), 1715.
11. D. G. Westlake and S. T. Ockers. "The Isotope Effect and the Influence of Interstitial Impurities on the Hydrogen Solubility Limit in Niobium and Vanadium," Met. Trans. 6A (1975) 399.
12. M. L. Grossbeck and H. K. Birnbaum, "Low Temperature Hydrogen Embrittlement of Niobium II–Microscopic Observations." Acta Met. 25 (1977) 135.
13. B. A. Lwmis, A. B. Hull. O. K. Chopra and D. L. Smith, "Hydrogen Concentration Distribution in Vanadium-Base Alloys after Surface Preparation and Exposure to Liquid Lithium," Fusion Reactor Materials Semiannual Progress Report for Period Ending March 31, 1988 (DOE/ER-0313/4), p. 160.
14. D. N. Braski and M. L. Grossbeck, "Analysis of Grain Boundaries in a V-5Cr-5Ti Alloy Using Auger Electron Spectroscopy,'' this document.

WELDING DEVELOPMENT FOR V-Cr-Ti ALLOYS – G. M. Goodwin and J. F. King (Oak Ridge National Laboratory)

OBJECTIVE

A vanadium structure, cooled with liquid helium, is the favored concept for an advanced breeding blanket for ITER. The objective of this task is to develop the metallurgical and technological basis for the welding of thick sections of V-Cr-Ti alloys.

SUMMARY

Welds have been produced and characterized using the gas-tungsten arc (GTA) and electron beam (EB) welding processes. Thin sheet (0.75 nun) welds were made with three levels of interstitial contamination, and hardness and tensile properties were found to k strongly affected by oxygen pickup. Thick-section (6 nun) welds have ken produced using both processes. and no embrittlement is experienced when high purity atmosphere is maintained. Metallographic examination shows a narrow. but coarse grained, heat affected zone for the GTA welds. Transition joint welding development between vanadium alloy and stainless steel has shown encouraging results.

PROGRESS AND STATUS

Introduction

The weldability of a V-Cr-Ti alloy is being characterized. The reactive nature of vanadium alloys causes concerns with welding the potentially large components of the ITER system, and the selection of weld processes and procedures will have strong economic impact on component fabrication. Several welding processes are being evaluated, with the primary consideration being the effect of interstitial pickup on mechanical properties.

Experimental

The starting material was an annealed plate, **7 mm** thick, of alloy **BL63** containing **4.6** wt % Cr, **5.1** wt % Ti, **440** wppm **0.28** wppm N, **73** wppm **C,** and **310** wppm Si. This material was also used to fabricate **0.75** nun thick sheet by warm rolling at ~300°C with intermediate anneals at **1125°C. Both** gas-tungsten arc (GTA) and electron beam (EB) processes are king investigated.

Results

Parameters established for full penetration autogeneous gas-tungsten arc welds in **0.75 mm** sheet were 90 amperes direct current electrode negative, **10.6 mm/sec** travel speed, and **1.1** nun arc length. Sensitivity to hot cracking was measured using the Sigmajig test, which gave a threshold cracking stress of **138-172** MPa. This level of cracking resistance is similar to some stainless steels, and indicates that hot cracking is unlikely to be a problem, except possibly in thick sections under high restraint.

Welds were then produced in argon using three levels of contamination: conventional gas shielding in the ambient environment, and **2%** and **<10** ppm oxygen in an atmosphere chamber. Tensile specimens were punched from the *sheets* with the weld bead located at the middle of the **12.7** nun gage length. Tests were performed on a Gleeble thermomechanical simulator at strain rates of **1.6** x 10^{-3}, **7.9** x 10^{-2}, and **1.6** per second. As summarized in Table **1,** increasing **strain rate** typically increased yield and ultimate strength and decreased total elongation by roughly 50%. Specimens made in the high purity atmosphere (**<10** ppm oxygen) **all** failed in the base metal while the other two environments (2% oxygen and conventional practice) resulted in all failures at the weld centerliie with less than **5%** total elongation. Microhardness measurements showed the high purity atmosphere welds to be approximately 200 dph at all locations, whereas the contaminated welds were hardened to levels of **650** dph in the heat affected zone and **1000** dph in the fusion zone. Additional testing will be required to determine more specifically how much oxygen can be tolerated, and what types of shielding techniques will be required.

Table 1. Summary of Tensile Properties (V-5Cr-5Ti Alloy Weldments)

		Strain rate, per second			Notes
		1.6×10^{-3}	7.0×10^{-2}	1.6	
Base metal	Yield (ksi)	37.7	40.2	42.7	
	Ultimate (ksi)	66.4	70.4	87.0	
	Total elongation (%)	19.3	17.1	13.7	
Glovebox weld <10 ppm O_2	Yield (ksi)	35.7	58.3	51.8	All base metal failures
	Ultimate (ksi)	46.3	77.4	92.5	
	Total elongation (%)	12.5	11.6	9.2	
Conventional gas shielded weld	Yield (ksi)	22.6	–	38.7	All weld centerline failures
	Ultimate (ksi)	61.9	72.9	68.9	
	Total elongation (%)	2.0	3.9	0.7	
Glove box weld in Argon + 2% O_2	Yield (ksi)	29.2	27.2	34.2	All weld centerline failures
	Ultimate (ksi)	47.8	39.2	34.2	
	Total elongation (%)	0.3	0.3	0.3	

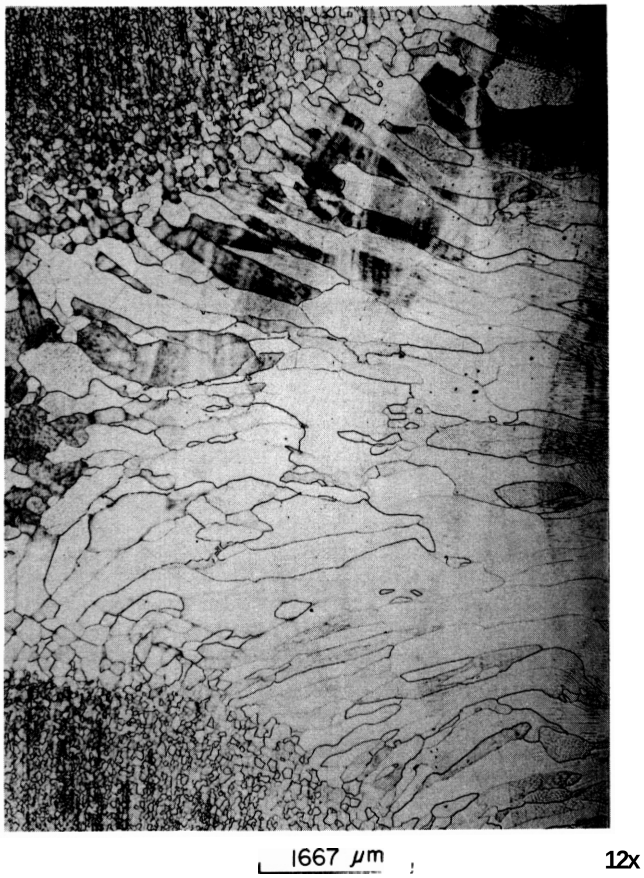

Fig. la. Fusion zone and heat affected zone of a multipass GTA weld in V-5Cr-5Ti.

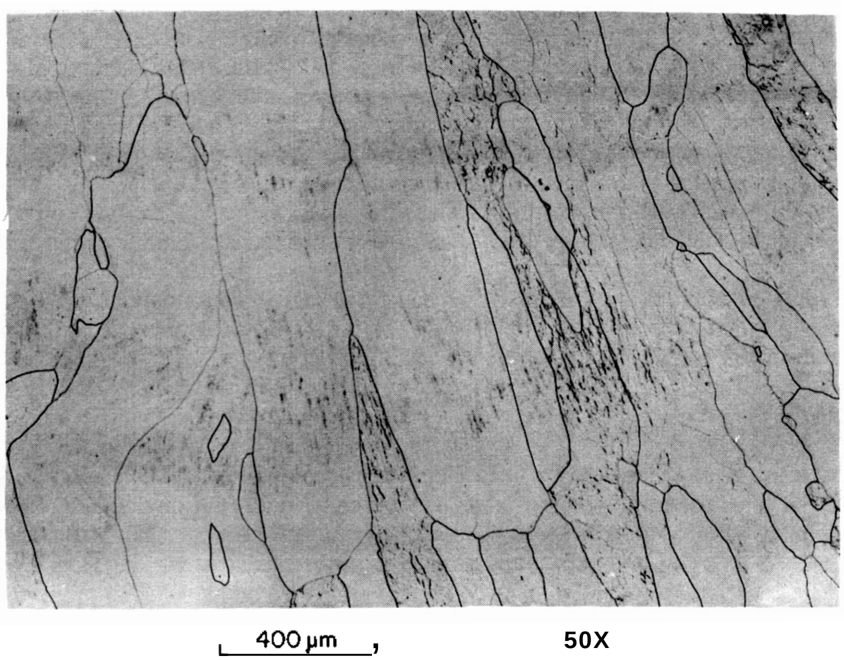

Fig. lb. Columnar grains in the fusion zone near the fusion line.

Welds have also been produced in 6 mm thick plate using both the EB and GTA processes. Autogeneous full penetration bead-on-plate EB welds were produced using 15 mA at 150 kV and a travel speed of 8.5 mm/s. Multipass single-vee groove GTA welds were made. using filler metal from the same heat, either sheared from 0.75 mm sheet, or machined from the thicker plate. The chamber atmosphere was maintained at less than 50 ppm water vapor plus oxygen throughout the welding operation. Using a welding current of 100 to 160 amperes, 8 to 10 passes were required to fill the 75" included angle groove. As was the case with the thin sheet welds produced in a high quality atmosphere, microhardness traverses across the weldment showed approximately 200 dph at all locations, indicating minimal interstitial embrittlement. Metallographic examination of a weld cross section (Fig. 1) shows large columnar fusion zone grains, and a narrow, but coarse grained. heat-affected zone.

In anticipation of the need for transition joints in the first wall/divertor structure, dissimilar metal welds have been produced between V-5Cr-5Ti and type 304L stainless steel. Initial results using type 308 filler metal look promising. Lap joints between 0.75 mm vanadium alloy sheet and 0.88 mm thick type 304L sheet were made with 1.13 mm diameter filler material in the glove box in pure argon.

Discussion and Outline of Weld Develonment Plan

The reactive nature of vanadium alloys with some elements at elevated temperature causes concerns with welding the potentially large components of the ITER system. Vanadium alloys have high solubilities for carbon, oxygen, nitrogen, and hydrogen, which dissolve interstitially. These elements can significantly effect the mechanical properties of these alloys. The weldability and weldment properties of vanadium and its alloys have not been studied extensively and it is important to have a basic understanding of weldability for potential ITER applications. The effect of alloy composition on weldability and weldment properties needs to be established. Joining processes must be identified that can be adapted to welding large, thick section components in both fabricating shops and during installation at the reactor site. Since little welding experience with vanadium alloys has been documented in the literature, it is essential that this technology be developed.

The effects of various concentrations of interstitial elements on vanadium alloy weld metal mechanical properties, including tensile and impact energy, will be determined. Weldments will be produced in a vacuum inert-gas purged glove box that bas welding amosphere monitoring instrumentation for oxygen, nitrogen, hydrogen. and water vapor. The environment in the chamber will be varied from high purity argon to argon containing intentionally higher concentrations of oxygen and nitrogen for a series of weldments produced by the gas tungsten arc process. Weld metal from these test plates will be examined by metallography and evaluated by microhardness measurements and Charpy V-notch testing. Weldment specimens will be tested both as-welded and after postweld heat treatment. Postweld heat treatment temperature will be evaluated to determine the effect on shifting the DBTT of weld metal. Postweld heat treatments near 400°C will be evaluated to remove hydrogen. Higher temperatures around 950°C will react the oxygen with the titanium. provide stress relief to the weldment, and remove the hydrogen. The concentration and distribution of the various alloying elements and the interstitial element contaminants in the weld metal will be determined for some of these specimens.

Weldability evaluations and weldment mechanical property determinations will be made for available alloys of the experimental compositions planned for the ITER program. These results will provide useful information for establishing vanadium filler metal compositions. It will be determined if a matching composition filler metal provides adequate properties and weldability or if a modified composition is desirable.

Comparisons of gas tungsten arc weld metal properties will be made to electron beam welded vanadium alloys. The electron beam welds produced in a high vacuum environment are not exposed to the interstitial contaminants found in weldments produced by the arc process. For experimental purposes, welding parameters can be adjusted to produce weldments with grain sizes varying from fme grain to coarse grain as in multipass arc welds. The effect of weldment grain sue on mechanical properties will be assessed. If it is determined that more extensive investigations are needed, the Gleeble thermomechanical test equipment will be utilized to produce similar microstructures in test coupons. This equipment has the capability of reproducing weld heating and cooling rates typical of the various welding processes in bulk specimens to produce varying grain sizes. Subsequent testing can then determine the effects of grain sizes on mechanical properties

The vanadium welding technology derived from this study will be necessary to support the selection of the applicable welding processes for fabrication of the ITER components. Determination of the requirements for welding environment purity, weldment properties, and heat treatments will be essential to both specifying the welding processes and developing the welding procedures. The economics of component fabrication will depend heavily on the findings of this effort. Three welding processes currently have the highest potential for joining the vanadium alloy components proposed for the ITER project. These are the gas tungsten arc (GTAW), electron beam (EBW), and laser beam (LBW) welding processes. For the EBW process. interstitial contamination is avoided, hut at a high price; welding systems cost in excess of $1 million and even the largest chambers available will not hold the full-sized ITER components. Fit-up of parts must be excellent and machining tolerances very tight. Properly applied, however, the EBW process should give the best possible weldment properties. With both of the gas-shielded processes, GTAW and LBW. the potential for interstitial pickup exists. The extent of protection offered is determined by the type of shielding, e.g. local trailing shields, flexible enclosures, or rigid chambers, both pumped and continuous flow. In general, the cost increases as shielding quality improves. Other welding processes may be identified for specific applications as the design process continues.

CHEMICAL AND MECHANICAL INTERACTIONS OF INTERSTITIALS IN V-5%Cr-5%Ti –

J. H. DeVan, J. R. DiStefano, and J. W. Hendricks (Oak Ridge National Laboratory)

OBJECTIVE

A vanadium alloy structure cooled with liquid Lithium is the favored concept for an advanced breeding blanket **for** ITER. The objective of this task is to determine the kinetics of reactions of vanadium alloys with hydrogen and oxygen **as** a function of alloy composition and TMT.

SUMMARY

Gas-metal reaction studies **of** V-5Cr-5Ti were conducted to determine the kinetics of reactions with H_2 and O_2, respectively, at 400-500°C. Reaction rates were determined through weight change measurements and chemical analyses, and effects on mechanical properties were evaluated by room temperature tensile tests. Exposure to hydrogen at pressures between 10^{-4} to 10^{-2} torr lowered the tensile ductility in the case **of** coarse-grained specimens but had little effect on finer-grained specimens. Similarly oxygen uptake at 500°C, at concentrations **as** low **as** 200 ppm (by weight), significantly lowered the ductility of the coarser-grained but not the finer-grained material.

INTRODUCTION

Materials and **procedures**

Interactions of the V-5Cr-5Ti alloy with hydrogen were investigated using an ultra-high vacuum Sievert's apparatus to control the hydrogen pressure **and** temperature at conditions prototypic **of** the ITER plasma-first wall interface and the divertor. High purity hydrogen was admitted to the apparatus through a controllable leak valve at the same rate **that** it was extracted by a turbomolecular pump, and the pressure at the specimen **was** fixed within the range 10^{-4} *to* 10^{-2} torr. Exposure temperatures were 400 and 500°C with times ranging from 24 to 150 **hours.** A similar apparatus was used to make controlled oxygen additions to the alloy. In this case the alloy was exposed at 500°C for a specified period (typically 4-24 h) to pure oxygen at 1-2 x 10^{-6} torr, and then was heat treated under ultra-high vacuum to flatten the oxygen concentration gradient. Reaction rates were determined **through** weight change measurements and chemical analyses, and **effects** on mechanical properties were evaluated by room temperature tensile tests.

Two different heats of the V-5Cr-5Ti alloy were investigated. The first was the Teledyne Wah Chang Albany heat 832394 (ANL designation BL63), and the second was a small 350 g heat that was drop cast and rolled to sheet at *Oak* Ridge National Laboratory (ORNL). Compositions are listed in Table 1. The compositions of major components are comparable for the two heats, but iron, silicon, carbon, and nitrogen contents are higher in the ORNL heat. Small tensile specimens (SS-3), nominally 0.76 mm thick with 1.5 mm x 7.6 mm gage sections, were machined or stamped from 40% warm-reduced sheet **stock of the** alloys. The specimens were then vacuum annealed for 1 h at 1125°C.

Heat ID	Concentration (wt%)			Concentration (wt ppm)			
	Cr	Ti	Fe	O	N	C	Si
ORNL 14272	4.0	5.6	0.11	324	512	204	1100
WC 832394	4.2	5.4	<0.045	427	***52***	40	<0.031

RESULTS ***AND*** DISCUSSION

Despite significant differences in grain size, discussed below, both heats showed quite similar room temperature elongations, which were consistently in the range 29±1 percent. Aging under vacuum ($<10^{-8}$ **torr) at** 500°C produced no significant change in room temperature elongation over times exceeding those of the gas exposures (up to **200 h).** V-5Cr-5Ti tensile specimens were exposed to H_2 at **500°C** at pressures from 10^{-2} to 10^{-4} torr and were chemically analyzed for hydrogen following tensile testing at room temperature. For any given exposure condition, the uptake of hydrogen was similar for the two heats of V-5Cr-5Ti and was strongly affected by the rate at which the specimens were cooled from 500°C to room temperature. As shown in Figure **1,** specimens left in the furnace zone and slowly cooled under the hydrogen exposure pressure showed significantly higher hydrogen concentrations than companion specimens moved quickly to a cold zone in the upper part of the furnace at the same hydrogen pressure. The hydrogen concentration of the faster cooled specimens was quite similar to that for pure vanadium at 500°C (based on published **data).**[1] Although the hydrogen concentrations of the two heats were comparable far a given H_2 exposure, the effect on room temperature ductility was quite different between the heats, as shown in Table **2.** The ORNL heat showed no effect of hydrogen on ductility up to concentrations of **20** ppm **(by** weight), and, unless the oxygen content also increased, ductility decreased only slightly at hydrogen concentrations approaching **80** ppm. In contrast, the effect of hydrogen on the ductility of beat **832394** was generally greater for a given concentration and varied from one group of specimens to another. The difference in the ductility response showed a strong correlation with grain size differences between the heats. Although there were no apparent differences in the annealing treatments prior to testing (1 h at **1125°C),** the resultant grain size of heat **832394** was much coarser (ASTM **5-6)** than the **ORNL** heat (ASTM **9).** Heat **832394** also showed variations in grain size between groups of specimens fabricated from the same sheet stock but annealed at different times. Again. the coarser the **grain** size of the specimen, the greater the effect of hydrogen on the ductility. For example, a specimen of ASTM grain size **5,** with 20 ppm hydrogen and a very minor uptake of oxygen, exhibited a ductility of only **3.1%,** while a specimen with ASTM grain size **6** with **47** ppm hydrogen showed a ductility of **6.8%** (Table **2).** The hydrogen embrittlement mechanism and the role of grain size has not been established, but it does not appear to relate to hydride formation, based on microscopic examinations of specimen cross sections and fracture surfaces.

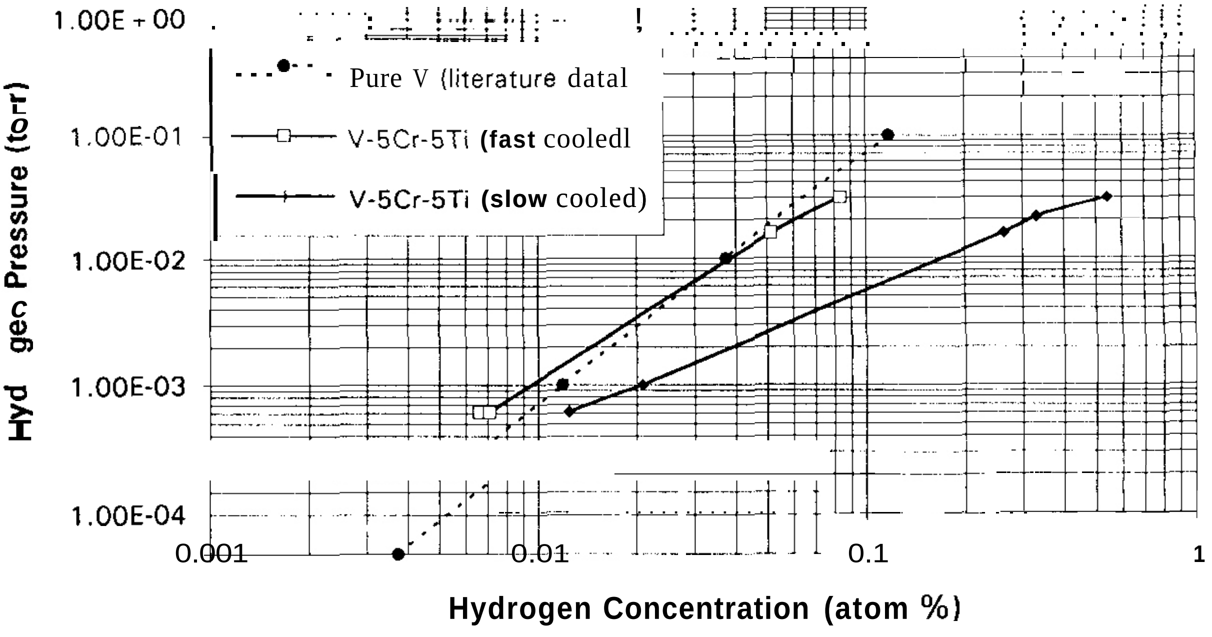

Fig. 1. Hydrogen concentration of V and V-5Cr-5Ti as a function of hydrogen pressure at **500°C.**

Table 2. Room Temperature Tensile Properties of V-5Cr-5Ti Alloys after Exposure to H_2 at 500°C

Heat	ASTM Grain Size	H Content (wt ppm)	O Content (wt ppm)	Yield Strength (MPa)	Ultimate Strength (MPa)	Elong (%)
ORNL	9	0.3*	324	376	456	30.8
ORNL	9	16	423	429	515	28.6
ORNL	9	77	458	491	568	21.7
832394	26	1*	421	410	490	34.7
832394	26	16	526	482	509	24.6
832394	26	47	654	511	465	6.8
832394	≤5	1*	410	391	48.3	25.3
832394	≤5	2	399	463	551	22.3
832394	55	20	445	432	455	3.1

*Unexposed specimens

The two V-5Cr-5Ti heats were exposed to oxygen at 1×10^{-6} and 2×10^{-6} torr, respectively, to establish rate of oxidation at 500°C and define appropriate boundary conditions for oxygen doping. Reaction rates with oxygen under these conditions were slightly greater for the ORNL finer grained heat; however, the effect of a given oxygen uptake on room temperature ductility was much less for the finer grained heat. Table 3 compares the oxygen uptake by the two heats after 24 h in 1×10^{-6} torr oxygen and after 4 h in 2×10^{-6} torr oxygen. The former exposure increased the oxygen content by 600-900 ppm (by weight), and the latter exposure, by approximately 200-300 ppm. In the as-oxidized condition, the tensile elongation of the ORNL heat decreased from 29% to 24% after the 24 h treatment However, after further aging for 96 h in vacuum at 500°C, the elongation dropped to 18%. The elongation of the ORNL heat was not affected by the initial 4 hour oxidation treatment at 500°C, but further aging for 100 h at 500°C decreased its elongation from 29 to 24%. Under the same conditions, the elongation of heat 832394 with ASTM grain size 5 was reduced from 29% to 7% by the 24 h oxidation treatment, and further aging for 96 h at 500°C resulted in fracture with essentially no yielding. The 4 h oxidation treatment at 2×10^{-6} torr reduced its elongation to 24%, and funher annealing in vacuum for 100 h at 5 W C again resulted in brittle fracture. Reducing the grain size of heat 832394 from ASTM 5 to ASTM 6 significantly increased the ductility for the same uptake of oxygen. The ductility of this finer grained material after the 4 h oxidation treatment and subsequent aging at 500°C was essentially the same as that of the ORNL heat.

Exposure to oxygen at 500°C for either 4 or 24 h resulted in near-surface pickup of oxygen, the specimen interior remaining relatively uncontaminated. Further annealing for 96-100 h at 500°C distributed the oxygen more uniformly over the specimen cross section. In this condition even the small amount of oxygen picked up in the 4 h exposures (which actually was less than the residual oxygen content of the alloys) substantially affected ductility, particularly in the case of coarse-grained material. It appears that oxygen introduced by the 500°C oxidation and aging treatment was retained in an interstitial, solid solution form, unliie the residual oxygen in the as-received specimen, which was present as an oxide precipitate. This conclusion was borne out by vacuum heat treating the 500°C-aged specimens for 4 h at 950°C. As shown in Table 3, the 950°C heat treatment essentially restored the ductility of a coarse-grained specimen of heat 832394, the elongation increasing from 0.7% before heat treatment lo 24% after heat treabnent. At the higher temperature oxygen was able to react with the titanium in the alloy to form an essentially insoluble precipitate, and its effect on ductility in this form was much less than in the interstitial form.

In the as-received condition, regardless of the grain size, the tensile specimens showed classic cup/cone fracture morphologies and relatively large reductions in area Higher magnification revealed that the failure mode was transgranular ductile tearing. However, in the case of the coarser-grained specimens with low ductility after hydrogen or oxygen uptake, the fractures were predominantly intergranular.

Table 3. Room Temperature Tensile Properties of V-5Cr-5Ti after Exposure to O_2 at 500°C

Heat	O_2 Exposure Conditions at 500°C		Post-Oxidation Annealing Treatment		O Content (wt ppm)	Yield Strength (MPa)	Ultimate Strength (MPa)	Elong (%)
	Pressure (torr)	Time (h)	Time (h)	Temp (°C)				
ORNL	Control		96	500	324	423	506	29.6
ORNL	1×10^{-6}	24	As-oxidized		1100	410	481	23.7
ORNL	1×10^{-6}	24	96	500	1180	427	485	18
ORNL	2×10^{-6}	4	As-oxidized		624	405	506	28.5
ORNL	2×10^{-6}	4	100	500	673	433	538	23.8
ORNL	2×10^{-6}	4	100 +4	500 950	624	379	485	28.8
832394	Control		96	500	410	402	506	28.3
832394	1×10^{-6}	24	As-oxidized		996	397	411	7.1
832394	1×10^{-6}	24	96	500	1070	409	431	0.3
832394	2×10^{-6}	4	As-oxidized		637	393	444	15.5
832394	2×10^{-6}	4	100	500	668	401	437	0.7
832394	2×10^{-6}	4	100	500	616	350	456	25.9

FUTURE WORK

Transmission electron microscopy will be used to investigate the mechanical and chemical nature of the grain boundaries before and after the ingress of hydrogen and oxygen in both the fine-grained and coarse-grained materials. The combined effects of hydrogen and oxygen doping at 500°C on room temperature ductility will also be investigated.

REFERENCES

1. E. Fromm and E. Gebhardt, Gase und Kohlenstoff in Metallen, Springer-Verlag, Berlin/Heidelberg **(1976).**

THE RELATIONSHIP BETWEEN RECRYSTALLIZATION TEMPERATURE, GRAIN SIZE, AND THE CHARPY IMPACT PROPERTIES OF V-Cr-Ti ALLOYS – M. L. Grossbeck, A. F. Rowcliffe, and D. J. Alexander

OBJECTIVE

A vanadium structure, cooled with liquid lithium is the favored concept for an advanced breeding blanket for ITER. The objective of thii task is to define the processing parameters for optimal alloy performance in the V-Cr-Ti alloy system.

SUMMARY

It is shown that the blunt notch Charpy impact properties of a V-5Cr-5Ti alloy are extremely sensitive to the grain size distribution developed during the final annealing treatment. Ductile behavior down to liquid nitrogen temperatures can be induced, for example, by a treatment at 950°C, rather than annealing at 1125°C. It is proposed that the resistance to irradiation-induced shift in DBTT reponed by Argonne National Laboratory (ANL) researchers for the V-4Cr-4Ti alloy is related primarily to the exceptionally fme-grained microstructure developed during the low temperature processing mute adopted for this alloy.

PROGRESS AND STATUS

Introduction

Because of their potential ability to accommodate higher heat loads than austenitic stainless steels, and their more favorable radio-activation properties, vanadium alloys are being developed for advanced blanket options for ITER. For many years a vanadium alloy containing 15 wt % Cr and 5 wt % Ti was the reference alloy in the U.S. alloy development program. However, data generated in the late 1980's indicated that this alloy was pmne to radiation-induced brittle fracture behavior at potential reactor operating temperatures.[1] Subsequent work by Loomis and coworkers[2] demonstrated that alloys containing a combined Cr and Ti content in the range 3 to 9 wt % were more resistant to both hydrogen and radiation-induced embrittlement. Further work, focusing on Charpy impact studies on a range of compositions, led to the recommendations of an alloy for structural applications in a fusion reactor with a composition of V-5Cr-5Ti (wt%) containing ~400 wppm O, –200 wppm N, and –900 wppm Si? In mid-1993, researchers at ANL proposed this alloy as the primary candidate for the development of an advanced blanket option for ITER. Under the 1994 ITER task agreements, major efforts were initiated in the U.S. and Russia, with supporting studies in the EC and Japan, to address critical issues in fabrication, welding, compatibility, insulator coatings, and irradiation performance of vanadium alloys (ITER R&D Task T13). The ANL recommendation for an alloy based upon V-5Cr-5Ti was modified later in 1993[4] on the basis of miniature Charpy V-notch (MCVN) impact data for a set of ten V-Cr-Ti alloys with titanium ranging from 1 to 15 wt % and chromium ranging from 5 to 15 wt %. Data were presented for annealed alloys with and without hydrogen charging; MCVN data were also presented for V-Cr-Ti alloys following irradiation to 34 to 44 dpa at ~420°C. The data presented (and reproduced here as Fig. 1) showed a very strong dependence of the ductile-to-brittle transition temperature (DBTT) on chromium concentrations for annealed, hydrogen charged, and for neutron irradiated alloys. Based on these findings, Loomis et al.[4] recommended the selection of a V-4Cr-4Ti alloy as having a near-optimal combination of physical and mechanical propenies for structural applications in a fusion reactor. It was speculated that the extremely low DBTT of the V-4Cr-4Ti alloy (heat BL47) may be related to a high volume fraction of non-coherent particles of the type (Ti(NCO)). A later report by Chung et al.[5], cast doubt on the hypothesis that fracture behavior is a sensitive function of Cr concentration in alloys containing 3 to 5 wt % Ti. Large variations in DBTT occurring within a relatively small band of Cr and Ti concentrations (3 to 5 wt %) were investigated. It was shown that the alloys with relatively high DBTTs (V-5Cr-3Ti and V-5Cr-5Ti) were characterized by high density precipitation of complex vanadium compounds containing Cl, S, Ca. Na. and K. It was suggested that (a) the formation of these deleterious compounds is favored in alloys containing significant levels of Cl, and (b) the absence of a DB1T in the V-4Cr-4Ti alloy tested down to liquid nitrogen temperatures was related to the use of higher quality raw materials low in Cl, S, P, Ca, Na, and K. It was also noted that the effect of post-fabrication annealing temperature on DBTT behavior was secondary, and that ductile behavior at liquid nitrogen temperatures could not be induced by laboratory annealing of the V-5Cr-5Ti and V-5Cr-3Ti alloys5

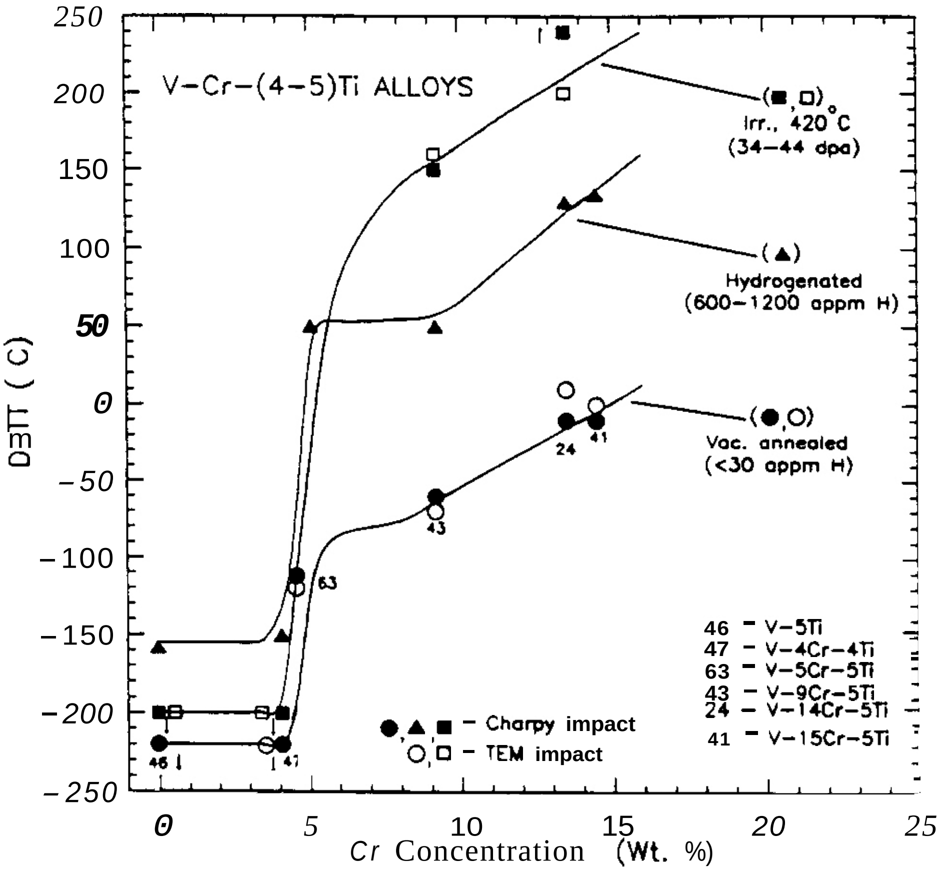

Fig. 1. Data of Loomis et al^4 on the **effects** of Cr concentration, hydrogen concentration, and irradiation on the Charpy impact properties of vanadium alloys containing **4** to **5 wt % Ti.**

The present work was undertaken to investigate further some of these ideas. Using the V-5Cr-5Ti alloy (heat BL63), two hypotheses were addressed. Firstly. a search was made for evidence that the presence of Cl plays a role in the fracture behavior of the beat **BL63** material. This topic is dealt with in a companion article in this document.^{6} Secondly, the *ANL* finding that post-fabrication annealing temperature has only a secondary effect on fracture properties was re-examined, since it is well known that in other refractory metal alloy systems, recovery/recrystallization treatments have a very strong influence on DB'IT.

Experimental

The starting material was in the form of an annealed plate –7 mm thick from Teledyne Wah Chang heat **832394, (ANL** designation BL63). The chemical analysis of heat BL63 provided by the manufacturer was 4.6 wt % Cr, 5.1 **wt 46** Ti. 440 wppm O, 28 wppm N, 73 wppm C, and 310 wppm Si. **An** overcheck carried out at **ORNL** gave impurity concentrations of 364 wppm O, 52 wppm N, 35 wppm C, and **1** wppm H. This material was **used** to fabricate **1/3-size** CVN specimens (MCVN) according to the processing schedule **shown** in Table **1.** Chemical analyses were carried out at several stages to check interstitial contamination. Rolling was carried out in air at **250** to 300°C and annealing carried **out** with Ta gettering in a vacuum of 10^{-5} to 10^{-4} Pa. Further discussion of processing methods may be found in a companion article in this document?

Table 1. Processing Schedule for V-5Cr-5Ti (Heat BL 63)

	Chemical Analysis (wppm)			
Stage	C	O	N	H
7 mm thick plate	35	364	52	1.1
↓				
Acetone clean				
↓				
Etch 5 min. (0.6 H_2O, 0.3 HNO_3, 0.1 HF)				
↓				
Ta foil wrap, anneal, $<10^{-4}$ Pa 1125°C, 1 h	37	374	50	0.5
↓				
Etch 5 min				
↓				
Roll at 250 to 300°C 12 to 13 passes to, 3.6 mm (46% RA)	42	384	54	0.6
↓				
Machine CVN L-T orientation				
↓				
Clean in Pet. Ether, Acetone				
↓				
Etch 5 min.				
↓				
Anneal 1125°C/1025°C/950°C Ta foil, $<10^{-4}$ Pa				
↓				
Test				

The impact specimens were third-size Charpy specimens, 3.33 by 3.33 by 25.4 mm long. They contained a 30°-included angle notch that was 0.51 mm deep with a root radius of 0.08 mm. All specimens were oriented so that crack extension was parallel to the rolling direction (L-T orientation). To prevent hydrogen pickup during fabrication, no water-based coolants were used, nor was electrodischarge machining employed.

The third-size specimens were tested in a semiautomated pendulum-type impact testing system modified for testing subsize specimens.[8,9] Gas from liquid nitrogen was used for cooling and a hot air gun for heating. After testing, the results were fitted with a hyperbolic tangent function to allow the DBTT and the upper-shelf energy (USE) to be determined. The lower-shelf energy was fixed at 0.2 J. The DBTT was determined at an energy level midway between the upper- and lower-shelf energy levels.

A few specimens were fatigue precracked prior to testing to determine the effect of a sharp crack as compared to a blunt notch. These specimens were precracked on a servohydraulic test machine operating in stroke control at 30 Hz with a sinusoidal waveform. The initial load was approximately 267 N. As the crack grew from the notch the load decreased. The final load was typically about 133 N. The stress intensity was estimated using the formulae for three-point bending.[10] The span (S) was 22.9 mm, so the ratio of span to width (S/W) was 6.87. Therefore, it was necessary to extrapolate between the given solutions for S/W values of 8 and 4. The initial maximum value of the stress intensity was calculated to be 9.9 $\mathrm{MPa}\sqrt{\mathrm{m}}$, for a crack to width ratio (a/W) of 0.15. For the final crack length of half the specimen width (a/W = 0.5) the maximum stress intensity was determined to be 12.9 $\mathrm{MPa}\sqrt{\mathrm{m}}$. Recracking required about 100,000 cycles.

Results

MCVN Impact Testing

Based upon the fabrication schedule shown in Table 1, four sets of MCVN specimens were fabricated. One set was tested in the 46% warm worked condition: the other three were given annealing treatments of one hour at 1125°C, 2 hours at 1050°C, or 2 hours at 950°C. The absorbed energy versus temperature data are shown in Fig. 2. The four thermomechanical treatment (TMT) conditions gave rise to four different types of fracture behavior. For the warm-worked material, absorbed energy increased with increasing test temperature without any indication of a transition regime. At all temperatures, fracture occurred by a mixture of ductile tearing and cleavage. The elongated and banded nature. of the as-rolled grain structure was evident in the fracture surface. (Fig. 3). Annealing for two hours at 950°C resulted in a large increase in absorbed energy so that specimens fractured in a completely ductile manner with bending and only partial separation of the two halves. although there was some decrease. in absorbed energy in going from -100 to -196°C. In this TMT condition, alloy BL63 was extremely resistant to brittle cleavage failure under the loading conditions and notch geometry of this test. Annealing at 1050°C for two hours resulted in the appearance of conventional DBlT behavior, with a transition temperature in the vicinity of -120°C. Annealing at 1125°C for one hour resulted in a large upward shift in transition temperature to around +75°C. In the transition region, the fracture surfaces contained a high proportion of intergranular cleavage fracture (Fig. 4). while transgranular fracture dominated the lower shelf region.

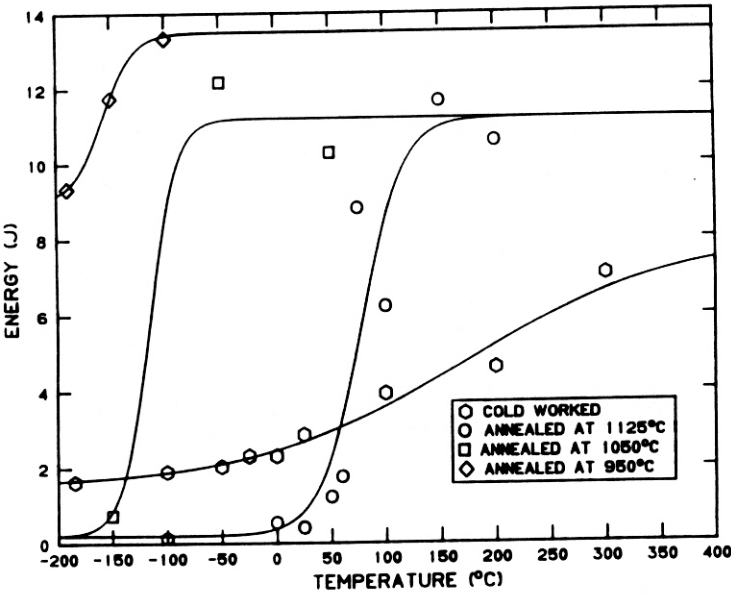

Fig. 2. Blunt-notch MCVN data for alloy BL63 in various TMT conditions.

The test results for the pre-cracked specimens for alloy BL63 following annealing at 1125°C for one hour are shown in Fig. 5. The results for the standard notch are included for comparison. Precracking resulted in a large increase in the transition temperature. from 76°C to 289°C, and a large decrease in the upper-shelf energy, from 8 J to 3.7 J. For example, a shift in the DBlT of 30°C and a drop in the USE by a factor of 3 have been observed for third-size specimens of HT-9 as a result of fatigue precracking.[11] The present results show a shift in DBlT of 161°C and a decrease in USE by a factor of 4.4, indicating that this alloy is very notch sensitive following the high temperature annealing treament.

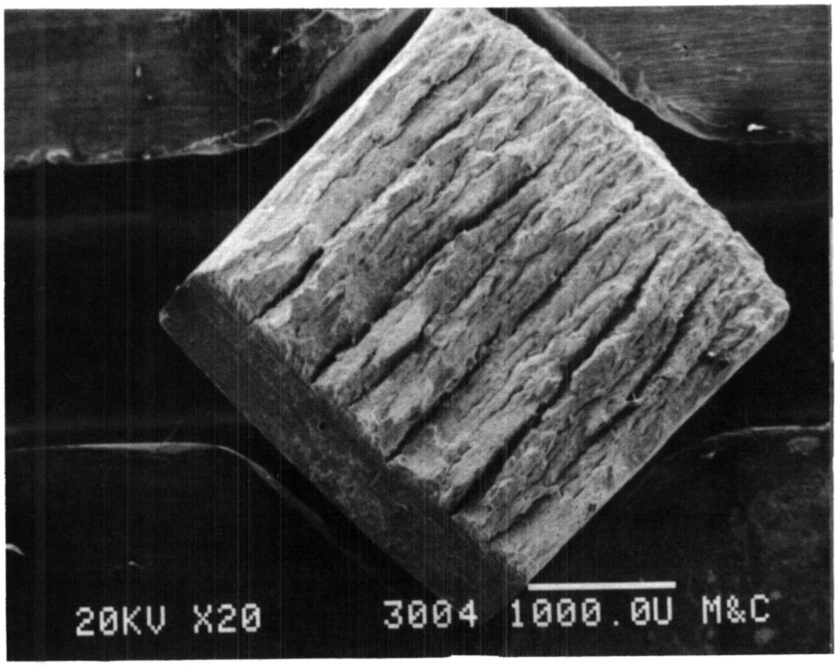

Fig. 3. **SEM** of **fracture surface** of alloy BL63 in the warm worked condition.

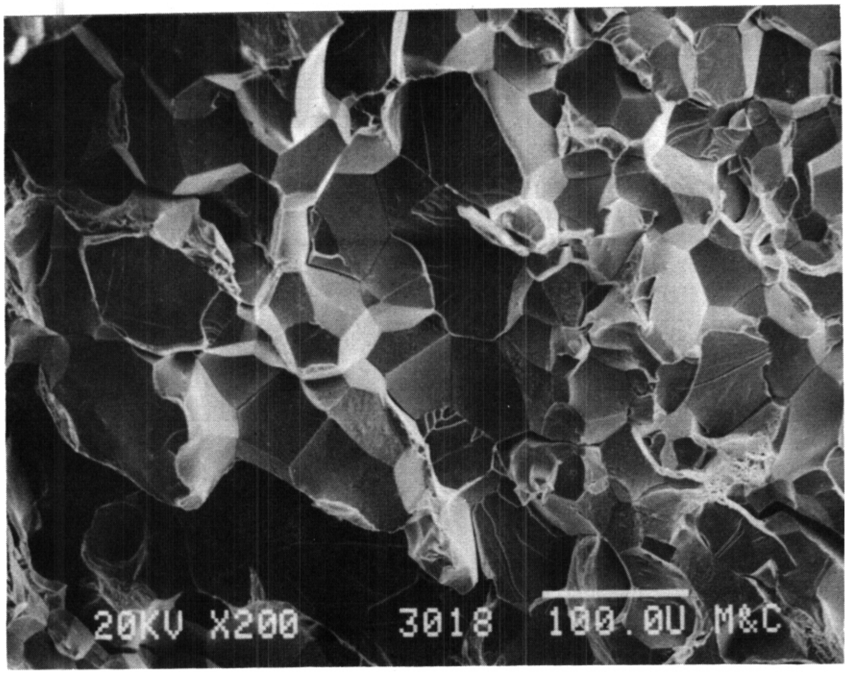

Fig. 4. SEM of transition region fracture **surface** of alloy BL63 in the **1125°C** annealed condition.

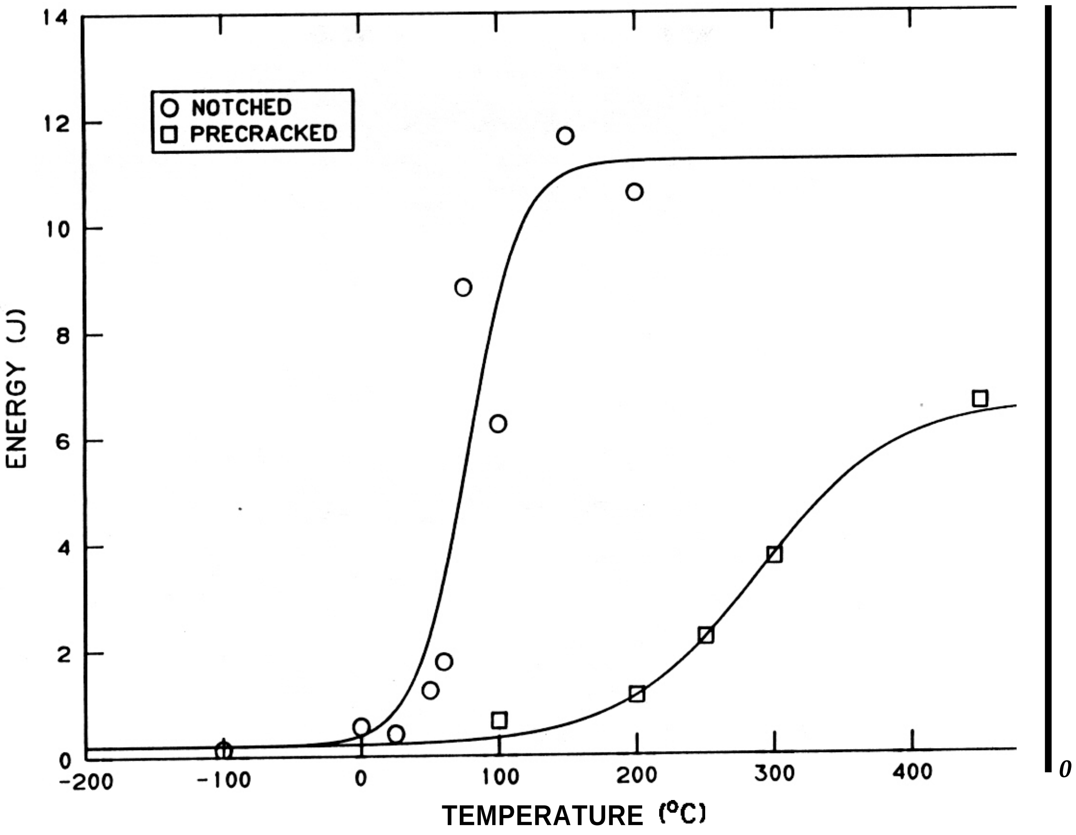

Fig. 5. Comparison of blunt-notch and precracked Charpy impact data for alloy BL63 in the 1125°C annealed condition. Absorbed energy values have been adjusted for the smaller ligament area remaining after pre-cracking.

Microstructure

Optical metallography showed that warm rolling to 46% reduction in thickness produced a layered plate-like grain structure with bands of dispersed phases, probably titanium oxy-carbonitrides, strung out in the rolling direction (Fig. 6a). The Vickers hardness number in this condition was ~224 DPH. Annealing at 950°C for two hours resulted in partial recrystallization and a reduction in hardness to –164 DPH. The microstructure (Fig. 6b) contained small (4 to 8 µm) recrystallized grains dispersed within the original elongated grains which contained a recovered dislocation structure.

The two hour anneal at 1050°C produced complete recrystallization and a hardness value of –174 DPN. The original elongated grain structure was not completely eliminated. Bands of smaller-than-average grains (10-20 µm) occurred in association with the bands of precipitate particles together with larger elongated grains in the range 50-100 µm dia (Fig. 7a). TEM examination showed a moderate dislocation density associated with the particle bands. A finely distributed phase precipitated on many of the new grain boundaries after recrystallization during the subsequent furnace cool to room temperature; this phase has not yet been identified. Annealing the warm-worked structure at 1125°C for one hour resulted in a more uniform and more qui-axed grain structure, although the average grain size was not much greater than that produced at 1050°C (Fig. 7b). The hardness of the annealed structure was –175 DPH.

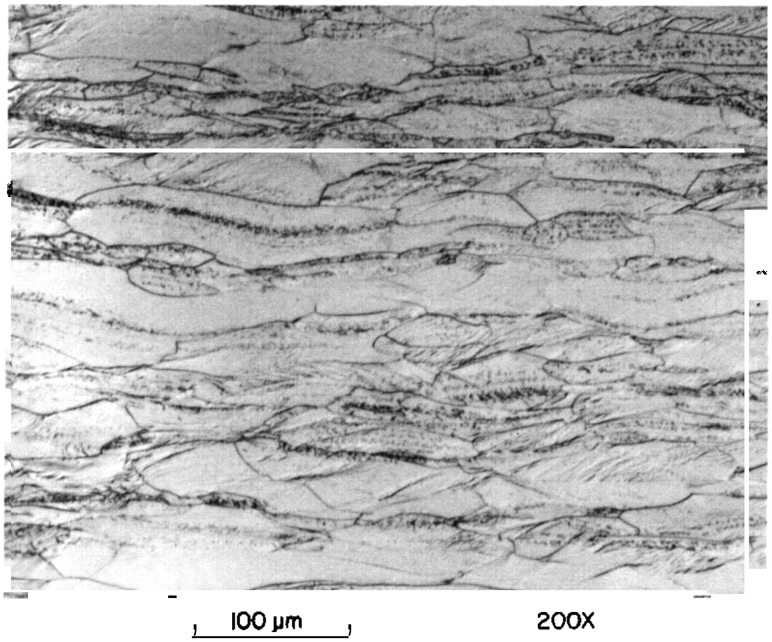

Fig. 6a. Optical micrograph of alloy BL63 in the 46% warm-rolled condition.

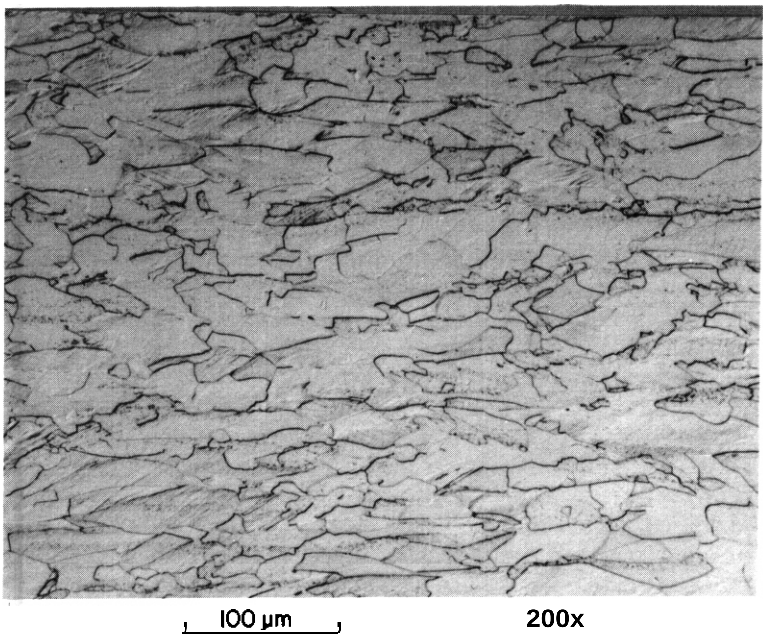

Fig. 6b. Optical micrograph of alloy BL63; warm-rolled 46% and annealed at 950°C for 2 hours.

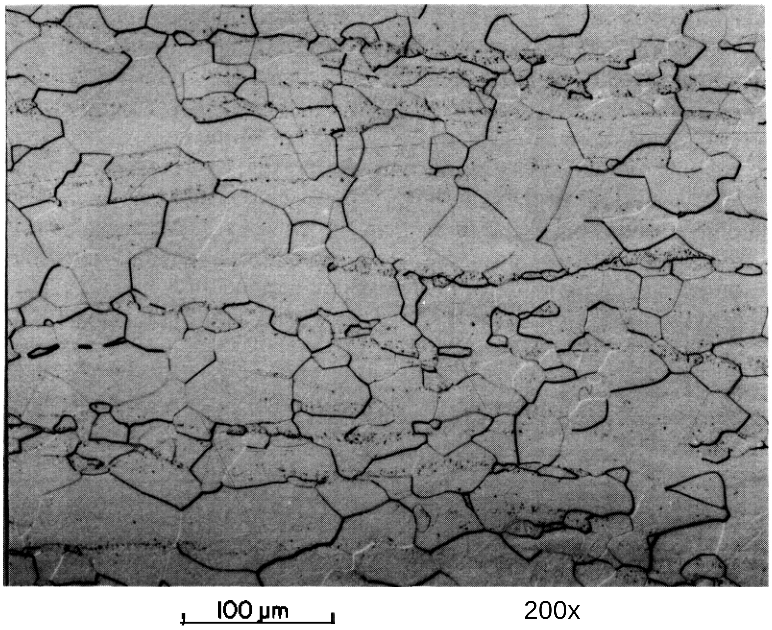

Fig. 7a. Optical micrograph of alloy BL63; warm-rolled 46% and annealed at 1050°C for 2 hours.

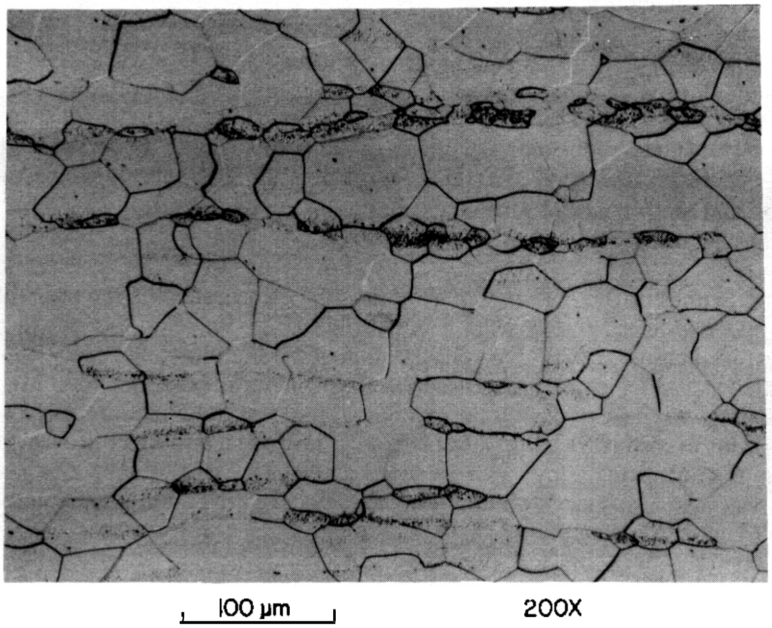

Fig. 7b. Optical micrograph of alloy BL63; warm-rolled 46% and annealed at 1125°C for 1 hour.

Discussion

The results described above need to be considered in the context of the data previously reported on heat BL63 and other alloys by researchers at ANL. Table 2 summarizes the DBTT data for a set of alloys reported by Loomis, et al.[3,4] and by Chung et al.[5] It should be pointed out that there is a discrepancy in the data previously reported for heat BL63. The unirradiated DBTT for heat BL63 (following an anneal at 1125°C) was reported by Loomis et al.[4] as -110°C. Subsequently, Chung et al[5] reported the DBTT as -30°C for an 1125°C anneal (Fig. 1 of reference 5). Accepting the latter as correct, the DBTT data in Table 2 are shown plotted as a function of Cr concentration in Fig. 8. It has been suggested that the DBTT of alloys in the V-Cr-Ti system depends strongly upon Cr concentration with a *sharp* increase in DBTT occurring for compositions containing more than ~4 wt % Cr.[4] An alternative interpretation (based on Fig. 8) is to regard the data as falling into two groups distinguished by their final recrystallization temperature. The group of alloys that were annealed at temperatures of 1125°C and above exhibit DBTTs in the range of zero to -100°C. On the other hand, the group of alloys annealed at 1100°C or lower showed ductile behavior at liquid nitrogen temperatures.

Table 2. Summary of ANL Data on DBTT of Vanadium Alloys

Heat ID	Cr wt %	Ti wt %	Anneal Temp (°C)	Unirradiated DBTT (°C)	Irradiated DBTT (°C)
BL 62	3.1	–	(4) 1100°C	-255	-220
BL 46	4.6	–	(4) 1100°C	-250	-220
BL 47	4.1	4.3	(5) 1050°C	-225	-225
BL 63	4.6	5.1	(5) 1125°C	-30	–
BL 54	5.1	3.0	(5) 1175°C	-85	–
BL 43	9.2	4.9	(3) 1125°C	-60	+150
BL 24	13.5	5.2	(3) 1125°C	-10	+240
BL 41	14.5	5.0	(3) 1125°C	-10	+240

()denotes literature reference

The room temperature yield stress data reported by *Gazda* et al.[12] show a trend of increasing yield stress with increasing Cr plus Ti concentration. A subset of their data is reproduced in Fig. 9 showing a linear increase in yield stress with Cr concentration. This increasing strength with Cr concentration might be expected to result in some dependency of DBTT on composition. However, the data in Fig. 8 strongly suggest that factors relating to the final recrystallization temperature are more dominant than Cr concentration and are probably instrumental in producing the previously reported[4] *sharp* discontinuity in behavior at around 4 to 6 wt % Cr.

A remarkable feature of the data reported by the ANL researchers is the radically different response to irradiation between these two groups of materials (Fig. 8). For the alloys annealed at the higher temperatures, irradiation at 420°C to -30 dpa induced a large increase (~250°C) in DBTT, whereas the alloys annealed at 1100°C or below showed ductile behavior in postirradiation MCVN tests down to liquid nitrogen temperatures. For both groups of alloys, the room-temperature yield stress increased by over 100% as a result of radiation hardening (Table 3): however. this level of hardening was insufficient to induce brittle fracture in the alloys with the lower annealing temperatures. It is particularly significant that alloy BL47 retains its resistance to brittle fracture even when the room-temperature yield stress is increased to 800 MPa by radiation hardening.

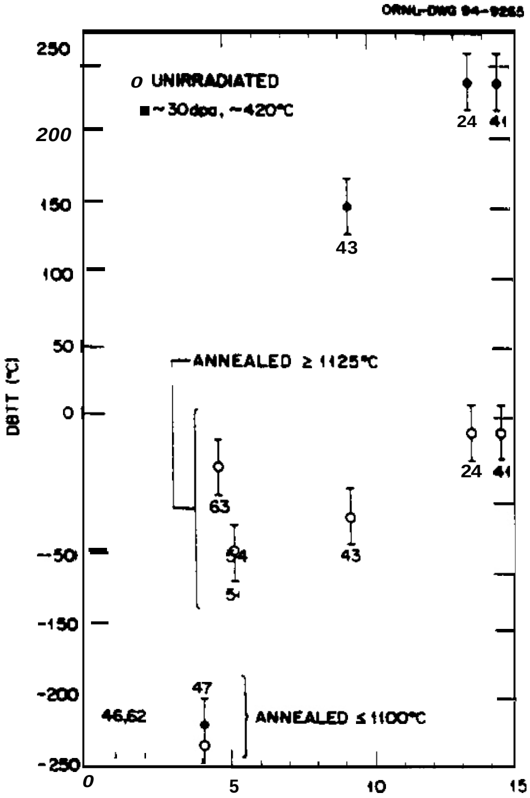

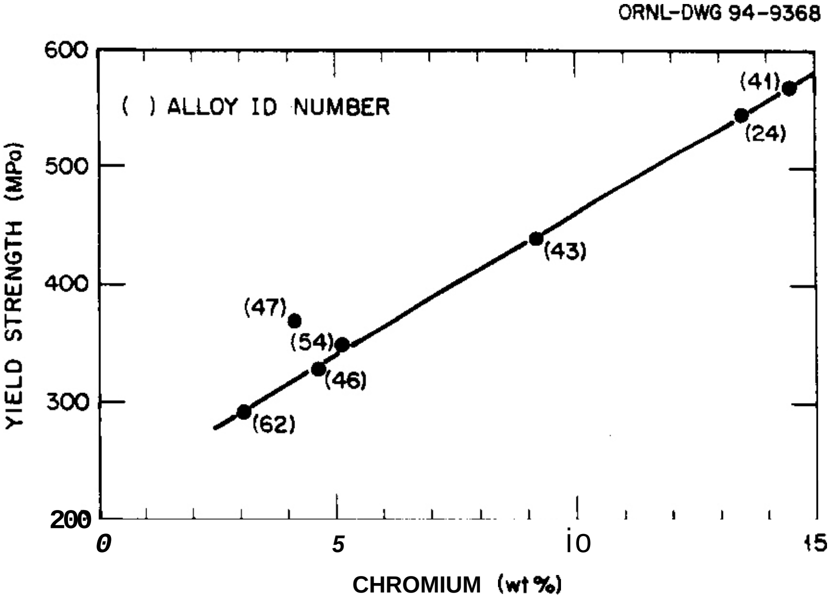

Fig. 9. Data of Gazda et al[12] on the dependence of room temperature yield strength on Cr concentration.

Table 3. *Summary* of ANL Data for RT Yield **Stress** and **DBTT** of Vanadium Alloys
(Irradiated at 420°C to –30 dpa)

Heat ID	**Cr** wt 90	Ti wt 90	**Unirradiated** YS (MPa)	**Irradiated** YS (MPa	ΔDBTT °C
BL 62	**3.1**	–	**290**	–	**0**
BL 46	**4.6**	–	**330**	**690**	**0**
BL 47	**4.1**	**4.3**	**370**	**800**	**0**
BL 54	**5.1**	**3.0**	**330**	–	–
BL 43	**9.2**	**4.9**	**440**	**1060**	**210**
BL 24	**13.5**	**5.2**	**550**	–	**250**
BL 41	**14.5**	**5.0**	**570**	**1180***	**250**

Current Data

The above discussion of previously reported ANL data indicates a possible strong influence of final annealing temperature on the fracture behavior during blunt-notch **MCVN** testing. The data reported here on the effects of final annealing temperature on the unirradiated **MCVN** properties **of heat BL63 clearly** demonstrate the importance of TMT on fracture behavior. It has been shown that **MCVN** properties of alloy **BL63** can be varied from **brittle** behavior at room temperature to ductile behavior at all temperatures down to **-150°C** simply by changing the final annealing temperature.

Following the **1125°C** treatment, the blunt notch transition temperature is **~75°C**. The precracked **MCVN** data show that the material is very notch-sensitive in this condition. Recracking of the specimens was difficult. The first attempt made at a maximum load of **311 N** resulted in permanent deflection of the specimen. At a lower loading of **267 N,** about **10,000** cycles were required. The fact that a crack would grow at such a low stress intensity indicates very limited resistance to fatigue crack growth in this condition. Patches of cleavage facets were observed in the pre-crack region, indicating that this alloy is susceptible to static fracture modes at very low stress intensities **at room** temperature. In fact, very low room-temperature static fracture toughness values for this alloy in **this** TMT condition have been reported by Li et **al.**[13]

Recovery and partial recrystallization at **950°C** of the heavily deformed microstructure of alloy **BL63** produces a highly ductile behavior very similar to that of the **BL47** alloy. A sample of this latter alloy in the form of a **MCVN** specimen was supplied by ANL. The manufacturer's records showed that the processing history of heat **BL47** was significantly different from that of heat **BL63.** The **120** mm dia ingot was extruded in a *64* mm square section following a solution treatment at **1150°C. Warm** rolling was carried out at ~400°C. However, the significant processing change was the introduction of inter-pass annealing treatments of 2 hours at **1050°C** rather than at **1100** to **1150°C.** The final recrystallization treatment was at 1050°C for **4** hours. Optical microscopy of this material showed a very fine-grained equiaxed microstructure containing bands of fine grains **(2** to **5 µm) associated** with stringers of particles that presumably became aligned during hot extrusion (Fig 10a). These bands were separated by regions of coarser grains **(15** to **20 µm)** where the precipitate density was relatively low (Fig. 10b). Thus, the microstructures of the **BL63** (after annealing at **950°C)** and **BL47** alloys, which are associated with highly ductile behavior, are similar in that they **both** contain a bimodal grain size distribution and bands of undissolved particles. In the case of the **BL47,** the microstructure is fully recrystallized and nearly equiaxed. In the case of the **BL63,** the microstructure produced by the **950°C** for **2** hours treatment contains small recrystallized grains mixed with larger grains containing a recovered dislocation cell structure; both types of grains are elongated in the working direction. It should be noted that the repeated working and **1050°C** anneal cycles adopted for alloy **BL47** produced a much finer grain size distribution than that developed in alloy **BL63** by single, final anneal **at 1050°C.**

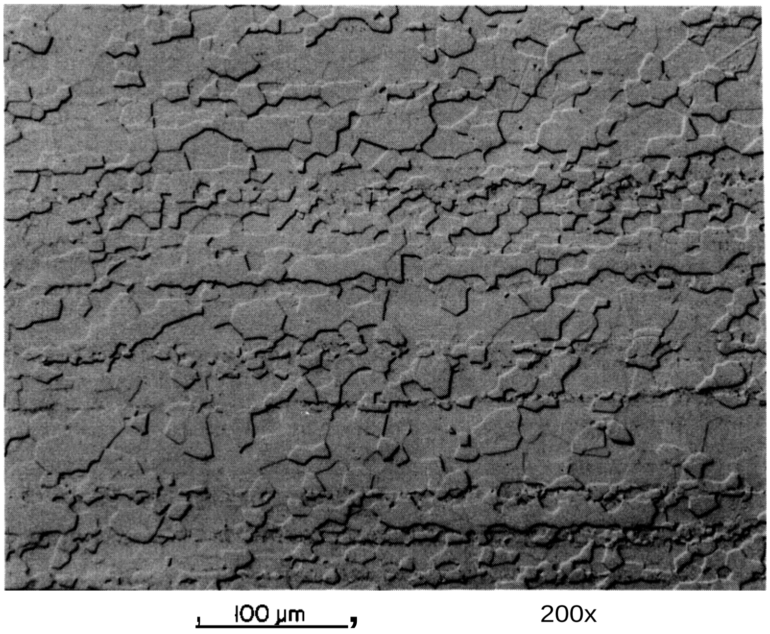

Fig. 10a. Optical micrograph of alloy **BL47** annealed at 1050°C **for 4 hours**.

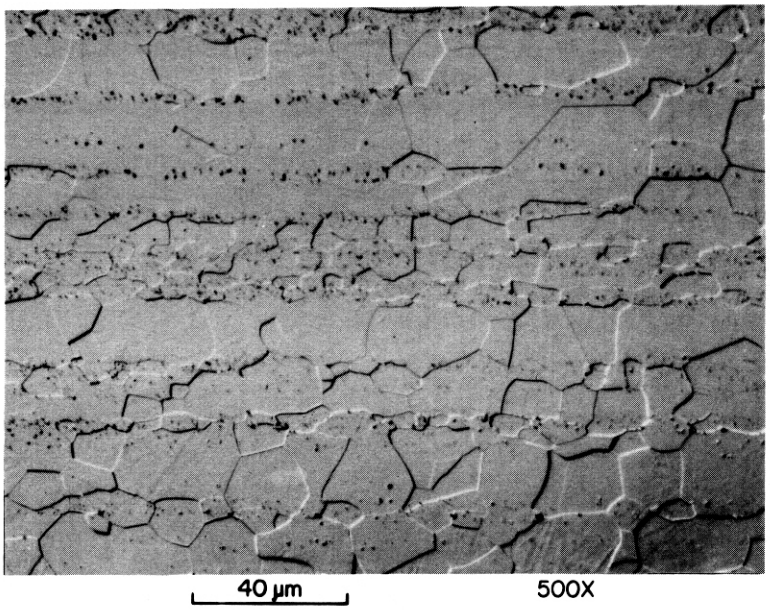

Fig. 10b Optical **micrograph** of alloy **BL47** annealed at **1050°C for 4 hours.**

It is well known that the DBTT of BCC metals such as W and Mo can be improved by the introduction of dislocations through plastic working. It has also been shown that postirradiation ductility in V-15Cr-Ti can be improved by cold-working.[14] It has been suggested that when the dislocation density is low, plasticity and blunting of the tip of a loaded crack may be prevented. At higher dislocation densities. when dislocations lie closer to any given crack tip, lattice resistance is exceeded by the crack tip field; dislocations move and multiply, thus blunting the crack.[15] The 950°C treatment of the BL63 alloy results in a material with a fairly high dislocation density compared with the material annealed at 1050°C. However, this is not believed to be a critical factor in the high toughness of the BL43 alloy under these testing conditions since the BL47 alloy does not contain a recovered microstructure and has a low overall dislocation density. Based upon current evidence, it is concluded that highly ductile behavior in these alloys is associated with a small average grain size and/or a bi-modal, banded grain size distribution. Differences in Cr and Ti concentration and the presence of <1 wppm Cl do not appear to be very significant. At the present time, we do not have sufficient information on the distribution of the interstitial elements O. N, and C between particles and solid solution. It is possible that annealing at temperatures ≤1050°C, besides reducing grain size, also leads to precipitation of a greater fraction of the interstitials in the form of titanium oxy-carbonitrides, thus lowering the concentration of O, C, and N in solid solution.

It is clear that final recrystallization treatments at temperatures that lead to a coarse qui-axed grain structure should be avoided. The large increase in DBTT that occurs in BL63 when the final heat treament is increased from 1050 to 1125°C may be the result of other phenomena since the average grain size increase is relatively small. Recently. H. Li et al.[13] reported brittle failure in room temperature fracture toughness tests of alloy BL63 following an anneal at 1125°C for one hour. Such behavior is consistent with the blunt notch CVN data reported here. Fracture surfaces contained a relatively large proportion of intergranular separation and preliminary Auger electron spectroscopy analysis showed significant enrichment of sulfur at grain boundaries.[6] Jones has suggested the possibility that above some critical processing temperature (~1100°C), a sulfur-containing compound dissociates and releases elemental sulfur which segregates to grain boundaries, and that the subsequent brittle behavior is initiated by grain boundary separation.[16]

CONCLUSIONS

In summary, the results presented here indicate that for alloys containing 4 to 5 wt % of Cr and of Ti fracture properties are very sensitive to the final recrystallization treatment. The resistance of alloy BL47 to irradiation induced shifts in DBTT is believed to be related to the exceptionally fine-grained microstructure developed during the low-temperature processing route adopted for this alloy. It is probable, however, that other factors, in addition to the small grain size are involved; lower temperature anneals may also affect the concentration of grain boundary segregants. particularly sulfur. The distribution of C. O, and N between solid solution and precipitate phases is almost certainly altered by the final annealing temperature and by the subsequent rate of cooling. Finally, it should be pointed out that, although the microstructures produced by low temperature annealing are very resistant to cleavage fracture during blunt-notch MCVN testing, fracture resistance in the presence of sharp cracks remains to be evaluated.

REFERENCES

1. D. N. Braski. J. Nucl. Mater. 141-143(1985) 1125-1131.
2. B. A. Loomis, L. J. Nowicki, and D. L. Smith. Fusion Reactor Materials Semiannual Progress Report for Period Ending September 30,1991 (DOE/ER-0313/11) 227.
3. B. A. Loomis, L. J. Nowicki, J. Gazda, and D. L. Smith, Fusion Reactor Materials Semiannual Progress Report for Period Ending March 31.1993 (DOE/ER-0313/14) 318.
4. B. A. Loomis. H. M. Chung, L. J. Nowicki, and D. L. Smith, "Effects of Neutron Irradiation and Hydrogen on Ductile-Brittle Transition Temperatures of V-Cr-Ti Alloys," to be published in the Proceedings of the Sixth International Conference on Fusion Reactor Materials, Stresa, Italy, September 27, 1993.
5. H. M. Chung, J. Gazda, L. J. Nowicki, J. E. Sanecki, and D. L. Smith, Fusion Reactor Materials Semiannual Progress Report for Period Ending September 30.1993 (DOE/ER-0313/15) 207.

6. D. N. Braski, and M. L. Grossbeck, "Analysis of Grain Boundaries in a V-5Cr-5Ti Alloy Using Auger Electron Spectroscopy," thii document
7. M. L. Grossbeck, T. K. Roche. W. S. Fatherly, F. F. Dyer, and N. H. Rouse, "Fabrication of Vanadium Alloy produce Forms for Specimen Fabrication," this document.
8. W. R. Corwin and A. M. Hougland, "Effect of Specimen Size and Material Condition on the Charpy Impact Properties of 9Cr-1Mo-V-Nb Steel," in The Use of Small-Scale Specimens for Testing Irradiated Material, ASTM STP 888, W. R. Corwin and G. E. Lucas, eds., American Society for Testing and Materials, Philadelphia, **(1986) 325-328.**
9. D. J. Alexander, R. K. Nanstad. W. R. Corwin, and J. T. Hutton, "A Semiantomated Computer-Interactive Dynamic Impact Testing System,'' in Applications of Automation Technology to Fatigue and Fracture Testing, ASTM STP **1092,** A. A. Braun, N. E. Asbbaugh, and F. M. Smith, eds., **American** Society for Testing and Materials, Philadelphia **(1990) 83-94.**
10. H. Tada, P. C. Paris, and G. R. Irwin, The Stress Analysis of Cracks Handbook, Del Research Corp., Hellertown, PA **(1973) 2.16.**
11. A. **S. Kumar.** B. S. Louden, F. A. Gamer, and M. L. Hamilton, "Recent Improvements in Size Effects Correlations for DBTT and Upper Shelf Energy of Ferritic Steels," in Small Specimen Test Techniques Applied to Nuclear Reactor Vessel Annealing and Plant Life Extension, **ASTM** STP 1204, W. R. Corwin. F. M. Haggag. and W. L. Server, eds., American Society for Testing and Materials, Philadelphia **(1993) 47-61.**
12. J. Gazda, **B.** A. Loomis, L. J. Nowicki. D. L. Smith, and S. Danyluk, Fusion Reactor Semiannual Progress **Report** for Period **Ending** September **30,1993 (DOE/ER-0313/15) 232.**
13. H. Li, **R.** H. Jones, and J. P. Hirth, this document.

14. M. L. Grossbeck and J. A. Horak, 'Tensile and Fracture Properties of EBR-11-Irradiated V-15Cr-5Ti Containing Helium." in Influence of Radiation on Materials Properties, ASTM **STP 956, ASTM,** Philadelphia **(1987),** p. **291.**
15. M. F. Ashby and J. D. Embury, The Influence of Dislocation Density on the Ductile-Brittle Transition in BCC Metals, Scripta Metallurgica **19 (1985) 557-562.**
16. **R.** H. Jones, private communication.

ROOM TEMPERATURE ELASTIC PROPERTIES OF V-5Cr-5Ti

–W.A. Simpson (Oak Ridge National Laboratory)

OBJECTIVE

The objective of this task is the measurement of the thermal and physical properties of a V-5Cr-5Ti alloy.

SUMMARY

Elastic moduli were measured for a specimen of the alloy V-5Cr-5Ti in the annealed condition using pulse-echo techniques. The value of Young's modulus was determined to be 125.6 GPa, the shear modulus was determined to be 45.9 GPa, and the Poisson's ratio to be 0.367.

PROGRESS AND STATUS

Introduction

Considerations such as thermal *stress* and thermal fatigue life require accurate values for physical properties such as thermal expansion, thermal conductivity, and Young's modulus. Thermal stress and thermal fatigue is necessary the determine the design lifetime for fust **wall** and **blanket** structures. It is also necessary to have accurate physical properties to compare the projected performance of candidate alloys. Sufficiently accurate data are required that data for pure vanadium cannot be used with making at least some measurements on the actual candidate alloys. This is the reason for the present measurements.

Experimental Procedure

A small coupon of V-5Cr-5Ti 6.35 mm in thickness was obtained for ultrasonic nondestructive determination of the elastic moduli. Because of the relatively low attenuation of this alloy for elastic waves in the frequency range 5 to 10 MHz, simple digital pulse-echo techniques were applied. The compressional wave velocity at 10 MHz and the transverse wave velocity at 5 MHz were measured using a digital oscilloscope for data acquisition and impulse excitation to the appropriate ultrasonic transducer. The density of the coupon was determined to be 6028 kg/m^3.

Results

The measured values for this sample were 6.023 ± 0.013 km/s and 2.760 ± 0.006 km/s for the compressional and transverse wave velocities, respectively. Employing the usual linear equations relating elastic wave velocities and elastic moduli, the mechanical properties were calculated to be: Young's modulus 125.6 ± 0.4 GPa, Shear modulus 45.9 ± 0.2 GPa, and Poisson's ratio 0.367 ± 0.001.

Discussion

Young's modulus for pure vanadium from room temperature to 1900 K and shear modulus from room temperature to about 950 K have been determined by Farraro and McLellan.[1] They give the following relations for the modulus values as a function of temperature:

$$E_y = ((1.28 - 9.61 \times 10^{-5} \times T) \pm 0.040) \times 10^{11}\ N/m^2$$

$$G = ((0.488 - 8.43 \times 10^{-5} \times T) \pm 0.011) \times 10^{11}\ N/m^2$$

E_y is Young's modulus, G is the shear modulus, and T is the temperature in Kelvin. At 300 K the value for E_y is 125 GPa and the value for G is 46.3 GPa. Both of these values agree with the measured values for V-5Cr-5Ti within the limits of error given by Farraro and McLellan. It is also apparent from the **data** of Farraro and McLellan that **the** moduli have a weak temperature dependence. Although a few high temperature measurements may be necessary, room temperature values are probably sufficient for most comparison studies and even most design studies. It is also apparent that the values are pure vanadium **are** very close to those of the alloy.

SUMMARY AND CONCLUSIONS

1. Values of room temperature elastic moduli and Poisson's ratio have been determined for the alloy **V-5Cr-5Ti.**

2. The values for elastic moduli do not differ significantly from those of pure vanadium.

3. The weak temperature dependence of elastic moduli over the range of first wall and blanket temperatures for next generation devices such **as** ITER will permit the use of room temperature values for many calculations.

REFERENCES

R. J. Farraro and Rex B. McLellan, "High Temperature Elastic Properties of Polycrystalline Niobium, Tantalum, and Vanadium," Met Trans 10A **(1979) 1699.**

Thermophysical Properties of V-5Cr-5Ti – W. D. Porter, R. B. Dinwiddie, and M. L. Grossbeck (Oak Ridge National Laboratory)

OBJECTIVE

Measurements of thermal expansion, specific heat, and thermal conductivity were made in order to provide a single source of data to support design efforts of vanadium alloy structures in fusion devices.

SUMMARY

Measurements of thermal expansion of V-5Cr-5Ti have been made from room temperature *to* 600°C, and specific heat and thermal conductivity have been measured over the range of 100 to 600°C. In each case, the results have been fitted to a polynomial expression to provide a convenient form for design studies.

PROGRESS AND STATUS

Introduction

Vanadium alloys offer a significant advantage over stainless steels in increased thermal conductivity which leads to lower thermal stress. However, thermophysical properties such as thermal conductivity have been reported only for pure vanadium and a few alloys containing higher concentrations of chromium and titanium. The present study provides the necessary data for the ITER candidate vanadium alloys.

Linear Thermal Expansion

Experimental Methods

The alloy V-5Cr-5Ti from Teledyne Wah Chang heat 832394. designated BL-63 by Argonne National Laboratory, was used for the measurements. The specimen was a rectangular solid ***25.0*** x ***5.84*** x ***5.84*** mm. It was used in the condition as received from Teledyne Wah Chang. annealed at 1100°C.

Measurements were made using a differential push-rod dilatometer that measures the linear thermal expansion. The thermal expansion of a test specimen is determined relative to that of a standard reference specimen. The two samples are placed side by side in a furnace, and two alumina push rods, that extend from the furnace to a thermally isolated linearly variable displacement transducer (LVDT), bear on the samples. The difference in expansion between the two specimens results in the differential movement of the push rods, thus allowing the linear thermal expansion of the unknown sample to be determined. The advantage of such a device is that instrument expansion is cancelled out. The dilatometer is of the horizontal configuration with push rods and sample holder constructed of high density alumina A sapphire rod with a length of 25 mm was used as the reference material. Differential changes in length between the sample and the reference are transmitted to the LVDT mounted on an Invar rod using separate pairs of leaf springs for the coil and core. The leaf springs provide frictionless movement of the LVDT and also maintain a push rod load of 25-30 g on the sample and reference. The LVDT *is* housed in an enclosure that is maintained at 40°C by means of water circulated from a constant temperature bath. A platinum/platinum-10% rhodium type S thermocouple was used to monitor the sample temperature. The accuracy of the expansion measurements was determined to be better than ±2% over the range of 20 to 1450°C by means of verification tests using sapphire and tungsten reference materials in the sample and reference positions.

Oxidation of the sample during the dilatometer runs was minimized by evacuating the system using a mechanical vacuum pump followed by back filling with titanium-gettered helium. This process was repeated three times prior *to* the dilatometer run. During the test a helium flow rate of 5 ml/min was maintained at a slight over pressure of 20.7 kPa.

Expansion measurements were made using a computerized **data** acquisition system while the sample was **heated and** cooled at a **rate** of **3°C/min.** The sample was healed to a maximum temperature of 600°C. **Data sets** were stored **at** 30 **sec** intervals. **After** the initial heating and cooling cycle, the sample was heated a **second** lime and **dam were** collected during heating only.

Results and Discussion

Results **for** the linear thermal expansion measurements appear in Table 1. The **data** are plotted as a **function** of temperature in Fig. 1 where a least **squares** fit curve is also **shown.** The polynomial expression describing the expansion is **as** follows:

$$\Delta L/L_0 = -179.97570689 + 9.0363848739\ T + 0.0015407532037\ T^2$$

where $\Delta L/L_0$ is the incremental thermal expansion in parts per million relative to the value at 20°C and T is the temperature in degrees Celsius. The instantaneous coefficient of expansion, expansivity, is shown in Fig. 2.

Table 1. Linear Thermal Expansion of V-5Cr-5Ti **Alloy** Referenced to 20°C*

Temperature	Specimen Exp. (ppm)	Average CTE (ppm/°C)	Instantaneous CTE (ppm/°C)
20	0	9.1	9.1
40	184	9.2	9.2
60	368	9.2	9.2
80	553	9.2	9.3
100	739	9.2	9.3
120	927	9.3	9.4
140	1116	9.3	9.5
160	1306	9.3	9.5
180	1497	9.4	9.6
200	1690	9.4	9.1
220	1884	9.4	9.7
240	2079	9.4	9.8
260	2275	9.5	9.9
280	2473	9.5	9.9
300	2672	9.5	***10.0***
320	2773	9.6	10.1
340	3074	9.6	10.1
360	3277	9.6	10.2
380	3487	9.7	10.3
400	3687	9.7	10.3
420	3894	9.7	10.4
440	4103	9.8	10.5
460	4312	9.8	10.5
480	4523	9.8	10.6
500	4736	9.9	10.7
520	4949	9.9	10.7
540	5164	9.9	10.8
560	5381	10.0	10.9
580	5598	10.0	11.0
600	5818	10.0	11.0

*Calculated values using fitted equations

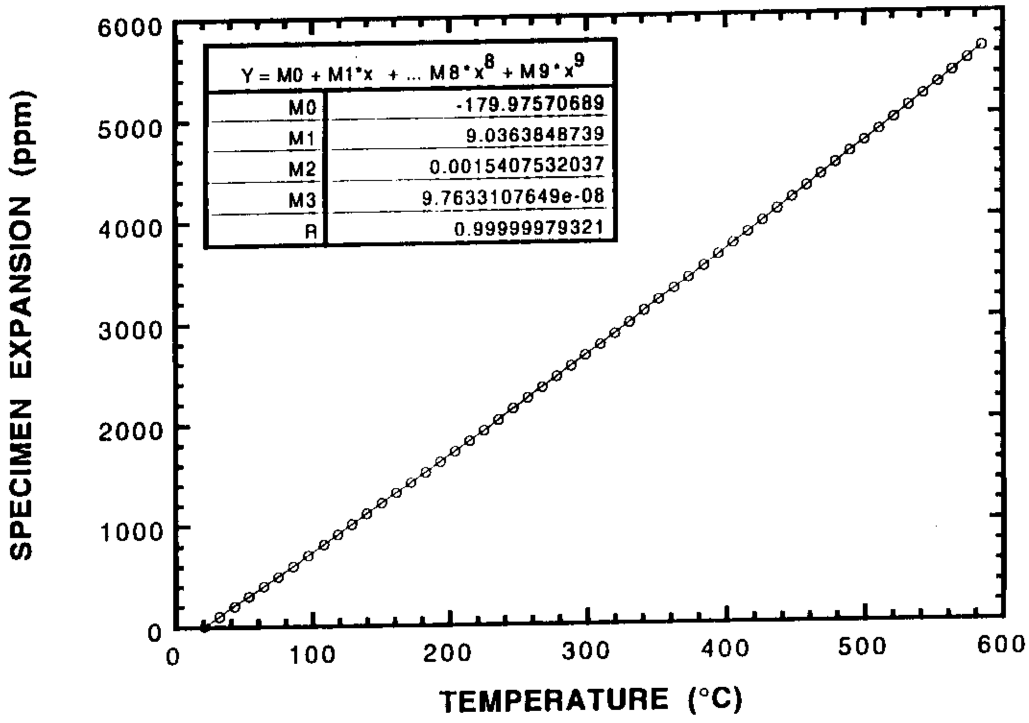

Y = M0 + M1*x + ... M8*x^8 + M9*x^9	
M0	-179.97570689
M1	9.0363848739
M2	0.0015407532037
M3	9.7633107649e-08
R	0.99999979321

Fig. 1. Linear Thermal Expansion of V-5Cr-5Ti (wt%).

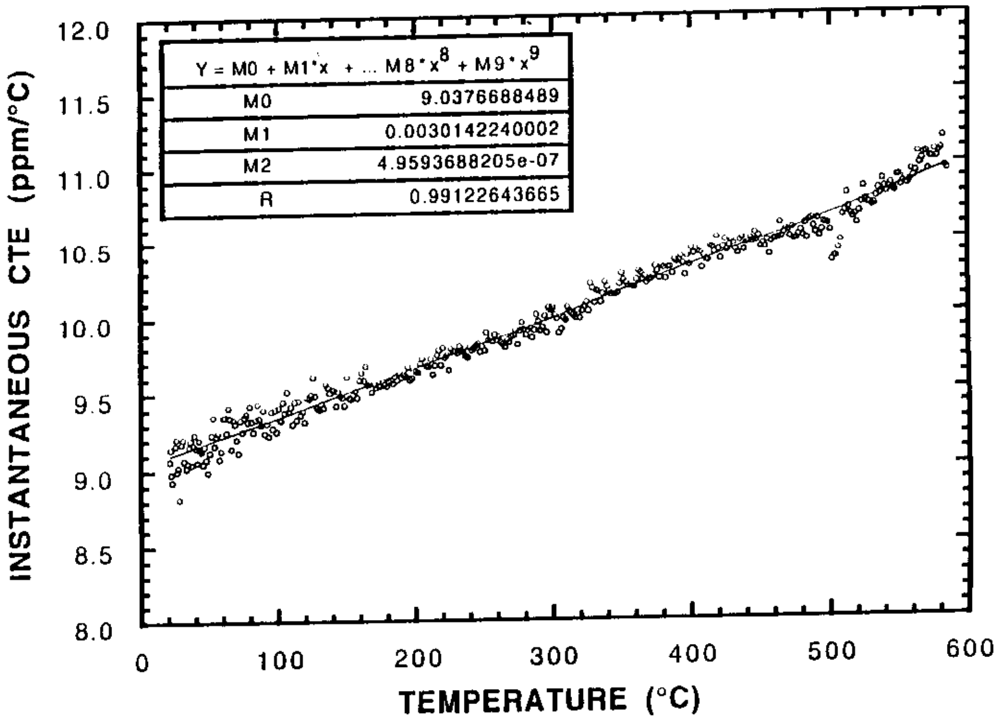

Y = M0 + M1*x + ... M8*x^8 + M9*x^9	
M0	9.0376688489
M1	0.0030142240002
M2	4.9593688205e-07
R	0.99122643665

Fig. 2. Instantaneous Coefficient of Expansion of V-5Cr-5Ti (wt%).

Figure 3 shows the curve for thermal expansion of V-5Cr-5Ti plotted with similar curves for pure vanadium[1] and for the alloys V-15Cr-5Ti and V-7.5Cr-15Ti.[2] The curves for V-5Cr-5Ti and V-7.5Cr-15Ti are nearly coincident, and the curve for pure vanadium is nearly coincident with the curves for the two previously mentioned alloys. This indicates that minor variations in alloy composition in the class of low alloy V-Cr-Ti alloys need not have thermal expansion evaluated for each composition. For many scoping studies, values for pure vanadium are sufficient.

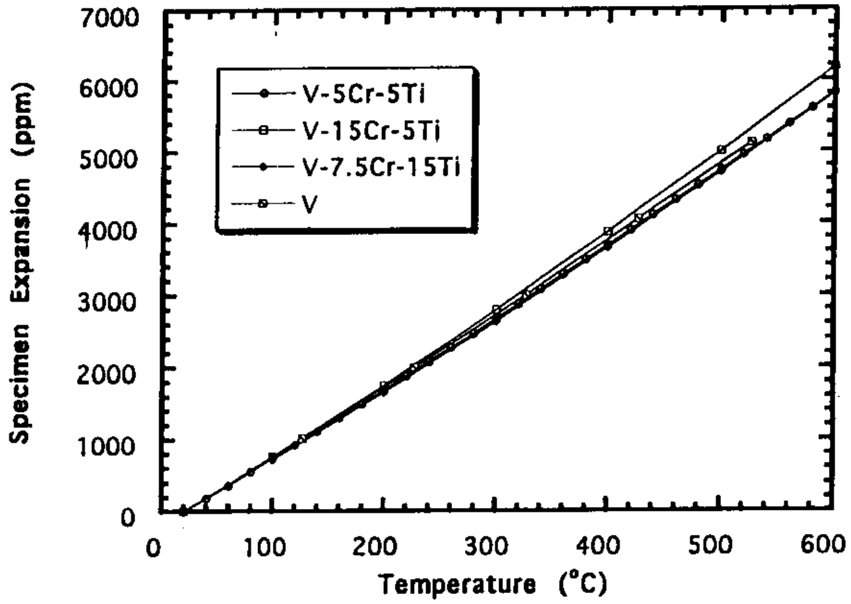

Fig. 3. Linear thermal expansion as a function of temperature for V-5Cr-5Ti as shown in Fig. 2 accompanied by similar values for pure vanadium (from Y.S. Touloukian, R.K. Kirby, R.E. Taylor, and P.D. Desai, Thermophysical properties of Matter Vol. 12, Plenum Press, New York (1975)) and for two V-Cr-Ti alloys (F.L. Yaggee, E.R. Gilbert, and J.W. Styles, "Thermal Expansivities, Thermal Conductivities, and Densities of Vanadium, Titanium, Chromium and some Vanadium-Base Alloys," J. Less Com. Metals 19 (1969) 39.)

Specific Heat

Experimental Method

Specific heat was measured with a Stanton-Redcroft differential scanning calorimeter. The operation of this instrument is based on measurement of the thermal response of an unknown specimen as compared with a standard when the two are heated uniformly at a constant rate. The instrument consists of a furnace containing two identical crucibles, each of which rests on a thin plate located inside the measurement head. Directly beneath the center of the crucible is the junction of a Pt vs Pt-10Rh differential thermocouple. Any difference in temperature between the two specimens is caused by differences in mass, specific heat, heats of reaction, or phase transitions.

To determine specific heat, a baseline is established by measuring the temperature differential of the empty crucibles as the temperature is changed at a constant rate over the temperature range of interest. Thermal response records are then acquired for a standard material, in this case sapphire, and an unknown under identical conditions. The ratio the departure of the standard and unknown from the baseline is then used to calculate the specific heat of the unknown.

Results and Discussion

The results of the measurement appear in Fig. 4. A least squares fit to these data result in the following relation:

$$C_p = 0.57551 - 21.094/T \ \ J/g\text{-}K$$

where C_p is the specific heat at constant pressure, and T is the temperature in Kelvin. This empirical expression is only valid over the range of the measurements.

Values of specific heat for pure vanadium are also plotted in Fig. 43 At fust it appears that the curves for the alloy and pure vanadium are very different in functional form. However, the ordinate is greatly expanded so that very small differences are magnified. Over a larger temperature range, the expected T^3 dependance at low temperature and the slow increase with increasing temperature at higher temperatures is apparent as shown in Fig. 5 for pure vanadium.

Thermal Conductivity

Introduction

It is necessary lo know thermal conductivity in order to calculate thermal stresses and to design a heal removal blanket. However, direct thermal conductivity measurements, especially at high temperatures, are difficult, time consuming, and they require relatively large specimens. Thermal conductivity, k, may be calculated from measurements of thermal diffusivity. a. specific heat, C„ and bulk density, ρ, by using the relationship $k=\alpha\rho C_p$. This method for obtaining thermal conductivity is relatively fast and requires only a small amount of material. The laser flash thermal diffusivity (LFTD) technique, used for elevated temperatures in this study, and the xenon flash technique, used for the room temperature measurements, have been used extensively to study a wide range of materials including glasses, plastics, metals, ceramics, composites, crystals, and foams.

Experimental Method

Two different systems were employed in obtaining thermal diffusivity at room temperature and at elevated temperatures. The elevated temperature system employs the LFTD technique. A small disk shaped specimen 12.45 x 1.9 mm thick was placed in an evacuated tube furnace, as shown in Fig. 6, and oriented with its flat surfaces perpendicular to the furnace axis. A neodymium glass laser was used to supply a high intensity. short-duration, pulse of thermal energy to one face of the test specimen. The intensity of the beam was controlled by varying the laser power supply and by use of attenuating filters. The resulting temperature rise of the other face of the test specimen was monitored as a function of time by an indium antimonide infared (IR) detector and stored in computer memory. The thermal diffusivity was then determined from a numerical analysis of the IR detector output.

The xenon flash system used for room temperature measurements was very similar in principle to the elevated temperature system. A short pulse (<1 ms) of heat was applied to the front face of the specimen, and the temperature change of the rear face was measured with an infared detector. The system was, of course, optimized for room temperature measurements. The system is illustrated by the sketch in Fig. 7.

The results of the measurements are shown in Fig. 8 where thermal conductivity has been calculated from the relation given above. $k=\alpha\rho C_p$. Also plotted in Fig. 8 are data for pure vanadium which fall within the limits of error for the V-5Cr-5Ti alloy.[4] Thermal conductivity increases slightly with temperature following the Wiedemann-Franz law relating thermal conductivity with electrical conductivity. Thermal conductivity of V-5Cr-5Ti may be expressed by:

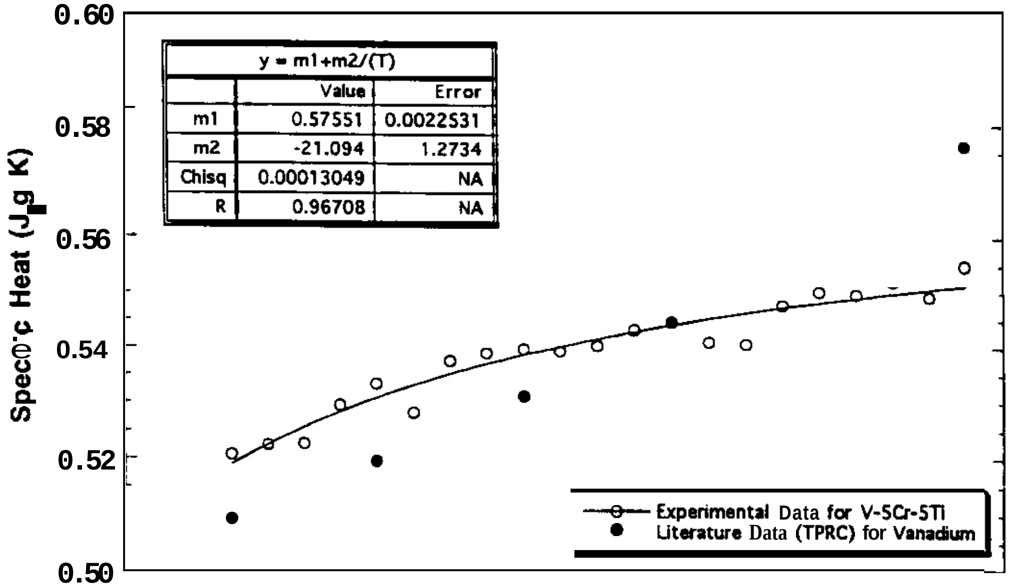

y = m1+m2/(T)		
	Value	Error
m1	0.57551	0.0022531
m2	-21.094	1.2734
Chisq	0.00013049	NA
R	0.96708	NA

Fig. 4. **Specific heat for V-5Cr-5Ti as a function of** temperature. **Data for pure vanadium are also** shown **for comparison (Y.S. Touloukian and E.H. Buyco,** Thermophysical Properties of Matter, Vol. 4, **Plenum Press, New York** (1970)).

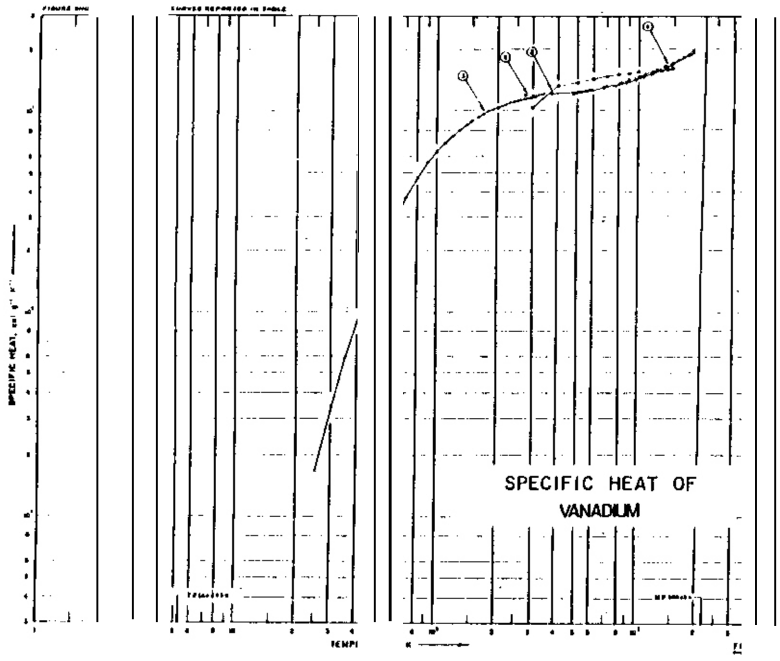

Fig. 5. **Specific heat of pure vanadium over a wide** temperature **range (Y.S. Touloukian and E.H. Buyco,** Thermophysical Properties of Matter, **Vol. 4 Plenum Press, New York (1970)).**

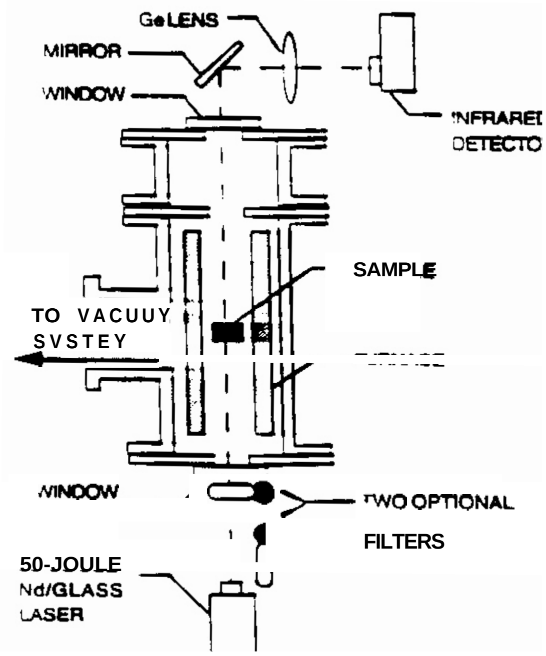

Fig. 6. Laser flash thermal diffusivity apparatus used for elevated temperature measurements.

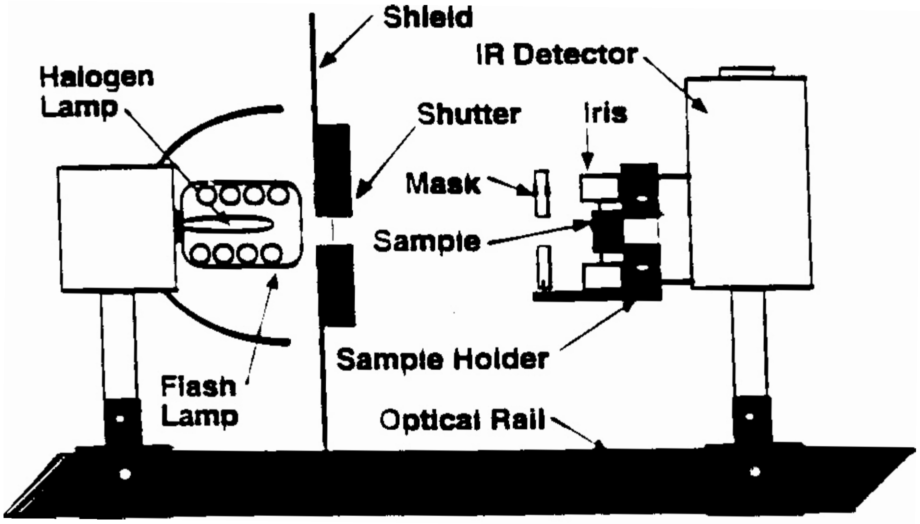

Fig. 7. Xenon flash thermal diffusivity system used for room temperature measurements.

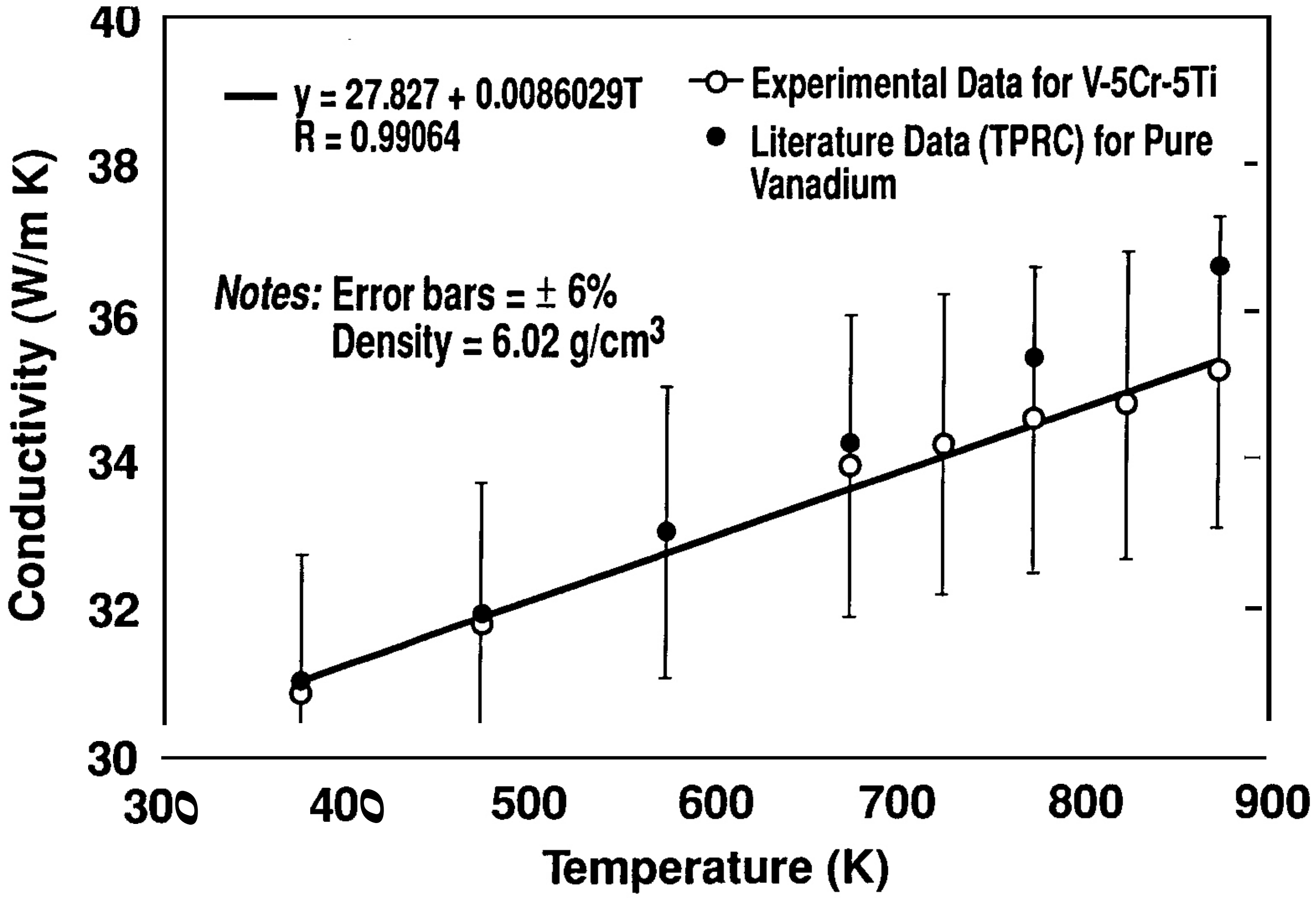

Fig. 8. Thermal conductivity of V-5Cr-5Ti as a function of temperature. Values for pure vanadium are also plotted for comparison (Y. S. Touloukian, R. W. Powell, C. Y. Ho, and P. G. Klemens, Thermophysical Properties of Matter, Vol. 1, Plenum Press, New York (1970).

$$k = 0.0086029\ T + 27.827\ \text{W/m-K}$$

where T is the temperature in Kelvin.

CONCLUSIONS

1. Linear thermal expansion

$$= \Delta L/L_0 = -179.97570689\ t\ 9.0363848739\ T + 0.0015407532037 T^2$$

where $\Delta L/L_0$ is the incremental thermal expansion in parts per million relative to the value at 20°C and T is the temperature in degrees Celsius.

2. Specific heat

$$= C_p = 0.57551 - 21.094/T\ \ \text{J/g-K}$$

where C_p is the specific heat at constant pressure and T is the temperature in Kelvin.

3. Thermal conductivity

$$= k = 0.0086029\ T + 27.827\ \text{W/m-K}$$

where T is the temperature in Kelvin.

FUTURE WORK

The requirements for physical property measurements will be guided by the needs of the designers of the ITER and other fusion devices. At the present time, no more measurements are planned until needs are expressed.

REFERENCES

1. Y. S. Touloukian. R. K. Kirby, R. E. Taylor, and P. D. Desai, Thermophysical Properties of Matter, Vol. 12, Plenum Press, New York (1975).

2. F. L. Yaggee, E. R. Gilbert, and J. W. Styles, “Thermal Expansivities. Thermal Conductivities, and Densities of Vanadium, Titanium, Chromium, and Some Vanadium-Base Alloys,” J. Less Com. Metals 19 (1969) 39.

3. Y. S. Touloukian and E. H. Buyko, Thermophysical Properties of Matter, Vol. 4, Plenum Press, New York (1970).

4. Y. S. Touloukian, R. W. Powell, C. Y. Ho, and P. G. Klemens, Thermophysical Properties of Matter, Vol. 1, Plenum Press, New York (1970).

Atom Probe Field Ion Microscopy Characterization of Vanadium-Titanium- Chromium Alloys -

M. K. Miller (Oak Ridge National Laboratory)

OBJECTIVE

This research was performed to help determine the underlying reasons for the differences in mechanical properties between two vanadium alloys of close composition: V-5Cr-5Ti and V-4Cr-4Ti.

SUMMARY

The atom probe field ion microscope was used to examine two V-Cr-Ti alloys (V- 5Cr-5Ti and V-4Cr-4Ti) which have been shown to have very different fracture properties. The alloys were examined for clustering to detect the presence of small precipitates as well as to determine the distribution of solute elements in the matrix. The elements Ti, Cr, and Si were examined and no clustering of any of these three elements was found.

PROGRESS AND STATUS

Introduction

Vanadium-chromium-titanium alloys of composition in the range of V-(4-5)Cr-(4-5)Ti are being considered as candidates for fusion reactor fust wall and blanket materials. Two alloys in this range are being investigated: V-4Cr-4Ti melted by Teledyne Wah Chang Corp. and designated BL-47 by Argonne National Laboratory (ANL), and V-5Cr-5Ti also melted by Teledyne Wah Chang Corp. as Heat 832394 and designated BL-63 by ANL. The fracture properties, as determined by Charpy testing. have been demonstrated to be very different with V-4Cr-4Ti having a ductile to brittle transition temperature (DBTT) about 100°C lower than V-5Cr-5Ti.[1] Since much of the fracture occurs intergranularly, depending upon test temperature, precipitation and segregation are king examined. In order to study these phenomena, an exploratory atom probe field ion microscopy (APFIM) characterization of two vanadium-titanium-chromium alloys was performed. The main emphasis of this characterization was to detect the presence of ultrafine scale precipitates and determine the distribution of the solute elements in the matrix.

Experimental Procedures

The atom probe field ion microscopy characterization was performed on two alloys: V-4Cr-4Ti (BL-47) and V-5Cr-5Ti (BL-63). The field ion specimens were prepared by fust cutting ~0.5 mm by ~0.5 mm square bar from the bulk material and then electropolishing those blanks into sharp needles with the use of a standard two stage procedure.[2] The conditions used were as follows: stage 1 - an electrolyte of 25% perchloric acid in glacial acetic acid, and stage 2 - an electrolyte of 2% perchloric acid in 2-butoxyethanol. Both stages were performed at room temperature with an applied voltage of 20 to 25 V. The characterization was performed in the ORNL energy-compensated atom probe field ion microscope.[3] This instrument has sufficient mass resolution to fully separate all the isotopes of the elements present in this material. Field ion microscopy was performed with the use of neon as the imaging gas and with a specimen temperature of approximately 60 K.

Good quality field ion micrographs were produced as shown in Figs. 1 and 2 for the BL-47 and BL-63 alloys, respectively. No evidence. of ultrafine scale precipitates is evident in these micrographs and no evidence was found in more extensive field evaporation sequences through the matrix. The dark lenticular areas evident in the micrograph of the BL-63 alloy, Fig. 2, were identified as vanadium hydrides by atom probe selected area analysis. These hydrides were frequently observed in the V-5Cr-5Ti alloy (BL-63) but

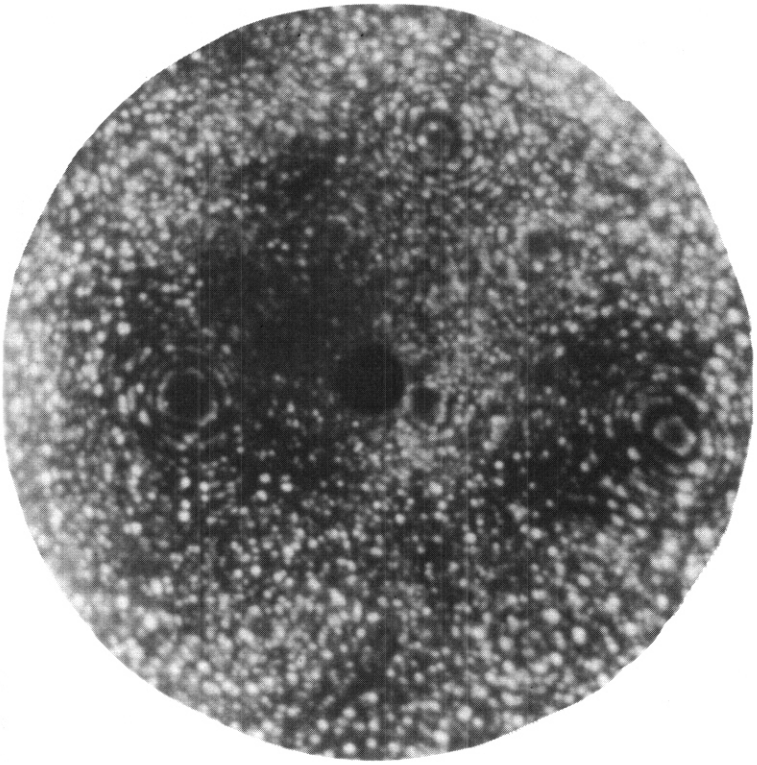

Fig. 1. Field ion micrograph of V-4Cr-4Ti (BL-47).

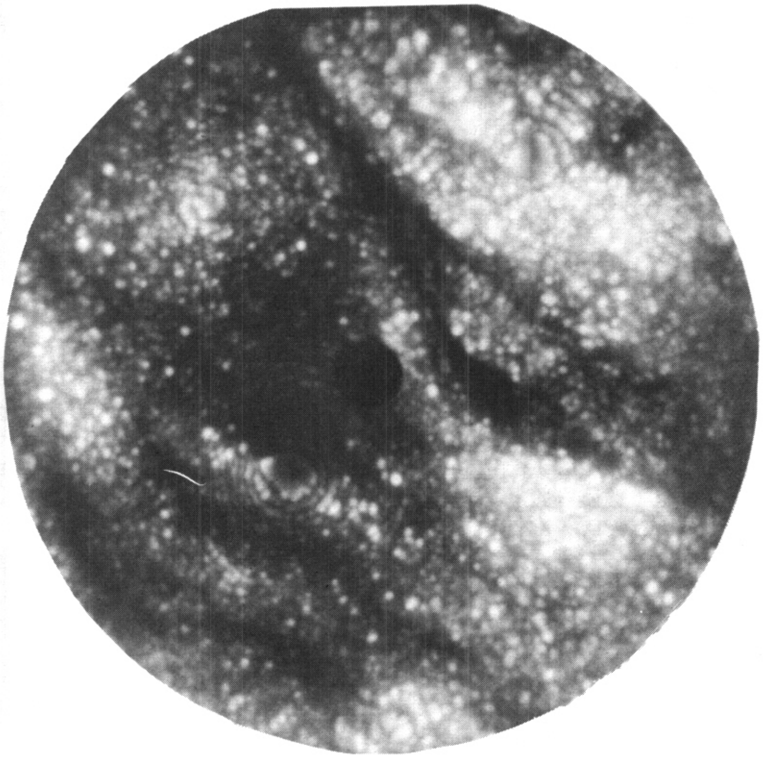

Fig. 2. Field ion micrograph of V-5Cr-5Ti (BL-63). The *dark* lenticular areas are vanadium hydrides.

were not observed in the V-4Cr-4Ti alloy **(BL-47).** However, it is likely that these features were introduced during the electropolishing process and the difference between the two alloys may not be representative of the hulk materials.

Analysis of the composition profiles also failed to reveal the presence of any ultrafine scale precipitates. The ion-by-ion data was also examined to determine the distribution of the major solute elements. Two different statistical methods were used. In the Johnson and Klotz method, the numbers of **AA,** AB, and **BB** pairs in the ion-by-ion data chain are examined and compared to those expected in a random solid solution? In the mean separation method, the variance of the separation of **like** solute atoms (e.g. Ti atoms) are compared to the expected variance from a random solid solution.[5,6] The Johnson and Klotz method was developed for concentrated solid solutions, whereas the mean separation method is more appropriate for dilute solid solutions. The results of these analyses are shown in Table 1. The numbers shown are the significance of the results and are the number of standard deviations from a random solid solution. Therefore, the result is considered to be a random solid solution if the result falls within the range (-2 > significance < 2). All values determined in these two materials fell within this range and therefore no evidence **was** found for clustering of titanium, chromium, and silicon.

Table 1. Clustering Analyses of V-4Cr-4Ti **(BL-47)** and V-5Cr-5Ti (BL-63)

Alloy	Element	Significance (Johnson & Klotz)	Significance (*Mean* Separation)
V-4Cr-4Ti (BL-47)	Ti	**-0.71**	**1.60**
	Cr	**-0.08**	0.55
	Si	**0.93**	**-0.32**
V-5Cr-5Ti (BL-63)	Ti	1.11	**0.45**
	Cr	**0.91**	**1.09**
	Si	–	**-0.73**

CONCLUSIONS

No evidence was found for ultrafine scale precipitates or clustering of the titanium, chromium, or silicon in **BL-47** or **BL-63.**

REFERENCES

1. J. Gazda. **B.** A. Loomis, **L.** J. Nowicki, D. L. Smith, and S. Danyluk, "Relationship of Microstructure and Mechanical Properties of V-Cr-Ti Alloys," Fusion Reactor Materials Semiannual Progress Report for Period Ending September **30,1993, DOE/ER-0313/15 (1994),** p. **232.**

2. M. K. Miller and G.D.W. Smith, Atom Probe Microanalysis: Principles and Applications to Materials Problems, Materials Research Society, Pittsburgh, PA **(1989).**

3. M. **K.** Miller, J. de Physique, **47-C2 (1986), 493.**

4. C. A. Johnson and J. H. Klotz, Technometrics, **16(4), 1974,483.**

5. M. G. Hetherington and M. K. Miller, J. de Physique, **48-C6 (1987), 559**

6. M. G. Hetherington and M. K. Miller, J. de Physique, **49-C6 (1988), 427.**

Analysis of Grain Boundaries in a V-5Cr-5Ti Alloy Using Auger Electron Spectroscopy - D. N. Braski and M. L. Grossbeck *(Oak* Ridge National Laboratory)

OBJECTIVE

The objective of this research was to investigate the mechanism of intergranular embrittlement associated with the relatively high ductile to brittle transition temperature (DBTT) in a V-5Cr-5Ti alloy.

SUMMARY

A V-5Cr-5Ti specimen was fractured in-situ below its DBTT and the fracture surfaces analyzed by Auger Electron Spectroscopy (AES). About 70% of the fresh fracture surfaces were intergranular while the remainder were characteristic of cleavage fracture. Sub-micron-sized particles appeared to cover most of the grain boundary surfaces along with a few larger particles. Only one of these larger particles, probably a Ti-V sulfide/phosphide combination, contained Cl, at a level of only a few at.%. **On** the other hand, S, which is known to cause embrittlement in many alloy systems, was detected on virtually **all** of the grain boundary surfaces.

INTRODUCTION

Recent research **has** led to the selection of low Cr-Ti vanadium alloys in the range of **V-(4-5Cr-(4-5)Ti.** The heat 832394 **of** V-5Cr-5Ti melted by Teledyne **Wah** Chang Albany Corporation (also referred to as alloy BL63) has been shown to have a high ductile--brittle transition temperature (DBTT) compared to an alloy of composition V-4Cr-4Ti.[1] In addition, it was found in the present study that in the transition temperature region, the fracture process is dominated by intergranular failure. These observations suggest that precipitation on or segregation to grain boundaries may be playing an important role. Previous investigators have observed chlorine-containing precipitates on grain boundaries and have attributed the poor fracture properties to **chlorine.**[2] The bulk concentration of chlorine was measured as part of this investigation and found to be below the 1 ppm **level.**[3] Nonetheless, it was considered necessary to investigate composition and structure of the grain boundary surfaces. **A** small bar of the annealed material was fractured in-situ and the fracture surfaces analyzed by AES.

EXPERIMENTAL

An *SS-3* (thickness of **0.76** mm and gage section **7.62** mm in length) tensile specimen of V-5Cr-5Ti from Heat #832394 was annealed for 1 hr at 1125°C and prepared for in-situ fracture by: (a) making two opposed cuts in the gage section with a slow-speed diamond saw, (b) trimming off excess material with heavy duty wire cutters so that the SS-3 specimen would fit into a fracture holder with a **3** mm diam. opening, and (c) securing the notched *SS-3* gage section in the holder using copper shims and a set screw. The holder was then inserted into a PHI 660 Scanning Auger Microprobe and pumped at a vacuum level of 4×10^{-8} Pa (3×10^{-10} torr) for three days. The specimen was then cooled to ≈-130°C with the liquid nitrogen cold stage and then fractured, in bending, using a built-in impact mechanism. The fracture process had no effect on the chamber pressure. The fresh fracture surfaces were analyzed immediately using an accelerating voltage of 10 kV and beam current of 15 nA. **A** beam aperture **of** 0.41 mm was used which produced a analysis spot size of ≈200 nm in diameter. Qualitative analysis was conducted using Auger spectra from the Handbook **of** Auger Electron Spectroscopy? and quantitative analysis was performed using the PHI software and sensitivity factors. The accuracy of the elemental analyses is estimated to be ≈±5 at. %. Scanning electron micrographs were taken of the areas of interest and of those that were analyzed.

RESULTS

The fracture surface that was analyzed is shown at low magnification in Fig. 1 and at slightly higher magnification in Fig. 2. The surface was estimated to be about 70% intergranular and 30% cleavage fracture. A few areas, probably <1%, showed some ductile tearing. Immediately after fracture, 20 to 25 particles lying on the grain boundaries and at triple point intersections were surveyed. One such area of intergranular fracture is illustrated in the micrograph in Fig. 3. Only one of these particles was found to contain Cl. It is marked as Particle #3 in Fig. 3 and is shown more clearly at higher magnification in Fig. 4. The Cl content of this particle was measured to be ≈1 at. % as shown in Table 1. This small amount of Cl detected by Auger generally agrees with a value of 1 ppm determined by neutron-activation analysis.[3] Besides Cl, a small amount of S was detected along with moderate amounts of TI, V, and C. This analysis not only represents that for Particle #3 but also reflects some of the adjacent grain boundary surface. The two compositions are combined because a portion of the analyzing beam extends beyond the edges of the small particle and excites Auger electrons from surrounding material. If the particle is thin enough, it is also possible for some electrons to scatter through the particle and excite material surrounding it. Analysis of the g.b. surface near Particle #3 produced values of V, Ti, C, and S that were nearly identical to the particle itself, except that no Cl was detected.

Table 1. AES Data (appm)

Sputter Time (min)	Feature	Fin.	V	Ti	Cr	C	S	P	Cl
0	Part. #3	3&4	27	39	–	27	6	–	1
0	g.b. sfc	4	22	43	–	28	7	–	–
17	Part. #3	4	73	16	–	–	2	6	3
17	g.b. sfc	4	77	9	4	10	–	–	–
17	Part.-A	5	65	14	4	17	–	–	–
17	Part.-B	5	65	16	1	18	–	–	–
17	cleavage	6	89	8	3	–	–	–	–

Additional information was obtained for Particle #3 and other areas by removing some of the outer layers of material by argon ion-sputtering. After sputtering for 17 min. (about 300 nm of material was removed), mostly V was detected for Particle #3, with smaller amounts Ti, S, P, and –3 at.% Cl (Table 1). Since S, P, and Cl were not detected on the adjacent g.b. surface (Table 1), it would appear that these elements are concentrated in Particle #3. Note that sputtering removed the C that was present in Particle #3 after fracture showing that it was probably just a part of a coating.

Figures 5 and 6 show typical grain boundaries which appeared to contain a large number of small (<1 µm) particles. A few larger particles were also observed, e.g. the cube-shaped particle in the center of the grain boundary surface in Fig. 6. Numerous other particles were surveyed after sputtering which contained C and are assumed to be some type of metallic carbides; the compositions of two "carbide" particles, "A" and " B in Fig. 7, are given in Table 1. As mentioned before. none of these particles appeared to contain Cl – or S and P, for that matter.

Finally, the cleavage fracture area in Fig. 8 was analyzed to check the bulk composition of the alloy (see Table 1). Remembering the ±5 at.% accuracy of the technique, it was found that the bulk composition of 8 and 3 at. % for Ti and Cr, respectively, compares favorably with the expected 5Cr-5Ti, by weight composition. (Note: since the atomic weights for V. Ti. and Cr are nearly the same, wt. % ≈ at. % for the alloy.)

Fig. 1. Macro **view** of fractured **specimen of** V-5Cr-5Ti.

Fig. **2. Fracture surface of the specimen in Fig.** 1. **Numbers refer to regions analyzed by AES.**

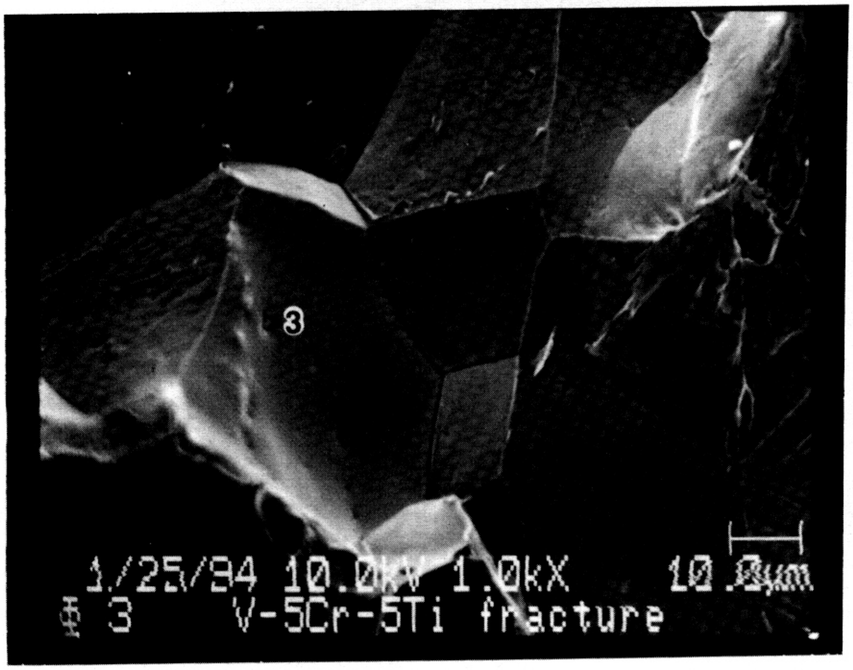

Fig. **3.** **Portion** of fracture surface between positions **2** and **3** of Fig. **2** showing precipitates on the grain boundary. Particle #3 is **a** CI-containing precipitate referred to in the text.

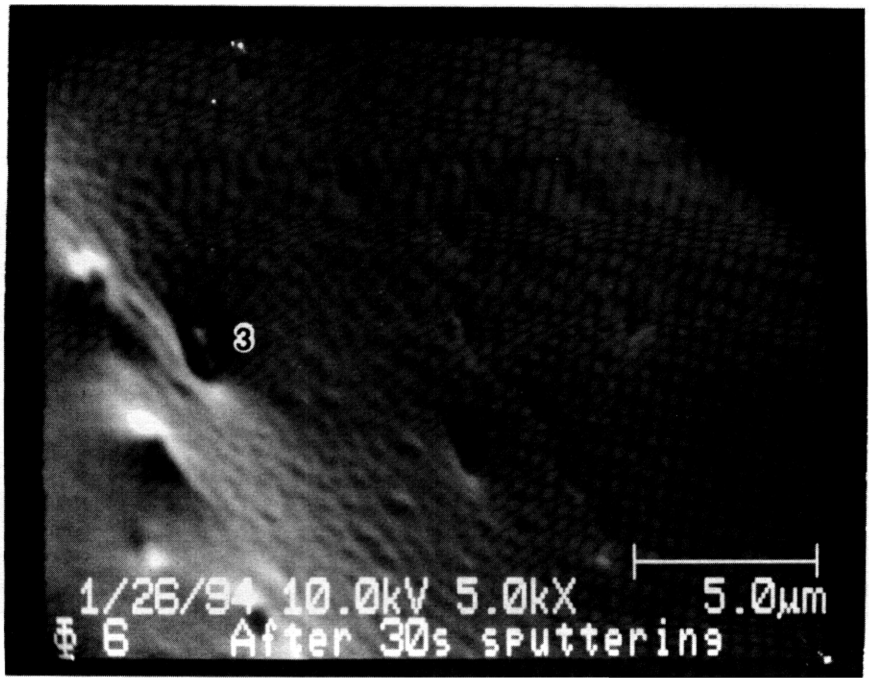

Fig. **4.** Higher magnification view **of** the region of Particle #3 in Fig. **3** following **30s** sputtering.

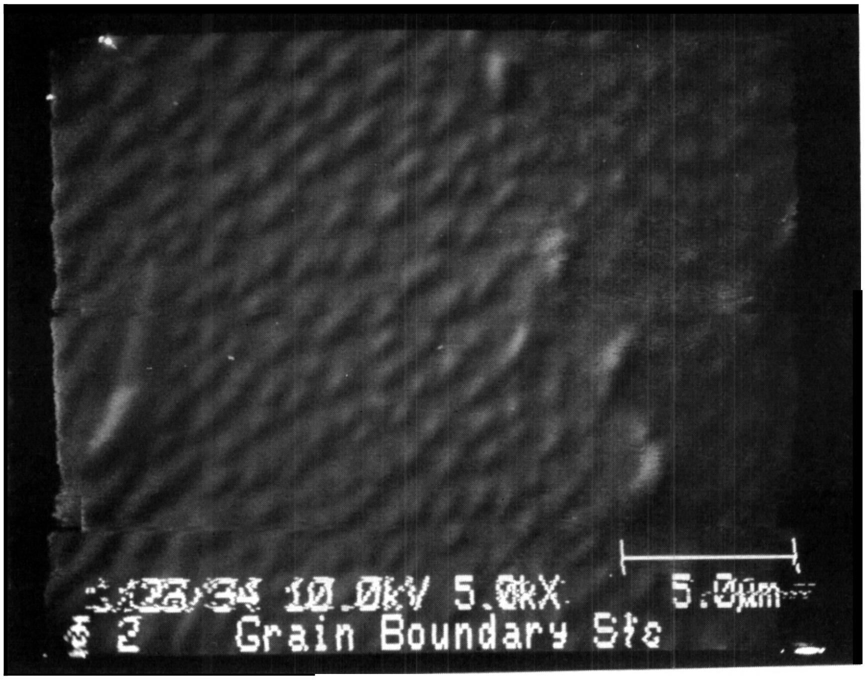

Fig. 5. Grain boundary surface showing < 1 µm size precipitates believed to be carbo-oxy-nitrides.

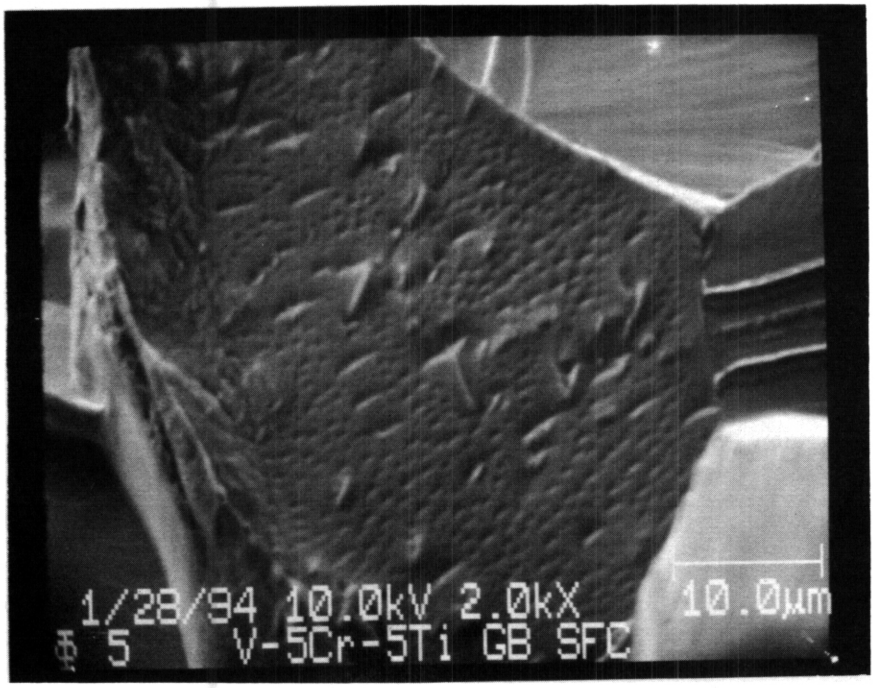

Fig. 6. Grain boundary surface showing < 1 µm size precipitates as well as cuboid precipitates determined to be metallic carbides.

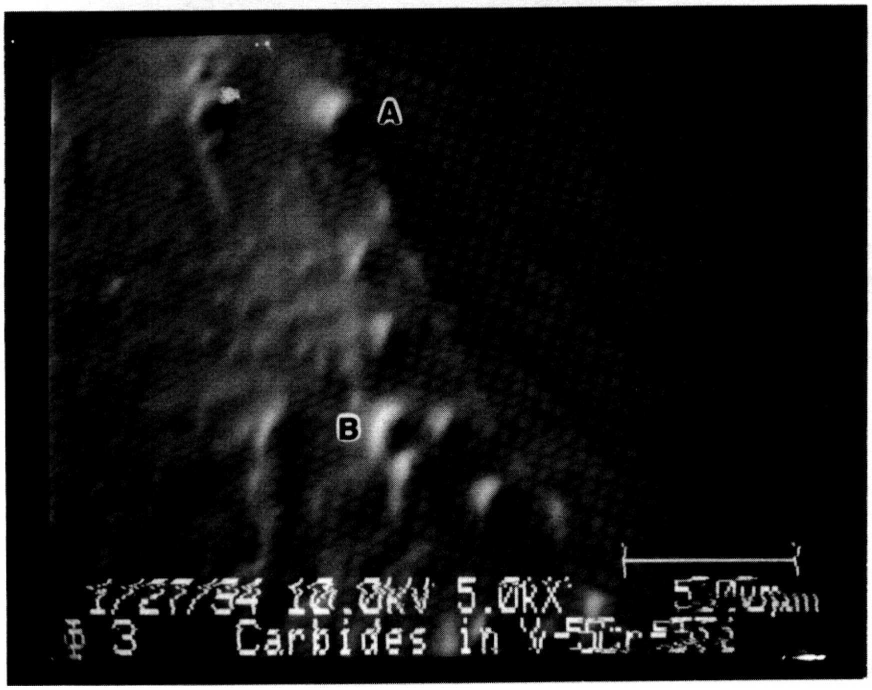

Fig. 7. Grain **boundary surface showing precipitates. The precipitates marked "** A **and "B" were analyzed and the data reponed in Table 1.**

Fig. 8. Cleavage fracture surface used for comparison with grain boundary **surfaces. The analysis appears in Table** 1.

DISCUSSION

Impact testing of the annealed V-5Cr-5Ti below its ductile-brittle transition temperature (DBTT) resulted in fracture along a substantial number of grain boundaries. Most boundaries appeared to contain a large number of submicron-sized precipitate particles while only a few had several moderately-sized particles (>1 µm). Only one of about 25 larger particles that were analyzed (Particle #3) contained a measurable amount of Cl. Because of the disappearance of C in Particle #3 after sputtering, it would appear that the particle may be a complex sulfide or phosphide of Ti with small amount of Cl. Schober and Braski[3] found both Ti-sulfides and Ti-phosphides as minor precipitates in three different vanadium alloys containing between 3 and 20 wt. % Ti. The major precipitate in the alloys was given as $Ti_{0.98}V_{0.02}N_{1-x-y}C_xO_y$. The more numerous particles along the V-5Cr-5Ti grain boundaries in this investigation could, indeed be Ti-V carbides a carbo-oxy-nitrides, but more work is needed to make a reliable identification. The main point is that these, more numerous particles, do not appear to contain Cl, which other investigators speculate to be the primary cause for elevated DBTT's in V-5Cr-5Ti.[2] Because only extremely small amounts of Cl were detected it seems unlikely that the observed brittle intergranular fracture below the DBlT was caused by this element. It would seem more likely that the weakening of the grain boundaries was caused by S. Sulfur was detected on all of the *grain* boundary surfaces analyzed in this and also in a previously analyzed V-5Cr5Ti specimen and is notorious for its embrittling effects in many different alloy systems. Sulfur was segregated on grain boundary surfaces as evidenced by its disappearance after sputtering. It would be interesting to look at other beats of V-5Cr-5Ti with different values of DBlT to see if S segregation can be correlated to toughness.

CONCLUSIONS

Auger electron spectrometry of grain boundary and cleavage fracture surfaces in V-5Cr-5Ti showed large concentrations of sulfur on the grain boundaries. A chlorine-containing precipitate was observed but only one, consistent with the measured chlorine concentration in the alloy. Numerous sub-micron size precipitates, that may be Ti-V carbo- oxy-nitrides, were observed in grain boundary surfaces. The role of sulfur in the fracture requires further investigation.

REFERENCES

1. J. *Gazda*, B.A. **Loomis,** L.J. Nowicki, D.L. Smith, and S. Danyluk, "Relationship of Microstructure and Mechanical Properties of V-Cr-Ti Alloys," Fusion Reactor Materials: Semiannual Progress Report for Period Ending September 30.1992 DOE/ER-0313/15 (1994) p. 232.

2. H.M. Chung, J. ***Gazda,*** L.J. Nowicki, **J.E.** Sanecki, and D.L. Smith. "Effects of Fabrication Variables on Impact Properties and Microstructure of V-Cr-Ti Alloys," Fusion Reactor Materials: Semiannual Progress Report for the Period Ending September 30.1993, DOE/ER-0313/15 (1994) p. 207.

3. **M.L. Grossbeck,** T.K. Roche, W.S. Eatherly, FF. Dyer, and N.H. Rouse, "Fabrication of Vanadium Alloy Product Forms for Specimen Preparation," This report.

4. L. E. Davis, N. C. MacDonald, P. W. Palmberg, G. E. Riach, and R. E. Weber, "Handbook of Auger Electron Spectroscopy," Physical Electronics Division. Perkin-Elmer Corp., 1976.

5. T. Schober and D. N. **Braski, "The** Microstructure of Selected Annealed Vanadium-Base Alloys," Met Trans-A, Vol. 20A, Oct. 1989 pp. 1927-1932.

FRACTURE TOUGHNESS OF V-5Cr-5Ti ALLOY AT ROOM TEMPERATURE AND 100°C -

Huaxin Li (Associated Western Universities--Northwest Division), R. H. Jones (Pacific Northwest Laboratories)’ and J. P. Hirth (Washington State University--Pullman)

OBJECTIVE

The purpose of this research is to investigate the mode I and mixed-mode I/III fracture toughness of a V-5Cr-5Ti alloy at room temperature and 100°C.

SUMMARY

The critical mixed-mode I/III fracture toughness, J-integrals (J_{MC}), at room temperature (RT) and 100°C were examined for a V-5Cr-5Ti alloy. Fracture toughness at 100°C was evaluated with a J-integral test and at RT with a K (the stress intensity factor) test. The determination of J„ was made using modified compact-tension specimens. Different ratios of tensionlshear stress were achieved by varying the principal axis of the crack plane between 0 and 45 degrees from the load line. Crack angles used in this study were 0, **15,** and 45 degrees. A specimen with 0 degree crack angle is the same as a standard mode I compact tension specimen. **In** this limit, J„ becomes J_{IC}. Specimens were annealed at 1125°C for **1** hour in a vacuum of 10^{-7} torr. J_{MC} and mixed-mode tearing moduli (T,) were determined at 100°C with the single specimen technique. Crack lengths were calculated with partial unloading compliances. The J„ values at RT were calculated from critical stress intensity factors (K_C). The results showed that at RT the V-5Cr-5Ti alloy was brittle and experienced unstable crack growth with a mixture of intergranular, cleavage and some microvoid coalescence (MVC) fracture while at 100°C it exhibited high fracture toughness and fractured with a mixture of MVC and intergranular failure. SEM investigation showed that some cleavage facets initiated at grain boundaries. The results suggest a low intergranular fracture strength and tendency towards cleavage fracture at room temperature. Preliminary data from Auger electron microscopy showed significant sulfur segregation on grain boundaries. The possible mechanism which might reduce intergranular fracture strength is discussed.

PROGRESS AND STATUS

Introduction

Vanadium-base alloys are being considered as a candidate structural material for the international thermonuclear experimental reactor (ITER). Besides retaining its good strength and ductility at both ambient and elevated temperatures, vanadium-base alloys possess some unique neutronic properties as compared to austenitic and ferritic steel. Low neutron activation in the short-term, and specially in intermediate and long terms, and low biological hazard potential are particularly attractive properties of vanadium alloys. Recently the research on vanadium-base alloys is very active in USA, Japan, and European Community [1]. Research in U.S. has concentrated on vanadium-base alloys which compositions base on V + 5-15Cr + 0-20Ti + < 1Si [2,3]. The optimal composition has been narrowed to **V-(4-5)Cr-(4-5)Ti** alloys. Tensile and impact toughness tests done by Loomis and eo-workers [2-6] showed that these alloys have good strength and ductility at RT and elevated temperatures, high upper shelf fracture toughness, and low ductile brittle transition

---

“Pacific Northwest Laboratory is operated for the U.S. Department of Energy by Battelle Memorial Institute under Contract DE-AC06-76RLO **1830.**

temperate (DBTT). It is known that fracture toughness values J_{IC} (critical J-integral for mode I) or K_{IC} (critical stress intensity factor for mode I) are important design criteria for structural applications. However, there is no such data in literature for V base alloys. This research is to evaluate the fracture toughness of V-5Cr-5Ti by measuring its critical J or/and K values.

Traditionally, mode I fracture has been used to study elastic-plastic fracture mechanics. However, in recent years, mixed-mode fracture has become a focus of many studies because many observed failures included shear components [7-16]. Fracture characteristics have been found to differ from one another when subjected to mixed-mode I/III loading, depending on the microstructure, strength, and toughness level of materials. In low-toughness high-strength alloys, such as 0.29C-0.83Cu steel, and 1.25C bainitic steel [13-16], mode III contributions to mode I loading had little or no effect on the overall value of J_{IC}, the mode I component of the J-integral for mixed-mode crack initiation, and tended to increase J_{MC}, the total J-integral for mixed-mode crack initiation. In tougher materials (such as 3.5NiCrMoV steel, A710A, a high-purity rotor steel (HPRS) and a reduced activation ferritic/martensitic stainless steel (F-82H) [7-15,17], which failed primarily by a microvoid nucleation and growth mechanism) mode III contributions lowered the J_{MC} values considerably from their mode I values. The J_{MC} values passed through a minimum at a position between mode I and mode III on a plot of J_{MC} vs crack inclination angle.

Tensile data for V-5Cr-5Ti [2,6] suggested that it might be a tough material and possibly sensitive to mixed-mode I/III stress. Furthermore, a crack in a real reactor can frequently be in a mixed-mode I/III condition. Therefore, both mode I and mixed-mode I/III fracture toughnesses were investigated in this study.

Material and Experimental Methods

1. Material

A 6.35 mm thick V-5Cr-5Ti alloy plate (ANL No. BL-63) was produced by Teledyne Wah Chang-Albany. The chemical composition of the plate (as provided) is listed in Table 1 (by wt%). Specimens used in this study were cut in the orientation of T-L as specified in ASTM E399-90 and were annealed at 1125°C for 1 hour in a vacuum of 10^{-7} torr. The heat-treatment produced an average intersection distance grain size of 34.5 μm (ASTM #6.4). Mechanical property data used for determination of critical J-integrals are quoted from Ref. 2 for another heat of V-5Cr-5Ti (ANL No. BL-47) and are listed in Table 2.

Table 1. Chemical Compositions of V-5Cr-5Ti (BL-63)

Wt%		ppm				
Cr	Ti	O	N	C	Si	V
4.6	5.1	440	28	73	310	bal.

Table 2. Mechanical Properties of a V-5Cr-5Ti Alloy (ANL No BL-47)

Temperature (°C)	Yield Strength (MPa)	UTS (MPa)	Elongation (%)
25	387	454	34
100	325	420	33

2. Experimental Methods

2.1 J Testing at 100°C

The details of experimental methods about mixed-mnde I/III J-integral test were reported in Ref. **18.** Only the important portions of experimental methods are summarized here.

The geometry of modified compact-tension (MCT) specimens used for mixed-mode I/III testing is schematically shown in Fig. **1.** The magnitude of mode III components can he varied by changing the crack slant angle Φ. An angle of 0 degree represents mode **1** loading and the geometry of a 0-degree specimen becomes the standard compact-tension (CT) specimen as specified in ASTM standard E813-89. As Φ increases, the contribution of mode III components increases. The crack-inclination angles used in this study were 0, **15,** and **45** degrees. Side grooves of 20% reduction of total thickness were incorporated in **all** specimens. These side grooves can increase the triaxiality at the edges of a growing crack and constrain the advancing crack in the original crack plane. Calculating the total J-integrals in mixed-mode **11111** requires measuring both vertical displacement (6,) and horizontal displacement (6,) of load points. A standard crack opening distance (COD) clip gage was positioned on the knife edges. It was found that the 6, increased with 6, in a linear mode [7,9]. Hence δ_hs were calculated approximately using a relation of 6, $= \alpha$ x δ_v, where a = δ_{hmax} IS,,,,. An electric discharge machine (EDM) was used to make thin cuts with a small radius (radius = 0.051 mm) and approximately **1.3** mm long. The cuts were used as a substitute for a pre-fatigued-crack (PFC) because a PFC tends to grow out of the original crack plane in mixed-mode specimens. The EDM cuts were made before final heat-treatment.

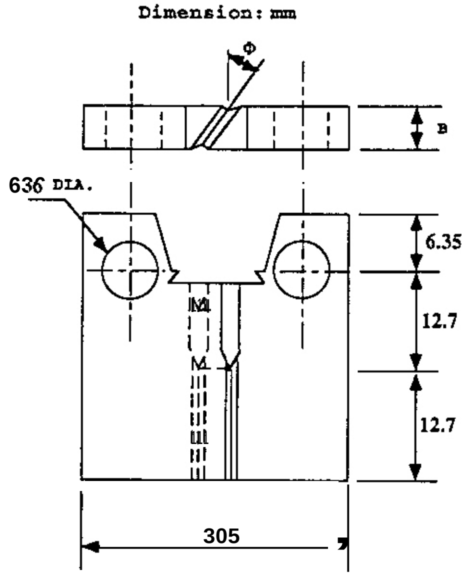

Fig. 1. The geometry of **a** modified compact tension specimen.

During **J** testing a specimen was heated up to 100°C with a heating tape surrounding it and temperature was controlled within **±5°C.** The single-specimen technique was used in this study, which allows a **J-R** curve (J vs crack extension Aa) to be generated with one specimen. During testing, the specimen was frequently and partially unloaded, and the partial unloading compliances were used to calculate the corresponding crack lengths following the procedure described in ASTM E813-89. Values of J matching those crack lengths were also calculated by means of Eq. **(1)** in the next section. At least 20 pairs of J-Aa data were used to construct **a** J-R curve.

The mixed mode I/III integral J_M were calculated from the area under the load vs load-line-displacement curve by means of Eq. (1) [19]:

$$J = \frac{2}{B_{net}\, b_o} \int_0^{6_v} P\, d\, V \qquad (1)$$

where

B_{net} = **$0.8B/\cos\Phi$** (the net crack front width excluding the **10%** side grooves on each side)
B = the overall specimen thickness
Φ = the crack-inclination angle
b_o = W - a, (the initial unbroken ligament)
W = the specimen width
a, = the initial physical crack length.

To construct J-R curves and determine critical J values **(J_{MC})**, ASTM **E813-89** was used. The slope of the blunting line for mixed mode I/III was calculated using Eq. (2):

$$m_{i/iii} = \frac{m_i \cos\Phi + m_{iii} \sin\Phi}{\sin\Phi + \cos\Phi} \tag{2}$$

where **m_i** = **$(\sigma_y + \sigma_{uts})$** and **$m_{iii}$** = **$(\sigma_y + \sigma_{uts})/2$**, which are blunting line slopes of pure mode I and mode III, respectively. When Φ equals **0** and 90, **$m_{i/iii}$** is equal to **m_i** and **m_{iii}**, respectively. ***A*** best fit straight line was also made using the J-Aa data between the upper and lower exclusion lines, and the slope of the straight line was taken as the nnnormalized mixed-mode 11111 tearing moduli (T,) for each specimen. The critical mode I and mode III J components (J_{iC} and J_{iiiC}) in mixed-mode specimens could also be calculated in terms of the corresponding resolved loads and displacements. The calculations of resolved mode I and mode III load and displacement and the determinations of J,, and J_{iiiC} have been reported in detail in Ref. **10, 11** and **15.**

2.1 K Testing at Room Temperature

Due to the brittleness and unstable crack growth of the V-5Cr-5Ti alloy at room temperature (RT), J„ could not be determined by ASTM **E813-89.** Therefore, **J_{MC}** at RT were calculated with Eq. **(3)**, **(4)** and ***(5):***

$$J_{MC} = J_{iC} + J_{iiiC} = \frac{1}{E}\left[K_{iC}^2 + (1+\nu)\, K_{iiiC}^2\right] \tag{3}$$

$$K_{iC} = \frac{P_Q}{B_{net}\sqrt{W}} f\left(\frac{a_o}{W}\right) \cos^2\phi \tag{4}$$

$$K_{iiiC} = \frac{P_Q}{B_{net}\sqrt{W}} f\left(\frac{a_o}{W}\right) \sin\phi\cos\phi \tag{5}$$

Where E is the Young's modulus which was provided by Grossbeck [20]; K„ and K_{IIIC} are mode I and mode III components of mixed-mode I/III; B_{net}, W and a, are the same as in Eq. 1; Φ is crack slant angle; P_Q is conditional load; f(a/W) is the correction function given in ASTM E399-89; here we assume f(a_o/W) is the same for both mode I and mode III.

K tests were done at RT by following the procedure specified in ASTM E399-90. Due to the shortage of material, the unbroken J specimens tested at 100°C were used for K testing at RT. After finishing J test at 100% and cooling the specimens down to RT, the specimens were fatigue-cracked at RT for a length of 0.5 to 1 mm. K„ and K„ values were calculated from Eq. (4) and (5). J„ was then calculated from K„ and K_{3C} by the means of Eq. (3). The J„ data at RT reported here might differ from those measured with a standard specimen because the specimens were deformed during J testing at 100°C and the ratios of crack length to specimen width were greater than 0.7.

Results

1. The Critical J Values

The dependence of J on crack angles and temperatures is shown in Fig. 2. In the limit of Φ = 0, J„ is equal to J„„ while for 0< Φ <90 degrees J_{MC} represents the total critical J values under mixed-mode I/III loading. Crack angles reported here include 0, 15, and 45 degrees. Each of the data points presented in Fig. 2 was obtained from a single specimen. The data reported here should be considered as exploratory. More tests are underway and will be presented in the next semiannual report. The RT fracture toughness data from F-82H steel (a ferriticlmartensitic stainless steel) are also included in Fig. 2 for comparison. From Fig. 2 it can be seen that J„ of the V-5Cr-5Ti at 100°C is comparable to those of F-82H steel at RT. Effect of introducing shear component on J„ is also similar to that of F-82H steel, i.e. introducing shear component decreased fracture toughness of V-5Cr-5Ti considerably from pure mode I counterpart. For example, J_{IC} at 100 C is about 470 kJ/m², however, the J„ at Φ=45 degree is only 180 kJ/m². The V-5Cr-5Ti alloy is brittle at RT and its fracture toughness shows only weak dependence on crack inclination angles. J„ varies from 61 to 43 kJ/m² when crack angles increase from 0 (mode I) to 45 degrees.

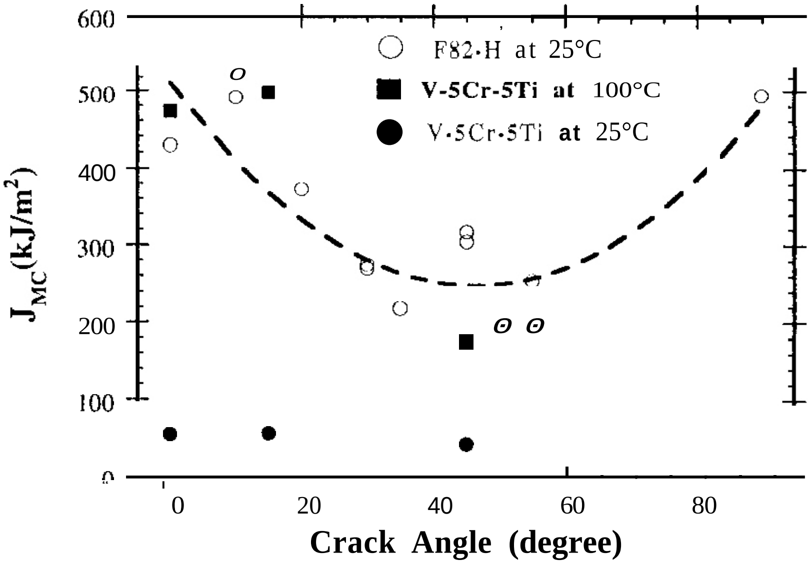

Fig. 2. The dependence of critical total J-integrals of V-5Cr-5Ti on crack inclination angles and temperatures. A reduced activation ferriticlmartensitic steel (F-82H) is included for comparison.

2. The Tearing Moduli (T,)

The dependence of unnormalized mixed-mode I/III tearing moduli (T_M) of the V-5Cr-5Ti at 100C on crack angles is shown in Fig. 3. RT T , could not be measured because the V-5Cr-5Ti was brittle and failed catastrophically. In this sense, the RT T_M should be close to zero. Once again the RT T„ data of F-82H steel are included in Fig. 3 for comparison. It can be seen that the 100°C T„ data ofthe V-5Cr-5Ti are also comparable to those of F-82H steel at RT, except for that of mode I ($\Phi=0$) which is much less than that of F-82H. The reason is unknown at this moment. More research is needed.

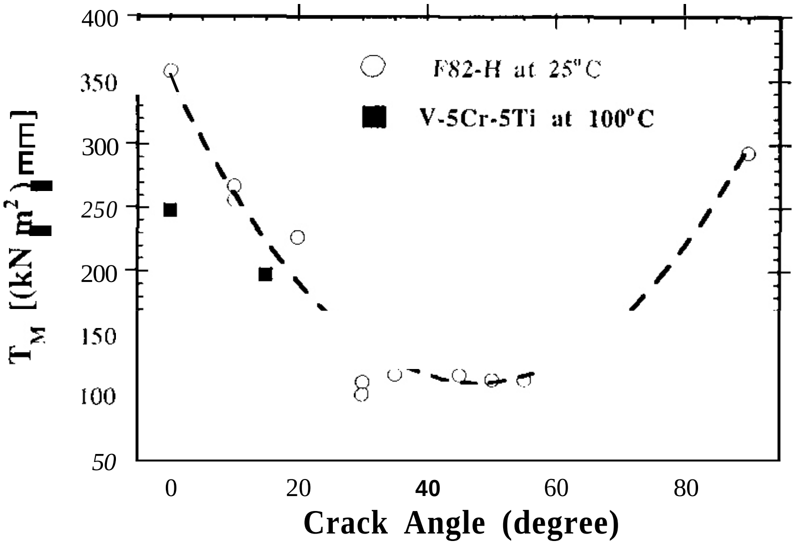

Fig. 3. The dependence of total tearing moduli of V-5Cr-5Ti on crack inclination angles. A reduced activation ferritic/martensitic steel (F-82H) is included for comparison.

3. Fractography

The crack fronts of all specimens remained in their initial orientation during J testing at 100°C and K testing at RT. At 100°C all specimens (regardless of crack angles) were fractured with a mixture of MVC and intergranular failure, as shown in Fig. 4. However, the morphology of fracture surface varied with crack extension during J testing. The fracture surface near the initial crack tip (the EDM cut tip) exhibited more MVC fracture than that close to the final crack tip. The fracture surface near the EDM cut tip is dominated with MVC fracture plus small amount of intergranular facets (Fig. 5a); as the crack propagated, intergranular fracture increased and MVC fracture decreased. Fig. 5b shows a fracture surface at the final crack tip. From Fig. 5 b one can see that while a large portion of the fracture surface is intergranular, the grains are heavily deformed and there are a lot of slip bauds on the intergranular facets. Therefore, although the V-5Cr-5Ti exhibited partially intergranular fracture at 100°C during J testing, its fracture toughness is still high. At RT the V-5Cr-5Ti fractured primarily with a mixture of intergranular, cleavage and some MVC mode, as shown in Fig. 6. Some cleavage facets apparently initiated at grain boundaries and propagated through adjacent grains, as shown in Fig. I. The tendency of the V-5Cr-5Ti to intergranular fracture at both RT and 100°C indicates that the intergranular bond strength is weak. The fracture data and fracture morphology at RT and 100°Cclearly indicate that the DBTT of the V-5Cr-5Ti annealed at 1125°C for 1 hour is above RT, which is consistent with the impact test

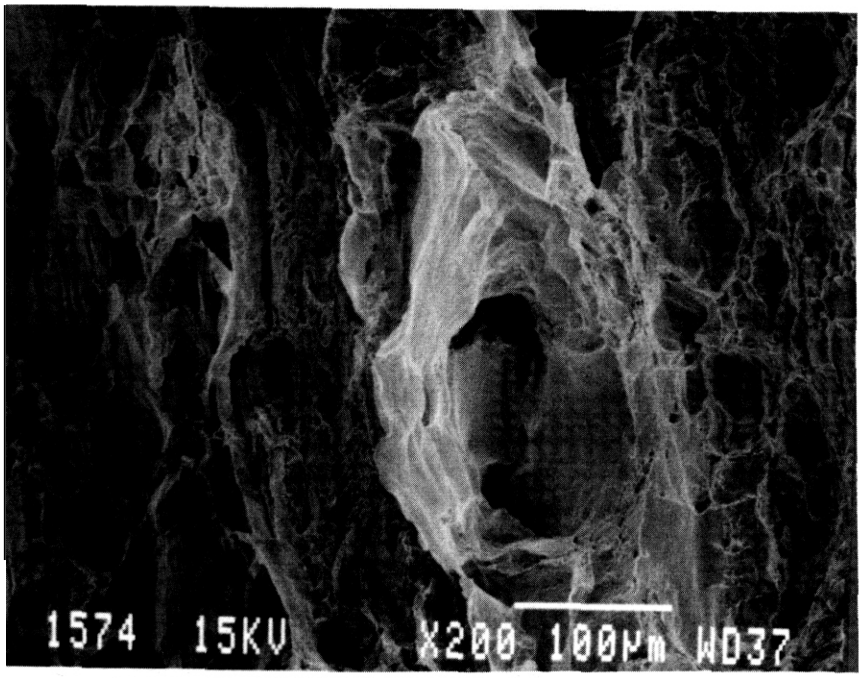

Fig. 4. A typical fracture surface of V-SCr-STi at 100°C, which shows a mixture of MCV and intergranular fracture.

results performed by Hamilton and Jones of Pacific Northwest Laboratories [21] and by Oak Ridge National Laboratories [22].

Discussion

Tensile properties reported by Argonne National Laboratory [2,6] (with thin sheet tensile specimens) showed that V-5Cr-5Ti annealed at either 1050 or 1125°C in vacuum for 1 hour were ductile at RT and 100°C, exhibiting MVC fracture with an elongation of about 34%. However, fracture toughness testing results in this study showed the alloy annealed at 1125°C for 1 hour was brittle at RT, experiencing a mixture of intergranular and cleavage failure. While the reason for this discrepancy is not fully understood, a trial J test conducted at RT suggests that notch sensitivity of V-5Cr-5Ti might play an important role in affecting its fracture behavior. One specimen with a crack angle of 15 degree was used for a J testing at RT and failed catastrophically shortly after a crack initiated from EDM cut. SEM investigation revealed that the area close to EDM cut tip experienced significant plastic deformation and fractured mainly by MVC fracture, as shown in Fig. Sa, however, after the crack propagated about 300 pm, it failed catastrophically with a mixture of intergranular and cleavage fracture, as shown in Fig. Sb. The reason for this change in fracture behavior is that the EDM cut was not very sharp, with a radius of about 50 pm, therefore, a relatively large amount of energy was consumed for a sharp crack to initiate; as a sharp crack formed, the fracture mode changed and the fracture energy decreased. Also, if a pre-fatigue pre-

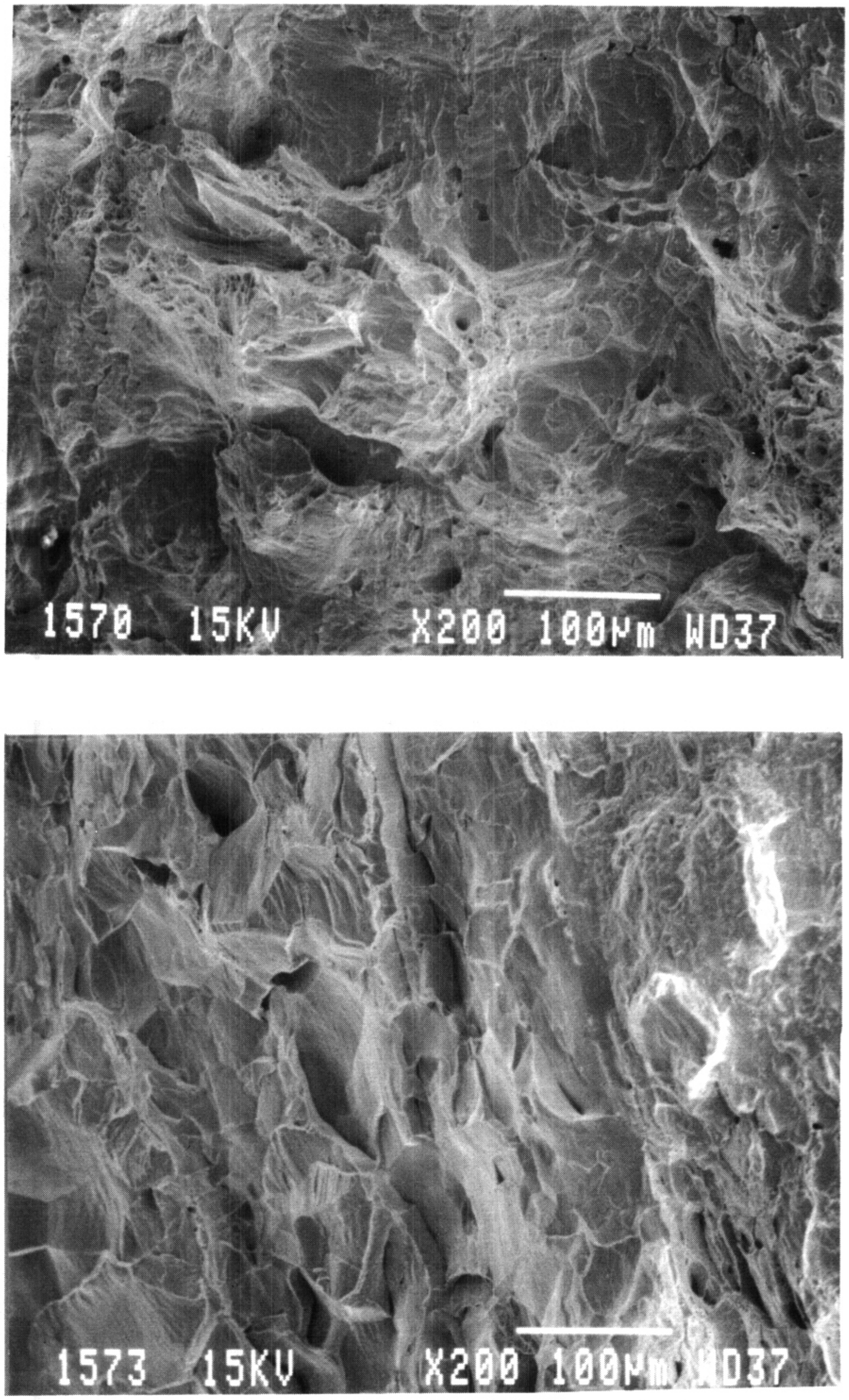

Fig. 5. Fracture surfaces of a zero degree J-integral sample fractured at 100°C during J testing: a. an area close to EDM cut tip which is dominated with MVC fracture; b. an area close to final crack tip which is a mixture of MVC and intergranular fracture.

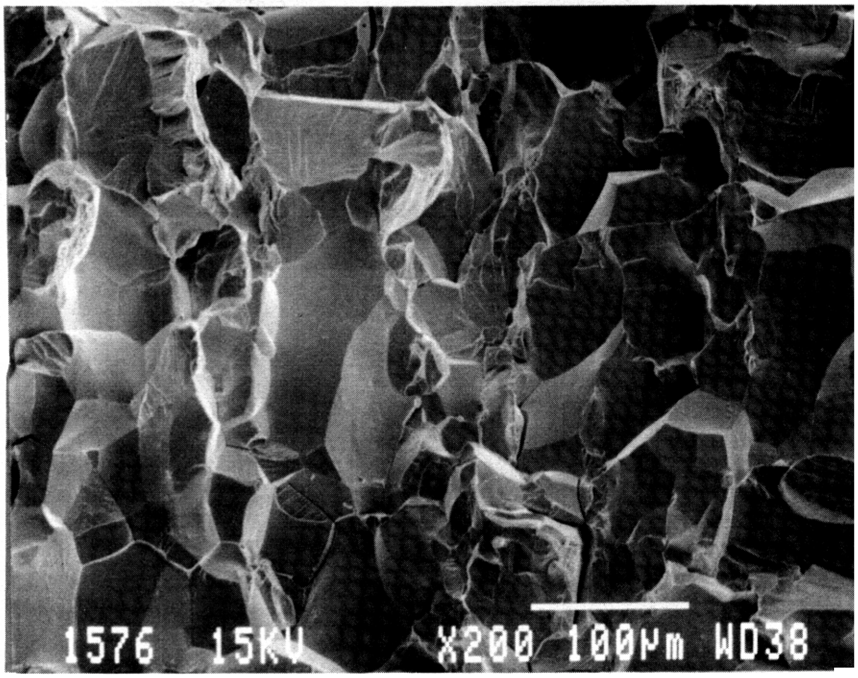

Fig. 6. A fracture surface of a zero degree sample which was fractured at room temperature during K testing. The fracture surface consists of a mixture of intergranular, cleavage and some MVC failure.

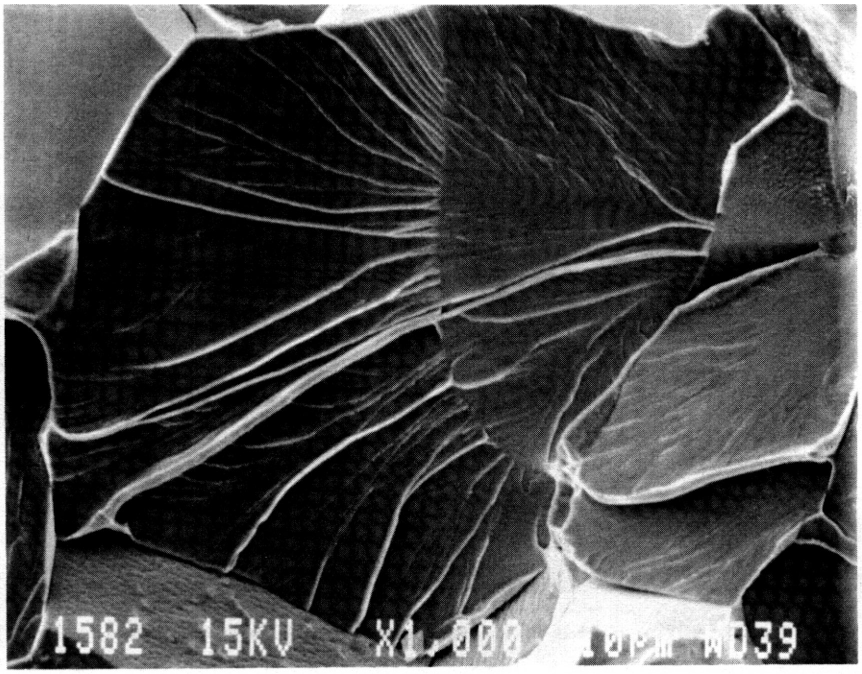

Fig. 7. A cleavage fracture facet which shows the cleavage crack initiates at grain boundary and passes through another grain boundary.

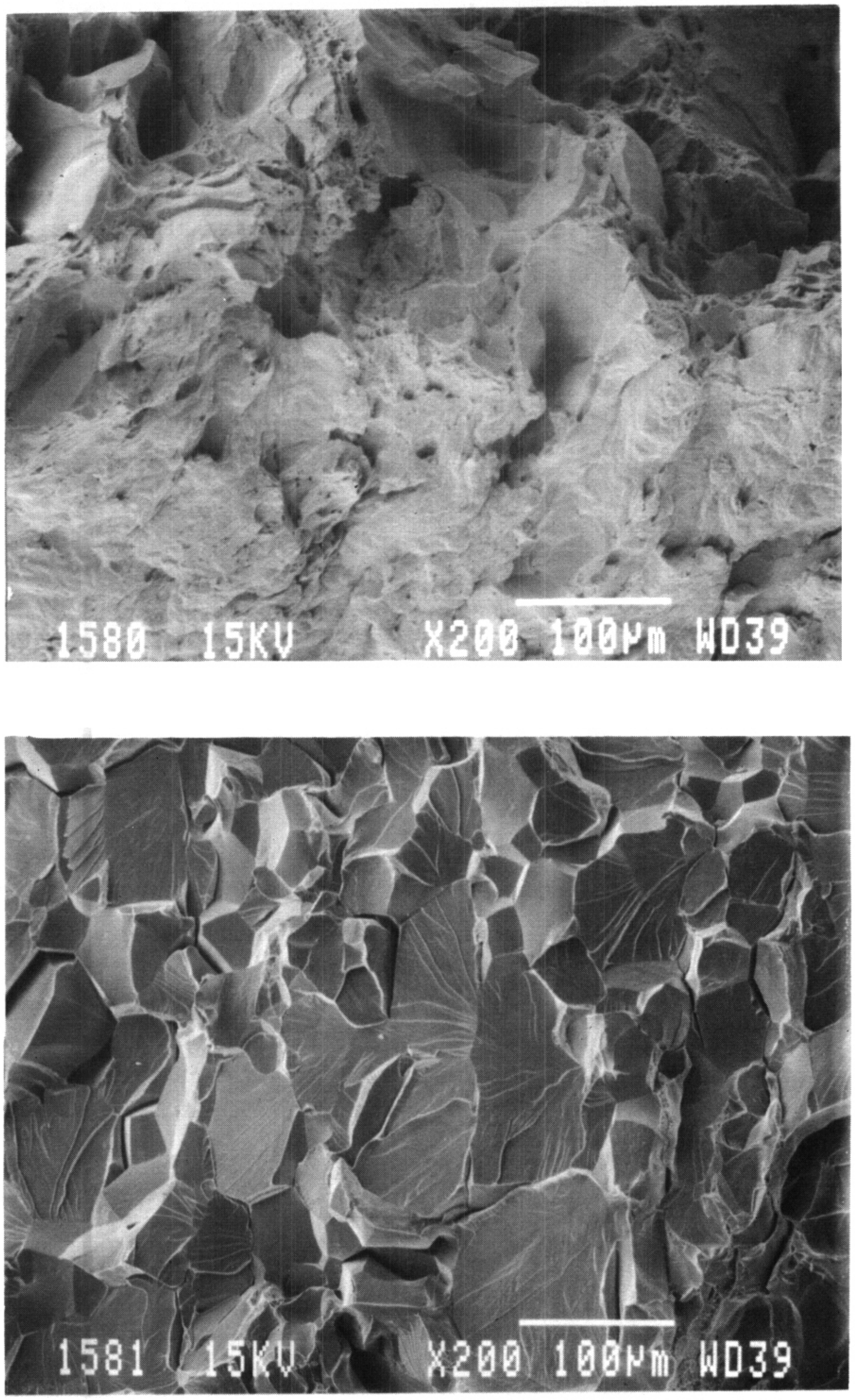

Fig. 8. Fracture surfaces of a 15 degree angle sample fractured during J testing at room temperature: a. an area close to EDM cut tip which is dominated with MVC fracture: b. an area close to final crack tip which is dominated with a mixture intergranular and cleavage fracture.

cracked specimen (such as in the case of K test at RT) was used, only a very small amount of MVC fracture was found near crack tip. The observation suggests that the V-5Cr-5Ti alloy is sensitive to crack sharpness. Another factor that could contribute to the brittleness of the V-5Cr-5Ti during K test at RT is the thickness of the specimen. Tensile tests were conducted with thin sheet specimens (1 mm) in which the state of stress is plane stress. On the other hand, a thick specimen with a sharp crack will result in a triaxial state of stress (plane strain) at crack tip. The triaxial stress will restrict plastic deformation and enhance brittle fracture. Sensitivity of a material to crack tip sharpness increases with the brittleness of material because of the reduced crack blunting during crack growth. Fracture toughness tests using fatigue pre-cracked specimens will be conducted in the future.

The brittleness of the V-5Cr-5Ti annealed at 1125°C seems to stem from the low grain boundary fracture strength. Increasing temperature can increase dislocation mobility and reduce or even eliminate cleavage fracture. However, a mixture of MVC and intergranular fracture at 100°C indicates the bond strength between grains is still weak. The possible mechanism which might reduce the grain boundary fracture strength will be discussed later and will be investigated systematically in the future.

It has been found recently that adding mode III component to mode I loading could increase, decrease, or have little or no effect on the J„, depending on the toughness of the materials. For brittle materials, such as glass [23], 0.29C-0.83Cu steel and 1.25C bainitic steels [10,14-16], where fracture was controlled by tensile stress and the local crack-opening displacements, adding mode III components had little or no effect on the J,, (mode I J component of J_{MC}), but tended to increase J_{MC}. For tough steels, such as HPRS [11] and F-82H steel [17], which failed primarily by microvoid coalescence, additional shear stress produced incompatibility stresses at the particle interfaces in the trajectory of the crack, causing decohesion or particle fracture (shear damage). This process led to void formation that limited the mode I plastic flow field and caused premature separation of voids by mode I stress. Accordingly, tough materials exhibited lower fracture toughness for a mixed-mode crack than that for mode I crack. For those materials with intermediate toughnesses, such as AISI 1090 steel [10], introducing a mode III component decreased J_{iC} moderately, and had little effect on J_{MC}.

At 100°C the V-5Cr-5Ti is ductile, introducing shear stress component decreases its J_{MC} considerably. While "shear damage" at interfaces between particles and matrix caused by shear stress component could lead to a lower mixed-mode fracture toughness than its mode I counterpart, it might not he the sole mechanism because there are fewer particles in this alloy than those in F-82H steel and a large portion of fracture surface is intergranular, not MVC fracture. One possible role of shear stress component might be to increase dislocation pile-ups rate at grain boundaries which promotes premature intergranular failure by tension stress component. How a mixed-mode I/III loading affects a ductile and partial intergranular fracture needs further investigation. Due to the low toughness at RT, introducing shear stress component did not reduce the total fracture toughness (J_{MC}) significantly. J,, keeps almost constant with crack angles between 0 to 45 degree, which is similar to that of AISI 1090 steel tested at RT [10]. The results are consistent with the theory of mixed-mode I/III fracture mechanics.

The relatively large proportion of intergranular fracture at both 100°C and RT indicates the low fracture strength of grain boundaries in the V-5Cr-5Ti annealed at 1125°C. It is known that intergranular fracture in a metallic material is usually caused by one or more of following reasons. 1. Impurity Segregation or/and secondary phase precipitation on grain boundaries, such as temper embrittlement in steels; 2. Hydrogen embrittlement; 3. Liquid metal embrittlement; 4. Environmental assisted cracking; and 5. Intergranular corrosion. The # 3, 4, and 5 mechanisms obviously can be excluded from this study. That all specimens annealed in a vacuum of 10^{-7} torr for 1 hour (which should outgas hydrogen thoroughly) and tested at 100°C still fractured with partial intergranular mode suggests hydrogen embrittlement mechanism probably is not responsible for the low fracture strength of grain boundaries. The most possible mechanism is the segregation of impurities (such as sulfur, phosphorous etc.) and/or precipitation of second phase to its grain boundaries. TEM analysis [22] revealed precipitation of Ti(O,C,N) on grain boundaries, and our preliminary Auger electron spectroscopy analysis showed a significant enrichment of sulfur on grain boundaries in a specimen annealed at 1125°C for 1 hour in vacuum. Jones [24] showed that sulfur segregation to grain boundaries can reduce the bond force between grains in steels and nickel. More research work will be devoted to evaluate the effects of heat treatments on sulfur segregation and second phase precipitation to grain boundaries, on intergranular fracture, fracture toughness and DBTT of the V-5Cr-5Ti alloy in the near future.

CONCLUSION

A V-5Cr-5Ti alloy annealed at 1125°C for 1 hour was brittle and experienced a mixture of intergranular, cleavage and some MVC fracture when tested at RT. Introducing shear stress had little effect on the total mixed-mode I/III fracture toughness (J_{MC}) at RT. J_{MC} decreased only from 61 to 43 kJ/m^2 when crack angle increased from 0 to 45 degrees. When tested at 100°C, V-5Cr-5Ti exhibited excellent fracture toughness while it still experienced a mixture of MVC and intergranular failure. Its J_{MC}'s are comparable to those of a tough ferritic/martensitic stainless steel, F-82H. Adding shear component reduced its J_{MC} and T , dramatically from its pure mode I counterpart (J_{IC}) and T,. J_{MC} and T_M dropped from 470 kJ/m^2 and 250 [(kJ/m^2)/mm] for pure mode I to 180 kJ/m^2 and 170 [(kJ/m^2)/mm] a mixed-mode I/III with a crack angle 45 degree, respectively.

FUTURE WORK

Further research is in progress to evaluate the effect of crack sharpness on fracture toughness and effect of heat treatments on sulfur segregation and second phase precipitation at grain boundaries, on the intergranular fracture, fracture toughness and DBTT of the V-5Cr-5Ti alloy. The effect of hydrogen and oxygen on mechanical properties will also be evaluated.

ACKNOWLEDGEMENTS

We are grateful to Dr. M. Grossbeck of ORNL for supplying us V-5Cr-5Ti alloy. The assistance of Mr. J. L. Humason at Pacific Northwest Laboratory in developing the test methods is gratefully acknowledged. This research was supported by the Office of Fusion Energy of the U. S. Department of Energy under Contract DE-AC06-76RLO 1830 with Battelle Memorial Institute.

REFERENCES

1. D. R. Harries, G. J. Butterworth, A. Hishinuma, and F. W. Wiffen, J. of Nuclear Materials, 191-194 (1992), pp. 92-99.

2. B. A. Loomis, L. J. Nowicki, and D. L. Smith, Fusion Reactor Materials Semiannual Progress Report DOE/ER-0313/10, Oak Ridge National Lab., Oak Ridge, TN (March, 1991).

3. B. A. Loomis and D. L. Smith, J. of Nuclear Materials, 191-194 (1992), pp. 84-91.

4. B. A. Loomis, L. J. Nowicki, and D. L. Smith, Fusion Reactor Materials Semiannual Progress Report DOE/ER-0313/13, Oak Ridge National Lab., Oak Ridge, TN (September, 1992).

5. B. A. Loomis, J. Gazda, L. J. Nowicki, and D. L. Smith, "Relationship of Microstructure and Mechanical Properties of V-Cr-Ti Alloys", CFRM-6/Ref. No. H016, Sixth International Conference on Fusion Reactor Materials, September 27-October 1, 1993, Stresa, Italy.

6. B. A. Loomis, "Anomalies of Dependence of Physical and Mechanical Properties of V-Ti and V-Cr-Ti Alloys of Titanium and Chromium Concentration", Argonne National Laboratory, November 6, 1993.

7. M. T. Miglin, I.-H. Lin, J. P. Hirth, and A. R. Rosenfield, Fracture Mechanics: 14th Symp.--Vol. II: Testing and Applications, ASTM STP 791, J. C. Lewis and G. Sines, Eds., ASTM, Philadelphia, 1983, pp. II-353-II-369.

8. M. T. Miglin, J. P. Hirth and A. R. Rosenfield, Res. Mech., 11 (1984), pp. 85-95.

9. J. G. Schroth, J. P. Hirth, R. G. Hoagland, and A. R. Rosenfield, Met. Trans. A, 18A (1987), pp. 1061-1072.

10. M. Manoharan, J. P. Hirth, and A. R. Rosenfield, J. of Test. and Eval., 18 (1990), No.2, pp. 106-114.

11. S. Raghavachary, A. R. Rosenfield, and J. P. Hirth, Met. Trans. A, 21A (1990), pp. 2539-45.

12. J. A. Gordon, J. P. Hirth, A. M. Kumar, and N. R. Moody, Jr., Met. Trans. A, 23A (1991), pp. 1013-1020.

13. M. Manoharan, S. Raghavachary, J. P. Hirth, and A. R. Rosenfield, J. Ene. Mater. Technol., 111 (1989), October, pp. 440-442.

14. A. M. Kumar and J. P. Hirth, Scripta Metall. Mater., 25 (1991), pp. 985-90.

15. M. Manoharan, Scripta Metall. Mater., 26 (1992). pp. 1187-1192.

16. M. Manoharan, J. P. Hirth and A. R. Rosenfield, Scripta Metall. Mater., 23 (1989), pp. 763-766 and pp. 1647-1648.

17. H. Li, R. H. Jones, P. J. Hirth and D. S. Gelles, Fusion Reactor Materials Semiannual Progress Report DOE/ER-0313/15, Oak Ridge National Lab., Oak Ridge, TN (October, 1993).

18. H. Li, R. H. Jones, P. J. Hirth and D. S. Gelles, Fusion Reactor Materials Semiannual Progress Report DOE/ER-0313/14, Oak Ridge National Lab., Oak Ridge, TN (March, 1993).

19. J. R. Rice, P. C. Paris, and J. G. Merkle, ASTM STP 536, ASTM, Philadelphia, 1973, pp. 231-235.

20. M. Grossbeck, Private Communication, March 1994.

21. M. L. Hamilton and R. **H.** Jones, Pacific Northwest Laboratories, 1994.

22. M. L. Grossbeck et al., "Vanadium Alloy Research **for** Fusion Reactors", Oak Ridge National Laboratories, March **17,** 1994.

23. A. R. Rosenfield and **W. H.** Duckworth, Int. J. Fract., 32, (1987), p. R59.

24. R. **H.** Jones, in Mechanical Properties and Phase Transformations in Engineering Materials, S. D. Antolovich, R. **O.** Ritchie and **W. W.** Gerberich, Eds. The Metallurgical Society of AIME, **1986,** pp. 227-249.

INFLUENCE OF TRANSMUTATION ON MICROSTRUCTURE, DENSITY CHANGE, AND EMBRITTLEMENT OF VANADIUM AND VANADIUM ALLOYS IRRADIATED IN HFIR -

S. Ohnuki and H. Takahashi (Hokkaido University, Sapporo, Japan), K. Shiba and A. Hishinuma (Japan Atomic Energy Research Institute, Tokai, Japan), J. Pawel (Oak Ridge National Laboratory, Oak Ridge, TN, USA), and F. A. Garner (Pacific Northwest Laboratory')

OBJECTIVE

The objective of this effort is to determine the factors which control the performance of vanadium alloys in fusion service.

SUMMARY

Addition of **1** at.% nickel to vanadium and V-10Ti, followed by irradiation along with the nickel-free metals in HFlR to **2.3** x 10^{22}n cm^{-2}, E>0.1MeV (corresponding to 17.7 dpa) at 400°C, has been used to study the influence of helium **on** microstructural evolution and embrittlement. Approximately **15.3%** of the vanadium transmuted to chromium in these alloys. The **–50** appm helium generated from the $^{58}Ni(n,\gamma)^{59}Ni(n,\alpha)^{56}Fe$ sequence was found to exert much less influence than either the nickel directly or the chromium formed by transmutation.

The V-10Ti and V-10Ti-1Ni alloys developed an extreme fragility and broke into smaller pieces in response to minor physical insults during density measurements. A similar behavior was not observed in pure **V** or V-1Ni. Helium's role in determination of mechanical properties and embrittlement of vanadium alloys in HFlR is overshadowed by the influence of alloying elements such as titanium and chromium. Both elements have been shown to increase the DBTT rather rapidly in the region of **10%** (Cr + Ti). Since Cr is produced by transmutation of **V,** this is a possible mechanism for the embrittlement. Large effects on the DBTT may have also resulted from uncontrolled accumulation of interstitial elements such as C, N, and **O** during irradiation.

PROGRESS AND STATUS

Introduction

Vanadium-base alloys are currently being investigated for potential applications as structural materials in fusion reactors **(1-3).** As with other alloy systems, however, there is concern that the relatively high levels of helium generated in fusion neutron spectra will strongly influence the microstructural evolution, dimensional stability and especially the mechanical properties. In order to study the potential influence of helium/dpa ratio while irradiating vanadium alloys in reactors whose spectra produce much lower levels of helium, a variety of helium enhancement techniques are being employed. Some involve the use of boron additions to produce helium via the $^{10}B(n,\alpha)^{7}Li$ reaction (4-6), while others involve the preiujection of 'He via the "tritium-trick" prior to neutron irradiation (7). The Dynamic Helium Charging Experiment utilizes pre-doping with tritium as well as continuous generation of tritium via transmutation of the 'Li-enriched lithium coolant surrounding the specimens ***(8).***

'Pacific Northwest Laboratory is operated for the **U.S.** Department of Energy by Battelle Memorial lnstitute under Contract DE-AC06-76RLO **1830.**

Another doping technique explored in the current study involves adding natural nickel to vanadium alloys and irradiating them in a mixed spectrum reactor such as the High Flux Isotope Reactor (HFIR) at Oak Ridge National Laboratory. Using this approach, helium is produced via the two-step $^{58}Ni(n,\gamma)^{59}Ni(n,\alpha)^{56}Fe$ sequence (9). To explore the feasibility of this approach, both pure vanadium and V-10Ti (at.%) were irradiated in HFIR, each as two variants, both with and without 1 at.% of natural nickel. As will be seen in the experimental results, however, the potential impact of gaseous transmutant helium was overshadowed by the action of solid transmutant chromium.

Experimental Details

One each of V, V-1Ni, V-10Ti, V-10Ti-1Ni (nominal compositions, all in at.%) specimens were irradiated side-by-side in a HFIR target position at a temperature of 400°C to 2.3 x 10^{22} n cm^{-2} (E>0.1 MeV) and 8.8 x 10^{22} n cm^{-2} (total) corresponding to 17.6 dpa in this spectrum calculated for austenitic stainless steel using the standard NRT model (10)]. The measured compositions are presented in Table 1. The specimens were irradiated in helium-filled stainless steel subcapsules in the form of 0.25 mm thick x 3.0 mm diameter microscopy disks. The residual radioactivity after two year's decay was ~10 mR/hr at contact for specimens without nickel and ~150 mR/hr for nickel-containing specimens. The calculated helium level for the nickel-containing specimens is ~50 appm; only 0.5 appm or less was calculated for the nickel-free specimens.

Table 1. Starting Composition* of Vanadium and Vanadium Alloys in at.%

Alloy	C	O	N	H	Al	Fe	Si	Ni	Ti
V	0.0051	0.0194	0.0083	0.0610	0.034	0.047	0.005	-	-
V-1Ni	-	-	-	-	-	-	-	0.91	-
V-10Ti	-	-	-	-	-	-	-	-	9.5
V-10Ti-1Ni	-	-	-	-	-	-	-	0.88	9.3

* Minor impurities measured only for vanadium.

Following post-irradiation removal from the subcapsules, the density of the irradiated specimens was measured at Oak Ridge National Laboratory using an immersion density technique shown to be accurate to ±0.1% change in density (11). The density of unirradiated specimens was measured at Pacific Northwest Laboratory using a similar technique.

During the density measurement process, the V-10Ti and V-10Ti-1Ni specimens each broke in a very brittle manner after the second of two density measurements was completed. The physical insult causing this breakage was considered to be minimal, however, since no other specimens have broken during similar handling. The procedure causing the breakage involved pneumatically transporting the specimen through a rubber tube dropping it into a wire mesh basket. Since such extreme embrittlement was unanticipated, repeat measurements were not performed on the V and V-1Ni specimens in order to preclude the possibility of further breakage.

The broken specimens were examined in a JSM 840 scanning electron microscope while the unbroken specimens were thinned for microscopy and examined in a JEOL 2000 FX electron microscope. Energy-dispersive x-ray (EDX) analysis was performed in each instrument to assess transmutation-induced changes in composition. Significant formation of chromium via transmutation of vanadium is expected during irradiation in HFIR. The thinning process and subsequent microscopy involve some stresses being placed on the specimens but fragility was not observed during thinning or examination of the V and V-1Ni specimens.

Results

The density change data are shown in Table 2. The changes in density are relatively small in V and V-1Ni, but significant decreases in density occurred in both V-10Ti and V-10Ti-1Ni; nickel additions appeared to decrease the change somewhat. Density changes are anticipated to result from both void swelling and transmutation-induced changes in lattice parameter.

Table 2. Density changes measured in vanadium and several alloys after irradiation to 17.7 dpa at 400°C in HFIR.

	Unirradiated density, g cm^{-3}	Irradiated density, g cm^{-3}	Change, %*
V	6.13038	6.1525	0.36
V-1Ni	6.19391	6.1784	-0.25
V-10Ti	5.97293	5.8336 5.8354**	-2.33 -2.30
V-10Ti-1Ni	5.98426	5.8955 5.8926**	-1.48 -1.53

Change contains contributions from both cavities and transmutation-induced changes in composition. A negative sign implies volumetric swelling.
Second independent measurement.

Figure 1 shows the broken specimens of both V-10Ti and V-10Ti-1Ni. Figure 2 shows typical fracture surfaces observed on two of the three major pieces of the V-10Ti specimen. The fracture surface is dominated primarily by transgranular cleavage facets and secondarily by grain boundary separation. With the exception of a few small precipitates on the grain boundary, there were no resolvable features on the facets or grain boundaries that would indicate the presence of voids or bubbles. Figure 3 shows similar micrographs for the V-10Ti-1Ni specimen. Once again there appeared to be no boundary or facet features that would provide evidence of cavities.

Figure 4 shows a comparison of the microstructure observed in pure V and V-1Ni. Each contained comparable densities ($\sim 5 \times 10^{16}\text{cm}^{-3}$) of small ($\leq 5$ nm) cavities. There appeared to be no refinement of the cavity structure due to helium generation from the nickel. The two specimens developed very different surfaces during electropolishing, however. While the V-1Ni specimen had a very smooth surface, the pure V specimen developed a very irregular surface, indicative of selective electropolishing. The regions protruding above the average surface plane appear to be related to be regions of higher chromium level.

As shown in Table 3, the bulk level of transmutant chromium determined by broad-beam electron scans in the JSM 840 of the surfaces of V, V-10Ti and V-10Ti-1Ni show that 15.35 ± 0.35% of the original vanadium having transmuted to chromium. Thin foil analyses of V and V-1Ni in the JEOL 2000 yielded comparable but somewhat more variable measurements of 16.0 and 14.0%, respectively. These results are in excellent agreement with the predictions of Greenwood and Garner (12), who predicted 19.3% at 22 dpa. When interpolated, this yields a predicted value of 15.5% at 17.7 dpa, compared to the measured mean of 15.3%.

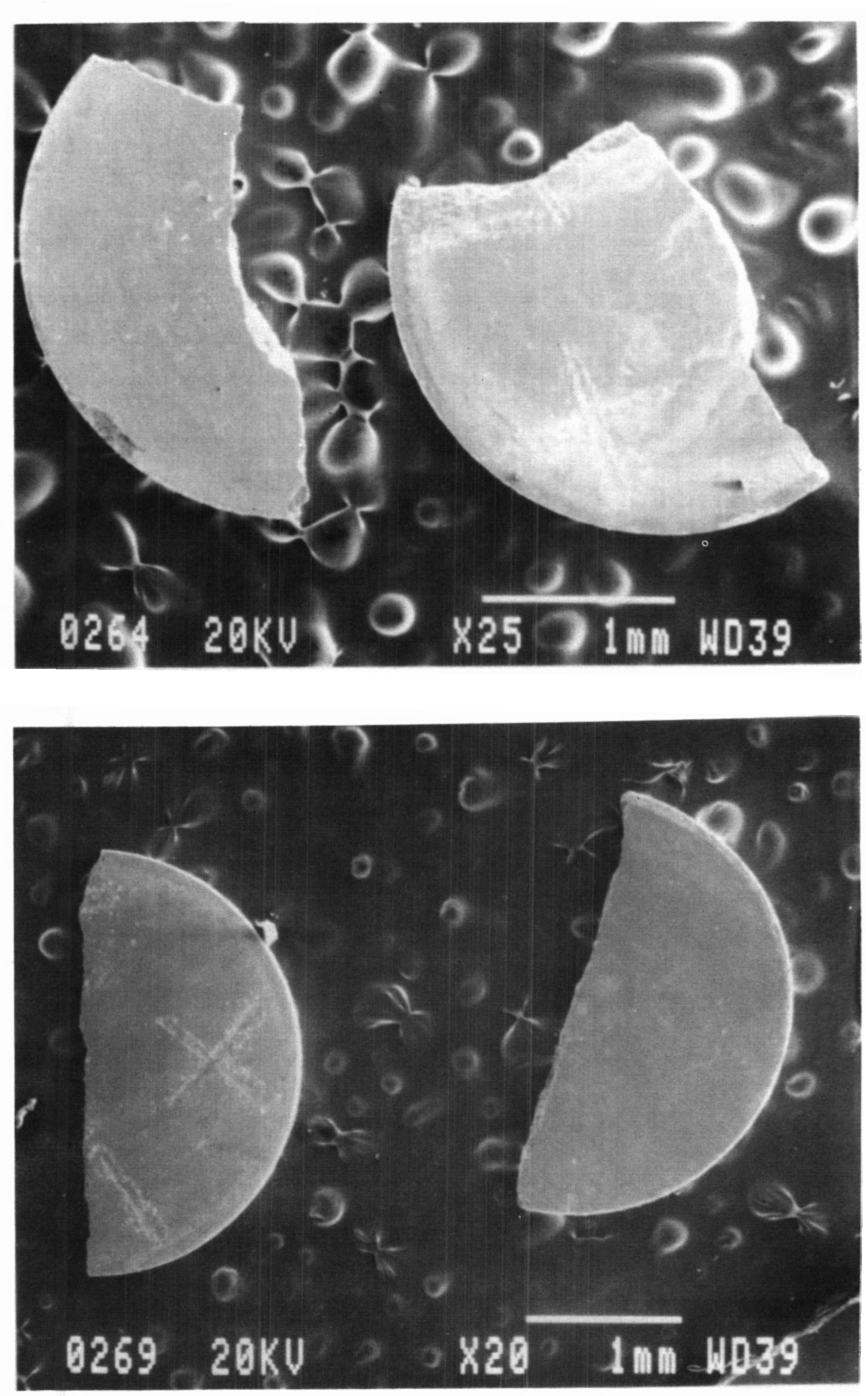

Fig. 1. Fragments of broken microscopy disks from irradiated V-10Ti (top) and V-10Ti-1Ni (bottom).

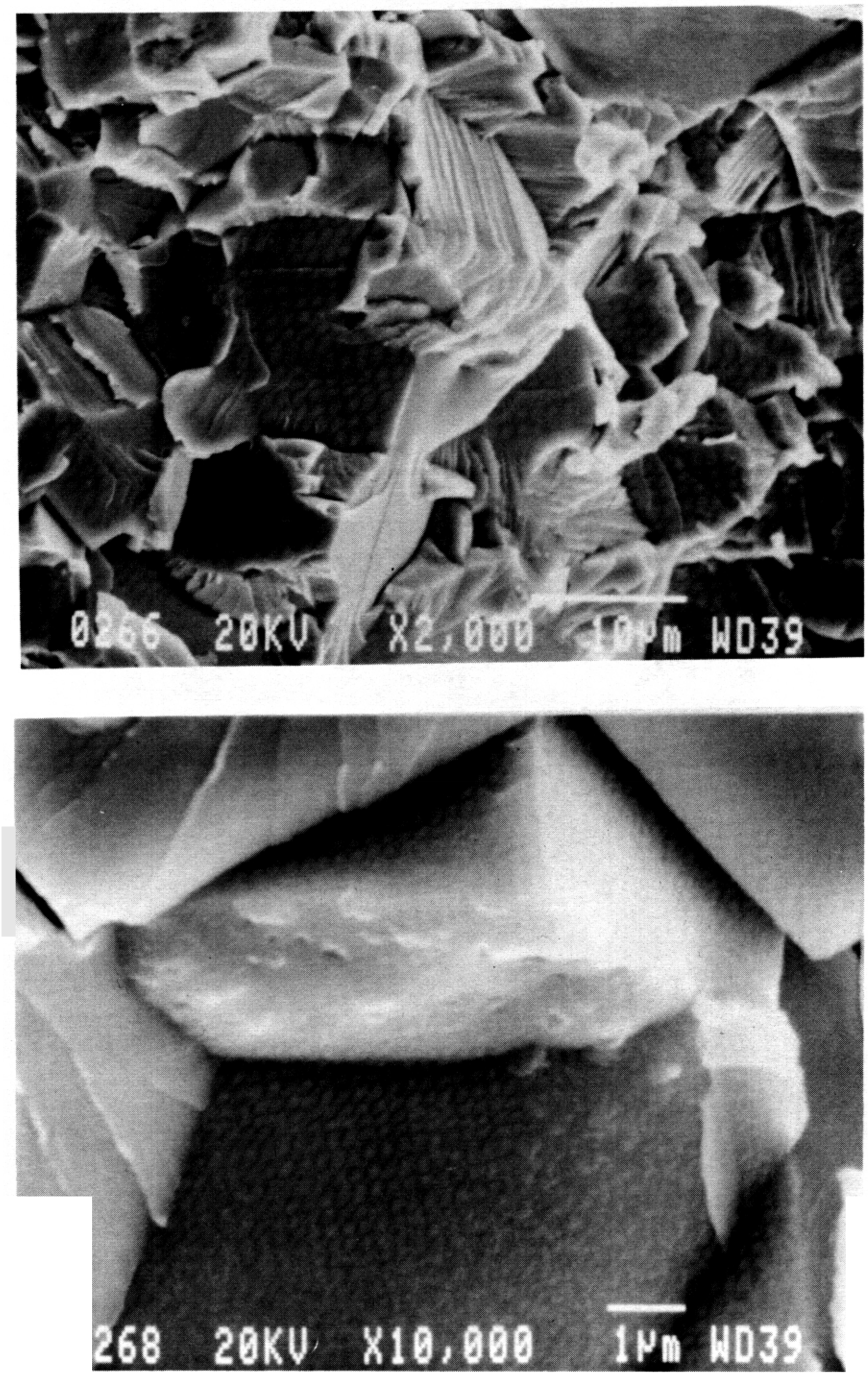

Fig. 2. Fracture surfaces of irradiated V-10Ti specimen.

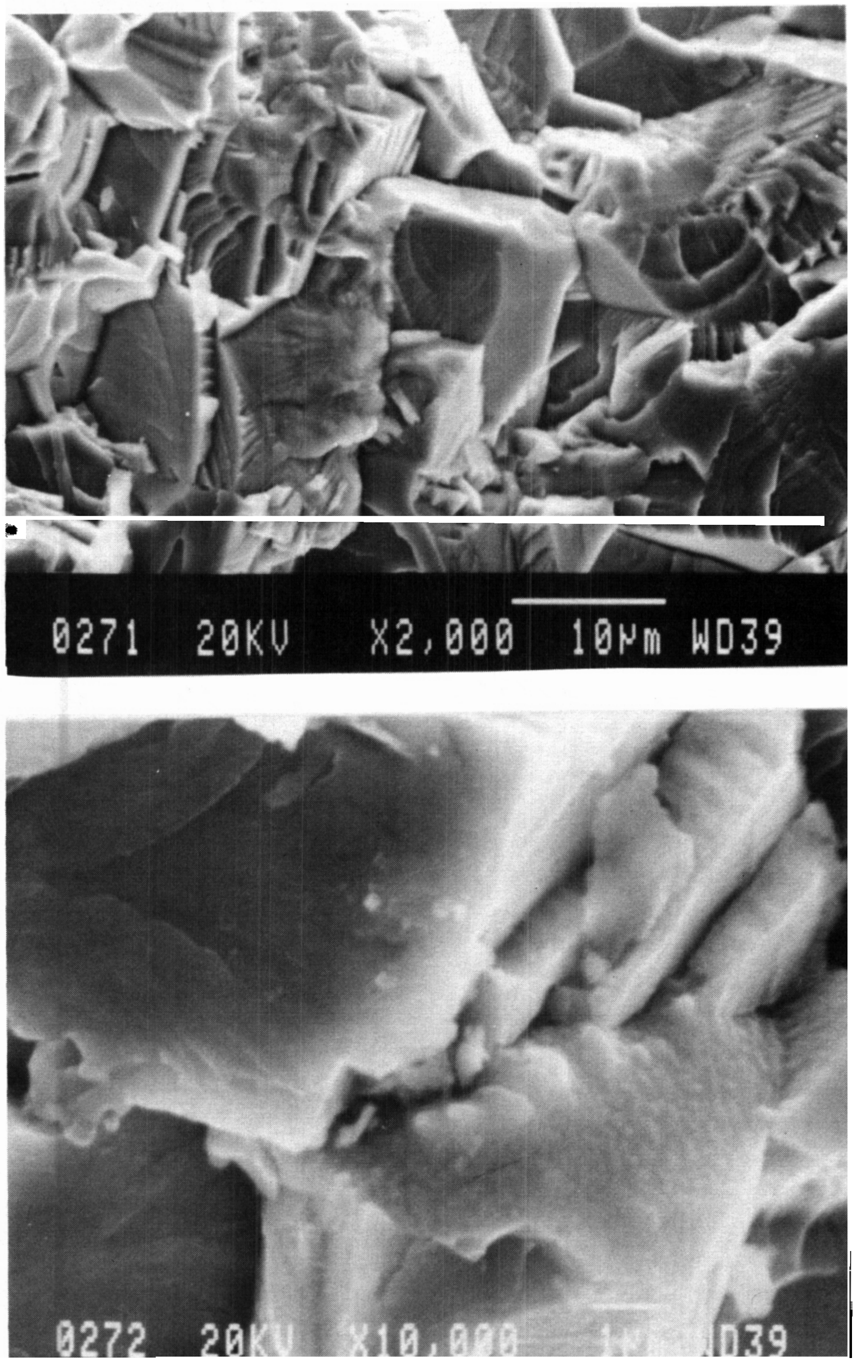

Fig. 3. Fracture surfaces of irradiated V-10Ti-1Ni specimen.

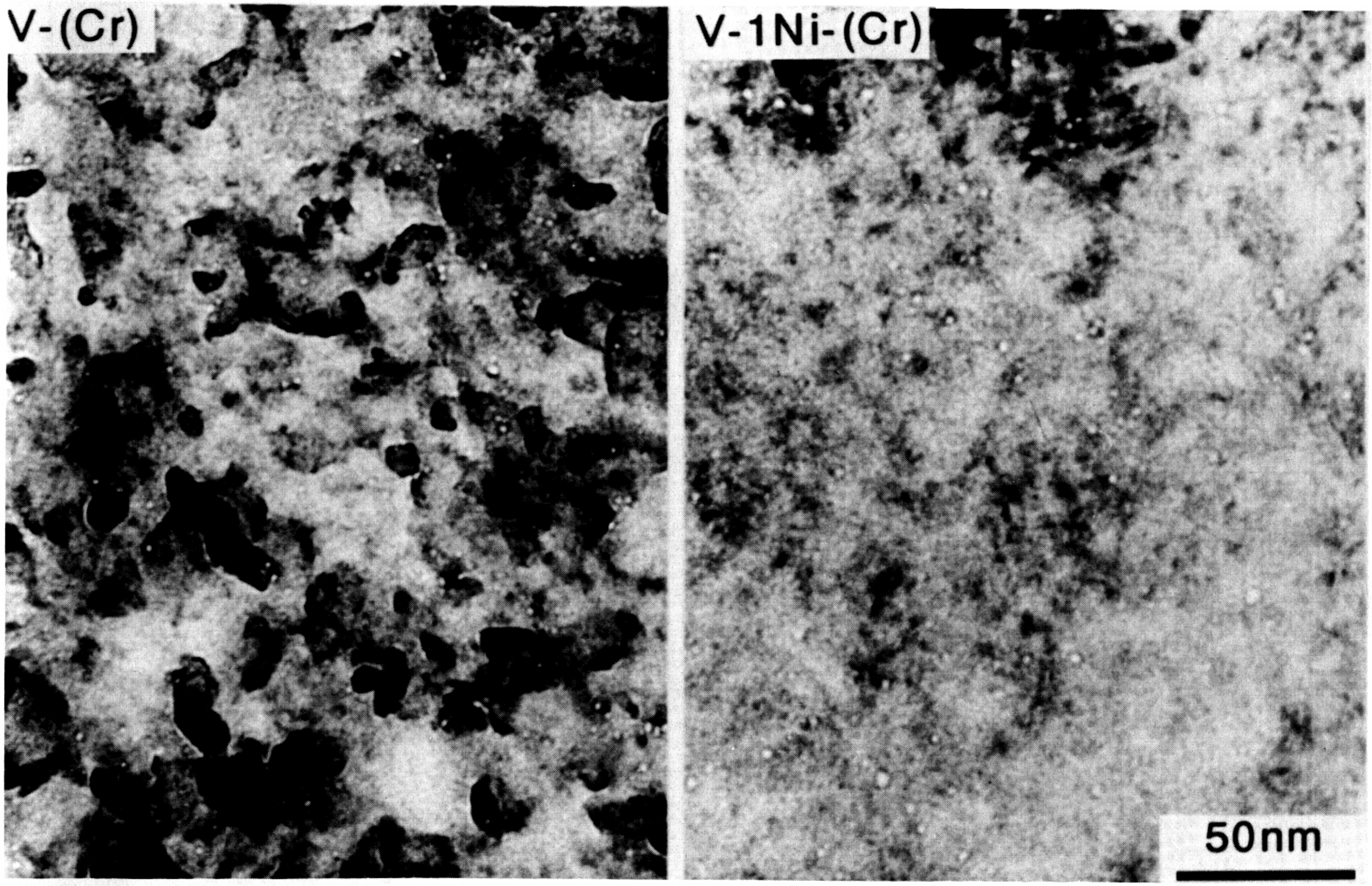

Fig. 4. Comparison of cavity microstructures observed in V and V-1Ni after irradiation. These alloys now contain ~15% chromium.

Table 3. **Compositions of HFIR-irradiated specimens** determined by EDX technique.

	V	Cr	Ti	Ni	Method*	%V→Cr
Pure V	84.3	15.7	-	-	SEM/EDS	15.7
Pure V	84.0	16.0	-	-	TEM/EDS	16.0
V-1Ni	80.0	13.9	-	0.9	TEM/EDS	14.0
V-10Ti	77.1	13.6	9.4	-	SEM/EDS	15.0
V-10Ti-1Ni	77.0	13.7	8.7	0.7	SEM/EDS	15.3

Scanning electron microscope or transmission electron microscope used to perform energy dispersive x-ray spectroscopy.

Typical EDX spectra from the scanning electron microscope are shown in Figure 5, and clearly show the significant amount of chromium formed. Figure 6 shows that chromium tends to segregate at grain boundaries in the absence of nickel, but not to segregate in nickel's presence. Nickel tends to segregate at grain boundaries, however.

Discussion

Although nickel was added to enhance the helium production, a significant role of helium on cavity nucleation is not evident in Figure 4. At this point, however, the helium build-up was not very large (~50 appm), due to the delay required to form the ^{59}Ni from ^{58}Ni. The small sizes of the cavities are consistent with their invisibility on the fracture surface. Even more important, the extreme fragility seems to be associated with the presence of titanium rather than with the presence of either nickel or helium. At this point, it is tempting also to preclude chromium as a cause of the embrittlement, since within ~10%, the chromium levels are all approximately equal io the four alloys. V-Cr binaries (Cr=5.0-14.1%) have been irradiated in the Fast Flux Test Facility (FFTF) to exposure levels ranging from 42 to 77 dpa at temperatures from 400 to 600°C in earlier studies, and did not exhibit such fragility (13,14).

The preferential polishing does appear to be associated with segregation of chromium, but the presence of nickel alters chromium segregation at grain boundaries and presumably at other sinks such as dislocations, thereby also influencing the electropolishing behavior.

While helium derived from nickel appears to play no large or direct role in cavity structure or density change in V and V-1Ni, nickel addition appears to depress swelling somewhat in V-10Ti. The density change values should not be interpreted to result from cavity swelling alone, however, since chromium additions tend to increase the density of vanadium alloys (15). Thus, the swelling of V-10Ti and V-10Ti-1Ni may actually be larger than inferred from the data in Table 2. Swelling appears to have been enhanced in V-10Ti by the transmutation, since only ≤1% swelling was observed after irradiation in FFTF at 420°C to exposures of 36-77 dpa (13).

Nickel additions tend to increase the density of vanadium alloys (15) but they also have been shown to exert a strong direct role in alteration of radiation-induced microstructure in electron irradiations (16) and fast reactor irradiations (17), neither of which lead to significant generation of helium.

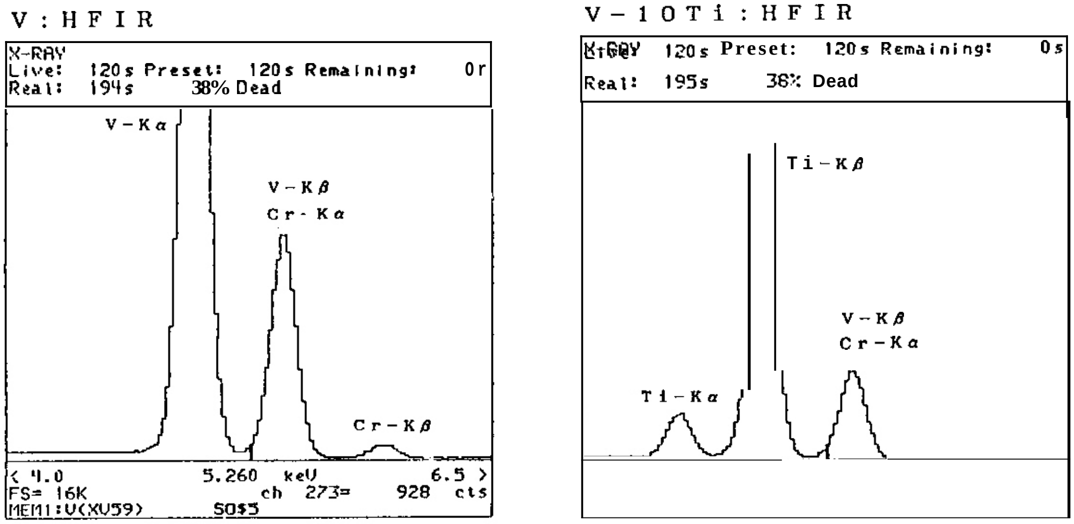

Fig. 5. EDX spectra observed in irradiated V and V-10Ti.

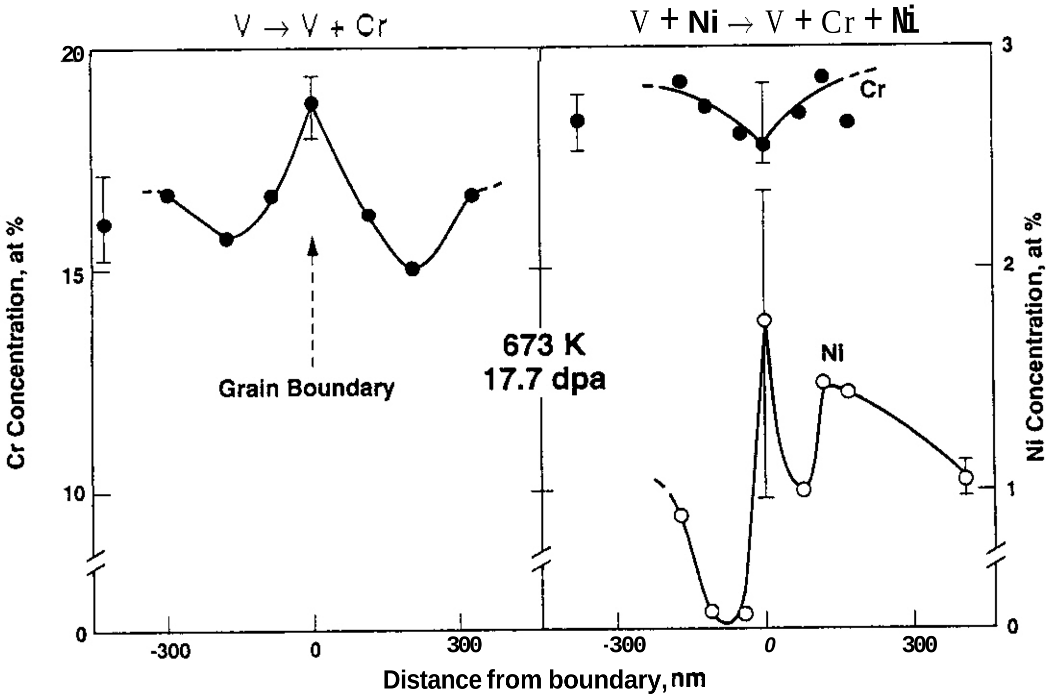

Fig. 6. Segregation profiles observed at grain boundaries in V and V-1Ni.

Loomis and coworkers **(18)** have shown that the ductile-to-brittle transition temperature (DBTT) of V-Ti binaries increases strongly for titanium concentrations greater than **5%** after fast reactor irradiation (no significant transmutation) at 420°C to 34-44 dpa, but increases even more strongly in V-Ti-Cr alloys for increasing chromium levels above **5%** Cr. For (Cr+Ti) levels above 9%, the DBTT after irradiation increases 200°C or more, as shown in Figure 7. Since the (Cr+Ti) level of the broken specimens after irradiation is on the order of 25%, the DBTT of these specimens may be 250°C or greater. Note that even before irradiation, the DBTT of such high solute alloys is near room temperature. It is interesting to note that vanadium alloys with high chromium and titanium levels irradiated in FFTF also showed significant embrittlement, but that V-3Ti-1Si resisted embrittlement (19,20).

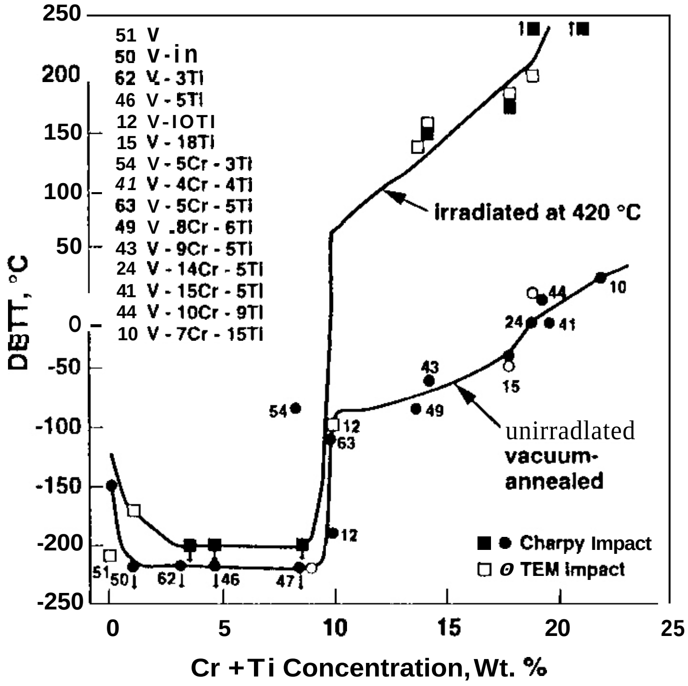

Fig. 7. Dependence of DBTT on solute concentration for V-Cr-Ti alloys irradiated at 420°C in FFTF to 32-44 dpa **(18).** Closed symbols denote Charpy impact data, open symbols denote TEM impact data.

As shown by Greenwood and Garner (12), however, the transmutation rates experienced by vanadium in HFIR are more than an order of magnitude greater than those expected in fusion neutron spectra or that of liquid metal cooled fission reactors. Mori (21) has calculated that for the International Thermonuclear Experiment Reactor (ITER), transmutation of vanadium to chromium would be less than **1%** per year at any position on the first wall when operating at 2 MW/m^2. Therefore, the extreme fragility exhibited by V-Ti alloys after irradiation in HFIR may be very atypical of the response that will occur in fusion reactors. Therefore, if fusion-relevant tests are to be successfully conducted in mixed spectrum reactors, the thermal component of the neutron flux must be reduced significantly by shielding the specimens with materials that are strong absorbers of low energy neutrons.

It must also be noted that interstitial impurity elements such as carbon, oxygen, and nitrogen cause embrittlement of vanadium alloys (19). The environmental pick-up of these elements was neither controlled nor measured in this HFIR experiment and thus may be a significant contributing factor to the embrittlement.

This experiment demonstrates once again that the possible influence of solid transmutation must be taken into account when designing and evaluating experiments that will be conducted in neutron spectra which are only surrogates for the spectrum of actual application. A summary of previously cited situations where transmutation was found to be an important concern is presented in other papers (22,23). Also demonstrated io this experiment is the principle that the impact of elemental tailoring of alloys to study the effects of transmutant helium is often overshadowed by the direct action of the tailoring agent itself.

CONCLUSIONS

The addition of nickel to vanadium and to V-10Ti appears to influence swelling of these alloys when irradiated at −400°C in HFIR, but its action appears to be related to nickel's direct influence on microstructural evolution, rather than to its role as **a** source of helium. Helium's role in determination of mechanical properties and embrittlement of vanadium alloys in HFIR is overshadowed by the influence of alloying elements such **as** titanium and chromium. Both elements have been shown to increase the DBTT rather rapidly in the region of 10% (Cr + Ti). Since Cr is produced by transmutation of V, this is **a** possible mechanism for the emhrittlement. Large effects on the DBTT may have also resulted from uncontrolled accumulation of interstitial elements, such **as** C, **N,** and **O** during irradiation.

The extreme emhrittlement observed in this experiment resulting from chromium formation will not be representative of that expected in fusion neutron spectra, where the V→Cr transmutation rate per dpa will be lower by more than an order of magnitude.

FUTURE WORK

Specimens irradiated in HFIR at temperatures above 400°C will he examined.

ACKNOWLEDGEMENTS

Work supported by the Japanese Ministry of Education, Science and Culture, under both the US/Japan Collaboration in Fusion Materials using Fission Reactors and the International Scientific Research Program. The U.S. participation was supported by the U.S. Department of Energy under Contracts DE-AC06-76RLO 1830 and DE-AC05-84OR21 400. The density measurements were performed at ORNL by L. T. Gibson and at PNL by **Gary** Whiting. The manuscript was prepared by Loree Swegle and Diane Forsyth.

REFERENCES

1. D. L. Smith, ***J. Nucl. Muter.,*** 122 **&** 123 (1984) **51.**
2. D. R. Diercks and B. A. Loomis, ***J. Nucl. Muter.,*** 141-143 (1986) 1117-1124.
3. B. A. Loomis, A. B. Hull and D. L. Smith, *J.* ***Nucl.*** Muter., 179-181 (1991) 148-154.
4. H. Kawanishi, Y. Arai and S. Ishino, **J. *Nucl. Muter.,*** 191-194 (1992) 933-937.
5. **N.** Sekimura and F. A. Garner, Fusion Reactor Materials Semiannual Progress Report DOE/ER-03131/13, 1990, pp. 235-237.

6. H. M. Chung, Fusion Reactor Materials Semiannual Progress Report DOWER-0313114, 1993, pp. 299-305.

7. M. Satou, K. Abe and H. Matsui, J. Nucl. *Muter.*, 191-194 (1992) 938-941.

8. D. L. Smith, **H.** Matsui, L. Greenwood and B. Loomis, J. Nucl. *Muter.*, 155-157 (1988) 1359.

9. **C.** H. De Raedt, Proc. Conf. on Fast, *Thermal and Fusion Reuctor Experiments*, Amer. Nucl. Soc., La Grange Park (1982). p. 226.

in. J. J. Norgett, J. T. Robinson and I. M. Torrens, Nucl. Eng. Design 33 (1975) **50.**

11. H. Kanazawa, T. Sawai and L. J. Turner, Fusion Reactor Materials Semiannual Progress Report DOE/ER-0313/8, 1990, pp. 17-20.

12. L. R. Greenwood and F. A. Garner, "Transmutation of Mo, Re, W, Hf, and V in Various Irradiation Test Facilities and STARFIRE," proceedings ICFRM-6, J. Nucl. *Mater.*, in press.

13. R. **A.** Loomis, D. L. Smith and F. **A.** Garner, *J. Nucl. Muter.*, 179-181 (1991) 771

14. F. A. Garner, D. S. Gelles, H. Takahashi, S. Ohnuki, H. Kinoshita and B. A. Loomis, *J. Nucl. Muter.*, 191-194 (1992) 948-951.

15. F. A. Garner and B. A. Loomis, in this semiannual report.

16. **D.** S. Gelles, S. Ohnuki, H. Takahashi, H. Matsni and **Y.** Kohno, J. Nucl. *Muter.*, 191-194 (1992) 1336-1341.

17. D. S. Gelles and J. F. Stubbins, proceedings ICFRM-6, J. Nucl, *Muter.*, in press.

1R. B. A. Loomis, H. M. Chung, L. J. Nowicki and D. L. Smith, Proceedings of ICFRM-6, J. Nucl. Muter.., in press.

19. D. N. Braski, in *Influence of Radiation on Material Properties: 13th Intern. Symp. (Part II)*, ASTM STP 956, F. A. Garner, C. H. Henager, Jr. and **N.** Igata, Eds., American Soc. of Testing and Materials, Philadelphia, 1987, pp. 271-290.

20. M. L. Grossbeck and J. **A.** Horak in *Influence of Radiation on Material Properties: 13th Intern. Symp. (Purl II)*, ASTM STP 956, F. A. Garner, C. H. Henager, Jr. and **N.** Igata, Eds., American Soc. of Testing and Materials, Philadelphia 1987, pp. 291-309.

21. M. Mori, ITER/EDA Design Data, JA93-JA0132.

22. F. A. Garner, H. L. Heinisch, R. L. Simons and F. M. Mann, *Radiation Effects and Defects in Solids*, 113 (1990) 229-255.

23. F. A. Garner and L. R. Greenwood, *Muter. Trans.*, JIM, 34 (1993) 985-998.

INFLUENCE OF FLUX-SPECTRA DIFFERENCES ON TRANSMUTATION AND SWELLING OF VANADIUM ALLOYS - F. A. Garner and L. R. Greenwood, (Pacific Northwest Laboratory)[a]

OBJECTIVE

The objective of this effort is to determine the factors that are relevant to the development of fission-fusion correlations for vanadium alloys.

SUMMARY

The swelling of vanadium and its alloys is known to he sensitive to the level of chromium in the alloy. Chromium is also the major transmutation product during neutron irradiation, however, and the production rate of chromium is very sensitive to neutron spectra. It appears that an apparent dependence of void swelling in pure vanadium irradiated in FFTF may arise in part from the spectral difference that accompanies changes in displacement rate.

PROGRESS AND STATUS

Introduction

In a recent joint Japan/U.S. study on swelling and microstructural evolution in V and V-5Cr, these metals were prepared with a variety of boron levels to assess the effect of helium (and lithium, unfortunately) on microstructural evolution and swelling. One rather surprising result of that study was a rather strong apparent influence of flux of swelling on pure vanadium, as shown in Figure 1, which compares data at (427°C, 46.4 dpa) and (411°C, 15.1 dpa).[1] The swelling rate per dpa appears to increase strongly at lower flux. Similar hints of a flux effect have surfaced in earlier U.S. MOTA studies and Japanese studies in JOYO. It is not known whether such a flux effect would exist for more complex alloys. The swelling data on V-5Cr at ~400°C in the current studies do not show enough swelling at either flux rate to see an effect of flux.

To this point, however, we have only considered the flux aspect of the flux/spectra differences encompassed in Figure 1. It now appears that the spectra aspect may he at least as important, or possibly even more important than the flux aspect. Note in Figure 2 that the transmutation rate for V→Cr is a strong function of position in FFTF.[2] (The midplane of the helow-core basket is at -66 cm). Is it possible that differences in chromium formation rates can act to accelerate swelling at different rates in pure vanadium or vanadium alloys that are irradiated in *slightly* different neutron spectra?

---

[a] Pacific Northwest Laboratory is operated for the U.S. Department of Energy by Battelle Memorial Institute under Contract DE-AC06-76RLO 1830.

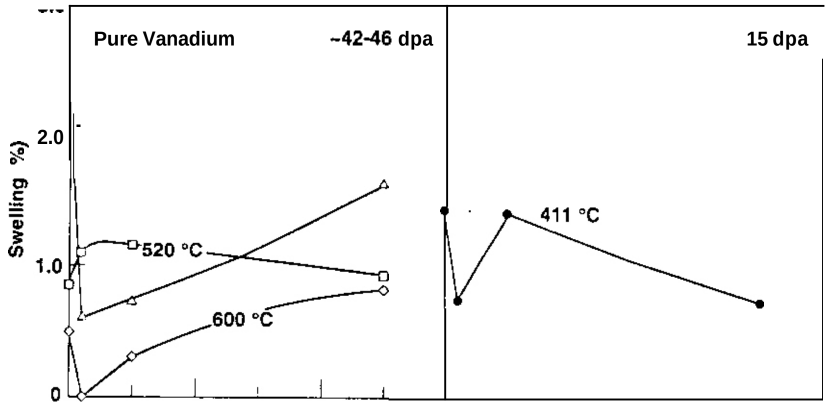

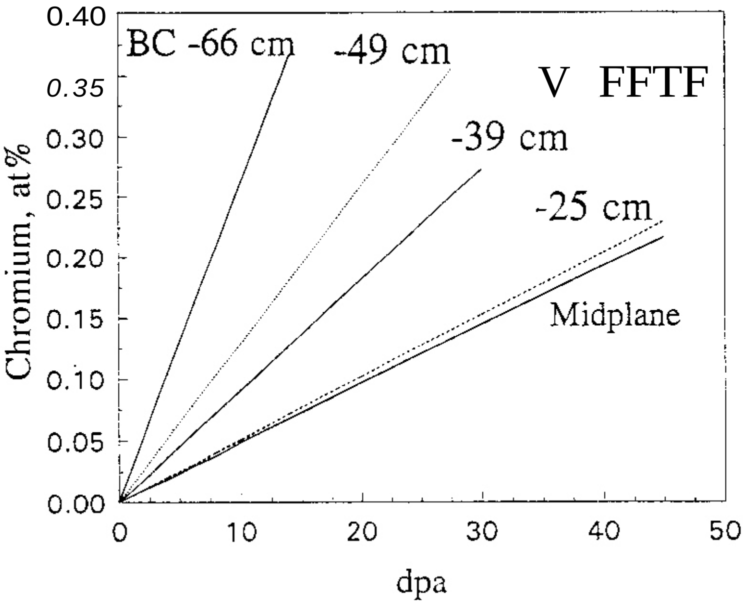

Fig. 2. Calculated Transmutation Rates.

Results and Discussion

Figure 3 shows swelling data at ~600°C, taken from various U.S. and joint U.S./Japan studies on V-Cr binary alloys in MOTA.[1,3-5] Note that the dependence of swelling on chromium content appears to be relatively weak at high chromium levels but much stronger at lower levels. Unfortunately, vanadium-chromium alloys at very low chromium levels (≤5%) have not been irradiated. Very high swelling V-xFe alloys (x=1,3,5,10) were recently irradiated in a joint

Tohoku/ANL experiment in EBR-II, however, and showed that most of iron's influence was realized already by 1% iron.[6]

Figure 3 suggests that the first small amount of chromium, including that produced by transmutation, strongly accelerates swelling. Since the transmutation rate per dpa increases as the flux falls, such an effect could be interpreted only in terms of a flux effect, but such an interpretation might be misleading.

Two applications of this discussion are relevant to currently on-going experiments.

a) The transmutation observed in V, V-1Ni, V-10Ti and V-10Ti-1Ni irradiated in HFIR at 400°C was –15.5% Cr at 17.7 dpa.[7] Swelling was low at 400°C, in agreement with that of FFTF studies at such high chromium levels. When the HFIR results at 500 and 600°C become available, the possible effect of V→Cr transmutation on swelling should be taken into account. For vanadium irradiated in spectral-tailored HFIR positions, a lower level of chromium will be formed, but this will still be an important factor due to chromium's strong effect at lower levels.

b) If the spectra difference is indeed more important than the flux difference for pure vanadium, then a lesser but still significant effect of spectra will probably exist for alloys already containing a significant amount of chromium. If not, however, flux effects may exert significant influence on the radiation response of more complex vanadium alloys. The answer must await analysis of other experiments conducted at different displacement rates.

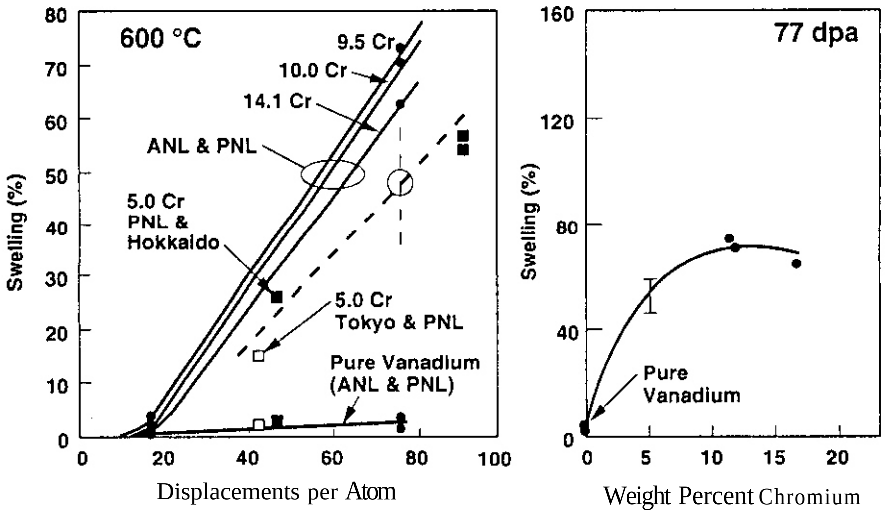

Fig. 3. Neutron-induced swelling of V-Cr alloys in FFTF.

FUTURE WORK

Measurements will be made of the density changes of V-B nd V-5Cr-B alloy series irradiated to higher fluence in FFTF. Densities will also be measured for pure V irradiated in HFIR at 500 and 600°C.

REFERENCES

1. N. Sekimnra and F. A. Garner, Fusion Reactor Materials Semiannual Progress Report DOE/ER-0313/13 (1992) 235-237.

2. L. R. Greenwood and F. A. Garner, Proc. ICFRM-6, *J.* Nucl. *Mater.,* in press.

3. B. A. Loomis. D. L. Smith and F. A. Garner, *J.* Nucl. *Mater.* 179-181 (1991) 771-774.

4. F. A. Garner, D. S. Gelles, H. Takahashi, S. Ohnuki, H. Kinoshita and B. A. Loomis, *J.* Nucl. *Mater.* 191-194 (1992) 948-951.

5. F. A. Garner, S. Ohnuki and H. Takahashi, unpublished data at 600°C; and 92 dpa.

6. H. Matsui, S. Yoshida, K. Nakai, A. Kimura, L. Nowicki, J. Gazda and H. Chung, to be presented at the ASTM International Symposium on Effects of Radiation, Sun Valley, ID, June 1994.

7. S. Ohnnki, H. Takahashi, K. Shiba, A. Hishinuma, J. E. Pawel and F. A. Garner, in this semiannual report.

DEPENDENCE OF VANADIUM ALLOY DENSITY ON STARTING COMPOSITION, TRANSMUTATION AND SEGREGATION - F. A. Garner (Pacific Northwest Laboratory[1]) and B. A. Loomis (Argonne National Laboratory)

OBJECTIVE

The objective of this effort is to assess the factors which contribute to density changes in irradiated vanadium alloys.

SUMMARY

The density of vanadium alloys is strongly dependent on solute identity and concentration, especially for additions of chromium and titanium. One consequence of this dependence is that radiation-induced density changes arise from segregation and precipitation. Transmutation of vanadium to chromium can also lead to significant increases in density and can therefore complicate somewhat the interpretation of swelling data derived using immersion density techniques.

PROGRESS and STATUS

Introduction

Vanadium alloys are currently under consideration for application in ITER One of the experimental techniques used to assess the behavior of these alloys after irradiation in EBR-II, FFTF and HFIR is that of immersion measurements to determine changes in density. Although the primary purpose of this technique is to determine the amount of void swelling, density changes arising from other non-void related phenomena also contribute to the measurement.

Segregation can sometimes lead to net changes in density if the partial molar volumes of the various elements are dependent in a nonlinear manner on the concentration of other elements in the alloy. If precipitation arises from such segregation, the potential for non-void density contributions increases strongly. Such changes occur in many irradiated alloys, ranging from several tenths of a percent to as much as 4%. These changes can be either positive or negative in sign.

Vanadium alloys are known to be susceptible to radiation - induced segregation and precipitation.[1-3] In addition, vanadium alloys are subject to large levels of transmutation of vanadium to chromium, especially in some neutron spectra.' For example, in a recent irradiation in HFIR, the composition of several vanadium alloys was altered significantly, with 16% of the vanadium converted to chromium at only 17 dpa' Even in the absence of precipitation, such a change will lead to a significant shift in alloy density.

In order to properly interpret density change data, it is necessary to determine the net effect of addition, removal or redistribution of various solutes on the lattice parameter of the alloy matrix. Such information is best gained from analysis of the compositional dependence of density under conditions where all solutes are uniformly distributed and no precipitation has yet occurred.

---

[1] Pacific Northwest Laboratory is operated for the U.S. Department of Energy by Battelle Memorial Institute under Contract DE-AC06-76RLO 1830.

Therefore, the density of archive specimens of a variety of binary and ternary alloys in the annealed condition has been measured. These data have been used to determine swelling values reported in various earlier studies, but most of the density data on unirradiated alloys have not previously been reported.

Results and Discussion

The data shown in Figure I are derived primarily from the Argonne National Laboratory binary and ternary alloy series (solid lines)' and partially from various joint Japanese/U.S. irradiation

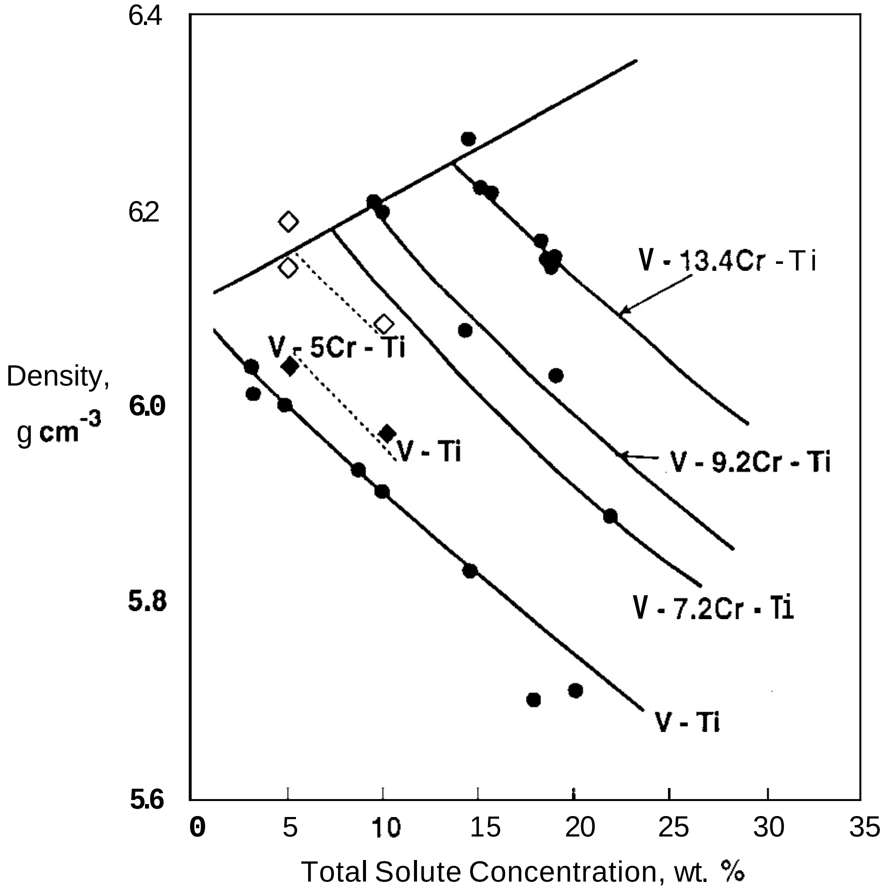

Fig. 1 Influence of chromium and titanium on the density of vanadium alloys. Solid lines represent data from the Argonne alloy series and the dotted lines represent data from various Japanese alloys.

studies, most of which have not yet been reported. Chromium additions clearly increase the density and titanium additions strongly decrease the density. Providing that no precipitation occurs, transmutation of vanadium to chromium will increase the density and thereby camouflage the onset of void swelling. Since the influence of chromium and titanium are of opposite sign, it appears possible to either increase or decrease the density upon precipitation, depending not only on the relative amount of titanium and chromium removed from the matrix but also on the crystal structure and lattice parameter of the precipitate Note that there appears to be some small differences in the density of the two V-Ti binary alloy series used in the Argoune series measured at Argoune and the Japanese alloys measured at PNL. This may be due to the faet that the Japanese alloys in general are of higher purity.

The V-Ti data on the Japanese alloys are presented again in Figure 2, along with data on a variety of alloys, all measured at PNL. The solutes Ni, Mo and Fe all cause increases in density while Si, Al and Y tend to cause decreases. Additions of 1% of either Y or Ni to various binary or ternary alloys lead to density changes consistent with the changes induced in the density of pure vanadium.

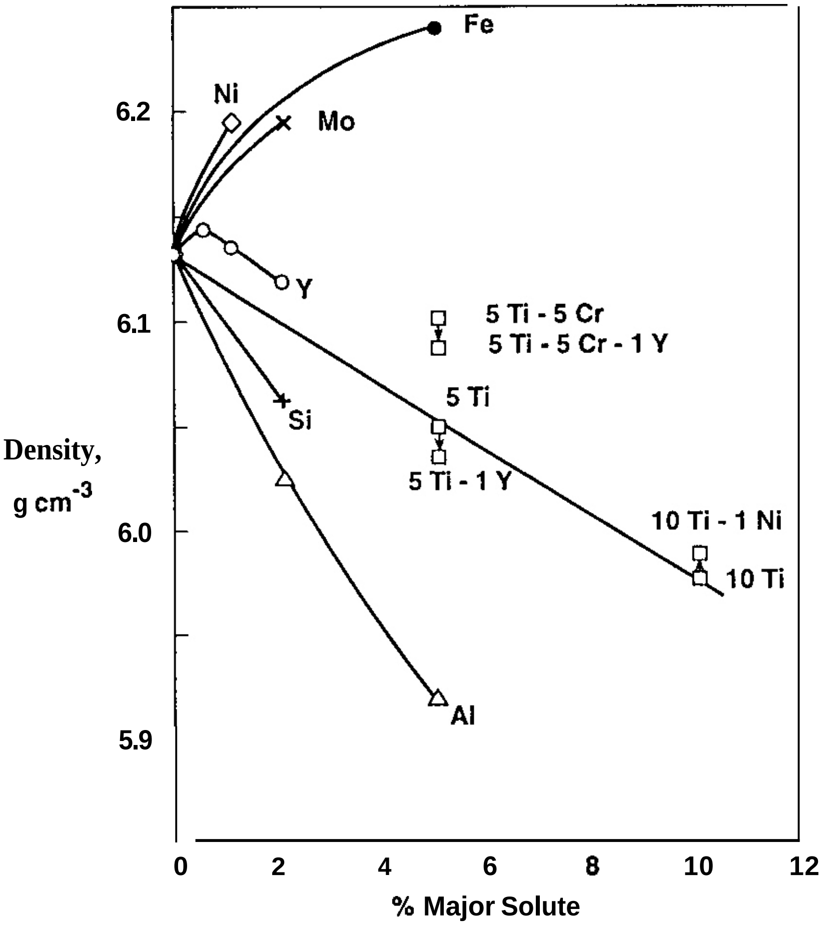

Fig. 2. Influence of various solutes on the density of annealed vanadium alloys.

FUTURE WORK

These data will be used in the interpretation of density change data derived from irradiated vanadium alloys. They will also be used to explain the impaet on swelling of various solutes, especially nickel, silicon and iron.

REFERENCES

1. S. Ohnuki, D. S. Gelles, B. A. Loomis, F. A. Garner and H. Takahashi, *J. Nucl. Muter.* 179-181 (1991) 775-778.

2. D. S. Gelles and J. F. Stubbins, *Fusion Reactor Materials Semiannual Progress Report DOE/ER-0313/15* (1994) 115-125.

3. H. M. Chuog, J. Gazda, L. J. Nowicki, J. E. Sanecki and D. L. Smith, *ibid* 207-218.

4. J. Gazda, B. A. Loomis, L. J. Nowicki, D. L. Smith and S. Danyluk, ibid 232-239.

5. H. Matsui, M. Tanno, J. Gazda and H. M. Chuog, *ibid* 240-246.

6. F. A. Garner and L. R Greenwood, in this semiannual report

7. S. Ohnuki, H. Takahashi, A. Hishinuma, K. Shiba, J. E. Pawel and F. A. Garner, in this semiannual report.

8. B. A. Lnnmis, D. L. Smith and F. A. Garner, *J. Nucl. Muter.* 179-181 (1991) 771-774.

6.4 Copper Alloys

COPPER ALLOYS FOR HIGH HEAT FLUX STRUCTURE APPLICATIONS - S.J. Zinkle *(Oak* Ridge National Laboratory) and S.A. Fabritsiev (D.V. Efremov Scientific Research Institute of Electrophysical Apparatus)

OBJECTIVE

The objective of this effort is to evaluate the unirradiated and irradiated properties of high-strength, high-conductivity copper alloys which are under consideration for first wall and divertor structural applications in ITER. This review was initiated in response to ITER technology R&D Task T7, "Assess Physical, Mechanical and Technological properties of the First Wall Candidate Cu Alloy".

SUMMARY

The mechanical and physical properties of copper alloys are reviewed and compared with the requirements for high heat flux structural applications in fusion reactors. High heat flux structural materials must possess a combination of high thermal conductivity and high mechanical strength. The three most promising copper alloys at the present time are oxide dispersion-strengthened copper ($Cu-Al_2O_3$) and two precipitation-hardened copper alloys (Cu-Cr-Zr and Cu-Ni-Be). These three alloys are capable of room temperature yield strengths > 400 MPa and thermal conductivities up to 350 W/m-K. All of these alloys require extensive cold working to achieve their optimum strength. Precipitation-hardened copper alloys such as Cu-Cr-Zr are susceptible to softening due to precipitate overaging and recrystallization during brazing, whereas the dislocation structure in $Cu-Al_2O_3$ remains stabilized during typical high temperature brazing cycles. All three alloys exhibit good resistance to irradiation-induced softening and void swelling at temperatures below 300°C. The precipitation-strengthened alloys typically soften during neutron irradiation at temperatures above about 3WC and therefore should only be considered for applications operating at temperatures <300°C. Dispersion-strengthened copper may be used up to temperatures in excess of 500°C. Based on the available data, dispersion-strengthened copper ($Cu-Al_2O_3$) is considered to be the best candidate for high heat flux structural applications.

PROGRESS AND STATUS

1. INTRODUCTION

High-strength copper-based alloys with high thermal conductivity are considered to be a promising class of materials for fusion reactor components which must withstand high levels of heat flux. Recent engineering design studies for the International Thermonuclear Experimental Reactor (ITER) have proposed copper alloys for the divertor structure and first wall regions. Relatively thick walls can be accommodated in the heat sink structure of the divertor or first wall if high-conductivity copper alloys are used instead of low-conductivity materials such as stainless steel: the temperature drop across a 10 mm plate of a high-conductivity copper alloy exposed to a heat flux of 1 MW/m^2 would be ~30°C. Copper alloys are well known for their high electrical and thermal conductivity, excellent resistance to corrosion, ease of fabrication, and good strength and fatigue resistance [1]. The manufacturing infrastructure for copper alloys is well established. The worldwide annual production (and consumption) of copper exceeds 10^{10} kg, with pure copper accounting for more than 50% of the applications. The annual production of specialized high strength, high conductivity alloys such as CuCrZr and $Cu-Al_2O_3$ is greater than 10^6 kg.

Reviews on the unirradiated and irradiated properties of copper alloys are. available from several different sources [1-6]. The general criteria for selection of a high heat flux structural material are summarized in a companion paper in this volume [7]. In the present paper, we will first summarize the physical and mechanical properties of copper alloys. Most of the remaining review concentrates on several high-strength, high-conductivity copper alloys which have the best mechanical and physical properties for fusion reactor high heat flux applications. Critical issues such as fabricability, joining, corrosion resistance and radiation effects are discussed. Property data quoted by the manufacturers of high-strength, high-conductivity copper alloys have generally been excluded from the present compilation, unless there was insufficient data from independent researchers to establish trend lines.

2. FABRICATION AND PROPERTIES OF COPPER ALLOYS

Table I summarizes the physical properties of pure copper [1,8,9]. The high thermal conductivity of copper (k_{th}~380 Wlm-K) is maintained over a wide range of temperatures, making thii material very useful for high heat flux applications. Since the free electrons in copper are mainly responsible for conduction of both thermal and electrical currents, the thermal conductivity and electrical resistivity (ρ_e) are conveniently related by the Wiedemann-Franz law, $k_{th}\,\rho_e = L\,T$, where T is the absolute temperature and L is the Lorentz number, which has a theoretical value of $2.45\text{x}10^{-8}$ W-Ω/K^2. Experimental measurements of the Lorentz number for copper indicate that it is slightly less than the theoretical value, ranging from $2.23\text{x}10^{-8}$ at 0°C to $2.38\text{x}10^{-8}$ at 500°C [8]. Electrical resistivity measurements can often he performed on specimens designed for another purpose (e.g., on neutron irradiated tensile specimens), and the Wiedemann-Franz relationship allows the thermal conductivity of copper and copper alloys to he estimated from the resistivity data without making a direct measurement of k_{th}.

Whereas pure copper exhibits very high thermal conductivity, the intrinsic strength of copper is relatively low. Solid solution additions are generally not effective in increasing the strength of copper by a significant amount and cause a concomitant decrease in thermal conductivity. Two general categories of high-strength, high-conductivity copper alloys are commercially available, namely precipitation-strengthened and dispersion-strengthened alloys. Since all of the copper alloys under consideration for high strength, high conductivity applications contain <3% solute additions, their thermophysical properties are the same as those listed for pure copper in Table I to within a few percent (except for k_{th} and ρ_e). Table II summarizes the chemical composition of several commercially available high-strength, high-conductivity copper alloys.

Since the copper mauix is intrinsically weak compared to more traditional structural materials such as iron- and nickel-based alloys, high-strength. high-conductivity copper alloys are generally produced in wrought form. The high dislocation density associated with wrought alloys can be pinned by precipitates or oxide particles, thereby producing high strengths. Precipitation-hardened alloys can in principle he cast and subsequently heat treated. which is advantageous for structural components with complex geometries that would he difficult to machine [20]. However, it must he recognized that the strength of the cast and aged alloy will be significantly less than the same alloy in wrought form. This issue will be discussed in more detail in Section 2.1 (e.g. Fig. 3). Precipitation-hardened copper alloys are generally aged at temperatures between 300 and 500°C. Exposure to temperatures near or above the aging temperature causes panicle coarsening in precipitation-hardened alloys, with accompanying softening.

TABLE I. Thermophysical properlies of pure copper [1,8,9].

Melting temperature	1083°C	
Boiling temperature	2567°C	
Heat of fusion	$2.05\text{x}10^5$ J/kg	
Heat of vaporization	$4.80\text{x}10^6$ J/kg	
Vapor pressure	$1.0\text{x}10^{-4}$ Pa @ 850°C 0.15 Pa @ 1150°C	0.015 Pa @ 1050°C
density	8950 kg/m^3 @ 20°C	
coefficient of thermal expansion (α)	$17.0\text{x}10^{-6}$ @ 20°C	$20.0\text{x}10^{-6}$ @ 500°C
Poisson's ratio (υ)	**0.345 @ 20°C**	**0.351** @ 500°C
Young's **modulus of** elasticity (E)	117 GPa @ 20°C	108 GPa @ 500°C
specific heat (C_p)	385 J/kg-K @ 20°C	431 J/kg-K @ 500°C
thermal conductivity (k_{th})	391 Wlm-K @ 20°C	370 Wlm-K @ 500°C
electrical resistivity (ρ_e)	17.1 nΩ-m @ 20°C	49.7 nΩ-m @ 500°C

TABLE II. Chemical composition of commercial high-strength, high-conductivity copper alloys.

Alloy tradename & manufacturer	Alloy type*	Composition (wt%)
Cu-Cr-Zr	PH	
MZC (AMAX copper, Inc.)		Cu - 0.8%Cr - 0.15%Zr - 0.04%Mg
ELBRODUR G (Kabelmetal)		Cu - 0.65%Cr - 0.10%Zr
Cu-Ni-Be	PH	
C17510 (Brush Wellman, Inc.)		Cu - 1.4 to 2.2%Ni - 0.2 to 0.6%Be
Oxide dispersion-strengthened Cu	DS	
GlidCop AL-15 (SCM Metals)		Cu - 0.15% Al as oxide particles (0.28%Al_2O_3)
GlidCop AL-25 (SCM Metals)		Cu - 0.25%Al as oxide particles (0.46%Al_2O_3)
GlidCop AL-60 (SCM Metals)		Cu - 0.60% Al as oxide particles (1.12%Al_2O_3)
MAGT 0.05 (Ultram-Golden)		Cu - 0.1%Al - 0.01%Hf - 0.03%Ti as oxide particles
MAGT 0.2 (Ultram-Golden)		Cu - 0.1 to 0.4%Al - 0.01 to 0.1%Hf -0.03 to 0.14%Ti as oxide particles

*precipitation-hardened (PH) or dispersion-strengthened (DS)

Dispersion-strengthened alloys cannot be cast since the oxide particles would not remain uniformly dispersed in the liquid phase. The fabrication process for the commercially available GlidCop™ oxide-dispersion-strengthened copper alloys utilizes powder metallurgy techniques [11]. The internally oxidized product is consolidated by hot extrusion or hot rolling of canned powder billets. The wrought precipitation-hardened or dispersion-strengthened copper alloys can be produced in a variety of forms. For example, sheets of dispersion-strengthened copper ($Cu-Al_2O_3$) are routinely available in cross-section sizes up to 6.3 x 50 cm [15], and moderately complex geometries can be produced by using custom-made extrusion dies.

It is worth emphasizing that many of the high strengths summarized in the following sections for precipitation-hardened and dispersion-strengthened copper alloys were obtained on thin strips which had been heavily cold-worked. These very high strengths (>500 MPa) generally cannot be achieved in large structural components fabricated from copper alloys, because large components cannot be heavily cold-rolled.

2.1 Room temperature strength and thermal conductivity

The thermal stress parameter (M) is a useful figure of merit for evaluating the suitability of candidate high heat flux structural materials:

$$M=\sigma_y k_{th}(1-\nu)/\alpha E \tag{1}$$

where σ_y is the yield strength, k_{th} is the thermal conductivity, ν is Poisson's ratio, α is the linear coefficient of thermal expansion, and E is Young's modulus. The values of σ_y and k_{th} are strongly dependent on the particular alloy and thermomechanical processing. Figure 1 shows the range of room temperature strengths and conductivities that can be achieved in various copper alloys and Type 316 stainless steel [1,2,4,5,6,10-21]. The range of possible strengths for a given alloy is due to different thermomechanical treatments: cold-worked (CW), cold-worked & aged (CWA), and solutionized & aged (SA) conditions. The high strength CuNiBe datum labeled TMT was obtained on thin sheet specimens of a high purity laboratory heat [12-14] and may not be achievable in large commercial heats. The wrought $Cu-Al_2O_3$ datum refers to hot extruded (M30 temper) GlidCop AL-25 plate of 13 cm thickness [1,15].

Cold working can greatly increase the room temperature strength of copper without any significant change in the thermal conductivity. However, pure cold-worked copper softens due to

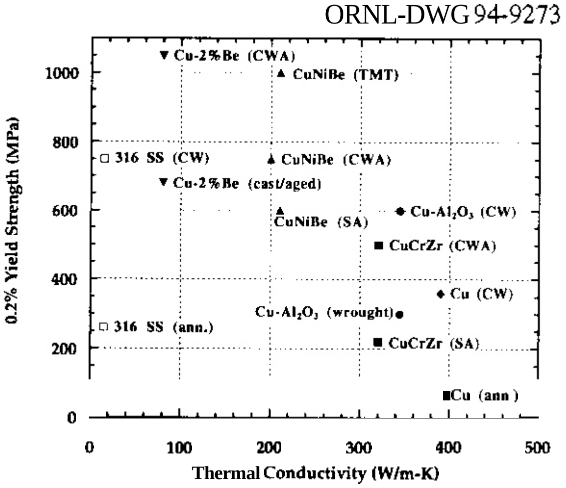

FIG. 1. Room temperature strength and thermal conductivity of copper [1], Cu-Cr-Zr [1,5,10,18-20], CuNiBe [1,12-14], Cu-Be [1,17], Cu-Al_2O_3 [1,11,15-18], and stainless steel [21].

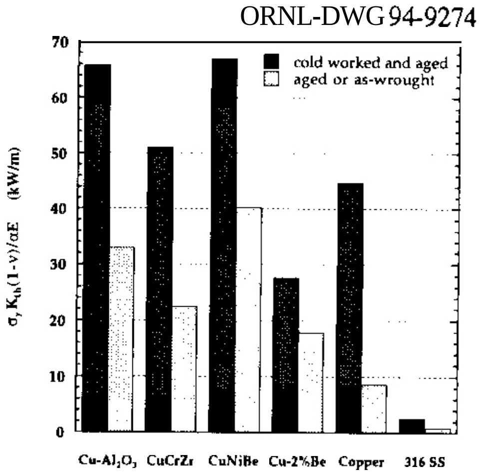

FIG. 2. Comparison of the room temperature thermal stress parameter for copper alloys and stainless steel. The copper alloy data were taken from Table I and Fig. 1.

recovery and recrystallization at temperatures above 100 to 200°C [22,23] and is therefore not suitable for applications above room temperature. The strength of copper alloys can be significantly increased by suitable combinations of heat treatment and cold working. Since the average amount of deformation that can be achieved in a thick plate or rod is less compared to a thin strip or wire, the strength of these alloys also depends on the product form [1]. For example, the as-consolidated yield strength of GlidCop AL-25 Cu-Al_2O_3 alloy varies from 345 MPa for 1 cm plate to 296 MPa for 13 cm plate. thickness [15]. Similarly, the room temperature yield streugth of solution quenched and aged (TF00 temper) Cu-Cr alloys can vary between 250 and 450 MPa depending on the product form and heat treatment conditions [1].

Figure 2 compares the room temperature thermal stress parameters of high-strength, high-conductivity copper alloys and stainless steel. Conventional precipitation-strengthened alloys such as Cu-2%Be have high strength but very low thermal conductivity compared to copper, resulting in a relatively low thermal stress parameter M. The highest combined strength and conductivity is achieved in cold-worked copper alloys that contain a uniformly distributed second phase of small particles. This is achieved in both precipitation-strengthened (e.g., CuCrZr and Cu-Be-Ni) and dispersion-strengthened (e.g., Cu-Al_2O_3) alloys. It can be seen from Fig. 2 that the room temperature thermal stress parameter of these copper alloys is more than an order of magnitude higher than the corresponding value for stainless steel.

It is worthwhile at this point to consider in more detail the influence of thermomechanical processing on the strength and conductivity of copper alloys. Several studies have shown that the yield strength in CuCrZr alloys which have been heat treated for maximum precipitation hardening (without cold working) is about 50 to 70% of the peak cold-worked and aged strength [10,24,25]. For example, the maximum yield strength in solution quenched and aged CuCrZr is about 350 MPa [20,25], whereas cold-worked and aged CuCrZr can have room temperature yield strengths up to at least 600 MPa [26]. Figure 3 compares the room temperature tensile curves of AMAX-MZC CuCrZr foil in the solutionized & aged condition (SA) and in the solutionized, cold worked & aged condition (CWA) [10]. The CWA treatment consisted of solution annealing at 950°C for 0.75 h, water quench, 90% cold roll, and aging at 400°C for 0.5 h. The SA alloy was annealed at 930°C for 0.75 h, water quenched, and aged at 500°C for 1 h. It can be seen that precipitation hardening in the absence of cold work produced yield strengths that were only about half of the cold-worked and aged strength. The room temperature thermal conductivities deduced from electrical resistivity measurements were 210 and 230 W/m-K, respectively for the SA and CWA conditions [10].

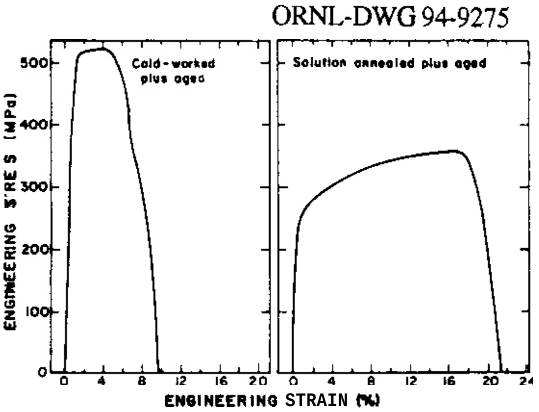

FIG. 3. **Room** temperature load-elongation curves for AMAX MZC Cu-Cr-Zr-Mg alloy [10].

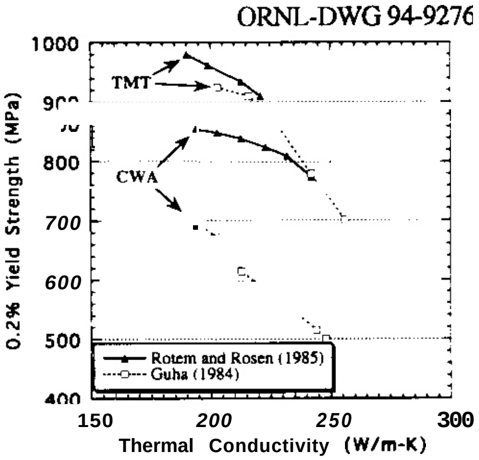

FIG. 4. **Room** temperature yield strength and thermal conductivity of Cu-2%Ni-0.4%Be thin sheet specimens subjected to different combinations of cold working and heat treament [13,14].

Thermomechanical processing can produce a wide range of strengths and conductivities in precipitation-hardened copper alloys [1,2,10,13,14,24,25]. Cold working *can* produce large **increases** in the alloy strength with only minor degradation in the thermal conductivity. Heat treatments which increase the alloy strength generally **cause** a concomitant decrease in the thermal conductivity. Figure 4 shows an example of the variation in room temperature yield strength and thermal conductivity that is achievable in Cu-2%Ni-0.4%Be subjected to different schedules of heat treatment and cold work [13,14]. The standard cold-work and aging (CWA) treatment produced lower strengths than thermomechanical treatment (TMT) consisting of preaging, cold work, and reaging. The thermal conductivity in Fig. 4 was estimated from electrical resistivity measurements using the Wiedemann-Franz law. Heat treatments which increased **the** thermal conductivity produced corresponding **decreases** in the alloy strength. **Similar** tradeoffs between yield strength and thermal conductivity **occur** for all precipitation-hardened copper alloys. The maximum in the thermal stress parameter (which is proportional to the product of the yield strength and thermal conductivity) in precipitation-hardened alloys can occur for either high-conductivity or high-strength heat treatments, depending on the alloy system.

2.2 Effects of annealing and test temperature on the tensile properties

The remainder of **this** review concentrates on the three copper alloys **that** have the best room temperature thermal stress resistance (Fig. 2). namely the precipitation-hardened alloys CuCrZr and CuNiBe and oxide dispersion-strengthened copper (primarily Cu-Al_2O_3). The optimum mechanical properties for the CuCrZr and CuNiBe alloys **are** produced by aging at temperatures of 320 to 500°C for *0.5* to 2 h [10,12,14,24,27]. Therefore. it *can* be anticipated that these alloys will be susceptible to softening after extended **exposure** to temperatures above 400°C due to precipitate coarsening (overaging) and recrystallization. On **the** other hand, the oxide particles in dispersion-strengthened copper are thermally stable up to the melting point of the copper matrix and therefore this type of copper alloy is inherently resistant to softening [28].

Figure **5** shows the **room** temperature yield strength of CuCrZr alloys following short term *(0.5* to 1 hour) annealing **at** temperatures between 300 and 750°C [10,19,29,30]. Significant softening begins to occur after **exposure** to temperatures above 400 to 500°C. Similar results have been reported for CuCrZr alloys by other researchers using Brinell hardness measurements [25], and this alloy has been shown to soften dramatically when aged for 1 h at temperatures above 500°C [e.g., 24,27]. Vandermeulen et al. [26] reported that annealing at 700°C for 15 minutes reduced the room temperature yield **strength** of CuCrZr from ***595*** MPa to 210 MPa. According to the **data** presented in

ORNL-DWG 94-9277

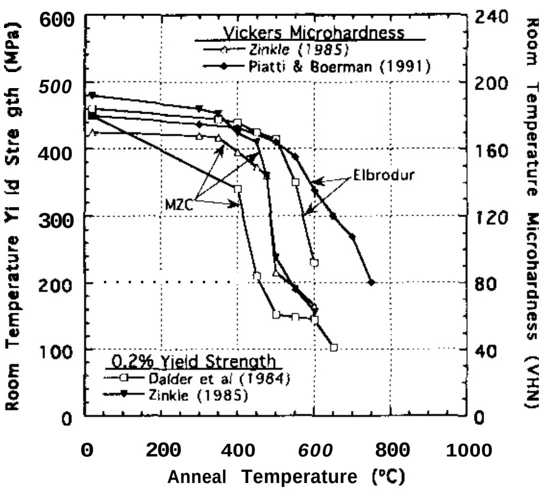

FIG. 5. Effect of annealing on the room temperature yield strength of MZC [10,29,30] and Elbrodur [19,30] CuCrZr alloys. The annealing times varied between 0.5 and 10 h.

ORNL-DWG 94-9278

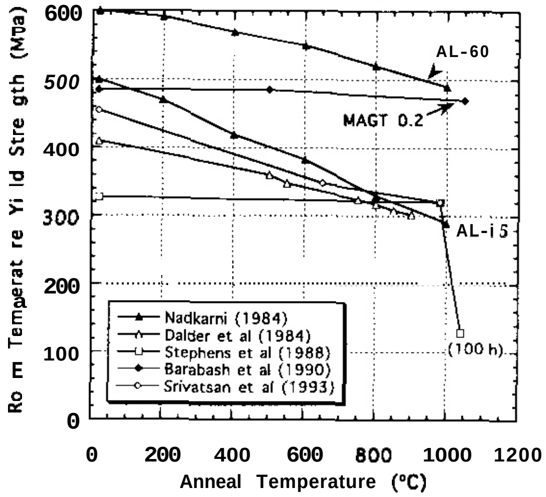

FIG. 6. Effect of annealing on the room temperature yield strength of GlidCop AL-15 and AL-60 [11,30-32] and MAGT [33] oxide dispersion-strengthened copper alloys. With the exception of the data point labeled 100 h, the annealing times varied between 0.25 and 10 h.

Fig. 5, Elbrodur CuCrZr appears to have somewhat better resistance to softening than MZC CuCrZr. Them is not sufficient annealing data on CuNiBe to determine its softening temperature. However, due to the similarity between CuCrZr and CuNiBe regarding precipitation hardening treatment temperatures, CuNiBe may be expected to behave similar to the softening trend shown in Fig. 5. The observed softening temperature for CuCrZr of 400 to 500°C is significantly higher than that of cold-worked copper: the corresponding softening temperature for high purity copper is only about 100°C [22,23], although small amounts of impurities can increase the softening temperature to 200°C or higher [1,22]. Unfortunately, the softening temperature of CuCrZr is too low to prevent significant loss of strength during joining by conventional furnace brazing or welding techniques. Conventional furnace brazing of copper alloys is performed at temperatures between 600 and 1000°C with typical bold times between 5 and 15 minutes. Some of the strength loss induced by the exposure to high temperatures can be recovered by subsequent heat treatment. The maximum room temperature yield strength that can be expected in a conventional furnace brazed or welded CuCrZr joint following heat treatment is the solutionized and aged value of 300 to 350 MPa [10,20,25].

The ultimate tensile strength (UTS) of CuCrZr alloys follows a similar softening behavior as the yield strength following exposure to temperatures above 400 to 500°C [10,26,30]. The room temperature LJTS of the as-fabricated alloy is typically 5 to 20% higher than the yield strength, with the lowest ratios of ultimate to yield strength occurring in heavily cold-worked (high strength) alloys. Following annealing at temperatures above 500 to 600°C, the room temperature UTS is generally –50% higher than the room temperature yield strength. Typical room temperature ultimate strengths of the annealed CuCrZr alloys are 300 to 350 MPa [10,26,30]. The total elongation to failure (e_{tot}) of the CuCrZr alloys increases *after* high-temperature annealing. Typical as-fabricated values of e_{tot} are 5 to 15%, with the lowest elongation occurring in the highest strength alloys [10,19,20,26, 30]. The room temperature elongation to failure in annealed CuCrZr alloys is generally >25% [10,26,30]. The measured reduction in area was >50% for cold-worked & aged MZC CuCrZr [25], which is indicative of a very ductile material.

Figure 6 shows the room temperature yield strength of commercial oxide dispersion-strengthened copper alloys following short-term annealing at elevated temperatures [11,30-33]. It can be seen that these Cu-Al_2O_3 alloys are resistant to softening up to temperatures close to the melting point of copper. Grant and coworkers [28] have found that the room temperature hardness of oxide dispersion-strengthened copper alloys remained within 5% of its original value following 1 h anneals at temperatures as high as 1000°C. Since these alloys do not recrystallize during exposure to temperatures as high as 1000°C, the room temperature ratio of the ultimate to yield strength remains nearly constant [11,30-33]. The room temperature UTS is typically 10 to 20% higher than the yield strength, depending on the amount of cold work induced during fabrication. The measured elongation to failure at room temperature in the dispersion-strengthened alloys generally ranges between 10 and 20% for the as-fabricated alloys and between 15 and 25% for the annealed alloys [11,30-33]. The reduction in area at room temperature is >50% in both the as-fabricated and annealed alloys [11,31].

Figure 7 shows the yield strength of CuCrZr alloys measured at elevated temperatures [19,20, 26,34-36]. The room temperature yield strength varied between 350 and 600 MPa, due to different thermomechanical fabrication procedures for the alloys. The lowest room temperature strength occurred in a cast and aged alloy [20], and the highest strength was produced in an alloy that was cold rolled after aging to achieve a 63% reduction in foil thickness [26]. The yield strength of all alloys decreased steadily with increasing test temperature, reaching a value of about 250 MPa at 500°C. Additional elevated temperature results. which are in good agreement with the average of the data shown in Fig. 7, have been obtained on MZC and Elbrodur CuCrZr alloys over the limited temperature range of 20 to 200°C [37]. Hot microhardness measurements obtained on CuCrZr alloys also exhibit a similar temperature dependence [27]. The typical strength of cast-and-aged Elbrodur plate is apparently lower than cast-and-aged tube or block moulds, with reported yield strengths of 300 and 165 MPa at test temperatures of 20 and 500°C, respectively, for plate material [20]. It is worth noting that high amounts of cold work are effective at increasing the room temperature strength of CuCrZr alloys. However, these cold-worked alloys suffer the largest decrease in strength with increasing test temperature, which may be attributed to the accelerated rate of recrystallization (and accompanying softening) that occurs with increasing amounts of initial cold work [22].

The ultimate tensile strength of CuCrZr alloys shows a similar dependence on test temperature as that shown for the yield strength in Fig. 7 [19,20,26]. The ratio of ultimate to yield strength depends on the thermomechanical treatment given to the alloy. For cold-worked alloys, the UTS is about 5% higher than the yield strength at room temperature and about 10% higher than the yield strength at 500°C [19,26]. For cast and aged alloys, the UTS is about 25 to 35% higher than the yield strength at room temperature and about 15 to 20% higher at 500°C [20]. Various studies on cold-worked CuCrZr alloys have reported either a decrease [18,19] or slight increase [26] of the total elongation to failure (e_{tot}) with increasing test temperature between 20 and 500°C. Typical values for the uniform and total elongation in the cold-worked alloys for this temperature range are 1 to 5% and 5 to 15%, respectively [18,19,26]. The typical e_{tot} for cast and aged CuCrZr over this temperature range is –18% [20].

The yield strength of oxide dispersion-strengthened copper alloys measured at elevated temperatures is shown in Fig. 8 [16,31,33,38-40]. Most of the data were obtained on GlidCop AL-15 and AL-20, which have lower strengths compared to the AL-25 and AL-60 alloys [11,15]. The room temperature yield strength varied between 300 and 600 MPa, mainly due to different amounts of cold work present in the alloys. The lowest room temperature strengths were obtained from as-wrought plates [16] and from an alloy consolidated from coarse particles that was cold worked 31% [39]. The highest strengths were obtained on 80%CW AL-20 [38], 86%CW AL-15 consolidated from fine particles [39], and the higher strength MAGT 0.2 alloy [33]. The yield strength of all of the dispersion-strengthened alloys decreased steadily with increasing test temperature. The average measured yield strength was about 200 MPa at 500°C. Additional tensile results on GlidCop dispersion-strengthened copper that agree with the average of the data shown in Fig. 8 have been reported for the temperature range of 20 to 2WC [37].

The ultimate tensile strength of the dispersion-strengthened alloys has been measured by several researchers at elevated temperature [16,31,33,38-40], with results that are similar to the yield strength behavior shown in Fig. 8. The UTS is about 5 to 15% higher than the yield strength at all test temperatures. Typical values of the uniform and total elongation are 1.5 to 5% and 5 to 15%, respectively, over the temperature range of 20 to 500°C. The total elongation has been observed to either decrease [39], increase [38], or remain roughly constant [16,31] with increasing test temperature. The reduction of area has been observed to decrease from –70% at room temperature to 10-50% at temperatures between 200 and 800°C for tests performed in air and high-purity argon environments [31,40]. The reduction of area at elevated temperatures in these non-vacuum environments was very sensitive to the strain rate, with the lowest reduction in area occurring at low strain rates [31,40].

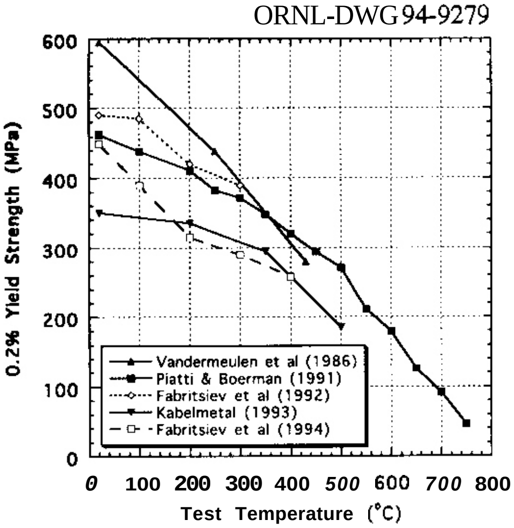

FIG. 7. Yield strength of Elbrodur [19,20,26] and Russian [34-36] CuCrZr alloys measured at elevated temperatures.

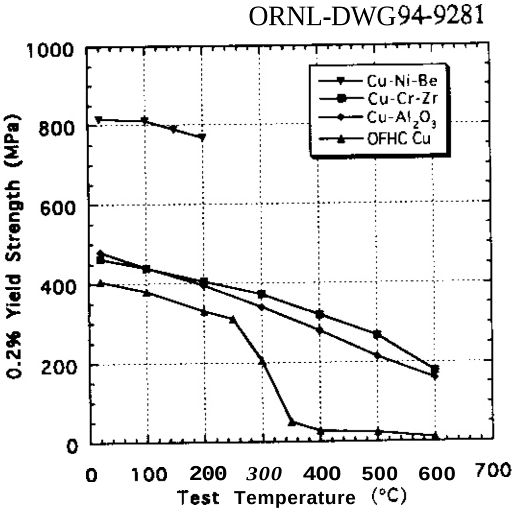

FIG. 9. Comparison of the elevated temperature yield strength of cold-worked copper and copper alloys. The data were obtained from Figs. 7 and 8 and refs. [1,41] for pure copper and refs. [37,42] for CuNiBe.

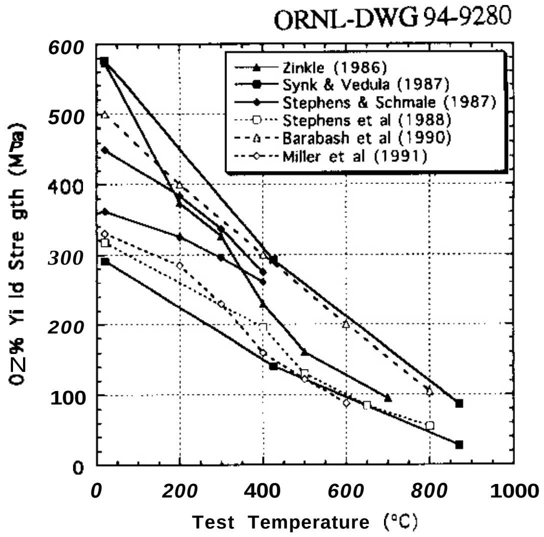

FIG. 8. Yield strength of GlidCop **AL-15** [16,31,39,40] and AL-20 [38] and MAGT 0.2 [33] oxide dispersion-strengthened copper alloys measured at elevated temperatures.

Figure 9 summarizes the effect of test temperature on the yield strength of cold-worked copper and the high strength copper alloys CuNiBe, CuCrZr and $Cu-Al_2O_3$. The data for pure copper were taken from refs. [1,41], and the data for CuCrZr and $Cu-Al_2O_3$ were obtained from an average of the data shown in Figs. 7 and 8, respectively. There are only limited data on the elevated temperature tensile properties of CuNiBe alloys, with no known data available at test temperatures above 200°C [12,37,42]. The most extensive results were presented by Rosenwasser and coworkers [37,42], and their data on conventional cold-worked and aged CuNiBe are shown in Fig. 9. Some caution should be exercised with these data. since their results are. about 100 MPa higher than the yield strength data at 20 and 150°C reported by Mollard et al [12] for a similar high-purity alloy. From the data trends summarized in Fig. 9, it can be surmised that CuNiBe has superior strength compared to the other alloys, at least over the temperature interval of 20 to 200°C. However, it should be kept in mind that the relatively low thermal conductivity of this alloy does not yield a superior resistance to thermal stress. The elevated temperature yield strength of CuCrZr and dispersion-strengthened copper is very similar over the temperature range of 20 to 600°C for these short term (< 1 h) exposures. The elevated temperature UTS, e_{tot}, and uniform elongation of CuCrZr and dispersion-strengthened copper measured during short-term exposures are also comparable.

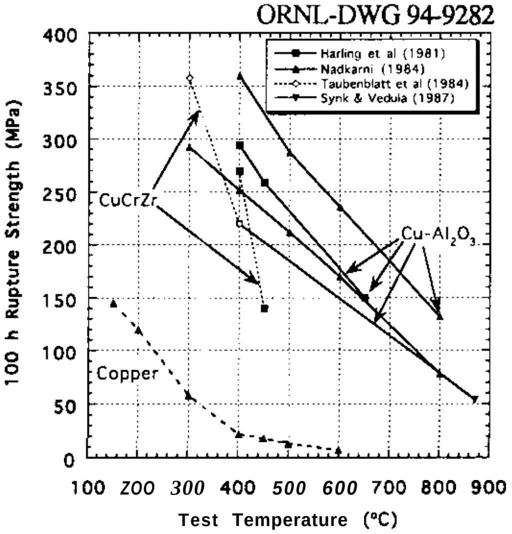

FIG. 10. Elevated temperature stress-rupture strength of copper [1,11], MZC CuCrZr [23,43], Cu-3.5 vol.% Al_2O_3 [43], and GlidCop AL-15 [11,39] and AL-60 [11].

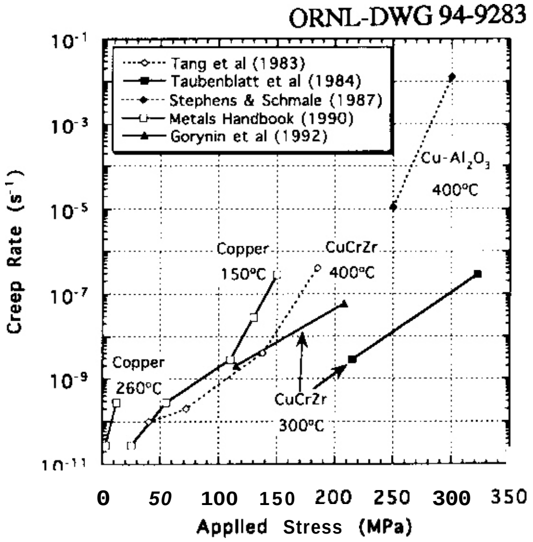

FIG. 11. Thermal creep rate in copper and copper alloys [1,18,23,40,45].

2.3 Creep and fatigue properties and fracture toughness

The maximum stress that can be safely applied to high-strength copper alloys during extended operation at elevated temperatures is less than the yield saength measured during short term exposures (Figs. 7-9), due to the phenomena of creep and fatigue. Figure 10 compares the mechanical stresses which produce creep failure within 100 hours in copper, CuCrZr and Cu-Al_2O_3 during exposure at elevated temperatures [1,11,23,39,43]. Both alloys have significantly higher rupture strengths than pure copper. The 100 hour rupture strength of both MZC CuCrZr [23,43] and GlidCop AL-15 Cu-Al_2O_3 [111 is approximately 300 MPa at 300°C. However, the rupture strength of CuCrZr decreases rapidly with increasing temperature above 300°C. Oxide dispersion-saengthened copper has superior 100 h rupture strengths at temperatures above 400°C. The higher-strength grades of dispersion-strengthened copper such as GlidCop ***AL-60*** have particularly good stress-rupture strengths. For example, the rupture strengths shown in Fig. 10 for GlidCop AL-60 and AL-15 at 400°C are about 360 and 240 MPa, respectively [11,39]. The impressive creep-rupture strengths of oxide dispersion-strengthened copper alloys such as GlidCop at elevated temperatures is due to the uniform dispersion of thermodynamically stable particles of -7 nm diameter, which is close to the optimum size for high creep saength [44].

The steady-state thermal creep rate in copper, CuCrZr and Cu-Al_2O_3 at temperatures between 150 and 4 W C is shown in Fig. 11 [1,18,23,40,45]. Pure copper creeps readily at low applied stress levels. For example, the creep rate of copper at 4 W C is nearly 10^{-4}/s for an applied stress of 100 MPa, and about 10^{-8}/s for an applied stress of only 15 MPa [46]. CuCrZr and oxide dispersion-strengthened copper alloys can be subjected to much higher stresses at elevated temperature without suffering excessive creep. The available data indicate that creep rates of ~$5x10^{-9}$/s are produced in CuCrZr [23] and oxide dispersion-strengthened copper [33] with applied stresses of about 200 MPa at 300°C. Unfortunately, there are not enough data to quantitatively compare the creep behavior of the various high-strength copper alloys over the ITER-relevant temperature range of 20 to 400°C. High strength copper alloys generally have a threshold stress below which creep deformation is negligible [44]. Further study is needed to determine the value of the threshold stress for the various copper alloys at temperatures between 20 and 400°C. The creep data reported by Nadkami [11] suggest that the threshold stress at 650°C is about 130 and 190MPa for cold-worked GlidCop AL-15 and AL-60, respectively. The data by Tang et al. [45] indicate that the threshold stress is about 100 MPa for MZC CuCrZr tested at 400°C.

A further factor which must be considered for the precipitation-hardened alloys is that their softening behavior at elevated temperatures due to overaging and recrystallization depends on both the exposure time and temperature. For example, extrapolation of short-term (0.25 to 100 h) annealing results on MZC CuCrZr indicates that the softening temperature is about 410°C for a 100 h exposure, but decreases to ~330°C for a 10 year exposure [10,29]. Therefore, although the creep rate or rupture strength of precipitation-hardened copper alloys such as CuCrZr may be acceptable at temperatures above 3 W C during short-term tests, the alloy could become unacceptably soft during extended exposure (>>100 h) at these temperatures due to overaging and recrystallization. The softening at elevated temperatures is accelerated by irradiation or the presence of stress [47].

The cyclic fatigue strength of copper alloys generally increases with increasing tensile strength, i.e., metallurgical changes which increase the tensile strength of copper alloys also increase the fatigue strength. Figure 12 shows the room temperature. cyclic fatigue strength of cold-worked pure copper, CuCrZr and CuNiBe [1,16,48]. The high-cycle fatigue strength of copper at room temperature is about 100 MPa [1,16,49], which is about 1/3 of the yield strength of the starting material (250 to 300 MPa). The corresponding high-cycle fatigue strength of MZC CuCrZr, with a yield strength of about 550 MPa, was reported to be 170 MPa [50]. There is a lack of fatigue data on CuCrZr and CuNiBe alloys, particularly at high cycles. The room temperature fatigue strengths of Elbrodur CuCrZr and Brush-Wellman CuNiBe alloys at intermediate (10^5) cycles are –280 and 400 MPa, respectively [48]. The fatigue strengths of normal and overaged CuNiBe were found to be comparable (–400 MPa) at 10^5 cycles, whereas the initial yield strengths were 770 and 570 MPa, respectively [48]. Additional low-cycle ($<3\times10^4$) fatigue data on CuNiBe have been reported by Rosenwasser and coworkers [37,42] using a minimum to maximum stress ratio of R=0. Their fatigue strengths were 200 to 250 MPa higher than the data reported by Bushnell and Ellis (Fig. 12) for a stress ratio of R=-1 [48].

The room temperature cyclic fatigue strength of GIidCop $Cu-Al_2O_3$ is shown in Fig. 13 [16,32, 48,51,52]. The fatigue data from refs. [48,52] were obtained under stress-controlled conditions, whereas the remaining data were obtained under strain-controlled conditions and converted to equivalent stress. All of the data were obtained on GlidCop AL-15 except for Singhal et al. [51], who examined GlidCop AL-25. The fatigue strengths of AL-15 and AL-25 appear to be comparable at intermediate (10^4 to 10^6) cycles. The high-cycle fatigue strength of $Cu-Al_2O_3$ with a yield strength of 330 MPa is about 175 MPa [16]. Nadkarni [11] reported somewhat higher fatigue strengths for GlidCop AL-15 and AL-60 compared to the data shown in Fig. 13 over the range of 3×10^4 to 2×10^7 cycles. His rotating-bending cantilever beam fatigue measurements indicated fatigue strengths at 2×10^7 cycles of about 205 and 230 MPa for AL-15 and AL-60, respectively. As discussed elsewhere [16], this discrepancy may be due to dynamic hysteresis effects associated with the rotating-bending beam measurements, or to the higher frequency (167 Hz vs. 1 to 10 Hz) of these measurements compared to the intermediate-to-high cycle data shown in Fig. 13. Alternatively, the higher fatigue strength may be due to a higher initial yield strength of Nadkarni's material (470 MPa for AL-15). The limited amount of data obtained on CuCrZr (Fig. 12) indicates that the room temperature fatigue behavior of this alloy is comparable to that of $Cu-Al_2O_3$ (Fig. 13).

There have only been a few studies of the fatigue behavior of CuCrZr [18,45,53,54], CuNiBe [37,42], and oxide dispersion-strengthened copper [16,18] at elevated temperatures. The high-cycle ($>10^6$) fatigue strength of GlidCop AL-15 was measured to be about 75 MPa at 6 W C [16]. Figure 14 summarizes the fatigue results obtained on high-strength copper alloys under strain-controlled conditions at temperatures between 20 and 3 W C [18,32,37,42,51]. Additional low-cycle strain-controlled data have been obtained on MZC CuCrZr at 400°C, with the results reported only in terms of the plastic strain range [45,53]. The low-cycle strain-controlled fatigue behavior of CuCrZr and oxide dispersion-strengthened copper appears to be very similar over the temperature range of 20 to 300°C. The results by Rosenwasser and coworkers [37,42] suggest that CuNiBe has superior low-cycle fatigue properties compared the other copper alloys. There does not appear to be a strong dependence on temperature between 20 and 300°C when the data are evaluated according to strain amplitude. All of the alloys have comparable or better fatigue properties than pure copper. For example, the fatigue lifetime of pure copper tested in the temperature range of 20 to 3 W C decreases from about 10^5 cycles to 10^3 cycles as the total strain amplitude increases from about 0.15% to 0.6% [55,56].

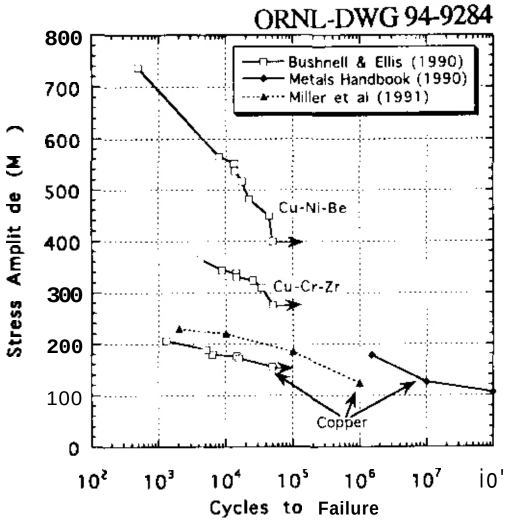

FIG. 12. Room temperature cyclic fatigue strength of copper [1,16,48], Elbrodur CuCrZr [48] and CuNiBe [48]. Fully reversed stress amplitude (R=-1). **All data** except for refs. [1,16] were stress-controlled. The **data** points with arrows denote specimens which did not **fail** during the test lifetime.

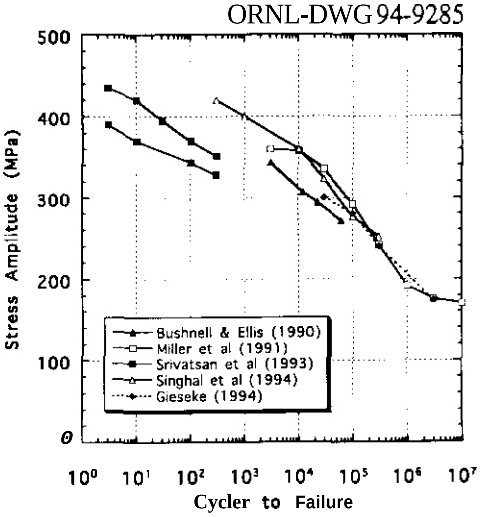

FIG. 13. Room temperature cyclic fatigue strength **of $Cu-Al_2O_3$** [16,32,48,51,52]. All of the **data** was obtained under fully reversed (R=-1) stress conditions except for ref. [16], which used a minimum to maximum stress ratio of R=0.

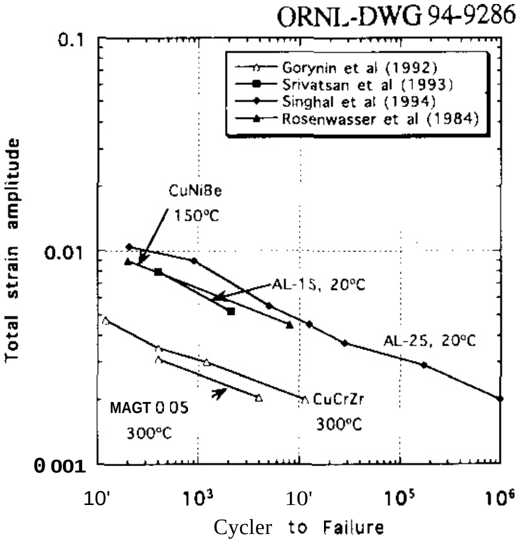

FIG. 14. Strain-controlled cyclic fatigue behavior of copper alloys [18,32,37,42,51].

We are not aware of any published measurements **of** the fracture toughness or fatigue crack growth behavior of CuCrZr, CuNiBe, or commercial oxide dispersion-strengthened copper. The room temperature fracture toughness of a medium-strength (σ_y=250 MPa) Cu-Zr alloy that should **be** comparable to CuCrZr was measured to be an impressive **420** MPadm, and the tearing modulus was 440 [57]. The fatigue crack growth rate was also found to be much better than pure copper. On the other hand, unpublished measurements on a cold-worked GlidCop AL-15 alloy (σ_y=330 MPa) indicate that **the** room temperature fracture toughness was only **20** to 50 MPadm [52,58], which is similar *to* values for high strength aluminum alloys [59].

3. IRRADIATION EFFECTS

Exposure to radiation generally produces small (<1%) changes in most of the copper alloy physical propenies such as the specific heat and coefficient of thermal expansion. On the other hand, large radiation-induced changes can he produced in the density (void swelling), thermal conductivity, and mechanical properties. The radiation stability of high-strength, high-conductivity copper alloys is directly linked to the stability of the precipitates or oxide particles. The interface between the particles and the copper matrix promotes the recombination of vacancies and interstitials, thereby imparting good resistance to void swelling. In addition, the particles are needed to stabilize whatever dislocation structure is present and to maintain high strength levels in the alloy.

Several studies have heen performed to investigate the stability of the second phase particles in irradiated CuCrZr [60-65], CuNiBe [61,66] and oxide dispersion-strengthened copper [60,61,63,66-69]. These studies are not in complete agreement regarding the structural stability of copper alloys. For example, either precipitate shrinkage [62,63,65] or coarsening [60] has been reported for the Cr precipitates in CuCrZr, and other studies [61,64] have found that the precipitates are not affected by irradiation. The most detailed studies of particle stability have been performed on irradiated oxide dispersion-strengthened copper [63,68,69]. These studies have found that a gradual reduction in oxide particle size occurs after irradiation to high doses (>10 displacements per atom) due to ballistic dissolution. However, the overall structural stability of the oxide dispersion-strengthened alloys remains very good even after damage levels in excess of 100 dpa [65,69,70]. The published investigations suggest that the oxide particles in dispersion-strengthened copper have somewhat better stability against radiation-induced dissolution than the precipitates in CuCrZr and CuNiBe.

3.1 Swelling

Copper alloys are susceptible to radiation-induced swelling due to microscopic void formation at temperatures between 180 and 550°C [6,71-74]. Figure 15 shows the temperature-dependent void swelling that occurred in copper and a dilute Cu-B alloy following fission neutron irradiation to a damage level of about 1.2 dpa (~1.2×10^{21} n/m^2, E>0.1 MeV) at a damage rate of ~2×10^{-7} dpa/s [71,72]. Void swelling in copper is maximized at intermediate temperatures of 275 to 325°C for this damage rate, which is comparable to the damage rate at the fust wall of ITER. It can be seen from Fig. 15 that significant levels of volumetric swelling (–0.5%) occur in pure copper at a damage level as low as –1 dpa. High dose studies performed on pure copper at temperatures near 400°C indicate that the steady-state swelling rate is about 0.5%/dpa [74], although even higher swelling rates have been reported [75]. Hence, it is obvious that pure copper is not suitable for high flnence (>1 dpa) applications at temperatures between –200 and 500°C due to unacceptable amounts of void swelling. Similar steady-state swelling rates have also been observed in simple copper alloys such as Cu-5%Ni [76].

The CuCrZr, CuNiBe and oxide dispersion-strengthened copper alloys have superior void swelling resistance compared to pure copper [4-6,17,18,36,61,67,70,74,76-79]. Figure 16 summarizes some of the swelling data obtained on these alloys following neutron irradiation to high damage levels [74,76,79]. Whereas irradiation to a damage level of 50 dpa near 4 W C produces radiation-induced density changes near 25% in pure copper and simple copper alloys such as Cu-5%Ni [74,76], the corresponding density changes in CuCrZr and Cu-Al_2O_3 alloys are generally less than 2%. Swelling levels below 2% have been maintained in some CuCrZr and Cu-Al_2O_3 alloys irradiated with fast fission neutrons up to a damage level of 150 dpa at 410 to 415°C [74,78]. The CuNiBe alloy shows a widely varying swelling behavior. depending on the initial thennomechanical treatment [74,79]. The measured swelling in CuNiBe after irradiation to –50 dpa at 410 to 430°C varied from about 0.4% for solutionized and solutionized & aged alloys [79] to 3.5 to 14% for solutionized & aged and cold-worked & aged alloys [74]. The CuCrZr alloys exhibit a similar, although less pronounced. dependence on thennomechanical treatment [74]. Swelling levels between 0 and 2% have been observed in CuCrZr alloys after irradiation to 50 dpa at ~410°C, depending on the detailed manufacturing procedure [74]. Ion irradiation studies performed over a wide range of temperatures and damage levels provide further evidence for the good swelling resistance of the precipitation- and dispersion-strengthened alloys [10,47,65,66]. Void formation was not observed in CuCrZr or MAGT 0.2 dispersion-strengthened copper alloys during ion irradiation up to 150 dpa at temperatures between 260 and 600°C [66]. Unfortunately, there are no high dose (>5 dpa) neutron irradiation swelling data on CuCrZr, CuNiBe or oxide dispersion-strengthened copper alloys at ITER-relevant temperatures of 50 to 350°C. Swelling levels between 0.2 and 3% have been reported for CuCrZr alloys after neutron irradiation to moderate damage levels of about 4 dpa at 300 to 350°C [18,36].

The good swellmg resistance of precipitation- and dispersion-strengthened copper alloys may be attributed to their high dislocation and particle densities, which promote recombination and annihilation of the point defects created by neutron irradiation [6]. The best swellmg resistance occurs in cold-worked alloys which retain their high dislocation density during irradiation. During high-

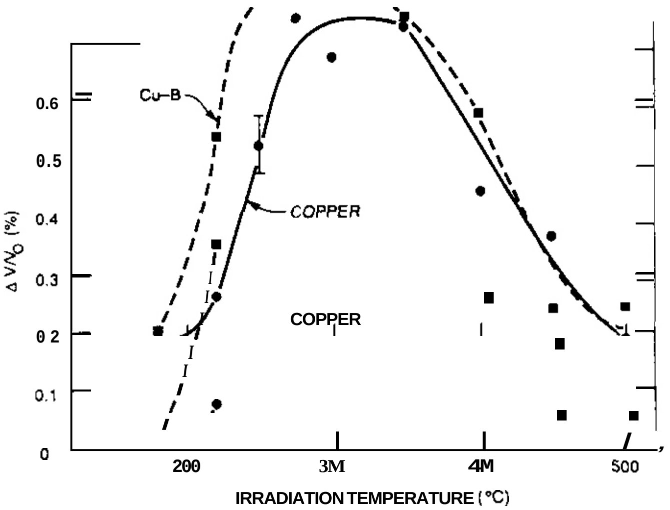

FIG. **15.** Temperature-dependent cavity swelling in copper and **Cu-100** appm ^{10}B irradiated with fission neutrons to **-1.2** dpa at ~$2x10^{-7}$ dpa/s [71,72]. The irradiation produced -0.2 and 100 appm He in the pure copper and **Cu-B** alloy, respectively.

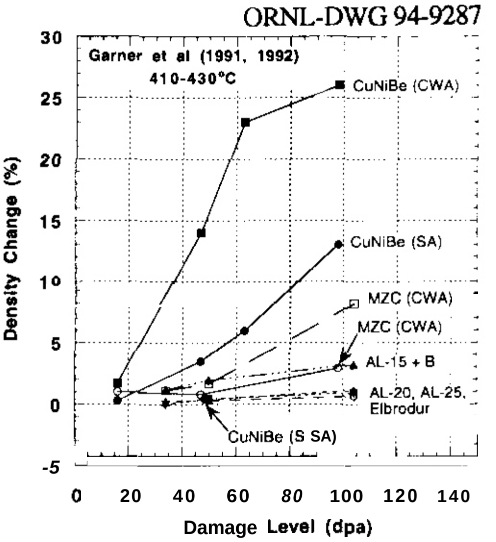

FIG. 16. Swelling behavior of CuCrZr, CuNiBe and $Cu\text{-}Al_2O_3$ alloys irradiated with neutrons at **400** to 430°C [74,76,79]. The materials were irradiated in solutionized (S), solutionized & quenched **(SA)** and cold-worked & aged (CWA) conditions.

fluence ion [66] or neutron [61,67,80] irradiation, void formation is initiated in regions of the matrix that have recrystallized (leaving a low defect sink density). Unfortunately, the precipitation-strengthened alloys are susceptible to radiation-enhanced recrystallization [47,81], which is due to a combination of radiation-enhanced precipitate overaging and dislocation recovery processes. The dislocation recovery and sweeping-up of precipitates by migrating grain boundaries during recrystallization can produce a relatively sink-free matrix that is susceptible to void swelling. The susceptibility to radiation-enhanced recrystallization increases with increasing amount of cold work. Since solutionized & aged alloys do not have a cold-worked dislocation structure, they will not suffer the dramatic microstructural changes associated with recrystallization. Therefore, in some cases solutionized & aged alloys may have lower levels of swelling than cold-worked & aged alloys which recrystallize during the irradiation. A large part of the swelling resistance of dispersion-strengthened copper alloys is due to their thermally stable particles, which impart superior resistance to recovery and recrystallization. Since precipitate overaging does not occur in the oxide dispersion-strengthened alloys, they are very resistant to radiation-enhanced recrystallization.

Further work is needed to determine if the precipitation- and dispersion-strengthened copper alloys remain swelling resistant in the presence of fusion-relevant levels of helium transmutation products. The helium generation rate in copper irradiated in fission reactors is **-0.2** appm/dpa, which is more than one order of magnitude smaller than the **ITER** fust wall generation rate of **-7** appm He/dpa. Spitznagel et al. [66] observed that dispersion-strengthened copper had about four times higher swelling **(0.8%***after* **20** dpa) following dual-ion **beam** irradiation at **30** appm He/dpa compared to specimens irradiated without helium coimplantation. The somewhat higher amounts of swelling that occurred in the GlidCop AL-15 alloy compared to **AL-20** and **AL-60** during high-dose neutron irradiation (Fig. **16)** may be partially due to helium generated via $^{10}B(n,\alpha)$ reactions with residual boron (<200 wt. ppm) in the **AL-15** alloy [6,80].

3.2 Mechanical properties

The general effect of neutron irradiation on the mechanical propenies of copper can be divided into two temperature regimes [6,34,82]. At irradiation temperatures below about 300°C, radiation hardening usually occurs along with a reduction in ductility. Radiation-enhanced softening generally occurs at irradiation temperatures above 300°C. The radiation hardening at low temperatures is due to the creation of a high density of small (<10 nm) dislocation loops and stacking fault tetrahedra. These so-called "black spot" defect clusters can increase the room temperature yield strength of annealed copper (unirradiated σ_y~60 MPa) to more than 350 MPa [6,83]. The radiation hardening associated with these small defect clusters approaches **a saturation** level after doses of –0.1 dpa [6,84,85]. The stacking fault tetrahedra are thermally unstable *at* temperatures above about 150°C [6,86]. Therefore, the radiation hardening in copper and copper alloys becomes progressively smaller with increasing irradiation temperature above ~150°C, and generally becomes insignificant above –3WC.

Figure 17 summarizes the available data on the elevated-temperature yield strength of CuCrZr following neutron irradiation at temperatures between 100 and 420°C [26,34-36,77,82]. All of the yield strength data **shown** in Fig. 17 were obtained at or near the irradiation temperature on cold-worked & aged specimens which had initial room temperature yield strengths between -400 and 500 MPa. The yield *strength steadily decreased* with increasing irradiation and test temperature, reaching a value **of** about 300 MPa at 3WC and –100 MPa at **4WC.**

It is instructive to compare the temperature-dependent strengths **of** irradiated and unirradiated alloys. Radiation-enhanced recrystallization can produce significant softening in cold-worked copper and copper alloys at irradiation temperatures above ~280°C **[6,17,18,26,34-36,67,74,77,81,87-90].** Figure **18** shows the measured change in yield strength in cold-worked & aged CuCrZr alloys following neutron irradiation at temperatures between 100 and 5WC [17,26,34-36,74,77,82,89,90]. The figure includes some alloy screening experiments that were **tested** at room temperature rather than at the irradiation temperature. The initial room temperature yield strengths of the CuCrZr alloys varied from –400 to 500 MPa, and the irradiation damage levels were between 1 and 150 dpa. Fabritsiev et al. [36] have **shown** that most of the radiation hardening or softening in CuCrZr occurs at relatively low neutron doses (**<1** dpa). The CuCrZr yield strength was increased by ***–5*** to ***25%*** after irradiation at temperatures below 260°C. Conversely. radiation softening occurred and became progressively more significant as the irradiation temperature was increased above 280°C. Approximately 80% of the initial alloy yield strength was lost after irradiation at temperatures above ~400°C. Similar radiation softening **has** been observed in CuNiBe alloys irradiated at temperatures above 400°C [17,74,89]. However, there **are** insufficient data on CuNiBe at irradiation temperatures below 400°C [91], ***so*** the overall temperature-dependent radiation softening behavior cannot be quantified at this time.

The oxide dispersion-strengthened alloys are very resistant to radiation softening compared to the precipitation-hardened alloys. Figure 19 shows the measured change in yield strength in oxide dispersion-suengthened copper following neutron irradiation at temperatures between 50 and 530°C [17,18,36,78,80,90,92]. The initial room temperature yield strengths ranged from 340 to 500 MPa, and the irradiation damage levels were between 1 and 150 dpa with the exception of the 0.04 dpa data of Heinisch et al. [92]. The available data are. consistent with the CuCrZr results that radiation hardening **occurs** for irradiation temperatures below ~300°C, and radiation softening occurs above ~300°C. However, the magnitude of radiation softening was much Less pronounced in the oxide dispersion-strengtheued alloys compared to CuCrZr. The radiation softening in oxide dispersion-strengthened capper was less than ***25%*** even after irradiation at 410 to 430°C to a **damage** level of 150 dpa [78] or irradiation at 530°C to a damage level of 32 **dpa** [80].

A loss of ductility is associated with the radiation hardening that occurs at irradiation temperatures below about 300°C. The uniform and **total** elongation of pure copper and Cu alloys **are** strongly reduced after neutron irradiation at temperatures below 250°C [6,18,34,36,82,92,93]. Cold-worked specimens appear to be particularly susceptible to radiation embrittlement. For example, Makin [93] found that **20%** cold-worked copper had a total elongation of only –1 to **2%** following irradiation near room temperature to an E>1 MeV neutron fluence of $4x10^{23}$ n/m^2 (–0.04 dpa). The corresponding **total** elongation in copper irradiated without any initial cold work was –16%. Figure **20** summarizes the uniform and total elongation measured in CuCrZr and oxide dispersion-strengthened copper alloys following irradiation at temperatures between 50 and 530°C [17,18,34-36,80,82,90, 921. Similar temperaturedependent trends have been observed for irradiated CuNiBe [17,89,91], but only a few scattered results are available. **Both** classes of alloys exhibit very low uniform elongation (<1%) after irradiation at temperatures below 250°C to damage levels in excess of **–1** dpa The corresponding total elongation in this radiation hardening temperature regime varied from –1 to **10%,** depending on the initial thermomechanical treatment given to the alloy. Irradiation at temperatures above 300°C generally produced high uniform and total elongation (>10%). The

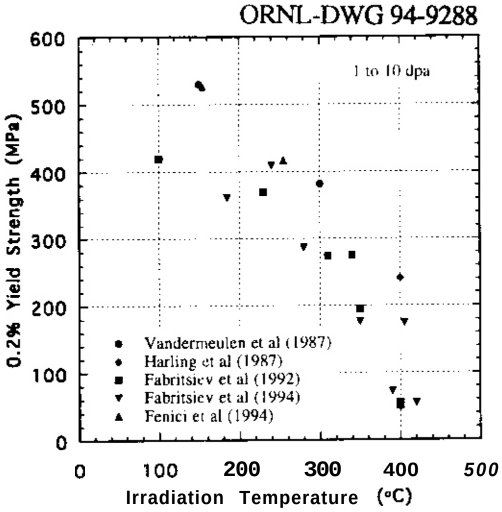

FIG. 17. Effect of irradiation temperature on the yield strength of neutron-irradiated CuCrZr alloys [26,34-36,77,82]. The tensile tests were performed at or near the irradiation temperature.

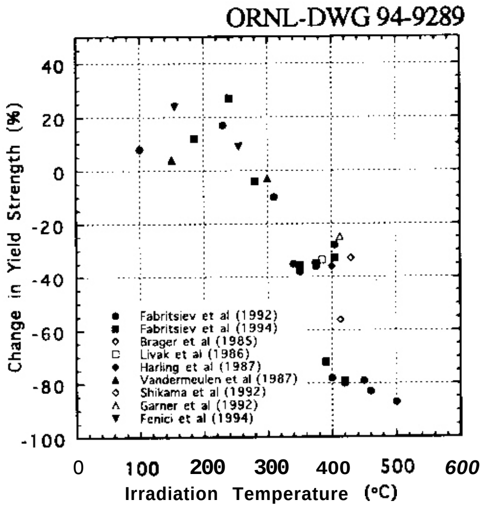

FIG. 18. Change in the yield strength of CuCrZr alloys following neutron irradiation at 100 to 500°C [17,26,34-36,74,77,82,89,90]. The filled symbols denote measurements made at or near the irradiation temperature, whereas the open symbols refer to room temperature tensile measurements.

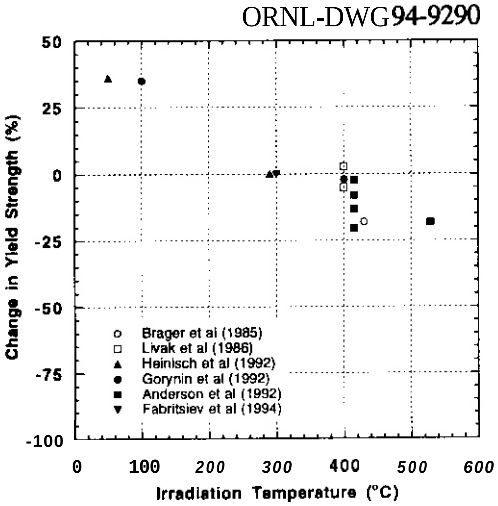

FIG. 19. Change in the yield strength of oxide dispersion-strengthened copper alloys after neutron irradiation at 50 to 530°C [17,18,36,78,80,90,92]. All of the tensile data except for refs. [18,36] were obtained at room temperature.

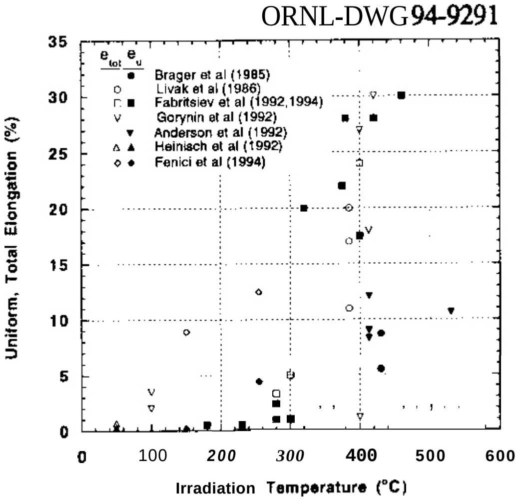

FIG. 20. Effect of irradiation temperature on the uniform (e_u) and total (e_{tot}) elongation of CuCrZr and oxide dispersion-strengthened copper alloys [17,18,34-36,80,82,90,92]. The tensile data from refs. [18,34-36,82] were made at or near the irradiation temperature, with the remaining data obtained from room temperature tests.

transition temperature between the low- and high-ductility regimes at 275 to 3 W C corresponds to the transition between radiation hardening and radiation softening (Figs. 18,19).

The relatively low ductility of the high strength (cold-worked) copper alloys in the ITER-relevant temperature range of 50 to 300°C may limit the applicability of these alloys for structural components. Unfortunately, there are no known published data on the important engineering properties of fracture toughness, fatigue strength, and fatigue crack growth rates in irradiated copper alloys. Conflicting results have been obtained on the fatigue properties of pure copper after low dose (~0.001 dpa) neutron irradiation near room temperature [94,95], although the overall effect of radiation on the fatigue strength was small due to the low damage level in these studies. There are no known published fatigue results on copper or copper alloys irradiated to damage levels >1 dpa. A recent unpublished study indicates that the fracture toughness of GlidCop AL-15 is severely reduced following irradiation to –3 dpa at 250°C [58]. Based on the observation that radiation embrittlement in the temperature range 50 to 250°C apparently becomes more severe with increasing cold work level [93], future irradiation studies should include the medium-strength as-wrought and cast & aged alloys. Whereas these alloys have less attractive unirradiated strengths compared to cold-worked alloys, it is possible that their irradiated properties may be superior to the cold-worked alloys due to higher ductility and work hardenability.

The presence of insoluble helium generated by transmutation reactions can produce additional embrittlement in copper and copper alloys [36,96-98]. However, helium embrittlement is generally most pronounced at elevated temperatures, where the overall ductility of irradiated copper and copper alloys is high. The threshold temperature for observable helium embrittlement decreases with increasing helium concentration [36,98]. For pure copper, the threshold temperature is about 500°C for a helium concentration of *2* appm and ~350°C for a He concentration of 60 appm. Alloys containing precipitates or oxide particles exhibit a significantly higher threshold temperature for observable He embrittlement compared to pure copper. For example, the threshold temperature for MAGT *0.2* dispersion-strengthened copper containing 60 appm He is – 9WC [98]. The increased resistance to helium embrittlement in the alloys is presumably due to effective partitioning of the helium among the numerous particle-matrix interfaces.

There are only a few published studies of radiation creep in copper [99,100], with no known studies on high-strength copper alloys. The magnitude of radiation *creep* in copper is comparable to other FCC metals such as Ni and austenitic stainless steel [99]. An irradiation-creep compliance of $\dot{\varepsilon}/\sigma P = 6.2\times10^{-11}$/Pa-dpa was obtained on *20%* cold-worked copper irradiated with light ions at 150°C [99], where P is the displacement damage rate and σ is the applied stress.

3.3 Transmutation effects and thermal conductivity degradation

The high energy neutrons produced in fusion reactors will produce significant concentrations of solid and gaseous transmutation products in copper, in addition to causing displacement damage. Table III summarizes the calculated displacement damage [101-103] and major transmutation products [5,102-106] for copper exposed to typical fusion reactor first wall irradiation spectra. For purposes of comparison, the corresponding values for copper irradiated in the EBR-II or FFTF fast fission reactors are also included in Table III [102,106]. The displacement damage calculations summarized in Table III used the recommended [107] average displacement energy of 30 eV for copper. The dominant transmutation products in both fusion and fission reactor spectra are nickel and zinc. The transmutation rates (appm/dpa) are lower in the fast fission spectrum for all of the major transmutation products. Water-cooled fission reactors produce significantly higher transmutation rates of copper to Ni and Zn (up to –5000 and 2000 appm/dpa, respectively) due to thermal neutron reactions, but produce similar amounts of Co, Fe, H and He as fast fission reactors [108,109]. Since fast fission reactors operate with liquid metal coolants, it is generally not possible to obtain irradiation data at temperatures below ~350°C. Water-cooled reactors can provide irradiation data in the ITER-relevant temperature range of 50 to 350°C, but spectral shielding of the thermal neutron flux is required for high-dose investigations (>1 dpa) to reduce the Ni and Zn transmutation rates to a level comparable to the fusion condition. As discussed in the following, the thermal conductivity of copper alloys is very sensitive to variations in the solid transmutation rate. Therefore. fission reactor thermal conductivity data must be corrected for solid transmutation differences before it can be applied for fusion design purposes.

TABLE III. Calculated displacement damage [101-103] and transmutation products [5,102-106] for copper in first wall fusion and fast fission reactor spectra. The dpa calculation for the fusion reactor is normalized to a neutron wall loading of 1 MW-yr/m^2 = 1 full power year (FPY) .

	Damage rate	Transmutation rate (appm/dpa)					
Spectrum	(dpa/FPY)	Ni	Zn	Co	Fe	H	He
Fusion 1st wall	15	190	90	7	0.02	40	7
Fast fission	54 to 73	51	46	0.1	...	7	0.1

TABLE IV. Experimental and calculated energies for hydrogen and helium migration (E_m), formation (E_f), binding energy to vacancies (E_{vB}) and vacancy-solute mutual diffusion (E_{vm}) in copper.

Solute	E_m (eV)	E_f (eV)	E_{vB} (eV)	E_{vm} (eV)	Reference
H	0.40	0.40	0.4	...	[113,114,116]
He	0.6	>2.0	2.1	2.1	[118-120]

The transmutation rates in CuCrZr, CuNiBe and oxide dispersion-strengthened copper will generally be very similar to the pure copper values given in Table III. The one notable exception is CuNiBe. where the Be will transmute during exposure to high energy neutrons (E> 2 MeV) via a threshold (n,2n) reaction and subsequent decay to produce two helium nuclei. Transmutation calculations indicate that this reaction will produce an additional 7 appm Hddpa in CuNiBe exposed to a fusion first wall spectrum and –5 appm He/dpa in a fission reactor spectrum [109].

Numerous studies have been performed on the solubility and diffusivity of hydrogen [110-117] and helium [118-120] isotopes in copper. Copper and its alloys are an effective barrier to tritium permeation compared to other metals such as austenitic stainless steel, due to the very low solubility of hydrogen in copper [121]. The solubility of hydrogen in copper is <100 appm at the melting point of copper, and –0.1 appm at 3 W C for an external hydrogen partial pressure of one amosphere [112, 117]. The combination of low tritium solubility and high tritium diffusivity in copper alloys produces a low tritium inventory. which is advantageous for accident scenarios. Table IV *summarizes* the diffusion and solubility data for hydrogen and helium in copper [110-120]. The solubility of hydrogen in copper obeys Sieverts Law, i.e. the solubility is proportional to the square root of hydrogen pressure. The pre-exponential factor for H diffusion is $D_0=1.06\text{x}10^{-6}$ m^2/s [113]. The activation energy for bulk permeation of hydrogen through copper is given by $E_\phi=E_m + E_f = 0.80$ eV, with a pre-exponential factor of $8.4\text{x}10^{-7}$ mol/(m-s-√Pa) [114]. Similar bulk permeation constants are obtained for tritium, with the exception that the pre-exponential factor is $4.9\text{x}10^{-7}$ [114]. In practice. the permeation of hydrogen isotopes through copper at temperatures below 4 W C is even lower than the bulk permeability [115]. The rate limiting step for low temperature hydrogen permeation is adsorption of molecular hydrogen at the surface of copper [115].

Although the hydrogen and helium produced by transmutation reactions are both insoluble in copper, their diffusion behavior creates two different responses. Hydrogen has a low migration energy, and its binding energy to traps such as vacancies and voids is –0.4 to 0.6 eV (Table IV and ref. [116]). Therefore. hydrogen can diffuse. rather easily at temperatures above room temperature and generally does not produce observable precipitation. On the other hand, helium has a somewhat higher migration energy and is strongly trapped by monovacancies and vacancy clusters. This behavior promotes the formation of cavities containing He in irradiated copper. Hydrogen generally does not produce any serious alterations in the mechanical properties of oxygen-free copper. Hydrogen embrittlement occurs in copper containing excess amounts of oxygen (>0.01%) in the form of copper oxide during exposure to hydrogen at temperatures >400°C [38].

TABLE V. **Room** temperature electrical resistivity contributions to pure copper (atomic fractions) [123,125,126]. The solute resistivities are valid for solute concentrations up to 30%. 3%. 1% and 1% for Ni, Zn, Co and Fe, respectively.

Solute resistivity (10^{-8} Ω-m)				Dislocation resistivity (Ω-m^3)	Stacking fault resistivity (Ω-m^2)	Frenkel pair resistivity (μΩ-m)
Ni	Zn	Co	Fe			
1.12	0.30	6.4	9.3	1.6×10^{-25}	1×10^{-19}	1.9

The **solutes** created by neutron transmutation reactions (Table III) produce **a** degradation in the electrical and thermal conductivity of copper. Additional radiation-induced processes such **as** void formation and precipitate dissolution can cause further decreases in the conductivity [122-124]. However, these contributions in radiation resistant copper alloys **are** generally small compared to the transmutation effects. The overall degradation in the thermal conductivity can be estimated by invoking Matthiesson's rule [125] and the Wiedemann-Franz law given in Section **2.** Table V summarizes experimental measurements of the specific resistivity of the principal **solutes** produced in neutron-irradiated copper, along with theoretical and experimental specific resistivity values for other radiation-induced defects [123,125,126]. According to Matthiesson's rule, the individual resistivity components *can* be independently **summed** *to* determine the overall resistivity degradation:

$$\rho=\rho_0+\rho_{Ni}X_{Ni}+\rho_{Zn}X_{Zn}+\rho_{Co}X_{Co}+\ldots. \qquad (2)$$

where ρ_0 is the electrical resistivity of pure copper (17.1 nΩ-m at 20°C), and ρ_i and X_i are the specific resistivity and atomic concentration of solute *i.* Similar **terms** can be written for the resistivity contribution from dislocation loops and network dislocations [123], but these terms typically produce less **than a 1%** increase in the resistivity of irradiated copper. Figure 21 shows the calculated degradation in the thermal conductivity of copper due to solid transmutations produced by exposure to **a** fusion reactor first wall neutron spectrum (Table III). The largest contribution to the thermal conductivity degradation is due to Ni. followed by Co and Zn. The accumulation of solid transmutation products alone causes the thermal conductivity of copper to be reduced to 66% of its initial value after 2 **MW-yr/m^2** (30 dpa). Figure 21 also shows the calculated change in the thermal conductivity of copper alloys with an initial thermal conductivity of 340 W/m-K (comparable to unirradiated CuCrZr and oxide dispersion-strengthened Cu, Fig. 1) and 210 W/m-K (comparable to unirradiated CuNiBe). The degraded thermal conductivity due *to* transmutation product formation after 2 MW-yr/m^2 in these two cases are 237 and 165 W/m-K, respectively.

Void swelling produces an additional degradation in **the** thermal conductivity of copper and copper alloys [17,18,77,122,124]. Experimental studies [122,124] have confirmed that the void swelling contribution to conductivity **loss** ***can*** be described by a simple mixing *rule* (originally derived by Maxwell), $\rho/\rho_m=[(1+0.5\ \Delta V)/(1-\Delta V)]$, where ρ_m is the matrix resistivity and AV is the volume fraction of cavities. **This** relationship is valid when the average cavity size is **larger** than the electron mean free path in the matrix material, which is –30 nm for pure copper at room temperature. Assuming a design limit for radiation-induced swelling of **5%.** the corresponding degradation in the thermal conductivity beyond that due to solid transmutation effects is 8%. Therefore, void swelling produces relatively minor changes in the thermal conductivity of swelling-resistant copper alloys.

A **final** factor that influences the thermal conductivity of irradiated copper alloys is the stability of the precipitate structure and its interaction with transmutation-produced solute. Experimental measurements have **shown** that the conductivity of neutron-irradiated copper alloys can be larger or smaller than the preirradiation value **[17,18,74,77,122,124].** The conductivity increases occur in some alloys with initial thermal conductivities below **–250** W/m-K, or ***in*** precipitation-strengthened alloys which were not heat treated to produce maximum conductivity. Radiation-enhanced precipitation and aging is the likely mechanism responsible for the conductivity increases in these low- to medium-conductivity alloys. It **has** been suggested that complex solute redistribution processes may occur in some irradiated alloys, involving the transmutation solute atoms and solute ejected from pre-existing precipitates (ballistic dissolution) [70,74,78]. These processes can produce decreases in the thermal conductivity of neutron-irradiated CuNiBe that are larger than predicted by Eq. 2 [74]. Large decreases in conductivity may occur if a high density of small precipitates are formed during irradiation, since this type of microstructure is very effective in reducing the conductivity [127].

Several studies have examined the radioactivation characteristics of copper and copper alloys exposed to a fusion fust wall neutron spectrum [5,105,128]. The overall radiological hazard of copper is comparable to other structural materials such as Type 316 austenitic stainless steel [5,128]. The alloying elements in the high-strength, high-conductivity copper alloys under consideration for fusion reactor applications (Table II) generate a radiation hazard that is similar to pure copper [105].

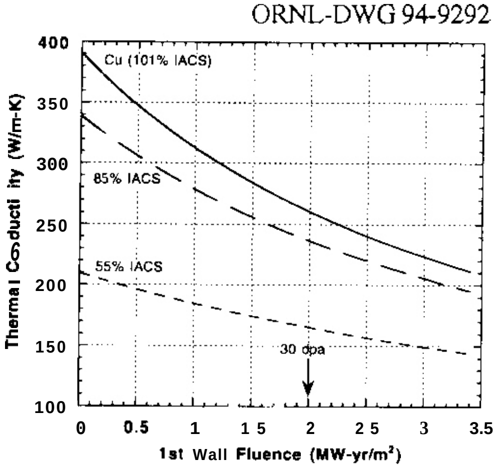

FIG. 21. Effect of solid transmutations on the thermal conductivity of copper at a fusion reactor first wall. The calculations were performed for three different initial conductivities, expressed in terms of percent International *Annealed* Copper **Standard** (IACS).

4. JOINING

Copper alloys can be joined by a variety of techniques, including welding, brazing and diffusion bonding [1,129]. Welding is generally not used for joining high-strength copper alloys, however, for several reasons. The precipitates in high-strength alloys such as CuCrZr and CuNiBe are subject to partial or complete dissolution in the melt layer of the weld joint. Therefore, the entire welded component must be solutionized and aged to recover some of the initial precipitation hardening in the joint. In addition, very high strengths generally cannot be achieved in the joint region after welding since the precipitation-strengthened copper alloys require cold working to attain their optimum strength. In some cases it is possible to design the joint region so that it can be cold worked after welding [130]. Oxide dispersion-strengthened copper cannot be welded by conventional techniques due to aggregation of the oxide particles in the melt layer, which destroys the uniform panicle spacing that is needed to produce high strength. Recrystallization would also occur in the melt layer. Welded GlidCop alloys have been shown to have very poor radiation resistance [70,78,80].

Brazing is the most common method for joining copper alloys. Copper alloys are typically brazed at temperatures between 600 and 950°C with hold times at the brazing temperature ranging from –10 seconds (torch, resistance, or induction brazing) to –10 minutes (furnace brazing). The most common brazing filler metals are Cu-, Ag- and Au-base alloys [129]. Oxide dispersion-strengthened copper has been successfully joined using torch [131,132], furnace [131], resistance [134] and induction [133,135] brazing. Due to the high recrystallization temperature of dispersion-strengthened copper, significant softening does not occur in the base metal at the brazing temperature (see, e.g. Fig. 6). On the other hand, precipitation-hardened copper alloys typically soften during furnace brazing (ref. [129] and Fig. *5).* The amount of softening in the base metal of precipitation-hardened alloys can be minimized by using torch, resistance or induction brazing, which limit the time that the base metal is at high temperature to less than one minute. Alternatively. the brazed component can be aged following furnace brazing to recover some of its initial strength. Complete recovery of high strength after furnace brazing by heat treatment is rather difficult in practice since the component must be heated to a temperature greater than typical brazing temperatures and rapidly quenched to create a supersaturation of solute prior to aging. For example, the strength of solutionized & aged CuCrZr alloys exposed to a solution anneal temperature of 900°C before aging is about 90% of the strength of alloys given a solution anneal at 1000°C [27]. As mentioned previously, the precipitation-hardened copper alloy would require cold working following furnace brazing in order to achieve the optimum strength.

The fine grain structure of wrought oxide dispersion-strengthened copper creates problems when trying to furnace braze with Ag-base braze alloys [131]. The grain boundary diffusion coefficient of Ag in copper is much larger than the bulk diffusion coefficient. Therefore, excessive diffusion of silver along grain boundaries can occur during furnace brazing of dispersion-strengthened copper. The rapid grain boundary diffusion of Ag can cause the formation of small voids in the braze region and poor joint strength. Cold-worked precipitation-hardened alloys have a fine grain structure that is similar to dispersion-strengthened copper. However, the precipitation-hardened alloys suffer recrystallization during the typical furnace braze cycle (with accompanying loss of strength). The resultant increase in the grain size during recrystallization minimizes the number of grain boundaries available for Ag diffusion, and effectively inhibits Ag depletion in the braze joint of precipitation-hardened alloys. The excessive diffusion of Ag from the braze region in furnace brazed dispersion-strengthened copper can be prevented by electroplating the joint surfaces with 10 to 50 μm of copper or nickel prior to brazing [131,135]. The large grain boundaries in the plated layer act as a banier for grain boundary diffusion of silver. Alternatively, joints with satisfactory shear strength can be obtained in dispersion-strengthened copper with Ag-base braze alloys by torch [131,132] or induction [133,135] brazing.

The highest mechanical strength braze joints in alloys such as oxide dispersion-strengthened copper are produced using Au-base braze alloys [131]. The grain boundary diffusion coefficient of gold in copper is low enough to prevent excessive depletion of An from the joint region during furnace brazing. Therefore. fme-grained high-strength copper alloys can be furnace brazed using Au-based alloys without prior electroplating. The measured room temperature shear strength of GlidCop AL-15 and AL-25 brazed with Au-Cu filler metals was 200 to 240 MPa [131]. The typical shear strength of GlidCop alloys brazed with Ag-base filler metals was 150 to 200 MPa [131,133, 135]. A room temperature tensile strength of 380 MPa was measured for a torch-brazed GlidCop AL-15 joint prepared with Ag-base foil, and the joint did not fail during fatigue testing up to 80,000 cycles at a stress amplitude of 276 MPa [132]. The fatigue strength of brazed copper joints is generally comparable to the base metal strength [55,56,132], although lower braze joint fatigue strengths have also been reported [133,134]. The ductility of the braze joint is generally much lower than the base metal [131,133-135]. Neutron irradiation studies on brazed GlidCop joints are in progress. Transmutation calculations indicate that significant burnup of the Ag and Au used in many braze alloys would occur in a fusion fust wall neutron spectrum [136], which could affect the mechanical properties of the braze joint. The calculations indicate that approximately 40% of Ag and 55% of Au would be burned up by exposure to a first wall fluence of 2 MW·yr/m^2 (30 dpa).

Joints with high mechanical strength can be produced in dispersion-strengthened copper alloys by diffusion bonding. Shear strengths comparable to that of the base metal (–300 MPa) have been obtained by applying 5 to 100 MPa pressure for –1 hour at 900 to 930°C [131,137]. These diffusion-bonding conditions are similar to the conditions normally employed for the hot isostatic pressure consolidation of GlidCop powder billets [131]. Diffusion bonding cannot be used to produce high strength joints in precipitation-hardened alloys, since unacceptable softening of the base metal occurs during exposure to the high temperatures necessary for effective solid state bonding. An attempt to diffusion bond precipitation-hardened Cu-Zr at 500°C produced a low hydrostatic bond strength of <17 MPa [138].

5. CORROSION

Copper and its alloys are widely known for their excellent corrosion resistance in water and other environments [1,139-141]. Surface corrosion rates below 10 μm/yr (–1 mg/dm^2-day) occur in copper exposed to water containing less than 1000 ppm oxygen at room temperature [139]. Pitting occurs in copper exposed to water containing high concenmtions of CO$_2$. The presence of aqueous ammonia causes preferential attack at grain boundaries [139] and stress corrosion cracking in copper alloys [140,141]. The corrosion behavior of the three high-strength copper alloys considered to be most promising for fusion applications (CuCrZr, CuNiBe and oxide dispersion-strengthened copper) should be similar to that of pure copper. However, residual stresses associated with cold working are known to increase the susceptibility of copper alloys to stress corrosion cracking [140].

Very little is known about the effect of irradiation on the corrosion of copper and copper alloys [18,139]. Satisfactory corrosion resistance was observed for several high strength copper alloys that were exposed to flowing water (–0.5 m/s) during neutron irradiation near 90°C to a damage level of –1 dpa [18]. The weight loss was about 5 times less in a CuCrZr alloy compared to MAGT 0.05 and MAGT 0.2 dispersion-strengthened copper. The possibility of irradiation-assisted stress corrosion cracking apparently has not been investigated in copper or copper alloys.

6. CONCLUSIONS

Most of the mechanical and physical properties of high-strength copper alloys needed for a qualitative evaluation of their suitability for high heat flux structural applications have been measured. Three types of copper alloys are commercially available which *appear* to have suitable properties for fusion reactor high heat flux applications: CuCrZr, CuNiBe, and oxide dispersion-strengthened copper. Due to the dependence of the physical and mechanical properties of these alloys on thermomechanical processing, additional property measurements would be required on specific prototypic heats in order to develop a comprehensive set of engineering design data for ITER. There are few available data on thermal fatigue, creep, fracture toughness, and near-threshold fatigue crack growth rates in high-strength copper alloys. In addition, there is a general lack of data on the effect of neutron irradiation on the properties of high-strength copper alloys at ITER-relevant temperatures of 50 to 350°C. The effects of irradiation on creep, fatigue, fracture toughness and corrosion of base metal and joints needs further study. In particular, the ductility reductions associated with neutron irradiation at 50 to 250°C needs to be quantified in cold-worked, wrought, and solutionized & aged alloys.

The precipitation-hardened CuCrZr and CuNiBe alloys are susceptible to significant radiation-enhanced softening during operation at temperatures above ~275°C. Both alloys appear to be promising for high heat flux structural applications if the operating temperature can be maintained below 275°C. The solutionized & aged strengths should be used for engineering design purposes rather than the more commonly quoted cold-worked & aged strengths of these two alloys, since joining operations will likely cause recrystallization with accompanying softening. The data base on CuNiBe is very limited compared to CuCrZr and dispersion-strengthened copper, which makes it difficult to evaluate its suitability for ITER.

Dispersion-strengthened copper and precipitation-hardened CuCrZr have similar mechanical and physical properties at temperatures between 20 and 300°C. Oxide dispersion-strengthened copper has a considerable advantage over all precipitation-hardened copper alloys in tams of high temperature creep resistance and strength retention after exposure to elevated temperatures. The main disadvantages associated with dispersion-strengthened copper are that it is only available in wrought form and it cannot be welded. Dispersion-strengthened copper can be satisfactorily joined by brazing or diffusion bonding. Considering the published data on mechanical properties (base metal and joints), thermal conductivity, and radiation stability, oxide dispersion-strengthened copper appears to be the most promising high strength copper alloy for high heat flux structural applications.

REFERENCES

1. ASM Metals Handbook, 10th ed., Vol. 2 , Properties and Selection: Nonferrous Alloys and Special-Purpose Materials, ASM International, Metals Park, OH (1990) 216-427.

2. E. Ling and P.W. Taubenblat (Eds), High Conductivity Copper and Aluminum Alloys, The Metallurgical Society of AIME, Warrendale, PA (1984).

3. S.J. Zinkle and R.W. Knoll, A Literature Review of Radiation Damage Data for Copper and Copper Alloys, UWFDM-578, Univ. Wisconsin Nucl. Eng. Dept., Madison, WI, June 1984.

4. K.R. Anderson and D.S. Gelles, ITER Materials Data Base for Irradiation Effects on the Design Properties of Cu-Ni-Be and $Cu-Al_2O_3$ Alloys, Fusion Reactor Mater. Semiann. Prog. Report DOE/ER-0313/5, April 1989, pp. 268-279.

5. G.J. Butterworth and C.B.A. Forty, J. Nucl. Mater. **189** (1992) 237.

6. S.J. Zinkle, in Effects of Radiation on Materials: 15th Int. Symp., ASTM STP 1125 (R.E. Stoller, et al., Eds.), American Soc. for Testing and Materials, Philadelphia (1992) 813-834.

7. W.B. Gauster, At. Plasma-Mater. Interact. Data Fusion, **5** (1994) in press.

8. CRC Handbook of Chemistry and Physics, 59th Ed. (R.C. Weast, Ed.), CRC Press, Boca Raton, Florida (1978).

9. G. Simmous and H. Wang, Single Crystal Elastic Constants and Calculated Aggregate Properties: A Handbook, MIT Press, Cambridge, MA (1971) p. 181.

10. S.J. Zinkle. Effects of Thermal Annealing and Ion Irradiation on the Properties and Microstructures of Copper Alloys, Ph.D. Thesis, Univ. Wisconsin-Madison Nucl. Eng. Dept. report UWFDM-642, May 1985.

11. A.V. Nadkami. in ref. [2], pp. 77-101.

12. F.R. Mollard. K.G. Wilke and A.R. Chaudry, in ref. [2], pp. 147-168.

13. A. Guha, in ref. [2], pp. 133-145.

14. A. Rotem and A. Rosen, Metall. Trans. A **16** (1985) 2073.

15. SCM Metal Products, Inc., technical data brochure on GlidCop® dispersion-strengthened copper

16. T.J. Miller, S.J. Zinkle and B.A. Chin, J. Nucl. Mater. **179-181** (1991) 263-266.

17. H.R. Brager, H.L. Heinisch and F.A. Gamer, J. Nucl. Mater. **133&134** (1985) 676-679.

18. I.V. Gorynin, S.A. Fabritsiev. V.V. Rybiu et al., J. Nucl. Mater. **191-194** (1992) 401-406.

19. G. Piatti and D. Boerman, J. Nucl. Mater. **185** (1991) 29-38.

20. KM-Kabelmetal, technical data brochure on Cu alloy moulds for continuous casting (Elbrodur® Cu-Cr-Zr alloys).

21. Materials Handbook for Fusion Energy Systems, DOE/TIC-10122, McDonnell Douglas, St. Louis, Missouri (1991).

22. R.E. Reed-Hill, Physical Metallurgy Principles, 2nd ed., Brooks/Cole-Wadsworth, Inc.. Monterey, California (1973) pp. 267-325.

23. P.W. Taubenblat, W.E. Smith and A.R. Graviano. in ref. 2, pp. 19-29

24. H. Suzuki, M. Kanno and I. Kawakatsu, J. Japan Inst. Metals **33** (1969) 628-633.

25. A.K. Lee and N.J. Grant Mater. Sci. and Engineering **60** (1983) 213-223.

26. W. Vandermeulen, V. Massaut, J. Van de Velde and W. Hendrix, in Proc. 14th Symp. on Fusion Technology, Pergamon Press, New York (1986) pp. 1031-1035.

27. H. Suzuki, I. Kawakatsu and H. Kitano, J. Japan Inst Metals 31 (1967) 342-346.

28. N.J. Grant, A. Lee and M. Lou, in ref. [2], pp. 103-117.

29. S.J. Zinkle, D.H. Plantz, AE. Bair, R.A. Dodd and G.L. Kulcinski, J. Nucl. Mater. **133&134** (1985) 685-689.

30. E.N.C. Dalder, W. Ludemann and B. Schumacher. in Proc. Workshop on Copper and Copper Alloys for Fusion Reactor Applications (F.W. Wiffen and R.E. Gold, Eds.), CONF-830466, National Tech. Information Service, Springfield, Virginia (1984) pp. 251-307.

31. J.J. Stephens, R.J. Bourcier, F.J. Vigil and D.T. Schmale, SAND88-1351, Sandia National Laboratories (1988).

32. T.S. Srivatsan, S. Anand and J.D. Troxell, Eng. Fracture Mechanics **46** (1993) 183-198.

33. V.R. Barabash, G.L. Saksagansky, Y.F. Shevakin et al., ITER Specialist Meeting on Materials Data Base, ITER-IL-NE-1-0-3 (Feb. 1990).

34. S.A. Fabritsiev, V.V. Rybin, V.A. Kasakov, A.S. Pokrovskii and V.R. Barahash, J. Nucl. Mater. **195** (1992) 173-178.

35. S.A. Fabritsiev, V.V. Rybin. V.A. Kasakov, A.S. Pokrovskii and V.R. Barabash, J. Nucl. Mater. **195** (1992) 179-183.

36. S.A. Fabritsiev, V.R. Barabash, Y.G. Prokofiev and AS. Pokrovsky, "Neutron Spectrum and Transmutation Effects on the Radiation Damage on Copper Alloys", Proc. 6th Int. Conf. on Fusion Reactor Materials, J. Nucl. Mater., in press (1994).

37. S.N. Rosenwasser, in ref. [30], pp. 309-329.

38. S.J. Zinkle, in Alloy Development for Irradiation Performance Semiann. Progress Report for period ending March 31, 1986, DOE/ER-0045/16, pp. 163-167.

39. JE. Synk and K. Vedula. Mater. Sci. and Technology **3** (1987) 72-75.

40. JJ. Stephens and D.T. Schmale, SAND87-1296, Sandia National Laboratories (1987).

41. G. Piatti and H.A. Weir, J. Nucl. Mater. **150** (1987) 1-9.

42. SN. Rosenwasser, R.D. Stevenson, G. Listvinsky, D.L. Vrable. J.E. McGregor and N. Nir, J. Nucl. Macer. **122&123** (1984) 1107-1120.

43. O.K. Harling, G.P. Yu, N.J. Grant and J.E. Meyer, J. Nucl. Mater. **103&104** (1981) 127.

44. J. Groza, J. Mater. Eng. and Performance **1** (1992) 113-121

45. N.Y. Tang, D.M.R. Taplin and G.L. Dunlop, in Proc. 6th Int. Conf. on Strength of Metals and Alloys, Vol. 2 (R.C. Gifkins, Ed.), Pergamon Press. New York (1983) pp. 665-670.

46. W.D. Nix and J.C. Gibeling, in Flow and Fracture at Elevated Temperatures (R. Raj, Ed.) Amer. Soc. for Metals, Metals Park, Ohio (1985) p. 50.

47. S.J. Zinkle, R.A. Dodd and G.L. Kulcinski, in 12th Int. Symp. on Effects of Radiation on Materials, Vol. 1, ASTM STP 870 (F.A. Gamer and J.S. Pemn, Eds.) Amer. Soc. for Testing and Mater.. Philadelphia (1985) 363-382.

48. C. Bushnell and R. Ellis, Princeton University reports F-900216-PPL-04 (GlidCop AL-15), F-900403-PPL-03 (Brush-Wellman CuNiBe), F-900404-PPL-03 (Elbrodur CuCrZr), F-900430-PPL-03 (Brush-Wellman overaged CuNiBe), and F-900518-PPL-04 (OFHC Cu), 1990.

49. A.J. Kennedy, **Processes** of Creep and Fatigue in Metals, John Wiley & Sons, Inc., New York **(1963)** pp. **289-313.**

50. P.W. Taubenblat, W.R. Opie and Y.T. Hsu, Met. Eng. Quarterly **12 (1972)** 4145.

51. A. Singhal. **J.F.** Stubbins, B.N. Singh and **F.A.** Gamer, **Proc.** 6th Int. Conf. on Fusion Reactor Materials, J. Nucl. Mater.. in press **(1994).**

52. B.G. Gieseke, Oak Ridge National Laboratory, private communication **(1994).**

53. A.L.W. Collins, D.M.R. Taplin and V. Singh, 2nd Int. Conf. on Mechanical Behavior of Materials, **Amer.** Soc. for Metals. Metals Park. Ohio **(1976)** pp. **871-875.**

54. V. **Singh** and D.M.R. Taplin, Bull. Electron Microsc. **Soc.** India **2 (1978) 17-18.**

55. K.C. **Liu** and C.M. Loring, Jr., J. Nucl. Mater. **122&123 (1984) 783-788.**

56. M. Seki, T. Horie, T. Tone et al., J. Nucl. Mater. **155-157 (1988)** 392-397.

57 W.A. Logsdon and P.K. Liaw. J. Mater. Eng. **9 (1987) 63-69.**

58. DJ. Alexander, *Oak* Ridge National Laboratory, private communication **(1994).**

59. J.G. Kaufman and J.S. Santner, in Application of Fracture Mechanics for Selection of Metallic Structural Materials **(JE.** Campbell. W.W. Gerberich and J.H. Underwood, Eds.), **Amer.** Soc. for Metals. Metals Park, Ohio **(1982)** pp. **169-211.**

60. T-S Lee, L.W. Hobbs, G. Kohse et al., **J.** Nucl. Mater. **141-143 (1986)** 179-183.

61. H.R. Brager. J. Nucl. Mater. **141-143 (1986) 163-168.**

62. N. Wanderka, C. Ramachandra, R.P. Wahi, and H. Wollenberger. **J.** Nucl. Mater. **189 (1992)** 9-**13.**

63. N. Wanderka, Y. Yuan, L. Jiao, R.P. Wahi and H. Wollenberger, J. Nucl. Mater. **191-194 (1992)** 1356-1359.

64. E.V. Nesterova, V.V. Rybin. **S.A.** Fabritsiev and V.R. Barabash. J. Nucl. Mater. **191-194 (1992)** 407-410.

65. V.R. Barabash, **A.A. Gervash, A.V.** Naberenkov et al., **J.** Nucl. Mater. **191-194 (1992)** 411.

66. **J.A.** Spitznagel, NJ. Doyle, WJ. Choyke et al., Nucl. Instr. Meth. B **16 (1986)** 279-287.

67. R.J. Livak. T.G. Zocco and L.W. Hobbs, J. Nucl. Mater. **144 (1987) 121-127.**

68. S.J. Zinkle, E.V. Nesterova, V.R. Barabash, V.V. Rybin and **A.V.** Naberenkov, J. Nucl. Mater. **208 (1994) 119-127.**

69. D.J. **Edwards, F.A.** Gamer, J.W. Newkirk and **A.** Nadkami, **Proc. 6th** Int. Conf. on Fusion Reactor Materials, J. Nucl. Mater., in press **(1994).**

70. D.J. **Edwards,** J.W. Newkirk, **F.A.** Gamer et al., in Effects of Radiation on Materials: **16th** Int. Symp., **ASTM** STP **1175 (A.S.** Kumar et al.. Eds.), American Soc. for Testing and Materials, Philadelphia **(1994) 1041-1060.**

71. **S.J.** Zinkle and K. Farrell, J. Nucl. Mater. **168** (1989) 262-267.

72. **SJ.** Zile, K. Farrell and H. Kanazawa, J. Nucl. Mater. **179-181** (1991) 994-997.

73. BN. Singh, A. Horsewell, D.S. Gelles and F.A. Gamer, **J.** Nucl. Mater. **191-194** (1992) 1172-1176.

74. F.A. Gamer, M.L. Hamilton, T. Shikama, DJ. Edwards and J.W. Newkirk, J. Nucl. Mater. **191-194** (1992) 386-390.

75. K. Yamakawa I. Mukouda and Y. Shimomura, J. Nucl. Mater. **191-194** (1992) 396-400

76. F.A. Gamer, H.R. Brager and K.R. Anderson, J. Nucl. Mater. **179-181** (1991) 250-253.

77. O.K. Harling, NJ. **Grant G.** Kohse et al., J. Mater. Res. **2** (1987) 568-579.

78. DJ. Edwards, K.R. Anderson, F.A. Gamer et al., J. Nucl. Mater. **191-194** (1992) 416-420.

79. F.A. Gamer, DJ. Edwards, B.N. Singh and H. Watanabe, in Fusion Reactor Materials Semiann. Prog. Report DOE/ER-0313/13, Sept. 1992, pp. 253-254.

80. K.R. Anderson, F.A. Gamer, M.L. Hamilton and J.F. Stubbins, in Effects of Radiation on Materials: 15th Int. Symp.. ASTM STP 1125 (R.E. Stoller, et al., **Eds.),** American Soc. for Testing **and** Materials, Philadelphia (1992) 854-874.

81. **SJ.** Zinkle, G.L. Kulcinski and L.K. Mansur. **J.** Nucl. Mater. **141-143** (1986) 188-192.

82. P. Fenici. D.J. Boerman, G.P. Tartaglia and J.D. Elen, in Proc. 6th Int. Conf. on Fusion Reactor Materials, J. Nucl. Mater., in press (1994).

83. J.C. Wilson, in Proc. 2nd UN Int. Conf. on Peaceful Uses of Atomic Energy, Vol. 5, United Nations, Geneva (1958) pp. 431-445.

84. I.A. El-Shanshoury. J. Nucl. Mater. **45** (1972/73) 245-257.

85. H.G. Mohamed, A.M. Hammad and F.H. Hammad, Trans. lnd. Inst. Metals **35** (1982) 258.

86. S.J. Zinkle, A. Horsewell, B.N. Singh and W.F. Sommer, in Proc. 6th lnt. Conf. on Fusion Reactor Materials, J. Nucl. Mater., in press (1994).

87. **SJ.** tinkle and W.C. Oliver, **J.** Nucl. Mater. **141-143** (1986) 548-552.

88. M. Appello and P. Fenici, J. Nucl. Mater. **152** (1988) 348-350.

89. T. Shikama, F.A. Garner, M.L. Hamilton and K.R. Anderson, in Effects of Radiation on Materials: 15th Int. Symp.. ASTM STP 1125 (R.E. Stoller, et al., Eds.), American Soc. for Testing and Materials, Philadelphia (1992) 846-853.

90. R.J. Livak, H.M. Frost, T.G. Zocco, J.C. Kennedy and L.W. **Hobbs,** J. Nucl. Mater. **141-143** (1986) 160-162.

91. H.L. Heinisch and C. Martinez, J. Nucl. Mater. **141-143** (1986) 883-887.

92. H.L. Heinisch, M.L. Hamilton, W.F. Sommer and P.D. Ferguson, J. Nucl. Mater. **191-194** (1992) 1177-1182.

93. M.J. Makin, in Radiation Effects (W.F. Sheely, Ed.), Gordon & Breach, New York (1967) 627-669.

94. R.B. Adamson, Trans. Metall. Soc. AIME 239 (1967) 714-720.

95. F.C. Strible and J.R. Cady, J. Appl. Phys. 43 (1972) 417424.

96. S.H. Goods, in Effects of Radiation on Materials: 14th Int. Symp., ASTM STP 1046, Vol. I (N.H. Packan et al., Eds.) American Soc. for Testing and Materials. Philadelphia (1989) 340-352.

97. S.H. Goods, Scripta Met 20 (1986) 565-569.

98. S.A. Fabritsiev, V.R. Barabash, Y.G. Prokofiev and A.S. Pokrovsky, "The Neutron Irradiation Induced 400 C Embrittlement of Copper Alloys". Proc. 6th Int. Conf. on Fusion Reactor Materials, J. Nucl. Mater., in press (1994).

99. P. Jung, J. Nucl. Mater. 200 (1993) 138-140.

100. Sh. Sh. Ibragimov, E.S. Aitkhozhin and Yu.S. Pyatiletov, in Influence of Radiation on Material Properties: 13th Int. Symp., Vol. II, ASTM STP 956 (F.A. Gamer et al., Eds.) American Soc. for Testing and Materials. Philadelphia (1987) 5-10.

101. L.R. Greenwood and R.K. Smither. ANL-FPP/TM-197 (Argonne National Lab., Argonne, IL, 1985).

102. T.A. Gabriel, B.L. Bishop and F.W. Wiffen. ORNL/TM-6361 *(Oak* Ridge National Lab., *Oak* Ridge, TN, 1979).

103. R.L. Hagenson and R.A. Krakowski, in ref. [30], 87-128.

104. L.J. Perkins, J. Nucl. Mater. 122&123 (1984) 1371-1375.

105. G.J. Butterworth, J. Nucl. Mater. 135 (1985) 160-172.

106. F.A. Garner, L.R. Greenwood and F.M. Mann. in Fusion Reactor Materials Semiann. Prog. Report DOE/ER-0313/13, Sept. 1992, pp. 4247.

107. Standard Practice for Neutron Radiation Damage Simulation by Charged Particle Irradiation, E521-89, Annual Book of ASTM Standards, Vol. 12.02, American Soc. for Testing and Materials, Philadelphia (1990).

108. F.A. Gamer, H.L. Heinisch. R.L. Simons and F.M. Mann. Rad. Effects Def. Solids 113 (1990) 229-255.

109. R.A. Lillie, *Oak* Ridge National Laboratory (1984, 1990) private communication.

110. E. Fromm and E. Gebhardt, Eds., Gase und Kohlenstoffe in Metallen, Springer-Verlag. New York (1976).

111. G.R. Caskey, Jr., A.H. Dester, M.L. Holzworth, M.R. Louthan, Jr. and R.G. Derrick, Corrosion-NACE 32 (1976) 370-374.

112. W.R. Wampler, T. Schober and B. Lengeler, Phil. Mag. 34 (1976) 129-141.

113. D.B. Butrymowicz, J.R. Manning and M.E. Read, Diffusion Rate Data and Mass Transport Phenomena for Copper Systems, INCRA Series on The Metallurgy of Copper. National Bureau of Standards, Washington, DC. (1977); also J. Phys. Chem. Ref. Data 4 (1975) 177-249.

114. S.A. Stewart, UCRL-53441. Lawrence Livermore National Lab., Livermore, California (1983)

115. T N. Kompaniets and A.A. Kurdyumov, Prog. **Surf.** Sci. **17** (1984) 75.

116. F. Besenbacher. S.M. Myers and J.K Nørskov, Nucl. Instr. Meth. B **7/8** (1985) 55-66.

117. W.A. Swansiger, Fusion Technol. **14** (1988) 631-636.

118. WD. Wilson and C.L. Bisson, Rad. Effects **19** (1973) 53-58.

119. M.I. Baskes and C.F. Melius, Phys. Rev. B **20** (1979) 3197-3204.

120. W.Th.M. Buters, A. van Veen and A. van den Beukel, Phys. Stat. Sol. (a) **100** (1987) 87-94

121. T. Tanabe, Y. Yamanishi, K. Sawada and S. Imoto, J. Nucl. Mater. **122&123** (1984) 1568.

122. H.M. Frost and J.C. Kennedy, J. Nncl. Mater. **141-143** (1986) 169-173.

123. S.J. Zinkle, J. Phys. F Met. Phys. **18** (1988) 377-391.

124. D.J. Edwards, F.A. Garner and L.R. Greenwood, Proc. 6th Int. Conf. on Fusion Reactor Materials, J. Nncl. Mater., in press (1994).

125. C.Y. Ho, M.W. Ackerman, K.Y. Wu et al., J. Phys. Chem. Ref. Data **12** (1983) 183-320.

126. K. Schroeder, CRC Handbook of Electrical Resistivities of Binary Metallic Alloys, CRC Press. Boca Raton, Florida (1983).

127. A.J. Hillel and P.L. Rossiter, Phil. Mag. B **44** (1981) 383-388.

128. S.J. Piet, E.T. Cheng and L.J. Porter, Fusion Technol. **17** (1990) 636-657.

129. MM. Schwartz, Brazing. ASM International, Metals **Park,** Ohio (1987)

130. H. Kimoto, H. Kojima, S. Hioki et al., Proc. 12th Symp. on Fusion Technology, Vol. 2, Pergamon Press, New York (1983) 1045-1050.

131. P.K. Samal, Brazing and Diffusion Bonding of GlidCop® Dispersion Strengthened Copper, SCM Metals, Research Triangle Park, North Carolina, in The Metal Science of Joining, The Minerals, Metals and Materials Society, Warrendale, PA (1992) 295-305.

132. T.J. McManamy, R.D. Benson, R.L. Brown, et al, Design and Fabrication of a Prototype Solenoid for the Spherical Torus Experiment, Oak Ridge National Lab. Oak Ridge, Tennessee (1987)

133. C-K Lee, B.A. Chin, S.J. Zinkle and R.C. Wilcox, in Effects of Radiation on Materials: 16th Int. Symp., ASTM STP 1175 (A.S. Kumar et al., Eds.), American Soc. for Testing and Materials, Philadelphia (1994) 1026-1040.

134. S.F. Chen, J.Y. Liu and B.A. Chin, Proc. 6th Int. Conf. on Fusion Reactor Materials, J. Nucl. Mater., in press (1994).

135. A.A. McFayden, **R.R.** Kapoor and T.W. Eagar, Welding J. ***69*** (1990) 399s-407s.

136. F.A. Gamer, L.R. Greenwood and D.J. Edwards, in Fusion Reactor Materials Semiann. Prog. Report DOE/ER-0313/16, April 1994, in press.

137. H. Nishi. Y. Muto and K. Sato, Proc. 6th Int. Conf. on Fusion Reactor Materials, J. Nucl. Mater.. in press (1994).

138. C. Logan, J. Dini, W. Ludemann et al., J. Nucl. Mater. 103&104 (1981) 1551-1556.

139. P.T. Gilbert, in Copper: The Science and Technology of the Metal, its Alloys and Compounds, (A. Butts. Ed.), Reinhold Publ., New York (1954) 379-409.

140. H. Leidheiser, Jr., The Corrosion of Copper, Tin and Their Alloys, Wiley & Sons, New York (1971).

141. J.A. Beavers, in Stress Corrosion Cracking (R.H. Jones. Ed.), ASM International, Metals Park, Ohio (1992) 211-231.

ROOM TEMPERATLJRE FATIGUE BEHAVIOR OF OFHC COPPER AND CUAL25 SPECIMENS OF TWO SIZES -

A. Singhal, and JF. Stubbins, (University of Illinois), B.N. Singh, (RISØ National Laboratory), and F.A. Gamer, (Pacific Northwest Laboratory')

OBJECTIVE

The objective of this effort is to determine the impact of specimen size on fatigue behavior of copper alloys now being irradiated in EBR-II and DR-3. These data and size effects correlations will be used to develop fatigue equations for application to ITER design.

SUMMARY

Copper and its alloys are appealing for application in fusion reactor systems for high heat flux components where high thermal conductivities are critical, for instance, in divertor components. The thermal and mechanical loading of such components will be, at least in part, cyclic in nature, thus requiring an understanding of their fatigue behavior. This report describes the room temperature fatigue behavior *of* unirradiated OFHC (oxygen free high conductivity) copper and CuAl25 (copper strengthened with a 0.25% atom fraction dispersion of alumina). The response of two fatigue specimen sires to strain controlled fatigue loading is examined, and differences in behavior are discussed. Specimens with the smaller sire are now being irradiated in several reactors.

PROGRESS AND STATUS

Introduction

Copper is attractive for a variety of high thermal loading applications due to its excellent thermal conductivity. Irradiation studies [1, 2] indicate that while the thermal conductivity degrades with increasing irradiation, the decline is predictable and not catastrophic even at very high doses. Alloys of copper show similar trends but usually possess somewhat lower initial thermal conductivities. There is, therefore, considerable interest in employing copper and its alloys for high heat flux applications. The alloy must also be capable of performing as a component structural material, withstanding thermal and mechanical loading under a variety of static and cyclic loading conditions to temperatures up to nearly half of its melting point.

The mechanical properties of copper and its alloys have been studied to a limited extent because of the intrinsic material behavior of copper, but not extensively for structural applications. This is due to copper's slip properties and stacking fault energy, which result in a low yield strength, a large degree of strain hardening, and a high sensitivity to multiaxial loading. Some of these limitations, however, can be offset by alloying or by dispersion strengthening.

This study examines the fatigue response of both unalloyed copper and an oxide dispersion-strengthened copper alloy to determine their suitability for potential fusion application in high heat flux components.

"Pacific Northwest Laboratory is operated for the U.S. Department of Energy by Battelle Memorial Institute under Contract DE-AC06-76RLO 1830.

Experimental Details

Oxygen-free high conductivity (OFHC) copper and CuA125 (Glidcop™) were fatigue tested under conditions of constant total strain amplitude at room temperature. The OFHC specimens were annealed at 550°C for two hours. The CuA125 was tested in the as-wrought condition characteristic of that which would most likely be used in component fabrication. Two specimen **sizes** were employed for both materials in order to establish the effect of specimen size on fatigue response. ASTM standard size fatigue specimens with 6.35 mm (0.25 in.) gauge diameter were compared with subsize specimens of 3.1 mm (0.12 in.) gauge diameter. The latter size was developed to fit in available irradiation capsules and is currently undergoing irradiation in DR-3 and EBR-II. Both specimens utilize uniform cross-section geometries. The specimen dimensions are shown in Figures 1 and 2.

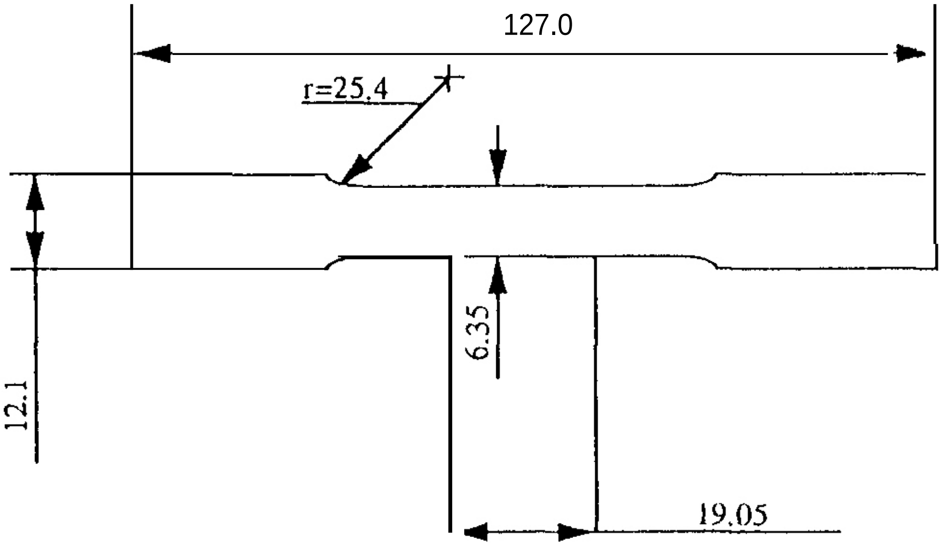

Fig. 1. ASTM standard size fatigue specimen dimensions.

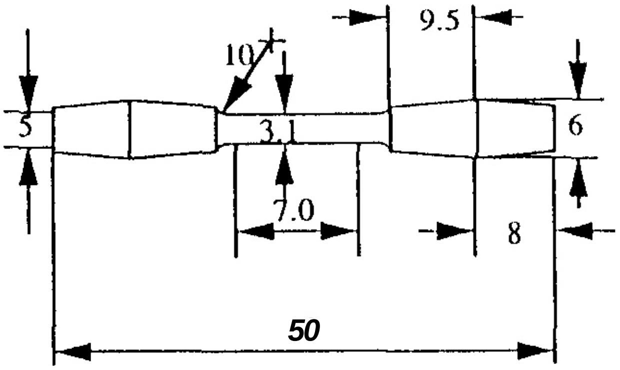

Fig. 2. Subsize fatigue specimen dimensions.

The fatigue experiments were performed on Instron closed-loop servohydraulic test frames, a different machine being used for each specimen size. Tests were performed in strain control and fully reversed ($R = -1$) with a frequency of 1 Hz. Strain ranges from 0.20 to 1.2% were examined for CuAl25 and from 0.10 to 0.35% for OFHC copper. The latter testing was limited by specimen stability at the higher strain ranges, where specimen buckling became unavoidable. Strain was monitored by using 7.62 mm (0.3 in.) and 12.70 (0.5 in.) gauge span extensometers for the small and large specimens, respectively. To prevent crack initiation at the point of contact of the extensometer arm to the specimen, small drops of epoxy were first placed on the specimen gauge section at the proper distance to accommodate the extensometer. The extensometer was then mounted on the epoxy drops. This method produced sound fatigue data which avoided early fatigue crack initiation due to the extensometry. Due to the tendency for buckling in the OFHC copper specimens, the specimens were cyclically loaded in increments of strain up to the test level. This also minimized the tendency for the development of mean loads due to the high strain-hardening response of OFHC copper. Full stress-strain hysteresis loops were recorded periodically throughout the test and were used to determine the elastic and plastic strain levels and the load levels throughout the test. The values reported for those parameters were taken at half the failure life ($N_f/2$) unless otherwise noted.

Results and Discussion

The fatigue response of the two materials and the two specimen sizes are shown in Figures 3 to 6. In addition to the plots of the life versus total strain, the dependence of the elastic and plastic portions of the strain ranges are shown. The fatigue behavior can be represented by the strain-life fatigue equation:

$$Ad2 = \sigma'_f/E \cdot (N_f)^b + \varepsilon'_f \cdot (N_f)^c,$$

where N_f is the number of cycles to failure, E is the elastic modulus, $\Delta\varepsilon/2$ is the total strain amplitude, and the other terms are material-dependent constants. The values of the constants are given in Table I for the test conditions examined here. The values of the exponents b and c are close to the commonly accepted values for a wide range of materials: $b \sim -0.1$ and $c \sim -0.5$. More data scatter arises for OFHC due to the smaller number of tests and the more limited range of strain amplitude that could be examined.

The elastic and plastic strain responses shown in Figures 3 through 6 indicate that the plastic response in CuAl25 does not contribute substantially to the failure life except at very short fatigue lives. The transition life (i.e., equal values of elastic and plastic strain range) occurs at about 1000 cycles for the larger specimens and around 400 cycles to failure for the smaller specimens. Thus the elastic response, which is principally controlled by material strength, dominates the fatigue response at intermediate and high lives.

In contrast, the plastic strain is the major contributor to fatigue response for OFHC copper at lives less than about 20,000 cycles to failure. This is consistent with the weaker, more ductile properties of this material compared to that of the dispersion-strengthened alloy.

The fatigue response of unalloyed copper has been examined in previous studies [3-9]. In most of these, the interest was in the high cycle fatigue behavior of this material where the relative contribution of plastic strain was small compared to the elastic component. However. some low cycle fatigue data are available for experimental conditions similar to those examined here [6-9]. The derived fatigue constants are given in Table I, and the fatigue life as a function of the plastic strain range is shown in Figure 7. The results of the present study are also shown. The lines in Figure 7 represent the best fit to the data over the range examined in the study. The present results are comparable with the two studies of Lukas and Kunz [7, 8]. In general, the results of Eckert et al. [9] deviate from those of other studies. Eckert has ascribed at least some of the differences to a change in the fracture mode at high strain ranges and low fatigue lives. Nevertheless, there are significant differences in the Eckert's results even in the range of fatigue lives where the failure lives overlap.

Previous examination of the fatigue response of dispersion-strengthened copper alloys is limited to CuAl15, an alloy with a lesser amount of dispersoid [10]. The results of the previous work, which was reported on the basis of maximum stress versus life, is compared in Figure 8 to the present results for CuAl25 based on the measured stress amplitude at half the failure life.

Table 1

Values of the Strain-Life Equation Constants

Material	Size	σ'_f/E*	b	E'f	c	Reference
CuAl25	Standard	780	-0.07	0.183	-0.55	This Study
CuAl25	Subsize	962	-0.10	0.148	-0.58	This Study
OFHC Cu	Standard	299	-0.08	0.106	-0.47	This Study
OFHC **Cu**	Subsize	378	-0.25	0.819	-0.69	This Study
OFHC Cu	Standard	**361**	-0.095	**0.455**	-0.581	Lukas and Kunz [7]
OFHC Cu	Standard	387	-0.107	0.0635	-0.457	Lukas and Kunz [8]
OFHC Cu	Standard	--	--	1.377	-0.25	Eckert et al. [9]

* assumes E = 129.8 GPa

The earlier work on CuAl15 was performed on miniature bend specimens [10], but the results have been confirmed by tests on standard size fatigue specimens of the same material [11]. The trend curves overlap **for** both materials at higher fatigue lives. In this region the elastic strain dominates and the ***data are*** well represented in the typical S-N fatigue format. The strain range, $\Delta\varepsilon/2$, can easily be converted to the stress amplitude, **S,** by multiplying it by the elastic modulus, E. It is not clear for CuAl25 whether a fatigue endurance limit is reached and, if it does occur, at what stress level. The data indicate that an endurance limit probably occurs, and at a stress level somewhat higher than that for CuAl15. Further testing is needed to confirm this conclusion.

At lower fatigue lives, the trend curves for the two materials diverge, most likely because of differences in their strength and ductility. In **this** range of fatigue lives, the S-N fatigue approach ceases to adequately represent the fatigue behavior, and life data are better correlated with plastic strain range (see Figures 3 and 4).

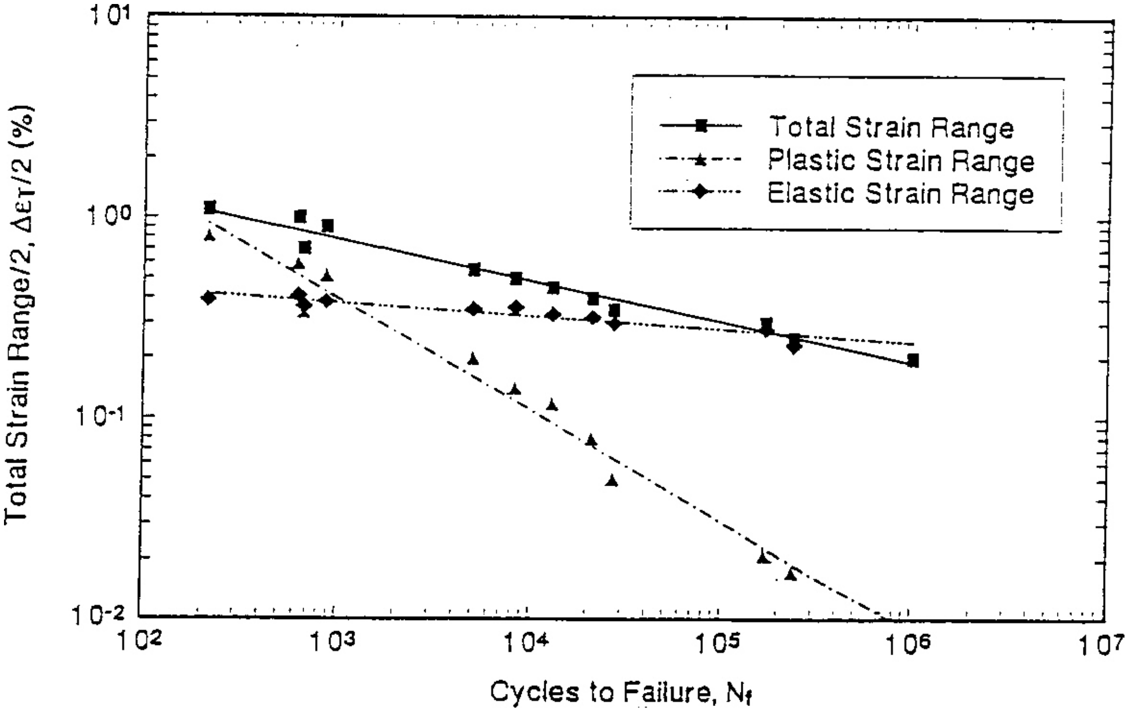

Fig. 3. Fatigue life results for standard size CuAl25 specimens.

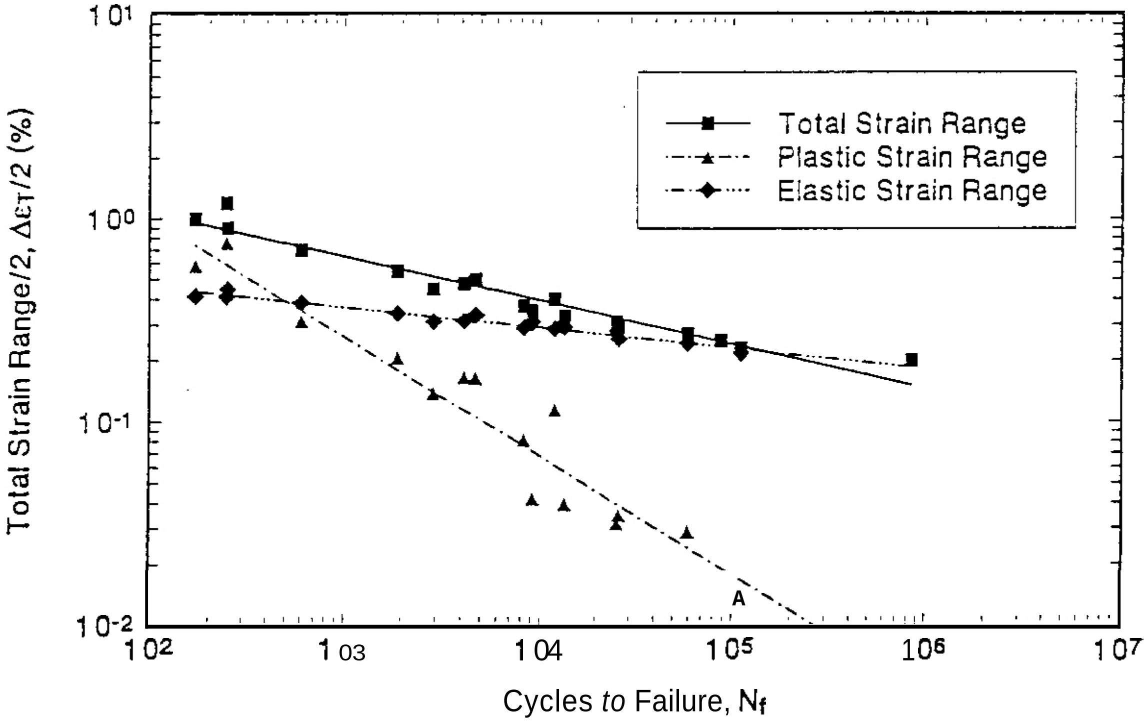

Fig. 4. Fatigue life results for subsize CuAl25 specimens.

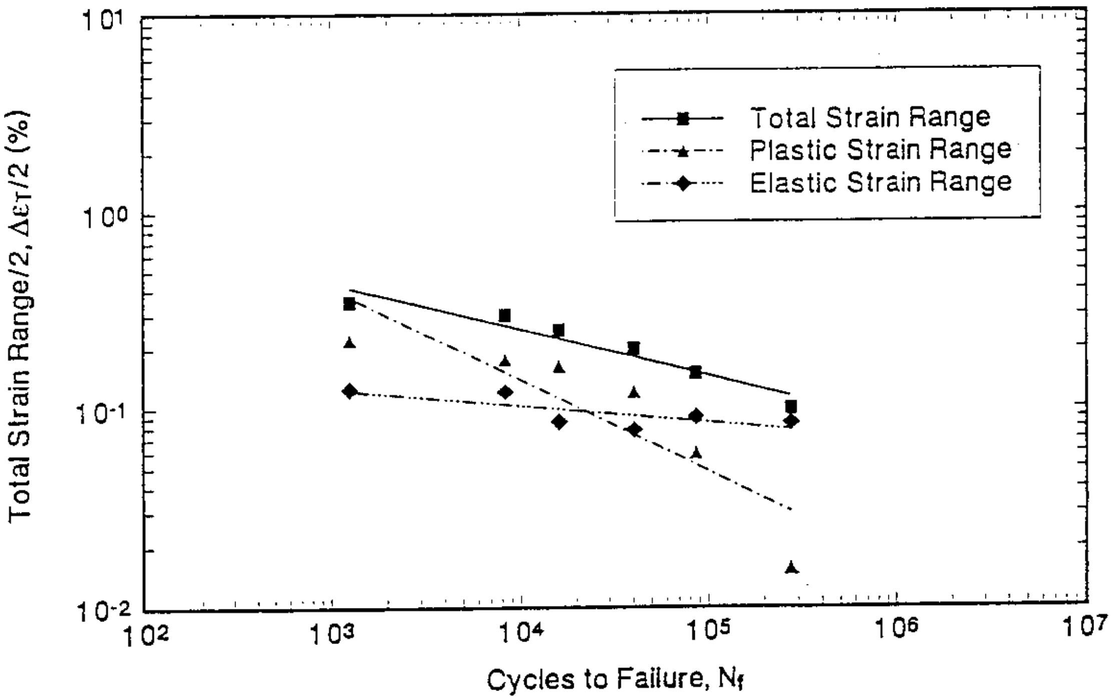

Fig. 5. Fatigue life results for standard size OFHC copper specimens.

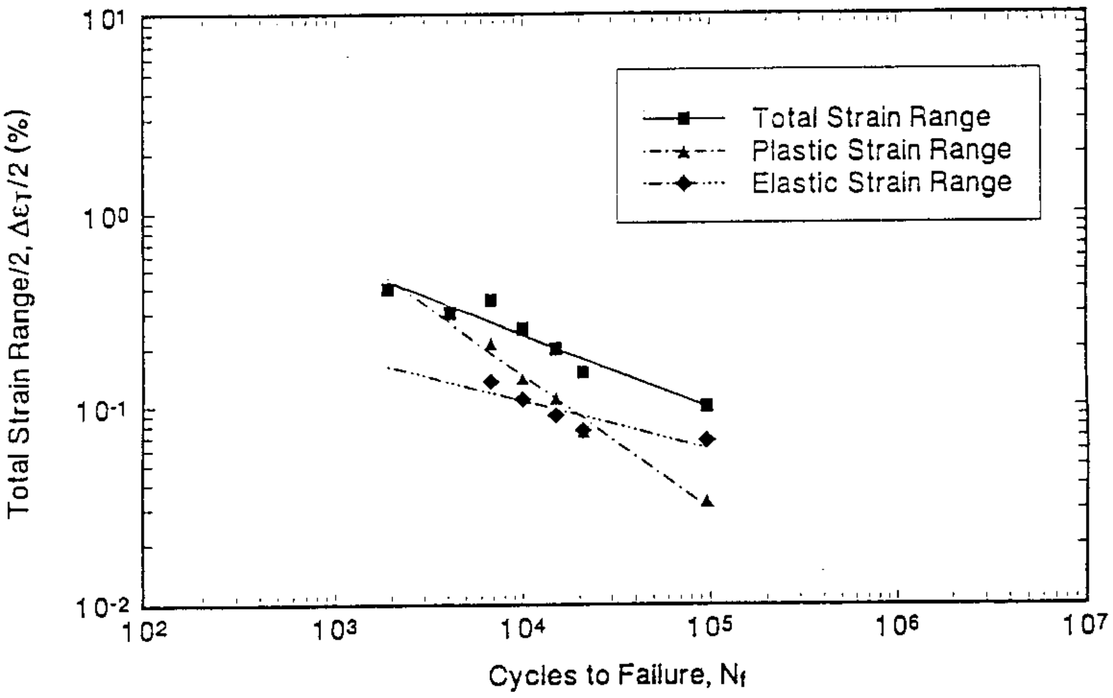

Fig. 6. Fatigue life results for subsize OFHC copper specimens.

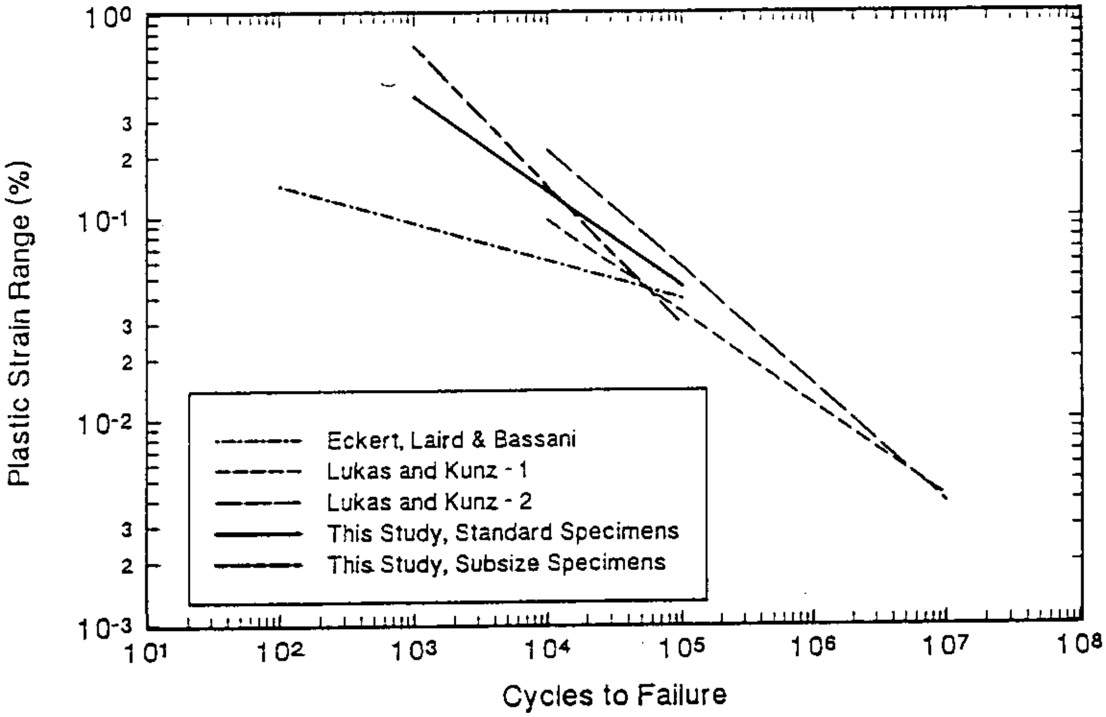

Fig. 7. Comparison of fatigue lives as a function of plastic strain range for the present study and the results of Lukas and Kunz [7, 8] and Eckert et al. [9].

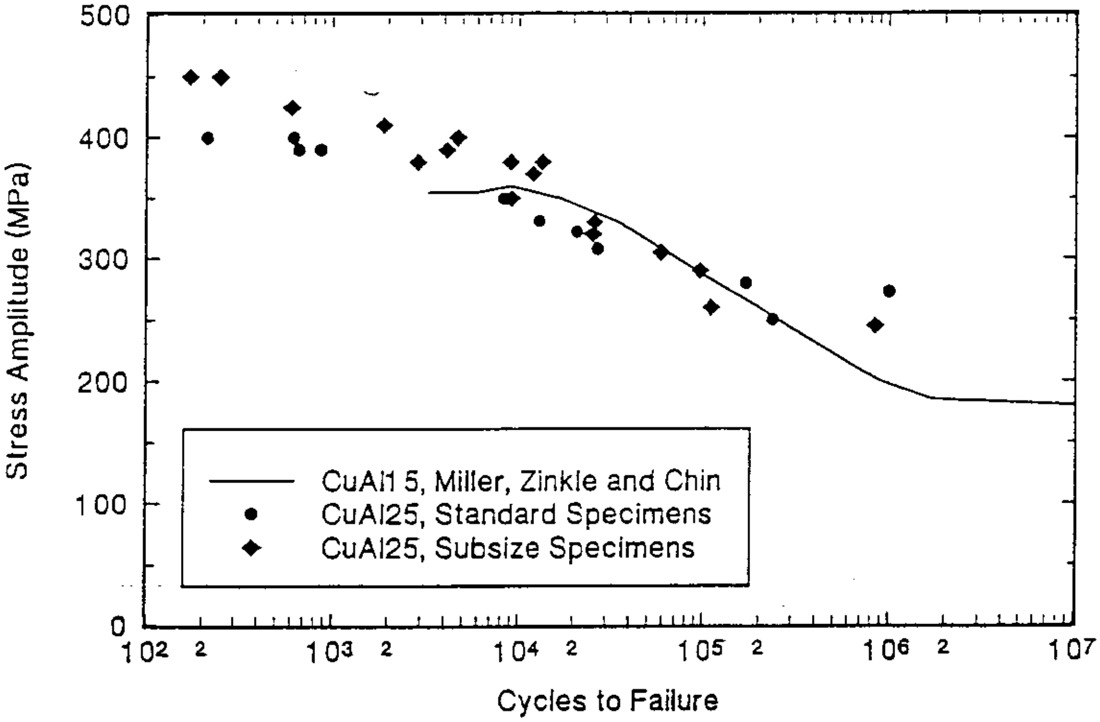

Fig. 8. Fatigue life as a function of the stress amplitude of CuAl15 [10] and CuAl25 in the present study.

A significant question in the present study is the influence of specimen size on fatigue response. Life comparisons for both materials show that longer lives were found for the larger specimens at equivalent strain ranges. Similar size effects were noted by Liu and Grossbeck [12] in a study of the fatigue response of 20% cold worked Type 316 stainless steel. They observed parallel slopes between the life vs. strain range behavior of small and large specimens. The larger specimens exhibited higher lives at a fixed value of strain range. This is exactly the same response to specimen size found in the present study. The reasons for the difference in lives as a function of specimen size are not readily apparent, but may be due in part to differences in surface to volume ratios. The surface to volume ratio is inversely proportional to the specimen diameter for right circular cross-section specimens. Since the fatigue process is dominated by surface effects and since fatigue cracks initiate and grow from the surface, a larger relative surface to volume ratio (i.e. smaller specimen diameter) could lead to a faster accumulation of fatigue damage even when the effect of gauge length is taken into account. Other factors may also be important in the process, and will be investigated in future studies.

CONCLUSIONS

From examination of the fatigue behavior of OFHC copper and an alumina dispersion-strengthened copper alloy, CuA125, at room temperature, the following conclusions can be drawn:

1. The dispersion-strengthened copper alloy shows superior fatigue performance compared to that of unalloyed copper. The higher strength of the alloy results in elastic strain-controlled fatigue response to lives as short as 1000 cycles to failure.

2. The fatigue results of both materials are consistent with the results of previous work

3. Useful fatigue data can be obtained from reduced-size specimens but complementary results on standard size specimens are needed for comparison.

4. Specimen size exerts influence on the failure lives of both materials. In all cases, the failure lives are shorter for the smaller specimens when compared to that of larger specimens tested under nominally identical experimental conditions but conducted on two different fatigue machines. For the dispersion-strengthened material, the difference in fatigue lives is relatively small but still significant. For the OFHC copper, larger differences in fatigue lives with specimen size are found and may be related to the larger influence of plastic strain in unalloyed copper.

ACKNOWLEDGEMENTS

This work was supported by the U.S. Department of Energy under contract DE-AC06-76RLO 1830 and also by Associated Western Universities under contract DE-FG06-89ER-75522.

REFERENCES

1. F.A. Gamer, H.R. Brager and K.R. Anderson, *J. **Nucl Muter.,*** 179 (1991) 250.

2. D.J. Edwards, **F.A.** Garner and L.R. Greenwood, Proceedings of ICFRM-6, ***J. Nucl. Muter,*** in press.

3. A.W. Thompson and W.A. Backofen, Acta Met., **19** (1971) 597.

4. H. Abdel-Raouf, A. Plumtree and T.H. Topper, Met. Trans., ***5*** (1974) 267.

5. F. Lorenzo and C. Laird, Mater. Sci. Eng., **62** (1984) 205.

6. P. Lukas and L. Kunr, Mater. Sci. Eng., ***85*** (1987) 67.

7. P. Lukas and L. Kunz, Mater. Sci. Eng., **A103** (1988) 233.

8. P. Lukas and L. Kunr, Int. J. Fat., **11,** I (1989) ***55.***

9. R. Ecken, C. Laird and J. Bassani, Mater. Sci. Eng., **91** (1987) 81.

10. T.J. Miller, S.J. Zinkle and B.A. Chin, ***J. Nucl. Mater.,*** 179-181 (1991) 263

11. ***S.*** Zinkle, private communication.

12. K.C. Liu and M.L. Grossbeck, in ***The Use of Small-Scale Specimens for Testing lrradiated Materials,*** ASTM STP 888, American Society for Testing and Materials, Philadelphia (1986) 276.

PREPARATION OF RUSSIAN COPPER ALLOY CREEP SPECIMENS - C. R. Eiholzer (Westinghouse Hanford Company), M. L. Hamilton (Pacific Northwest Laboratory)”, and V. Barabash (D. V. Efremov Institute)

OBJECTIVE

The objective **of** this effort is to complete the fabrication of pressurized tnhe specimens from copper alloy tubing provided by the Efremov Institute, for irradiation in the joint US/RF experiment being conducted in the SM-3 reactor.

SUMMARY

Eleven creep specimens **of** the Russian copper alloy MAGT-0.2 were pressurized and welded closed. The specimens were pressurized to levels ranging from 7.2 to 15.6 MPa (1052 to 2267 psia). These pressures will produce hoop stresses between ***55*** and **185** MPa (7,977 to 26,830 psia) when irradiated at 120°C.

PROGRESS AND STATUS

Introduction

As part **of** a collaborative effort between the United States and Russian governments, eleven Russian creep specimens were sent **to** the United States for pressurization and closure welding. The collaborative program focuses on the development **of** structural materials for fusion reactors. These eleven specimens will be used to study irradiation creep in a copper alloy at low temperature. The specimens will be irradiated in an in-core position in the Russian SM-3 reactor. The specimens will be irradiated at –100°C in direct contact with the water coolant for –45 days, producing ***–5*** dpa at a fluence **of** 8 x 10^{21} nlcm’.

The creep specimens have a gauge section made of a Russian copper alloy (MAGT-0.2) and stainless steel end caps. The alloy has **a** copper matrix with a dispersion **of** $(AlHfTi)_2O_3$ particles that have an average diameter **of** 6 nm. The mechanical and physical properties of the alloy are very similar to those of the U.S. GlidCop alloy CuAl20.

Eleven tubes were supplied to the US with the end caps already attached. The end caps had been brazed to the copper tubes in Russia with **a** Cu-Mn-Ti brazing alloy. Westinghouse Hanford Company (WHC) pressurized the specimens and closed them by laser welding. This report documents the fabrication steps. The report also provides pre-test data such as **fill** pressures and the outside diameters of the specimens before and after pressurization.

Fabrication Steps

The end cap/tube assemblies were fabricated and leak tested in Russia. The tubes were machined from rods while the end caps were machined from **a** Russian 316Ti stainless steel. The tubes were

---

‘Pacific Northwest Laboratory is operated for the **U.S.** Department of Energy by Battelle Memorial Institute under Contract DE-AC06-76RLO 1830.

joined to the end caps by vacuum capillary brazing at 930°C using brazing alloy PM-63, which is a copper alloy containing manganese, nickel, silicon, and iron. The inside of the tube was coated electrochemically with a thin layer of nickel prior to the brazing. The brazed tubes were leak tested with pressurized water (10 hours at pressures of up to 10 MPa) to verify the integrity of the brazed joints, after which the outer surfaces of the finished tubes were polished electrolytically to remove the oxide that formed during the leak test. Similarly brazed tubular tensile specimens were also tested to failure at room temperature; failures were consistently in the tube rather than the brazing joint, indicating that the joint was stronger than the alloy itself.

Fabrication of the creep specimens at WHC from the end capltube assemblies included the following steps:

- Identification numbers were laser engraved on the specimens.
- The fill pressures for the specimens were calculated.
- The specimens were cleaned, pressurized, and laser welded closed.
- The laser welds were inspected.
- The outside diameters of the specimens were also measured before and after pressurization.

The following sections give the details for each fabrication step.

Identification Numbers and Engraving. A laser engraver was used to place identification (ID) numbers on the top and bottom end caps of each specimen. The specimens were numbered consecutively from 01 to 11. The specimens identified as numbers 10 and 11 are the tubes fabricated with a slightly larger outer diameter and therefore a slightly larger wall thickness (Ref. 1).

Cleaning. Residual grease was observed on the top (gas fill) end caps on all the as-received specimens. All specimens were therefore cleaned hefore pressurization and closure welding. All the specimens were hand wiped with alcohol to remove any grease and dirt. Both the end caps and the tube of each specimen were cleaned. The specimens were hand cleaned so that liquid would not get into the specimens through the open gas fill hole in the top end caps.

Determination of Stresses and Fill Pressures. The nominal hoop stresses and corresponding. fill pressures were determined before the specimens were pressurized with helium. Pacific Northwest Laboratory (PNL) and WHC personnel determined the desired nominal hoop stresses for the test matrix on the basis of the tensile data provided with the tubes (Ref. 1). The uniaxial yield strength was given as 320 MPa at 100°C. The corresponding effective (biaxial) hoop strength was determined as $320 * (\sqrt{3}/2) = 277$ MPa (Ref. 2). It was agreed that the maximum hoop stress in the test matrix would he two thirds (213) of the hoop strength corresponding to the uniaxial yield condition. The rest of the nominal matrix consists of stresses that are approximately 85%, 75%, 65%, 50%, and 30% of the maximum hoop stress. Two specimens were prepared at each of the five lower stress levels; only one was prepared at the highest stress level. The test matrix is shown in Table 1.

A WHC computer code was used to determine the fill pressures of each specimen. The program determines the fill pressure required for obtaining a specific hoop stress at a given test temperature. The program allows the user to input fill gas type, specimen diameter, material type, and external pressure. The hoop stress calculations can he based on either the thin walled or thick walled elastic stress/strain relationships. The computer code has been approved and verified as required by WHC procedures.

Table **1**. Summary of Russian Copper Alloy Creep Specimen Fabrication Data.

TUBE ID NUMBER	HOOP STRESS[1] (MPa)		TEST TEMP (°C)	FILL PRESSURE[2]		AVERAGE DIAMETER BEFORE PRESSURIZATION (mm)	AVERAGE DIAMETER AFTER PRESSURIZATION (mm)
	NOMINAL	ACTUAL		MPa	psia[3]		
01	55	48	120	7.2	1052.5	4.402	4.410
02	55	45	120	7.2	1052.5	4.423	4.429
03	90	83	120	9.5	1379.5	4.376	4.383
04	90	82	120	9.5	1379.5	4.380	4.387
05	120	114	120	11.4	1660.5	4.365	4.381
06	120	107	120	11.4	1660.5	4.389	4.405
07	140	113	120	12.3	1847.5	4.436	4.440
08	140	134	120	12.3	1847.5	4.362	4.365
09	155	132	120	13.7	1987.5	4.410	4.419
10	155	118	120	13.7	1987.5	4.460	4.475
11	185	146	120	15.6	2267.5	4.446	4.474

[1] Nominal hoop stress calculations were based on the average of the diameter measurements made with a micrometer on the six smallest tubes prior to filling. Actual hoop stress calculations were based on the diameter measurement made with the laser system on each individual tube prior to filling.

[2] Ultra-pure helium was the pressurization gas.

[3] Actual **fill** pressures are recorded in psig; **14.7** psi was added to the actual fill pressures to get the pressures given in the table.

The following input data were used to determine the fill pressures for the specimens:

- Temperature assumed during filling:	22.2°C
- Atmospheric pressure assumed during filling:	**14.513** psia **(0.1** MPa)
- Outside diameter:	**0.171** in. **(4.34** mm)
- Inside diameter:	**0.157** in. **(3.988** mm)
- Linear thermal expansion: (the handbook value for wrought copper was assumed)	**9.18 µin./in./°F (16.5** µin./in./°C)
- External pressure on specimen during irradiation:	**711** psia **(4.9** MPa)
- Irradiation temperature:	120°C

The thin walled approximation was used to determine the hoop stresses. The ideal gas law was used to model the helium behavior in the creep specimens. All the specimens were successfully pressurized to the goal pressures. Table **1** gives the fill pressures.

Nominal pressures were calculated on the basis of preliminary diameter measurements taken with a hand-held micrometer. Because of the variability in the diameters that resulted from the electropolishing, the average diameter of the six smallest tubes was used as the specimen diameter in the calculation of the pressure required to achieve the nominal stresses. Unfortunately, these diameters were sometimes significantly different than the diameters obtained in the laser system immediately prior to specimen pressurization. In addition, the dimensional differences in specimens 10 and 11 were not taken into account in the pressurization calculations. Thus the actual hoop stresses vary somewhat from the nominal hoop stresses, as shown in Table 1.

Gas Pressurization of Creep Specimens. The creep specimens were pressurized in a laser weld chamber. The specimens were placed in a pressure vessel that has a quartz port on top. The chamber was evacuated three times and then pressurized with ultra-pure helium. Helium was added until the lowest fill pressure was achieved. Then the openings in two specimens were laser welded closed. More helium was added until the next fill pressure was achieved and two more specimens were welded closed. This procedure continued until all eleven specimens were pressurized and welded. All welds were made according to WHC procedure MT5-254.

Weld Inspections. Two inspections were performed on each laser weld. All the welds were examined visually at 10x by a quality engineer checking for cracks, incomplete welding, or other visual defects. All specimens passed the visual inspection.

All the specimens were also helium leak checked. The acceptance criterion was that a specimen not have a detectable leak rate of 10^{-8} atm-cclsec or greater. All the specimens passed the helium leak check.

Diameter Measurements. A laser micrometer system was used to measure the pre-test outer diameters of the specimens. Each specimen was measured at least once before and after pressurization. Each diameter determination requires measuring the specimen in five places. The five measurements were 4.88 mm apart, with the third measurement at the center of the specimen. Measurements 2, 3, and 4 were averaged to give the average diameter for each specimen.

Most specimens were measured twice before and twice after pressurization. In accordance with standard procedure, a given specimen was remeasnred when the center three measurements varied from each other 0.00127 mm (0.00005 in.) or more. The use of this tolerance band ensures valid and self-consistent measurements. For all specimens measured twice, the second set of center values varied 0.00127 mm (0.00005 in.) or more but closely repeated the first set of measurements. The two average diameters (one from each set of measurements) were averaged to give the average diameters reported in Table 1.

FUTURE WORK

The difficulties encountered in delivering the specimens to Russia have significantly delayed the start of the irradiation. The specimens were finally sent to Russia by air and successfully arrived at the Efremov Institute after a lengthy delay in Russian customs. Pre-test diameters will be measured in Russia for comparison with the WHC-measured values prior to insertion in a core position in the SM-3 reactor. The tubes will he irradiated for 45 days at –100°C in direct contact with coolant water. If the tubes survive the initial irradiation without rupture or excessive bulging, they may be reinserted for further irradiation. No collaborative plans have been established yet for post-irradiation examination.

REFERENCES

1. Letter, Vladimir Barabash to M. L. Hamilton and F. A. Garner, dated August 1993.
2. E. R. Gilbert and L. D. Blackburn, *J. Eng. Muter. Techno/.*, Vol. 99 (1977), 168.

VOID SWELLING OF PURE COPPER, CU-5NI AND CU-5MN ALLOYS IRRADIATED WITH FAST NEUTRONS - H. Watanabe (Kyushu University) and F. A. Garner (Pacific Northwest Laboratory")

OBJECTIVE

The objective of this effort is to determine the factors which influence the response to irradiation of copper and copper alloys intended as candidates for high heat flux applications in fusion devices.

SUMMARY

The effects of cold-work level and solute addition (nickel or manganese) on pure copper under fast neutron irradiation have been investigated. Neutron irradiation was conducted in the Fast Flux Test Facility (FFTF) **at** temperatures from 638 to 873K to doses ranging from 8 to 98 dpa. In purc copper, the void swelling behavior was investigated as a function of cold-work level. At 638 and 703K, 10% cold-work reduced swelling somewhat with little influence at higher cold-work levels. In comparison with pure copper, void swelling was suppressed by 5% nickel addition at 648K but slightly increased at 696K. Cu-5Mn resisted swelling in both annealed and **40%** cold-worked specimens in all temperatures examined. At 648K, void formation was not detected. Only stacking fault tetrahedra were observed in this specimen.

PROGRESS AND STATUS

Introduction

Copper and copper alloys are being considered for high heat flux applications in fusion reactors. It has been recognized that void formation and growth in copper are influenced by gaseous impurities such as oxygen and helium''', nongaseous solutes' and cold-working'. Leffers et. **al**[6,7] demonstrated the effect of cold-work level (ranging from 10 to 90%) on swelling of pure copper (99.999%) during electron irradiation. At 523 and 623K, both the incubation period and steady-state swelling rate were sensitive to the cold-work level. Cold-working first increased swelling at these temperatures, hut the swelling reached a peak and then declined with increasing levels of cold-work. It is not certain, however, that such behavior would be expected at the higher temperatures and lower displacement rates typical of neutron irradiation.

It is also known that the behavior of point defects in many materials, i.e., mobility of vacancies and interstitials, is influenced **by** addition of over-sized and/or sub-sized solutes. Recently, Muroga et al.[8] have investigated the effect **of** nickel and zinc addition in copper **on** microstructural evolution under electron irradiation. Interstitial type dislocation **loop** densities increased with increasing sub-sized nickel content hut were independent of over-sized zinc content. The enhanced loop nucleation by nickel addition was explained by the strong interaction between interstitials and nickel.

Electron irradiation using a high voltage electron microscope (HVEM) is a powerful technique to investigate the fundamental processes during irradiation, hut at higher temperatures where void

---

'Pacific Northwest Laboratory is operated for the U.S. Department of Energy by Battelle Memorial Institute under Contract DE-AC06-76RLO 1830.

swelling is prominent, the two specimen surfaces play an important role for loss of both dislocations and radiation-induced point defects. Moreover, irradiation doses in HVEM experiments are limited to lower displacement levels.

The objective of the present study is, therefore, to understand the effect of cold-work level on pure copper, and the effect of sub-sized solute (nickel) and over-sized solute (manganese) additions on void swelling behavior at high temperatures to fluences on the order of **100** dpa.

Experimental Procedures

Archive specimens of Leffcr's study[6,7] were used to study the influence of cold-work level. They used 99.999% pure copper (Johnson Matthey) with different degrees of cold-work produced by rolling. The conditions examined were annealed, three different levels (**10, 25, 50%** reduction) of cold-work and **25%** cold-work followed **by** aging at 573K for **2** hours. These specimens were irradiated in the Fast Flux Test Facility using the Material Open Test Assembly (MOTA) at 696, 793 and 873K.

In addition, MARZ grade pure copper (annealed), Cu-5Ni and Cu-5Mn specimens (annealed and 40% cold-worked) were also irradiated at 648K (**12.7** and **21.2** dpa) and 696K (**48.0** and 95.4 dpa). Swelling values were obtained by density measurement. Microscopy was performed with the JEM-**2000FX** electron microscope.

Results

Assuming that the 648 and 696K swelling data are independent of temperature, swelling of annealed MARZ grade pure copper appears to be consistent with **0.5%** dpa swelling rate usually observed for pure copper at about 673K[9].

Fig. **1** shows swelling observed in neutron-irradiated pure copper as a function of cold-work level. At 638K (16.9 dpa) and 706K (47.3 dpa), swelling is initially reduced by **10%** cold-working, with very little influence of cold-work observed at higher levels. On the other hand, an influence of cold-work level on swelling was not detected at 793 and 873K. Aging at 573K for **2** hours appeared **to** have no significant effect on swelling of **25%** cold-worked pure copper.

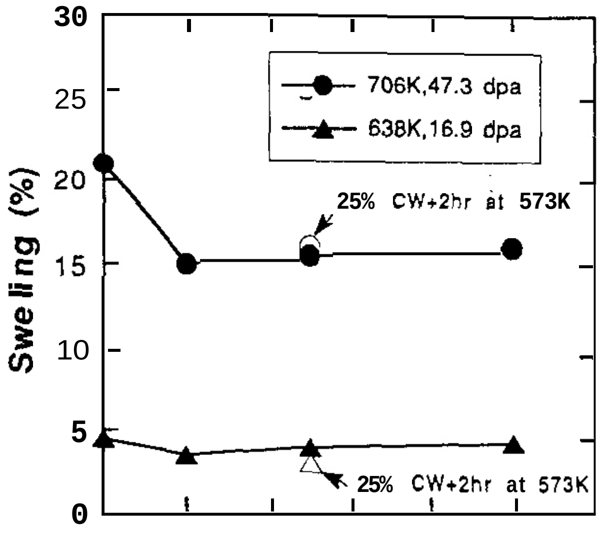

Fig. **2** shows the swelling of annealed and cold-worked Cu-5Ni, as well as **Cu-5Mn,** at 648 and 698K. At 648K, swelling was suppressed by nickel addition. However, a slight enhancement was detected at 696K. Reduced swelling by cold-work was found at both irradiation temperatures.

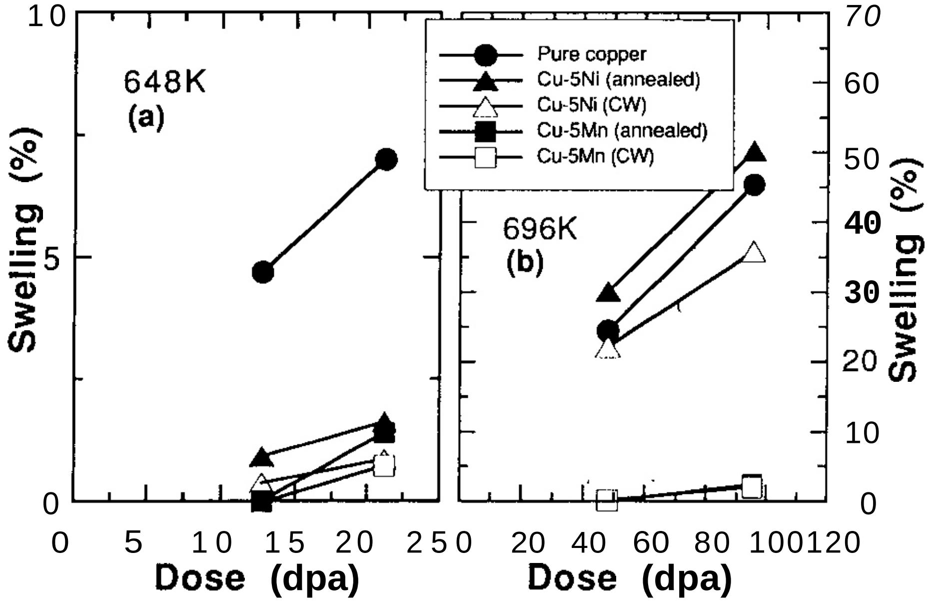

Fig. 2. Dose dependence of swelling in annealed pure copper and copper alloys irradiated at (a) 648K and (b) 696K.

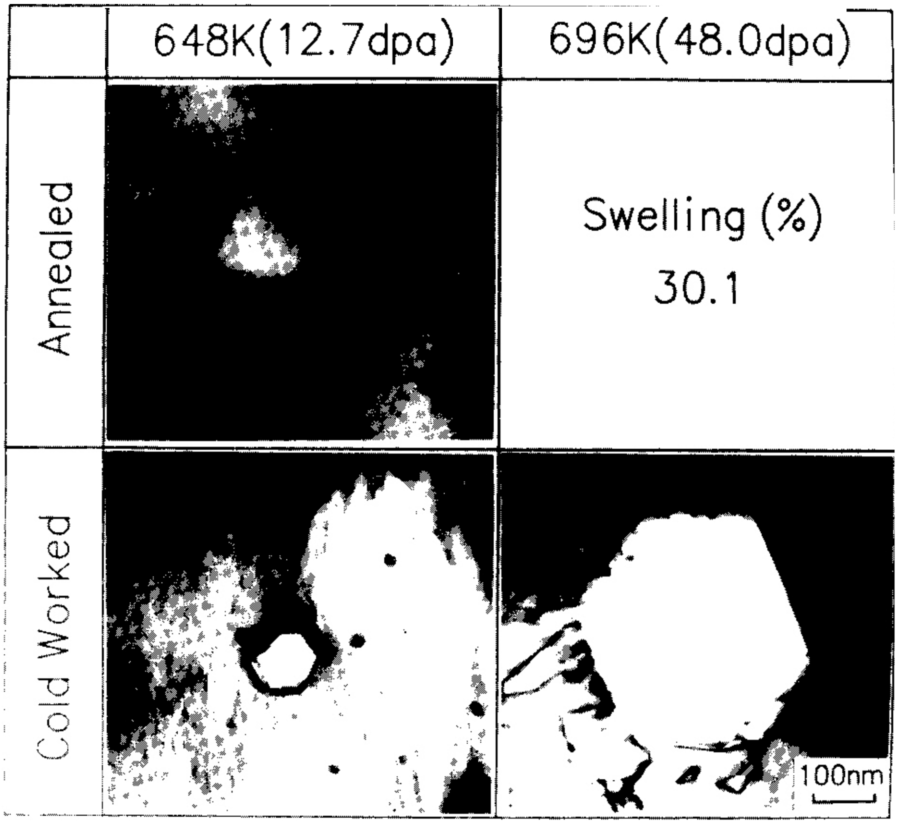

Fig. 3. Microstructure of annealed and cold-worked Cu-5Ni irradiated at 648K (12.7 dpa) and 696K (48.0 dpa).

Fig. 3 shows the microstructure of annealed and cold-worked Cu-SNi alloys irradiated at 648K (12.7 dpa) and 698K (48.0 dpa). Electron microscopy for an annealed specimen with 30.1% swelling irradiated at 698K to 48 dpa was not successful due to its higher swelling value. Fig. 4 shows dark field images of annealed and cold-worked Cu-SNi alloys irradiated at 638K (12.7 dpa) and shows the cold-worked induced dislocation structure before irradiation. The reduced swelling by cold-work is due to a smaller void size. At 648K (12.7 dpa), the average void sizes in the annealed specimen and the cold-worked specimen were 230 nm and 120 nm, respectively. It was also shown that cell structures of dislocations were formed and that preferential void formation occurred at dislocations irradiated at 696K (48.0 dpa). Isolated voids were also observed in a cold-worked specimen irradiated at 648K to 12.7 dpa.

Cu-5Mn exhibited strong resistance to swelling in both the annealed and 40% cold-worked specimens. Density measurement revealed that swelling at 698K to 95.4 dpa was 2.4 and 2.0% for the annealed and cold-worked conditions, respectively. Void formation was only detected in the specimen irradiated at 696K. Figs. 5 (a) and (h) show the microstructures of an annealed and cold-worked specimen irradiated at 696K to 48.0 dpa. The micrographs were taken in a void image condition. In the annealed specimen, small voids of about 10 nm were observed. Much larger void sizes of about 100 nm were observed in the cold-worked specimen. However, dislocation networks and preferential void formation at dislocations, which were commonly observed in Cu-5Ni, were not detected. Fig. 6 shows the dark field images of the specimens irradiated at 648K and 696K. The

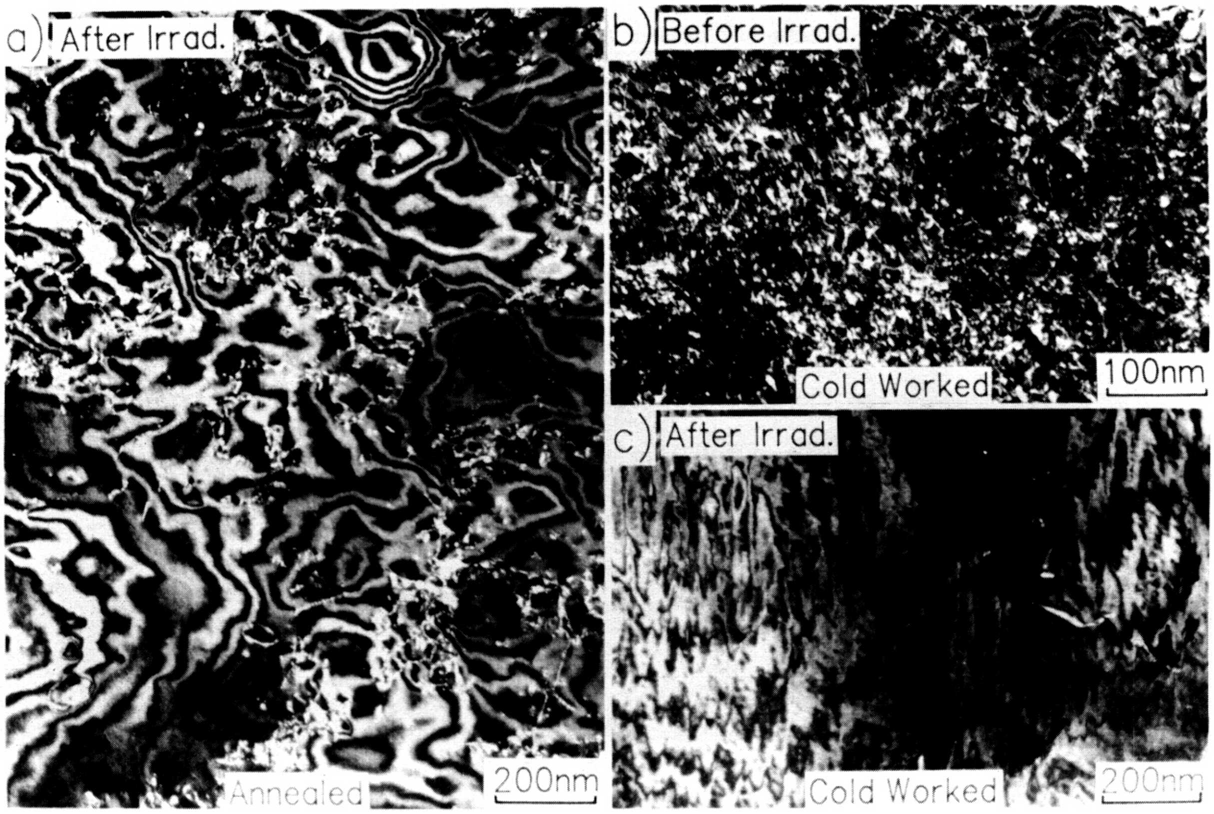

Fig. 4. Dislocation structure of Cu-5Ni irradiated at 648K to 12.7 dpa (a)

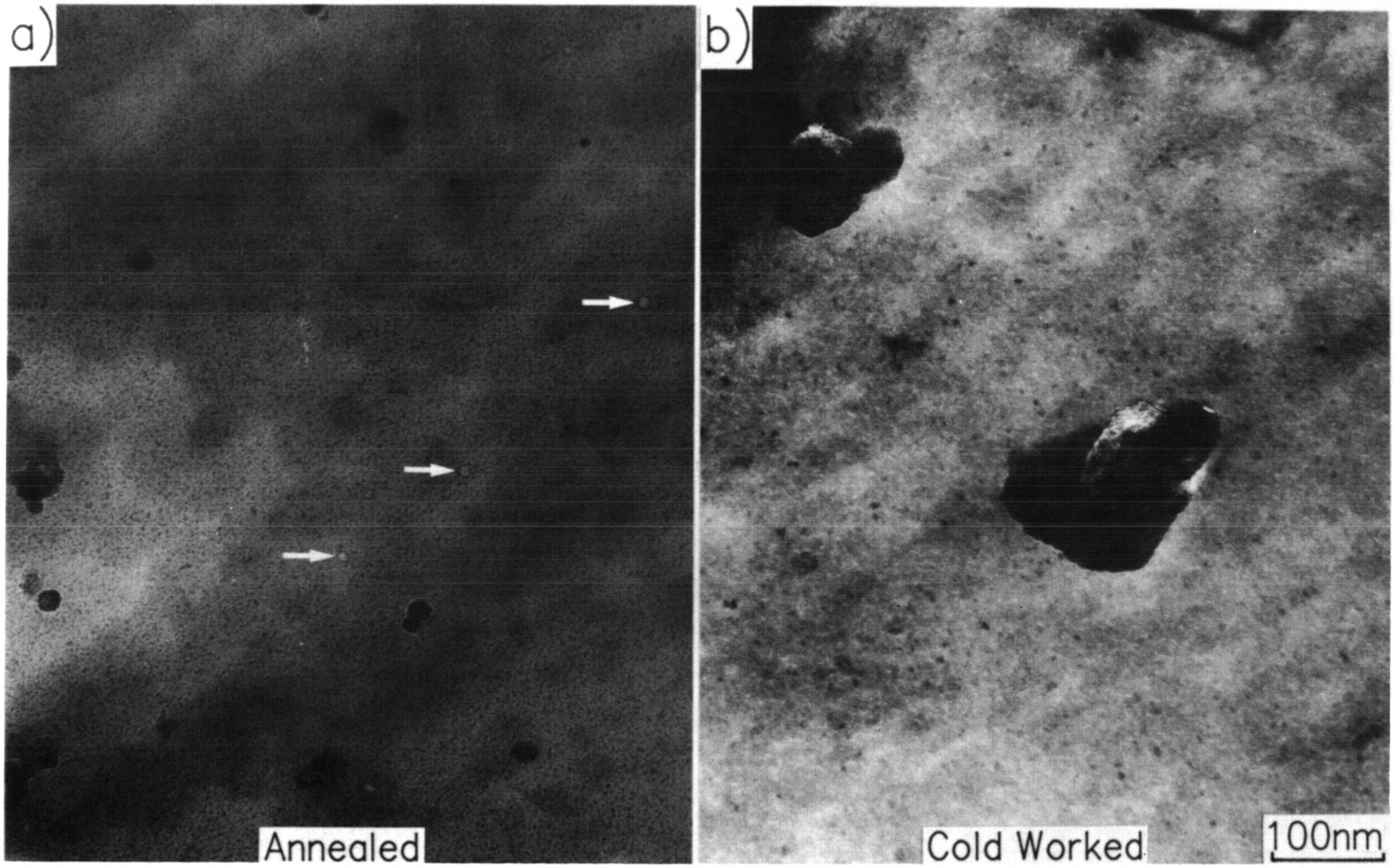

Fig. 5. Microstructure of annealed (a) and cold-worked (b) Cu-5Mn irradiated at 696K (48.0 dpa). The arrows in the figure show a small void formed in an annealed specimen.

observed dislocation density was about **1.0** x 10^{13} m $^{-2}$, which was almost the same in the annealed and cold-worked conditions. The arrows in the figure show the stacking fault tetrahedra (SFT) formed at **696K.**

Discussion

Swelling during fast neutron irradiation at **638** and **706K,** is initially reduced by **10%** cold-working, with very little influence of cold-work observed at higher levels. On the other hand, during electron irradiation[6,7], both the incubation period and steady-state swelling rate at **523** and **623K,** were found to be sensitive to cold-work level. Cold-working first increased swelling at these temperatures, but swelling reached a peak and declined with increasing cold-work. The different behavior observed in electron and neutron irradiations may arise from a different dislocation structure in these two experiments.

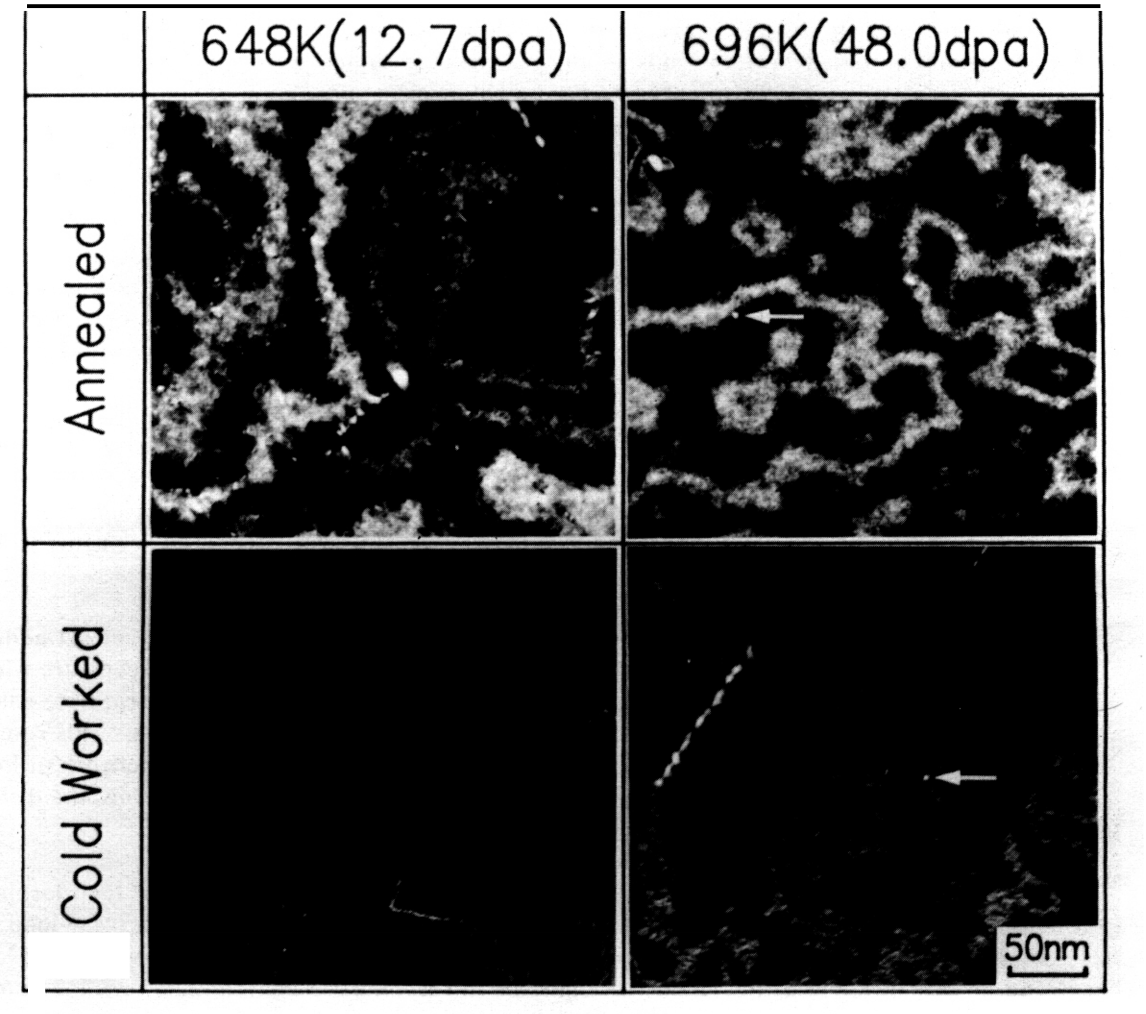

Fig. **6.** Microstructure of annealed and cold-worked Cu-5Mn irradiated at **648K (12.7** dpa) and **696K (48.0** dpa). The arrows indicate stacking fault tetrahedra.

During electron irradiation, Leffers et al.[6,7] confirmed that the cold-worked structure survives up to the dose of about **30** dpa. Maximum void swelling was observed in the **50%** cold-worked specimen.

Preferential void formation at dislocations in 10% cold-worked copper at **523K** was also detected. It is reasonable to believe that the cold-work dependence during electron irradiation is related to the cold-work induced dislocation networks and enhanced void formation near dislocations. Residual gases play an important role for stability of void nuclei. If the temperature is high enough, gas atoms diffuse and are trapped at the dislocations. Preferential void formation near dislocations may be explained by the high concentration of gas atoms near dislocations. Moreover, it is also known that void growth is strongest when the sink strength of dislocations is comparable to that of voids. It might he possible that the dislocation density of the ***50%*** cold-worked specimen, where maximum swelling was observed, is most appropriate for promoting void swelling.

On the other hand, electron microscopy of Cu-5Ni and Cu-5Mn revealed that a higher dislocation density was observed in the annealed specimen but not in the cold-worked specimen. This means that the dislocation structure induced by cold-working was presumably annihilated by absorbing point defect during an early stage of irradiation at **638** and **706K.** We believe that the network dislocations observed around voids in the annealed specimen were introduced during neutron irradiation. Microscopy was not performed on cold-worked pure copper, but annihilation of cold-worked induced dislocations might be the reason for the slight influence of cold-work on swelling in pure copper at higher cold-work levels.

Void swelling was suppressed by nickel addition at **648K,** but a slight enhancement of swelling was observed at **696K.** On the other hand, Cu-5Mn resist swelling very strongly at **648** and **696K** in both the annealed and cold-worked conditions. On the assumption that the impact of the order of magnitude difference in displacement rate associated with these two irradiation temperatures **(648** and **696K)** is negligibly small, suppressed void swelling by nickel or manganese addition might be explained by difference in dislocation density of the two specimens.

Very few voids were detected in the specimens with very low dislocation density. On the other hand, preferential void formation and growth at dislocations were observed in specimens where network dislocations were detected. Once dislocations were formed by irradiation, nucleation of voids on the compression side of dislocations may occur. In this case, if a higher concentration of gas impurities are present at dislocations, void nuclei might be stabilized with gas.

In Cu-5Ni, Muroga et al.[8] demonstrated that loop formation was enhanced **by** nickel addition at relatively lower temperatures. The loop density decreased with increasing temperature where the processes of trapping and detrapping of nickel is strongest. At these temperatures, cold-work induced dislocation structures will be rearranged by absorption of point defects. This results in a reduction of dislocation density in cold-worked specimen. Io the present study, network dislocations were not observed at **648K** but were observed at **696K.** This means that at **696K** the dislocation density was increased to the level where void growth became prominent.

Preliminary results of another study using HVEM irradiation has revealed that loop formation in Cu-5Mn was strongly enhanced by over-sized manganese addition at **373K.** But, the loop density dropped off more quickly than in Cu-5Ni with increasing irradiation temperature. At **573K,** the loop density of Cu-5Mn was almost comparable to that of pnre copper. The very low nucleation rate of dislocation loops at above **573K** might be one reason for the lower dislocation density and suppressed swelling observed in Cu-5Mn.

CONCLUSIONS

Cold working and nickel additions have a relatively small effect on neutron-induced swelling of pure copper, but manganese additions appear to suppress swelling very effectively. The question remains whether the suppression effect can operate at lower manganese levels.

FUTURE WORK

Examination of irradiated specimens containing lower levels of manganese will proceed in Japan.

ACKNOWLEDGEMENTS

This work was supported in part by the Japan-U.S. Fusion Cooperation Program, sponsored by Monbusho, the Japanese Ministry of Education, Science and Culture. This work was also supported by the U.S. Department of Energy under Contract DE-AC06-76RLO-1830. The authors would like to thank Professor B. N. Singh of Rise National Laboratory, Denmark for supplying the cold worked pure copper specimens.

REFERENCES

1. D. I. R. Norris, Radiation Effects, 15 (1972) 1.

2. S. J. Zinkle and E. H. Lee, Metallurgical Trans., **21A** (1990) 1037.

3. K. Yamakawa, I. Mukouda and Y. Shimomura, ***J. Nucl. Muter.,*** 191-194 (1992) 396.

4. F. A. Garner, H. R. Brager, K. R. Anderson, **J. *Nucl. Mater.,*** 179-181 (1991) 250.

5. A. Risbet and V. Levy, ***J. Nucl. Muter.,*** 46 (1973) 341.

6. T. Leffers, B. N. Singh, S. N. Buckley, and S. A. Manthorpe, ***J. Nucl. Muter..*** **118** (1983) ***60.***

7. T. Leffers, B. N. Singh, P. Barlow, RISØ National Laboratory Report RISØ-M-1937, May 1977.

8. T. Muroga, E. Ishimaru and N. Yoshida, presented at the ***16th International Symposium on Effects of Radiation on Materials,*** ASTM STP 1175 (1993) pp. 1013-1025.

9. F. A. Garner, M. L. Hamilton, T. Shikama, D. J. Edwards and J. W. Newkirk, **J. *Nucl. Muter.,*** 191-194 (1992) 386.

INFLUENCE OF NICKEL AND BERYLLIUM CONTENT ON SWELLING OF COPPER IRRADIATED IN COBRA-IA - F.A. Garner (Pacific Northwest Laboratory”) and B.N. Singh (RISØ National Laboratory)

OBJECTIVE

The objective of this effort is to determine the influence of solid transmutants on the swelling of copper, and then to use this information to develop fission-fusion correlations for copper and its alloys employed for high heat flux applications in ITER.

SUMMARY

A series of annealed Cu-Ni dilute binary alloys were irradiated in COBRA-IA in EBR-II at temperatures of 373, 420 and **500°C.** Density measurements have been performed for specimens irradiated at 373°C to 1.78 x 10^{22}n cm” (–11.3 dpa for pure copper). At this temperature and dose level nickel additions suppress swelling. There is a possible indication that some type of segregation-related phenomenon also occurs, yielding radiation-induced densification.

PROGRESS AND STATUS

Introduction

When pure copper is irradiated with neutrons, the elements nickel, zinc and cobalt (in order of decreasing formation rate) are formed by transmutation. The levels of these transmutants are determined by the total neutron exposure and the neutron spectrum.’.’ The thermal and electrical conductivities of copper then decline as the transmutant levels increase and also as void swelling develops. Nickel has the greatest effect per atom on conductivity. It is expected, however, that void swelling may be sensitive to the level of transmutants, especially nickel.’.’ This possible interaction of the two largest contributions to degradation of conductivity complicates somewhat the development of fission-fusion correlations for copper and its alloys. Therefore, a series of studies are in progress in the U.S., Denmark and Japan to determine the separate and synergistic effects of the various transmutants and microstructural processes involved in the radiation response of copper and its alloys.

Experimental Details

In this experiment five Cu-xNi alloys, where x=0 0.17, 1.0, 2.0, 5.0 and 10.0 atomic percent, were irradiated in COBRA-1A in EBR-II at 385°C and 1.78 X10^{22}n cm^{-2}, which corresponds to **–11.3** dpa for pure copper. Cu-0.5 at.% Be was also included. The density of these specimens was measured using an immersion density technique known to be accurate to ±0.2% change in density. These foils were supplied by RISØ National Laboratory from the archives used for a previous series of electron irradiation experiments.

‘Pacific Northwest Laboratory is operated for the U.S. Department of Energy by Battelle Memorial Institute under Contract DE-AC06-76RLO 1830.

Packet ID	Temperature (°C)	Neutron Fluence [n cm^{-2} (E>0.1MeV)]	dpa (Cu)
76	393	1.78×10^{22}	11.3
9A	497	1.78×10^{22}	11.3
79	517	0.64×10^{22}	3.5

Results and Discussion

Figure 1 shows that the density of Cu-Ni alloys in their original state depends somewhat on the level of nickel and reaches a minimum at ~5%Ni. This finding was somewhat surprising, since an earlier measurement of the density of Cu-5Ni showed it to be somewhat different from that measured in this study, as also shown in Figure 1. Measurements were performed on two separate specimens of each alloy, however, and there is no reason to suspect errors in any individual measurement. If real, this difference may signal the presence of some type of ordering or segregation, which often results in a change in overall density.

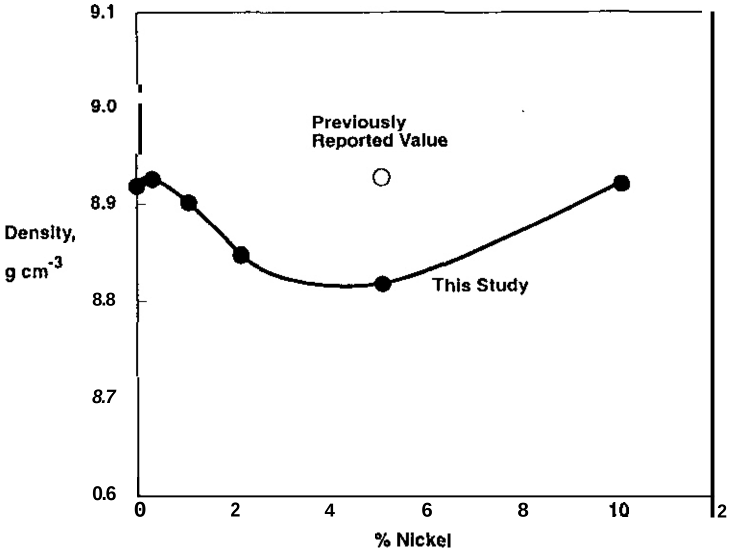

Fig. 1. Density of Cu-Ni alloys prior to irradiation.

As shown in Figure 2 and Table 2, the swelling of pure copper at 373°C and 11.3 dpa was 7.7%, a little higher than the 5.6% that would be expected on the basis of the 0.5%/dpa swelling rate usually observed at ~400°C. This relatively small difference may he due to the fact that the dose of 11.3 dpa was determined for the center of the experimental packet, which was located in a large flux gradient in the below-core basket of MOTA. There is no way to know which end of the packet was in the higher flux position, however, and therefore there is some uncertainty in the dpa level.

Figure 2 also shows that addition of nickel strongly depresses the swelling of copper in the range 0.17 to 2%. At 5%, a densification of –1.4% appears to have developed. This is a most surprising result and requires microscopy to determine its origin. It is significant to note, however, that if the value of 8.93g/cm^3 used in earlier studies was employed, there would be no densification. Unless some systematic error is found in the current set of density measurements, this suggests that some process, possibly involving segregation or most likely ordering, affects the density of Cu binary alloys. Therefore the resulting lattice parameter may be sensitive to the details of the annealing process.

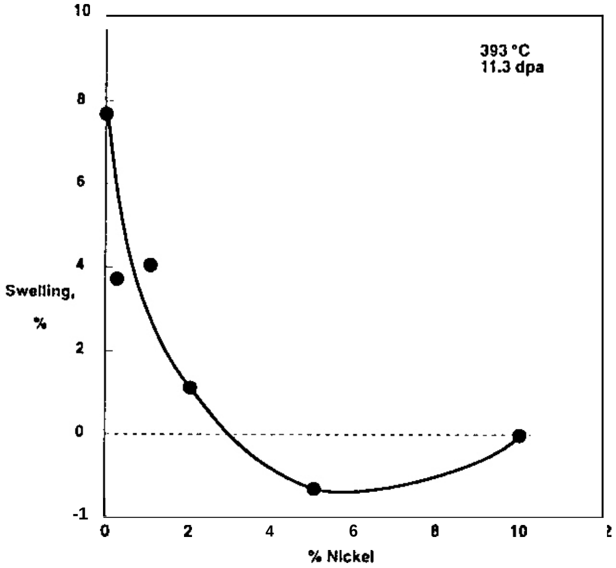

	Archive (g/cm^3)	Irradiated (g/cm^3)	Swelling (%)
Cu(OFHC)	8.9192	8.27820	7.74
Cu-0.17Ni	8.93281	8.61513	3.69
Cu-1.0Ni	8.90567	8.56423	3.99
Cu-2.0Ni	8.85680	8.75733	1.14
Cu-5.0Ni	8.82240	8.94760	-1.4
Cu-10Ni	8.92329	8.93229	-0.10
Cu-0.5Be	8.59121	8.77122	-2.05

Table 2 shows that Cu-0.5Be also densified significantly, but this effect most likely arises from the formation of beryllide precipitates.

FUTURE WORK

The details of specimen preparation and density measurement will be pursued in the next reporting period. Microscopy will also proceed in Denmark and will be used to check for segregation, ordering or other microstructural processes that might explain the behavior observed in this study.

REFERENCES

1. F. A. Garner and L. R. Greenwood, ***Mater. Trans. JIM*** **34** (1993) 985-998.

2. D. J. Edwards, F. A. Garner and L. R. Greenwood, ***J. Nucl. Mater.*** (proc. of ICFRM-6), in press.

3. F. A. Garner, ***J. Nucl. Muter.,*** **174** (1990) 229-239.

4. F. A. Garner, M. L. Hamilton, T. Shikama, D. J. Edwards and J. W. Newkirk, ***J. Nucl. Mater.,*** 191-194 (1992) 386-390.

6.5 Environmental Effects in Structural Materials

FABRICATION OF ALUMINUM NITRIDE AND ITS STABILITY IN LIQUID ALKALI METALS*

K. Natesan and D. L. Rink (Argonne National Laboratory)

OBJECTIVE

The objectives of this task are to (a) evaluate several fabrication procedures for development of aluminum nitride (AlN) coatings on the candidate first–wall structural material V-5wt.%Cr-5wt.%Ti; (b) evaluate the stability of coatings, which were fabricated by various methods, in contact with the structural alloy as a function of temperature and time; (c) evaluate the stability of the coatings in a liquid Li environment at temperatures between 200 and 400°C; (d) measure the electrical resistivity of the coated films after exposure to liquid Li; (e) evaluate the effects of defects in the coating on electrical resistivity of the coating; and (e) establish in-situ repair procedures to maintain adequate insulating properties for the coatings.

SUMMARY

AlN has been selected as a prime candidate for electrically insulating the V–alloy first wall in the self-cooled ITER concept. Several methods are being evaluated for fabricating coatings that have adequate thickness and desirable physical, electrical, chemical, and mechanical properties. Coatings developed thus far are being exposed to liquid Li at 350 and 400°C.

BACKGROUND

Extensive thermodynamic calculations have been made to evaluate potential candidates that (a) are chemically compatible in a liquid Li and (b) possess adequate insulating characteristics for use as a coating on the first–wall and blanket structural material. A review of available information on the electrical resistivity values for several oxides, nitrides, and oxynitrides showed that a number of oxides (e.g., CaO, MgO, SiO_2, Al_2O_3, $MgAl_2O_4$) and nitrides (e.g., AlN, Si_3N_4) have resistivities $>10^5$ ohm-m at temperatures below ≈600°C. The requirement is that the product of the coating's electrical resistivity and thickness should exceed a nominal value of 0.1 ohm m^2 under operating conditions. This translates to a minimum resistivity value of 10^5 ohm-m for a coating thickness of 1 µm, and 10^4 ohm-m for a thickness of 10µm. Based on the resistivity values of the materials listed above, a coating layer of <1 µm thickness of any of these materials would be adequate from the insulating standpoint, provided that resistivity is not reduced during operation, i.e., by irradiation. Figure 1 is a comparison of resistance of several materials, along with the requirements for ITER application.

Based on chemical compatibility in a liquid sodium-potassium (NaK) alloy and the need for adequate electrical resistivity, materials such as Al_2O_3, CaO, MgO, and Y_2O_3, and nitrides such as AlN and Si_3N_4 will be acceptable. On the other hand, Al_2O_3 is not stable in liquid Li and other candidate oxides and nitrides need to be considered. While the bulk oxides mentioned above are potential candidates, it is difficult to apply them with sufficient bonding onto first–wall structural material such as Type 316 stainless steel, martensitic steel such as MANET, and V-5wt.%Cr-5wt.%Ti alloy so that the coating will remain intact for long time periods under thermal cycling conditions.

The primary candidate for application in Li is AlN. The thermodynamic stability of several of the nitrides as a function of temperature is shown in Fig. 2; superimposed on this diagram are lines corresponding to different concentrations of N in Li. It is evident that AlN will be stable in Li with a wide range of N concentrations, while Si_3N_4 will be stable up to ≈400°C in Li that contains >300 ppm N. Calculations show that Ti in the V alloy can also form a nitride in the same Li, but the resulting TiN is not viable as an

---

*This work has been supported by the U.S. Department of Energy, Office of Fusion Energy Research under Contract W-31-109-Eng-38.

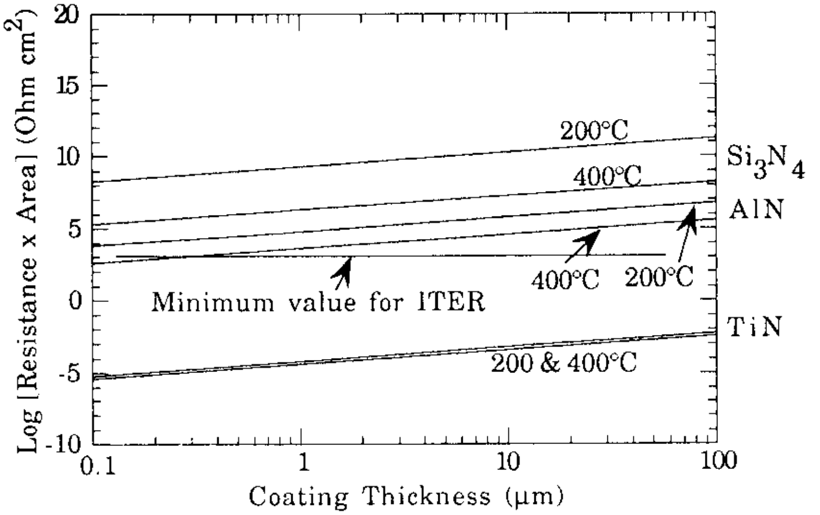

Figure 1. Resistance of several nitrides as a function of coating thickness; requirements for ITER application shown for reference

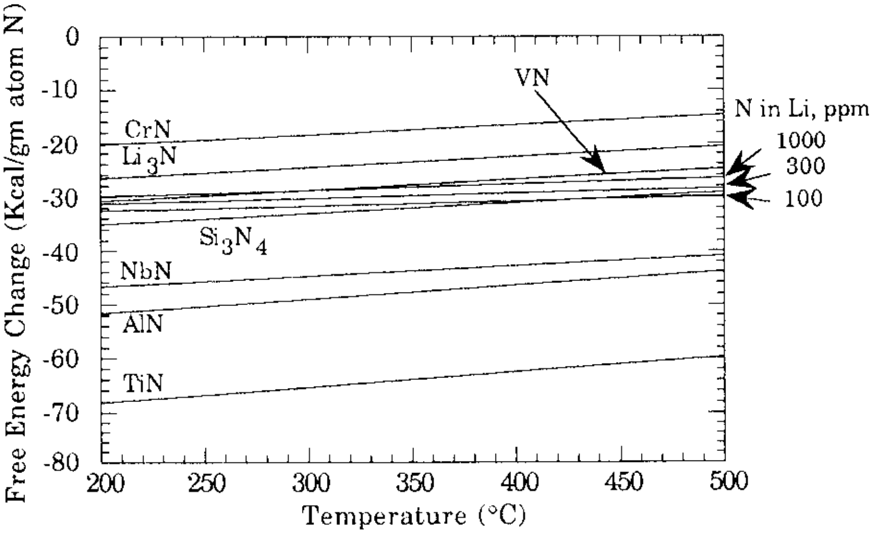

Figure 2. Thermodynamic stability of several nitrides compared with different levels of nitrogen concentration in lithium

electrical insulator. As a result, it is desirable to aluminize the surface regions of the first-wall alloy and to nitride the surface Al to form the insulating layer. Further, Al is favored because a reservoir of Al can be built into the alloy surface by different techniques; if the coating layer cracks or spalls, the Al-enriched surface could be renitrided by adding N to the Li.

EXPERIMENTAL PROGRAM

Several possible approaches are being examined to develop an AlN coating on the structural material: (a) prealuminization of the material surface by a (pack) diffusion process and subsequently conversion to a nitride in an external gas atmosphere; (b) physical vapor deposition with and without bond coats; (c) chemical vapor deposition at temperatures between 600 and 900°C; (d) a low-temperature method involving sequential reactions; (e) prealuminization of the surface of the alloy and conversion to a nitride in a high-N Li environment; (f) preexposing the material to liquid Al and subsequent conversion to a nitride in Li; (g) in-situ formation in Li with high thermodynamic activities for Al and N; and (h) prealuminization of specimens of structural material and nitriding with N_2 cover gas during Li exposure.

RESULTS

Fabrication of Coatings. The pack process is a well-established approach used to cover stainless steels and Ni–base alloys with layers of an intermediate phase [1]. The substrate materials are covered with a pack of powders and heated for 4-12 h at temperatures of ≈900°C. The composition of such powders (e.g., 65 wt.% Al_2O_3, 33 wt.% Al, 2 wt.% NH_4Cl) includes metallic Al, alumina as filler material, and NH_4Cl as an activator. The amount of Al can be reduced by partial replacement with Ni. Al deposited on the substrate surface diffuses into the subsurface regions of the material, where it forms intermetallic phases as aluminides of Fe or Ni. Because the substrate materials are heated to temperatures close to the annealing range for times sufficient to cause solution processes in the matrix, the materials need a final treatment in order to optimize the structure. The aluminide layers reach thicknesses of 0.025–0.20 mm, depending on the composition of the substrate materials. Figure 3 shows elemental concentration profiles for Al, V. Cr. and Ti in a V-5Cr-5Ti alloy sample after an aluminizing [2]. The diffusion processes lead to layers with very good adhesion to the substrate. The high temperature of the formation process creates layers that develop compressive stresses at lower temperatures and thus do not contain cracks after preparation process is finished.

The aluminizing of V and its alloys by the "hot-dip" process covers the substrate materials at –800°C in 1-2 min with a layer of solid solutions of the substrate metals in Al, or of aluminides of the alloying elements [3]. The process requires clean surfaces on the structural materials to achieve proper wetting and adherent layers. Adherence can be improved by a thermal treatment of at 500 to 600°C, although this may cause pores or cavities in the outer part of the layer. The aluminide layer consists of an the inner part in close contact with substrate by diffusion bonding and an outer part which contains pores and cavities due to diffusion effects. The complete layers have a thickness of –0.2 mm and the inner ones –0.12 mm. The aluminide layers must be oxidized to obtain an insulating surface layer. Specimens of V alloy are being aluminized by this process at KfK in Germany.

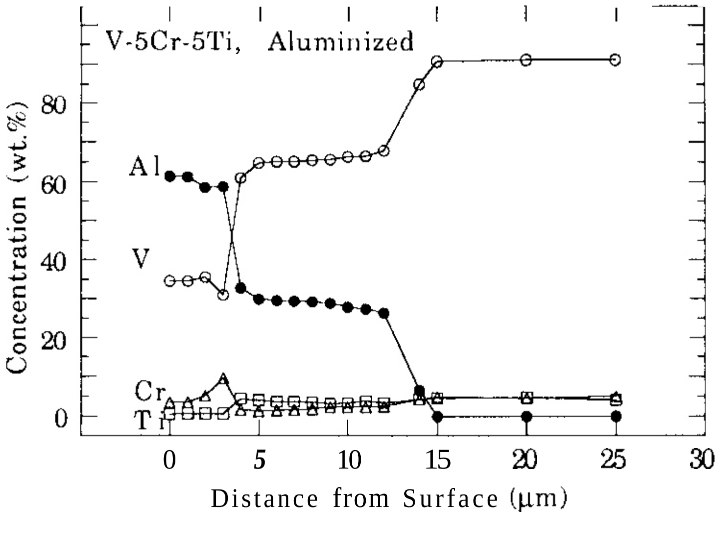

Figure 3. Depth profiles for Al, V, Cr. and Ti in an aluminized specimen of V-5Cr-5Ti alloy

Aluminum nitride coatings were also made by reaction sputtering in low-pressure N_2 atmosphere at temperatures of 350, 400, and 450°C. Coating thicknesses after 1 h of deposition were 0.8-1.4 µm. The coating covered the entire surface of the V-alloy specimen and was found to have very high electrical resistance, indicating adequate insulating properties. The coatings developed at 350 and 450°C tended to crack, but the one developed at 400°C was fairly adherent and mechanically hard. Additional specimens are being prepared by this approach, with an emphasis on optimizing coating parameters to achieve 5-10-µm-thick coatings without defects.

Aluminum nitride coatings on a V alloy were also prepared by a commercial physical deposition technique. The specimens used ≈10-µm-thick coatings of pure AlN, that were found to be electrically insulating. Procedures are now being developed to characterize these coated samples and also measure their electrical resistivity as a function of temperature and thermal cycling exposures.

Testing of Coatings in Liquid Metals Aluminized layers have been found to be stable in liquid Li at 400°C in a recirculating Li loop [6]. However, the kinetics of layer growth and chemical/mechanical integrity of the layer must be determined, especially at the temperatures of interest for the ITER (250-400°C). Bulk samples of AlN have been exposed to liquid Li at 400°C and found to be intact after 100 h of exposure [7]. Further, Al transport/deposition to a specimen surface was achieved by additions of 2-5 wt.% Al to liquid Li [8]. This indicates that if the externally formed AlN layer cracks or spalls in flowing Li, in-situ repair or self-healing is possible by controlling the activities of Al and N in the Li. Bulk samples of AlN have been exposed for up to 750 h to liquid Li at Argonne National Laboratory and the specimens have shown negligible weight change. Preliminary results indicate that any breakdown of AlN and dissolution of Al and N from the coating is fairly slow at 350°C. Further, V-alloy specimens were exposed in contact with bulk AlN material for 900 h at 500°C in vacuum. Figure 4 shows the EDX elemental profiles for V, Al, Ti, and Cr for the exposed specimen. It is evident that no significant reaction is noted between the alloy and AlN. Specimens with AlN coatings developed by reaction sputtering and physical deposition are being exposed in liquid Li at 350°C and have accumulated 150 h to date. Additional specimens will be exposed in a second Li vessel at 400°C. All specimens will be retrieved periodically and their chemical, electrical, and

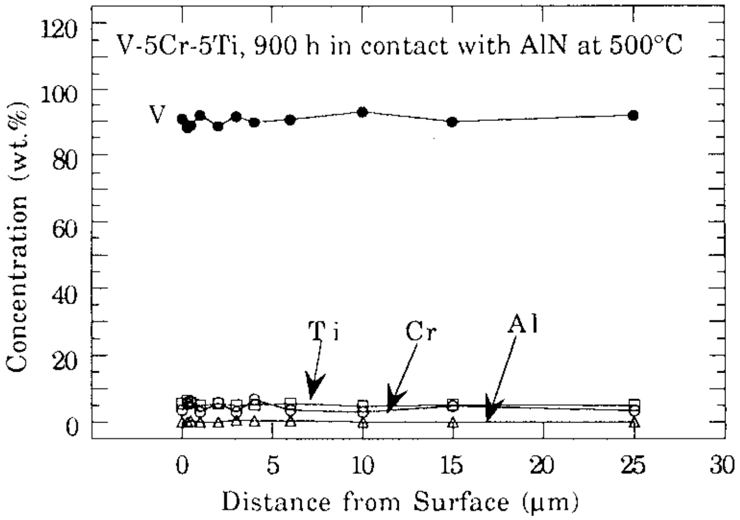

Figure 4. Energy-dispersive X-ray elemental profiles for V, Cr, Ti, and Al in a V-alloy specimen after 900 h exposure at 500°C in contact with bulk AlN

mechanical integrity evaluated. Further. experiments are underway to determine the repair procedures for in-**situ** reformation of layers by controlling the thermodynamic activities of N and **Al** in Li, level of N_2 in the cover gas, and exposure temperature

REFERENCES

1. S. R. Levine and R. M. Caves, J. CS 121 [1974] 1051-1064
2. K. Natesan, Argonne National Laboratory, unpublished work.
3. H. Glassbrenner and H. U. Borgstedt, J. Nucl. Mater., accepted for publication
4. H. Glassbrenner and H. U. Borgstedt, unpublished results.
5. H. U. Borgstedt, H. Glassbrenner, and Z. Peric, I. Nucl. Mater., accepted for publication
6. G. **C.** Burrow, M. G. Down, and C. Bagnall, I. Nucl. Mater. 103 & 104, [1981] 657-662.
7. R. J. Lauf and J. H. DeVan, J. Electrochemical Soc. 139, [1992] 2087-2091.
8. P. F. Tortorelli, J. H. DeVan, J. E. Selle, and H. D. Upton, Proc. 8th Symp. on Engineering Problems of Fusion Research, eds. C. K. McGregor and T. H. Batzer, Vol. III, IEEE, 1979.

DEVELOPMENT OF ELECTRICAL INSULATOR COATINGS: IN-SITU ELECTRICAL RESISTANCE MEASUREMENTS ON CaO–COATED V-5%Cr-5%Ti IN LIQUID LITHIUM*

J.-H. Park, G. Dragel, and R. W. Clark (Argonne National Laboratory)

OBJECTIVE

Corrosion resistance of structural materials and the magnetohydrodynamic (MHD) force and its influence on thermal hydraulics and corrosion are major concerns in the design of liquid–metal blankets for magnetic fusion reactors (MFRs). The objective of this study is to develop in–situ stable coatings at the liquid-metallstructural-material interface, with emphasis on coatings that can he converted to an electrically insulating film to prevent adverse currents generated by the MHD force from passing through the structural walls.[1-3]

SUMMARY

The electrical resistance of CaO coatings produced on V-5%Cr-5%Ti by exposure of the alloy to liquid Li that contained 4 at.% dissolved Ca was measured as a function of time at temperatures of 250 to 698°C. The solute element, Ca in liquid Li, reacted with the alloy substrate at 420°C to produce a CaO coating. The resistance of the coating layer was = 0.4 and 35.7 R a t 267 and 698°C. respectively. Thermal cycling between 267 and 698°C changed the resistance of the coating layer, which followed insulator behavior. These results and those reported previously[4,5] suggest that thin homogeneous coatings can be produced on variously shaped surfaces by controlling the exposure time, temperature, and composition of the liquid metal. This coating method is applicable to reactor components of various shapes (e.g., inside/outside of tubes, complex geometrical shapes) because the coating is formed by liquid-phase reaction. The liquid metal can he used over and over because only the solutes are consumed within the liquid metal.

INTRODUCTION

Corrosion resistance of structural materials and magnetohydrodynamic (MHD) force and its influence on thermal hydraulics are major concerns in the design of liquid–metal cooling systems for fusion first–wall/blanket applications.[1-3] Vanadium and V-hase alloys (V-Ti or V-Ti-Cr) are leading candidate materials for structural applications in a fusion reactor.[6] The objective of this study is in-situ development of stable corrosion–resistant coatings, as well as insulator coatings at the liquid-metallstructural-material interface. The electrically insulating coatings should he capable of forming on various shapes such as the inside of tubes or irregular shapes during operational conditions to prevent adverse currents that are generated by MHD forces from passing through the structural walls. The coatings could also improve general corrosion resistance and act as a diffusion barrier for hydrogen isotopes, viz., deuterium and tritium.

EXPERIMENTAL PROCEDURE

Three types of experiments have been conducted for fabrication of electrical insulator coatings to be used in liquid-Li environments, i.e., (a) a screening test for candidate ceramic materials in liquid Li, (b) in-situ fabrication CaO coatings by first charging oxygen into the V–base alloy in Ar gas containing O_2/H_2O impurities and subsequently exposing the alloy to liquid Li containing dissolved Ca to form the CaO layer on surface of the material, and (c) in-situ electrical resistance measurements of CaO coatings on V-5%Cr-5%Ti in Li environments. Thermal cycling tests were also conducted to investigate the integrity of coating layers that formed in–situ.

---

*This work has been supported by the U.S. Department of Energy, Office of Fusion Energy Research, under Contract W-31-109-Eng-38.

Compatibility tests on electrically insulating ceramics

Results of compatibility tests on electrically insulating ceramics in liquid Li are shown in Table I. In general, compatibility of ceramic insulators with liquid Li follows the criterion for thermodynamic stability. Although some ceramic materials fall into the category of thermodynamically stable materials, e.g., sintered AIN and SiC (applied by chemical vapor deposition), they were not compatible with liquid Li in screening tests. We conclude that this behavior is caused by grain boundaries in AIN and SiC that are enriched in **O**, Si, C, or impurities that react with liquid Li. An example **is** sintered AIN. Electron–energy–dispersive–spectroscopy (EDS) analysis indicated that **O** contamination was predominant in AIN. Oxygen may form Al_2O_3, which is not stable in liquid Li, in the grain-boundary area. Al_2O_3, if present at grain boundaries, reacts with Li and thereby weakens the mechanical strength of AIN. As a result, O–enriched AIN appears to he brittle after exposure in liquid Li. When the **O** is gettered by the Y/Y_2O_3 phase present in AIN, sintered AIN remains intact after exposure lo liquid Li. This presumably indicates that both AIN and Y_2O_3 are compatible with Li, as indicated in Table I. Based on results of the liquid-Li compatibility tests, we proceeded with work to develop an in-situ coating method for various alloys by forming intermetallic phases, which are then converted to ceramic insulators in liquid-Li environments.

Table 1. *Liquid-Li* ***compatibility*** *of* ***insulator materials***

Material	Composition (Form)	Vendor	Compatibility1 Test Method”	Observation
SiC	SiC (CVD)	Northern	1/1	Reacted
	SiC (Si-enriched)	Northern	1/1	Reacted heavily
	SiC (Hot–pressed)	Northern	3/1	Intact
Si3N4	Si3N4 (Hoc–pressed)	Northern	0/1	Specimen not recovered
	Si-N-0 (IBAD-coating)	*ANL*	0/1	Coating layer totally dissolved
Quartz	SiO_2 (Quartz tube)		0/1 and 2	Specimen not recovered
Rutile	Ti02 (Single crystal)		0/1	Specimen not recovered
Yttria	Y_2O_3 (Sintered)	Ceres	3/1	Intact
	Y_2O_3 (Hot-pressed)	*ANL*	3/1	Intact
YSZ	ZrO_2-10%Y_2O_3			
	(Sintered)	Coors	1/1	Reacted heavily
	(Single crystal)	Ceres	1/1	Reacted heavily
Chromia	Cr_2O_3 (Hot–pressed)	ANL	WI	Specimen not recovered
AIN	AIN	ORNL	*3r2*	Intact [7]
	AIN^b (1-3% **Y** incorporated)	ANL	3/1	Intact
	AIN (Sintered-oxygen enriched)	ANL	2/1	Reacted
	Al(V)N or AIN Al-O-C-N	*ANL*	*3r2*	AIN, Al(V)N, or Al-O-C-N formed in-situ on V-5Cr-5Ti

Table I. continued

Material	Composition (Form)	Vendor	Compatibility/ Test Method[a]	Observation
BN	BN (Hexagonal)	Northern	0/1	Specimen not recovered Coating totally dissolved
	BN (IBAD–coating)	ANL	0/1	
Si	Si (Single crystal)	ANL	0/1	Specimen not recovered
Al_2O_3	Al_2O_3 (AD 998-sintered)	Coors	0/1	Specimen not recovered
TiN[c]	[d]TiN (pure & doped with Si, Mg, Al, and O)	ANL	3/2	TiN formed on Ti in Li at >650°C
CaO	CaO	ANL	3/2	700°C, 266 h CaO formed on V-15Cr-5Ti[e]
	CaO or Ca(V)O	ANL	3/2	416°C CaO or Ca(V)O formed in-situ on V-5Cr-5Ti in Li
MgO	MgO	B&W	3/2	Intact [7]
	MgO	ORNL	3/2	Intact [7]
	MgO or Mg(V)O	ANL	3/2	416°C MgO or Mg(V)O formed in-situ on V-5Cr-5Ti in Li
BeO	BeO	General Ceramics	3/2	Intact [7]
	BeO	Coors	3/2	Intact [7]
	BeO or Be(V)O	ANL	3/1 and 2	416°C BeO or Be(V)O formed in situ on V-5Cr-5Ti in Li
Y-Al garnet	$Y_3Al_2O_{12}$	Union Carbide	3/2	Intact [7]

[a] Compatibility with liquid-Li: 0 and 3 indicate not compatible and compatible. respectively. Test method; 1 indicates a test in flowing Li at 450°C for 315 to 617 h; 2 denotes capsule tests at 400°C for 100 h.

[b] ICP-Spectrochemical analysis of AlN indicated impurity levels (in wt.%); As <0.05, Ba 0.005, Be <0.001, Ca 0.54, Co <0.002, Cr <0.002, Cu 0.006, Fe 0.015, Y 3.77, Y_2O_3 4.79, Mg 0.004, Mn <0.001, Ni 0.002, Pb <0.02, Sb <0.05, Sn <0.02, Sr <0.001, Ti 0.022, V <0.002, Zn <0.002, Zr <0.002, and Te <0.05. Before and after the test, only the Li was analyzed again. The Li contents were <0.01 and 6.85, respectively.

[c] TiN is an electrical conductor.

[d] Type 304/316 stainless steel container for Li + N

[e] Li + Ca used for this study.

CaO coating on V-5%Cr-5%Ti

In the event that metallic solutes (e.g., Ca. Be, **Y,** or **Mg)** dissolved in Li cannot produce intermetallic phases by reaction with V or its **alloys,** another fabrication approach can be adapted to facilitate formation of the insulating coating. It is well known that O can be incorporated into the interstitial sublattice in body-centered-cubic (bcc) V and its alloys.[8] Thus, **if** O or N **is** present in the alloy **(as** a reactant), it may have a higher affinity for solutes such **as** Ca or Mg dissolved in Li than do the alloy elements (i.e., V, Cr, and Ti). Several experiments were performed to test this hypothesis. Samples of V-5%Cr-5%Ti were heat–treated in flowing N_2 or **Ar** at temperatures of **510** to 1030°C to charge the surface of the alloy with N or **O.** Then the samples were immersed in Ca-bearing liquid Li for four days at 420°C to investigate the formation of CaO. Figure 1 shows SEM photomicrographs of the surface and cross section of CaO on a V-5%Cr-5%Ti specimen, together with an EDS spectrum from the CaO layer.

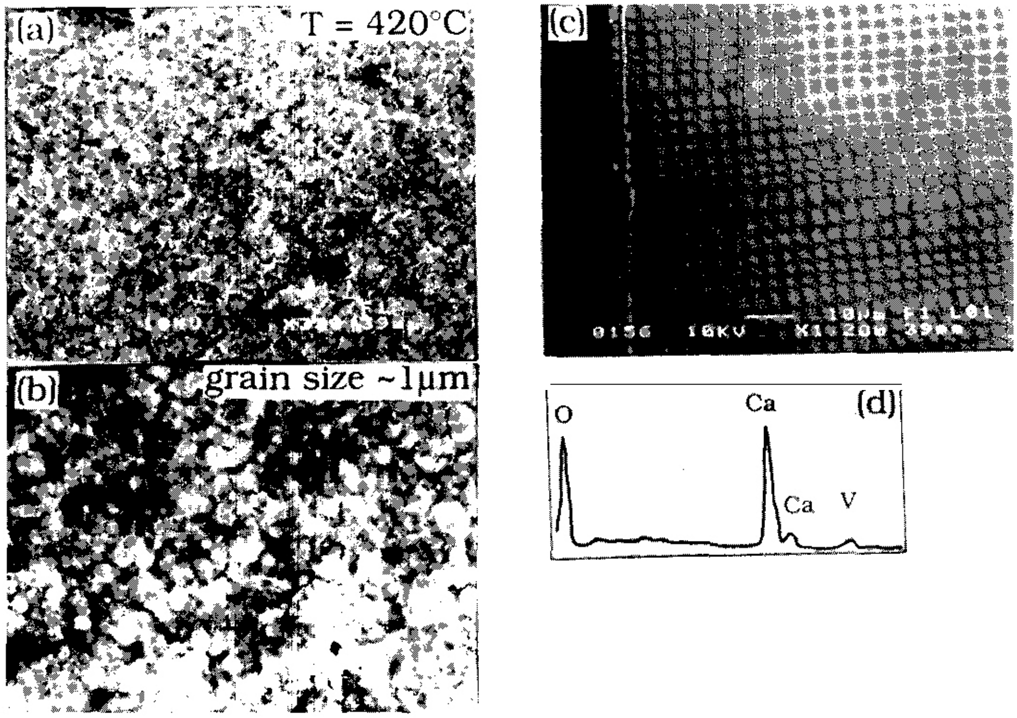

Figure 1. ***(a) SEM photomicrograph of surface of CaO layers on V-5%Cr-5%Ti formed in Li containing ≈4 at.% Ca, (b) enlargement of part of (a), (c) cross-sectional view, and (d) EDS spectrum from CaO layer***

Electrical resistance **of** the films was ≈ 0.4 to 3.5 Ω, and temperature–dependent electrical resistance showed predominantly ceramic-insulator behavior (Fig. 2). When direct current was supplied through the electrodes at 539°C, polarization behavior was observed and the ohmic values increased to 35.7 Ω for the 3–cm^2 area. **A** calculated value of 107 Ω-cm^2 may satisfy the required resistivity (r) times thickness (t), or rt criterion of ≥25 to 100 Ω-cm^2 for fusion reactor applications? if the thickness is assumed to be ≈3 μm. **A** problem that still requires attention is depicted in Fig. **3,** namely, decrease in resistance as temperature increases. Two temperature–cycling runs showed that ohmic values dropped abruptly at ≈500°C in the first run and at ≈400°C in the second run. This problem will be explored over an extended temperature range from the fabrication temperature to the freezing point of the liquid metal, and down to room temperature.

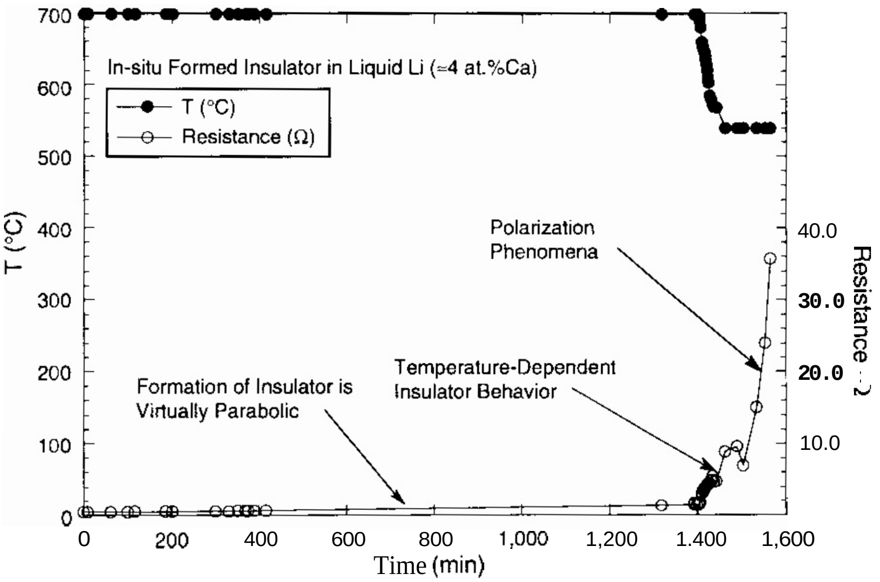

Figure 2. *Temperature and in-situ electrical resistance of CaO coating in liquid Li containing 4 at.% Ca, as a function of time*

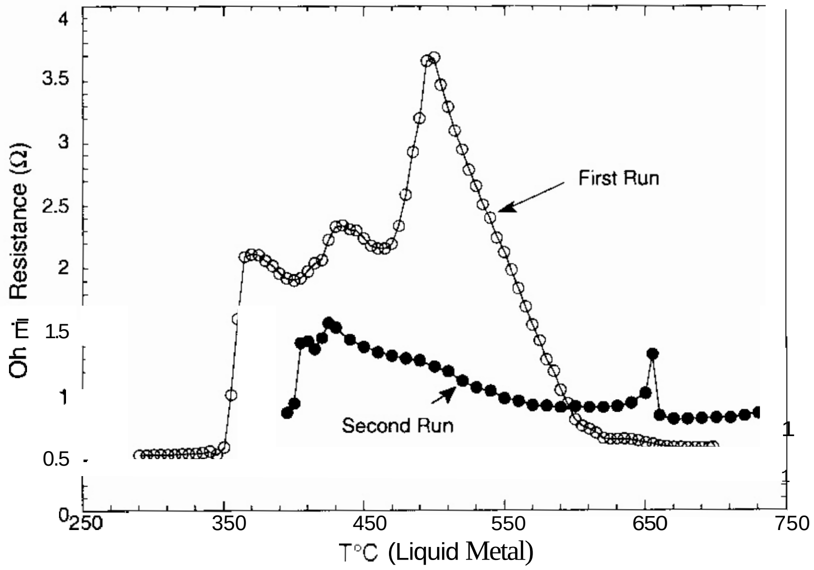

Figure 3. *Ohmic values for CaO layer on V-5%Cr-5%Ti in liquid Li vs. temperature during cooling in two runs*

CONCLUSIONS

Based on liquid-Li compatibility tests of coatings produced on V–base alloys, a method was developed for in-situ fabrication of insulator coatings in a liquid-Li environment. Surface modification via high-temperature liquid–phase deposition can provide intermetallic and/or ceramic phases on V–base alloys. This process is facilitated in liquid Li because surface contamination by O or oxide films is virtually eliminated, and the process to produce homogeneous coatings on various surface shapes can he controlled by exposure time, temperature, and composition of the liquid metal. Conversion of intermetallic or O and N enriched layers to an electrically insulating coating (CaO for surface O–enriched V–5%Cr–5%Ti) in liquid Li was demonstrated in the temperature range of 416°C to 880°C. A CaO layer formed relatively easily in liquid Li containing Ca at 416°C. Additional work will be performed to improve the mechanical stability of the coatings during thermal cycling and to establish the mechanisms for self-healing of the coatings.

REFERENCES

[1]. C. C. Baker et al., *Tokamak Power System Studies FY 1985,* Argonne National Laboratory Report ANL/FPP-85-2 (December 1985).

[2]. **Y. Y.** Liu and D. L. Smith, *Ceramic Electrical Insulators for Liquid Metal Blankets.* J. Nucl. Mater., **141-143**, 38 (1986).

[3]. T. Kammash, *Fusion Reactor Physics,* Chapter 15, Ann Arbor Science Pub. Inc., Ann Arbor, MI (1975), pp. 405-439.

[4]. J.-H. Park and G. Dragel, *Development of Electrical-Insulator Coatings: In-situ Electrical Resistance Measurements on V-5%Cr-5%Ti in Liquid Lithium,* Fusion Reactor Materials Semiannual Progress Report for the Period Ending September 30, 1993, DOE/ER–0313/15, pp. 321–325 (1993).

[5]. J.-H. Park and G. Dragel, *Development of Aluminide Coatings on Vanadium–Base Alloys in Liquid Lithium,* Fusion Reactor Materials Semiannual Progress Report for the Period Ending March 31, 1993, DOE/ER–0313/14, pp. 405–410 (1993).

[6]. R. F. Mattas, B. A. Loomis, and **D. L.** Smith, *Vanadium Alloys for Fusion Reactor Applications, JOM,* **44**(8), 26 (1992).

[7]. R. J. Lauf and J. **H.** DeVan, *Evaluation of Ceramic Insulator for Lithium Electrochemical Reduction Cells.* J. Electrochem. Soc., 139,2087-2091 (1992).

[8]. A. U. Seybolt and H. T. Sumsion, *Vanadium-Oxygen Solid Solutions,* J. Metals Trans. AIME, 292-299 (1953).

[9]. B. F. Picologlou, Argonne National Laboratory, personal communication (1991)

7.0 SOLID BREEDING MATERIALS AND BERYLLIUM

Performance of Ceramic Breeder Materials in the SIBELIUS Experiment

J. P. Kopasz and C. E. Johnson (Argonne National Laboratory) and D. L. Baldwin (Pacific Northwest Laboratories)

OBJECTIVE

The objective of this work is to obtain performance information on the candidate ceramics from the SIBELIUS experiment.

SUMMARY

Lithium containing ceramics are among the leading candidates for use as tritium breeding materials in a fusion reactor. An issue affecting both the safety and economics of the reactor is the tritium inventory. The SIBELIUS experiment was designed to examine material compatibility between different components of a breeder blanket and to examine the tritium inventory in the components of the blanket. The tritium inventory in each of the ceramics was determined by measurements at end of life and were found to be quite low and in agreement with those determined in tests with no beryllium present. The inventory increased in the order lithium zirconate < lithium oxide< lithium orthosilicate<lithium aluminate with the inventory in the zirconate less than 0.03 wppm at 550°C.

PROGRESS AND STATUS

Introduction

Lithium containing ceramics are among the leading candidates for use as tritium breeding materials in a fusion reactor. Breeder blanket designs utilizing lithium ceramics also employ a beryllium neutron multiplier to ensure a tritium breeding ratio greater than one. In order for these designs to be acceptable from an economic and safety perspective, the tritium inventory in the ceramic and in the beryllium should be low. The SIBELIUS experiment is an EU/USA collaborative test designed to assess the compatibility of beryllium/lithium ceramics and beryllium/steel compacts in a neutron environment. The test also provided the opportunity to assess the tritium inventory in several candidate ceramic breeder materials and in beryllium, and determine if there are any interactions between the ceramics and beryllium which may effect the tritium inventory in either of these materials.

End-of-life inventory measurements are less ambiguous than those determined from in-pile temperature change tests, and provide crucial tritium inventory data for designers and modelers. However, sample characteristics such as grain size may be affected by changes in the test conditions, such as temperature or purge gas composition changes, which may complicate the interpretation of the end-of-life inventories. The SIBELIUS data set is unique in that the samples were subjected to a minimal number of temperature changes and operated under constant purge gas Composition.

Experimental

The irradiation vehicle consisted of eight capsules, seven of which were independently purged with a He - 0.1% H_2 gas mixture. The eighth capsule was not purged and contained Be pellets for lifetime and void swelling tests. Two capsules contained only ceramic (Li_2O and $LiAlO_2$), for comparison of tritium release and inventory with the samples in contact with beryllium. One capsule contained Li_4SiO_4 pebbles in contact with Be disks, and the other four contained alternating disks of beryllium, steel, and ceramic in the order beryllium, steel, beryllium, ceramic. One capsule contained lithium orthosilicate, a second capsule lithium aluminate, a third capsule lithium oxide and a fourth capsule contained lithium zirconate. The design of the irradiation capsules and the experimental conditions have been reported previously.[1,2] A summary of the ceramic properties is given in Table I. The irradiation temperature was controlled by a gap gas and was maintained at 550°C for most of the experiment. One set of temperature transients was performed, with the temperature for the aluminate decreased to 500°C then returned to 550°C, and the silicate and zirconate decreased to 450°C then increased back to 550°C, while the temperature for the oxide sample remained constant. The temperature at the end of the experiment was **550°C.** The specimens were irradiated for **1690** h with a neutron flux at mid-plane of 1.1 x 10^{14} n $cm^{-2}s^{-1}$ (thermal) and **1.0** x 10^{14} n $cm^{-2}s^{-1}$ (fast, > 1 MeV).

Table I: **Sample Characteristics**

Material	Li_2ZrO_3	Li_2O	Li_4SiO_4	LiAlO,
Grain size (µm)	1	–20	–20	**0.4**
Density (%TD)	**70**	80	**91**	**75**

Sample	Anneal Temperatures, °C	Anneal Times	% of total released at each temperature
Li Aluminate	550 650 750 850	-24 h -24 h -24 h -48 h	42.4 52.0 5.0 0.6
Li Zirconate	550 850	-24 h -24 h	84.9 15.1
Li Oxide	850 only	-17 h	100
Li Silicate	850 only	-3 days	100

^{54}Mn, and ^{65}Zn on all of the ceramic samples, indicating contamination from steel activation products. In addition, the gamma spectroscopy indicated a small amount of activity due to ^{125}Sb and ^{152}Eu, ^{154}Eu, and ^{155}Eu in the oxide sample. For the zirconate sample, the activation was due mainly to the ^{95}Zr and ^{95}Nb species which would not be removed by any surface treatment, so dissolution was not attempted.

The samples used for the dissolution tests were broken in pieces and each piece placed in a tared glass vial and weighed. The lithium oxide samples were dissolved in **5 ml** of distilled water in closed screw cap vials to prevent escape of HTO vapor. The solutions were transferred to **25 ml** volumetric flasks and diluted to the appropriate volume. Aliquots were taken for liquid scintillation counting. The lithium aluminate and lithium silicate samples would not dissolve completely. Tritium inventories were obtained by adding 10 ml of an acid solution (approximately 6 N $HNO3$), closing the vial and heating for about 6 hrs. The acid solution was decanted from the solid into a 100 ml volumetric flask and a second 10 ml of acid solution added. The procedure was repeated and the remaining solid washed with 10 ml of distilled water. The solid and vial were then dried and weighed to determine the amount of solid which had dissolved.

During the dissolution there is the possibility that some HT may form. If this occurs, calculations indicate that due to the equilibrium between HT, H, HTO and H_2O only a small fraction ($<<1\%$) of tritium will be expected to remain in the form of HT. Therefore, this procedure does not take any special precautions to collect tritium in the form of HT gas formed during the dissolution, such as oxidation followed by collection of the HTO formed. In addition, estimates of the HTO vapor pressure above the solution under the conditions of the dissolution (closed vial) are expected to lead to errors less than 1%.

Results

For the lithium aluminate sample, the first anneal was performed at **850C** for **24** h where the bulk of the tritium was released. A final anneal was performed at 850°C for 48 h. During the second 24 h period of this anneal an additional 0.1% of the tritium was released. For the lithium zirconate, one anneal was performed for 24 h at 550°C, followed by a second 24 h anneal at 850 C. The majority of the tritium (84.9%) was released during the anneal at 550°C. For lithium oxide only one anneal at 850°C was performed. No additional release was observed after 17 h. For the lithium silicate, the sample was annealed at 850°C. After 48 h tritium was still being released, so the anneal was continued. After 72 h no additional release was observed.

The tritium inventory values determined from the dissolutions and the anneals are tabulated in Table III. The lithium oxide results have been corrected to give tritium per gram of Li_2O prior to any hydrolysis of the sample. The amount of hydrolysis was determined by titration of the lithium oxide sample solutions. For lithium oxide, two moles of hydroxide would be formed for each mole of oxide upon dissolution, giving 0.067 moles hydroxide/gram of sample. If the sample was already hydrolyzed to lithium hydroxide there would be 0.042 moles hydroxide/gram of sample.

Sample	inventorydissolution	Inventory -Anneals	Average
LiAlO,	2029 ± 203	1659 ± 116 MBq/g	1844 i 185 MBq/g
Li_4SiO_4	874 ± 87	947 ± 66 MBq/g	911 ± 37 MBq/g
Li_2O	34.8i3.5 MBq/g	36.2i 2.6 MBq/g	35.5 ± 0.7 MBq/g
Li_2ZrO_3		7.8 ± 0.6 MBq/g	

Titration of the solutions formed upon dissolution indicated a hydroxide concentration of 0.041 moles/gram of sample. This corresponds with the concentration of lithium hydroxide of 0.042 moles/g indicating that the lithium oxide samples had fully hydrolyzed prior to the analysis. Most likely this hydrolysis occurred during the handling and storage of the samples and not during the irradiation. Correcting the inventory to tritium/gram of lithium oxide increases the inventory from 21.7 to 34.8 MBq/g Li_2O for the dissolution tests and from 22.6 to 36.2 MBq/g Li_2O for the anneal samples, assuming the same amount of hydrolysis occurred in each sample. The ternary ceramics are much less hygroscopic than lithium oxide, and are expected to have undergone only slight hydrolysis during handling and storage. In addition, if hydrolysis occurred the percentage of weight gained due to hydrolysis is much less than that for lithium oxide, so errors in determining the tritium per unit weight of sample are reduced. It is estimated that the errors in the inventories due to any hydrolysis of the ternary ceramics is less than 10%.

Discussion

Overall performance

The system Be/ceramic appears stable at 550°C under irradiation. The lithium ceramics survived the irradiation intact without fractures. The ceramic disks were easily separated from the adjacent beryllium disks, with no macroscopic evidence for interactions between the ceramic and beryllium. SEM examinations indicated no changes in the ceramic microstructure at the Be/ceramic interface, however some roughening of the Be surfaces was noted.[2],[5] The stability is probably due to the protective coating of BeO which appears to be unaffected by irradiation damage at the fluence investigated. The tritium inventory increased in the order $Li_2ZrO_3 < Li_2O < Li_4SiO_4 < LiAlO$, These inventories were all within the range of values observed for in-pile tests where beryllium was absent, suggesting the beryllium has little or no effect on the tritium retention in the ceramic.

Comparison of methods

The tritium inventory in lithium oxide was determined by two separate methods, high temperature anneals and dissolution, at two different laboratories. The results are in excellent agreement, with differences of less than 5%. This indicates that all of the tritium was released during the high temperature anneals and that losses due to tritium in the gas phase (either as HT or HTO) for the dissolution method are insignificant. For the silicate, the agreement between the two methods is also very good. The greatest difference was found in the inventories determined for the aluminate samples, with a difference of about 20%. This difference is most likely due to the small amount of aluminate sample which dissolved (6 mg) and the inherent errors involved in the partial dissolution.

Comparisons with other SIBELIUS determinations

Inventory values determined for the oxide (35.5 MBq/g) and the silicate (910 MBq/g) are lower than those determined by Dienst et al. for SIBELIUS samples from the same capsules (70.5 and 1219 MBq/g respectively) [5]. The differences in the inventories for the SIBELIUS samples does not appear to be attributable to any differences in the samples or irradiation environment. One might expect the position in the capsule to have an effect on the inventory. since there is an increasing tritium partial pressure as one moves from the purge gas inlet where the tritium partial pressure is very low to the purge gas outlet where the tritium partial pressure is high. This has been proposed as the reason for the increase in tritium inventory going from the purge inlet to the purge outlet observed for the BEATRIX thin-ring [6]. A similar gradient was observed in the CRITIC-I experiment [7]. If solubility was a main factor in determining tritium inventory, the samples analyzed by Dienst et al. located near the purge gas inlet would be expected to have a lower inventory than the samples analyzed in this work as they were positioned near the purge gas outlet. Also, the differences between the inventory values can not be attributed to reaction of the hygroscopic lithium oxide samples with water, as the values reported here have already been corrected and any hydrolysis experienced by Dienst's samples would increase the discrepancy.

Comparisons with other in-pile tests

The tritium inventory determined for the SIBELIUS lithium oxide sample of 35.5 MBq/g (0.096 wppm) is in agreement with the inventory determined in BEATRIX-II of 0.06 wppm for the portion of the solid (temperature gradient) lithium oxide specimen in temperature regions calculated to be from 532 to 649" C [6,] and for the EXOTIC-2 lithium oxide of 0.05 wppm (at 590-

630°C) [8]. The agreement is exceptional if one uses the SIBELIUS inventory prior to correction for hydrolysis of 22.2 MBq/g (0.064 wppm). This raises the possibility that hydrolysis may have also occurred for the BEATRIX temperature gradient and EXOTIC-2 samples. The SIBELIUS inventory values are about a factor of two to six lower than the values reported for the BEATRIX-II thin ring specimen of 0.23-0.61 wppm [6], even though the average temperature in the thin ring at shutdown was 630°C. The value obtained by Dienst et al. (0.20 wppm)[5] is comparable to the value reported for the BEATRIX-II thin ring sample for the sample positioned at the bottom near the purge inlet (0.23 wppm),[6]. These inventories are less than those determined in CRITIC-1 of 0.3 to 1 wppm [7] (at 600°C) and VOM-15H of 0.5-1.0 wppm at 740°C [9], which were under purge gases with lower hydrogen concentrations. The differences in tritium inventory for the experiments run under He + 0.1% H_2 do not correlate with differences in grain size. The reasons for the variations in inventory are not understood at this time.

Comparisons of tritium inventory values for lithium aluminate samples shows an even larger variation. For the SIBELIUS lithium aluminate sample a tritium inventory of 1844 MBq/g (5.2 wppm) was determined. In the TRIO experiment an inventory of 16.7 MBq/g was found (at 650°C, grain size 0.2 µm)[10] while in the EXOTIC-6 experiment the inventory ranged from 148 MBq/g (at 495 C) for the CEA prepared aluminate to 2405 MBq/g (at 485 C) for ENEA prepared material. Kwast [11] suggests the difference in inventory for the EXOTIC aluminates is related to differences in grain size (CEA aluminate grain size 0.4 µm, ENEA aluminate grain size 1-10 µm). However, the SIBELIUS sample, although at slightly higher temperature and with a grain size comparable to that of the CEA aluminate in EXOTIC, has an inventory comparable to the ENEA aluminate. This suggests another variable may be responsible for the difference in tritium inventory for the aluminate samples. The SIBELIUS generation rate is about seventy percent higher than in EXOTIC, so from a desorption release mechanism, the inventory values would be expected to be proportionately higher. However, this difference in generation rates does not account for the more than order of magnitude difference in the inventory values of similarly sized materials.

For the lithium orthosilicate the tritium inventory values determined at the end-of-life are in good agreement; however, these values do not agree with the inventory determined from temperature transient tests. We determined an inventory of 910 MBq/g for the SIBELIUS lithium orthosilicate pellet. Dienst et al. [5] determined a slightly higher inventory of 1219 MBq/g for a second SIBELIUS lithium orthosilicate pellet and Kwast et al. reported an inventory of 1776 MBq/g at the end-of-life for lithium orthosilicate at 360 C in EXOTIC-6.[11] These values are higher than expected based on calculations from in-pile tritium release transients after temperature changes. In SIBELIUS the temperature transients indicate a tritium inventory of 442 MBq/g at 550°C (residence time of 1 h)[12]. This suggests tritium inventories determined from temperature transient tests may substantially under predict tritium inventories.

A tritium inventory of 7.84 MBq/g was determined for the SIBELIUS lithium zirconate from annealing studies. This is slightly greater than those determined by Kwast et al. of 2.96 MBq/g for CEA zirconate (1 µm grain diameter) and 7.03 MBq/g for ENEA zirconate, (2 µm grain diameter) at temperatures of 450 and 455 C.[11] The SIBELIUS zirconate was similar to the CEA zirconate used in EXOTIC, however the inventory is more comparable to that for the larger ENEA zirconate. Again, the reasons for these variations is unknown.

Conclusions

Intimate contact between beryllium and lithium ceramics considered for tritium breeding materials appears to have no detrimental effects on the performance of the ceramics. Although

Ab initio calculations for hydrogen adsorption on lithium oxide surfaces - A. Sutjianto. S.W. Tam. L. Curtiss. and C.E. Johnson (Argonne National Laboratory) and R. Pandey (Michigan Technological University)

OBJECTIVE

The objective of this work was to investigate the hydrogen adsorption on the lithium oxide surfaces. The surfaces were described by using the so-called slab model; a finite number of atomic layers parallel to the exposed face.

SUMMARY

The study of hydrogen chemisorption on the (110) and (111) lithium oxide surfaces have been investigated by means of ab initio Hartree-Fock calculations. In general, for the n-layer slab (where n = 2 and 3) of the neutral (110) and for the three-layer slab of the neutral (111) surfaces, there is no hydrogen chemisorption. The oxygen 2p band of the (110) surface is stabilized by the presence of more stacking sequences of layers which prevents charge transfer to the hydrogen. In the case of a neutral (1 10) layer due to low coordination of the anion, there is hydrogen chemisorption in the form of OH- and $Li^+H^-Li^+$ with the chemisorption energy of 0.93 eV. For the neutral (I 11j surface, there is no hydrogen chemisorption since the oxygen layer is screened by the cation layers hindering the charge transfer to the hydrogen.

PROGRESS AND STATUS

Introduction

Lithium ceramics is one of the leading class of materials being considered as tritium breeders for fusion technology application. Hydrogen has been known to be able to enhance the release of tritium from lithium ceramics materials. This ‘accelerator’ role of hydrogen has been demonstrated in numerous in-pile experiments on tritium release [1-5]. The enhancement effect is usually accomplished via the addition of hydrogen (typically at a level of around **0.1%)** to the helium purge gas. Despite this positive benefit the use of hydrogen in this way is not without problems. Chief among them are the issues of tritium management via isotopic separation (due to the large hydrogenltritium ratio) and tritium containment (arising from the presence of reduced form of tritium and the potential permeation **loss).**

In order to maximize the benefit/liability ratio of hydrogen utilization to enhance tritium release one needs to gain an understanding of the mechanism through which hydrogen is able to accomplish this role. Increased understanding would also benefit the search for alternative ‘accelerator’ materials beside hydrogen. Therefore we have initiated a program to investigate the process of hydrogen adsorption onto lithium oxide surfaces. Concurrent to an experimental component using temperature programmed description technique we have **also** utilized the method of computer simulations to simulate the hydrogen adsorption process. This work reports the result of the computer simulation.

Method

The technique that we have employed is the self-consistent-field Hartree-Fock linear-combination-atomic-orbitals (SCF-HF-LCAO) method modified to a crystalline environment. This is an ***ab*** *initio* method meaning that it contains no ***ad hoc*** adjustable parameters. Instead of basing on molecular orbitals (MOs) crystal orbitals (COs) are used. These COs are defined (similar to the quantum molecular approach) as a linear-combination-of-atomic-orbitals (LCAO) but with the periodic environment of the crystal built in. This has the advantage of taking the extended nature of the crystalline materials into account. The CRYSTAL code [6] that we have utilized has adopted this CO approach.

However, for some low symmetry configurations such as kinks and ledges on surface step structures it may not be practical to use the CRYSTAL approach. For these situations the GAUSSIAN code [7] which is based on a finite quantum cluster approach would be more suited to simulate these low symmetry configurations. Both approaches have been utilized in a complementary manner. The main emphasis to the present work is on hydrogen chemisorption processes on the terrace sites on Li_2O surfaces in which

CRYSTAL would be the principal tool utilized.

One of the keys to a successful ab initio calculation is using a good basis set to represent the electronic structure of the species. In the case of the lithium oxide its bonding characteristic is strongly ionic. However the O^{2-} being an unstable ion is actually stabilized by the surrounding cation (in our case Li) environment. In this situation the two extra electrons on the oxygen ion would induce a relaxation of the valence electrons. This particular consideration for O^{2-} is necessary for any oxide that involves this oxygen ion in which the bonding is reasonably ionic. The effect **is** taken into account in an optimized basis set designed for the oxygen ion in a Li_2O environment. [8,9] Recent calculations on bulk crystalline Li_2O done by Dovesi [9] have indicated that the optimized basis set is able to give the lattice constant, bulk modulus and elastic constant in good agreement with experimental values. Table 1 listed the results of the calculations and the corresponding experimental data. **We** have therefore adopted this crystalline basis set [9] for all our subsequent calculations involving lithium oxide. For the hydrogen, we have used the basis set obtained by Dovesi [11] where the calculated equilibrium Hartree-Fock bondlength of H_2 of 0.738 Å is in good agreement with its experimental value of 0.742 Å [12]

Table 1. The energy and geometrical parameters from both Hartree-Fock calculations and experiment.

	Dovesi[9]	Experiment
Total energy (eV)	-2447.920	
HF cohesive energy (eV)	7.864	11.755*
Lattice parameter (Å)	4.57	4.57[14]
Bulk modulus (dyne cm^{-2})	0.93×10^{12}	0.85×10^{12} [14]

*obtained with an atomic reference from thermochemical data [12]

Results and discussion

The geometrical and the electronic structures of the bulk, the surfaces **of** Li_2O and the study **of** the chemisorption of H_2 on the Li_2O surfaces are discussed successively.

The crystalline and the electronic structure of Li_2O

There has been a number of theoretical calculations and experiments [13-15] being done to understand the bulk properties of the crystalline Li_2O. The crystalline structure of lithium oxide **is** in the anti-fluorite configuration with the space group *Fm3m*. The experimental lattice constant a_0 at T = 0 K **is** 4.573 Å [14] obtained by extrapolating the a_0 versus **T** curve measured in the range of 293-1300 K. For the lattice constant of 4.573 Å, the nearest Li-Li, O-O and Li-0 distances are 2.286, 3.224 and 1.980 Å respectively.

Fig.1 shows the density of states for the valence bands of the bulk Li_2O calculated using CRYSTAL. This figure identifies the order of the occupied bands of the lithium and oxygen respected to their energies. It also describes the number of states within an interval of energies between E and E+dE. The deepest band, not shown in the figure, at **-555.910** eV, is the **Is** type core orbital from oxygen and it is followed by the two bands, in the interval of -63.451 to -63.105 eV, which are attributed to the **Is** core orbital from both lithiums **(Is** Li). The band that characterized by 2s type orbital of oxygen (2s **O)**is appeared in the interval of -31.231 to -30.810 eV and, finally, the highest bands are located between -13.554 to -10.025 eV are the p type orbitals of oxygen (2p **O).**

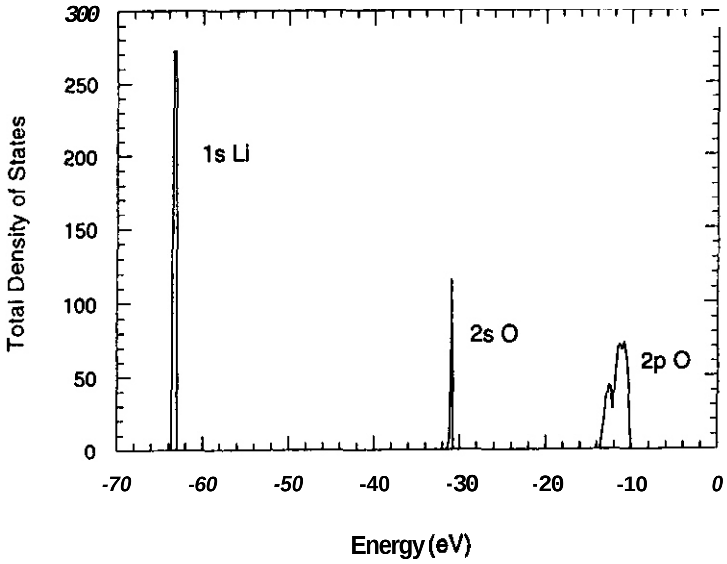

Fig. 1 The Hartree-Fock total density of states of crystalline Li_2O. The bandwidths for 1s Li and 2s O, and 2p O are 0.35 eV and 3.55 eV respectively.

The Li_2O is an ionic material because of the following reasons: first. there is little overlap of the ionic charge distribution indicated by the small and negative (-0.01) bond population between the nearest Li-0 neighbor which confirms the very limited presence of covalency. Secondly, as a consequence, the crystalline Li_2O energy bands are well separated and no contribution of the lithium band to the uppermost valence band of oxygen (Fig.1, 2p O).Finally, from a Mulliken analysis of the charge distribution, the net charge of oxygen is -1.94 e, very close to the value of -2 e expected from ideal ionic bonding.

The stability of Li_2O crystal surfaces

The surface study was carried out by using the slab model available in the CRYSTAL program; the semi-infinite crystal was simulated by a finite number of atomic layers parallel to the exposed face and reproducing the crystal geometry.

There are three planes, namely, (100).(I 10) and (1 11), that will be discussed in this section. The (100) planes consist of alternating lithium layers and oxygen layers. The distance between the two layers is 1.143 A. Each layer of (110) planes is neutral where both lithium and oxygen are on the same plane. The layer separation is 1.617 Å. The (11 I) planes, for the smallest neutral system. have two lithium layers and one oxygen layer. The distance between the lithium and the oxygen layers is 0.660 Å and the distance between the two adjacent lithium layers is 1.320A. The stacking of the layers for these different surfaces are shown in Fig.2. The neutral stacking unit of (100), (110) and (I 11) planes, along the perpendicular to the planes, are two layers (one lithium layer, and one oxygen layer), one layer, and three layers (two lithium layers and one oxygen layer) respectively.

Tasker [16] classified the arrangements of the charged layers into three classes, depending on the stacking sequences of the charged planes as one moves into the bulk. The stacks of the (100) planes are charged and there is a dipole moment (m) perpendicular to the planes (Fig.2a). This creates a potential. called Madelung potential, where addition of an extra neutral unit of two planes to the (100) surface of the crystal will affect the energy of ions in the bulk of the crystal. As there are no cancellations and the potential does not diminish with distance from the top layer then the Madelung potential at an ion in the crystal contains contributions from all the planes out to the external (100) surface. The potential therefore never settles to reliable inventory data are few in number so one has difficulty drawing firm conclusions at this time, it appears that the triiium inventories in the ceramics are unaffected by contact with beryllium. Chemical interactions between the ceramics and the beryllium also appear to be negligible. The tritium inventories determined for the SIBELIUS lithium zirconate and lithium oxide samples were extremely low, at 7.8 MBq/g (0.02 wppm) and 35.5 MBq/g (0.096 wppm). While the inventory for the orthosilicate and aluminate are about two orders of magnitude higher, 910 and 1844 MBq/g (**2.6** and 5.2 wppm) they are still quite low and below levels which would cause safety or economic problems.

FUTURE WORK

Additional inventory data will be obtained for the lithium zirconate sample

REFERENCES

[1] N. Roux. M. Briec, M. Bruet, T. Flament, C. Johnson, M. Masson, A. Terlain, and F. Tournebize, J. Nucl. Mater. 179 (1991) 329.

[2] N. Roux, J. J. Abassin, M. Briec, D. Cruz, T. Flament, and I. Schuster, "Compatibility behavior of beryllium with $LiAlO_2$ and Li_2ZrO_3 ceramics, with 316 L and 1.4914 steels in SIBELIUS" J. Nucl. Mater. 191-194(1992)

[3].D.L. Baldwin. O.D. Slagle and **D.S.** Gelles, J. Nucl. Mater. 179&181 (1991) 329-334.

[4].D.L. Baldwin and M.C. Billone, presented at ICFRM6, to be published in J. Nucl. Mater.

[5] W. Dienst, D. Schild and H. Werle , Kernforschungszentrum, Karlsruhe, Report KfK-5109, December 1992.

[6] O. D. Slagle, **T.** Takahashi, F. D. Hobbs, K. Noda, D. L. Baldwin, G. W. Hollenberg, and R. A. Verrall, "Postirradiation Examination of BEATRIX-II, Phase I" . to be published in J. Nucl. Mater.

[7] R. A. Verrall, J. M. Miller, I. J. hastings, **D.** S. MacDonald adn D. H. Rose, in Advances in Ceramics: Fabrication and Properties of Lithium Ceramics, Vol. 27, eds. G. W. Hollenberg and **I.** J. Hastings (American Ceramic Society, Inc, Westerville, OH, 1990) p. 299

[8] H. Kwast, A. Kout, R. P. Muis, M. P. Stijkel, A . J. Flipot. and J. D. Elen, Fusion Engineering and Design, 8,(1989)359-364.

[9] T. Kurasawa, H. Yoshida. H. Takeshita, H. Walanabe, T. Miyauchi, **T.** Matui, H. Umei and Y. Naruse, J. Nucl. Mater. 133-134 (1985) 196.

[9] R. G. Clemmer. P. **A.** Finn, R. F. Malecha, B. Misra. M.C. Billone, **D.** L. Bowers, A.K. Fischer, L. R. Greenwood, R. F. Mattas. S.W. Tam, R.B. Poeppel, G. T. Reedy, I. T. Dudley, F. **F.** Dyer, **E.** D. Clemmer, J. S. Watson, P. W. Fisher, J. R. Conlin, R. L. Childs, J. L. Scott, R. M. Arons and A. E. Scandora, "The **TRIO** Experiment" Argonne Natrional Laboratory. Argonne, Report ANL-84-55, September, 1984

[10] H. Kwast, R. Conrad, R. May, S. Casadio, N. Roux, and H. Werle, "The Behaviour of Ceramic Breeder Materials with Respect to Tritium Release and Pellet/Pebble Mechanical Integrity" ICFRM-6 to be published in J. Nucl. Mater.

[11] N. Roux, personnal communication , April, 1994.

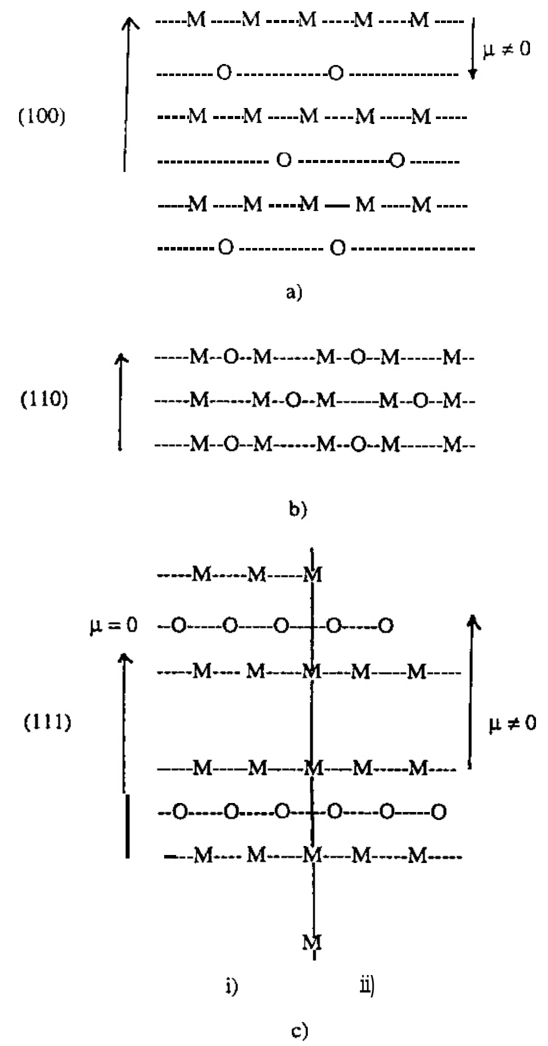

Fig.2 Stacking sequence of planes in the a) (100), b) (110) and c) (111) directions. The non-zero dipole moment, μ, is shown perpendicular to planer (100) direction and (111) direction of stack terminated with anion plane (c,ii). Dipole moment is zero in (111) direction for stack terminated with cation plane (c,i). M denotes the Li^+ and O is O^{2-}

its normal bulk value and the surface energy does not converge. Thus, in this discussion, the (100) surface can be easily ruled out since it is unstable. Unlike the (100) planes, the (110) layers are built up from a stack of neutral layers (Fig.2b). Both lithium and oxygen ions occur on each plane whose total charge is therefore zero. This means that the (110) surface is stable since there is no dipole moment created by the layer and the addition of extra (110) planes on the surface will have no effect to first order electrostatically on an ion in the bulk. Fig.2c shows the stacking sequence in the (111) . Based on the type of the surface layer, one can obtain the (111) layers in two different stackings, namely, the one which begins with the cation layer (Fig.2c (i)) where the system is stable since there is no dipole moment. The other which starts with the anion layer (Fig.2c (ii)) where the dipole moment is not zero and causes the surface to be unstable.

Fig.3 shows the convergency of the total energy per Li_2O of the stable (110) and (111) surfaces as the number of layers increases. In the case of $n = 3, 6, 9, \ldots$ for both (110) and (111) planes, their total energies

Table 2. The Hartree-Fock surface energy SE(Jm^{-2}) for the (110)and (111) planes.

Surface	n	SE(Jm^{-2})	
		present work	Lichanot et al.[10]
(111)			
	3	0.657	0.785
	6	0.680	0.804
	9	0.679	0.804
	12	0.679	0.804
	15	0.679	0.804
(110)			
	2	1.410	1.630
	4	1.443	1.630
	6	1.443	1.630

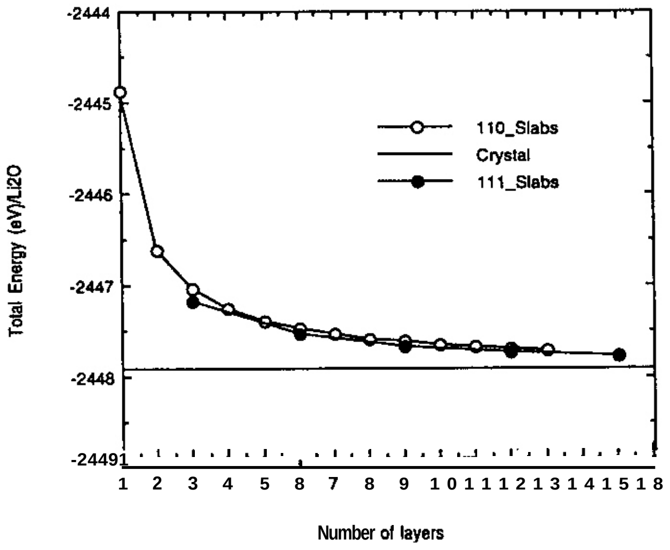

Fig.3 The Hartree-Fock total energy (eV) per Li$_2$O versus number of layers plot of both (110) and (111) planes.

are very close to each other, A drastic change in the total energy per Li$_2$O occurs from one to two (110) layers by about 1.74eV due to the uncoordinated ions on the single layer.

The surface energy (SE)[17] is defined as,

$$SE = (nE^b - E^n)/2, \tag{1}$$

where the denominator 2 is given such that the surface energy is calculated respected to one surface only. n denotes the number of layers, in this case $n = 1,2,3, \ldots$ for (110) and $n = 3, 6, 9. \ldots$ for (111). E^b is the total energy of the bulk and E^n represents the total energy n-layer slab. The present calculated surface energies with the extended basis set [9] are about **15%** and 11% for (111) and (110), respectively. lower than the surface energies calculated by Lichanot et al.[10] In this work, the (111) surface energy is 0.7 Jm^{-2} lower than the (110). This is due to the fact that the (111) surface is the natural cleavage plane in the anti-fluorite structure. Although, the (111) surface is energetically more favorable, in reality, one expects that there is a mix of (110) and (111) surfaces.

The electronic charge density contour plot of the three-layer (110) slab is shown in Fig.4. The lack of covalency is observed with a clear charge separation between the nearest Li-O neighbors. **A** similar ionic characteristic is observed for the (111) surface.

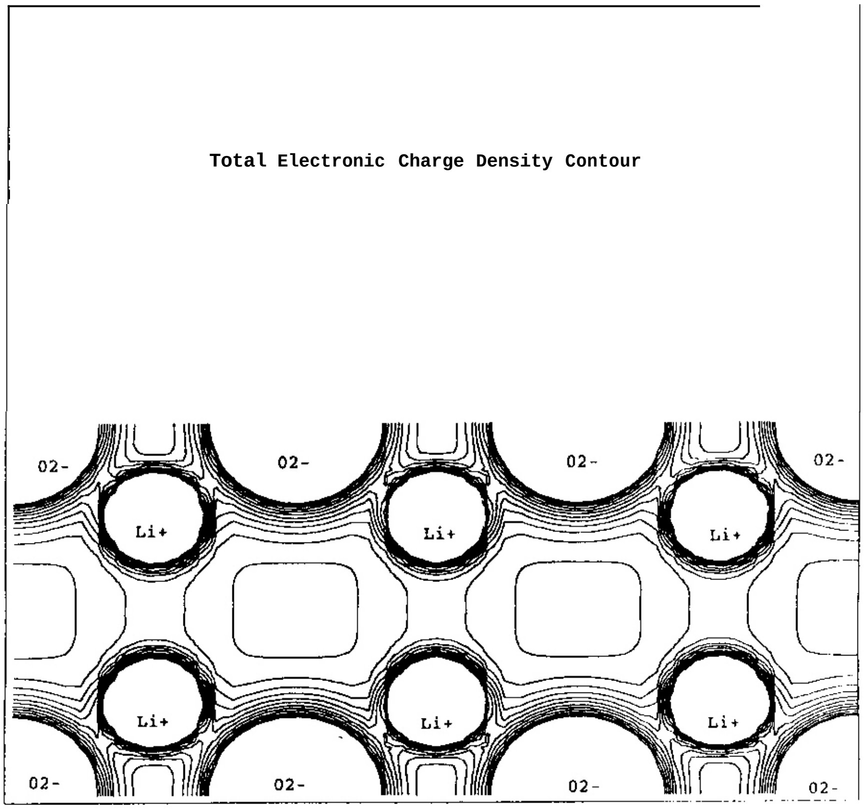

Fig.4 Total electronic charge density map of the (110) surface with 0.003 Å interval **from one isoelectronic to the nearest isoelectronic.**

The studies of H_2 chemisorption on (110) and (111) terraces

The stability of crystal surface that has been discussed in the previous part of this section is very important for further investigation on the possibility of H_2 chemisorption on these stable (110) and (111) terraces, Terraces are atomically flat planes on a crystalline surface. Terraces may terminate at structures called steps.

Fig.5 and Fig.6 show a part of the extended top layer of the (1 10) terrace and the projection of the three (1 11) layers. To study the H_2 chemisorption on the surfaces, each atom of the hydrogen molecule is inserted to the locations of the interested sites within the unit-cell. The adsorption locations (denoted by 1, *2,* 3 and 4) of the hydrogen atom being considered are also shown in these figures. Thus, the configurations of the hydrogen molecule are H(1)H(2), H(1)H(3) and H(1)H(4), where, for example, H(1)H(2) means that. at location 1, one of the hydrogen atom is on top of the oxygen and the other hydrogen is on top of lithium. at location 2, similarly for the other configurations. For each given adsorption location, the calculations were done for one, two and three (110) layers and three (111) layers. The height of the hydrogens were optimized respected to the given locations on the surface to obtain the lowest total energy. Different surface coverages of 100% and 50% were also considered for the n-layer slab (where n = 2 and 3) for (110) surface and for three-layer (I 11) surface. The 100% surface coverage means that within each unit cell of the slab there is a hydrogen molecule. For 50% surface coverage, a hydrogen molecule is within each repeated cell that is two times larger than the original unit cell.

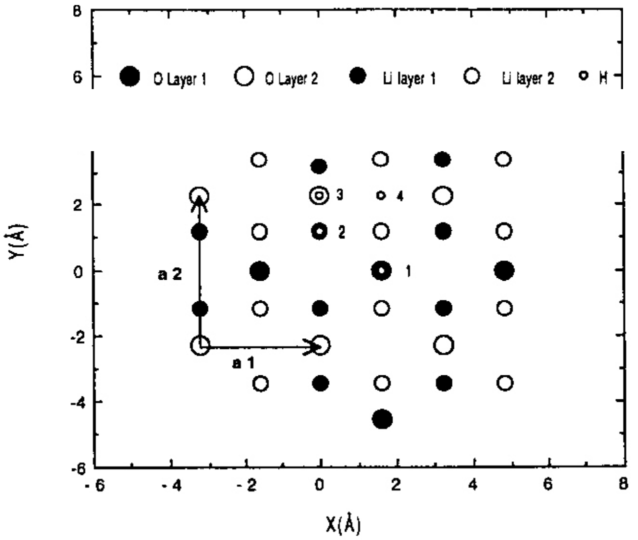

Fig.5.The geometry ofthe two (110) planes. The unit-cell is defined by basis vectors a_1= (3.23.0.0.0.0)Å and a_2 = (0.0,4.57) Å. Along the perpendicular direction to the planer. the stacking sequence is obtained by repeating these two layers.The locations of the strectched hydrogens are represented by 1.2.3 and 4.

The binding energy (BE) of the hydrogen at each given location on each different number of layers is calculated by employing the following equation,

$$BE = [E^n+E(H_2)]- E^n(H_2), \qquad (2)$$

where the first two term denotes the total energies of an n-layer slab, **E".** and that of the adsorbent , $E(H_2)$. Respectively the third term represents the total energy of the hydrogen at the given locations. The convention for (2) is as follows: if BE is a positive value then the system is bound otherwise the system is unbound. The location of the stretched hydrogen which gives the largest value of the binding energy is where the chemisorption occurs. Table 3 lists the calculated binding energies at the given locations (Fig.5 and Fig.6) for the (I 10) and (1 11) terraces.

Table 3 The calculated Hartree-Fock LCAO-CO bondlengths d (Å) of the stretched H2, located above the (110) and (111) surfaces (figs.5 and 6), and the binding energies BE(eV) for n = 1, 2, and 3 layers obtained from CRYSTAL.

Surface	n	Locations of H	d(OH)	d(LiH)	d(H-H)	BE*
(110) [fig.5]						
	1	H(1)H(2)	0.96	1.54	2.06	-0.94
		H(1)H(3)	0.96	1.59	2.08	+0.93
		H(1)H(4)	0.96	2.04	2.33	+0.64
	2	H(1)H(2)	0.98 (0.97)	1.57 (1.57)	2.07 (2.07)	-1.71 (-2.27)
		H(1)H(3)	0.96 (0.96)	1.69 (1.73)	2.89 (2.90)	-0.57 (-1.02)
		H(1)H(4)	0.96 (0.96)	2.20 (2.21)	2.60 (2.60)	-0.86 (-1.43)
	3	H(1)H(2)	0.97 (0.97)	1.57 (1.58)	2.07 (2.07)	-1.54 (-1.82)
		H(1)H(3)	0.96 (0.96)	1.65 (1.72)	2.88 (2.90)	-0.33 (-0.79)
		H(1)H(4)	0.96 (0.96)	2.18 (2.21)	2.59 (2.61)	-0.61 (-1.05)
(111) [fig.6]						
	3	H(1)H(2)	1.1 (1.0) [1.0]	1.48 (1.55) [1.70]	2.14 (2.17) [2.31]	-3.65 (-2.96) [-2.70]
		H(1)H(3)	1.0 (1.0) [1.0]	1.60 (1.60) [1.65]	2.77 (2.77) [2.80]	-3.24 (-2.24) [-1.95]
		H(1)H(4)	1.0 (1.0) [1.0]	2.22 (2.25) [2.33]	1.27 (1.30) [1.41]	-2.73 (-2.10) [-1.74]

---

* The calculated binding energies are listed for various surface coverages: the 25% (represented by the data in the square bracket), 50% defined by the data in the bracket and 100% for the data with no bracket.

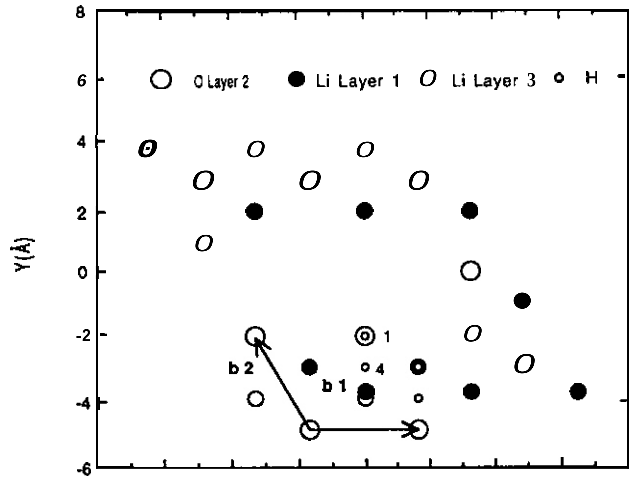

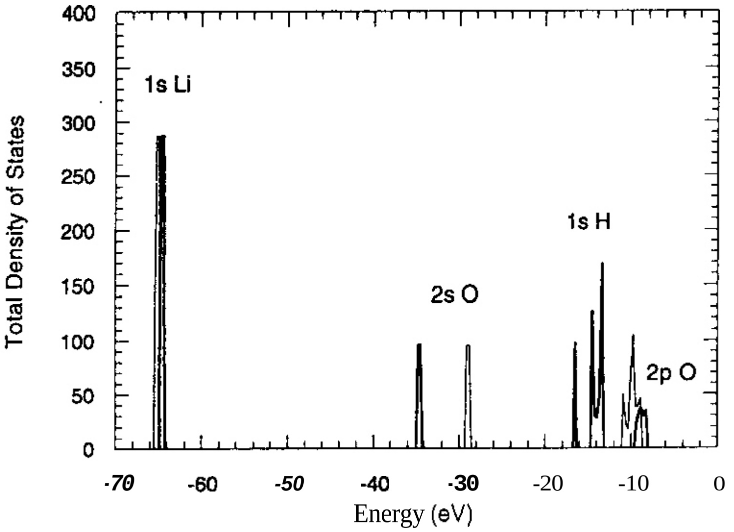

Fig.7 The Hartree-Fock density of states of one-layer (110) surface. The total density of states of the surface is represented by the light curves. The total density of states of the chemisorped hydrogen on the surface is illustrated by the bold curves.

Although a one-layer (110) surface is not a realistic model for a surface, the characteristic of this configuration could be used as a reference to understand the role of the lower coordination number of lithium and oxygen in the hydrogen chemisorption processes. On the monolayer (110) structure with 100% surface coverage of H_2, there is chemisorption state with the energy of 0.93eV at the location where one hydrogen attaches to the oxygen and the other hydrogen is attached in-between two lithium (Fig.5(ii)). Fig.7

illustrates successively the density of states of the situations on the surface before and after chemisorption The particular interest is that the 2p **O** is split. This process indicates that the oxygen plays a major role in transferring some of its valence electron to the hydrogen to form H^-. The H^- bands are indicated by the two bands appeared between the gaps of the **2s O** and 2p **O.** From a Mulliken analysis, the resulting H^- is due to charge transfers of about -0.75 e from the oxygen site and **of -0.22** e of intramolecular charge transfer within the H_2 as it approached the Li-0 site. It seems that as the hydrogen approaches the Li-0 site, there is an initiation of the hydrogen molecule to stretch with charge transfer within the hydrogen molecule itself due to the crystal field arising from the influence of the local Li-0 sites. There is a gap of 2.5 eV between the upper limit valence band of H^- and the lower limit of the 2p **O.** The other band that is close to the **2s O** is the core electron band of the hydrogen which causes the **2s** band to be shifted about **4.5**eV further down. There is no significant change on the lithium core band. The other hydrogen, H^+, that makes bond to the oxygen has no band because there is no electron left. The electronic charge densities of the OH^- and $Li^+H^-Li^+$ are shown in Fig.8 and Fig.9. **A** covalent type of bonding appears for OH- with a very localized electronic charge density, while for $Li^+H^-Li^+$ the bonding is more ionic with a distinctive clear-cut charge separation between Li^+ and H^-. The **OH** and LiH bondlengths are 0.96 and **1.54 *8,*** successively which are closely comparable with the **OH** (0.97 Å) and LiH (1.595 Å) [12] in the gas phase

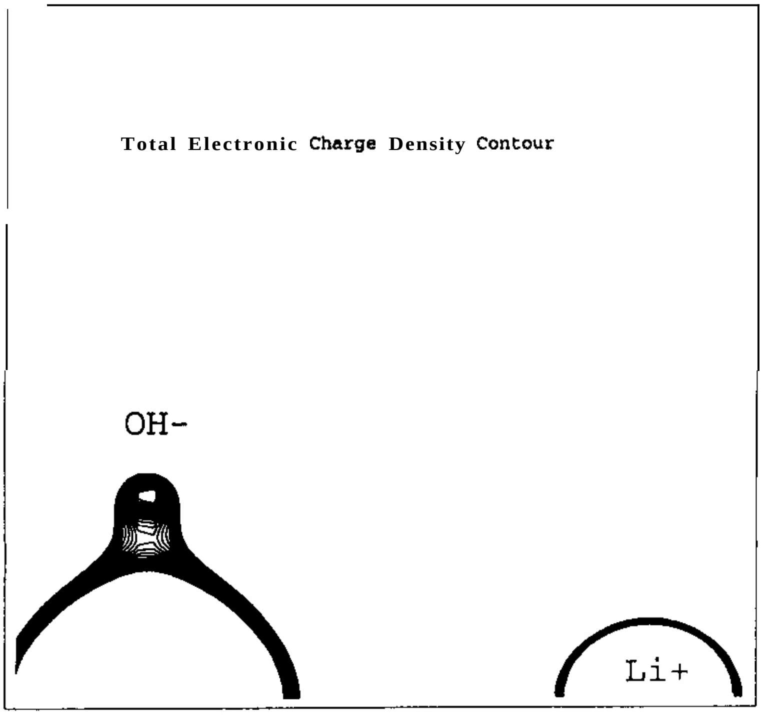

Fig.8 The total electronic *charge* density map of OH bond on the one (I 10) **layer. The figure shows strong** covalent type **of** OH- **bond. The interval between the nearest** isoelectronic contours **is** 0.003 **Å.**

The surfaces of (1 10) with the n-layer slab (where n = **2** and 3) do not allow the H_2 to be chemisorped. The density of states of the 2p **O** of the (110) surface in the one, two, and three layer system (Fig.10) indicate that the 2p **O** is shifted downward (more negative) as additional layers are introduced. For example, in the case of two and three layers, the shifts are about **2** and ***2.6*** eV, successively, with respect to the upper limit 2p **O** of the monolayer. This means that as more layers are introduced to the surface the more stable

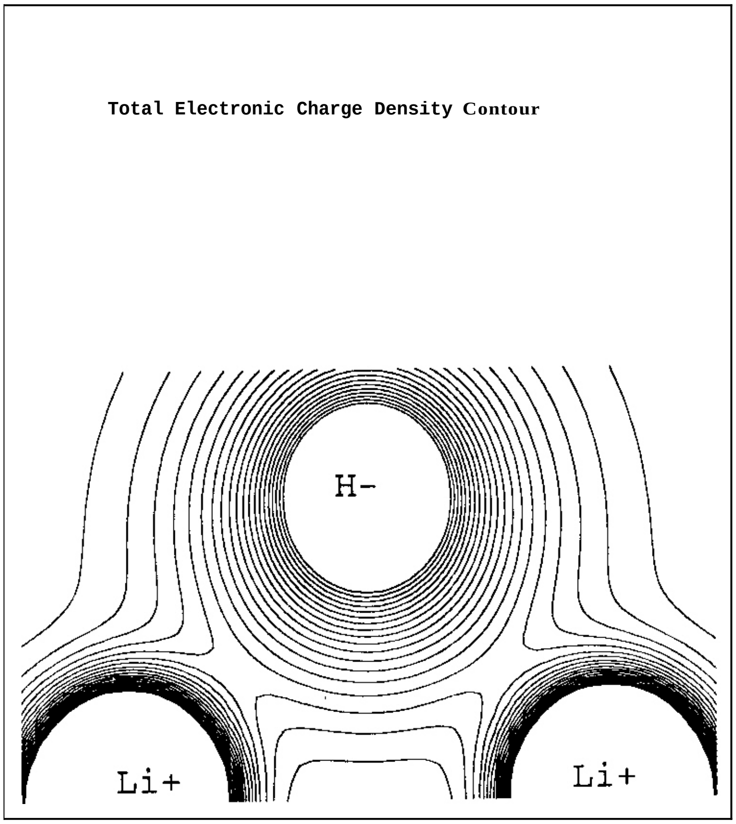

Fig.9 The total electronic charge density map of the ionic bonding of Li$^+$H$^-$Li$^+$ with 0.003 A interval between the nearest isoelectronic contours.

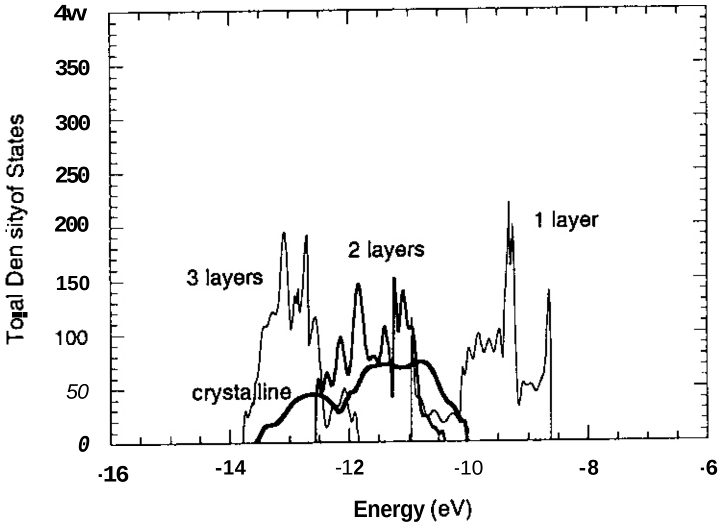

Fig.10 Schematic diagram of the total charge density of 2p O far the one-, two- and three-layer slab of the (110) surfacer.

the surface becomes. This is as expected. For lower surface coverage (50%) there is no chemisorption and based on its calculated binding energy is highly unbound (Table 3).

For the (111) surface, the 2p O lies in the range close to the 2p O of one-layer slab for the (110). at -10.638 to -8.086 eV. However, there is no hydrogen chemisorption on that surface, namely the (111). One important reason is the location of the oxygen layer which is sandwiched between the two cation layers. The oxygen is screened by the lithium layers and as a result the H^+ finds it energetically unfavorable to move close to the positively charged Li^+ layer before it can be chemisorped by the O^{2-}.

Calculations on the homolytic sites of the terrace, such as. Li-Li and O-O, indicate that there is no H_2 chemisorption. As it has been discussed previously, for the case of (110) represented by n-layer slab (where n = 2 and *3)*, there is no chemisorption on O-O site since the 2p O surface is stabilized in the presence of additional layers (*Fig.10*) such that the oxygen is difficult transferring charge to the hydrogen. The chemisorption on Li-Li site is very unlikely to occur since the 1s Li is the stable core band. For H_2 chemisorption could take place on the homolytic sites, it has to be in the form of either two H^+ or two H^- where each of them attaches to two oxygens or to two lithiums. respectively. This means that for the case of O-O site each oxygen has to release its valence electron, or each hydrogen also releases its electron to the crystal environment. For the Li-Li site, each hydrogen would need to capture an electron from oxygen to form H^-.

Table 4 The calculated Hartree-Fock LCAO-MO bondlengths d (Å) of the stretched H_2, located above the (110) and (111) surfaces (figs.5 and 6), and the binding energies BE(eV) obtained from GAUSSIAN.

Surface	Clusters	Locations of *H*	d(OH)	d(LiH)	d(H-H)	**BE**
(110) [fig.5]						
	$Li_{22}O_{11}$†	H(1)H(2)	0.97	1.73	2.12	-2.13
		H(1)H(3)	0.96	1.72	2.82	-1.44
		H(1)H(4)	0.96	2.28	2.29	-2.11
	$Li_{32}O_{16}$††	H(1)H(2)	0.97	1.75	2.13	-1.91
		H(1)H(3)	0.96	1.74	2.90	-1.50
		H(1)H(4)	0.96	2.28	2.29	-1.96
(111) [fig.6]						
	$Li_{18}O_9$†††	H(1)H(2)	1.0	1.90	2.43	-1.60
		H(1)H(3)	1.0	2.30	2.56	-2.23
		H(1)H(4)	1.0	2.28	1.56	-1.0

†representing the finite two (110) layers.

††representing the finite three (110) layers by adding the two (110) layers with its first layer denoted by the shaded circles (fig.5).

†††representing the finite three (111) layers.

Such phenomena does not occur for this material under equilibrium conditions since it would require transferring electrons into the surrounding crystal environment.This is equivalent to creation of electronic defects, (for example neutral Li). The surface band structure that we have obtained indicate that electronic disorder is energetically unfavorable. It may occur under certain condition such **as** by irradiation where it may create electronic structure defects on the crystal surface. Thus, under equilibrium condition one expects no homolytic chemisorption.

To investigate chemisorption of a hydrogen molecule on the terrace (no absorbent-absorbent interactions), the finite neutral clusters model were employed. The calculations were done by employing the GAUSSIAN program [7] and the same basis set for both lithium and oxygen as they were used for the extended system. Care is taken to construct a cluster in which the reaction sites has the correct environment to at least first nearest neighbors in both the cation and anion species. At the same time enough ions are included to render the cluster neutral. The geometrical structure of the clusters representing the (110) and (111) terraces are shown in Fig.5 and Fig.6 respectively. The Li-Li, Li-0 and O-O distances are maintained the same as the value on crystal surface. At present work, the $Li_{22}O_{11}$ cluster (Fig.5) is defined to represent the two layer (110) terrace, and for the three layers, the $Li_{32}O_{16}$ cluster is obtained by adding the first layer (defined by the shaded circles, Fig.5) to the $Li_{22}O_{11}$ cluster. The three (111) layers are represented by $Li_{18}O_9$ cluster. The calculated data of the given locations of the hydrogen molecule is listed in Table 4.

The corresponding calculated binding energies (at the given locations of the hydrogen) obtained from the slab and the cluster models (Table *3* and Table **4,** respectively) indicate that there is no hydrogen chemisorption. In both tables show that the OH bondlength is relatively the same of about 0.96 Å obtained from both models.

Conclusions

The study of the hydrogen chemisorption **on** the (110) and (111) terraces have been calculated primarily using molecular orbital technique. The finite and extended models provide qualitative agreement that, in general. there is no hydrogen chemisorption on the terrace. In the case of (110) terraces of n-layer slab model calculations (where n = 2 and 3), the chemisorption does not occur for Li-Li, Li-0 and O-O sites due to the stable 2p **O** on the surface such that the oxygen **is** difficult to transfer charge to the hydrogen. The chemisorption takes place for the case of one-layer (110) surface around the Li-0 site due to the low coordination of the oxygen. The intramolecular charge transfer in hydrogen plays important to initiate the chemisorption. The one (110) layer model could be use to further understand in any lower coordination case due to the presence of kinks and ledges on surface step structure.

Although the oxygen of (111) terrace has the same local coordination and similar energy range of 2p **O** as it does in the (110) terrace. there is no hydrogen chemisorption.The oxygen layer is screened by the lithium layers preventing the hydrogen chemisorption to occur.

FUTURE WORK

Further investigations on the hydrogen chemisorption on the defect surfaces such **as** steps and kinks will be considered. For the steps, the investigations will be done by using both the Hartree-Fock techniques for the extended and finite systems. The kinks will be studied by employing the molecular Hartree-Fock method.

References

[1] W. Dienst, D. Schild and H. Werle, Kernforschungszentrum, Karlsruhe. Report KfK-5109, December 1992.

[2] O.D. Slagle, T. Takahashi. F.D. Hobbs. K. Noda. D.L. Baldwin, G.W. Hollenberg. and R.A. Verrall, "Postirradition Examination of BEATRIX-II, Phase I", to be published in J. Nucl. Mater.

[3] **H.** Kwast, A. Kout, R.P. Muis, M.P. Stijkel, A.J. Flipot, and J.D. Elen, Fusion Engineering and Design, 8, (1989)359-364.

[4] R.G. Clemmer. P.A. Finn, R.F. Malecha, B. Misra. M.C. Billone, D.L. Bowers,

A.K. Fischer, L.R. Greenwood, R.F. Mattas. S.W. Tam, R.B. Poeppel, G.T. Reedy. LT. Dudley, F.F. Dyer, E.D. Clemmer. **J.S.** Watson, P.W. Fischer, J.R. Conlin, R.L. Childs, J.L. Scott, R.M. Arons and A.E. Scandora. “The TRIO Experiment” Argonne National Laboratory, Argonne, Report ANL-84-85. September 1984.

[5] H. Kwast, R. Conrad, R. May, S. Casadio, N. Roux, and H. Werle, “The Behaviour of Ceramic Breeder Materials with Respect to Tritium Release and Pellet/Pebble Mechanical Integrity” ICFRM-6 to be published in J. Nucl. Mater.

[6] R. Dovesi, C. Roetti and V.R. Saunders, CRYSTAL92 program.

[7] M.J. Frisch, M. Head-Gordon, G.W. Trucks, J.B. Foresman, H.B. Schlegel, K.Ragavachari, M.A. Robb, **J.S.** Binkley, C. Gonzalez, D.J. Freeze, D.J. Fox, R.A. Whiteside, R. Seeger, C.F. Melius, J. Baker, R.L. Martin, L.R. Kahn, J.J.P. Stewart, S. Topiol. and J.A. Pople (Gaussian, Inc., Pittsburgh PA, 1990).

[8] R. Dovesi, Solid State Comm. 54 (1985) 183.

[9] R. Dovesi, C. Roetti, C. Freyria-Fava. M. Prencipe, Chem. Phys. 156 (1991) 11.

[10] Albert Lichanot. Michel Gelize, Christiane Larrieu and Cesare Pisani, **J.** Phys. Chem. Solids ***52*** (1991) 1155.

[11] R. Dovesi, C. Ermondi, **E.** Ferrero, C. Pisani and C. Roetti. Phys. Rev. B 29 (1984)

[12] Warren J. Hehre et al., Ab Initio Molecular Orbital Theory (Wiley. N.Y., 1986) pp.138 and pp.210.

[13] T.W.D. Farley, W. Hayes,. S. Hull, R. Ward, M.T. Hutchings and M. Alba, Solid State Ionics, 28-30(1988)189.

[14] S. Hull. T.W.D. Farley. W. Hayes and M.T. Hutchings, J. Nucl. Mater. 160 (1988) **125.**

[15] T.W.D. Farley, W. Hayes,. S. Hull, M.T. Hutchings, M. Alba and M. Vrtis, Physica **B** 156 &157 (1989) 99.

[16] P.W. Tasker. Surface Science 78 (1979) 315.

[17] C. Pisani et al., Hartree-Fock Ab Initio Treatment **of** Crystalline Structure (Springer-Verlag. Berlin Heidelberg, 1988) pp.136.

IRRADIATION OF LITHIUM ZIRCONATE PEBBLE-BED IN BEATRIX-II, PHASE II -

R. A. Verrall[1], O. D. Slagle[2], G. W. Hollenberg[2], T. Kurasawa[3], and J. D. Sullivan[1]

[1] AECL Research, Chalk River Laboratories, Chalk River, Ontario, K0J 1J0, Canada
[2] Pacific Northwest Laboratory[(a)], Richland, Washington 99352, USA
[3] Japan Atomic Energy Research Institute, Tokai-mura, Ibaraki-ken, Japan

OBJECTIVE

The objective of the BEATRIX-II, Phase II temperature-gradient canister irradiation was to characterize the tritium release behavior and the physical stability of a Li_2ZrO_3 pebble-bed in a fast neutron flux.

SUMMARY

BEATRIX-II was an in situ tritium recovery experiment that was designed to characterize the behavior of lithium ceramics irradiated to a high burnup, and to assess their suitability for use in a fusion reactor blanket. This paper describes the results from a vented canister containing lithium enriched lithium zirconate spheres (85% ^6Li) that were irradiated to a burnup of 5.2% (total lithium) in a steep temperature profile—400°C edge, 1100°C center. The reference sweep gas was He-0.1%H_2, with systematic tests using alternate compositions: He-0.01%H_2 and pure He (maximum duration 8 days). Tritium recovery decreased slightly at lower H_2 concentrations. For example, the buildup of inventory during a 4-day test in pure He was 0.8 Ci which was approximately 6.5% of the tritium generated in the lithium zirconate during that period. The steadiness of the bed central temperature and the high tritium release rate, together with low moisture release rate, indicate good performance of the zirconate bed.

PROGRESS AND STATUS

Introduction

The BEATRIX-II experiment, a joint U.S., Japan, and Canada collaboration, was an irradiation of lithium ceramic breeding materials in a fast flux neutron reactor to simulate the environment of a fusion blanket. Phase II consisted of two swept, vented canisters, containing lithium oxide and lithium zirconate, and a number of closed canisters, all irradiated in FFTF (Fast Flux Test Facility). The vented canisters were irradiated to burnups of 5.2% (total lithium) for the lithium zirconate and 4.8% for the Li_2O. The irradiation of the vented canister of lithium zirconate is described here.

The lithium zirconate was in the form of a pebble bed; i.e., 1.2 mm diameter spheres[1] filling an annular volume 13.2 mm OD, 2.3 mm ID (as a thermocouple well) and 103 mm long. The objective was to evaluate the in situ recovery of tritium and the physical, chemical, and mechanical performance of the lithium zirconate. The tritium and moisture concentration in the sweep gas

---

(a) Pacific Northwest Laboratory is operated for the U.S. Department of Energy by Battelle Memorial Institute under Contract DE-AC06-76RLO 1830.

and the temperature of the lithium zirconate were monitored continuously. The dimensions of the lithium zirconate region were chosen to provide a large temperature difference (and temperature gradient) in the sample, thus providing engineering data for a blanket. The surface and central temperatures were 400° C and 1100° C, respectively, chosen to exceed temperatures and temperature gradients that would be expected in a solid breeder blanket. Accommodations for temperature-change tests were deliberately not designed into the canister.

The main results from this irradiation were obtained from the continuous monitoring of the zirconate temperature and the tritium concentrations in the sweep gas downstream from the canister. The reference sweep gas was 0.1% H_2 in He, but tests with 0.01% H_2 in He and pure He provided information on the dependence of the tritium release on sweep gas composition. Important further results will be obtained when post-irradiation examination (PIE) is done in 1994 to evaluate the condition of the irradiated lithium zirconate. Indications are that the lithium zirconate performed very well in the fast-neutron flux, and that tritium inventory was never large, but that it increased slowly when concentrations of H_2 lower than 0.1% were used. These conclusions are supported generally by lower burnup experiments on tritium release from lithium zirconate.[2-5]

Experimental

The canister was irradiated in level 2 (below the mid-plane) of the Materials Open Test Assembly (MOTA) of FFTF during operational cycle 12. The irradiation consisted of four 50-day subcycles for a total of 203 effective full-power days. The nominal fast-neutron fluence (E > 0.1 MeV) at this position was 4.5×10^{22} n/cm^2. Table 1 gives measured characteristics of the lithium zirconate spheres. The zirconate spheres were prepared by a process of wet extrusion followed by spheronizing and sintering.' The process had been developed previously and it was designed to permit easy scale-up for large-quantity production.

Table 1. Sphere and Pebble-Bed Characteristics

Grain Sue	10 μm
Sphere diameter	1.2 mm average
^{6}Li enrichment	85 at%
Sphere density	82% TD
Sphere packing density	63%
Smear density	52 %TD
Outer diameter	1.32 cm
Inner diameter	0.23 cm
Total Weight	29.47 g

Figure 1 is a schematic diagram of the irradiation canister. A detailed description **has** been published elsewhere? The canister was made primarily from stainless steel. Nickel screens at the top and bottom served to contain the spheres and to permit passage of sweep gas. The central-thermocouple well accommodated two thermocouples: one a standard type-K thermocouple and the other a Nb-1%Zr/Mo thermocouple, designed and constructed at Westinghouse Hanford Company. This latter thermocouple was thought to provide a longer lifetime in-reactor at temperatures of 1200° C. Advance mockup tests showed that the central hole would not decrease the density **of** spheres in the bed. The actual packing density obtained was 63%. The Lithium zirconate spheres were vibration packed into the canister and vacuum outgassed while heating to 600° C. Argon backfills were carried out at 300° C and 500°C. The tritium analysis and recovery system **has** been described previously?

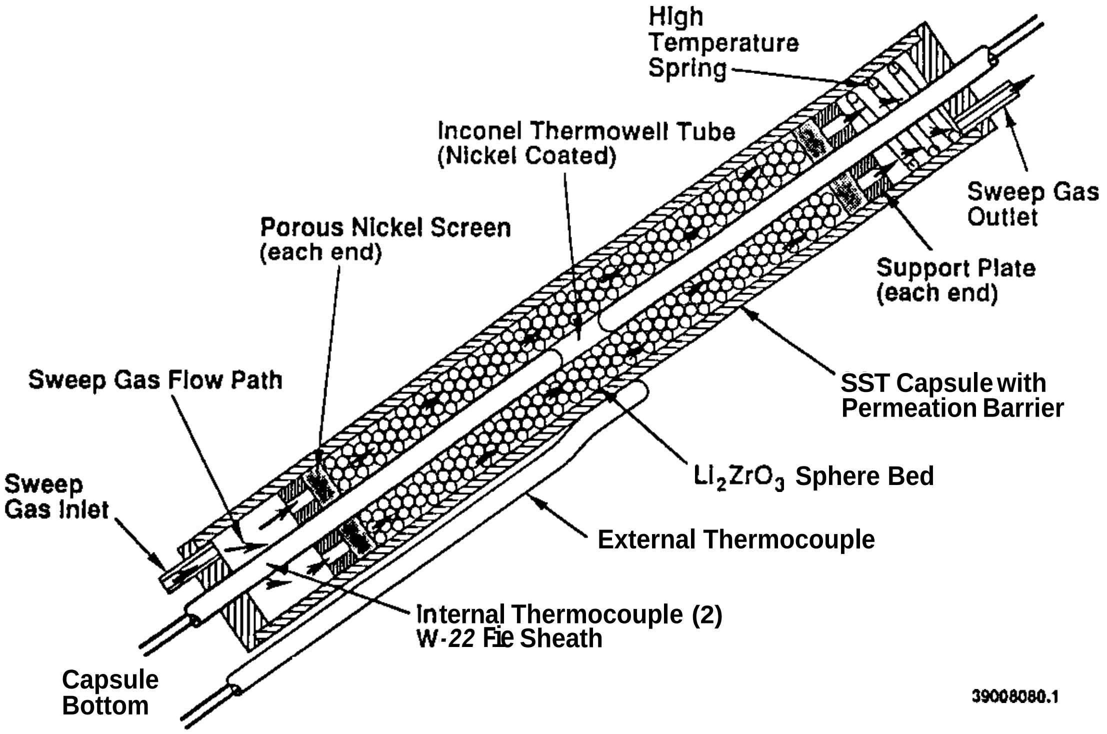

Fig. **1.** Schematic Diagram of the BEATRIX-II, Phase II Temperature-Gradient Canister

Results and Discussion

Temperatures - Figure **2** is a plot of the readings from the two central thermocouples for the four irradiation cycles. The measured central temperatures of approximately 1100°C were unexpectedly close to the pretest calculated values of 1030–1160° C, given the uncertainties in bed thermal conductivities, heat generation, and irradiation effects. The difference in temperatures between the two thermocouples is attributed to the axial flux gradient in the sample. The gradual decrease in temperature during each cycle was due to burnup of the fuel and a decreasing flux at this position in the reactor. **Similar** thermal behavior was also observed in a the Phase **I** irradiation of Li_2O [6,8] and this behavior was interpreted as an indicator of stable performance.

- When switching from the reference sweep gas to pure He, all tests showed a sharp transient drop in tritium recovery rate, followed by a return to a new steady-state rate, slightly lower than in the reference gas.

- AU exhibited a double peak upon reintroduction of the reference sweep gas, and a return to the same steady-state recovery as before the test.

- The integrated areas under the peaks, and the peak heights increased with the duration in the He sweep gas.

The double peak was thought to be due to a rapid HT peak and a slower HTO peak. The rapidity of the HT peak may reflect the kinetics of release from the ceramic or a more rapid transit through the piping to the ionization chamber, due possibly to an "open-tube chromatographic" effect of the HTO gas. That is, the HTO continuously adsorbs and desorbs from the walls as it moves through the piping while the HT is less reactive with the walls.

The tritium recovery rate was approximately constant, i.e., steady state recovery, after only a few hours in the He sweep gas at a value that was apparently slightly lower than in reference sweep gas. This implies a steady buildup of tritium with time in He. The relative steady-state recovery rates in the alternate sweep gases have an uncertainty of 5-10% because the relative ionization-chamber calibration factors for the alternate gases are not known to within that uncertainty. Despite this uncertainty, the tritium recovery rate in He is measurable lower than the steady-state recovery rate in reference gas. Evidence is provided by the large recovery peak at the reintroduction of the reference sweep gas, which is a clear indication of inventory buildup in the He sweep gas due to a lower recovery rate in He.

Test Series II - Test Series II was a comparison of the tritium recovery for 4 days in He-0.01%H_2 versus 4 days in He sweep gases. The tritium recovery curves are given in Figure 4. The steady-state recovery in He-0.01%H_2 gas is appears to be approximately equal to that in He, but the smaller recovery peak for He-0.01%H_2 upon reintroduction of the reference gas is a clear indication that the inventory buildup in He-0.01%H_2 gas was less than in He. This suggests that the recovery rate for He may be slightly less than that for He-0.01% H_2.

Test Series III - Test series III involved the gas composition sequence of 4 days in He followed by 2 days in He-0.01%H_2. The tritium recovery curves indicated a 20% reduction of recovery rate in He gas followed by a recovery rate in He-0.01%H_2 gas which was only 8% less than the reference gas. Upon re-introduction of reference gas, the recovery rate returned to its original value.

Observations are consistent with a tritium release rate that decreases with decreasing H_2 concentration in the He sweep gas. We have assumed that, in the reference gas, tritium is released and recovered at or near the generation rate in the ceramic. Residual tritium inventory measurements from postirradiation examination (PIE) will test this. PIE measurements on Phase I Li_2O showed no large tritium inventory buildup' which is consistent with a similar interpretation as this one.

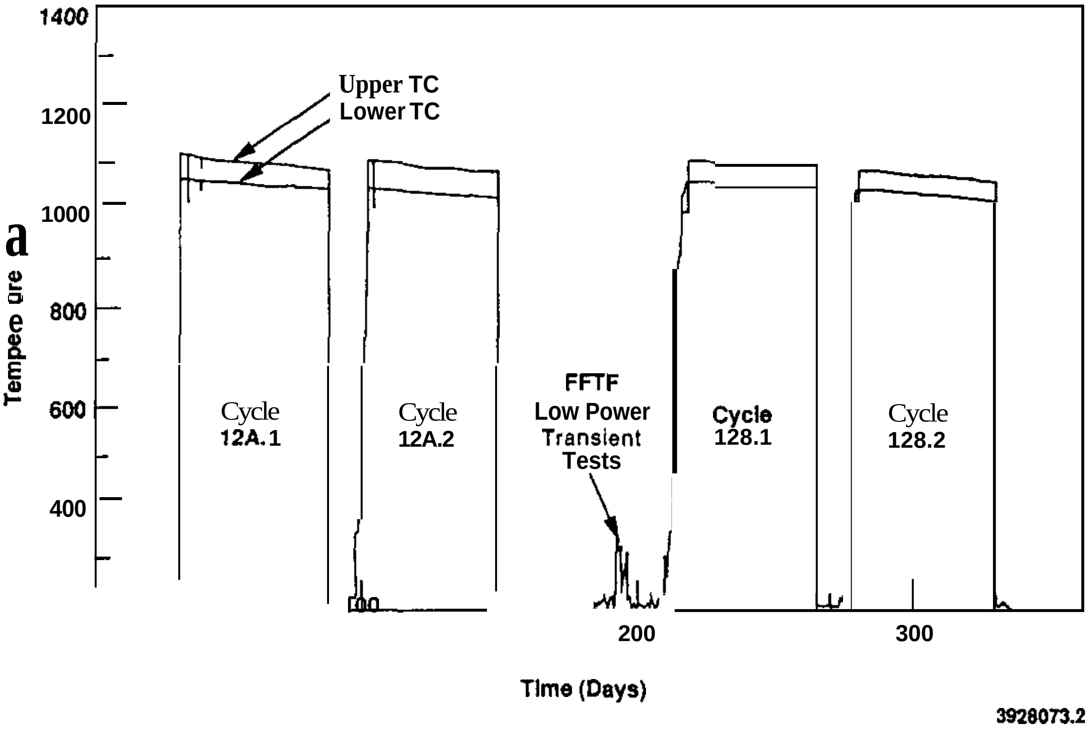

Fig. 2. Central Temperature Readings from Two Thermocouples for the Four Irradiation Cycles.

Moisture Release - During the initial reactor startup at the beginning of the experiment, a 2400 ppm spike in the sweep gas moisture concentration was observed. However, the moisture concentration had decreased to less than 1% of that value after 1 Effective Full Power Day (EFPD) of operation. After 7 EFPD, the reading was less than 0.02 ppm (nominal), well below the instrument's limit of resolution. Because sweep gas had been flowing for several days before reactor startup to dry all system components, we believe the moisture release during startup emanated from the ceramic. This spike is much smaller than that at startup in CRITIC-11,[3] another vented canister irradiation of lithium zirconate in which loading was done in air with predrying done at 200°C. The source for this moisture may be residual $(OH)^{-1}$ in the ceramic remaining after dryout. For the rest of the BEATRIX irradiation, the release of moisture was extremely low, the moisture meter output indicating a few parts per billion, but this is below its limit of resolution. During sweep gas composition changes that involved increased H_2 concentrations, small apparent peaks of moisture were recorded; but the indicated levels were less than 0.05 ppm. These small peaks in moisture release were consistently observed during sweep gas composition changes and coincided with a rise in both total tritium release and tritiated water release. Although the absolute accuracy of standard moisture meters does not extend to these low levels, these peaks probably indicated real release of moisture. The source for this moisture may be oxygen, freed by lithium burnup, which combines with hydrogen in the sweep gas. Calculations show the burnup rate of lithium is sufficient to account for this moisture. Low moisture release was a notable feature of the Li_2ZrO_3 test. Li_2O also released low levels of moisture in the BEATRIX-II Phase I and Phase II tests, but not as low as Li_2ZrO_3.

Tritium Release - Systematic changes in the sweep gas composition were made to determine the effect of composition on tritium release. The results from three series of tests are described here. All test series started and ended with the reference gas (He-0.1% H_2). In Test Series I, the composition was switched to He for varying lengths of time. Periods of 2, 4, and 8 days in He were used. In Test Series II, 4 days in pure He were compared to 4 days in He-0.01%H_2. In Test Series III, 4 days in He were followed by 2 days in He-0.01%H_2. Sweep gas flow rate was fixed at 100 ml/min throughout.

The tritium recovery rate was constant and in agreement with the calculated generation rate except when sweep gas composition changes were made. The tritium was recovered primarily in the reduced form (HT). The rest of this section describes the results of sweep gas composition changes on the tritium recovery rate and, therefore, on the tritium inventory in the ceramic. Observed changes in tritium recovery rate could potentially be due to inventory changes elsewhere in the system (e.g., the piping); however, laboratory tests at AECL have shown that changes in inventory on piping do not readily occur from changes in H_2 concentration in the sweep gas. Moisture additions to the sweep gas are required to effect sizable inventory changes on the piping. For this reason the observed tritium recovery data can be expected to reflect the tritium release from the Li_2ZrO_3 spheres. All tritium recovery data have been corrected for the effect of sweep gas composition on ionization chamber calibrations and for background buildup, as described in section 3.5.

Test Series I - Test series I compared the tritium recovery behavior for 2, 4, and 8 days in pure He. The results are shown in Figure 3 and indicate:

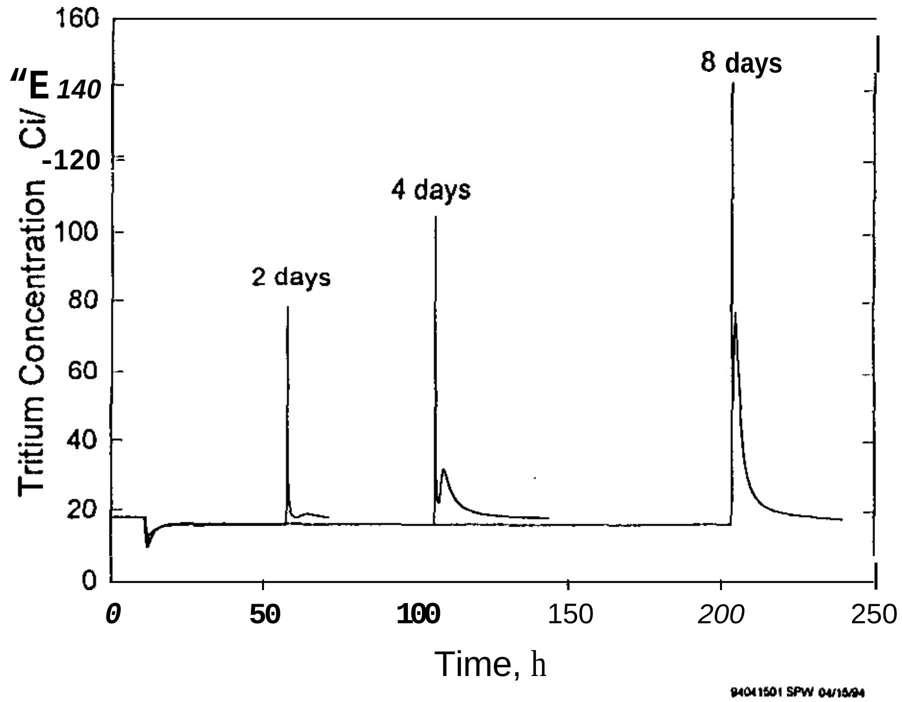

Fig. 3. Superposition of the results of three tests in He for 2, 4, and 8 days in He sweep gas, preceded and followed by He-0.5%H_2.

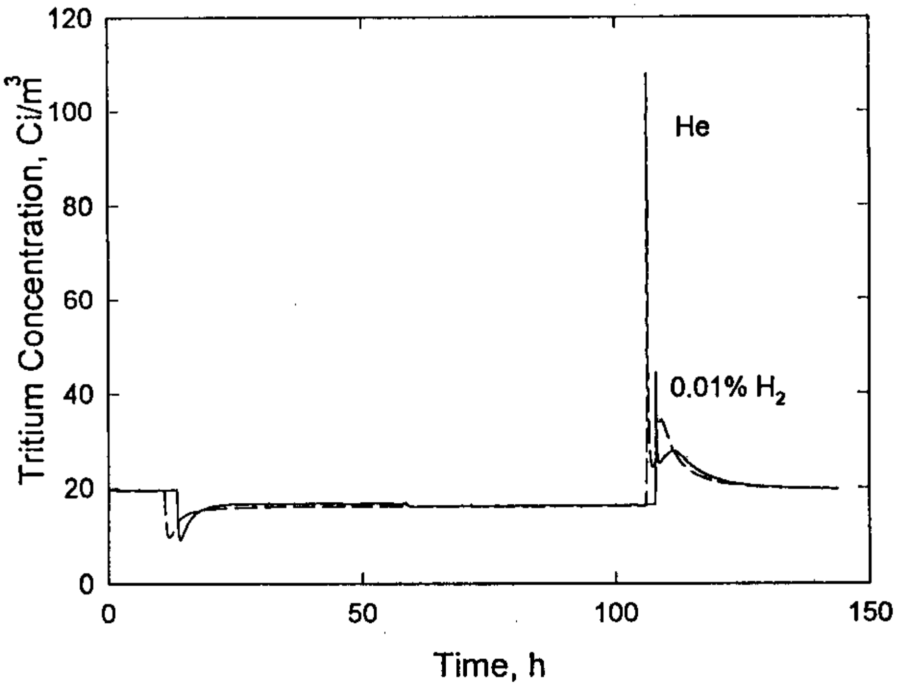

94041602.8PW 04/15/94

Fig. 4. Superposition of the results of two tests, one using He and one using He-0.01%H_2 sweep gas.

Comparison of Li_2ZrO_3 and Li_2O

Figure 5 is a superposition of the tritium recovery data for 4 days in He for the Phase II canister containing Li_2ZrO_3 spheres and a very similar Phase I canister containing solid Li_2O. The main difference in the recovery curves is that the integrated areas under the peaks, both the negative peak at the introduction of He sweep gas and the positive peak at the return to He-0.1%H_2, are smaller for Li_2ZrO_3. The inventory change for the large positive Li_2O peak is 14.4 Ci, while that for the Li_2ZrO_3 peak is 0.76 Ci. Centerline temperatures in the Phase I Li_2O were less than 1000°C and the tritium generation rate was about 3 times as large in the Li_2O. Thus, tritium inventory increases in a helium sweep gas for both ceramics, but the buildup is smaller for the lithium zirconate. Note that the small secondary HTO peak does occur for Li_2O at reintroduction of He-0.1% H_2 but it is masked by the width of the large HT peak.

Ionization Chamber Corrections

Ionization chambers used for measuring tritium concentration in carrier gases have calibration factors that can depend on concentrations of impurities and additives to the carrier gas.[10,11] This effect is called the Jesse effect and results when carrier gas atoms (e.g., He) that have been excited to metastable states by tritium decays, but not ionized, contact and ionize impurity (additive) atoms. Whether this effect occurs depends on the relative energies of the metastable states of the carrier gas versus the ionization energy of the impurities (additives). For the effect to occur, the metastable state of the carrier gas must be higher in energy than the ionization energy of the impurity.

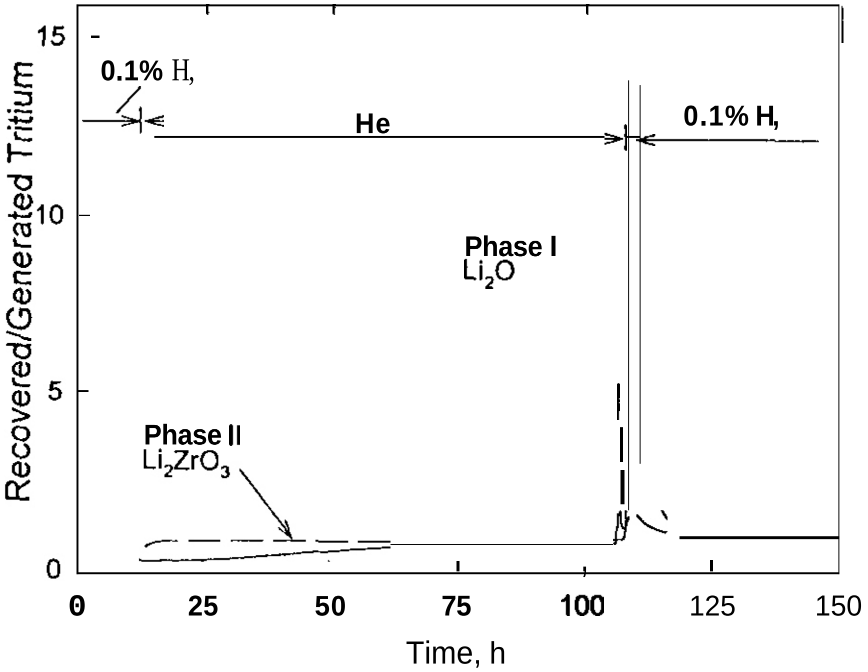

94041403.SPW 04/14/94

Fig. 5. Superposition of the Results of Two Tests, Both Using He Sweep Gas for 4 Days. One is for the BEATRIX-II Phase II Lithium Zirconate and One is for BEATRIX-II Phase I Li$_2$O. The Tritium Recovery Rate Axis is Normalized to the Generation Rates for the Two Materials.

During this experiment, grab samples of sweep gas containing tritium were systematically taken and analyzed for tritium content, to check the calibration of the ionization chambers in the analysis stream. These tests confirmed that there were different calibration factors for different sweep gases.'' Laboratory measurements[10,11] and the grab sampler calibrations gave approximately the same values: increases in the calibration constant by factors of 1.3 and 1.1 for He-0.1%H$_2$ and He-0.01%H$_2$ over that for pure He. These factors were used to correct all data presented here.

During the experiment, background readings tended to increase in the ionization chambers; i.e., tritium became sorbed on the walls of the chamber and gave a nonzero tritium reading even when no tritium was present in the sweep gas. When FFTF was shut down and the sweep gas contained no tritium, the value of the background could be determined. *Also*, on occasion, a non-tritiated gas was substituted for the sweep gas passing through the ionization chamber *to* determine the background. These background values along with others were established by comparing the tritium recovery rates in the reference sweep gas with the calculated generation rates and were used to correct the data presented here. These methods have previously been described more completely.[13]

Conclusions

The lithium zirconate pebble-bed performed very well to the terminal burnup of 5.2% total Li The observations that led to this conclusion are:

- Steady tritium release in the reference sweep gas (He-0.1% H_2) throughout the experiment.
- Steady centerline temperature, as measured by two central thermocouples, throughout the irradiation.
- Extremely low moisture release

The steady-state tritium release from the Li_2ZrO_3 spheres decreased with decreasing H_2 concentration in the He sweep gas for the three sweep gas compositions *used* 0, 0.01% and 0.1% The effect of gas composition on tritium release was less for the Phase II Li_2ZrO_3 spheres than observed for the Li_2O solid in BEATRIX-II Phase I.

FUTURE WORK

Postirradiation examination of the Phase II temperature-gradient canister will be carried out to characterize the tritium retention and physical stability of the Li_2ZrO_3 spheres during irradiation.

ACKNOWLEDGEMENTS

Funding was provided by a number of sources: the institutions of the authors; US Department of Energy; the federal government of Japan; the Canadian National Fusion Program; and the Canadian Fusion Fuels Technology Project. We acknowledge the many persons who contributed to this experiment, and especially thank D. Baker (Westinghouse) and J. M. Miller (AECL Research).

REFERENCES

1. J. D. Sullivan, C. L. Brayman, R. A. Verrall, J. M. Miller, P. Gierszewski, F. Londry, and A. Slavin. 1991. ***Fusion Eng. Design,*** 17:79.
2. H. Kwast. 1993. In ***Proc. Int. Workshop*** on ***Ceramic Breeder Blanket Interactions,*** p. 55, University of Tokyo.
3. W. Krug, et al. 1991. ***Fusion Eng. Design,*** 1765.
4. J. M. Miller, and R. A. Verrall. 1993. "Performance of a Li_2ZrO_3 Sphere-Pac Assembly in the CRITIC-I1 Irradiation Experiment." Presented at the Sixth International Conference of Fusion Reactor Materials, September 27-October 1, 1993 in Stresa, Italy. To be published in ***J. Nucl Mater.***

5. J. Kopasz, J. M. Miller, and C. E. Johnson. 1993. "Tritium Release from Lithium Titanate, a Low Activation Tritium Breeding Material." Presented at the **Sixth** International Conference of Fusion Reactor Materials, September 27-October 1, 1993, in Stresa, Italy. To be published in ***1.*** Nucl. ***Mater.***

6. T. Kurasawa, O. D. Slagle, G. W. Hollenberg, and R. A. Verrall. 1992. "Fabrication and Properties ***of*** Lithium Ceramics III." In *Ceramic Transactions*, Vol. 27, eds. I. J. Hastings, and G. W. Hollenberg, p. 299. Westerville, Ohio.

7. D. E. Baker, T. Kurasawa, J. M. Miller and O. D. Slagle. 1991. ***Fusion Technol.*** 19:1640.

8. ***G.*** W. Hollenberg, H. Watanabe, I. J. Hastings, and S. E. Berk. 1992. ***J.*** Nucl. ***Mater.*** 23, p. 191-194.

9. O. D. Slagle, T. Takahashi, F. D. Hobbs, K. Noda, D. L. Baldwin, G. W. Hollenberg, and R. A. Verrall. 1993. "Postirradiation Examination ***of*** BEATRIX-II, Phase I Presented at the Sixth International Conference ***of*** Fusion Reactor Materials, September 27-October 1, 1993 in Stresa, Italy. To be published in ***1.*** Nucl. ***Mater.***

10. L. Rodrigo, J. M. Miller, and D. Yin. 1993. ***Proc. Int. Workshop on Ceramic Breeder Blanket Interactions,*** p. 213, University ***of*** Tokyo.

11. L. Rodrigo, and D. Yin. 1993. "Canadian Fusion Fuels Technology," Report CFFTP G-9199 and AECL-10764.

12. O. D. Slagle, G. W. Hollenberg, D. E. Baker, T. Kurasawa, and R. A. Verrall. 1993. ***Proc. Int. Workshop on Ceramic Breeder Blanket Interactions,*** p. 204, University ***of*** Tokyo.

13. O. D. Slagle, T. Kurasawa, R. A. Verrall, and G. W. Hollenberg. 1993. "BEATRIX-II: In Situ Tritium Recovery Data Correction," presented at the 2nd Int. Workshop on Ceramic Breeder Blanket Interactions, Paris, September 22-24, 1993. To be published by Commissariat a l'Energie Atomique, Saclay, Gif sur Yvette, France.

8.0 CERAMICS

FATIGUE CRACK GROWTH RATE (FCGR) BEHAVIOR OF NICALON/SiC COMPOSITES –

N. Miriyala, P. K. Liaw and C. J. McHargue (University of Tennessee). **L. L.** Snead *(Oak* Ridge National **Laboratory),** and D. K. **Hsu** and V. K. Saini (Iowa **State** University).

OBJECTIVE

To develop a basic understanding of fatigue crack growth **characteristics** of NicalodSiC composites in both **irradiated as** well **as** non-irradiated **conditions.**

SUMMARY

Ultrasonic measurements were carried out **on** the NicalodSiC composite specimens to correlate elastic moduli with percentage porosity in the in-plane **as** well **as** through-thickness directions. Compact type C(T) specimens were cyclically loaded to study the fatigue crack growth behavior. However, it was difficult to initiate the crack in the specimens.

PROGRESS AND STATUS

Introduction

The development of toughened ceramics over the past few years is arguably one of the most important material design breakthroughs of recent times.[1] Using techniques **on** fundamental understanding of phenomena, such **as** ***in-situ*** **phase** transformation, **fiber** bridging, ductile particle toughening and so forth, monolithic and composite ceramic materials have been processed with fracture toughness in many cases up to an **order** of magnitude higher than those available about two decades ago. Although ceramics can now be considered seriously for many potential structural applications, they *can,* contrary to popular belief, be susceptible to degradation under cyclic fatigue loading, even when such loading is fully compressive. In view of the importance of cyclic loading in many structural applications, the topic of "fatigue in ceramics" **has** received considerable attention of researchers. However, since the field is still in its infancy, understanding of salient mechanisms **has** not **been** achieved and the design of microstructures for optimum fatigue resistance has yet to **be** attempted.[1]

There **are** only a very few reports in literature concerning the fatigue and fracture behavior of Nicalon/SiC composites. Also, standard methods for fatigue crack growth testing of ceramic matrix composites have yet to **be** developed. In view of the above, it **has** been decided to study the fatigue crack propagation behavior **of** Nicalon/SiC composites processed by the Forced Chemical Vapor Infiltration (FCVI) technique, using the ASTM standard **E 647-92** for the measurement of fatigue crack growth rate in metallic materials.

Present Status

Nicalon/SiC composites processed by FCVI technique have a fabric lay-up of $[0\text{-}30/30\text{-}120/60\text{-}150]_n$. Metallographic examination of a few composite specimens was carried out to examine the type and distribution of porosity in the samples. Planar and cross-sectional views of **a** composite specimen are **shown** in Fig. 1. It can be. seen from Fig. 1 that there **are** two major types of porosity in the NicalodSiC composites, viz. porosity between the fiber tows (Figure 1a) and interlaminar porosity (Fig. 1b). The composite is highly anisotropic and. hence, it can be expected that the mechanical properties of the Nicalon/SiC composites will vary significantly along the in-plane and through-thickness directions.

Compliance measurements **are** widely **used** to measure **the** *crack* length **as** well **as** characterize the near crack **tip** field phenomena. However, the elastic modulus of each sample **has** to be known to permit the use of the technique. In view of the variation in density values and consequently moduli values from specimen to specimen. which is inherent from the manufacturing process, and also to develop an indirect method for measuring the moduli values, ultrasonic measurements have been carried out on the specimens.

Based on acoustic wave theory,[2,3] the elastic modulus (E) can be expressed as a function of ultrasonic velocity as

$$E = \rho * \frac{V_S^2(3V_L^2 - 4V_S^2)}{V_L^2 - V_S^2}$$

Where r = density of the material,
V_S = *shear* velocity , and
V_L = longitudinal velocity

Longitudinal waves were used to carry out the ultrasonic measurements. The longitudinal modulus(C) is related to the longitudinal velocity as

$$C = \rho V_L^2$$

The longitudinal modulus is not the same as elastic modulus. It is called "elastic stiffness constant" or "longitudinal modulus of elasticity."[2,3] To calculate the elastic moduli, it is necessary to make ultrasonic measurements using **shear** waves. However. it was difficult to make the shear velocity measurements due to the **porous** nature of the samples.

Ultrasonic measurement?, were performed by *dry* coupling to avoid contamination by couplant. A "pulse-echo overlap method" was used to measure the wave velocities. A schematic of the experimental set **up** is shown in Fig. 2. The reference signal is obtained by passing ultrasonic waves through a reference test system comprised of a rubber sheet and a fused **quartz** piece. The test sample is then placed between the transmitting transducer and the rubber sheet reference test system and ultrasonic waves are passed through the setup. The signals are received by the receiving transducer and captured by an oscilloscope. The signal **peaks** from the reference and test samples, with and without **the** sample in *the* reference system, are matched as closely as possible, and from the phase shift between the two the time **taken** by the ultrasonic waves to travel through the sample is measured. The thickness of the sample divided by the lime taken for the ultrasonic waves to pass through the sample is **taken** as the ultrasonic velocity through the sample. Since the two signals are matched as closely as possible (i.e. overlapped), this technique is referred to as the pulse-echo overlap method.

The longitudinal moduli of the composites were determined in both in-plane and through-thickness orientations. The results are summarized in Table 1. The density of **the** samples varied from **2.06** to 2.63 g/cc and the porosity from **11.5** to 30.4%. The ultrasonic velocities and longitudinal moduli values are plotted against % porosity in Figs. 3 and 4. It can be seen the ultrasonic velocities (0.799 to 0.994 cm/msec) were greater in the in-plane direction than in the through-thickness direction (0.167 to 0.725 cm/msec). Consequently, the longitudinal moduli (129 to 248 GPa) were greater than through-thickness longitudinal moduli (5.6 to 138.2 GPa), as could be expected from the fabric lay-up. It can also be seen that porosity has a greater effect in reducing the moduli in the through-thickness direction than in the in-plane direction.

One of the ***primary*** objectives of the present investigations is to determine the smallest specimen size that can be tested, the results from which are representative of the composite system under study. A new MTS servo-hydraulic system has been recently installed, which will be used to conduct both ambient and elevated temperature (up to 2000°C in air and vacuum) tests. Also a 'Questar' traveling microscope bas been acquired, which enables the measurement of the *crack* lengths, as well as video imaging of the crack Up phenomena.

Machining of Nicalon/SiC samples, apart from being expensive, is well known to be a difficult **task.** Also, the fabrication difficulties are accentuated by the small ***size*** of the specimens, which call for special tools, pushing up the machining costs even higher. An attempt was made to develop in-house fabrication capability to machine the NicalodSiC compact type C(T) specimens (see Fig. 5) using existing facilities. Diamond tools were used to machine the test specimens.

C(T) specimens were cyclically loaded to initiate and then propagate the crack to study the fatigue crack growth behavior of the Nicalon/SiC composites. Initiation of cracks in ceramic specimens is usually done in compression-compression loading. However, the crack initiation under compression-compression has the potentially deleterious effect of leaving residual tensile tensile stresses at the crack tip, on unloading of the specimen, which can exceed the tensile suength of the material over a distance of the order of notch tip radius.[4] It was difficult to initiate the crack in the Nicalon/SiC composite specimens tested. with premature failure emanating from the pin holes. The inability to initiate the crack can be attributed to the shallow notches (a/w = 0.2) in the specimens and relatively blunt notch tips (–200 mm root radius). However, we have recently been able to machine specimens with relatively deep notches (a/W=0.5) and sharp notch tips (–75 nun root radius) using the laser processing facilities at the Y-12 plant of ORNL. The laser-machined C(T) specimens will be tested shortly.

FUTURE WORK

(i) Continuation of fatigue crack growth testing of the C(T) specimens under different loading conditions at ambient as well as elevated temperatures.

(ii) Fractography of the specimens to assess the various damage and crack shielding mechanisms that govern the fatigue and fracture behavior of the NicalodSiC composites.

(iii) Investigation of the fatigue crack propagation behavior of the irradiated Nicalon/SiC specimens and their characterization.

ACKNOWLEDGMENTS

This work is supported by the Department of Energy under contract No. Martin Marietta 11X-SL261V. The authors are very grateful to H. R. Hartman for kindly supplying the KRAK GAGE/FRACOMAT system. They sincerely appreciate the help of Mike Tuck of Y-12/ORNL in machining the compact specimens. They would like to thank Greg Jones, Ted Long, Dong Fielden and Bill Matlin of the University of Tennessee and Marcelo Cescon of Instituto de Pesquisas Tecnologicas, Brazil for their help and support in pursuing this work. They are also grateful to Dr. Arthur Rowcliffe and Dr. Everett Bloom of ORNL for their encouragement and support.

REFERENCES

1. R. H. Duaskardt, R. O. Ritchie and B. N. Cox, Advanced Materials and Processes, Vol. 144, No. 2, 1993. pp 30-35.

2. H. Jeong, D. K. Hsu, R. E. Shannon and P. K. Liaw. Metallurgical Transactions A, Vol. 25A, April 1994, pp 799-809.

3. H. Jeong, D. K. Hsu, R. E. Shannon and P. K. Liaw, Metallurgical Transactions A, Vol. 25A, April 1994, pp 811-819.

4. S. Suresh, Fatigue of Materials, Cambridge University Press, 1991. pp 441-443.

Table 1 In-plane and through-thickness longitudinal of Nicalon/SiC Composites

Sample No.	Vel (cm/μsec),1*	Vel (cm/μsec), 2*	Density (g/cc)	% Porosity	Modulus (GPa),1*	Modulus (GPa), 2*
1	0.987	0.471	2.55	13.85	248.41	56.57
2	0.990	0.477	2.45	17.23	239.83	55.68
3	0.994	0.465	2.45	17.23	242.56	53.08
4	0.927	0.364	2.32	21.62	197.65	30.47
5	0.927	0.377	2.33	21.28	200.22	33.12
6	0.936	0.378	2.37	19.93	205.88	33.58
7	0.814	0.220	2.13	28.04	137.16	10.02
8	0.799	0.219	2.06	30.41	129.60	9.74
9	0.812	0.227	2.07	30.07	133.85	10.46
10	0.972	0.512	2.41	18.58	228.64	63.44
11	0.957	0.442	2.39	19.26	217.97	46.50
12	0.972	0.552	2.44	17.57	226.75	73.13
13	0.877	0.167	2.09	29.39	155.36	5.83
14	0.897	0.195	2.07	30.07	165.75	7.83
15	0.873	0.179	2.10	29.05	159.28	6.70
16	0.967	0.725	2.63	11.15	245.93	130.24
17	0.950	0.685	2.62	11.49	236.82	123.12
18	0.956	0.653	2.60	12.16	237.35	110.74
19	0.940	0.629	2.46	16.89	203.90	89.57
20	0.951	0.525	2.34	20.95	211.18	64.36

*

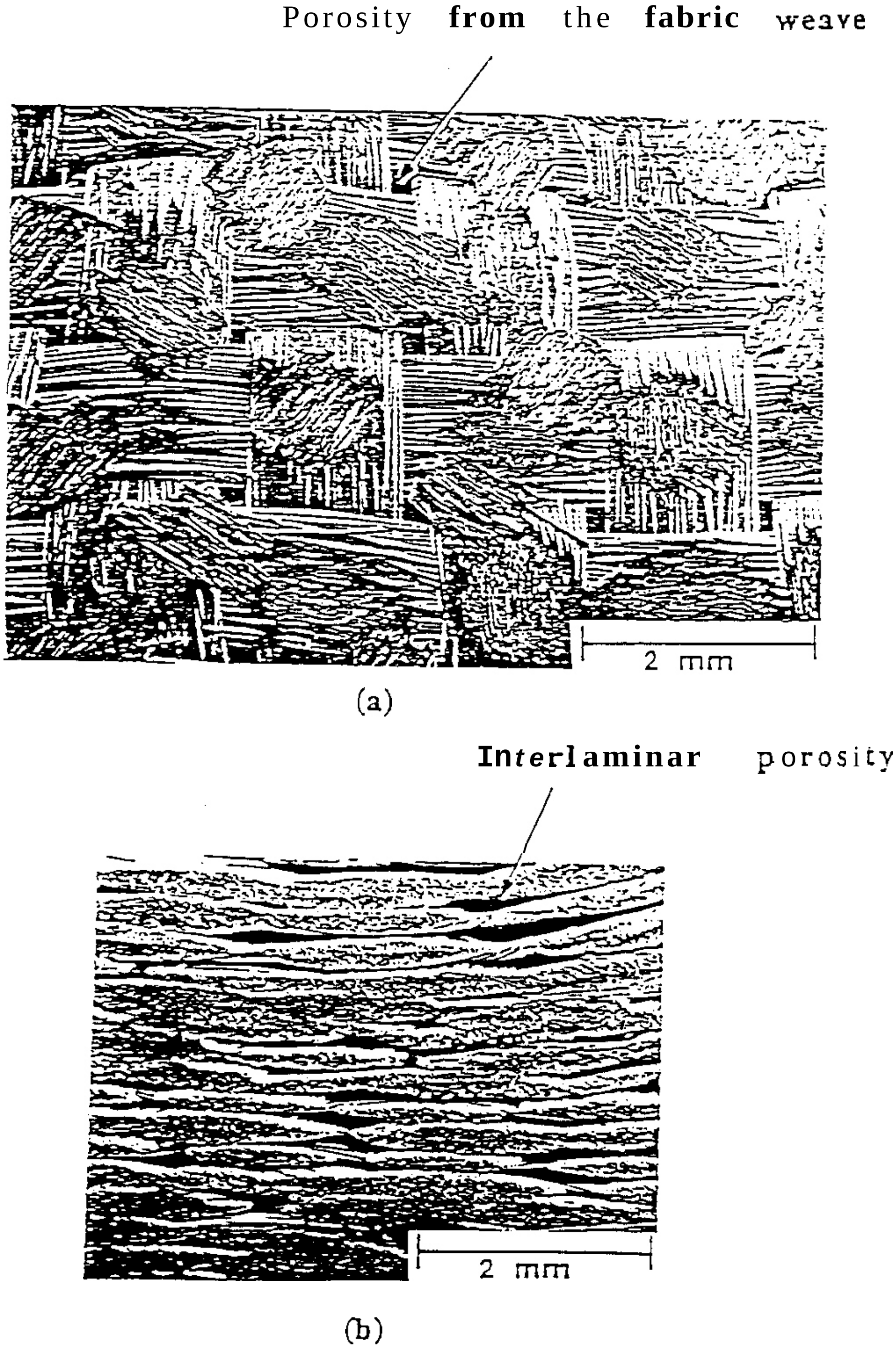

Figure 1. Fabric **Architecture** of Nicalon/SiC Composites
(a) **Plane** View, (b) Goss-Sectional **View**

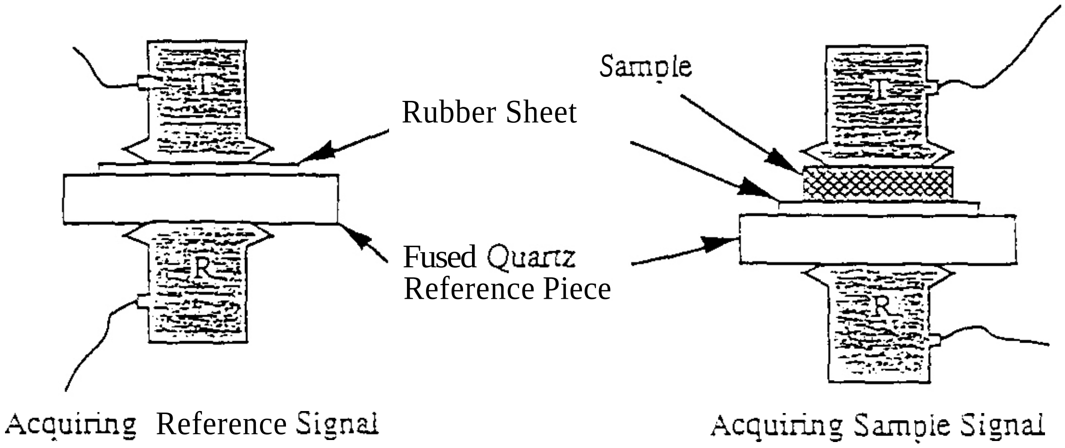

Figure 2. Schematic of **the** Ultrasonic Measurement **set** up

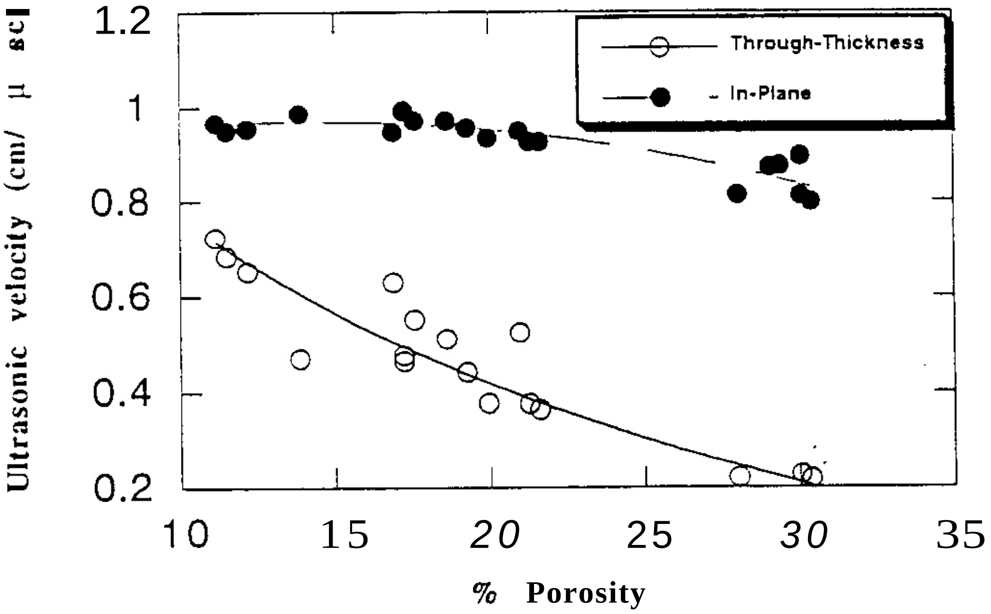

Figure 3. Ultrasonic Velocity vs % Porosity

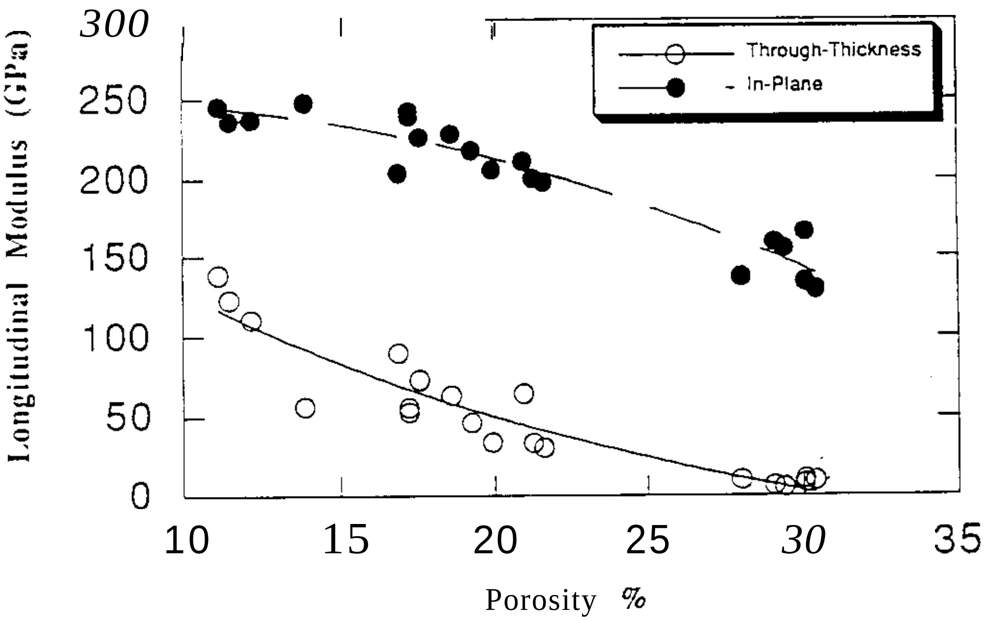

Figure 4. Longitudinal Moduli vs % Porosity in Nicalon/SiC Composites

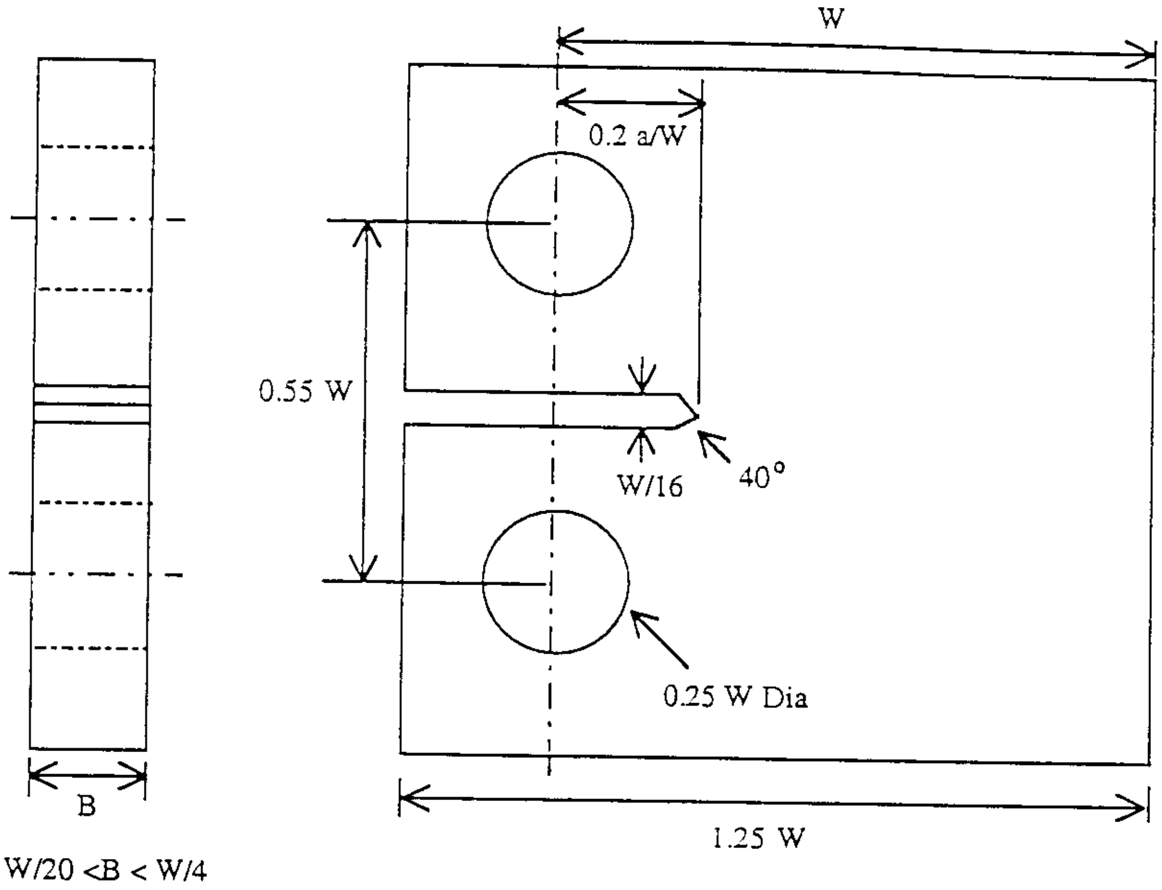

Figure 5. Compact C(T) Specimen for Fatigue Crack Growth Testing

TENSILE BEHAVIOR OF IRRADIATED SIC **FIBERS** - M. C. Osborne (Rensselaer Polytechnic Institute), L. L. Snead (Oak Ridge National **Laboratory),** and D. Steiner (Rensselaer Polytechnic Institute)

OBJECTIVE

The strength and toughness of continuous fiber reinforced ceramic composites(CFCC's) are highly dependent on the fiber strength distribution. To first order, **weaker** fibers lead to low strength but higher toughness while stronger fibers lead to high strength composites of relatively low toughness. Toughness is associated with pullout of the fibers from the ceramic matrix. It **has** been shown previously that both strength and toughness of SiC/Nicalon^{TM} composites are drastically changed following irradiation. The object of this investigation is to investigate the effects of low level neutron irradiation **has** on the microstructure and mechanical properties of low oxygen Nicalon fibers.

SUMMARY

Tensile results **are** presented for low oxygen Nicalon fibers neutron irradiated at damage levels of 0.013 displacements per atom (dpa), 0.13 dpa and 0.32 dpa. Single fibers were tensile **tested** and analyzed, using Weibull statistics, for mean strength and distribution. Tensile modulus was also determined. Using a diffractometer. the fiber **grain** size and percent crystallinity were determined. The mean strength and modulus decreased by 20% but then increased with **the** highest damage level **tested.** Both grain sue and crystallinity decreased **as** dose increased. These initial results of low level neutron irradiation of **low** oxygen Nicalon fibers exhibit no substantial degradation of the properties investigated. Therefore, continued research at **higher doses** is recommended.

STATUS *AND* PROGRESS

Introduction

Silicon carbide(SiC) has been considered **as** a low-activation structural material for fusion reactor about twenty years [1-5]. Bulk ceramics' fracture strength is highly dependent on the flaw population and they fail with no plastic deformation. Therefore, bulk **SiC** is processed with **SiC** fibers to produce a continuous fiber reinforced ceramic composite (CFCC) which has significantly higher toughness **than** monolithic SiC and can lead to more graceful failure. The tensile behavior of SiC fibers used in these composites needs to be studied to allow prediction of composite behavior and tailoring of composite properties.

The work of fracture (WOF) which is related to toughness due to pullout is dependent on the pullout length, h, **as** shown below in equation 1 [6]

$$WOF = \frac{V_f h^2 t}{3 \ r} \qquad (1)$$

where **r** is the fiber radius and t is the frictional shear stress. Although the fiber pullout length is highly dependent on the characteristics of the fiber-matrix interface, the pullout length is also dependent on the statistical distribution of the fiber strength. This study primarily investigates the strength variations of a recently developed **SiC** fiber. low oxygen Nicalon. with different levels of neutron irradiation.

Ceramic grade Nicalon has been studied extensively [7-11] and **has** adequate mechanical properties up *to* 1100-1200C. However, studies of the low temperature neutron irradiation behavior of Nicalon [11] have shown that the fiber is unstable. Neutron irradiation densifies the fiber which increases strength and modulus but also reduces the fracture toughness of the fiber. In the radiation induced densification process, the fiber diameter also decreases which causes the fiber to pull away from the interface, thus significantly reducing the composite strength and in many cases also the toughness [11].

A recently developed experimental fiber produced by the Nippon Carbon Company employs the same processing as Nicalon except that the fiber is crosslinked using electron irradiation and cured in an inert atmosphere [12,13]. This new processing technique elimanates most of the oxygen which is normally found in ceramic grade Nicalon. The oxygen content is reduced from >10 wt% in ceramic grade Nicalon to <0.5 wt% in the low oxygen Nicalon. The low oxygen concentration allows a greater amount of the Si and C to combine with each other rather than with oxygen, resulting in higher crystallinity for the low oxygen Nicalon compared to that of ceramic grade Nicalon.

The irradiation behavior of these newer fibers needs to be investigated to determine if they would be stable in a neutron radiation field. A recent study [14] found that low oxygen Nicalon does not densify under low levels of neutron irradiation. Thus, this fiber shows promise for use in neutron enviroments but the irradiation behavior of this fiber needs to be further investigated. This paper will discuss the properties of low oxygen Nicalon after low level neutron irradiation. The properties investigated are tensile strength, tensile modulus, grain size and percent crystallinity.

Experimental Setup and Data Reduction

The tensile testing was performed on an Instron[a] Model **1130** in accordance with test procedures described in ASTM **3379-75 [15].** The load was measured with a two pound (4.4 N) Entran[b] load cell and the displacement was measured with a laser micrometer made by Keyence[c] Corporation. The load and displacement were recorded and controlled by a computer using Instron Series IX software.

The fiber gauge length was set by cutting a rectangle into an index card with one of the dimensions *25* mm (gauge length) and epoxying the individual fibers across this rectangular hole. The fiber was vertically aligned in pneumatic grips and the edges of the index card carefully cut. The crosshead diplacement speed was set at 0.5 mm/min.

Fiber diameters were measured after fiber failure to reduce the possibilities of surface damage. A picture was taken of the broken fiber in an optical microscope and magnified to 400X. The fiber diameter on the magnified picture could be measured using vernier calipers to an accuracy of 0.001 in. (0.025 mm). The me fiber diameter was calculated by dividing the measured value by 400.

Strength was calculated by dividing the load by the fiber cross sectional area and the modulus was calculated as the stress divided by strain where the **strain** is displacement divided by the gauge length. Weibull statistics (the two parameter model) [16-18] were used to reduce the raw strength data. The average tensile modulus was calculated as the simple average of the moduli which assumes a Gaussian distribution.

X-ray diffraction **data** were obtained by placing a powder sample in a diffractometer and measuring the intensities at various angles. This is accomplished automatically on a diffractometer. The diffraction scan was performed at 35 kV and 15 mA using Cu K, radiation. To mount a sample, a pulverized fiber is mixed with toluene in a mortar to allow the crushed fiber to flow. The mixture was poured onto a Si wafer which has a low background signal. The chamber was flooded with He to lower the background scattering which would occur in air. This background reduction is necessary when investigating the crystallinity of the fibers. Scattering of non-crystalline **material** (glass) produces a halo which peaks at about 20 degrees. Scattering from air will *mask* this effect and make the amorphous peak indistingishable from the scattering due to air.

---

[a] Instron Corp., Canton, MA

[b] Entran Devices Inc., Fairfield, NJ

[c] Keyence Corp.. Fair Lawn, NJ

The range of scattering angle, **2q,** was chosen to be from **10** to **110** degrees to include the amorphous halo and several low intensity SiC peaks at **100** and 105 degrees. The data were reduced using Scintagg[d] software which de-convolutes the **peaks** from background and from one another. The software gives peak intensity, full width at half maximum. **2q** and the integrated intensities. The crystal ***size*** was calculated using Sherrer's formula [19] including the effect of lattice strains. Percent crystallinity was calculated by dividing the integrated intensity for the peaks due to diffraction of SiC by the total integrated intensity which includes the amorphous halo.

Fibers were irradiated in the hydraulic rabbit tube (HT3) at the High Flux Isotope Reactor (HFIR) at ORNL. The fibers were enclosed in an aluminum tube which was welded shut in an argon amosphere. The neutron flux ($E > 0.1$ MeV) was **7.8** x 10^{18} n/(m^2 s). The conversion of fluence to dpa **for** SiC used the approximation of 1 x 10^{25} n/m^2 per **1** dpa. Low oxygen fibers were tested prior to irradiion and also for various irradiation conditions which included **1.28** x 10^{23} n/m^2 **(0.013** dpa), **12.8 x** 10^{23} n/m^2 **(0.13** dpa) and **32.2** x 10^{23} n/m^2 **(0.32** dpa). The test temperature was estimated to be 100°C which is about 40°C higher than the core coolant temperature. There is some uncertainty in the irradiation temperature of the fibers. If the fibers had good contact with the walls of the capsule, there would be sufficient heat transfer to keep the fibers at or below 100°C to offset any heating due to the irradiation. There was some evidence that the fibers were at a higher temperature which caused the fusing of the fibers' sizing hut the temperature was not greater than 200°C.

Results and Discussion

Table 1 presents the reduced data **from** the tensile tests. The mean strength and modulus are plotted versus dose. in Figure **1.** The experimental error for the suength and modulus calculations is **1.7%** for the strength and **3.5%** for the modulus. The main contribution to the experimental error in the determination of the elastic modulus is from the displacement measurement (about **2%). The** standard deviations may appear high for mean strength but this behavior is typical of materials with low Weibull moduli. Figure **2** presents **a** sample load-displacement curve and note that the figure is linear to failure indicating that the fibers do not exhibit plastic deformation. Figures **3-6** present Wiebull plots for the various conditions.

Table 1. Reduced Tensile Data for Low Oxygen Nicalon Fibers (Standard Deviations are in Parenthesis)

Fiber Designation	Wiebull Modulus for Strength	Mean Strength (GPa)	Tensile Modulus (GPa)
Unirradiated	**3.00**	**2.41 (0.764)**	**238.2 (62.8)**
0.013 dpa	**2.69**	**2.26 (0.903)**	**208.1 (47.6)**
0.13 dpa	**2.58**	**2.03 (0.844)**	**167.9 (47.3)**
0.32 dpa	**3.99**	**2.79 (0.623)**	**222.7 (61.0)**

For the tensile modulus. the standard deviation relates the intrinsic differences in the fiber structure. If all the fibers had exactly the Same structure then the moduli would be the same for each batch tested. With higher standard deviations the internal structure of the fibers may vary and the numbers presented in Table 1 represent an average **property.** The reason for averaging the bulk properlies is that the x-ray diffraction dala yields property averages. The x-ray diffraction data represent information on grains of differing size and orientation and for fibers of differing composition. Thus, this data gives an average of the bulk structure.

Table **2** presents the reduced **results** from the diffraction data. The family of planes investigated **was** {111}. The **0.13** dpa fibers had noisy data (not enough material to get significant diffraction) and were not analyzed. Crystal sizes are in nanometers and the lengths correspond **to** the [111] direction. **Strain** is not reported in **this** table hut it was calculated to increase with higher dose.

---

[d] Scintag Corp.. Sunnyvale, CA

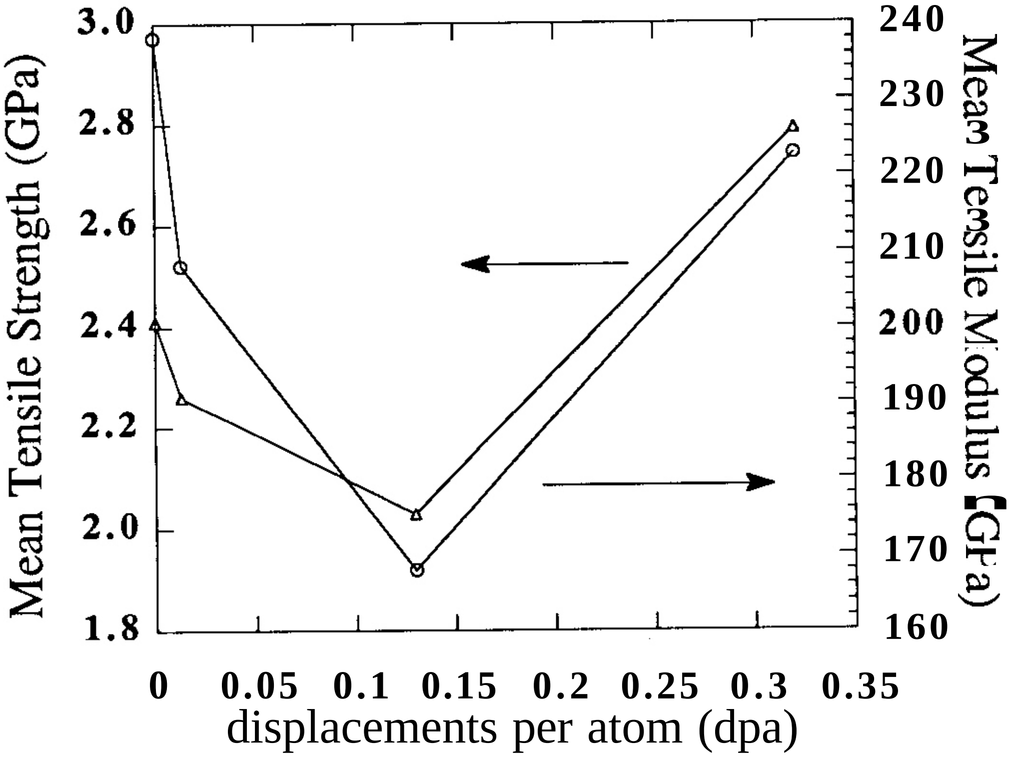

Fig. 1. Mean Strength and Modulus versus Damage Level

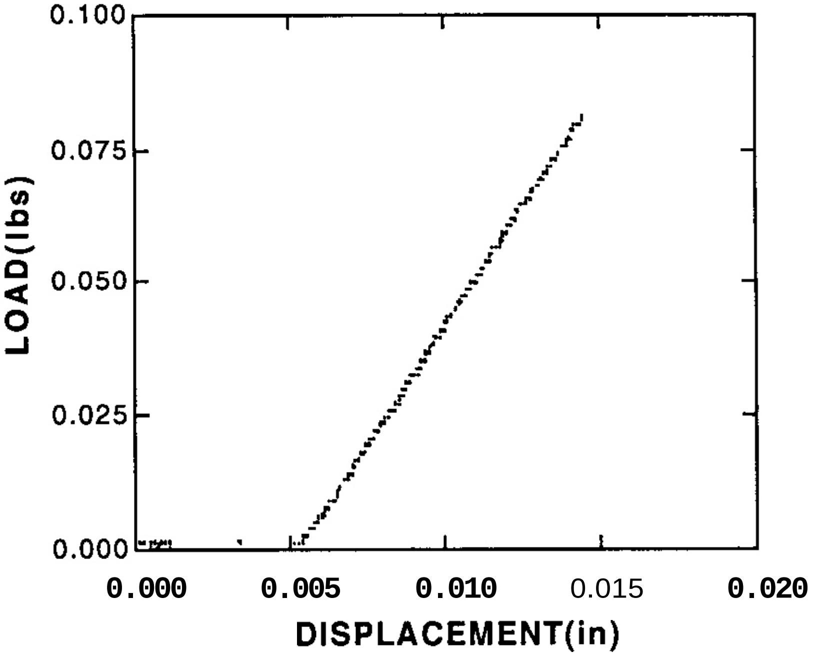

Figure 2. Typical Load-Displacement *Curve* for Single **Fiber** Test of Low Oxygen Nicalon

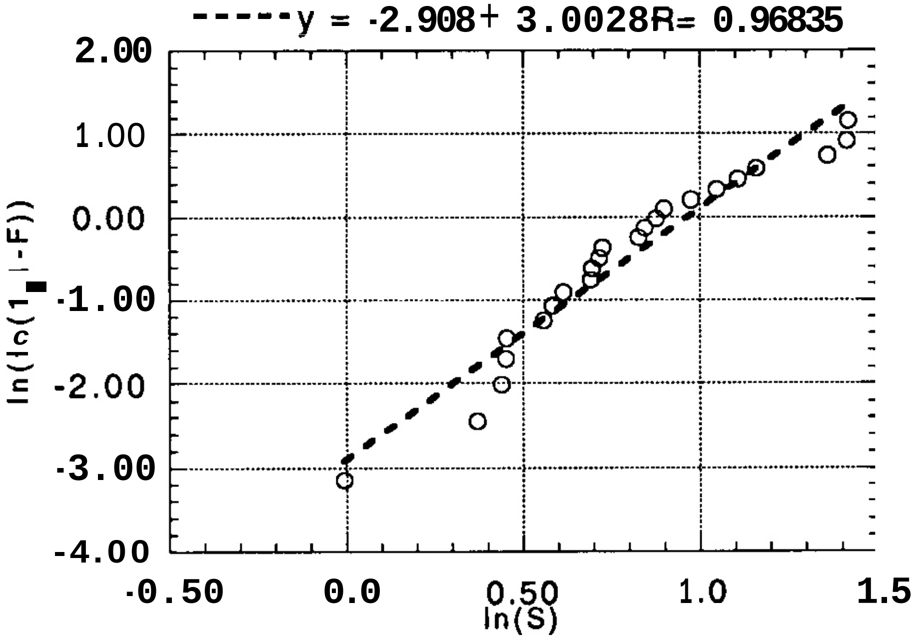

Figure 3. Unirradiated Low Oxygen Nicalon Wiebull Plot (“ R is goodness of fit).

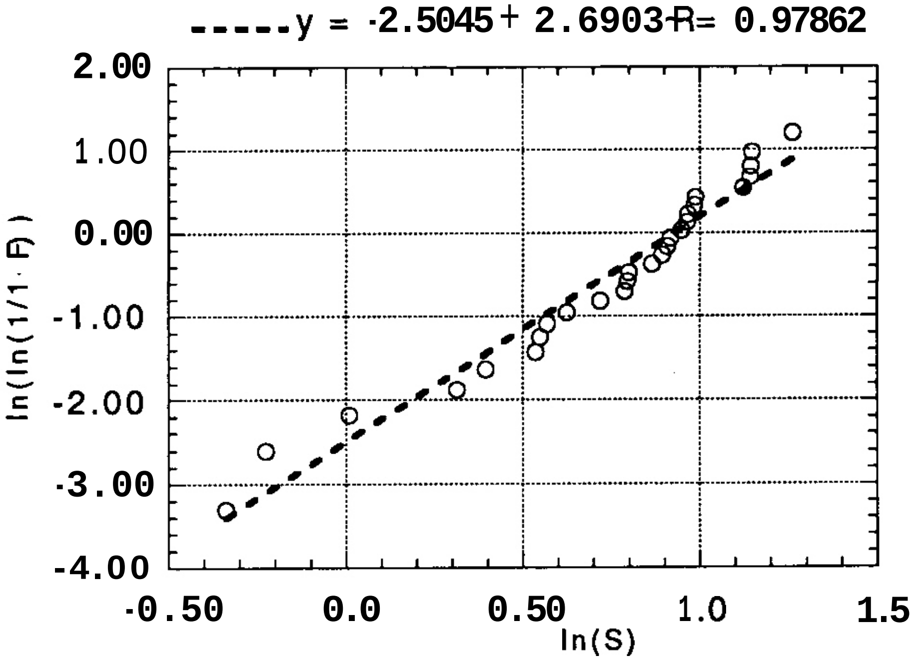

Figure 4. Irradiated Low Oxygen Nicalon (0.013 dpa) Wiebull Plot (“R” is goodness of fit).

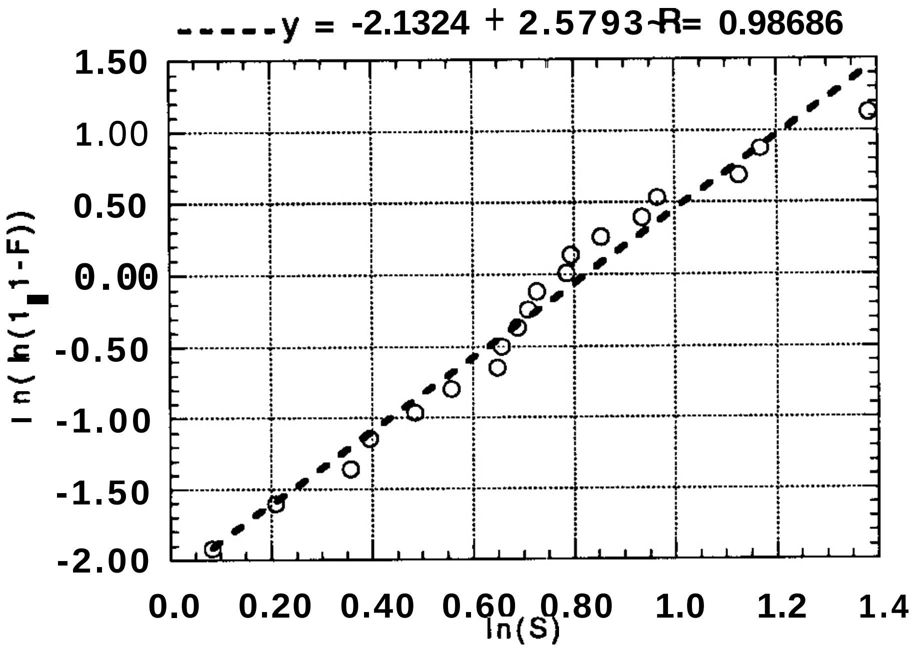

Figure 5. **Irradiated** Low Oxygen Nicalon(0.13 **dpa)** Wiebull **Plot ("R"** is goodness of fit).

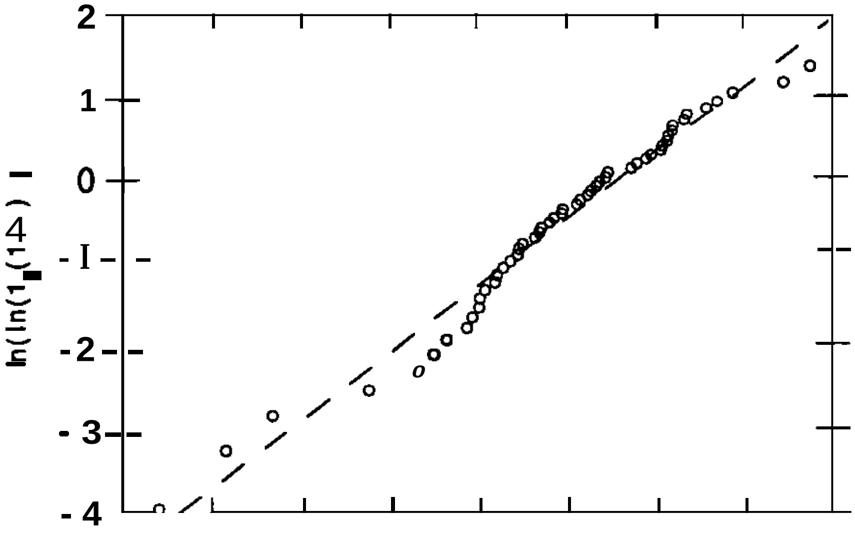

Table 2. Reduced X-Ray Data for Low Oxygen Nicalon Fibers

Fiber Designation	Crystal size (nm)	Percent Crystallinity
Unirradiated	3.04 - 3.16	97.5
0.013 dpa	3.09 - 3.20	
0.32 dpa	2.71 - 2.81	93.6

Crystallite sizes were calculated as described previously and the ranges in size correspond to the difference between the Gaussian and Cauchy fits to the peaks. Percent crystallinity was not reported for the low dose fibers due to problems with the experimental setup, i.e., the amorphous halo around 20-25 degrees was masked by some residue of adhesive tape on the Si wafer. This problem was corrected for the higher doses, but due to the limited amount of material available, the low dose irradiation could not be repeated.

The tensile data show a decrease in mean strength and increase in scatter about the mean strength (lower Wiebull parameter) at low doses but at the highest dose the strength increases and the fibers show less scatter in the strength. At the highest dose tested, the strength and reliability were higher than for the unirradiated condition. The change in reliability, shown by the different Weibull moduli, suggests that there is a different controlling mechanism for failure and this failure mechanism will be discussed later. The strength increase of the fibers is consistent with observations by other authors for irradiated ceramic grade Nicalon [20-22]. The strength increase in the ceramic grade Nicalon may be attributed to densification. The strength increase at the high dose for the low oxygen Nicalon is not fully understood but a possible explanation is presented below.

The strength increase with irradiation is normal for most materials. Metals considered for fusion **reactors** show embrittlement and strength increases with increases in dose [23-25]. However, the embrittlement mechanism is different for metals than for ceramics. Metal embrittlement is due to irradiation induced clusteres of interstitials and vacancies which pin dislocations or act as barriers to dislocation movement resulting in a reduction of plastic deformation and an increase in strength. In most ceramics. especially SiC, there is little or no macroscopic plastic deformation. *so* this dislocation mechanism is not valid.

From the x-ray data, the unstrained average crystal size was calculated and **shown** to have decreased slightly at the highest dose but to have no significant change at the lowest dose. Since the low-oxygen fibers are nearly all crystalline, the cause of failure could be due to changes in crystal size which could change the flaw population at the crystal boundries. This assumes that the flaw population is controled by the grain size. This would be the case if the surface flaws are insignificant compared to the flaws due to the grains and if there are no large inclusions in the bulk of the fiber which could cause stress concentration .

Orowan and Petch [26] have shown that strength of normally ductile or semibrittle materials is proportional to $d^{-1/2}$, where d is the average grain size. Figure 7 shows a plot of mean strength versus the reciprocal of the square root of the crystal size for the varying test conditions. The plot follows linearity for the three data points obtained in this study which suggests that change in crystal size could be a mechanism for strength increase in the irradiated fibers. The data would be more convincing if there were more points, however, it does appear that crystal size has an effect on the strength of the fibers.

The decrease in **crystal** size and corresponding crystallinity decrease at the highest dose can possibly be partially explained via the fact that the neutron bombardment causes atom displacements which result in a reduction of the effective size of grains by disordering atoms in the crystal lattice. This phenomena known as ballistic dissolution could be the cause of the crystallite sue reduction and the decrease in crystallinity. Ballistic dissolution is the cascade effect caused by an energetic particle (neutrons in this study) striking and displacing the primary knockon atom (PKA) [27]. The PKA strikes other atoms causing more displacements and this process continues until the atoms involved have insufficient energy to cause displacements. This cascade effect causes a balloon-like region of damage in the material in the direction in which the PKA recoils after being struck by the neutron. The damaged region has a size of tens of nanometers. If this small volume of disordering passes near or through a crystallite, the crystallite will become completely or partially disordered which reduces the crystal size and overall crystallinity of the material. If enough damage occurs then the material could become totally amorphous providing that

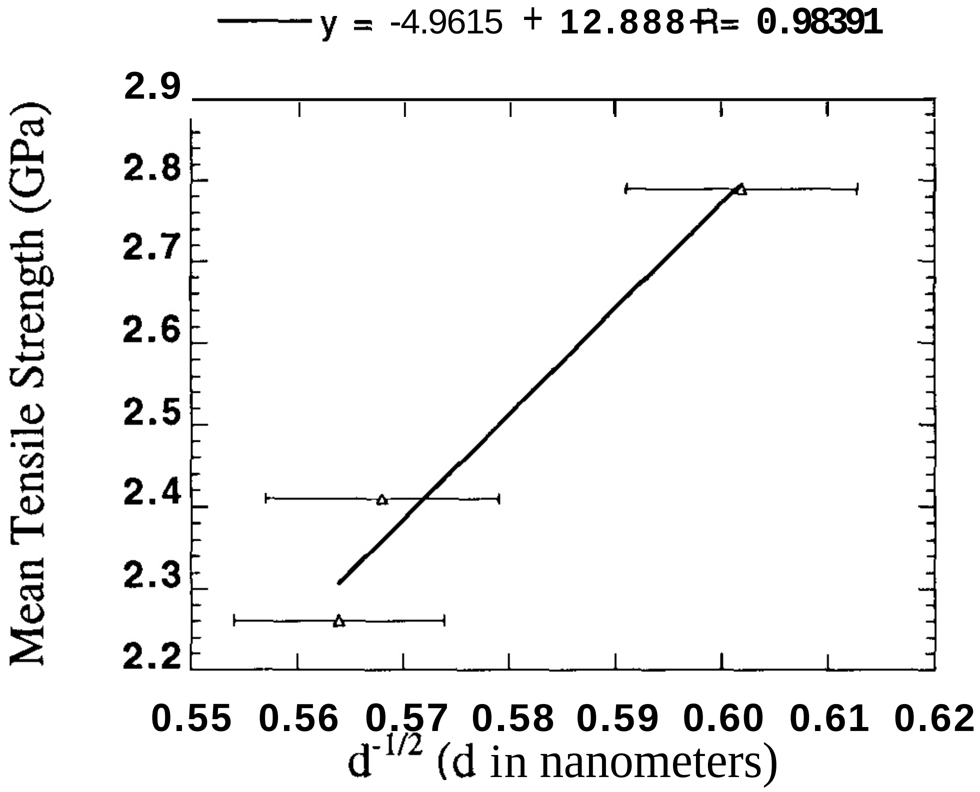

Figure 7. Mean Strength versus Reciprocal Square Root of Crystal Size, d ("R" is goodness of fit).

recrystallization does not take place. The amount of recrystallization is highly dependent on the irradiation temperature. At the liquid nitrogen temperature (-210°C), the atoms would remain in their displaced positions. At the temperatures of this experiment (about 100°C), the atoms will come back to lattice positions with very small amounts of disordering remaining. Therefore large numbers of neutrons need to strike the fiber for significant microstructural changes to occur.

The change in crystallinity would affect the tensile modulus. The initial decrease in modulus corresponds to the decrease in crystallinity. The reason for the modulus increase at 0.32 dpa is not completely understood. The modulus is a measure of the average bond suength but it is not linear with atomic spacing [28]. A possible explanation for the modulus increase is that at the low dpa levels, the average bond length increases due to the creation of vacancies and interstitials as discussed above. As the damage increases, more vacancies are filled in than created, but not necessarily with the original occupant of the lattice site(i.e. Si goes to C position and vice versa) and therefore, the modulus would increase again but crystallinity would continue to decrease. Additional microstructural characterization using TEM, EXAFS or Raman spectroscopy is needed to help clarify the possible physical mechanism for modulus changes, crystallite size decrease and crystallinity decrease.

Another cause of microstructural changes which would affect the modulus is possible variations in the irradiation temperature. The temperature in the irradiation capsule must be known to a reasonable accuracy (within 20 degrees or so) such that there are no microstructural changes due to temperature. The temperature for this study was not measured directly but was estimated to be about 100°C.

An unresolved issue in this study is the appearance of the fracture surfaces of the broken fibers because the fracture surfaces were not examined with a scanning electron microscope (SEM) due to time constraints. The fiber fracture surfaces would have given information on where the flaw which caused failure occured. This information determines the mode of failure (surface or hulk) of the fiber. Previous investigations with ceramic grade Nicalon suggested that there was a changing flaw population in the fibers with increasing irradiation [19,20]. A change in failure mode was seen in the data at the highest dose for this study. A failure mode change is detected in two ways: (1) by observing a bend in the Weibull plot; and (2) by tensile testing fibers at different lengths to see if there is a surface effect on the strength. Potential bends in the Weibull plots occur at ln S = 0.9 in Figure 3 (unirradiated fibers). 0.8 in Figure 5 (0.13 dpa), and 1.2 in Figure 6 (0.32 dpa), suggesting that there is a varying mechanism for fiber failure. Although with more data the tailing off on the end regions on the plots may not be a significant effect and therefore not show mode changes. The actual flaws would also have been picked up by SEM of the fiber fracture surfaces. If there is no observable flaw when viewing the fracture surface, then the failure could be due to the change in crystal size which would help justify the above hypothesis on crystal size and mean strength.

The change in the Weibull moduli suggests a changing flaw population in the fibers. At the highest damage level, 0.32 dpa. the Weibull modulus was higher. Using the two parameter model for data analysis may not be appropriate due to the bends in the plots as discussed above. The overall increase in Weibull modulus at the highest damage level indicates that neutron irradiation reduces the spread in the controlling flaw population so that the fibers will fail closer to the same mean stress.

CONCLUSIONS AND FUTURE WORK

Low dose (< 0.3 dpa) neutron irradiation of low oxygen Nicalon show the mean strength and modulus decrease by about **20%** and then both increasing with increasing **damage.** X-ray diffraction data show that the crystallinity and crystal size of the fibers decreased with increasing dose but as the percent crystallinity decreases the strength distribution was reduced as shown by the increase in Weibull modulus. Overall, the irradiated data do not exhibit drastic changes in properties but rather represent small variations around the unirradiated values.

The absence of significant degradation of properties with irradiation suggests that the low oxygen Nicalon SiC fiber has potential for use in a neutron radiation enviroment. The effects of higher neutron doses need to be investigated before employment in CFCC's for nuclear reactors. Besides higher dose testing, future studies would include tensile testing, x-ray diffraction and density measurements but they would also need additional information to develop a complete picture of the fiber's behavior. The additional information desired would include SEM of fracture surfaces, TEM of the fibers, testing fibers at different gauge lengths, Raman spectroscopy or EXAFS, and precise. control and measurement of the irradiation temperature.

ACKNOWLEDGEMENTS

Research sponsored by the Office of Fusion Energy, U. S. Department of Energy, under contract DE-AC05-84OR21400 with Martin Marietta Energy Systems, Inc., and with RPI under subcontract DE-FG02-92ER54181. The authors would like to thank **S.J.** Zinkle and E. Lara-Curzio for helpful comments.

REFERENCES

1. L.H. Rovner and G.R. Hopkins, Nuclear Technology 29 (1976) 274.
2. F. Porz et al, Materials Sci. and Engineering 71 (1985) 273.
3. G.R. Hopkins and J. Chin, J. Nucl. Matl. 141-143 (1986) 148.
4. J. Linke et al, High Temp.-High Press. 21 (1989) 533.
5. The ARIES I Tokamak Reactor Study, UCLA-PPG-1323 (1991).
6. R.W. Davidge and J.J.R. Davies. Mechanical Testing of Engineering Ceramics at High Temperatures. eds. B.F. Dyson, R.D. Lohr, and R. Morrell, Elsevier, New York, (1989) 255.
7. G. Simon and A.R. **Bunsell.** J. Matr. Sci. 19 (1984) 3649.
8. H. Kim and A.J. Moorhead, J. *Am.* Ceram. Soc. 74 (1991) 666.
9. T. Mah et al, J. Matr. Sci. 19 (1984) 1191.

10. L.C. Sawyer et al, J. Am. Ceram. Soc. 70 (1987) 798.
11. L.L. Snead. Investigation of SiC Composites as Structural Materials for Nuclear Applications, (Doctoral Thesis, Rensselaer Polytechnic Institute, December (1993) 133.
12. K.K. Chawla, Composite Materials, (Springer-Verlag. New York (1987) 181.
13. K. Okamura and T. Seguchi, J of Inorganic and Organometallic Polymers 2 (1991) 171.
14. L.L. Snead and K L More, J. Nucl. Matl.. to be published.
15. ASTM D 3379-75, "Standard Test Method for Tensile Strength and Young's Modulus for High-Modulus Materials," [15.03] (1986) 181-185.
16. S.N. Patankar, J. Matl. Sci. Letters 10 (1991) 1176.
17. E.M. Asloun et al, J. Matr. Sci. 24 (1989) 3504.
18. H.F. Wu and AN. Netravali, J. Matr. Sci. 27 (1992) 3318.
19. B.E. Warren, X-Ray Diffraction (Addison-Wesley Publishing Co., Reading, MA (1969) 258.
20. A. Kohyama et al. Effects of Radiation on Materials, 15th International Symposium, eds: RE. Stoller. A.S. Kumar and D.S. Gelles, ASTM STP 1125, ASTM, Philadelphia (1992) 785.
21. K. Okamura et al, J. Nucl. Mat. 141-143 (1986) 102.
22. K. Okamura et al, J. Nucl. Mat. 155-157 (1988) 329.
23. S.Jitsukawa et al, J. Nucl. Mat. 191-194 (1992) 771.
24. Y. Zvezdin et al. J. Nucl. Mat. 191-194 (1992) 855.
25. B.A. Loomis and D.L. Smith et al, J. Nucl. Mar 191-194 (1992) 84.
26. W.D. Kingery , H.K. Bowen and D.R Uhlmann, Introduction to Ceramics, Second Edition, John Wiley and Sons, New York (1991) 794-795.
27. K.C. Russell, Prog. Mater. Sci. 28 (1984) 229.
28. H.W. Hayden, W.G. Moffatt and J. Wulff, The Structure and Properties of Materials, Vol. 3, Mechanical Behavior. John Wiley and Sons, New York (1965). 28.

TEMPERATURE DEPENDENCE OF THE SUBCRITICAL CRACK GROWTH RATE OF A SiClSiC COMPOSITE - R. H. Jones and C. H. Henager, Jr., (Pacific Northwest Laboratory)

OBJECTIVE

The objective of this study is to evaluate the high-temperature mechanical properties of SiClSiC composite materials for fusion structural applications.

SUMMARY

The long term stability of SiC/SiC composites is an issue regarding their use for fusion structural applications only because there is insufficient data to determine if there is really a problem. Crack growth measurements have been made over the temperature range of **800** to 1100°C, in high-purity Ar, to help assess the long term stability of these materials. Stage **II** crack growth rates ranging from 2 x 10^{-9} m/s at 1100°C down to 3 x 10^{-11} m/s at 800°C were found for a 2-D SiC/SiC composite reinforced with 40% Nicalon fibers. The stage **II** velocities obeyed an Arrhenius relationship over this temperature range with an activation energy of 235 kJ/mol. At a fusion relevant temperature of 800°C, the crack velocity will result in a crack growth of 1 mmlyr. More creep resistant fibers are expected to reduce this crack growth amount to less than **1** x 10^{-2} mmlyr. at 800°C. This is not an excessive amount of crack extension for a material with a fracture toughness of about 20 MPa $m^{1/2}$.

PROGRESS AND STATUS

The crack growth rates of SiClSiC samples were measured over a temperature range of **800** to 1100°C in high-purity Ar in a manner consistent with that reported previously (1). The material is that reported on previously and is a 40% continuous SiC fiber reinforced SiC. The fibers were Nicalon and the matrix was produced **by** chemical vapor infiltration. Tests were conducted at constant load instead of increasing load steps as performed previously. A starting load corresponding to a stress intensity of about 10 MPa $m^{1/2}$ was chosen as the starting condition. The velocity utilized for this analysis was the minimum obtained as a function of time. With increasing time, the crack extension increases the stress intensity and drives the crack into the stage III regime. This behavior is demonstrated in Figure 1 where the **K** independent regime is referred to as stage II and the strongly **K** dependent behavior is stage III. An example of the change in crack velocity with time at a constant load is shown in Figure 2. This behavior has been discussed previously and is explained by the creep relaxation of the fibers bridging the crack and the resulting increase in the crack bridging zone (2).

The crack length was measured by the compliance method as explained previously (1). However, more recent data supports the relevance of this type of measurement

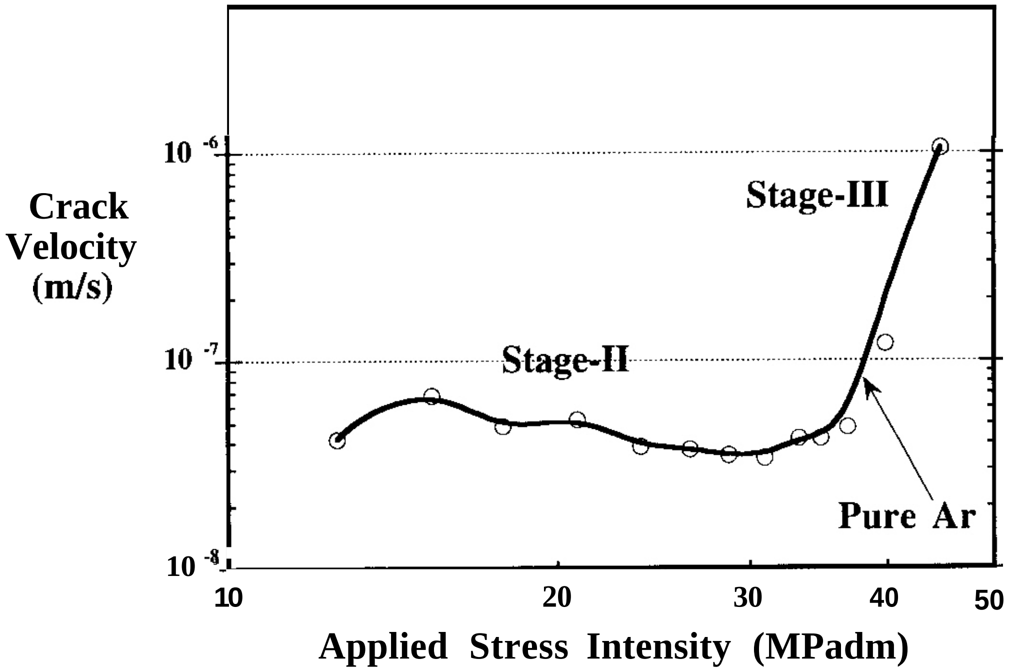

Figure 1. Crack velocity as function of stress intensity for SiClSiC composite reinforced with Nicalon fibers.

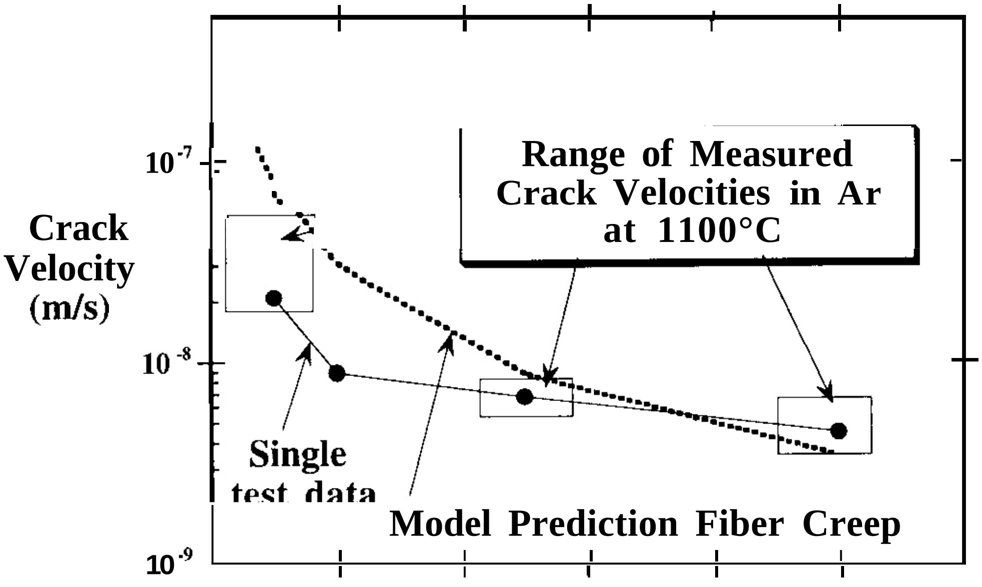

Figure 2. Crack velocity as a function of time for SiClSiC composite reinforced with Nicalon fibers.

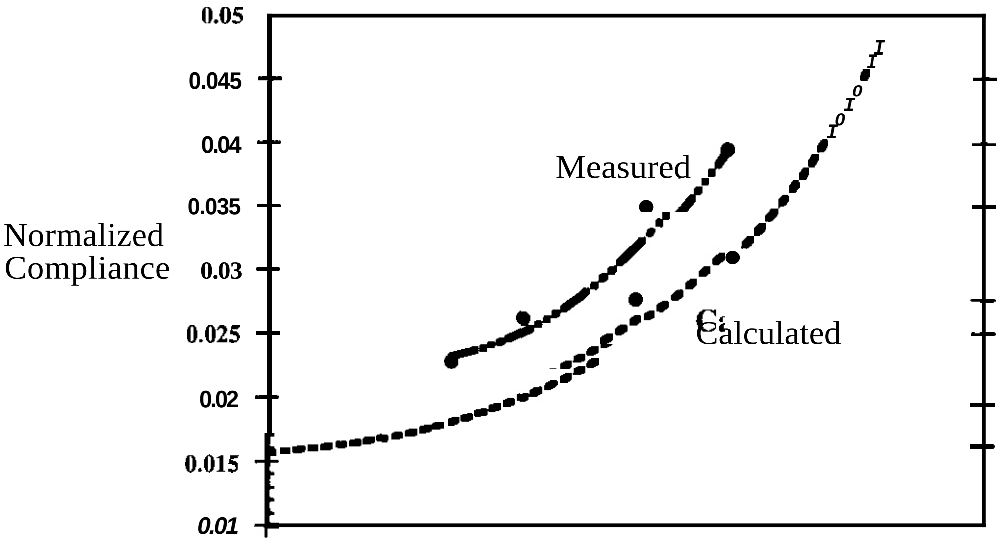

Figure 3. Calculated and measured crack lengths as a function of normalized SENB specimen compliance. Cracks were measured from sectioned and polished post-test specimens and calculated lengths were determined from instantaneous compliance during testing.

(Figure 3). The dashed curve is the calculated compliance as a function of a/W based on the 4-point bend geometry used in these tests and the properties of SiC/SiC. This curve was based on a calibration for the test fixture using a steel sample with variable a/W. This curve was then converted to that for SiC/SiC. The experimental data points were obtained from SiC/SiC samples in which cracks were grown at 1100°C by subcritical crack growth to various a/W values. The compliance was measured at the end of the test and the samples sectioned and the mid-plane crack depth measured. The difference between the measured and calculated curves is consistent with the presence of the multiple cracks observed in these samples. The multiple cracks emanating from the sample notch and propagating in a mostly parallel direction cause the sample to be more compliant than the calculated compliance. Nevertheless, the difference between the measured and calculated curves is not very large and the shape of the curves are quite similar.

Experimental Results

The sample displacement rate, which is a measure of the crack growth rate, is shown as a function of 1/T in Figure 4. The range of crack velocities associated with the data in Figure 4 are 2 x 10^{-9} m/s at 1100°C to 3 x 10^{-11} m/s at 800°C. This result produced a plot that follows an Arrhenius relationship with an activation energy of 234 ± 50 kJ/mol. Previous research on the creep of Nicalon fibers by Bunsell (3) resulted in an activation energy of 490 kJ/mol. The reason for this nearly factor of 2 difference between the composite and fiber activation energy is not

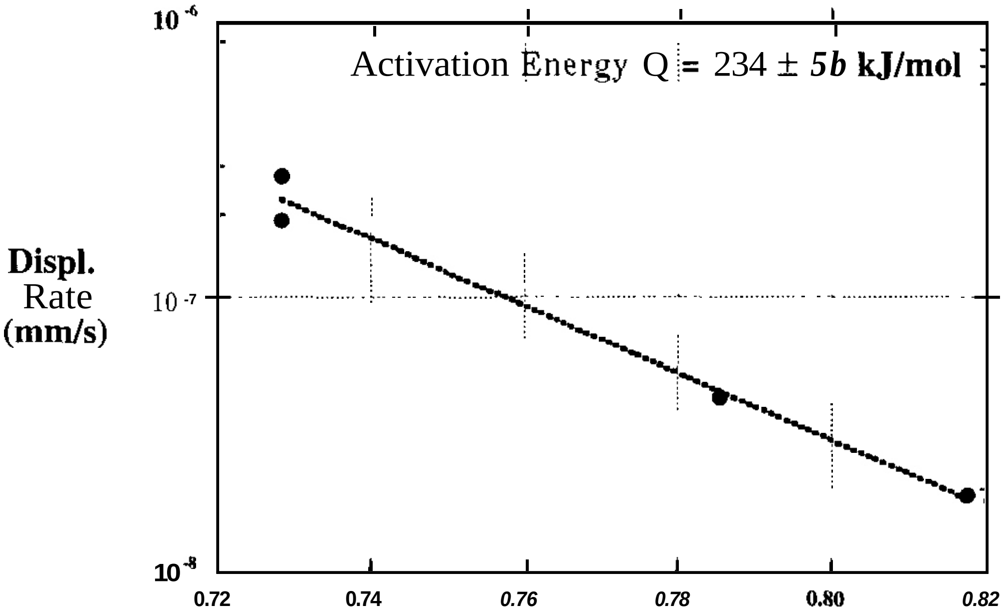

Figure 4. Displacement rate as a function of 1000/T to determine activation energy for slow crack growth rate in SiClSiC composite reinforced with Nicalon fibers. This rate would change depending on reinforcing fiber used in composite.

known; however, there are several factors that could be involved. These factors include: 1) the role of the fiber/matrix interface, 2) changes in the Nicalon during processing of the composite and 3) changes in the composition and microstructure of Nicalon fibers over the last 10 years.

Discussion

The upper use temperature for SiClSiC in a radiation environment will be around 1000°C because this represents the minimum in the dimensional change observed for beta SIC. Void formation occurs at temperatures above 1000°C in beta SiC and this results in large dimensional changes. Therefore, without attempts to modify the void formation regime in SiC by compositional adjustments, 1000°C becomes a radiation stability defined upper use temperature. Also, a lithium silicate that forms at 1026°C between Si-Li and O so for liquid lithium cooled SiC/SiC structures 1000°C is also a corrosion defined upper use temperature. For a He cooled blanket, the corrosion temperature limit may be higher than 1000°C.

An upper temperature limit for the use of SiC/SiC is therefore likely to be around 1000°C. Based on the crack growth rate data presented here, the flaw growth rate is about 15 mmlyr. at 1000°C and about 1 mm/yr. at 800°C. These crack growth rates are higher than a designer is likely to accept depending on the failure criteria for a SiC/SiC blanket. Newer SiC fibers such as Nippon Carbon's Hi-Nicalon, Dow Corning's alpha SiC and MER's beta SiC all exhibit superior creep resistance to the currently available Nicalon. These newer fibers exhibit at least a 200°C shift for a comparable creep rate and in the case of MER's beta SiC a 400' C shift. These temperature shifts would translate into about a factor of 5 decrease in the creep rates per 100°C so that a composite made with the Hi-Nicalon and Dow Corning fibers could exhibit a crack growth rate of 1.5 and .1 mm/yr. at 1000 and 800°C, respectively, and a composite with the MER fiber could exhibit crack growth rates of .15 and 0.010 mm/yr. at 1000 and 800°C, respectively, Of course these rates must be determined for the composite material but a material with the crack growth rates possible with the MER fiber are very acceptable while those with the Hi-Nicalon and Dow Corning fibers probably acceptable at 800°C but less acceptable at 1000°C.

The acceptable flaw growth rate in SiC/SiC and maximum allowable flaw size will depend on the failure criteria for this material. If the failure criteria is based on a fracture mechanics or fracture stress criteria, these materials exhibit novel behavior because the continuous fibers bridge the crack. The effect of these bridging fibers on the fracture stress of SiC/SiC is demonstrated in Figure 5. These results demonstrate the difference between a machined notch and an equal depth notch produced by slow crack growth at 1100°C. The peak stress is based on the failure load and the unnotched cross-sectional area. These results clearly show that samples with cracks grown slowly at 1100°C to equal depths to machined notches retain their original fracture strength. This strength retention results from fibers bridging the

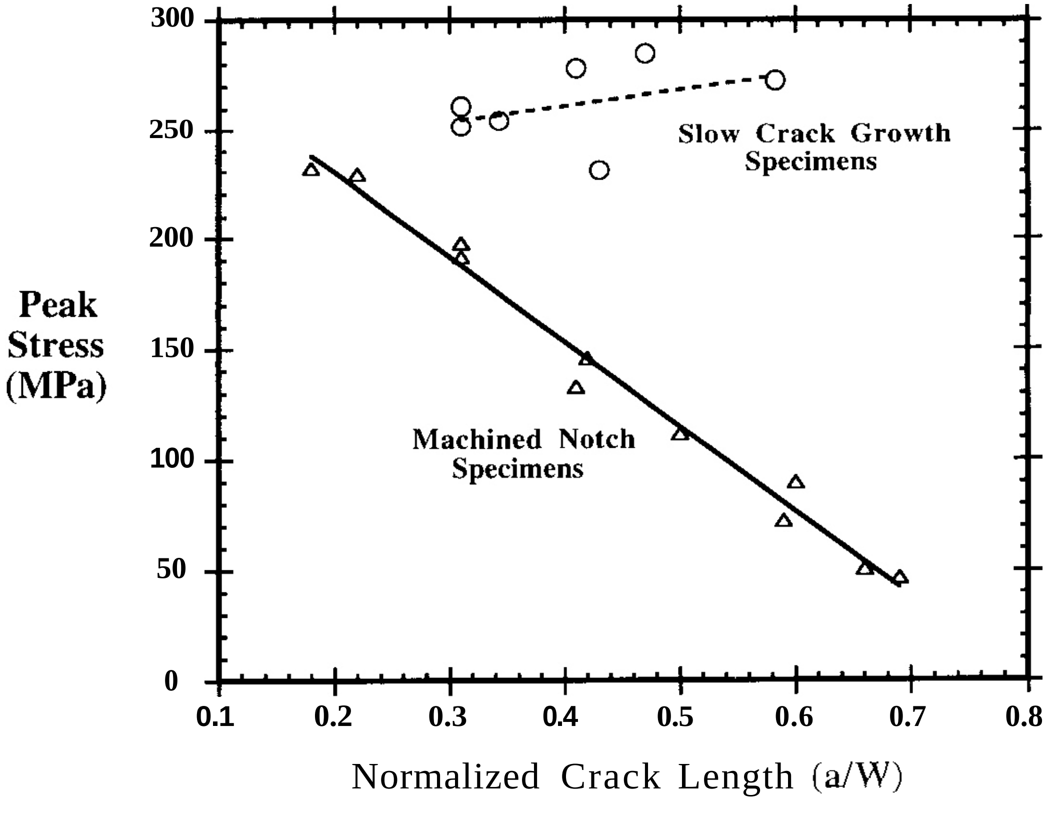

Figure 5. Comparison between slowly grown cracks and machine-notched specimens showing ability of slowly grown cracks to carry much higher loads due to increased crack bridging.

crack. With slowly grown cracks, the stress in the fibers is relaxed by creep and fibers bridge the entire crack. With a fast loading rate, some fraction of the fibers are fractured and a reduction in the peak stress results. A more complete description of the data presented in Figure **5** was reported by Jones et al. (4). The significance of this result is that these materials become independent of matrix crack lengths and therefore structural failure is related to fiber fracture and not matrix fracture. The crack velocities presented in Figure 4 may therefore not directly impact a structural failure criteria but would be more relevant for a leak rate, fatigue failure, or stiffness failure criteria. Clearly, the determination of a failure criteria for a SiClSiC structure must consider the novel behavior of these materials.

FUTURE DIRECTION

Future tests will he conducted to evaluate the stability of SiClSiC composites with carbon as the fiber/matrix interface in low oxygen partial pressure environments. Weight change and crack growth measurements will be made in argon plus 10 to **100** ppm of O_2. Also, crack growth measurements will he made on a wide variety of SiC/SiC material for comparison purposes. A new test facility will be purchased and assembled to allow subcritical crack growth measurements using compact tension type samples with either static or cycle loading. This system will he adaptable to a cross-head or servohydraulic load frames with controlled atmosphere environments. The coupling to a servo-hydraulic load frame will allow variable frequency testing along with the ability to test compressive stress effects. The current SiClSiC system can only achieve 0.1 Hz or less so accumulating a large number of cycles is very time consuming. Also, the 4-point bend apparatus does not allow compressive stress cycles to he applied.

ACKNOWLEDGMENTS

The assistance of J.L. Humason in performing the crack growth experiments and Diane Forsyth, Barbara Braby and Loree Swegle for manuscript preparation is gratefully acknowledged. This work was supported by the Office of Fusion Energy and the Office of Basic Energy Sciences of the U.S. Department of Energy under contract DE-AC06-76RLO 1830 with Battelle Memorial Institute which operates Pacific Northwest Laboratory.

REFERENCES

1. R.H. Jones and C.H. Henager, Jr. "High Temperature Properties of SiClSiC for Fusion Applications", Fusion Reactor Materials Semiannual Progress Report for Period Ending March **31,** 1993, DOE/ER-0313/14, p. 451.

2. C.H. Henager, Jr. and R.H. Jones, "Time-Dependent Subcritical Crack Growth of CVI SiC Reinforced with Nicalon Fibers", J. of the Am. Ceram. Soc., in press.

3. G. Simon and A.R. Bunsell, "Creep Behavior and Structural Characterization at High Temperatures of Nicalon SiC Fibers", J. Mater. Sci. 19 (1984) 3658-3670.

4. C.R. Jones, R.H. Jones and C.H. Henager, Jr., "Toughening of Ceramic Composites With Slow Crack Growth" Fusion Reactor Materials Semiannual Progress Report for Period Ending Oct. 31, 1993, DOE/ER-0313/14.

DEFECT ENERGETICS CALCULATIONS OF SiC USING THREE REPRESENTATIVE EMPIRICAL POTENTIALS,

Hanchen Huang, Jimmy Wong, Nasr Ghoniem (Mechanical Aerospace and Nuclear Engineering Department University of California, Los Angeles, CA 90024), and Michael Basks (Sandia National Laboratories Livermore, CA 94550)

OBJECTIVE

The objectives of the present work are: (1) to establish a reliable data base for defect energetics in SiC; and (2) to compare three representative empirical potentials.

SUMMARY

Defect energetics is a critical issue not only for irradiation damage but also for semiconductor applications. Calculations of defect energetics rely mainly on using empirical potentials, which are developed based on information from equilibrium crystal configurations and which may not be suitable for investigating defected configurations. Therefore, not all potentials give accurate enough results. This paper fust calibrates MEAM for silicon carbide. Calculations are then made for defect energetics of silicon carbide using the MEAM and two other representative empirical potentials. Results obtained with these potentials are compared with available first principle calculations and experimental data. The results not only provide more information for defect formation and migration in silicon carbide, but also provide a critical assessment of the three empirical potentials. The results are analyzed in terms of construction and calibration of the empirical potentials.

PROGRESS AND STATUS

Introduction

Silicon carbide (SiC) has been proposed as a candidate for fusion reactor components [1,2], which face intensive neutron irradiation damage[3]. Evolution of defects so produced determines macroscopic properties of the components. Studying of defect energetics that dominates the defect evolution processes is therefore crucial to understanding responses of silicon carbide components to radiation damage. There are several ways of studying defect energetics: experimental measurement[4,5]; fust principle calculation[6,7]; and computer simulation with empirical potentials[e.g., reference 81. Experimental results are affected by many uncertain factors, and their interpretation is usually not unique. First principle calculation is quite accurate, but requires very intensive computational effort. Molecular Dynamics (MD) simulation using an empirical potential is commonly used to study defect energetics with reasonable computational time and accuracy. The empirical potential used in the MD simulation is usually calibrated with a group of physical parameters. quality of which is determined by how it is constructed and calibrated. Empirical pair potentials have been successfully applied to metals. but have failed in describing covalent systems. There are quite a few empirical potentials proposed to describe many body effects that are very important in covalent materials. This paper investigates defect energetics of SiC using three representative potentials: Pearson potential; Modified Embedded Atom Method (MEAM); and Tersoff potential. Formation energies and migration energies of point defects, and anti-site defect formation energies are calculated. Possible defect migration mechanisms are investigated. The results show that a single vacancy can hardly move due to the two sub-lattices existing in SiC. With assistance of another vacancy on different sub-lattice, migration energy of the vacancy is dramatically reduced. Formation energies of the defects are compared with available first principle calculations and experimental data. Although not perfect, the results obtained with MEAM and Tersoff potential are more reasonable than that obtained with Pearson potential. The three representative potentials will be described in more detail in Section 2. The calculated results, available data of experimental investigation and first principle calculation are summarized in Section 3. Success and failures of the potentials are discussed according to their construction and calibration in Section 4.

The Three Representative Potentials

The Pearson Potential

Pair potentials (Lennard-Jones [9], Morse [10], etc.) have been successfully used in studying metals, and are able to explain close packed structures that are common for metals. More open structures in semiconductors turned out to be a challenge for pair potentials. To account for many body interactions, Born and Oppenheimer[11] proposed a general form interatomic potential:

$$\Phi_i(\vec{r}_1,\vec{r}_2,......,\vec{r}_n)=\frac{1}{2!}\sum_{j\neq i}V^{(2)}(\vec{r}_{ij})+\frac{1}{3!}\sum_{k\neq}\sum_{j\neq i}V^{(3)}(\vec{r}_{ij},\vec{r}_{ik},\vec{r}_{jk})$$
$$+......+\frac{1}{n!}\sum_{q\neq}\cdots\sum_{m\neq}\cdots\sum_{j\neq i}V^{(n)}(\vec{r}_{ij},\ldots,\vec{r}_{iq},\ldots,\vec{r}_{mq})$$

Environmental effects are included in the many body interactions. To make this many body potential practical in its applications, Pearson et al[12] truncated the expansion up to the three-body level. For SiC, they combined the Lennard-Jones(6-12) two-body potential[9] and Axilrod-Teller three-body potential[13] in the form:

$$V^{(2)}(\vec{r}_{ij}) = \frac{\varepsilon}{m-n}\left[n\left(\frac{R_o}{r_{ij}}\right)^{m} - m\left(\frac{R_o}{r_{ij}}\right)^{n} \right]$$

$$V^{(3)}(\vec{r}_{ij},\vec{r}_{ik},\vec{r}_{jk}) = Z\left[\frac{1+3\cos\theta_{ij}\cos\theta_{ik}\cos\theta_{jk}}{\left(r_{ij}r_{ik}r_{jk}\right)^{3}} \right]$$

where the energy parameters (ε, Z) and the two-body structure parameter (R_O) were adjusted to fit experimental data for bulk solid and atomic clusters (sublimation energies and bond length). The three body potential is a simple form that favors open structures. A small modification was made by Huang and Ghoniem[8] to fit the sublimation energy exactly without affecting other parameters. The potential parameters are listed in Table 1. The Stillinger-Weber potential [14], similar to Pearson potential, is another example of this type of potentials. The Pearson potential has proven to be successful in some applications[15,16,17]. Unfortunately, it fails in some other cases in which the systems are far away from equilibrium configurations[18].

Table 1 Parameters of Pearson Potential

	ε (eV)	R_O (Å)	Z (eVÅ^9)
Si-Si	2.8127	2.2951	N/A
Si-C	3.895	1.7400	N/A
C-C	5.437	1.4806	N/A
Si-Si-Si	N/A	N/A	3484.0
Si-Si-C	N/A	N/A	796.8
Si-C-C	N/A	N/A	597.5
C-C-C	N/A	N/A	167.3

The Modified Embedded Atom Method

Embedded Atom Method (EAM) was developed and named by Daw and Baskes[19,20]. In the EAM, potential energy of an atom in a crystal is divided into two parts: (1) two-body core-core interactions with lattice atoms; *(2)* energy needed to embed the atom into background electron sea of the lattice. Improvements and applications are pursued at Sandia National Laboratories[21-30], University of Virginia[31-34], and other institutions[35-37]. At the beginning, EAM was developed to use central potential and central electron density. It was then modified to use angular dependent electron density in order to model covalent structure. The angular dependence automatically disappears for FCC and BCC structure. Later on. s-p-d-f components of electron density were introduced to account for the angular dependence of inter-atomic interactions, which gave a more physical description of the spatial asymmetry.

Total configuration energy of a crystal section is written as sum of direct contributions from all atoms, each of which is divided into two parts:

$$E = \sum_i E_i \quad \text{with} \quad E_i = F_i(\bar{\rho}_i) + \frac{1}{2}\sum_{j \neq i} \phi_{ij}(R_{ij})$$

where the first part corresponds to environment dependent energy of embedding an electron, while the second part is the conventional pair potential. The embedding energy is assumed to be represented by:

$$F_i(\bar{\rho}_i) = A_i E_i^0 \frac{\bar{\rho}_i}{Z_i \rho_{i0}} \ln \frac{\bar{\rho}_i}{Z_i \rho_{i0}}$$

$$Z_i = Z_{i0} e^{-\frac{1}{2}\sum_{k=1}^{3} s^{(k)} t_i^{(k)} / z_{i0}^{2}}$$

$$\bar{\rho}_i = \bar{\rho}_i^{(0)} e^{-\frac{1}{2}\sum_{k=1}^{3} \bar{\rho}_i^{(k)} t_i^{(k)} / \bar{\rho}_i^{(0)2}}$$

$$t_i^{(k)} = \frac{\sum_{j \neq i} t_{0,j}^{(k)} \rho_j^{(0)} S_{ji}}{\sum_{j \neq i} \rho_j^{(0)} S_{ji}}$$

$$\bar{\rho}_i^{(0)} = \sum_{j \neq i} \rho_j^{(0)} S_{ji}$$

$$\left(\bar{\rho}_i^{(1)}\right)^2 = \sum_{\alpha=1}^{3} \left[\sum_{j \neq i} x_{ij}^{\alpha} \rho_j^{(1)} S_{ji}\right]^2$$

$$\left(\bar{\rho}_i^{(2)}\right)^2 = \sum_{\alpha,p=1}^{3} \left[\sum_{j \neq i} x_{ij}^{\alpha} x_{ij}^{p} \rho_j^{(2)} S_{ji}\right]^2 - \frac{1}{3}\left[\sum_{j \neq i} \rho_j^{(2)} S_{ji}\right]^2$$

$$\left(\bar{\rho}_i^{(3)}\right)^2 = \sum_{\alpha,p,q=1}^{3} \left[\sum_{j \neq i} x_{ij}^{\alpha} x_{ij}^{p} x_{ij}^{q} \rho_j^{(3)} S_{ji}\right]^2 \quad \text{with } \alpha, p, q = 1,2,3$$

$$\rho_i^{(k)} = e^{-\beta_i^{(k)}\left(\frac{R}{R_i^0} - 1\right)} \quad \text{with } k = 0,1,2,3$$

$$x_{ij}^1 = \frac{x_j - x_i}{r_{ij}}, \quad x_{ij}^2 = \frac{y_j - y_i}{r_{ij}}, \quad x_{ij}^3 = \frac{z_j - z_i}{r_{ij}}$$

$$S_{ji} = \prod_{k \neq j,i} e^{-\left[\frac{C_{max} - C}{C - C_{min}}\right]^2} \quad \text{with } C = 1 + 2\frac{r_{jk}^2 r_{ji}^2 + r_{ki}^2 r_{ji}^2 - r_{ji}^4}{r_{ji}^4 - (r_{jk}^2 - r_{ki}^2)^2}$$

The averaging of the weighting factors. $t_i^{(k)}$, considers the effect of electrons from dissimilar atoms in a multicomponent system, The screening function, S_{ji}, introduced to account for relative contributions from atoms at different locations can be though of as a force cut-off technique.

Table 2: Parameters of MEAM

	Si-Si	C-C	Si-C
A	1	1	N/A
ρ_0	1.0	3.2	N/A
Z	4	4	4
R_0	2.3517	1.5446	1.8878
E_0	4.63	7.37	6.433
α	4.87	4.38	5.53
β_0	4.8	4.5	N/A
β_1	4.8	3.9	N/A
β_2	4.8	3.5	N/A
β_3	4.8	4.8	N/A
$t_0^{(0)}$	1.3	1.0	N/A
$t_0^{(1)}$	3.3	11.5	N/A
$t_0^{(2)}$	5.105	1.59	N/A
$t_0^{(3)}$	-0.8	-8.75	N/A
$s^{(0)}$	1	1	N/A
$s^{(1)}$	0	0	N/A
$s^{(2)}$	0	0	N/A
$s^{(3)}$	32/9	32/9	N/A
C_{min}	2.0	2.0	2.0
C_{max}	2.8	2.8	2.8

The pair potential is derived from the universal equation of state[38,39]:

$$E_i^u(R) = -E_i^0\left[1+\alpha_i\left(\frac{R}{R_i^0}-1\right)\right]e^{-\alpha_i\left(\frac{R}{R_i^0}-1\right)}$$

$$E_i(R) = \frac{1}{2}\left\{F_i\left[\frac{Z_{ij0}}{Z_{i0}}\bar{\rho}_j\right] + F_j\left[\frac{Z_{ij0}}{Z_{j0}}\bar{\rho}_i\right] + Z_{ij0}\phi_{ij}(R)\right\}$$

and with screening effects it is given as:

$$\phi_{ij}(R) = \frac{1}{Z_{ij0}}\left\{2E_i^u(R) - F_i\left[\frac{Z_{ij0}}{Z_{i0}}\bar{\rho}_j\right] + F_j\left[\frac{Z_{ij0}}{Z_{j0}}\bar{\rho}_i\right]\right\}S_{ji}$$

It is worthwhile to mention that the pair potential is defined using the embedding function at a reference structure. For a detailed explanation, readers are referred to reference 29. For single elements. the parameters are determined by fitting to sublimation energy, lattice constant, bulk modulus, two shear constants, two structure energy differences, and vacancy formation energy. Only one parameter is introduced to interpolate potential in diatomic system from those in single element systems. The parameter, relative magnitudes of ρ_{10} and ρ_{20}, is determined by fitting to the vacancy formation energy of an atom pair in the diatomic system. The parameters of MEAM for SiC are listed in Table 2.

The Tersoff Potential

The conventional pair potential was extended to describe many body effects by setting the pair potential coefficients dependent on environment [40,41]. Computational time of Molecular Dynamics simulation with pair-like potential is dramatically reduced compared to that employing three body potentials. The potential is composed of two parts: repulsive and attractive interactions. Local environment is described by a measure of bond order in the attractive interaction. Bond strength is explicitly related to coordination number, which makes close packed structure or open structure a natural result of competition between bond strength and coordination number. The effective coordination number is both distance dependent and angular dependent, which makes open structure like diamond possible. The potential, after being successfully used for pure elements [42,43], was extended to multicomponent systems by interpolation [44-46]. Only one parameter was introduced to scale the relative bond order of the elements involved. The general potential function for multicomponent systems can be written as:

$$E = \sum_i E_i = \frac{1}{2}\sum_{i,j\neq i} E_{ij}$$

$$E_{ij} = f_c(r_{ij})\left[A_{ij}e^{-\lambda_1 r_{ij}} - B_{ij}b_{ij}e^{-\lambda_2 r_{ij}}\right]$$

$$f_c(r_{ij}) = \begin{cases} 1, & \text{for } r_{ij} < R_{ij} \\ \frac{1}{2} + \frac{1}{2}\cos\left(\frac{r_{ij} - R_{ij}}{S_{ij} - R_{ij}}\pi\right), & \text{for } R_{ij} < r_{ij} < S_{ij} \\ 0, & \text{for } r_{ij} > S_{ij} \end{cases}$$

$$b_{ij} = \chi_{ij}\left(1 + \beta_i^{n_i}\zeta_{ij}^{n_i}\right)^{-1/2n_i}$$

$$\zeta_{ij} = \sum_{k \neq i,j} f_c(r_{ik})g(\theta_{ijk})$$

$$g(\theta_{ijk}) = 1 + \frac{c_i^2}{d_i^2} - \frac{c_i^2}{d_i^2 + (h_i - \cos\theta_{ijk})}$$

Table 3: Parameters of Tersoff Potential

	Carbon	Silicon
A (eV)	$1.5448\text{x}10^3$	$1.8308\text{x}10^3$
B (eV)	$3.8963\text{x}10^2$	$4.7118\text{x}10^2$
λ (Å^{-1})	3.4653	2.4799
μ (Å^{-1})	2.3064	1.7322
β	$4.1612\text{x}10^{-6}$	$1.1000\text{x}10^{-6}$
n	$9.9054\text{x}10^{-1}$	$7.7834\text{x}10^{-1}$
c	$1.9981\text{x}10^4$	$1.0039\text{x}10^5$
d	7.0340	$1.6217\text{x}10^1$
h	$-3.9953\text{x}10^{-1}$	$-5.9825\text{x}10^{-1}$
R (Å)	1.8	2.7
S (Å)	2.1	3.0

$\chi_{C-Si}=1.0121$

*The original value from Tersoff was 1.0320, which gives 13.3 eV sublimation energy. To make comparison of the potentials consistently, we calibrate the c to fit 12.865 eV of experimental sublimation energy, which is used in the other two potentials. Difference in results caused by this modification is samll (mostly 3 - 5%)

where parameters for multicomponent systems are related to those for single elements by:

$$\lambda_{ij} = \frac{\lambda_i + \lambda_j}{2}$$

$$\mu_{ij} = \frac{\mu_i + \mu_j}{2}$$

$$A_{ij} = (A_i A_j)^{1/2}$$

$$B_{ij} = (B_i B_j)^{1/2}$$

$$R_{ij} = (R_i R_j)^{1/2}$$
$$S_{ij} = (S_i S_j)^{1/2}$$

Parameters for single elements are detennined by fitting to sublimation energy, lattice constant, and bulk modulus of diamond structure, and cohesive energies of other polytypes (dimmer, SC, FCC) of the material. The single parameter (χ_{ij}) for each pair of dissimilar atoms is determined by fitting to the correct heat of formation. The parameters determined by Tersoff [46,47] are listed in Table 3.

Results and Conclusions

Defect energetics of beta silicon carbide are calculated using the three representative potentials. The energy recovered when a single atom is placed on a crystal surface of a compound is ambiguous. Depending on the surface condition, amount of the surface recovery could vary [e.g., references 6 and 71. To avoid any confusion in defining defect energetics, an infmite vacuum rather than a real crystal surface is taken as a reference system. That is. an atom will be taken to a vacuum at infinity to form a vacancy. Similarly, an interstitial is formed by taking an atom from infinity and putting it at an interstitial site. It is worthwhile to mention that defect migration energies are independent of the reference system, whereas defect formation energies are dependent Formation energies of vacancies and interstitials at TC (Tetrahedral site surrounded by four Carbon atoms) and TSi (Tetrahedral site surrounded by four Silicon atoms), and migration energies of vacancies and interstitials are calculated. H and B interstitial configurations are asymmetrical in SiC and therefore unstable. The numerical results are summarized in table 4. Several salient conclusions can be draw directly from the results:

(1) Direct migration of a vacancy in SiC is very difficult due to a high migration barrier. But the migration of the same vacancy assisted by an opposite type vacancy is much easier. In irradiated materials, vacancy concentration can be very high and this indirect vacancy migration mechanism is likely to operate. Other mechanisms (e.g., anti-site mechanism) are also proposed, and may be operative under some conditions.

(2) Interstitials migrate from one tetrahedral site to another equivalent tetrahedral site through the other type tetrahedral site. Migration energy of an interstitial is much lower than that of a vacancy, and interstitial clustering is liely to happen prior to vacancy clustering in irradiated SiC.

(3) When excess carbon atoms are present in SiC, anti-site C defect (C replaces Si) can be formed quite easily. Because of large formation energy of an anti-site defect pair (a C and a distant Si are switched), zinc-blend structure SiC is a thermodynamically favored configuration.

(4) Results based on MEAM agree the best with the first principle calculations. Those based on Tersoff potential are also in good agreement with the first principle calculations. Some results from

Pearson potential are reasonable while others (e.g., very small anti-site defect formation energies) are not.

Table 4: Results of Defect Energetics of SiC

	Pearson et al	MEAM	Tersoff	first principle	experimental
$E^f(V_{Si})$	6.70	11.48	12.46	12.60	N/A
$E^f(V_C)$	5.26	12.13	11.61	11.70	N/A
$E^{d\text{-}m}(V_{Si})$	7.39	7.85	5.83	N/A	$E^f+E^m=9.5$
$E^{d\text{-}m}(V_C)$	6.10	6.74	8.94	N/A	$E^f+E^m=8.7$
$E^{i\text{-}m}(V_{Si})$	4.30	2.46	6.08	N/A	N/A
$E^{i\text{-}m}(V_C)$	-0.50	3.42	3.48	N/A	N/A
$E^f(I_{Si}\ T_C)$	3.23	-0.76	4.08	8.00	N/A
$E^f(I_C\ T_C)$	3.37	-3.15	2.29	4.4	N/A
$E^f(I_{Si}\ T_{Si})$	10.55	10.51	8.00	8.30	N/A
$E^f(I_C\ T_{Si})$	3.80	2.56	0.23	1.90	N/A
$E^m(I_{Si})$	6.04	11.27	3.95	N/A	N/A
$E^m(I_C)$	1.47	6.01	3.58	N/A	N/A
E(Si antisite)	3.66	7.65	5.55	6.40	N/A
E(C antisite)	-3.33	0.85	0.61	0.20	N/A

I=Interstitial, V=Vacancy, m=Migration, d-m=Direct Migration, i-d=Indirect Migration

The experimental data are from references 4 and 5. The first principle calculations are from references 6 and 7

Discussions

These numerical results not only provide us with a more reliable data base for studying defect evolution processes in SiC, but are a practical test to the potentials as well. The successes and failure of the potentials in defect calculations are related to physical bases of construction and calibration of the function forms. There are something that are commonly shared by the three potentials, and other things that make all the differences.

(1) Developers of all the three potentials tried to consider effects of local environment (many body interactions). MEAM was developed based on the quantum mechanical results that spatial

distribution of outer electrons is generally angular dependent. It is the electron distribution that determines the local environment. Tersoff potential was developed based on the physical base *that* bond order depends on coordination number. Trade off of these two factors makes both close packed and open structures possible. Angular dependence was introduced to account for the fact that bond order is affected by relative angles of neighboring bonds. Pearson potential was obtained by brutally truncating the Born-Oppenheimer expansion at the three body level. All higher order effects (many body interaction) are assumed to be either *small* or represented by the three body interaction form.

(2) In calibration of MEAM, data of equilibrium configuration (e.g., sublimation energy, lattice constants, etc.) and defected configuration (e.g., vacancy formation energy) are used. For Tersoff potential, only data of equilibrium configuration are used. Pearson et al calibrated their potential by using both bulk properties and cluster properties. The number of these. data fitted is more than the number of free parameters. Therefore, none of the properties was perfectly fitted in original form of the Pearson potential.

(3) The *three* potentials have quite different approaches to account for the fact that atoms far away from a site have smaller contributions. MEAM employed a screening function such that when atoms are blocked from a site, they can hardly "see" the site and therefore have little contributions. Tersoff potential used a smooth cut-off function such that as an atom is farther away from the site, its influence to the site becomes smaller. There is no explicit form of cut-off in Pearson potential that makes it unnecessarily *short* ranged.

(4) One of the most important indices measuring an empirical potential's quality is its computational simplicity. In Molecular Dynamics simulation, each step cakes about $1.2x10^{-3}$ sec/atom with Pearson potential, $4.7x10^{-4}$ sec/atom with MEAM, and $3.9x10^{-4}$ sec/atom with Tersoff potential (all are in CPU of CRAY-A at NERSC). Computational effort is greatly reduced using Tersoff potential or MEAM. in comparison to that employing Pearson potential.

(5) MEAM has been mainly used for metals and found great success there. With simple calibration. it also describes covalent systems very well. Tersoff potential and Pearson potential are primarily developed for covalent systems. while Tersoff potential gives better prediction than Pearson potential.

(6) According to defect energetics calculations, results based on both MEAM and Tersoff potential are in good agreement with the fist principle calculations, while results based on Pearson potential are not as good. The fact that MEAM gives better prediction than Tersoff potential may be atnibuted to the different calibration procedures since the two potential functions are quite similar in essence [48]. We recommend that Pearson potential should be avoid, at least in studying defected configurations.

FUTURE WORK

Defect evolution processes in SiC will be studied based on the defect energetics results obtained in the present work. Effort will be extended to interpreting experimental data of radiation damage on SiC.

ACKNOWLEDGMENT

Partial support of US DOE under contract DE-FG03-91ER54115 with UCLA, and partial support of US DOE under contract DE-AC04-94AL85000 with Sandia National Laboratories are greatly appreciated. It is a great pleasure to thank Dr. J. Tersoff at IBM for providing us with updated potential parameters prior to publication. Thanks are extended to Dr. M. Guinan, and many other participants of Santa Barbara Workshop on SiC (Summer 1993) for their stimulating comments on this topic.

REFERENCES

1 S. Sharafat, C. Wong, and E. Reis, "Sic-Composite First-wall Design for the ARIES-I Reactors", Fusion Tech. 19(1991)901-907

2 G. Trantina, "Ceramics for Fusion Reactors - Design Methodology and Analysis", J. Nucl. Mater. 85&86(1979)415-420

3 H. Huang and N. Ghoniem, "Neutron Displacement Damage Cross Section for SiC", J. Nucl. Mater. 199(1993)221-230

4 M. Hon and R. Davis, "Self-diffusion of ^{30}Si in Polycrystalline β-SiC", J. Mater. Sci. 14(1979)2411

5 M. Hon and R. Davis. "Self-diffusion of ^{14}C in Polycrystalline β-SiC", J. Mater. Sci. 15(1980)2073

6 C. Wang. J. Bernholc, and R. Davis, "Formation Energies, Abundances, and the Electronic Structure of Native Defects in Cubic Sic", Phys. Rev. B38(1988) 12752-12755

7 J. Bernholc, S. Kajihara, C. Wang, A. Antonelli, and R. Davis, "Theory of Native Defects, Doping and Diffusion in Diamond and Silicon Carbide", Mater. Sci. Engr. B11(1992)265-272

8 H. Huang and N. Ghoniem, "Molecular Dynamics Calculation of Defect Energetics in SiC", J. Nucl. Mater., in print

9 J. Lennard-Jones. Interatomic Forces, Special Publication No. VIII, Indian Association for the Cultivation of Science, Calcutta, India. 1939

10 D. **Olander,** Fundamental Aspects of Nuclear Reactor Fuel Elements. Technical Information Center, Energy Research and Development Administration. 1976, Chapter 4

11 J. Ziman, Principles of the Theory of Solids, Cambridge University Press, 1965, Chapter 6.10

12 E. Pearson, T. Takai, T. Halicioglu and W. Tiller, "Computer Modeling of Si and SiC Surfaces and Surface Processes Relevant to Crystal Growth from the Vapor". J. Crystal Growth 70(1984)33-40

13 B. Axilrod and E. Teller. "Interaction of the van der Waals Type Between Three Atoms", J. Chem. Phys. 11(1943)299-300

14 F. Stillinger and T. Weber, "Computer Simulation of Local Order in Condensed Phase of Silicon", Phys. Rev. B31(1985)5262-5271

15 **W. Tiller.** "Point Defect Roles in the Growth and Nucleation of SiO_2 Precipitates in Si". Proceedings of the Second Symposium on Defects in Silicon: Defects in Silicon II, Washington, DC, USA, 5-10 May 1991, Edited by W. Bullis and U. Gosele, 1991. pp 237-254.

16 P. Ungar, T. Takai, T. Halicioglu, and W. Tiller. "Point Defect Structures and Energetics in Si Using an Empirical Potential", J. Vacuum Sci. Tech. A11(1993)224-230.

17 S. Erkoc, T. Halicioglu. and W. Tiller. "Simulation Calculations for Gold Clusters on the GaAs(110) Surface", Surface Sci. 274(1992)359-62.

18 R. Biswas and D. Hamann, "Interatomic Potentials for Silicon Structural Energies", Phys. Rev. Lett. 55(1985)2001-2004

19 M. Daw and M. Baskes. "Semiempirical Quantum Mechanical Calculation of Hydrogen Embrittlement in Metals", Phys. Rev. Lett. 50(1983)1285-1292

20 M. Daw and M. Baskes, "Embedded-atom Method: Derivation and Application to Impurities, Surfaces. and other Defects in Metals", Phys. Rev. B 29(1984)6443-6453

21 S. Foiles, M. Baskes. and M. Daw, "Embeded-atom Method Functions for the FCC Metals Cu, Ag, Au, Ni, Pd, Pt, and Their Alloys", Phys. Rev. B 33(1986)7983-7991

22 M. Baskes. "Application of the Emkded-atom Method to Covalent Materials: A Semiempirical Potential for Silicon", Phys. Rev. Lett. 59(1987)2666-2669

23 S. Foiles, M. Baskes. and M. Daw, "Atomistic Studies of Interfacial Structure and Properties", Mater. Res. Soc. Symp. Proc. 122(1988)343-354

24 M. Daw, "Model of Metallic Cohesion: The Embeded-atom Method", Phys. Rev. B39(1989)7441-7452

25 M. Baskes, J. Nelson, and A. Wright, "Semiempirical Modified Embeded-atom Potentials for Silicon and Germanium", Phys. Rev. B40(1989)6085-6100

26 S. Foiles. M. Baskes, and M. Daw, "The Calculation of the Equilibrium Interface Structure of Alloys". Mater. Sci. Forum 37(1989)223-234

27 M. Daw, "Embeded Atom Method: Many-atom Description of Metallic Cohesion". Atomic Simulation of Materials, edit by V. Vitek and D. Srolovitz. Plenum Press, New York. 1989, pp181-191

28 M. Baskes. M. Daw, and M. Foiles, "The Embeded Atom Method: Theory and Applications", Mater. Res. Soc. Symp. Proc. 141(1989)31-41

29 M. Baskes, "Modified Embeded-atom Potentials for Cubic Materials and Impurities", Phys. Rev. B 46(1992)2727

30 M. Baskes and R. Johnson, "Modified Embeded Atom Potential for HCP Metals", Modeling and Simulation in Mater. Sci. Engr. J. 2(1994)147-163

31 R. Johnson, "Analytic Nearest-Neighbor Model for FCC Metals", Phys. Rev. B37(1988)3924

32 D. Oh and R. Johnson, "Simple Embedded Atom Method Model for FCC and HCP Metals", J. Mater. Res. 3(1988)471

33 R. Johnson and D. Oh, "Analytic Embedded Atom Method Model for BCC Metals", J. Mater. Res, 4(1989)1195

34 D. Oh and R. Johnson, "A Semi-empirical Potential for Graphite". Mater. Res. Soc. Symp. Proc 141(1989)31

35 A. Voter and S-P. Chen, "Accurate Interatomic Potentials for Ni, Al, and Ni_3Al", Mater. Res. Symp. Proc. 82(1987)175

36 M. Yoo, M. Daw, and M. Baskes, "Atomistic Simulation of Supperdislocation in Ni_3Al", Atomic Simulation of Materials, edited by V. Vilek and Srolovitz, Plenum Press, New York. 1989. p401

37 E. Savino, S. Rao. and R. Pasinot, "Beyond the Embedded Atom Interatomic Potential", Mater. Res. Symp. Proc. 141(1987)43

38 J. Rose, J. Smith, F. Guinea, and J. Ferrante, "Universal Features of the Equation of State of Metals". Phys. Rev. B 29(1984)2963

39 A. Banerjea and J. Smith. "Origins of the Universal Binding-energy Relation", Phys. Rev. B37(1988)6632

40 J. Tersoff, "New Empirical Model for the Structural Properties of Silicon". Phys. Rev. Lett. 56(1986)632-635

41 J. Tersoff, "New Empirical Approach for the Structure and Energy of Covalent System", Phys. Rev. B37(1988)6991-7000

42 J. Tersoff, "Empirical Interatomic Potential for Carbon, with Application to Amorphous Carbon". Phys. Rev. Lett. 61(1988)2879-2882

43 J. Tersoff. "Empirical Interatomic Potential for Silicon with Improved Elastic Properties", Phys. Rev. B38(1988)9902-9905

44 P. Kelires and J. Tersoff, "Equilibrium Alloy Properties by Direct Simulation: Oscillatory Segregation at the Si-Ge (100) 2x1 Surface". Phys. Rev. Lett. 63(1989)1164-1167

45 J. Tersoff, "Carbon Defects and Defect Reactions in Silicon", Phys. Rev. Lett. 64(1990)1757-1760

46 J. Tersoff, "Modeling Solid-State Chemistry: Interatomic Potentials for Multicomponent Systems". Phys. Rev. B39(1989)556-5568

47 J. Tersoff. Phys. Rev. B, in press

48 D. Brenner, "Relationship Between the Embedded-Atom Method and Tersoff Potentials", Phy. Rev. Lett. 63(1989)1022-1022

PHENOMENOLOGICAL INELASTIC CONSTITUTIVE EQUATIONS FOR SiC AND SiC FIBERS UNDER IRRADIATION --- A. El-Azab and N.M Ghoniem (University of California, Los Angeles)

OBJECTIVE

The objectives of this work are to develop a set of constituitive equations for the time-dependent deformation characteristics of monolithic SiC, representing the matx of SiC/SiC composites, and SiC fibers. Two representative types of fibers are considered; Nicalon and SCS-6 fibers.

SUMMARY

Experimental data on irradiation-induced dimensional changes and creep in β-SiC and SiC fibers is analyzed, with the objective of studying the constitutive behavior of these materials under high-temperature irradiation. The data analysis includes empirical representation of irradiation-induced dimensional changes in SiC matrix and SiC fibers as function of time and irradiation temperature. The analysis also includes formulation of simple scaling laws to extrapolate the existing data to fusion conditions on the basis of the physical mechanisms of radiation effects on crystalline solids. Inelastic constitutive equations are then developed for SCS-6 SiC fibers, Nicalon fibers and CVD SiC. The effects of applied stress, temperature, and irradiation fields on the deformation behavior of this class of materials are simultaneously represented. Numerical results are presented for the relevant creep functions under the conditions of the fusion reactor (ARIES IV) first wall. The developed equations can be used in estimating the macro mechanical properties of Sic-Sic composite systems as well as in performing time-dependent micro mechanical analysis that is relevant to slow crack growth and fiber pull-out under fusion conditions.

INTRODUCTION

SiC has been considered as a primary candidate for ***structural*** applications in fusion reactors. In addition to being a low activation material, SiC has many other promising features. Among these features are its high temperature resistance to corrosive actions, high modulus-to-weight ratio, and its resistance to neutron irradiation damage. It is undesirable to construct fusion components from monolithic SiC because of its relatively low fracture toughness, that is characteristic to ceramics. However, recent progress in composite material manufacturing makes it possible to develop SiC-SiC composite components of high reliability. This approach offers a high degree of flexibility in designing with SiC materials. In particular, it is now possible to "engineer" the material in such a way that the desired thermal, mechanical, chemical, and irradiation constitutive behavior is achievable.

Sic-Sic composites have been considered for the first wall and blanket structures in two major reactor studies; ARIES IV Tokamak Fusion Reactor' and PROMETHEUS Inertial Fusion Reactor [2]. The structural design conducted in these two studies involved only the assessment of the thermoelastic response of the structural elements in the first wall, blanket and in the ARIES IV diverter. However, in both of these fusion reactor studies, there was no attempt to perform any formal inelastic structural analysis due to the lack of constitutive equations of Sic-Sic composites in the fusion environment. Inelastic structural analysis would predict the evolution of time- dependent stress and deformation fields, which eventually results in accurate definition of failure criteria and limiting properties, and in turn, an estimate of the life time of structural components. In this context, it is essential to analyze the irradiation-induced dimensional changes, irradiation and thermal creep of the composite micro constituents (fibers and matrix) and include these effects, simultaneously, in a formal set of constitutive equations that describe the overall mechanical response.

Direct experimental studies on the irradiation effects on Sic-Sic composites are not available. A rich variety of initial manufacturing conditions may lead to a wide spectrum of radiation responses, which may make it difficult to even interpret this data. Obviously, as irradiation data becomes available, the general understanding of various factors which influence the irradiation stability of the composite will improve. In this paper we assemble the available data base on the effects of neutron irradiation on monolithic SiC. Most of this data resulted from the HTGR program, and as such may only be indicative of possible effects of high energy neutrons on SiC. However. we will use the general understanding of radiation effects on materials to derive constitutive relationships for Sic-Sic composites. The present accuracy of these relationships may not be high. As data becomes available, these relationships should be updated.

In this paper, we focus on two major areas: (1) Analysis of the existing data on irradiation-induced dimensional changes and creep in β- SiC and SiC fibers, and (2) Development of phenomenological constitutive equations which incorporate the effects of the applied stress, temperature, and irradiation fields on the deformation behavior of the composite material. The analysis of this data includes empirical representation of the irradiation swelling and creep in terms of the neutron flux, time, and temperature, and formulation of appropriate scaling laws for extrapolation to fusion conditions. The latter step is based on our understanding of the phenomenological models of irradiation effects in crystalline solids. The extrapolation of irradiation data is performed for AFUES IV first wall conditions, based on data from **Ref.** 3 for the neutron damage in SiC and from Ref. **4** for the first wall neutron flux. Similar analysis is also performed for limited irradiation data on SiC fibers obtained from recent irradiation experiments. Numerical results are then presented for the relevant creep functions. The developed constitutive equations are readily usable in the following modeling areas: (1) Micro mechanical formulation of the theory of macroscopic constitutive properties of Sic-Sic composites under fusion conditions. In that theory, the effects of thermal creep, irradiation-induced swelling and creep on the time evolution of internal stress fields in composite phases are considered. (2) Time-dependent micromechanics (viscoelastic) modeling of fiber pull-out and slow crack growth in Sic-Sic composites at high temperature and under neutron irradiation, where time-dependent inelastic strains dominate the composite response.

IRRADIATION-INDUCED SWELLING IN β-SiC

Irradiation-induced dimensional changes in β-SiC has been considered in three areas of research: (1) particle coating of HTGR fuels, (2) temperature monitoring of irradiation experiments, and (3) structural fusion energy applications. Experimental studies of irradiation-induced dimensional changes in β-SiC have been mostly conducted to assess the performance of SiC-coated HTGR fuels. These experiments used fast fission neutrons irradiation facilities. Little work has been done with regard to fusion applications. In what follows we summarize the results from those studies and formulate some scaling laws to extrapolate the fission neutron irradiation data to fusion conditions.

A. Swelling of β-SiC by Neutron Irradiation Below 1000 °C

SiC was irradiated at temperatures between **460** and 1040 °C, and neutron fluences up to $2\text{-}4.2\times10^{21}$ n/cm^2 (E, > 0.18 MeV)$^{5-8}$. Isotropic swelling of irradiated samples was observed and was attributed to the formation of dislocation loops (planar defect clusters) parallel to the {111} crystallographic planes. It has also been observed that SiC swelling below 1000-1050 °C saturates and becomes independent of neutron exposure above a neutron fluence of ~2×10^{20} nlcm'. The saturation swelling depends on the irradiation temperature only, and decreases as the temperature increases below 1000 °C, as shown in Fig. 1. The reproducibility of these swelling characteristics qualified SiC to be used as an *irradiation* temperature monitor in this temperature range'.". Irradiation-induced swelling of SiC irradiated below 1000 °C can be annealed out and the annealing is complete at ~1500 °C ^{8}. Electron micrographs showed that Frank-type dislocation loops still exist at lower densities, which have a mean diameter of ***50-60*** **Å** compared to 35 A before annealing.

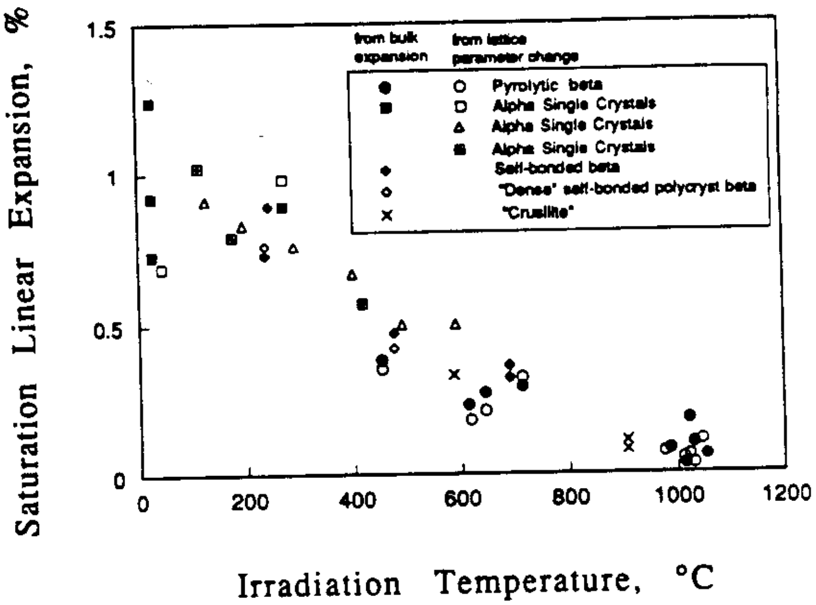

Fig. 1. Saturation linear expansion of neutron-irradiated SiC as a function of irradiation temperature (Fluence between $3x10^{20}$ and $5x10^{21}$ n-cm^{-2}). Data from Ref. 8.

B. Swelling of β-SiC by Neutron Irradiation Above 1000 °C

In Ref. 7 β-SiC samples were neutron irradiated in the temperature range 1250-1550 °C and neutron fluences up to $12x10^{21}$ n/cm^2 ($E_n > 0.18$ MeV). Tetrahedral voids which are bounded by {111} crystallographic planes were observed. Void sizes increased with increasing fluences and with increasing the irradiation temperature, while void concentrations decreased with increasing temperature. SiC samples irradiated at 1250-1550 °C contained a high density of uniformly distributed voids. Void densities of $(14\pm5)x10^{16}$ cm^{-3} and $(3.8\pm1.2)x10^{16}$ cm^{-3} were measured in samples irradiated at 1250 °C (up to $4.3x10^{21}$ n-cm^{-2}) and 1500 °C (up to $8.8x10^{21}$ n-cm^{-2}), respectively[7]. Stereo-micrographs showed that some of the large voids were truncated across the corners and that their projected shape was hexagonal. The distribution of voids was somewhat heterogeneous in samples irradiated at 1500 °C. Also, in these samples, there was an occasional tendency for formation to of planar clusters of voids parallel to the {111} planes, suggesting preferential nucleation on stacking faults. Voids below 30-40 Å could not be resolved. The calculated void volume fraction was 2 and 20 times smaller than the volume fraction increase calculated from density measurements at 1500 °C and 1275 °C, respectively. This discrepancy is attributed to errors in resolving and counting small voids and in measuring the void size. Dislocation loops were not observed in this temperature range. Fig. 2 shows the swelling data of neutron-irradiated SiC obtained by Price[7] as a function of the neutron fluence and irradiation temperature. The data shows that void swelling takes place in β-SiC and that swelling is a maximum in the neighborhood of 1300 °C, which resembles void swelling in metals maximizing at a homologous temperature $T_H \approx 0.5$.

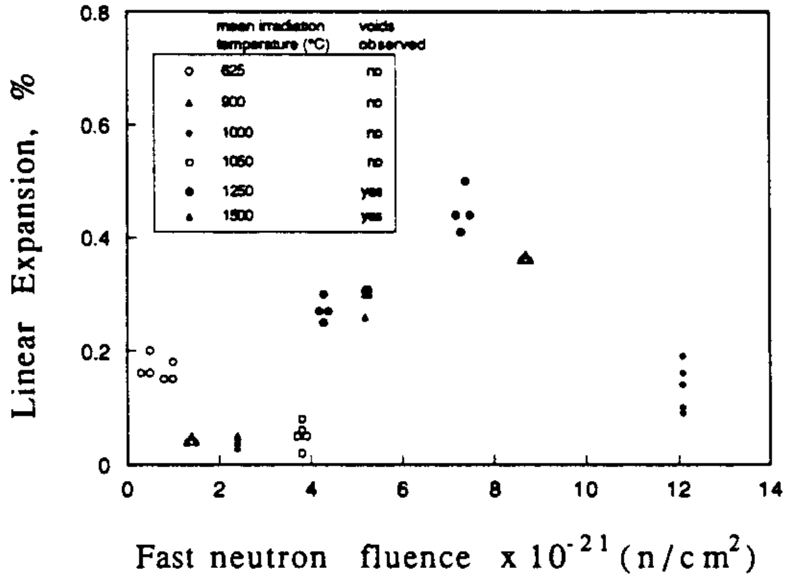

Fig. 2. Linear expansion of β-SiC as a function of fast neutron fluence and temperature. Data from Ref. 7.

Void annealing experiments showed that in the samples irradiated at 1250 °C voids are resistant to annealing. Annealing starts at ~ 1700 °C and was complete at 2100 °C. For those irradiated at 1500 °C annealing starts at ~ 1800 °C and was not complete at 2100 °C (Figs. 3 and 4). The fact that voids can be annealed out, although at very high temperatures, suggests that they do not contain gas atoms. Experimental evidences on helium stabilizing effect on voids are reported in Ref. 11 and 12. In Ref. 11 an experimental study was carried out to determine the effects of sintering aids on the length change of SiC under neutron irradiation. Samples of pressure-less sintered (PLS) SiC containing boron and carbon exhibited significant length increase upon annealing over 1300 °C (see Figs. 5 and 6). Such an annealing behavior was explained as a combined effect of availability of helium atoms produced by $^{10}B(n,\alpha)^{7}Li$ reactions which migrate to voids, and the thermal equilibrium vacancies over 1300 °C required for bubble growth [13].

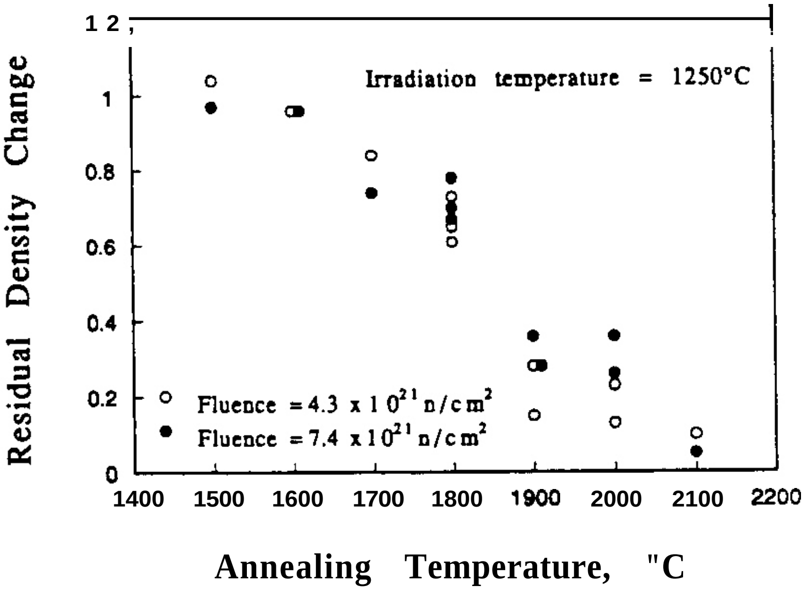

Fig. 3. Recovery of the density of irradiated β-SiC during one hour post-irradiation anneals, as a function of annealing temperature. Irradiation temperature = 1250 °C. Residual density change = (original density - annealed density)/(original density - irradiated density). Data from Ref. 7.

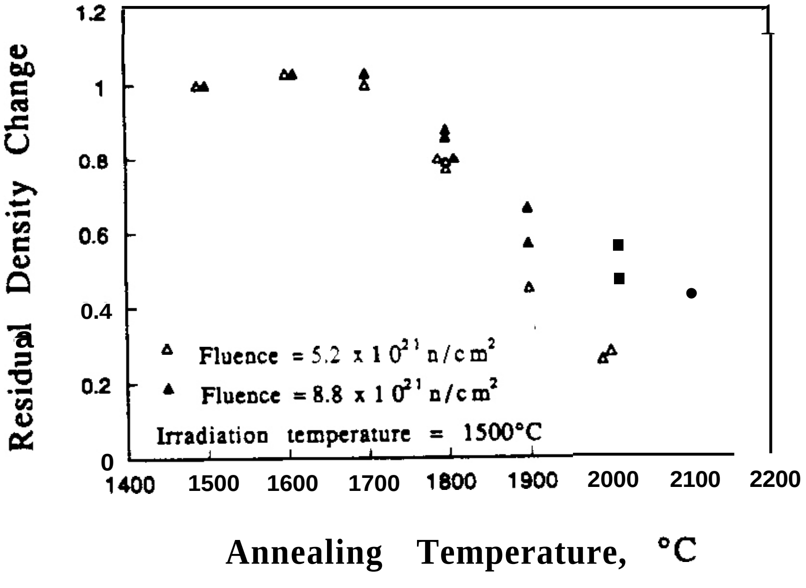

Fig. 4. Recovery of the density of irradiated β-SiC during one hour post-irradiation anneals, as a function of annealing temperature. Irradiation temperature = 1500 °C. Residual density change = (original density - annealed density)/(original density - irradiated density). Data from Ref. 7.

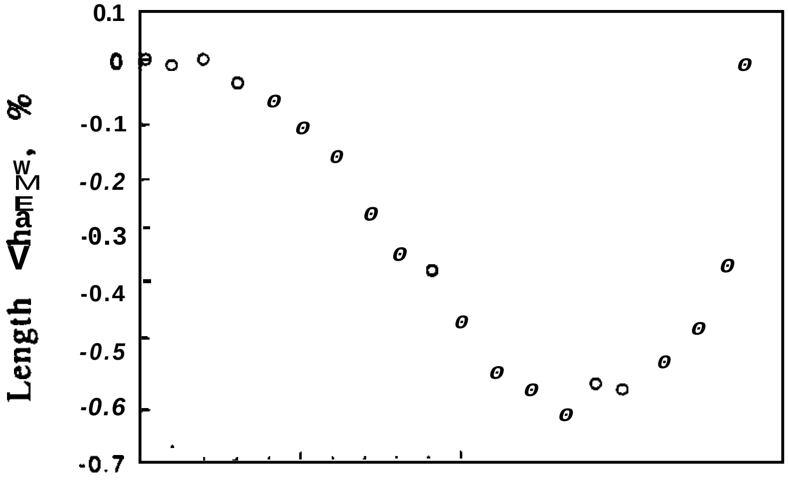

Fig. 5. Macroscopic length change against annealing temperature for pressure-less sintered SiC containing B and C and irradiated to a neutron fluence of ~8×10^{19} n/cm^2 at ~ 280 oC. Data from Ref. 11.

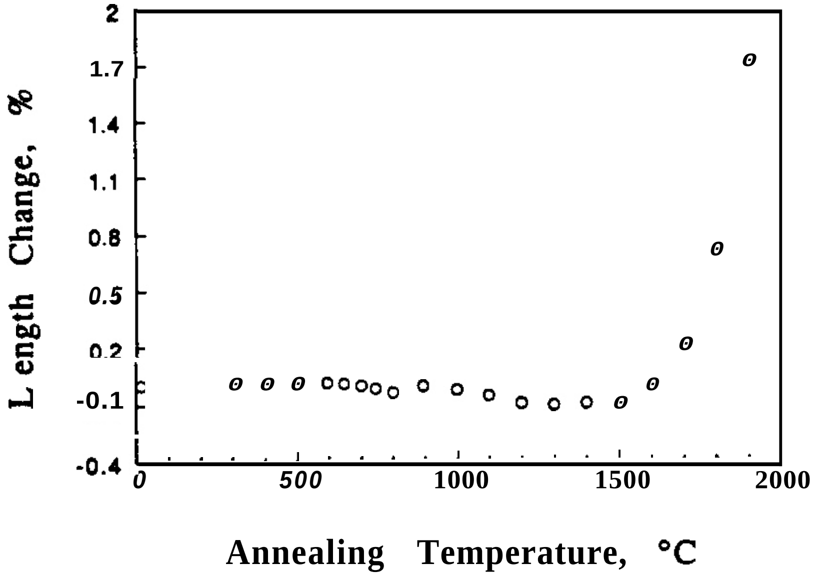

Fig. 6. Macroscopic length change against annealing temperature for pressure-less sintered SiC containing B and C and irradiated to a neutron fluence of ~6×10^{20} n/cm^2 at ~ 640 °C. Data from Ref. 11.

C. Empirical Representation of Swelling Data

(i) Loop swelling below 1000 °C

In the absence of helium, **two** swelling mechanisms of neutron irradiated SiC were observed. Dislocation loop (or lattice) swelling, which saturates at a neutron fluence of ~$2\mathrm{x}10^{20}$ $\mathrm{n/cm}^2$ [14] below 1000 "C, and void swelling, which increases monotonically with fluence and temperature above a 1000 "C. Based on Fig. 1, the percent linear dimensional change associated with loop swelling can be represented empirically by:

$$\left[\frac{\Delta L}{L}\right]_{Loop}=(1.05-10^{-3}(T-273))(1-e^{-\frac{\phi t}{\Phi_0}}) \tag{1}$$

where T is the temperature in K, Φ_0 is a fraction of the saturation fluence, ϕ is the operating neutron **flux,** and *I* is the time into irradiation. In the present treatment of data, Φ_0 is related to the saturation fluence, **a,,,, as** follows:

$$\Phi_0=\frac{1}{n}\Phi_{sat} \tag{2}$$

where n = **3** in the present analysis. In the representation given by Eq. (1), the time required to saturate loop swelling is governed by the operating flux ϕ. If $\Phi_0 = \phi t_o$, where *I*, is a time constant, then Eq. (I) becomes:

$$\left[\frac{\Delta L}{L}\right]_{Loop}=(1.05-10^{-3}(T-273))(1-e^{-\frac{t}{t_0}}) \tag{3}$$

where the time constant t_o is given by:

$$t_0=\frac{1}{n}\frac{\Phi_{sat}}{\phi} \tag{4}$$

The saturation level of loop swelling can be regarded to correspond to a certain amount of atomic displacements. Point defect production in SiC under fusion conditions is faster than that under fission conditions for the same nominal flux values. Therefore loop swelling saturation is expected to be faster in a fusion environment. This is based on the fact that the fusion neutron spectrum is harder. An exprapolation procedure to fusion conditions can be based on the effects of the neutron spectrum on point defect production. **A** scaling law for the saturation fusion fluence may be formulated **as** follows:

$$\left(\Phi_{sat}\int_{E_n}\sigma_d(E_n)\phi(E_n)dE_n\right)_{fis}=\left(\Phi_{sat}\int_{E_n}\sigma_d(E_n)\phi(E_n)dE_n\right)_{fus} \tag{5}$$

where $\sigma_d(E_n)$ **is** the neutron displacement cross section and $\phi(E_n)$ **is** the neutron spectrum.The subscripts *fis* and ***fus*** denote fission and fusion, respectively. Eq. *(5)* **is** based on the assumption that the loop swelling saturation level. at the same irradiation temperature, corresponds to the same amount of atomic displacements under fission and fusion conditions. The time constant for saturation under fusion conditions can then be written **as:**

$$(t_0)_{fus} = \frac{1}{n\phi_{fus}} (\Phi_{sat})_{fis} \frac{\left(\int_{E_n} \sigma_d(E_n)\phi(E_n)dE_n \right)_{fis}}{\left(\int_{E_n} \sigma_d(E_n)\phi(E_n)dE_n \right)_{fus}} \tag{6}$$

The integral ratio in **Eq.** (6) is determined on the basis of detailed calculations by Huang and Ghoniem [3] for the neutron displacement damage cross sections in SiC under fission and fusion conditions. The ratio is found to be in the range 0.03-0.04 for **ARIES** IV first wall. Based on a saturation fission fluence of ~2×10^{20} n/cm^2 and a fusion neutron flux of 1.65×10^{15} n/cm^2.s, the time constant for saturation of loop swelling **was** estimated to be –30 minutes. Fig. 7 shows the estimated linear dimensional change associated with loop swelling in SiC for **ARIES** IV first wall. From the figure and the estimated time constant, it can be shown that in the first few hours of operation the matrix of Sic-Sic composites undergoes a linear dimensional change of − **0.3** - 0.05 **%** in the first wall of **ARIES** IV, in the temperature range 750-1000°C. The internal misfit stresses are highly dependent on such strains. Therefore, the dimensional changes of the prospective SiC fusion fibers must be compatible with such matrix swelling.

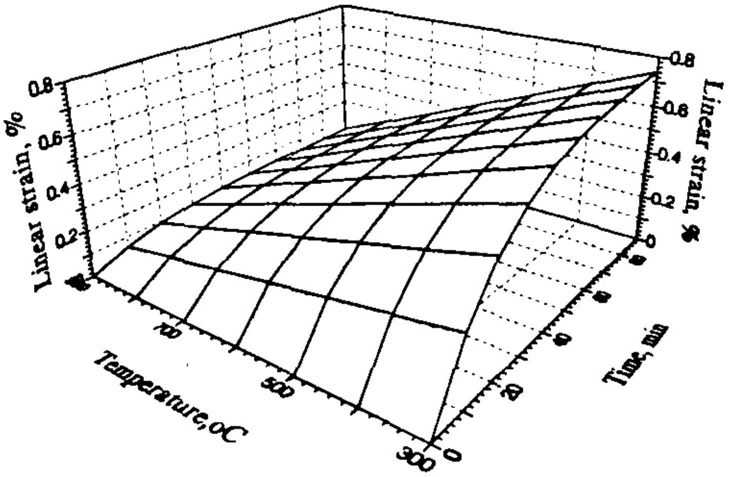

Fig. **7.** Estimated linear dimensional expansion of CVD SiC due to dislocation loop swelling based on ARIES IV first wall neutron flux, as a function **of** irradiation time and temperature. Operating neutron flux − 1.65×10^{15} nicm' s.

(ii) Helium swelling in β-SiC

As has been observed experimentally [11-13], helium bubbles grow if a vacancy supply is available. Such a growth process depends on the stress, temperature, and irradiation fields. Under fusion irradiation large numbers of vacancies are produced continuously by neutron-induced atomic displacements. **Also** significant amounts of helium are expected to be produced by (n,xα) reactions in carbon and silicon atoms. Thus, highly mobile helium atoms in SiC matrix at high temperatures can be a deriving force for gas bubble swelling. Therefore, cavity induced swelling in SiC under fusion conditions is expected to be of the helium bubble-type.

A simple phenomenological equation which describes helium swelling in crystalline ceramics is developed by Ghoniem et al.[15] , and was used to study heliume swelling in solid breeders in fusion blankets. The equation is written as:

$$\left(\frac{\Delta L}{L}\right)_{Helium} = \left(\frac{1}{12\pi}\right)^{1/2} \left(\frac{kT\ fGt}{2\gamma\ N^{1/3}}\right)^{3/2} \qquad (7)$$

where γ is the surface energy, f is the fraction of helium atoms retained in bubbles, G is the helium generation rate, N is the bubble density and t is the time into irradiation. The assumptions made in obtaining this equation are summarized as follows:

- All bubbles are of the same average size.
- Ideal gas equation of state is used for helium in bubbles.
- Bubbles are in mechanical equilibrium with the solid.
- Re-solution of helium atoms from the bubbles is neglected.

Fig. 8 shows the estimated helium swelling in CVD SiC, as a function of temperature and time for ARIES IV first wall neutron flux, based on a bubble density of 10^{22} m^{-3} (Ref. 7) and a retained helium fraction of 0.2. The helium generation rate was determined to be 2.898×10^{13} atoms/cm^3.s for ARIES IV first wall, based on the data given in Ref. 3. As the data in Ref. 7 shows, the bubble density can be represented in terms of irradiation temperature by $N = N_o \exp(g/kT)$, where g is an activation energy. There is no adequate data to support this representation of bubble density. However, as a first order estimate, the data obtained by Price[7] for the void density in the temperature range 1250 - 1500°C is used. Based on this data. the constant N_o is found to be 5.18×10^{17} m^{-3}, and g = 1.642 eV. An upper bound value of 5×10^{23} m^{-3} for bubble density is chosen which allows the use of the Arrhenius representation of bubble density fo T > 1150 °C only. With this representation of bubble density, Fig. 9 shows the estimated helium swelling in SiC based on ARIES IV first wall neutron flux. Helium swelling as presented in Figs. 8 and 9 is an estimation which may not be adequately accurate and still need to be confirmed by experimental data. No voids were observed below 1000 °C under fission spectra [7] where no helium is generated(Fig. 2). This may be the case also under fusion conditions if no helium is present. However, significant amounts of helium are expected to be generated in SiC in a fusion environment. In the present analysis we assume that helium can stabilize small vacancy clusters, which would exist under large scale cascades and high dpa rates in a fusion environment, leading to formation and growth of helium bubbles even below 1000 °C. Thus the temperature range for helium bubble formation and growth may be extended to below that temperature as given in Figs. 8 and 9.

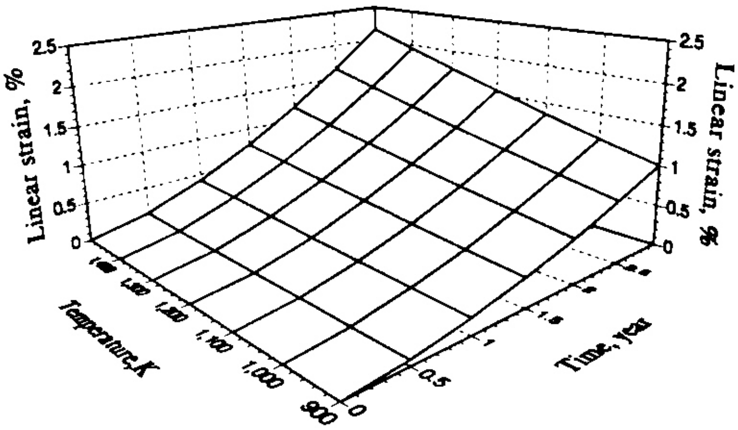

Fig. **8.** Estimated linear dimensional expansion of CVD SiC due to helium swelling based on **ARIES** IV first wall neutron flux, as a function of irradiation time and temperature. Operating neutron flux - 1.65x1015 n/cm2 s.

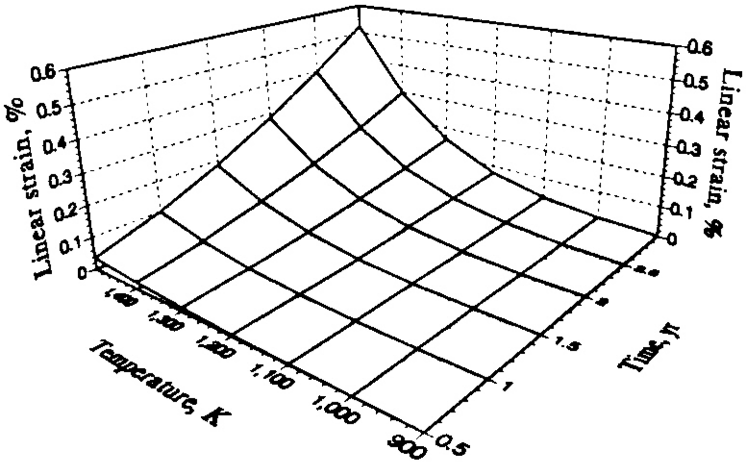

Fig. 9. Estimated linear dimensional expansion **of** CVD SiC due to helium swelling based on **ARIES** IV first wall neutron flux with Arrhenius helium bubble density.

IRRADIATION CREEP OF β-SiC

Irradiation creep experiments were performed in order to determine the irradiation creep characteristics of β-SiC for the HTGR fuel program', where creep samples were irradiated up to 7.7×10^{21} nlcm' **(E,** > 0.18 MeV). The experimental results have shown that the irradiation creep strain, ε_{irr}, in β-SiC is linearly related to the applied stress, σ, as shown below:

$$\epsilon_{irr}=K\sigma\phi t \tag{8}$$

where *K* is the irradiation creep constant. For an irradiation temperature of 650 °C a creep constant on the order of 2×10^{-37} (Pa-nm^{-2})$^{-1}$ was estimated. At 900 °C, an upper limit of 4×10^{-37} (Pa-nm^{-2})$^{-1}$ was inferred'. Other experiments mentioned in Ref. *8* have confirmed the estimated results and showed that the temperature sensitivity of the creep constant *K* can be neglected. A value of $K = 3\times10^{-37}$ (Pa-nm^{-2})$^{-1}$ will be used in the present analysis.

It is well known that irradiation creep in crystalline solids can be explained in terms of a dislocation glide process which is assisted by dislocation climb. This creep mechanism depends on point defect concentrations as well **as** the defect mobilities in the vicinity of the dislocation core. The absorption (or emission) of point defects at the dislocation core result in a climb process which enables the dislocation to move past different **types** of pinning centers. Therefore, **one** would expect a higher creep constant under fusion conditions, where the atomic displacements take place at higher rates, and the mobility of point defects is enhanced by the irradiation field. Irradiation creep can be described by the following relation [16]:

$$\dot{\epsilon} = \sigma(Z_iD_iC_i - Z_vD_vC_v) \tag{9}$$

where **Z,** is the dislocation bias factor for interstitials and D_i and C, are the diffusion coefficient and **the** concentration of interstitials. Z_v , D_v and C_v have the same definitions for vacancies. Under the condition of steady-state irradiation, defect concentrations are proportional to the defect generation rate and depend on other microstructural extended defects which are sinks for point defects. Assuming similar extended defect microstructures, the irradiation creep rate can be scaled by considering the defect generation **rate** alone. Therefore, a scaling law for the creep constant is proposed **as:**

$$K_{fus}=K_{fis}\frac{\left(\int_{E_n}\sigma_d(E_n)\phi(E_n)dE_n\right)_{fus}}{\left(\int_{E_n}\sigma_d(E_n)\phi(E_n)dE_n\right)_{fis}} \tag{10}$$

The integral ratio in Eq. (10) **is** found in the range 25-35 for ARIES IV first wall. Therefore the estimated irradiation creep constant for SiC is ≈ 10^{-35} (Pa-nm^{-2})$^{-1}$ under fusion conditions.

IRRADIATION EFFECTS IN SiC FIBERS

SiC fibers are produced by two methods; the polymer pyrolysis method in which a polycarbosilane polymer precursor material is used to obtain fibers, and the Chemical Vapor Deposition (CVD) method. The SCS-6 and the SCS-8 silicon carbide fibers are produced by CVD of β-SiC on a turbostatic carbon core. The carbon core is -40 μ in diameter while the β-SiC sheath outer diameter is around 140 μ. The carbon core is about 8% of the fiber volume. The class of SiC fibers derived from the pyrolysis of polycarbosilane(PCS) are known as Nicalon fibers. Nicalon fibers are oxygen-rich, which makes these fiber thermally unstable at high temperatures. These fibers are –10 μ in diameter. A newer class of Nicalon fibers. which contain less than 1% oxygen are now available. These fibers are – 14 μ in diameter, and are cured by electron beams, which funher lower their oxygen-content and enhances their high-temperature stability. However, CVD SiC fibers and Nicalon fibers are expected to behave differently in a fusion environment. In this section we review the available data on fiber irradiation experiments and propose constitutive equations for the irradiation creep and dimensional changes in these fibers.

A. Nicalon Fibers

Okamura et al.[18 19] presented experimental results on the neutron irradiation of Nicalon fibers. Two types of fibers were tested (amorphous and partially microcrystalline) in the Japanese Materials Test Reactor, JMTR, (E, > 1 MeV), up to 2×10^{20} n-cm^{-2} at 150 °C, and 9×10^{20} n-cm^{-2} at 650 "C. Both materials exhibited significant increase in density by irradiation leading to a substantial increase in the Young's modulus and the tensile strength. Similar results were reported by Kohyama et al.[20]. The fiber densification under neutron irradiation is due to nucleation and growth of β-SiC microcrystallites at the expense of the amorphous phase [20]. Therefore, the irradiation-induced dimensional change of such fibers may be regarded to consist of two components; a shrinkage component associated with the atomic ordering, and a swelling component due to the expected dislocation loop formation and helium bubble growth in the ordered phase. The latter is considered to be that of β-SiC but occurs in the ordered phase only.

An empirical representation for the irradiation densification data presented by Okamura et al.[19] may be written as:

$$p = \rho_0 + a\Phi^2 \tag{11}$$

where ρ_0 is the initial density of the fiber material ($\rho_0 = 2.56$ g.cm^{-3}), a is a constant to be determined from the experimental data, and Φ is the neutron fluence. The constant a is found to be $a = 0.21/\Phi_0^2$, where $\Phi_0 = 10^{21}$ n-cm^{-2}. It can be shown that the densification of fibers by neutron irradiation is saturable at the neutron fluence at which the entire amorphous phase is consumed. This fluence can be approximately taken equal to Φ_0 , since at that level of exposure both kinds of fibers which were tested (initially amorphous and partially microcrystalline fibers) reached the same density level [19]. The relative volumetric change corresponding to the densification process is then given by:

$$\frac{\Delta V}{V} = -1 + \rho_0\left(\rho_0 + a\Phi^2\right)^{-1} = -1 + \rho_0\left[\rho_0 + 0.21\left(\frac{\Phi}{\Phi_0}\right)^2\right]^{-1} \tag{12}$$

The fiber densification process under irradiation is faster at higher atomic displacement rates associated with the fusion neutrons. In this case, the constant Φ_0 shown in the last equation will have a lower value, given by a relation similar to Eq. *(5)*. Thus the linear dimensional shrinkage strain may be written in terms of the operating fusion flux, ϕ, and time, t, as follows:

$$\left(\frac{\Delta L}{L}\right)_{Nic}=-\frac{1}{3}\left(\frac{0.21\left(\frac{\phi t}{\Phi_0}\right)^2 R^2}{\rho_0+0.21\left(\frac{\phi t}{\Phi_0}\right)^2 R^2}\right) \tag{13}$$

where R is given by:

$$R=\frac{\left(\int_{E_n}\sigma_d(E_n)\phi(E_n)dE_n\right)_{fus}}{\left(\int_{E_n}\sigma_d(E_n)\phi(E_n)dE_n\right)_{JMTR}} \tag{14}$$

This equation is valid until the densification process is complete, which corresponds to a maximum value of shrinkage strain equal to ~ 2.4%. This value corresponds to the maximum density from Okamura's data [19]. Under ARIES IV first wall neutron flux, this is estimated to occur after the first 28 hours of operation.

There is no data reponed on the irradiation creep of these fibers. However, a reasonable irradiation creep constant may be taken to be equal to that of β-SiC.

B. SCS-6 Fibers

Experimental studies have shown that the fast densification of Nicalon fibers under irradiation results in fiber-matrix interface debonding [31]. To avoid this problem SiC fibers must have higher initial content of crystalline SiC. In this case slower fiber densification is expected and the integrity of the interface may be kept. In fact, this is the reason SCS-6 fibers are considered in the present analysis. This kind of fiber containes –92% β-SiC, which is desirable from the irradiation stand point.

The carbon core in this fibers is ~ 8% by volume. Therefore it is not expected to contribute much to the irradiation creep and swelling. This statement is justified below . If we assume that the swelling of these fibers under neutron irradiation is controlled by the swelling of the SiC sheath, then the following linear dimensional changes associated with sheath swelling can be obtained for these fibers:

$$\left(\frac{\Delta L}{L}\right)_{tr}=(1-f_c)\left(\frac{\Delta L}{L}\right)_{SiC}$$

$$\left(\frac{\Delta L}{L}\right)_{ax}=\left(\frac{\Delta L}{L}\right)_{SiC} \tag{15}$$

where

$$\left[\frac{\Delta L}{L}\right]_{SiC} = \left[\frac{\Delta L}{L}\right]_{Loop} + \left[\frac{\Delta L}{L}\right]_{Helium} \tag{16}$$

The subscript tr and ax refer to the transverse (in the plane of fiber cross section) and axial directions, respectively, and f_c is the volume fraction of the carbon core. In Eq. **(15)** the $(1\text{-}f_c)$ factor is considered since we have neglected the dimensional changes in the carbon core, and assumed that the induced swelling, contributed by the SiC sheath. is uniformly distributed over the fiber cross sectional area. including the carbon core itself. The reason behind this assumption is that the carbon core is much softer in comparison to the SiC sheath. Therefore, the swelling of the core would be suppressed by the the surrounding sheath. If the fiber is used in a composite, the matrix surrounding the fiber would resist the swelling induced by the SiC sheath only. Thus, the irradiation-induced swelling in SCS-6 fiber can be anisotropic.

The irradiation creep constant for the SCS fibers can be obtained by analyzing the fiber as a composite cylinder. In this case the axial creep constant can be obtained as:

$$K_{ax} = \frac{K_{SiC} K_C}{f_c K_{SiC} + (1 - f_c) K_C} \tag{17}$$

The irradiation creep constant for isotropic graphite is found, both theoretically [21] and experimentally [22-24], to be in the range $(4.4 \pm 1.5) \times 10^{-35}$ $(\text{Pa n-m}^{-2})^{-1}$, which is a factor of 5 greater then that of SiC. Also, since f_c is considerably small, Eq. (17) can be simplified to give the fiber creep constant as follows:

$$K_{ax} = \left[\frac{K_{SiC}}{1 - f_c}\right] \tag{18}$$

which means that the fiber irradiation creep is controlled by the slower creep response of the SiC sheath. For the transverse direction. $K_{tr} = K_{SiC}$ is a good approximation.

MELASTIC CONSTITUTIVE EQUATIONS

In this section a set of inelastic constitutive equations, which is suitable for micromechanics problem formulation in SiC fiber-reinforced SiC matrix. is developed. In addition to irradiation-induced creep and dimensional changes, we focus on thermal creep. The parameters representing the constitutive behavior, which are determined from experiments, are also listed. A cylinderical system of coordinates is adopted in the present analysis since micromechanical theories of fiber-reinforced composites are mostly based on concentric cylider models.

It has been experimentally observed that SCS-6 fibers exhibit linear relationship between thermal creep strain and the applied stress at high temperatures”. Nicalon fibers showed a non-linear relationship between the stress and creep strain”, with a stress exponent of 1.9. In a recent experiement[28] a stress exponent of 1.2 was measured. In the present analysis, it will be assumed that the stress strain relation is linear which makes it possible to apply the linear theory of viscoelasticity . Since irradiation creep is also linearly dependent on the applied stress, SiC fibers can be regarded as linear viscoelastic solids under high-temperature neutron irradiation. For a linear anisotropic viscoelastic solid, the stress-strain relationship takes the form":

$$\epsilon_{ij}=\int_{-\infty}^{t} J_{ijkl}(t-t')\frac{\partial\sigma_{kl}(t')}{\partial t'}dt' \tag{19}$$

in which J_{ijkl} are creep compliance functions which characterize the time-dependent response of the material and t is the time at which the strains are evaluated. If other non-viscoelastic strain components such as thermal expansion and irradiation-induced dimensional changes are present the stress-strain relation becomes:

$$\epsilon_{ij}-\epsilon_{ij}^{s}-\epsilon_{ij}^{th}=\int_{-\infty}^{t} J_{ijkl}(t-t')\frac{\partial\sigma_{kl}(t')}{\partial t'}dt' \tag{20}$$

where the superscripts s and th represent swelling and thermal expansion, respectively. By virtue of the linearity of the stress-strain relationship, the compliance function J_{ijkl} can be decomposed into three components; the elastic, thermal creep and irradiation creep components, as below:

$$J_{ijkl}=J_{ijkl}^{e}+J_{ijkl}^{th}+J_{ijkl}^{irr} \tag{21}$$

The last two equations are used to formulate the constitutive equations for CVD SiC matrix, Nicalon fibers and SCS SiC fibers in this section.

A. Constitutive Equations for SCS Fibers.

It has been previously mentioned that SCS fibers are expected to be transversely isotropic from the point of view of irradiation creep and swelling. Proposed inelastic constitutive equations for SCS fibers are written in the form:

$$\epsilon_r-\epsilon_r^{s}-\alpha_r\Delta T=\frac{\left(\sigma_r(t)-\nu_{SCS}[\sigma_z(t)+\sigma_\theta(t)]\right)}{E_{SCS}}+\int_0^{t}\left([\sigma_r(t')-\nu_{SCS}\sigma_\theta(t')]\dot{J}_{tr}(t-t')-\nu_{SCS}\sigma_z(t')\dot{J}_{ax}(t-t')\right)dt'$$

$$\epsilon_z-\epsilon_z^{s}-\alpha_z\Delta T=\frac{\left(\sigma_z(t)-\nu_{SCS}[\sigma_r(t)+\sigma_\theta(t)]\right)}{E_{SCS}}+\int_0^{t}\left(\sigma_z(t')\dot{J}_{ax}(t-t')-\nu_{SCS}[\sigma_r(t')+\sigma_\theta(t')]\dot{J}_{tr}(t-t')\right)dt'$$

$$\epsilon_\theta-\epsilon_\theta^{s}-\alpha_\theta\Delta T=\frac{\left(\sigma_\theta(t)-\nu_{SCS}[\sigma_z(t)+\sigma_r(t)]\right)}{E_{SCS}}+\int_0^{t}\left([\sigma_\theta(t')-\nu_{SCS}\sigma_r(t')]\dot{J}_{tr}(t-t')-\nu_{SCS}\sigma_z(t')\dot{J}_{ax}(t-t')\right)dt'$$

(22)

where *E*„„ **is** Young's mudulus and ν_{SCS} **is an** effective viscoelastic Poisson's ratio. The first term to the right hand side of any of Eqs. (22) is the elastic (prompt) component of the strain, while the integral term represents the hereditary component. In writing down these equations, it has been assumed that the Poisson's ratio is independent of time. This assumption is also applicable for Nicalon fibers and CVD SiC. J_{ax} and J_{tr} are the axial and transverse creep compliance functions of *SCS* fibers, which are given by:

$$J_{ax}=\frac{1}{E_{SCS}}+\frac{K_{SiC}}{(1-f_c)}\phi t+C_{SCS}(T)t^{p}$$

$$J_{tr}=\frac{1}{E_{SCS}}+K_{SiC}\phi t+C_{SCS}(T)t^{p} \qquad (23)$$

where the first term in the above equation is the elastic compliance, the second term is the irradiation creep compliance and the third term **is** the thermal creep compliance. $C_{SCS}(T)$ is a function of temperature, and given by Dicarlo and Morscher [28] **as:**

$$C_{SCS}(T)=A_{SCS}\exp\left[-\frac{25800}{T}\right] \qquad (24)$$

in which A_{SCS} = 13.112 , $p = 0.36$ and, for stress in MPa, time in seconds and T in K. Figs. 10 and 11 show the estimated creep compliance of *SCS-6* fibers in **ARIES** IV first wall conditions at 1000 "C and 1200 °C, respectively. It is noticed that thermal contribution becomes important over **1000 °C** (Fig. 1**1),** while the irradiation component dominates the creep response of this material at **lower** temperatures (Fig. 10). The difference between the axial and transverse creep functions is small since f_c in **Eq. (23)** is **small** (f_c=0.08). However, this difference may be important for the time-evolution of internal mismatch stresses in Sic-Sic composites, which influences the deformation and fracture behavior of SiC-SiC materials. The time-dependent dimensional changes associated with fiber swelling, ϵ^s are given by:

$$\epsilon_r^s=\epsilon_\theta^s=(1-f_c)\left[\frac{\Delta L}{L}\right]_{SiC} \qquad (25)$$

$$\epsilon_z^s=\left[\frac{\Delta L}{L}\right]_{SiC}$$

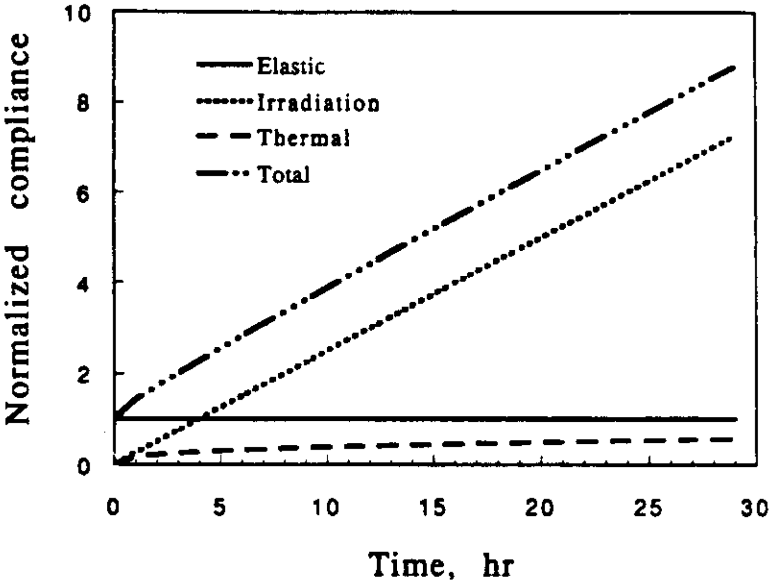

Fig. 10. Estimated axial creep compliance of SCS-6 fibers in ARIES IV first wall at 1000 °C.

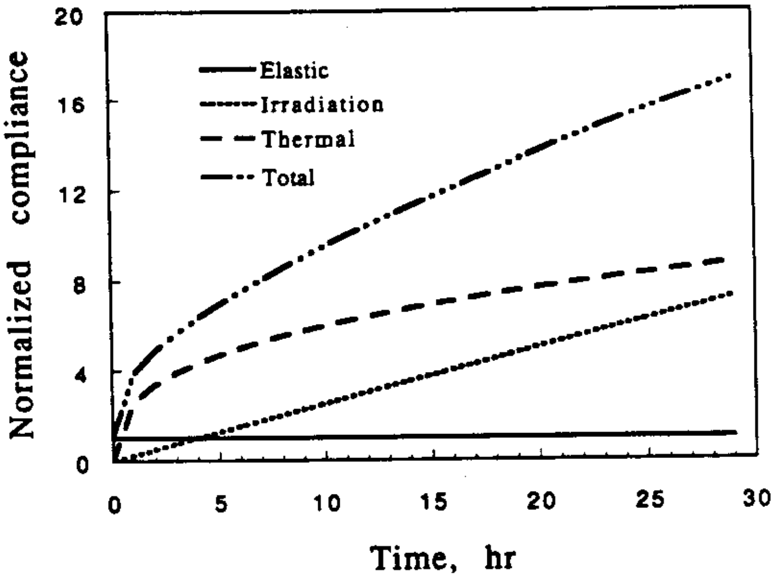

Fig. 11. Estimated axial creep compliance of SCS-6 fibers in ARIES IV first wall at 1200 °C.

B. Constitutive Equations for Nicalon Fibers.

Nicalon fibers are considered isotropic. In this case, the inelastic constitutive equations are written as:

$$\epsilon_z - \epsilon^s - \alpha\Delta T = \frac{\left(\sigma_z(t) - \nu_{Nic}[\sigma_r(t)+\sigma_\theta(t)]\right)}{E_{Nic}} + \int_0^t \left(\sigma_z(t') - \nu_{Nic}[\sigma_r(t')+\sigma_\theta(t')]\right)\dot{J}_{Nic}(t-t')dt'$$

$$\epsilon_r - \epsilon^s - \alpha\Delta T = \frac{\left(\sigma_r(t) - \nu_{Nic}[\sigma_z(t)+\sigma_\theta(t)]\right)}{E_{Nic}} + \int_0^t \left(\sigma_r(t') - \nu_{Nic}[\sigma_z(t')+\sigma_\theta(t')]\right)\dot{J}_{Nic}(t-t')dt'$$

$$\epsilon_\theta - \epsilon^s - \alpha\Delta T = \frac{\left(\sigma_\theta(t) - \nu_{Nic}[\sigma_z(t)+\sigma_r(t)]\right)}{E_{Nic}} + \int_0^t \left(\sigma_\theta(t') - \nu_{Nic}[\sigma_z(t')+\sigma_r(t')]\right)\dot{J}_{Nic}(t-t')dt' \quad (26)$$

where E,, and ν_{Nic} are the Young's modulus and Poisson's ratio of Nicalon fibers. J_{Nic} is the total fiber compliance, which is written as:

$$J_{Nic} = \frac{1}{E_{Nic}} + K_{SiC}\phi t + C_{Nic}(T)t^m \quad (27)$$

where $C_{Nic}(T)$ is given by[28]:

$$C_{Nic}(T) = A_{Nic}\exp\left[-\frac{24200}{T}\right] \quad (28)$$

in which A,, = 8.316 , m = 0.4, for stress in MPa, time in seconds and T in K. **Figs.** 12 and 13 show the creep function of Nicalon fibers in **ARIES** IV first wall above a 1000 °C. The time-dependent dimensional changes associated with shrinkage/swelling of Nicalon fibers are given by:

$$\epsilon_z^s = \epsilon_r^s = \epsilon_\theta^s = \left[\frac{\Delta L}{L}\right]_{Nic} + \left[\frac{\Delta L}{L}\right]_{SiC} f_{conv}(t) \quad (29)$$

where the first term represents the shrinkage given by Eq. (13) and the second represents the swelling component in the ordered phase and $f_{conv}(t)$ is the fraction densified at time t. It must be noticed that the thermal creep components for both Nicalon and *SCS* fibers are operable starting at temperatures above 1000 °C, while the irradiation component **is** fairly independent of temperature.

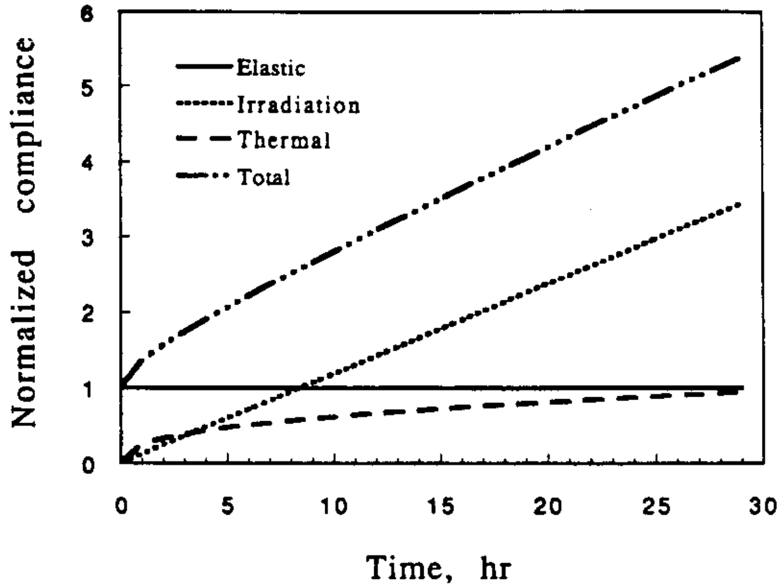

Fig. 12. Estimated creep compliance of Nicalon fibers in ARIES IV first wall at 1000 °C.

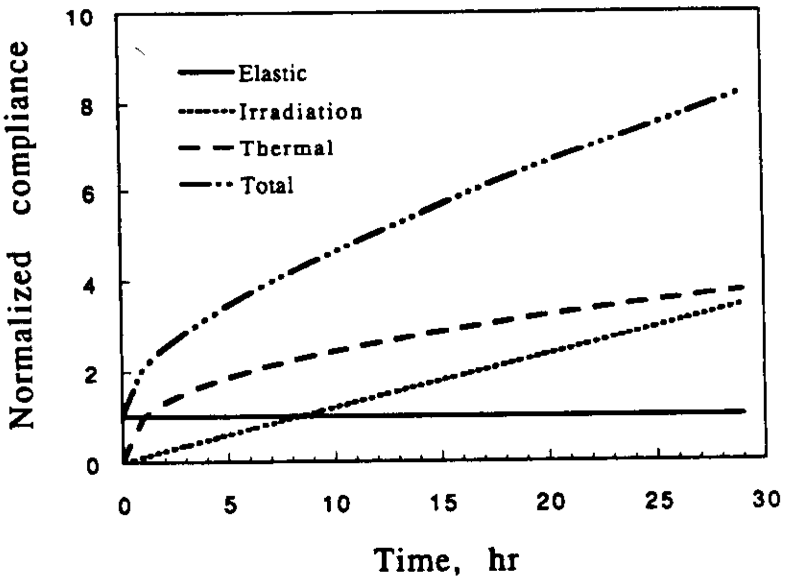

Fig. 13. Estimated creep compliance of Nicalon fibers in ARIES IV first wall at 1100 °C.

C. Constitutive Equations for CVD SiC

CVD SiC has been tested in compression by Carter and Davis [29] in the temperature range 1550 °C - 1750 “C and in bending by Gulden and Driscoll [30] in the temperature range 1200 °C - 1500 °C. Gulden and Driscoll interpreted the creep of CVD SiC in term of Nabarro-Herring creep mechanism which follows a linear viscous deformation law of the form?

$$\epsilon = \frac{13.3\sigma D\Omega}{kTd^2} t = C_{SiC}(T)\sigma t \tag{30}$$

where σ **is** the applied stress. ***D*** is the diffusion coefficient of the rate-controling species, **Ω is** the atomic volume, ***k*** **is** the Boltzmann constant and ***d*** is the grain size. Carter and Davis observed a power law behavior, for which the creep rate is written as[29]:

$$\dot{\epsilon} - \sigma^n exp(-Q/RT) \tag{31}$$

which represents a dislocation creep mechanism. Q is the acivation energy and *R* is the gas constant. In the present analysis the data of Gulden and Driscoll [30] **is** analyzed and compared to the thermal creep data of SCS-6 and Nicalon fibers obtained by Dicarlo and Morscher” (Figs. 14 through16). It is **observed** that the thermal creep rate of CVD SiC matrix is a few to several orders of magnitude slower than **that** of SCS and Nicalon fibers below 1500 “C. The constitutive equations for CVD SiC are written as:

$$\epsilon_z - \epsilon^s - \alpha\Delta T = \frac{\left(\sigma_z(t) - \nu_{SiC}[\sigma_r(t) + \sigma_\theta(t)]\right)}{E_{SiC}} + \int_0^t \left(\sigma_z(t') - \nu_{SiC}[\sigma_r(t') + \sigma_\theta(t')]\right)\dot{J}_{SiC}(t-t')dt'$$

$$\epsilon_r - \epsilon^s - \alpha\Delta T = \frac{\left(\sigma_r(t) - \nu_{SiC}[\sigma_z(t) + \sigma_\theta(t)]\right)}{E_{SiC}} + \int_0^t \left(\sigma_r(t') - \nu_{SiC}[\sigma_z(t') + \sigma_\theta(t')]\right)\dot{J}_{SiC}(t-t')dt'$$

$$\epsilon_\theta - \epsilon^s - \alpha\Delta T = \frac{\left(\sigma_\theta(t) - \nu_{SiC}[\sigma_z(t) + \sigma_r(t)]\right)}{E_{SiC}} + \int_0^t \left(\sigma_\theta(t') - \nu_{SiC}[\sigma_z(t') + \sigma_r(t')]\right)\dot{J}_{SiC}(t-t')dt' \tag{32}$$

where the irradiation-induced swelling is given by **Eq.** (16) and J_{SiC} is the compliance of CVD SiC, which is given by:

$$J_{SiC} = \frac{1}{E_{SiC}} + K_{SiC}\phi t + C_{SiC}(T)t \tag{33}$$

in which $C_{SiC}(T)$ **is** defined in Eq. (30). The constitutive shear relations are written as:

$$\epsilon_{ij}=\frac{\sigma_{ij}(t)}{2G_{SiC}}+\int_0^t\sigma_{ij}(t')\frac{\partial Y_{SiC}(t-t')}{\partial(t-t')}dt' \tag{34}$$

(for $i \neq j$). G„„ is the shear modulus of SiC and Y_{SiC} (t) is the creep compliance of that material in shear, which is readily obtainable from the compliance J_{SiC} and the poisson's ratio as follows:

$$Y_{SiC}(t)=(1+\nu_{SiC})J_{SiC}(t) \tag{35}$$

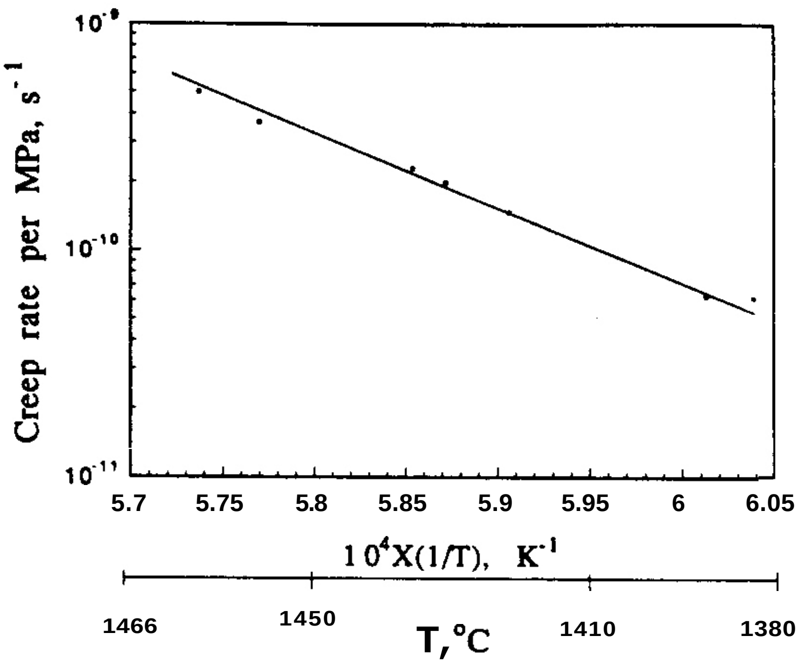

Fig. 14. Thermal creep data of CVD-SiC obtained by Gulden and Driscoll [Ref. 30].

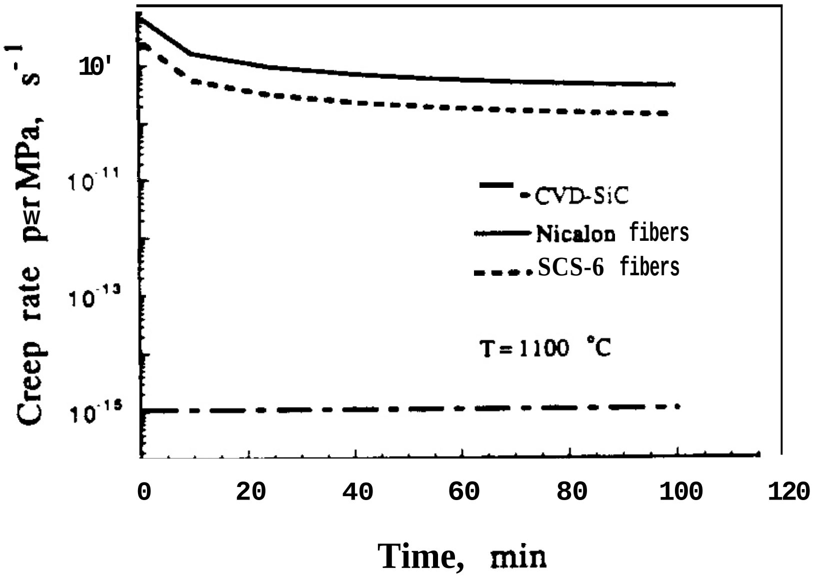

Fig. 15. Comaprison of thermal creep rates of CVD-SiC [Ref. 30], Nicalon and SCS-6 fibers[Ref. 28] at 1100 °C.

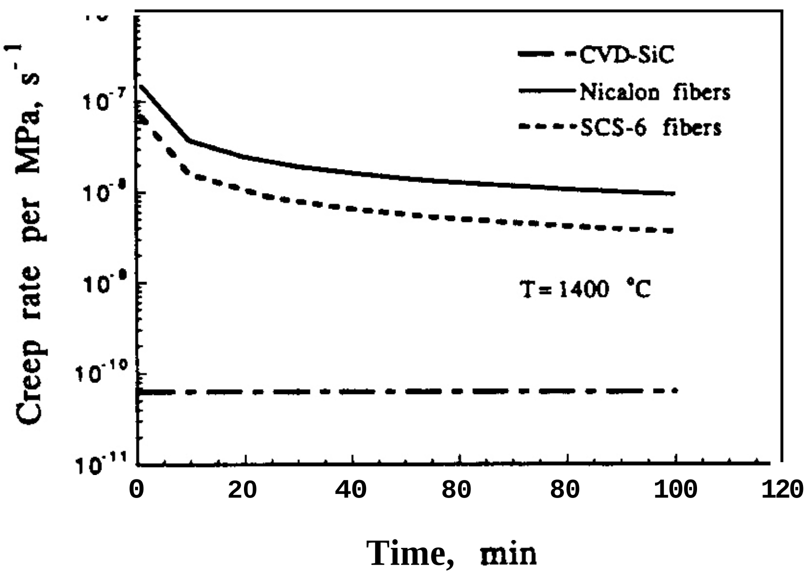

Fig. 16. Comparison of thermal creep rates of CVD-SiC [Ref. 30], Nicalon and SCS-6 fibers[Ref. 28] at 1400 °C.

CONCLUSIONS

Even though the data base for irradiation effects on SiC and SiC fibers under fusion conditions is not available, an effort is made in this paper to develop constitutive equations for its mechanical behavior, on the basis of available fission reactor data. Phenomenological and empirical models are used to describe the stress-temperature-time-deformation characteristics of the composite. The work could be useful in a number of ways: (1) stimulate conceptualization of proper experimental conditions to test the irradiation response of these materials, (2) give first-order estimates of possible mechanical behavior in the fusion environment, (3) help in the formulation of proper micro mechanical models to study the overall constitutive behavior of Sic-Sic composites and to study slow crack growth and fiber pull-out under irradiation.

Based on the results for swelling and irradiation creep, two other conclusions are drawn. Firstly, the time scale for loop swelling in CVD SiC matrix and SCS fibers is of the order of a few hours, which means that an SCS(fiber)-CVD SiC (matrix)composite would undergo significant changes in the internal mismatch stresses very early during service. This requires careful determination of the initial mismatch strains. The same conclusion is also applicable to the initial densification process of Nicalon fibers. Secondly, the total creep compliance for SiC fibers is dominated by thermal creep above 1000 °C, while irradiation creep dominates below this temperature. In a fusion reactor, where the structure temperature is below 1000 °C, the response of the composite will be mainly determined by irradiation creep and helium swelling.

FUTURE WORK

The developed phenomenological equations will be used in conjunction with micro-mechanical models of cracks, bridged by creeping fibers, to determine the conditions for sub-critical crack growth under fusion conditions.

ACKNOWLEDGEMENT

Support of U.S. D.O.E. research grant #DE-FGO3-9ER54115 with U.C.L.A. is greatly acknowledged.

REFERENCES

1. F. NAJMABADI, R. W. CONN et al., " The ARIES IV Tokamak Reactor Study: Final Report," to be published **(1993).**

2. M. **S.** TILLACK et al., " Design and Analysis of the PROMETHEUS Wetted Wall IFE Reactor Cavity, " ***The 14th IEEE/NPSS Symposium of Fusion Engineering,*** Vol. **I,** San Diego, California **1991, p. 223.**

3. HANCHEN HUANG and N. M. GHONIEM, " Neutron Displacement Damage Cross section for SiC," *J* ***Nucl. Mater..*** **199,** 221(1993).

4. LAILA EL-GUEBALY, ARIES IV Team Researcher, University of Wisconsin-Madison, Private Communication.

5. R. J. PRICE, " Effects of Fast Neutron Irradiation on Pyrolytic Silicon Carbide," *J* ***Nucl. Mater.,*** **33, 17 (1969).**

6. R. BLACKSTONE and E. H.VOICE, "The expansion of Silicon Carbide by Neutron Irradiation at High Temperature," *J* ***Nucl. Mater.,*** **39, 319 (1971).**

7. R. J. PRICE, " Neutron Irradiation-Induced Voids in β-Silicon Carbide," *J.* ***Nucl. Muter..*** **48,** 47 **(1973).**

8. R. J. PRICE, " Properties of Silicon Carbide for Nuclear Fuel Particle Coatings," ***Nucl. Tech., 35,*** **320 (1977).**

9. R. J. PRICE, " Annealing Behavior of Neutron-Irradiated Silicon Carbide Temperature Monitors," ***Nucl. Tech..*** **16, 536 (1972).**

10. J. E. PALENTINE, " The Calibration of Fast Reactor Irradiation SiC Temperature Monitors Using Length Measurement Technique, " *J.* ***Nucl. Mater.,*** **92, 43 (1980).**

11. T. SUZUKI, T. YANO, T. MARUYAMA, T. **ISEKI,** and T. MORI," Effects of Sintering Aids on the Length Change of Neutron Irradiated SiC Ceramics During Annealing at High Temperature," *J.* ***Nucl. Mafer.,*** **165, 247 (1989).**

12. S. D. HARISON and J. C. CORELLI, " Microstructure of Neutron Irradiation-Induced Defects in Sintered and Siliconized SiC," J. Nucl. *Muter.*, **122&123**, 833 (1984).

13. T. SUZUKI, T. ISEKI, T. MORI and J. H. EVANS, " The Influence of Thermal Vacancies on Helium-Induced Volume Swelling in Silicon Carbide." *J. Nucl. Marer.*, **170,** I13 (1990).

14. T. YANO, T. SUZUKI, T. MARUYAMA and T. ISEKI, " Microstructure and Annealing Behavior of Heavily Neutron-Irradiated β-SiC," J. Nucl. *Mater.*, **155-157**, 311 (1988).

15. "TOKamak Reactor Operations Study ' TOKOPS', ' The Influence of Reactor Operations on the Design and Performance of Tokamaks with Solid-Breeder Blankets," UCLA/ENG-86-38 PPG-1009 (1986).

16. N. M. GHONIEM, "Nuclear Materials Engineering," **Class** Notes UCLA - MANE Graduate Course.

17. M. TAEDA, Y. IMAI, et al., " Thermal Stability of the Low Oxygen Silicon Carbide Fibers Derived fro Polycarbosilane," *Ceram. Enging. & Sci. Proc.*, **13 No.** *7-8,* 209 (1992).

18. K. OKAMURA, T. MATSUZAWA, M. SATO, Y. HIGASHIGUCHI and S. MOROZUMI, " Effects of Neutron Irradiation on SiC Fibers," *J. Nucl. Mater.*, **133&134**, 705 (1985).

19. K. OKAMURA, T. MATSUZAWA, M. SATO, H. KAYANO, S. MOROZUMI, H. TEZUKA and A. KOHYAMA," Effects of Neutron Irradiation on the Fine Structure and Strength of SiC Fibers," *J. Nucl. Marer.*, **155-157**, 329 (1988).

20. A. KOHYAMA, H. TEZUKA and S. SATO, " Radiation Induced Microstructural Evolution in SiC/Al Composites," *J. Nucl. Muter.*, **155-157**, 334 (1988).

21. B. T. KELLY and A. J. E. FOREMAN, "The Theory of Irradiation Creep in Reactor Graphite–The Dislocation Pinning-Unpinning Model, " *Carbon*, **12**, 151 (1974).

22. J. KAAE," The Mechanical Behavior of Biso-Coated Fuel Particles During Irradiation. Part I: Analysis of Stresses and Strains Generated in the Coating of A Biso Fuel Particle During Irradiation," *Nucl. Tech.*, **35, 359** (1977).

23. J. KAAE, R. E. BULLOCK, C. B. SCOTT and D. P. HARMON," The Mechanical Behavior of Biso-

Coated Fuel Particles During Irradiation. **Part** II: Prediction of Biso Particle Behavior During Irradiation With a Stress Analysis Model," ***Nucl. Tech., 35*** **, 368 (1977).**

24 J. KAAE, " On Irradiation-Induced Creep of pyrolytic Carbon in a General State of Stress," ***J. Nucl. Muter.,*** **34 , 206 (1970).**

25. JAMES A. DICARLO, " Creep of Chemically Vapor Deposited SiC Fibers," ***J. Muter. Sci.,*** **21,** 217 **(1986).**

26. G. SIMON and A. R. BUNSELL, " Creep Behavior and Structural Characterization at High Temperatures of Nicalon SiC Fibers, " ***J. Mater. Sci.,*** **19, 3658 (1984).**

27. R. M. CHRISTENSEN, "Theory of Viscoelasticity: An Introduction," Academic Press, **(1971).**

28. JAMES A. DICARLO and GREGORY N. MORSCHER, "Creep and Stress Relaxation Modeling of Polycrystalline Ceramic Fibers," in '*Failure Mechanisms in High Temperature Composite Materials,*' ASME **AD-Vol. 22, AMD-Vol.** 122, **1991,** Editors: G. K. **HARJTOS,** G. NEWAZ and S. **MALL.**

29. C. H. CARTER and R. F. DAVIS, " Kinetics and Mechanisms of High-Temperature Creep in Silicon Carbide: II, Chemically Vapor Deposited," ***J Amer. Ceram. Soc.,*** **67 No. 11 ,** 732 **(1984).**

30. T. D. GULDEN and C. F. DRISCOLL, "Creep of Chemically Vapor-Deposited **b-SiC** with an Analysis of Creep in Bending" Gulf General Atomic Company, **CA-10366 ,** February **16, 1971.**

31. R. JONES, " SiC-SiC Composite Development **for** Fusion Structural Applications," ***Presented in the US-Japan Workshop on Power Reactor Studies,*** March **14-17, 1994,** University of California, San Diego, USA.

Tritium transport and retention in silicon carbide - S.W. Tam, J. Kopasz, and C.E. Johnson (Argonne National Laboratory)

OBJECTIVE

The objective of this work was to develop a theoretical framework that would serve as an analytical tool for describing trapping, diffusion, and desorption of tritium from vapor deposited silicon carbide.

SUMMARY

A theoretical framework describing trapping, diffusion and desorption of tritium from vapor-deposited 0-silicon carbide has been proposed and an analytical version of this model was derived. This analytical model was used to extract trapping, diffusion, and desorption parameters from a limited part of the experimental data set. The resulting parameter-free model was then used to test its predictive capability by calculating the time-dependent release behavior for the high temperature regimes. General agreement with the release data was found supporting the suitability of the present approach. Tritium trapping was found to be strong. Both bulk diffusion and surface desorption make comparable contributions to tritium release from the silicon carbide. Improvements beyond the present analytical model to include dynamical detrapping can be achieved with the proposed framework.

PROGRESS AND STATUS

Introduction

Silicon carbide(SiC) has been proposed for application in various areas of fusion reactor technology, ranging from structural materials [1] to tritium containment barriers [2]. In most applications, the silicon carbide is likely to be in close proximity to tritium in its various forms. Therefore, understanding the behavior of tritium in SiC is of interest to fusion technology. Recent literature reports on tritium release from and dissolution in vapor-deposited β-silicon carbide have provided extensive data on the behavior of tritium in this form of material [2]. Depending upon temperature of the annealing experiment[2], the amount of the tritium released, expressed as a fraction of the quantity of tritium originally present, approaches a constant value substantially less than one (0.4-0.60) after 3000 to 4000 seconds. This seems to indicate that a substantial amount of the tritium remains trapped in the β-silicon carbide samples despite extensive high temperature anneals. The presence of such strong traps is very different from the behavior of tritium in most lithium ceramics which are being considered as tritium breeders for fusion technology. For most lithium ceramics, such as lithium oxide, tritium release is relatively rapid and the final tritium inventory is typically low [3]. Despite the fact that the vapor deposition method leads to sample materials that are very near theoretical density, this lack of porosity is unlikely to be the primary reason that tritium species find it difficult to migrate out of the solid as the samples only have a thickness of 80 μm [2, 4].

A theoretical framework has been constructed that describes the tritium transport processes in vapor deposited silicon carbide wherein trapping in the bulk is an important component. Diffusion and surface desorption processes are also included. Use of this model leads to analytical results which are particularly suited for analysis and understanding of time dependent behavior involving many process parameters that cannot be known a priori. Included in this model beside a description of the transport process there is also a statistical mechanical analysis of the trapping phenomenon. A careful discussion of how the quantity 'fractional release' should he defined by looking at how this same quantity has been determined experimentally completes the description of the model. The model was utilized to analyze and to understand the available experimental data. The characteristics of the trap were determined. The transport parameters were determined using release data at only two temperatures (1200 ^{0}C and 1300 ^{0}C). The model was then tested in a predictive mode on the detailed time dependence of the tritium release process at a higher(1500 ^{0}C) temperature. The merits and limitation of the model in the light of the confrontation between theory and data were discussed.

Theory

One of the main characteristics of the tritium release data from vapor deposited SiC in isothermal anneal experiments is that the fractional release seems to reach a saturated value significantly below unity. This seems to indicate at various temperatures substantial fraction of the tritium is unable to escape from the vapor-deposited SiC materials. Strong traps for tritium species in this type of materials would provide a natural explanation [2]. A general description of this class of transport process can be formulated in terms of a diffusion-trapping-desorption model. The bulk diffusion process is described with the following equation;

$$\frac{\partial n_f}{at} = D\frac{\partial^2 n_f}{\partial x^2} + K_d n_t - K_a n_f \qquad (1)$$

where n_f is the fraction of mobile tritium in the solid, n, is the fraction of trapped tritium, D is the diffusion coefficient for the mobile tritium, and K_d and K_a are the detrapping and trapping rate constants respectively. Note that within the present model the trapping and detrapping processes are assumed to be first order. The dynamics of the trapping/detrapping process are described by the following equation;

$$\frac{\partial n_t}{\partial t} = K_a n_f - K_d n_t \qquad (2)$$

There is no diffusive term for n, since one expects that the trapped tritium would be immobile within the time frame of the experiments. At the surface of the crystal a first order desorption process is used to model the departure of the tritium from the SiC surface into a He+ 0.1% Hydrogen purge **gas** stream [2]. The model assumes that the purge **gas** flow is efficient in removing the tritium from the solid and, therefore, it is not the rate-limiting step in the dynamics. This type of argument fixes the boundary condition for equation 1 to he of the following form:

$$D\frac{\partial n_f}{\partial x}\Big|_0 = K_{des} n_f \qquad (3)$$

where K_{des} is the surface desorption rate constant. This set of coupled equations together with the initial conditions which specify the distribution of n_f and n_t at time t = 0 would give a general description of the transport, retention and release of tritium from vapor deposited silicon carbide. However this general model is composed of coupled partial and ordinary differential equations which contain no less than four transport or solid state reaction parameters, namely D,K_a,K_d and K_{des}. These four parameters are in Arrhenius form, each having its own unknown preexponential and activation energy factors. Practical application of this model towards understanding the available tritium release data [2,4] would be nontrivial at best. To make further progress one needs to derive a well-justified approximation to this general model. This simplified model would be described below with a careful discussion of its physical basis.

By adding equations 1 and 2 one obtains the following equation;

$$\frac{a}{a\,t}(n_f+n_t)=D\frac{\partial^2 n_f}{\partial x^2} \qquad (4)$$

Note that at this point equation **4** is still 'exact' within the general model. No approximation has yet been made. However, as it stands, equation **4** is not useful because one does not know the relationship between n_f and n_t. To proceed further one needs to introduce a 'closure' relation between n_f and n_t so that equation **4** becomes solvable. There are two limiting cases to our general model in which this closure relationship can be derived. We shall discuss each of them in turn and utilize the physics of the release data to settle on the choice.

If the diffusion process **is** slow compared to the trapping-detrapping process then local equilibrium between the mobile and the trapped tritium would be maintained at all times within the silicon carbide as tritium migration proceeds. This equilibrium relationship is given by the following equation;

$$\frac{n_f}{n_T}=\frac{1}{(1+0.2231\frac{N_t}{N_f}\exp(\frac{E_B}{k_bT}))} \qquad (5)$$

Where $n_T = (n_f + n_t)$ is the total tritium present in the solid, N_t is the total number of traps, N_f is the total number of interstitial sites in which tritium is mobile, and E_B is the trap binding energy. $P_f = n_f/n_T$ represents the probability that a tritium is mobile. With the relation expressed in equation **5** one could rewrite equation **4** in the following form;

$$\frac{\partial n_T}{\partial t}=D_{eff}\frac{\partial^2 n_T}{\partial x^2} \qquad (6)$$

Here D_{eff} can be regarded as the effective diffusion coefficient of the tritium and is defined by $D_{eff}=DP_f$. Physically equation **6** describes the diffusion of the entire tritium population in the solid **as** if there is no trap present but with a apparent diffusion coefficient D_{eff} that has a decidedly nonarrhenius character. **More** importantly, as the tritium is released from the silicon carbide the trapped portion of the tritium population (i.e. n_t) would continue to be depleted via detrapping into the mobile state *so* as to maintain the required equilibrium between the mobile and the trapped tritium population. In this way the entire tritium content would be depleted eventually. Experimentally one should observe the fractional release as a function of time to approach a plateau of the value one. However this **is** in substantial contradiction to the observed behavior of tritium release from SiC [2]. **As** discussed in the introduction, the fractional release at 1300°C saturates at around 0.61. Similar behavior has been observed at other temperatures [2,4]. This implies that substantial fraction of the tritium population was held immobile in the solid during the entire annealing experiments. Therefore, the underlying assumption of equation 6 must be incorrect. That is, the mobile and the trapped tritium cannot be in equilibrium with each other during the entire release experiment. This leads to the other limiting case to **our** general model.

If the diffusion process is fast compared to the trapping/detrapping process, and that the traps are strong traps then n_f is only in equilibrium with n_T at t=0, the beginning of an experimental run. Subsequently, the only tritium that would be released is that already in the mobile state at the beginning of the experiment. In this model, all the mobile tritium would be released at long time at the end of the experiment. But the trapped tritium would remain trapped throughout the course of the experiment. This would provide a natural explanation of the saturation of the fractional release data that are much below unity. **Thus** within this model the release process is described with this equation;

$$\frac{\partial n_f}{\partial t}=D\frac{\partial^2 n_f}{\partial x^2} \tag{7}$$

Note that only the mobile tritium is involved in this equation. Likewise the desorption boundary condition involves only the mobile component of the tritium population at the surface. Equation 7 has the following analytical solution [5];

$$\frac{n_f(t)}{n_f(0)}=1-\sum_{n=1}^{\infty}\frac{2L^2}{\beta_n^2(\beta_n^2+L^2+L)}\exp\left(\frac{-\beta_n^2 Dt}{l^2}\right) \tag{8}$$

where $n_f(0)$ is the mobile tritium present at the beginning of the experiment, β_n is the n_{th} solution (n=0,1,2,...) to the equation $\beta\tan(\beta)=L$, $L=lK_{des}/D$, and l is the thickness of the SiC slab which in the present case is 40 μm[2].

The initial condition is a uniform distribution of tritium, $n_f(0)$, which is determined by the equilibrium between trapped and mobile state at temperature T of the particular release experiment. In the experimental approach the sample is brought to the furnace already at temperature [2,4]. Thermal equilibrium would be achieved in a short time but not instantaneously. So in the application of the present model only release data obtained at time *250* seconds or more after the start of the experiment would be utilized.

As it stands, equation 8 cannot yet be used to analyze the experimental data since the fractional release data was not normalized to $n_f(0)$ as was assumed in equation 8. The experimental normalization factor was obtained by first performing the release experiment (say at 1300°C) until saturation occurs. Then the temperature of the system was raised to 1600°C and all the releasable tritium at that temperature was collected and the sum total of the amount collected at both 1300 and 1600 degrees then is used as the normalization factor. The key is that the amount collected at 1600 degrees may represent most but not necessarily all the tritium remaining in the system.

Using equation 5 and the present discussion the correct renormalization factor R(T) at temperature T within our model is given by

$$R(T)=\frac{P_f(T)}{P_f(1600)\left[1+P_f(T)\left(\frac{1}{P_f(1600)}-1\right)\right]} \tag{9}$$

where $P_f(T)$ is simply the value of P_f evaluated at temperature T. Using this renormalization factor and equation 8 one finally obtains the fractional release F_{th} within our model. This is the quantity to be compared to the experimental data.

$$F_{th}=R(T)\,\frac{n_f(t)}{n_f(0)} \tag{10}$$

Equations 5, 8.9, and 10 represent the principal results of this paper. They are analytical in nature and therefore relatively easier to utilize. They are expressed in terms of the diffusion, desorption parameters and the trap characteristics (i.e. binding energy and concentration). In the next section this model would be utilized to extract these parameters and the predictive capability of the model would be determined.

Results and discussion

The present model implies that when the experimental release data as a function of time reaches a plateau it indicates that the mobile tritium has been released (relative to the normalization factor discussed in the last section). This means that the experimental value of the fractional release at saturation should be described by equation . The two data points at 1200 C (at 4000 seconds) and at 1300 ^{0}C(at 2800 seconds) were utilized in conjunction with equation to obtain a trap binding energy of 1.61 eV with a trap fractional concentration of 2.16×10^{-5} . The energetics indicates fairly strong traps for tritium with a reasonably high trap concentration which is consistent with the fundamental thesis of the model, namely that trapping is strong and is important in the release of tritium from vapor-deposited β-SiC. A plot of the fraction of mobile tritium, P_f is shown in Figure 1. A clear non-arrhenius behavior can be seen throughout the plotted temperature range of 1000 "C and 1700 "C. Note that at 1600 ^{0}C most (over 90%) hut not all of the tritium is mobile. This supports the notion discussed in the last section that caution is needed in analyzing fractional release data since it depends on the way the results are normalized.

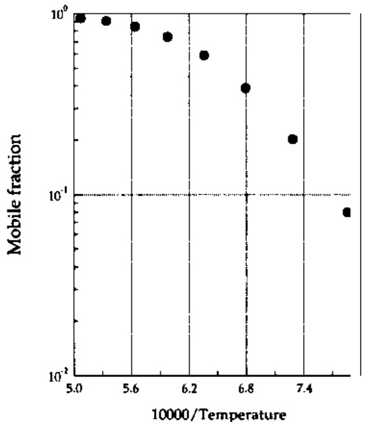

gure 1 Fraction of mobile tritium versus reciprocal temperature ($^0K^{-1}$)

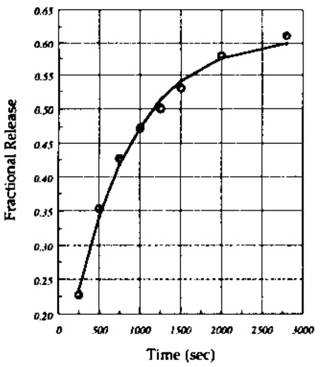

igure 2 Calculated release curve fitted to release data at 1300 ^{0}C (,solid curve - calculation; circle - data [2])

Once the trap characteristics have been determined, one can utilize the tritium release spectra at two temperatures (eg. 1200 "C and 1300 ^{0}C) and equation 10 to extract the diffusion and desorption parameters D and K_{des} respectively. Figure 2 indicates excellent tit to the data has been obtained with the following results for the two transport parameters, where $D = 1.688\times10^{-4} \exp(-1.11\ eV/K_bT)\ cm^2$ per sec., $K_{des} = 0.0322 \exp(-1.174\ eV/K_bT)$ cm per sec, and K_B is the Boltzmann constant and T is temperature in degree Kelvin.

A plot of log D with respect to the inverse temperature is shown in Figure 3. The diffusivity lies between the range of 10^{-7} and 10^{-8} **cm^2 per** sec in the temperature range of 1100 to 1600 ^{0}C. This indicates relatively rapid diffusion which is not surprising at such high temperatures . The range of values is **in-**between several sets of data on tritium diffusion in SiC reported in the literature [6]. The result is consistent with the physical basis of the present model which postulates that diffusion is fast relative to trapping/detrapping.

More importantly the determination of D and K_{des} allow one to estimate L. Physically L is a measure of the relative contribution of diffusion versus desorption to the transport process of tritium in silicon carbide. **A** large value of L (say, 10 or larger) would indicate diffusion-limited process while a small value(say 0.1 or smaller) would suggest surface desorption to be rate-limiting. If L is of the same order of unity then one may say both processes are important and no one process is dominant. Figure **4** indicates that throughout the temperature regime of interest. L is of the order of unity. This suggests that for the present system diffusion and desorption processes are of comparable importance. Note that the system size l enters into the consideration for L. In the present case a small diffusion distance of 40 μm plays a part in rendering diffusion not to be the dominant process.

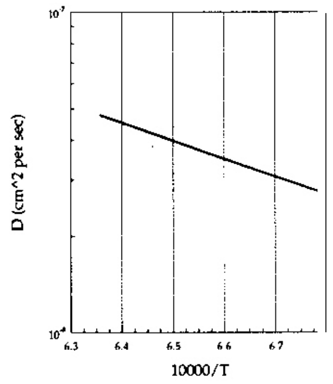

gure 3 Diffusion coefficient D versus reciprocal temperature ($^0K^{-1}$)

With the determination of all the trapping and transport characteristics, the present framework becomes a model with no adjustable parameters . In order to test its validity, the model was then applied to estimate the complete time dependent release behavior of tritium from silicon carbide at a higher (1500 ^{0}C)temperature regime. The comparison with experimental data [2,4] is shown in Figure **5**.

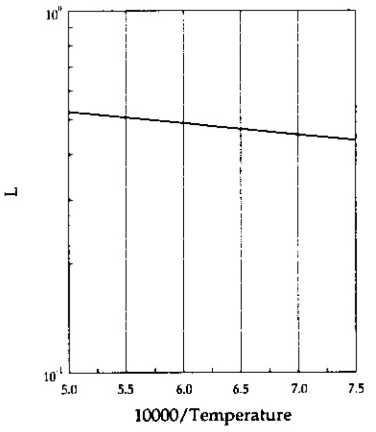

igure **4** The parameter L = 1 K_{des} I D versus reciprocal temperatures ($^0K^{-1}$)

The agreement with experiment is very good up to about 2000 seconds into the release process. Thereafter there appears a relatively small(a maximum of 15%) but systematic deviation between theory and experiment. To understand this point one recalls that the present theory is based on the assumption that no trapped tritium would be released during the entire experimental run. The amount that is releasable can only come from tritium that is already mobile near the start of the experiment. This argument is likely to work very well for lower temperature release (eg. those at 1300 "C or below). Indeed, the present direct calculations have confirmed this. However, for higher temperatures(such **as** at 1500^0C) one would expect, on physical grounds, that as the mobile tritium was depleted detrapping would become increasingly strong. This effect would become increasingly important in the latter stages of the release. As a result the good agreement between theory and experiment would diminish. This corresponds precisely to the observed behavior. To remedy this effect one would need to describe the actual dynamics of the trapping/detrapping process. This is already incorporated within the general framework as represented by equation 1 and 2. Thus, should high levels of accuracy be required in future analysis (say better than 15%), the general model is already available as presented here. However, the computational effort required would be substantially more than is allowed by the approximate version used in this work. At the same time. the relatively small deviation between our analytical model and experimental data clearly indicates that the dynamical detrapping effect, while not negligible, is not likely to he an overwhelming part of the process.

Conclusion

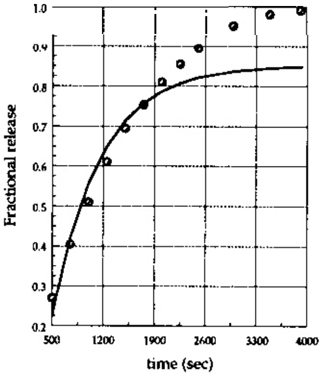

Figure **5** Calculated release curve (with no adjustable parameter) compared to data at 1500 "C (solid curve - calculation; circle - **data** [4])

A general theoretical framework for describing trapping, diffusion and desorption of tritium from vapor-deposited β-silicon carbide has been proposed. An approximate analytical version of this model was derived. The model develops from the assumption that diffusion is fast relative to trapping/detrapping, an assumption that is based on features of the available experimental release data. This analytical model was then used to extract trapping, diffusion and desorption parameters from a limited part of the experimental data set. The resulting parameter-free model was then tested against other parts of the data sets. Calculations were performed with no adjustable parameters to obtain time-dependent release behavior at the high temperature regimes. Good general agreement with the release data was found. This provides supports for the general validity of the present approach. The results indicate that trapping is strong in vapor-deposited β-silicon carbide. Both diffusion and surface desorption plays a comparable role in tritium release from this material. A **15%** underestimate of the fractional release data was observed for the high temperature case **at** the long time limit. It was argued that this deviation between theory and experiment arose from dynamical detrapping effect which was neglected in the analytical model. However the deviation though not negligible, nevertheless does not represent a large effect thereby suggesting that dynamical detrapping cannot be an overwhelming part of the release process even at the higher temperature regime. It was suggested that for a proper inclusion of dynamical detrapping it is necessary to return to the general framework originally proposed.

FUTURE ACTIVITIES

Future activities would include an implementation of the full dynamical model as contained in equation (1) and (2). The nature of the traps in SiC for tritium as discussed here would be investigated via ab initio quantum cluster calculations.

References

1. "The ARIES-I Tokamak Reactor Study, Final Report," Vol. I and II, UCLA-PPG-1323 (1991).
2. R. A. Causey, W. R. Wampler, J. R. Retelle, and J. L. Kaae. J. Nucl. Mater., 203 106 (1993).
3. J. P. Kopasz, C. E. Johnson, and D L. Baldwin, this conference (1994).
4. R. A. Causey, private communication (1994).
5. J. Crank, "The Mathematics of Diffusion." Clarendon Press, Oxford (1979).
6. See reference 2 and references therein.
7. N. F. Mott and R. W. Gurney, "Electronic Processes in Ionic Crystals," Clarendon Press, Oxford (1950).

RADIATION-INDUCED CHANGES IN ELECTRIC, DIELECTRIC AND OPTICAL PROPERTIES OF CERAMICS -- S.J. Zinkle (Oak Ridge National Laboratory)

OBJECTIVE

The objective of this study is to review published data on several key physical properties of ceramic insulators.

SUMMARY

The data base on radialion-induced changes in the electric and dielectric propenies of ceramic insulators is reviewed. Ionizing radiation causes a prompt increase in the electrical conductivity that is generally proportional to the ionizing dose rate. The precise magnitude of the radiation induced conductivity is sensitive to the detailed manufacturing process and impurity content. The conflicting evidence regarding the possibility of permanent radiation induced electrical degradation (RIED) is summarized. Further work is needed to define the physical mechanism and practical operating limits of the RIED phenomenon. Displacement damage associated with neutron irradiation produces significant increases in the room temperature dielectric loss tangent of oxide ceramics for fast neutron fluences above $1x10^{22}$ n/m^2 (~0.001 dpa). A brief summary of the effects of irradiation on the optical properties of ceramics and silica optical fibers is also presented.

PROGRESS AND STATUS

1. Electrical Conductivity

It has long been known that the electrical conductivity of insulating and semiconducting materials can be dramatically increased by energetic radiation, due to the excitation of valence electrons into the conduction band. The phenomenon of radiation induced conductivity (RIC) was apparently fist discovered in 1873, when the semiconductor selenium was observed to become more conductive during exposure to light [1]. Similar photoconductivity experiments on different insulating materials followed around the turn of the century using X-ray [2] and gamma ray [3] sources. Radiation induced conductivity was subsequently observed to be a general phenomenon in insulators irradiated with ionizing radiation, including electron and alpha particle sources [4,5]. Despite these early experimental observations, a sound theoretical understanding of RIC incorporating the general features of carrier excitation, trapping and recombination did not occur until the 1950s when models by Rose [6] and Fowler [7] were published. There are numerous books and review articles devoted to photoconductivity and RIC [8-15]. The term photoconductivity has historically been limited to induced conductivity associated with photon radiation sources, i.e., light. X-rays and gamma rays, whereas RIC is the more general term for any type of ionizing radiation source [9].

Accurate measurement of RIC in ceramic insulators requires several experimental precautions. A suitable guard ring geometry [16] is required to minimize surface leakage currents. However, it should be recognized that significant surface leakage currents may occur during irradiation even when guard rings are utilized, due to the deposition of conductive surface films from the surrounding atmosphere [17]. Ionization of the surrounding atmosphere can produce spurious currents unless the pressure is below about 0.1 Pa, and the maximum ionization currents occur at intermediate pressures of ~10 to 100 Pa [18]. This gas ionization is a particularly difficult problem for fission reactor RIC measurements. The measured radiation-induced current depends strongly on the behavior of the metallic electrodes that are in contact with the insulator [9-12]. Two general categories of electrode behavior are possible. depending on specimen surface preparation, the method of electrode deposition, and the relative work functions (electron affinities) of the electrode and insulator. Many vacuum-deposited metals act as *blocking electrodes* (also known as rectifying contacts) at low and intermediate field strengths, i.e., charge carriers are not easily transferred from the electrode to the insulator, but charge carriers may he removed from the insulator by the electrode [11]. This can lead to the formation of Schottky barriers at the electrode-insulator interface. The preferred contacts are *ohmic electrodes,* which produce a linear relation between current and voltage.

However, all ohmic contacts tend to inject excess charge carriers into the insulator when the applied electric field exceeds a certain value [9,10]. This leads to space-charge-limited current flow and non-ohmic behavior. RIC associated with ionizing radiation tends to increase the upper limit of the electric field for ohmic behavior by reducing space-charge effects in the insulator. In practice, ohmic behavior must be experimentally verified (with and without ionizing radiation) in both the forward and reverse current direction to determine the allowable range of electric fields.

1.1 Transient Radiation Induced Conductivity

Any source of radiation that is sufficiently energetic to ionize the atoms in a ceramic insulator by imparting kinetic energy to the valence electrons in excess of the band gap energy (typically a few eV) can produce radiation induced conductivity. Many of the ionized electrons and associated holes recombine within ~10^{-11} s in the vicinity of their parent ion and do not contribute to any current flow (geminate recombination) [12]. Electrons and holes that escape geminate recombination can diffuse under an applied electric field and produce RIC. Structural imperfections in the crystal, such as impurities, create trapping sites for the diffusing electrons and holes which further modifies the RIC behavior. Two types of trapping sites are possible: ***recombination centers***, where the captured charge carrier recombines with a carrier of opposite charge, and ***trapping centers***, where a charge carrier is temporarily captured and is thermally reexcited into the conduction band before recombination occurs [10, 12]. The demarcation between ***recombination*** and ***trapping centers*** is approximately the Fermi energy level (E_F). Electrons captured in sites more than E_F from the conduction band will generally experience recombination with a hole since thermal reexcitation into the conduction band is negligible, whereas electrons lying in sites within E_F from the conduction band will generally be thermally excited back into the conduction band before recombination occurs and are therefore temporary *trapping centers* [10].

There is a large data base on the instantaneous increase in electrical conductivity of ceramics induced by exposure to ionizing radiation [9, 12-15, 18-34]. The high mobility and capture cross sections of electrons and holes in the conduction band generally results in recombination of the electron-hole pairs created by ionizing radiation within <10^{-9} s [12]. Hence, RIC measurements must be performed in-situ while the specimen is being irradiated. The electrical conductivity of the ceramic generally reverts to a value very near its preirradiation value immediately after the irradiation source is turned off [12, 18, 28], although in some cases the time constant for decay of the RIC can be seconds or days [11, 35]. This delayed conductivity is due to thermal emission of charge carriers from *trapping centers* which are located near the Fermi energy level ("deep traps").

Figure 1 shows a typical example of the temperature-dependent RIC of alumina measured during exposure to ionizing radiation [26]. The RIC is only weakly dependent on temperature at low irradiation temperatures, which is an indication of predominantly deep trapping sites. Various studies have observed either a slight increase [25,26,30, 33] or decrease [25] in the RIC with increasing temperature in the range of 25 to 400°C. At high irradiation temperatures, the RIC curve gradually merges with the nonirradiated electrical conductivity curve.

The electrical conductivity measured during irradiation can generally be described by the simple power law relation

$$\sigma=\sigma_0 + K R^{\delta} , \tag{1}$$

where σ_0 is the conductivity in the absence of irradiation, R is the ionizing dose rate, and K and δ are constants which depend on the material and irradiation conditions [6, 12, 14, 24]. The proportionality constant K has typical room temperature values of 10^{-12} to 10^{-9} s/(Gy Ω m) for ceramic insulators. The dose rate exponent δ has been observed to vary between 0.5 and 1 for most materials [9, 10, 12, 15]. Several experimental studies have shown that the detailed behavior of δ depends on both temperature and defect concentration [10, 14, 25, 26, 32, 33], with reported values as low as 0.5 and as high as 3 to 5. The supralinear behavior is generally only observed over a narrow range of ionizing fluxes [10, 33] Theoretical models incorporating multiple trap levels have been developed to explain the different dose rate responses [10, 12, 25].

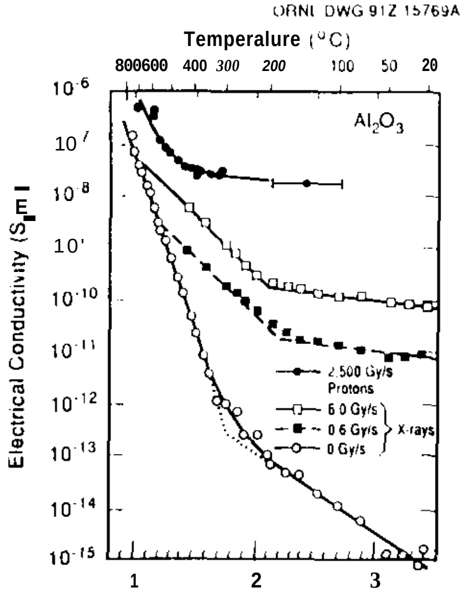

Fig. 1. Electrical conductivity of polycrystalline alumina versus reciprocal temperature, with and without ionizing radiation [26]. The 18 MeV proton ionizing dose rate given in the originally published paper has been corrected using the revised dose rate relation 1 nA/cm^2 = 21 Gy/s [33].

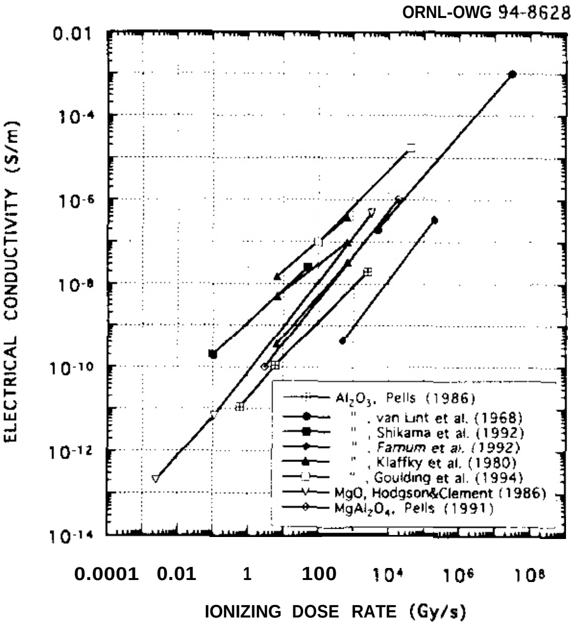

Fig. 2. Radiation induced conductivity of pure oxide ceramics measured during irradiation near room temperature [18,24-28,32,33]. All of the measurements were made on Al_2O_3 except for Hodgson and Clement [32] and Pells [33] which were made on MgO and $MgAl_2O_4$, respectively. The data by Farnum et al. [28] are previously unpublished results on a specimen irradiated at 25°C to 10^{-3} dpa with 3 MeV protons.

Figure 2 summarizes RIC data that has been obtained on high-purity Al_2O_3, MgO, and $MgAl_2O_4$ during irradiation near room temperature [18, 24-28, 32, 33]. The room temperature conductivity in the absence of radiation was $<10^{-13}$ S/m in these materials. It can be seen that the RIC for these three oxide insulators is approximately proportional to the ionizing dose rate ($\delta \sim 1$) over a very wide range (10 orders of magnitude) of ionizing flux. The precise magnitude of the RIC depends on the concentration and nature of impurities in the ceramics, which act as trapping and recombination centers for the electron and hole charge carriers. For example, *Klaffky* et al. [25, 29] observed that the RIC in single crystal Al_2O_3 (sapphire) was decreased by more than an order of magnitude by the addition of 0.03 wt% Cr_2O_3. On the other hand, Goulding et al. [18] found similar values of RIC in pure sapphire and polycrystalline Al_2O_3 containing between 0.02 and 3 wt% impurities. Hence, the most important factor for charge carrier trapping is not necessarily the bulk concentration of the impurity but rather its spatial distribution and chemical bonding state (valence, etc.). Prolonged exposure of a sample to radiation sources that produce displacement damage generally has been found to produce a decrease in RIC, due to the creation of point defects and defect aggregates that act as charge carrier trapping or recombination centers [15, 17, 20, 28, 29, 36, 37]. For example, the RIC data by Farnum et al. [28] in Fig. 2 was obtained on a sapphire specimen irradiated with protons at room temperature to a damage level of about 10^{-3} dpa, and had about a factor of 40 lower RIC than the virgin material. The apparent exception to this behavior is radiation induced electrical degradation [36], which only occurs if a sufficiently large electric field is applied during the irradiation, and will be discussed in the following section.

Most RIC studies performed to date have only considered the overall magnitude of the ionizing radiation, and have assumed that the spatial distribution of the ionization is not important. There is some theoretical [38] and experimental [21] evidence that the prompt RIC may be less in insulators exposed to densely ionizing radiation sources compared to diffuse or weakly ionizing radiation. due to enhanced electron-ion geminate recombination. However, the overall effect of ionization density appears to be small, since there is no correlation between ionization density and RIC behavior for high purity Al_2O_3 irradiated with X-rays, gamma rays, electrons, protons, and neutrons (e.g. Fig. 2) [18, 24-28].

1.2 *Permanent Electrical Conductivity Changes*

There have been numerous studies of the effect of prolonged irradiation on the electrical conductivity of ceramic insulators. Under certain irradiation conditions. it is possible to inject charge carriers into the insulator and thereby increase the postirradiation electrical conductivity for a limited period of time [11]. However, prolonged irradiation without an applied electric field generally produces either no change or a moderate *decrease* in the postirradiation electrical conductivity compared to the preirradiation value [15, 17, 20, 28, 29, 36, 37, 391. The decrease in conductivity occurs in specimens subjected to displacement damage, which produces !sapping sites for the charge carriers.

Several recent studies indicate that severe permanent increases in the electrical conductivity of ceramic insulators may occur during extended irradiation if an electric field is applied during the irradiation [36, 37, 40-49]. This radiation induced electrical degradation (RIED) apparently develops in oxide ceramics at moderate temperatures of about 200 to 600°C after irradiation to rather low damage levels of 10^{-5} to 0.1 dpa. RIED has been reported for single crystal and polycrystal Al_2O_3 [36, 37, 40-49], MgO [40] and $MgAl_2O_4$ [37] irradiated with electric fields greater than about 20 V/mm. The effect of RIED is to increase the base conductivity (σ_0 in eq. 1). Some studies have reponed permanent postirradiation electrical conductivities $>10^{-4}$ S/m in degraded samples [37], which could severely limit the usefulness of ceramic insulators in radiation environments.

Significant degradation in the electrical resistivity of electron irradiated Al_2O_3 has been reported for electric fields as low as ~20 V/mm, and the degradation process is accelerated if the electric field is greater than ~75 V/mm [43, 44]. It is worth noting that most insulator applications in nuclear radiation environments require continuously applied electric fields of 10 to 1000 V/mm [e.g., 15]. In contrast to the well-known phenomenon of electrothermal dielectric breakdown in nonirradiated ceramics [50], RIED has been reported to occur not only in dc electric fields, but also ac fields up to at least 126 MHz [43, 44].

There is apparently a strong temperatnre dependence to the RIED process, with the largest degradation in insulators such as Al_2O_3 occurring near 450°C [15, 45, 46]. Little or no degradation has been observed in Al_2O_3 or Y_2O_3 for neumn doses of 0.01 to 0.5 dpa at temperatures of 615 to 1100°C with an applied dc electric field of ~40 to 150 V/mm [51-54]. Similarly, RIED was not observed in $MgAl_2O_4$ or Al_2O_3 irradiated with 18 MeV protons at temperatures >600°C [55]. Electron irradiation studies indicate that the lower temperature limit for RIED in Al_2O_3 is about 150°C [46], whereas proton irradiations conducted at a somewhat higher damage rate found that significant levels of RIED did not occur if the irradiation temperature was below ~3WC [37]. RIED was not observed in Al_2O_3 irradiated with fission neutrons at 80°C up to ~0.11 dpa with an applied electric field of 130 V/mm [56].

The phenomenon of RED has only been observed in specimens subjected to radiation sources which produce displacement damage, which suggests that the physical degradation mechanism involves some type of point defect aggregation. Unfortunately. the physical process responsible for the electrical degradation remains uncertain. Hodgson [36, 42-47] has suggested that colloid (small metallic precipitate) formation may be the cause, based on optical microscopy, the general temperature and dose rate dependence of the process, and optical absorption (F and F^+ center) measurements. However, transmission electron microscopy has failed to detect colloid formation in either degraded or nondegraded samples irradiated with an applied electric field [49, 55,571. Furthermore, the irradiation temperature corresponding to the peak amount of electrical degradation (~450°C) is several hundred degrees below the peak void swelling temperature for these materials [58]. Since colloid formation and void swelling both involve nucleation and growth of vacancy type defects. a similar temperature dependence would be expected for both processes.

Figure 3 compares the results of several RIED studies on Al_2O_3 that were performed near the peak degradation temperature of 450 to 500°C [36, 37, 48, 57]. Significant permanent degradation was observed in the electron irradiated specimens after $<10^{-4}$ dpa, whereas ~0.1 dpa was required to induce RIED during fission neutron irradiation. The inability to correlate the RIED results obtained in different irradiation sources with displacement damage level suggests that additional physical processes need to be considered, such as damage rate [47] and irradiation spectrum [59]. From Fig. 3. is appears that irradiation sources such as electrons which produce isolated point defects and high levels of ionization per atomic displacement may cause accelerated RED kinetics compared to fission neutrons, which produce relatively dense populations of defects in spatially localized regions and low levels of ionization per atomic displacement. It is well established that irradiation spectrum can have a strong influence on the microstructural evolution of ceramic insulators such as Al_2O_3 and $MgAl_2O_4$, and that point defect diffusion in ceramics can be greatly enhanced by ionizing radiation [59]. Hodgson [47] has also recently noted that the lower damage rates employed in the electron irradiation experiments would he expected to induce RIED at lower damage levels compared to high damage rate (fission neutron) experiments, if point defect aggregation is responsible for RIED (simple chemical rate theory predicts a square root dependence on dose rate).

ORNL-DWG 92M 12122R2

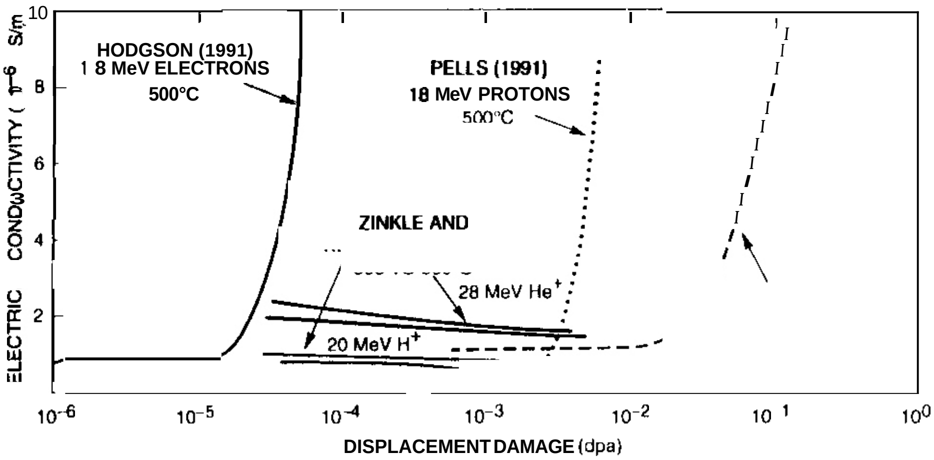

Fig. 3. Effect of extended irradiation in different radiation fields on the electrical conductivity of Al_2O_3. The electric fields present during irradiation ranged from 130 V/mm [36] to 500 V/mm [37,48,57]. The displacement damage rates ranged from $\sim 5\times10^{-10}$ dpa/s for the electron irradiation to about 1.5×10^{-7} dpa/s for the neutron irradiation.

Several recent studies have suggested the possibility that RIED may be due to surface leakage currents, instead of hulk conductivity changes [17,60]. It was concluded in these studies that hydrocarbon deposition onto the specimen surface from residual gases in an evacuated target chamber could modify the optical absorption and surface electrical conductivity during irradiation, thereby creating an apparent "bulk" RED effect. Application of an electric field during irradiation was found to dramatically increase the electrical conductance of the surface film compared to the zero field case (perhaps by modifying the chemical nature of the deposited film) [60]. Further support for the importance of atmospheric contamination was obtained from a side-by side neutron irradiation experiment on Al_2O_3 [54]. No evidence for RED was obtained in capsules filled with Ar gas during irradiition to about 0.03 dpa at temperatures of 395. 615, and 655°C with a dc applied field of 50 and 150 V/mm. On the other hand, conductivity increases similar to the RIED curves (Fig. 3) were observed in specimens irradiated with an ac applied field of 130 V/mm in capsules that were evacuated and sealed before irradiation. Postirradiation examination of the specimens from the evacuated capsules is currently in progress, and will help determine if a conductive surface film caused the RIED-like behavior for these specimens. It should be noted that the neutron irradiation study shown in Fig. 3 which reported evidence for RIED was performed in a capsule that was evacuated and sealed prior to irradiation [48].

Further work is clearly needed to resolve the questions surrounding the RIED phenomenon, namely: *Is* RIED a bulk or a surface irradiation effect, and what are the physical mechanism responsible for RIED? Colloid formation does not appear to be a likely mechanism for the electrical degradation, since a high volume fraction of metallic precipitates would be required to increase the electrical conductivity of Al_2O_3 to $>10^{-5}$ S/m. In addition, colloid formation has not been observed by electron microscopy, even in specimens which have apparently suffered RIED [49]. On the other band, the work by Zong et al. [49] indicates that specimens subjected to an electric field during irradiation experience significant bulk microstructural changes in their dislocation density. The average dislocation density in single crystal Al_2O_3 irradiated with an electric field of –210 V/mm was found to be $\sim 10^{13}/m^2$, compared to $\sim 10^8/m^2$ in regions irradiated without an electric field. The dislocations were heterogeneously grouped in low-angle subgrains [49], suggesting that RIED may he somehow associated with polygonization. The microstructure observed in the regions exposed to the electric field are reminiscent of the microstructure observed in dielectrics subjected to high temperature thermoelectric breakdown [61].

Recent work by Hodgson [45, 46] suggests that the production of F^+ centers (anion vacancy containing a trapped electron) is enhanced during irradiation with an applied electric field. The F^+ center is expected to be more mobile than the F center [62], which could lead to defect aggregation at lower temperatures than normally occurs (i.e., without an applied electric field) and could explain the discrepancy between the location of the RIED and void swelling temperature peaks. Radiation effects studies on semiconductors suggest that applied electric fields may also enhance the defect production rate [62]. Finally. the possible role of space charge effects on the development of RIED needs funher study. Large inhomogeneous electric fields can be induced in dielectrics by trapped charges [63] and by electromagnetic radiation [64,65]. It is conceivable that local amplification of the electric field applied during the RIED experiments may occur, which could lead to localized dielectric breakdown.

2. Dielectric breakdown strength

Most ceramic insulators can withstand electric fields up to about 10^7 V/m at room temperature without suffering permanent dielectric breakdown. Bulk dielectric breakdown occurs by either the avalanche or thermal (joule heating) mechanism, depending on the material, temperature, and duration of applied voltage [66]. The avalanche mechanism is dominant at low temperatures and for short voltage pulses, and occurs when electron motion induced by the electric field is sufficiently energetic to produce ionization from electron-electron collisions. The thermal mechanism is associated with the increased electrical conductivity that occurs with increasing temperature in insulators. If the joule heating associated with current flow in a dielectric is sufficiently high to increase the bulk temperature, further increases in current are produced until runaway and breakdown occur. The dielectric breakdown strength of ceramics generally decreases with increasing temperature. due to the increased importance of thermal breakdown at elevated temperatures. Typical breakdown strengths for oxide insulators at 1200°C are – 1 6V/m [67].

Irradiation appears to have a relatively minor effect on the dielectric breakdown strength of ceramic insulators. Postirradiation tests have shown that the room temperature breakdown strength was essentially unchanged in Al_2O_3 and other oxide ceramics following irradiation at 100 to 340°C to a fluence of 0.15 to 2.2×10^{26} n/m^2 (E>0.1 MeV) [68]. Similar results were also obtained for Al_2O_3 irradiated at 650 and 830°C to a flnence of 1 to 2×10^{26} n/m^2 (E>0.1 MeV) [69]. A slight degradation in the dielectric breakdown strength of Al_2O_3, ThO_2 and ZrO_2 was found during exposure to an X-ray field of about 5 Gy/s at temperatures below 200°C [70]. The X-rays did not affect the breakdown strength at temperatures above 200°C, due to the increased importance of field-enhanced thermal emission compared to RIC effects [70]. Concurrent ionizing radiation of 0.5 Gy/s did not affect the breakdown strength of BeO or Al_2O_3 at any temperature between 25 and 650°C [30].

3. Dielectric properties: dielectric constant and loss tangent

The power **absorbed** by a low-loss dielectric from an incident electromagnetic wave is dependent on two material parameters, the dielectric permittivity (ε) and the **loss** tangent ($\tan\delta$). The **loss** angle, 6. is related to the phase difference between the applied ac field and the resulting current. For an ideal loss-free dielectric, the current leads the voltage by 90' and the **loss** angle $\delta=0$, whereas in real dielectrics the phase difference **between** the current and voltage is $90^{\circ}-\delta$ [71]. Rigorously, the loss tangent is defined **as** the ratio $\varepsilon''/\varepsilon'$ **of** the imaginary to the real part of the permittivity, where $\varepsilon=\varepsilon'-i\varepsilon''$. From an integration **of** the product of **the** voltage and current, the power absorbed in the dielectric is given by [71]

$$P=\omega\,\varepsilon\,\tan6\,E^2 \qquad (2)$$

where ω is the angular frequency of the ac electric field with root mean square amplitude E. The product ε tan6 is commonly referred to **as** the dielectric **loss** factor.

For high power applications such **as** radio frequency beating of the plasma in fusion reactors, it is desirable to have the lowest possible **loss** factor in order to minimize thermal stresses associated with power absorption. The dielectric permittivity of most ceramic insulators is approximately $10\,\varepsilon$, over a wide range of temperature and frequency, where ε_0 is the permittivity of free space [71]. On the other hand, the value of tan6 exhibits a pronounced dependence on temperature and frequency [72-74]. Impurities have a relatively minor effect on the permittivity, but *can* cause dramatic increases in the loss tangent over several decades in frequency [71-74]. The **loss** tangent can be represented **as** the **sum** of contributions from electrical conduction and polarization losses [71, 76]:

$$\tan\delta=\frac{\sigma}{\varepsilon\omega}+\frac{\chi''\varepsilon_o}{\varepsilon} \qquad (3)$$

where σ is the electrical conductivity (eq. 1) and χ'' is the imaginary part of the electric susceptibility. The electrical conductivity term is generally negligible compared to the polarization term unless there is a large amount **of** RIC. A typical loss tangent for **a** low-loss dielectric such **as** Al_2O_3 at 100 MHz is $\tan\delta\sim10^{-4}$ at room temperature, and the electrical conductivity required to produce this **large** of a **loss tangent** would be $\sigma\sim5\times10^{-6}$ S/m. The **loss** tangent generally decreases at all frequencies with decreasing temperature below room temperature. **Loss** peaks associated with impurities *can* produce complex behavior in the **loss** tangent at elevated temperatures, but the general trend is an increase in the **loss** tangent with increasing temperature [72-74].

Postirradiation measurements indicate that radiation-induced changes in the permittivity are generally **small** (~1 to *5%)*. with either slight increases [76, 78-80] **or** decreases [77] reported. **A** slight decrease (–1%) in the permittivity of several ceramic insulators was measured during pulsed neutron irradiation with peak ionizing dose rates *up* to 4×10^4 *Gy/s* at room temperature. due to electrical conductivity increases **associated** with RIC [18].

Displacement damage *can* produce large increases in the **loss** tangent, with the magnitude of the increase depending on the **material,** irradiation conditions, and measurement frequency [73, 75-88]. Most of the irradiated **loss** tangent measurements have been performed on Al_2O_3, with relatively few studies performed on $MgAl_2O_4$ [18, 82. 86. 881. BeO [77, 85], AlN [18, 82], Si_3N_4 [18, 86, 88] and AlON [84, 86. 88]. All **of** the ceramic materials appear to behave in a qualitatively similar manner, although significant quantitative differences *can* occur (due mainly to **as** yet unresolved impurity effects). Figure 4 summarizes some *of* the postirradiation **loss** tangent measurements made at frequencies greater **than** 1 *MHz* on Al_2O_3 **irradiated near** room temperature [75, 76, 81, 82]. Neutron irradiation fluences up to about 1×10^{22} n/m^2 (–0.001 dpa) produce only small increases in the **room** temperature **loss** tangent. Large increases in the loss tangent occur over a wide frequency range for neutron fluences above 1×10^{22} n/m^2.

Irradiation at elevated temperatures requires progressively higher neutron fluences to induce comparable degradation in the loss tangent. For example, the room temperature loss tangent of Al_2O_3 measured at 95 GHz increased from 3.9×10^{-4} to 8.3×10^{-4} after irradiation to a neutron fluence of 1×10^{26} n/m^2 (E>0.1 MeV) at 385°C [77], whereas a similar amount of degradation was observed in this frequency range for Al_2O_3 irradiated to only ~3.5×10^{23} n/m^2 (E>0.1 MeV) at 60°C [81]. Radiation-induced point defects that contribute strongly to dielectric loss are known to be thermally unstable at temperatures above room temperature from postirradiation annealing experiments on Al_2O_3 [81, 89, 90]. This causes the rate of loss tangent degradation to decrease with increasing temperature above room temperature. In addition, the predominant type of defect produced during irradiation changes from point defects at low temperatures (which are effective at increasing the loss tangent) to defect aggregates and dislocation loops at elevated temperatures (which are less effective at increasing the loss tangent per atomic defect).

There is evidence that significant annealing of the induced loss tangent degradation in ceramics may occur at room temperature. Postirradiation measurements on Al_2O_3, $MgAl_2O_4$ and AlON irradiated with protons near room temperature to damage levels of ~0.02 dpa found that a substantial part of the loss tangent increase at 100 MHz was recovered within a matter of hours [86, 88]. Since most loss tangent measurements on neutron irradiated samples are typically made several months after the irradiation (to allow for the decay of radioactivity), postirradiation measurements made on samples irradiated near or below room temperature may be an underestimate of the in-situ loss tangent. There have only been a few attempts to measure the in-situ loss tangent of ceramics during irradiation [18, 85, 87]. Pulsed fission reactor irradiation at very high damage rates (~4×10^4 Gy/s) caused a significant prompt increase in the loss tangent at 100 MHz of several ceramics due to radiation induced conductivity (cf. eq. 3), but the damage levels in this study were not high enough to investigate point defect annealing behavior [18]. A measurable increase in the loss tangent of Al_2O_3 was detected during proton irradiation at 300 K for damage levels greater than ~10^{-4} dpa, and the loss tangent became larger than 10^{-3} for damage levels $>10^{-3}$ dpa [87]. This in-situ degradation is about an order of magnitude higher than that determined from postirradiation tests performed on neutron irradiated samples (cf. Fig. 4).

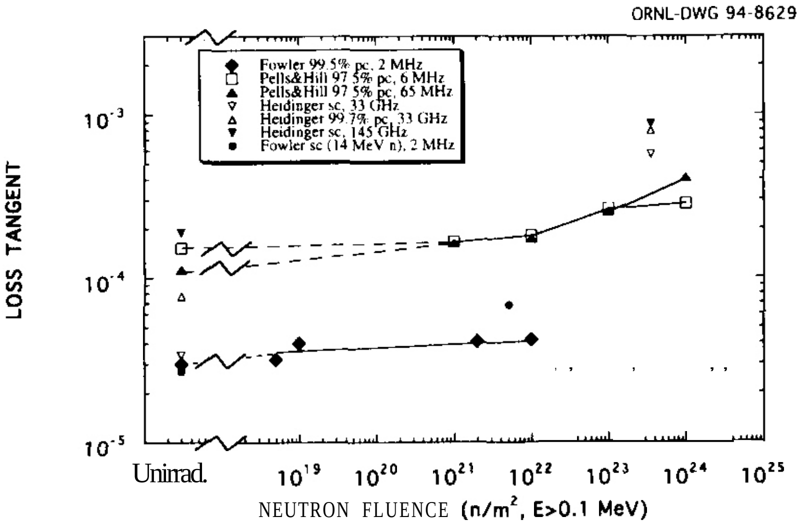

Fig. 4 Effect of neutron irradiation near room temperature on the loss tangent of polycrystalline (pc) and single crystal (sc) Al_2O_3 [75,76,81,82]. All of the measurements were performed postirradiation at room temperature at the indicated frequency.

4. Optical properties

One of the characteristic features of dielectric materials is their good transmission at frequencies corresponding to the optical part of the electromagnetic spectrum [91]. Absorption of light is generally small in ceramic dielectrics between the infrared and ultraviolet wavelengths of ~100 µm and ~100 nm, respectively. Irradiation-induced defects in dielectric materials can reduce transparency by serving as resonant absorption and scattering centers. The strong coloration of irradiated ceramics results from defects having energy levels of opposite parity within the band gap [92, 93]. This produces a unique resonant scattering frequency for each individual type of point defect (anion vacancy, anion vacancy with one trapped electron, etc.). Much of the present understanding of point defects in non-metals has been obtained from studies on the optical absorption and luminescence associated with irradiation. Defect concentrations below $10^{22}/m^3$ (0.1 appm) can be detected by optical techniques [49, 94]. Vacancies on the anion sublattice in oxides are historically referred to as F-type centers, whereas vacancies on the cation sublattice are called V-type centers [93]. Numerous reviews on the optical properlies of irradiated ceramics have been published [92, 93. 95. 961.

Optical absorption and luminescence measurements have been used to determine fundamental parameters such as the threshold displacement damage energy in Al_2O_3 [14,97, 981 and the effect of irradiation spectrum [99-101] and temperature [14,90, 101] on the defect production rate in Al_2O_3 and MgO. These studies have shown that the defect production rate decreases with increasing temperature. and that energetic collision cascades generally produce a smaller fraction of the calculated Kinchin-Pease displacements compared to low energy displacement events. The aggregation of point defects into defect clusters during annealing at elevated temperatures bas also been studied by optical techniques in ceramics such as Al_2O_3 [90, 1021.

Numerous radiation effects studies have been performed on quartz and SiO_2 optical fibers, due to their technological importance [93, 96. 103-113]. The optical fibers are often glassy silicates with significant concentrations of dopants such as Ge, P and OH and low concentrations of other impurities. The basic design of an optical fiber consists of a transparent core surrounded by a concentric transparent clading which has a lower index of refraction. This causes transmitted light to be confined to the core due to reflection at the interface between the core and cladding. Optical fibers composed of pure silica (SiO_2) cores and fluorine-doped silica cladding have been found to have the best transmission properlies in a radiation environment [107, 112, 113]. Since SiO_2 suffers permanent damage during exposure to ionizing radiation, most studies have been conducted with X-rays or gamma rays. Several neutron irradiation studies have also been performed [103-106]. The fluence required to produce significant degradation in optical transmission depends on the wavelength of interest. For example. an attenuation of 10 dB/m is produced at 500 nm and 700 nm in silica fibers after room temperature neutron irradiation to fast neutron fluences of $1x10^{21}$ and $1x10^{22}$ n/m^2, respectively [106].

Radiolytic damage in optical fibers is characterized by breaking of bonds, which are then available as charge-trapping sites. Resonances for these absorption centers which occur in the optical spectrum (usually centered near the infrared) cause degradation in the transmission. Doping with multivalent elements to form electron or hole traps with absorption bands outside of the wavelengths of interest has been used to decrease the sensitivity of optical fibers to radiation [109]. However, more recent work has shown that pure silica bas superior radiation resistance compared to silica doped with elements such as Ge or P [112, 113]. Similarly, low levels (~1 ppm) of impurities such as Al or the alkali metals or moderate levels (~100 ppm) of Cl can greatly reduce the radiation resistance of silica at certain wavelengths. Silica containing up to 1000 ppm OH (a common natural impurity) has better transmission characteristics than pure silica for wavelengths below 650 nm, but there are conflicting results on whether high-OH silica maintains this advantage after irradiation [112].

For most optical fibers, the transmission is significantly better at long wavelengths (1.5 µm) compared to short wavelengths (0.2 µm), and this wavelength dependence is maintained after irradiation [106, 111-113]. The effect of irradiation temperature on optical absorption is complex. Point defect annealing generally results in reduced optical degradation with increasing temperature. particularly above 200°C [112]. However, severe optical degradation can occur at high temperatures (above about 300°C), most likely due to deterioration in the optical cladding [107]. Periodic exposure of the irradiated optical fiber to an intense light source can cause significant recovery of the radiation induced attenuation by a process known as photobleaching [1081.

REFERENCES

1. W. Smith, Nature 7 (1873) 303.
2. J.J. Thomson and R. McClelland, Proc. Cambridge Philos. Soc. 9 (1896) 15.
3. H. Becquerel, C.R. Acad. Sci., 136 (1903) 1173.
4. A. Becker. Ann. d. Physik 13 (1904) 394.
5. G. Jaffé, J. de Phys. 5 (1906) 263.
6. A. Rose, RCA Rev. 12 (1951) 362; Pbys. Rev. 97 (1955) 322. 1538.
7. JF. Fowler. Proc. Roy. Soc. London A 236 (1956) 464.
8. R. Hofstadter, Nucleonics 4 (1949) 2.
9. R.H. Bube, Photoconductivity of Solids (Wiley & Sons, New York, 1960).
10. A. Rose, Concepts in Photoconductivity and Allied Problems (Interscience/Wiley, New York, 1963).
11. B. Gross, in Electrets, Topics in Applied Physics Vol. 33, ed. GM. Sessler (Springer-Verlag, New York, 1980) p. 217.
12. V.A.J. van Lint T.M. Flanagan, RE. Leadon, J.A. Nabor and V.C. Rogers, Mechanisms of Radiation Effects in Electronic Materials, Vol. 1 (Wiley, New York, 1980).
13. G.C. Messenger and M.S. Ash. The Effects of Radiation on Electronic Systems (Van Nostrand Reinhold, New York. 1986).
14. G.P. Pells, J. Nucl. Mater. 155-157 (1988) 67.
15. SJ. Zinkle and E.R. Hodgson, J. Nucl. Mater. 191-194 (1992) 58.
16. ASTM Standard Test Methods for DC Resistance or Conductance of Insulating Materials, D-257-91 (ASTM, Philadelphia, 1991).
17. W. Kesternich, F. Scheuermann and SJ. Zinkle, J. Nucl. Mater. 206 (1993) 68.
18. R.H. Goulding. S.J. Zinkle, D.A. Rasmussen and R.E. Stoller, Phys. Rev. B, submitted; also Fusion Reactor Materials semiannual prog. report for period ending Sept. 30,1993, DOE/ER-0313/15, p. 434.
19. H.J. Wintle, Brit. J. Radiol. 33 (1960) 706.
20. R.A. Wullaert, et al., in Effects of Radiation on Materials and Components, eds. J.F. Kircher and R.E. Bowman (Reinhold Publ., New York, 1964) p. 277.
21. S.E. Harrison. FN. Coppage and A.W. Snyder, IEEE Trans. Nucl. Sci. NS-10 (Nov. 1963) 118.
22. H.W. Wicklein, H. Nutley and J.M Ferry, IEEE Trans. Nucl. Sci. NS-10 (Nov. 1963) 131.
23. D.J. Huntley and J.R. Andrews, Can. J. Phys. 46 (1968) 147.
24. V.AJ. van Lint J.W. Hanity and T.M. Flanagan. IEEE Trans. Nucl. Sci. NS-15, No. 6 (1968) 194.
25. R.W. Klaffky. B.H. Rose, AN. Goland and G.J. Dienes, Phys. Rev. B 21 (1980) 3610.
26. G.P. Pells, Rad. Effects 97 (1986) 199.
27. T. Shikama, M. Narui, Y. Endo, A. Ochiai and H. Kayano, J. Nucl. Mater. 191-194 (1992) 544.
28. E.H. Farnum, J.C. Kennedy, F.W. Cliiard and H.M. Frost, J. Nucl. Mater. 191-194 (1992) 548; and private communication (1993).
29. R.W. Klaffky, in Special Purpose Materials ann. prog. report, DOE/ER-0048/1 (1980) 19.
30. M.V. Davis. in Nuclear Applications of Nonfissionable Ceramics, eds. A. Boltax and J.H. Handwerk (Amer. Nucl. Soc., Hinsdale, IL. 1966) p. 229.
31. T.J. Ahrens and F. Wooten, IEEE Trans. Nucl. Sci. NS-23, No. 6 (1976) 1268.
32. E.R. Hodgson and S. Clement Rad. Effects 97 (1986) 251.
33. G.P. Pells, J. Nucl. Mater. 184 (1991) 183.
34. S. Kasahara, Y. Katano, S. Shimanuki, K. Nakata and H. Ohno, J. Nucl. Mater. 191-194 (1992) 579.
35. J.C. King and H.H. Sander, IEEE Trans. Nucl. Sci. NS-20, No. 6 (1973) 117.
36. E.R. Hodgson, J. Nucl. Mater. 179-181 (1991) 383.
37. G.P. Pells, J. Nucl. Mater. 184 (1991) 177.
38. D.K. Nichols and V.A.J. van Lint, IEEE Trans. Nucl. Sci. NS-13, No. 6 (1966) 119.
39. Yu. K. Gus'kov and V.F. Sachkov, Sov. J. Atomic Energy 6 (1959) 120.
40. E.R. Hodgson, Cryst. Lattice Defects Amorphous Mater. 18 (1989) 169.
41. V.M. Ivanov et al., Inorg. Mater. 17 (1981) 1203.
42. E.R. Hodgson, Radial. Effects Defects Solids 119-121 (1991) 822.
43. E.R. Hodgson, Nucl. Instr. Methods B 65 (1992) 298.
44. E.R. Hodgson, J. Nucl. Mater. 191-194 (1992) 552.
45. E.R. Hodgson, in Defects in Insulating Materials, Vol. 2, eds. O. Kanert and J-M Spaeth (World Scientific, 1993) p. 332.

46. A. Moroño and E.R. Hodgson, ICFRM-6 proceedings, J. Nucl. Mater., in press.
47. E.R. Hodgson, **ICFRM-6** proceedings, J. Nucl. **Mater.,** in press.
48. T. **Shikama,** M. Narui, **Y.** Endo. T. Sagawa and H. Kayano, J. Nucl. Mater. **191-194 (1992) 575.**
49. X-F Zong, C-F Shen, S. Liu. Z-C Wu, **Y.** Chen, **Y.** Chen, B.D. Evans, R. Gonzalez and C.H. Sellers, Phys. Rev. B (June **1994)** in press.
50. K.L. **Tsang, Y.** Chen and J.J. O'Dwyer, Phys. Rev. B **26 (1982) 6909.**
51. LN. **Grossman** and A.I. Kaznoff, ref. **30.,** p. **421.**
52. W.A. Ranken and A.R. Veca, in Space Nuclear Power Systems. eds. M.S. El-Genk and M.D. Hoover (Orbit Book Co., Malabar, FL, **1988)** p. **329.**
53. W.A. Ranken, **Proc.** DOE Workshop on Electrical Breakdown of Insulating Ceramics in a High Radiation Field, May, **1991,** eds. **Y.** Chen and F.W. Wiffen, **CONF-9105176,** p. **433.**
54. E.H. Farnum, F.W. Clinard, Jr., W.F. Sommer, J.C. Kennedy, and T. Shikama, ICFRM-6 proceedings. J. Nucl. Mater.. in press.
55. G.P. Pells. IEA Workshop on Radiation Effects in Ceramic Insulators, Stresa, **Italy.** Sept. **27. 1993** (private communication).
56. L.L. Snead, D.P. White and SJ. Zinkle, **ICFRM-6** proceedings. J. Nucl. Mater., in press.
57. **S.J.** Zinkle and W. Kesternich, in Fusion Reactor Materials semiann. prog. report **DOE/ER-0313/14 (1993)** p. **437.**
58. L.W. Hobbs. J. ***Am.*** Cer. **Soc. 62 (1979) 267.**
59. **S.J.** Zinkle, **REI-7** proceedings, Nucl. Instr. Meth. B, in press.
60. P. **Jung.** Z. Zhu and H. Klein, J. Nucl. Mater. **206 (1993) 72.**
61. J. Narayan, R.A. Weeks and E. Sonder, J. Appl. Phys. **49 (1978) 5977.**
62. J.W. Corhett and J.C. Bourgoin, **IEEE** Trans. Nucl. **Sci. NS-18,** No. **6 (1971) 11.**
63. **K.G.** McKay, Phys. Rev. **74 (1948) 1606.**
64. E.W. Van Stryland, M. Bass. M.J. Soileau and C.C. Tang, in Laser-Induced Optical Damage in Optical Materials, **NBS** Special Publ. 509 (National Bureau of **Standards,** Washington DC, **1977)** p. **118.**
65. S.A. Basun, A.A. Kapianskii and S.P. Feofilov, Sov. Phys. **JETP 60 (1984) 1182.**
66. **JJ.** O'Dwyer, The **Theory** of Electrical Conduction and Breakdown in Solid Dielectrics (Clarendon Press, Oxford, **1973).**
67. E. Sonder and R.A. Weeks, J. Appl. Phys. **56 (1984) 2365.**
68. P.A Fefelov. **Yu.G.** Prokov'ev, A.S. Pokrovsky and **V.S.** Sandakov, private communication **(1993).**
69. JM. Bunch, LASL Controlled Thermonuclear Research Program prog. report **LA-7474** (Los Alamos Scientific Laboratory, **1977)** p. **166.**
70. EJ. Britt and **M.V.** Davis. in Proc. Thermionic Conversion Specialists Conf., **IEEE** report **71C63-ED** (Inst Electrical and Electronic Engineers, New York. **1971)** p. **137.**
71. WD. Kingery, H.K. Bowen and D.R. Uhlmann, Introduction to Ceramics, 2nd Ed. (Wiley & Sons, New York, **1976)** p. **913.**
72. W.W. Ho. Millimeter Wave Dielectric Property Measurement of Gyrotron Window Materials, **ORNL/SUB/83-51926/1** (April **1984)** and **ORNL/SUB/83-51926/2** (April **1985).**
73. R. Heidinger, J. Nucl. **Mater. 179-181 (1991) 64.**
74. J. **Mollá,** R. Heidinger and A. Ibarra, ICFRM-6 proceedings, J. Nucl. Mater., in press.
75. JD. Fowler, Jr., J. Nucl. Mater. **122&123 (1984) 1359.**
76. G.P. Pells and GJ. Hill, J. Nncl. Maw. **141-143 (1986) 375.**
77. **H.M.** Frost and F.W. Clinard Jr., J. Nucl. Mater. **155-157 (1988) 315.**
78. R. Heidinger and F. Königer, J. Nucl. Mater. **155-157 (1988) 344.**
79. R. Heidinger, J. Nucl. Mater. **173 (1990) 243.**
80. W. Dienst T. Fett, R Heidinger. H.D. Röhrig and B. Schulz. J. Nucl. Mater. **174 (1990)** 102.
81. **R.** Heidinger, Rad. Eff. Defects Solids **119-121 (1991) 861.**
82. **G.P.** Pells, ITER Tech. Meeting on Radiation Effects on In Vessel Components, Garching, Germany, Nov. **1993.**
83. P.P. Budnikov, F.G. Kerhe and N.S. Kostyukov. Izvest. Akad. Nauk SSSR. Neorgan. Mater. **3 (1967) 94.**
84. G.J. Hill, G.P. Pells and M.A. Barnett, **Rad.** Effects **97 (1986) 221.**
85. D. Edelson, RE. Jaeger and J.C. Williams, J. Amer. Cer. **Soc. 52 (1969) 359.**
86. S.N. Buckley and P. Agnew. J. Nucl. Mater. **155-157 (1988) 361.**

87. S.N. Buckley and P. Agnew, in Microwave Processing of Materials II, **MRS** Symp. Proc. Vol. 189, *eds.* W.B. Snyder, Jr., et al. (Mat. Res. Soc., Pittsburgh, 1991) 503.
88. G.P. Pells et al., Harwell **report** AERE-R13222, Sept. 1988.
89. J.M. Bunch and F.W. Clinard. Jr., J. **Amer.** Cer. Soc. 57 (1974) 279.
90. K. Atobe and M. Nakagawa, **Cryst** Latt. Def. and Amorph. Mar 17 (1987) 229.
91. WD. Kingery. H.K. Bowen and D.R. Uhlmann. Introduction to Ceramics, 2nd Ed. (Wiley & Sons. New **York.** 1976) p. 646.
92. A.E. Hughes, in Defects and Their Structure in Non-Metallic Solids, NATO ASI Series B, Vol. 19, *eds.* B. Henderson and AE. Hughes (Plenum Press. New York, 1976) p. 133.
93. B. Henderson, Rad. Effects 64 (1982) 35.
94. B. Henderson and D.H. Bowen, J. Phys. C Solid St. Phys. 4 (1971) 1487.
95. J.H. Crawford, Jr., **J.** Nucl. Mater. **108&109** (1982) 644.
96. N. Itoh and K. Tanimura, Rad. **Effects** 98 (1986) 269.
97. P. Agnew, Phi. Mag. A 65 (1992) 355.
98. K.J. Caulfield, R. Cooper and J.F. Boas, Phys. Rev. B 47 (1993) 55.
99. **Y.** Chen, M.M. Abraham, M.T. Robinson, J.B. Mitchell and R.A. VanKonynenburg, **in** Radiation Effects and Tritium Technology for Fusion Reactors, CONF-750989, Vol. II, eds. J.S. Watson and F.W. Wiffen (National Tech. Inf. Service, Springfield, VA. 1976) p. 492.
100. B.D. Evans and M. Stapelbroek, J. Nucl. Mater. 85&86 (1979) 497.
101. P. Agnew. Nucl. Instr. Meth. Phys. Res. B 65 (1992) 305.
102. K. Atobe. N. Nishimoto and M. Nakagawa, Phys. Stat. Sol. (a) 89 (1985) 155.
103. M.G. Jani and L.E. Halliburton, J. Appl. Pbys. 56 (1984) 942.
104. P.L. Mattern, J.E. Shelby. GJ. **Thomas** and W. Bauer, J. Nucl. Mater. 63 (1976) 317.
105. T. Iida, S. Ire, K. Sumita, T. Matsubara, D.W. Heikkinen and D.W. Short, IEEE Trans. Nucl. Sci. 35, No. 1 (1988) 898.
106. W.P. Unruh, in Dynamic Effects of Radiation in Ceramics, ed. E.H. Famum, Los Alamos National Lab. **report** LA-UR-92-4400 (1992) p. 289.
107. R Toossi and D. Modarress, IEEE Trans. Nucl. Sci. 38, No. 5 (1991) 985.
108. S. Hayashi, **Y.** Wada, **Y.** Chigusa, K. Fujiwara, **Y.** Hattori and **Y.** Matsuda. in Influence of Radiation **on** Material **Properties,** Part II, ASTM **STP** 956, eds. F.A. Gamer, C.H. Henager, Jr. and N. Igata ***(her.*** Soc. for Testing and Mater., Philadelphia 1987) p. 647.
109. J.A. Wall, H. Posen and J. Jaeger, in Physics of Fiber Optics, Advances in Ceramics, Vol. 2, *eds.* B. Bendow and S. Mitra (Amer. Ceram. Soc., Columbus, OH, 1981) p. 393.
110. J.A. Wall, H. Posen and J. Jaeger, in Physics of Fiber Optics, Advances in Ceramics, Vol. 2, eds. B. Bendow and S. Mitra (her. Ceram. Soc., Columbus, OH, 1981) p. 398.
111. EJ. Friebele and M.E. Gingerich. in Physics of Fiber Optics, Advances in Ceramics, Vol. 2, eds. B. Bendow and **S.** Mitra (Amer. Ceram. Soc., Columbus, OH, 1981) p. 387.
112. D.L. Griscom, J. Ceram. Soc. Japan 99 (1991) 923.
113. E.J. Friebele. in Optical Properties of Glass. eds. D.R. Uhlmann and N.J. Kreidl (Amer. Ceram. Soc., Westerville, OH, 1991) p. 205.

NEUTRON DAMAGE TO DIAGNOSTIC MIRRORS -- E. H. Famum and F. W. Chard. Jr. (Los Alamos National Laboratory), S. P. Regan (Johns Hopkins University, Baltimore, MD), and B. Schunke (JET Joint Undertaking, Abingdon, Ox., UK.)

OBJECTIVE

The objective of this work is to assess changes in multilayered mirrors of the type that will he used in fusion reactor diagnostic systems, after exposure to neutron damage.

SUMMARY

Diagnostic systems for fusion reactors will require mirrors capable of reflecting electromagnetic radiation in the soft x-ray, near uv, visible, and ir wavelengths. These components will be exposed to significant fluences of fast neutrons during use. Mirrors made from alternating layers of low-2 and high-Z materials were irradiated to a fluence of 1.1×10^{23} n/m^2 at 270-300°C, and subsequently evaluated for structural changes and in some cases changes in optical properties. Short-wavelength mirrors retained their structural integrity while exhibiting slight changes in reflectance: some long-wavelength mirrors showed structural degradation. while others did not. **These** results are discussed in terms of materials damage effects and possibilities for improvement of mirror performance under Severe operating conditions.

PROGRESS AND STATUS

Introduction

Fusion reactors will require a number of diagnostic systems to monitor plasma performance and. through feedback systems, to control plasma parameters for optimal performance. Mirrors play an important role in diagnostic systems by reflecting to detectors information on characteristic electromagnetic emissions (for example, emissions from carbon impurities in the plasma). The information to be transmitted can encompass wavelengths ranging from soft x-ray (typically 1 to 30 nm) to ultraviolet, visible, and infrared emissions (30 to 1200 nm).

Although a variety of materials and mirror designs *can* he used for this purpose, layered synthetic microstructures (LSMs) are especially attractive because of their dispersive qualities, high reflectance, and high throughput. Multilayered mirrors **are** made up of alternating layers of high-Z and low-Z materials, the former for the purpose of reflecting the incident radiation and the latter to serve **as** spacers to tune the reflectance to specific wavelengths. Figure 1 illustrates schematically the structure and function of an LSM mirror system.

Experimental Procedures

Test materials

A total of nine mirrors were subjected to neutron irradiation testing. Included were four mirrors designed to serve **as** soft x-ray reflectors and five for use at near-uv, visible, and/or ir wavelengths. The sort x-ray mirrors were produced by T. Barbee at Lawrence Livermore National Laboratory. In all cases the multilayers were deposited using dc magnetron sputtering in an Ar plasma. Substrates used were made from Si, glassy SiO_2, or Zerodur [1], whereas low-2 spacing layers were composed of Si, SiO_2, B_4C, or C. High-2 layers were of composition Mo, W, HfO_2, ZrO_2, or TiO_2. Specifications and characteristics of these mirrors are given in Table 1.

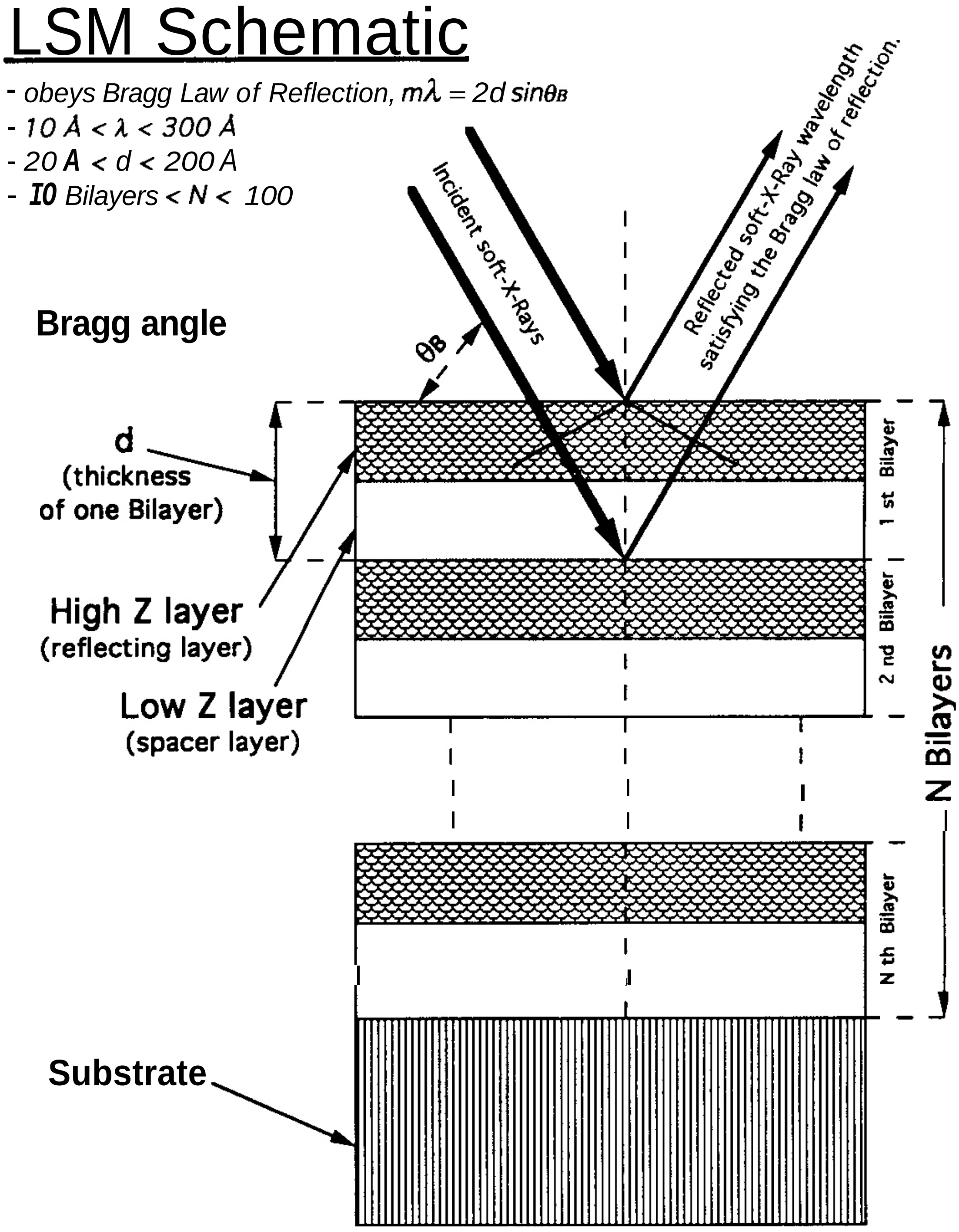

Fig. 1. Schematic drawing of the structure and function of a layered synthetic mirror (LSM), here as used in a soft x-ray diagnostic system.

Table 1. Characteristics of the Mirrors Tested Here

Materials system	d-spacing (nm)	Number of bilayers
Short-wavelength mirrors		
Mo/Si on Zerodur	8.78	50
W/B_4C on Si	2.275	100
W/C on Si	2.53	100
Mo/Si on Si	18.66	25
Long-wavelength mirrors		
HfO_2/SiO_2 on SiO_2	448	37
ZrO_2/SiO_2 on SiO_2	389	121
ZrO_2/SiO_2 on SiO_2	332	29
TiO_2/SiO_2 on SiO_2	491	39
TiO_2/SiO_2 on SiO_2*	642	39

*Plate polarizer

Irradiation testing

The nine test mirrors were irradiated at the Los Alamos Spallation Radiation Effects Facility. LASREF is located at the beam stop of the Los Alamos Meson Physics Facility, where 800 MeV protons are stopped in a water-cooled copper block. Nuclear reactions between incident protons and Cu nuclei result in production of spallation neutrons, the energy spectrum of which can be characterized as similar to that of a fast fission reactor but with the addition of a high-energy tail. A typical neutron spectrum for LASREF is shown in Fig. 2. The LASREF facility has been further described by Sommer et al. [2].

The proton beam at LASREF is pulsed, being on for 0.5 ms every 8 ms. The neutron flux averaged over this duty cycle at the location of the mirror samples was 2×10^{16} n/m^{2}s, and the gamma flux was 200 Gy/s. The accumulated neutron fluence was 1.1×10^{23} n/m^2, while the gamma fluence was 1.1×10^{9} Gy. Total elapsed time for the experiment, including periods when the beam was off, was approximately 2000 h.

The mirrors were irradiated inside a stainless steel capsule filled with Ar gas. Nuclear heating resulted in a significant temperature increase of the samples above ambient; judging from temperatures measured by thermocouple in another, similar capsule, the maximum temperature reached in the mirror capsule was 270-300°C.

Results

The four short-wavelength mirrors were examined visually before and after irradiation. The coatings appeared smooth and featureless before irradiation; no changes in appearance were observed after exposure.

The optical properties of two of these mirrors, The Mo/Si-coated, Zerodur-substrate system and the Mo/Si coated, Si substrate system. were measured by C. Tarrio and R. Watts of the Electron and Optical Physics Division, the National Institute for Standards and Testing, Gaithersburg, MD, and compared with data obtained from control samples. Results are shown in Fig 3. It may be seen that in each case the intensity of the peak reflectivity was decreased slightly by exposure at LAMPF, as was the associated wavelength.

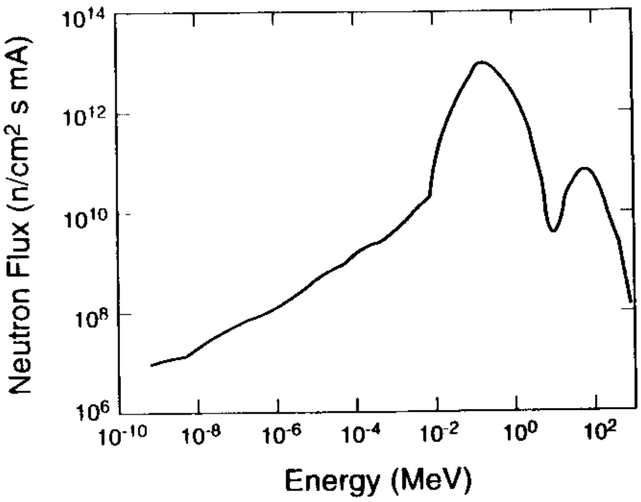

Fig. 2. Neutron spectrum (flux vs. energy) for a typical sample location at the Los Alamos Spallation Radiation Effects Facility (LASREF). The vertical scale represents flux per mA of proton beam current: the present experiments were carried out at 0.2 to 0.75 mA.

The five long-wavelength mirrors in their as-received condition exhibited smooth, featureless multilayer coatings. The appearance of the mirrors after irradiation is described below:

HfO_2/SiO_2, 37 layers -- slight crazing

ZrO_2/SiO_2, 121 layers -- coating almost totally flaked off

ZrO_2/SiO_2, 29 layers -- moderate crazing and chipping

$TiO_2//SiO_2$, 39 layers -- no obvious LASREF-induced damage

TiO_2/SiO_2, 39 layers, plate polarizer -- no discernable damage.

The small amount of damage visible on the fourth mirror probably resulted from remote handling of the samples after irradiation.

Discussion

Short-wavelength mirrors

The changes in optical properties of the short-wavelength mirrors (Fig. 3) may be attributable to either of two effects: neutron damage or exposure to elevated temperatures. With respect to the second explanation, Rosen et al. [3] recently demonstrated that Mo/Si-on-Si mirrors of d-spacing 6.96 nm showed significant changes in microstructure when heated for times up to 3000 h at temperatures of 260 to 342°C. The major change involved significant growth of a Mo-Si compound interlayer (probably $MoSi_2$) at the expense of the surrounding Mo and Si layers. Such a reaction would be expected to result in a net densification, with the effect on optical properties being to shift the d-spacing and therefore reflectivity peak to lower wavelengths as observed here after 2000 h at 270-300°C (Fig. 3). Concurrent irradiation could through displacement processes have assisted the kinetics of formation of the Mo-Si compound; for that reason the extent of that reaction may be greater in the present work than was observed by Rosen et al. With respect to the observed decrease in intensity of peak reflectivity, that change may be due to irregularities in d-spacing resulting from uneven growth of the interlayer.

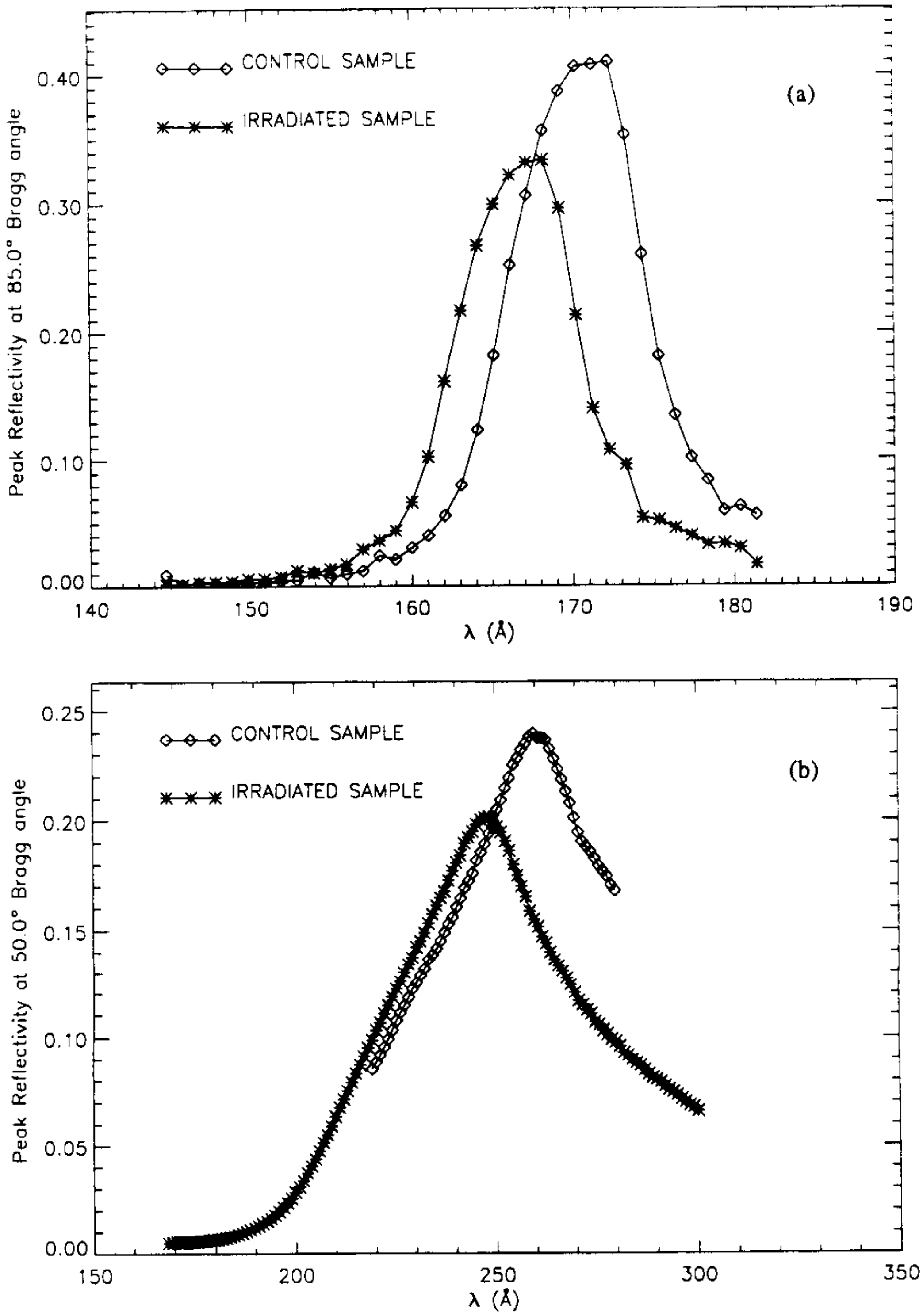

Fig. 3. Peak reflectivity vs. wavelength λ for two of the short-wavelength mirrors tested here, as measured before and after irradiation: (a) Mo/Si on Zerodur substrate; (b) Mo/Si on Si substrate.

Some materials deposited by thin-film techniques exhibit an amorphous structure, as was the case for the Si layers in the study by Rosen et al. [3]. Amorphous materials when heated can convert to a higher-density crystalline condition, thus adding another source of dimensional change in the direction observed.

It is not obvious that irradiation to the neutron and gamma fluences employed here had a significant effect on the short-wavelength mirrors. The changes in optical properties could have resulted from irradiation-induced changes in density of the starting materials; however, most materials exhibit swelling upon hdiation, and such a change would have resulted in an increase in wavelength at **peak** intensity. Also, most materials do not show significant dimensional changes at the low fluence attained here.

Long-wavelength mirrors

Results for the long-wavelength mirrors show that exposure to a fluence of $1.1x10^{23}$ n/m^2 at 270-300°C resulted in visible damage to three of the five reflectors. Differential swelling between substrates and their layered structures, and within layered structures, could be a source of damage here because the SiO_2 substrate and low-Z layer material is highly damage-sensitive: glassy SiO_2 exhibits densification, at least near room temperature, of approximately 1 vol. % at the present test fluence of $1.1x10^{23}$ n/m^2 [4]. Further degradation could have resulted from swelling of the high-Z layers; however, the high-Z materials used here are not expected to show significant dimensional changes at this low fluence.

The most likely source of changes in the Mo-Si-coated short-wavelength mirrors, namely chemical reaction between the layers, is less likely to apply to the long-wavelength mirrors, since relatively stable high-Z compound layers were used.

Another factor that may contribute to damage of the long-wavelength mirrors is the much greater thickness of the bilayers (i.e., d spacings) compared with that for the short-wavelength mirrors (Table 1). It has been observed that when differential swelling occurs, coarse microstructures exhibit greater sensitivity to structural damage than do fine microstructures. An example is the ocurrence of enhanced microcracking in coarse-grained polycrystalline Al_2O_3 [5], a hexagonal-structure material in which c-axis swelling predominates [6]. The relatively coarse microstructures of these mirrors may thus exacerbate the effect of swelling mismatches among the component materials.

Variations in bilayer thickness among the long-wavelength mirrors do not correlate with the observed damage effects (that is, a greater thickness does not lead to greater damage). On the other hand, it may be significant that the most severe damage occurred in the reflector that had the greatest number of layers (121, for one of the two ZrO_2/SiO_2 systems); the same materials system in 29-layer form showed significantly less damage. If the **121** layers behave as a single hulk phase, then differential swelling between that thick phase and the $Si02$ substrate could explain the near-complete delamination of this coating.

Conclusions

The following tentative conclusions can be drawn from this work

1. Short-wavelength mirrors are relatively resistant to damage.
2. In a multi-layered mirror. fewer and thinner bilayers give best performance.
3. Materials used in the bilayers and substrates should be selected according to their resistance to both irradiation and heat-induced structural changes (e.g., crystallization from the amorphous condition and formation of interlayer compounds).
4. Significant benefits may result if substrates made from radiation-sensitive SiO_2 can be replaced with relatively radiation-stable low-Z interlayer and substrate materials. such as Al_2O_3, MgO, or $MgAl_2O_4$ spinel.

5. Alterations in fabrication procedures (*e.g.*, heating the substrate to induce crystallization of deposited layers) could result in a more structurally-stable materials system.
6. To the extent possible. mirrors used in fusion devices should be located in areas that are remote from the source of the irradiation (the plasma), or be well-shielded. For some materials systems, operation near room temperature will extend usable lifetime; in these cases the possibility of supplying external cooling should be considered.

REFERENCES

[1] Zerodur is a pore-free glass-ceramic material that has both glass-like and crystalline phases. It is a product of Schott Glass Technologies, Inc., Duryea, PA 18642.

[2] W. F. Sommer, W. Lohmann, K. Graf, I. K. Taylor, and R. M. Chavez, Proc. 13th Int. Symp. on Influence of Radiation on Material Properties, ASTM-STP 956, F. A. Gamer, C. H. Henager, Jr., and N. Igata, eds. (American Society for Testing and Materials, Philadelphia, 1987)pp. 718-729.

[3] R. S. Rosen, D. G. Steams, M. E. Kassner. J.-I. Koike, Y. Cheng, and S. P. Vernon, Nanostructured Materials 3(1993) 195.

[4] E. Lell, N. J. Kriedel, and J. R. Hensler, Progress in Ceramic Science Vol. 4, ed. J. E. Burke (Pergamon Press, New York, 1966)p. 1.

[5] G. W. Keilholtz, R. E. Moore, and H. E. Robertson, Nucl. Technology 17 (1973) 234.

[6] F. W. Clinard, Jr., G. F. Hurley and L. W. Hobbs, J. Nucl. Mater. 108&109 (1982) 655.

ELECTRICAL PROPERTIES OF AL_2O_3 DURING IRRADIATION WITH SPALLATION NEUTRONS -- E. H. Famum and F. W. Clinard, Jr. (Los Alamos National Laboratory)

OBJECTIVE

The objective of this work is to determine the changes in electrical properties of Al_2O_3 ceramics during neutron irradiation, and to interpret these results in terms of damage mechanisms and experimental variables. It is of particular importance to establish whether the apparent radiation-induced electrical degradation (RIED) observed in ac measurements is a real effect.

SUMMARY

DC and AC conductivity of Al_2O_3 ceramics were measured at elevated temperatures during irradiation with neutrons and gamma rays at the Los Alamos Spallation Radiation Effects Facility. DC conductivity was increased at *start* of irradiation, **but** was subsequently reduced **as** displacement damage was accumulated. AC conductivity appeared **to** increase at high levels of damage. The observed dc behavior is attributed to excitation of electrons into the conduction band by ionizing radiation, followed by charge trapping and recombination at damage sites. The ac behavior, which resembles RIED, is attributed to conductivity in the residual gas surrounding the samples. Surface conductivity, while not the source of the apparent RIED, nevertheless is of sufficient magnitude to be of concern for fusion applications.

PROGRESS AND STATUS

Introduction

Insulating ceramics used in fusion reactors **must** retain adequate insulating properlies during **and** after irradiation with intense fluxes and fluences of neutrons and gamma rays. The principal influence of high fluences is to induce mechanical degradation (**e.g.,** fracture), which could render an insulator useless. The effect of ionizing fluxes is to excite electrons into the conduction hand; thus when an electric field is applied, radiation-induced conductivity (RIC) is observed. The combined effect of flux, electric field. and fluence (the latter short of causing structural failure), is to bring on radiation-induced electrical degradation (RIED), **a** phenomenon leading to increases in conductivity that are heyond those attributable to RIC and that are retained after removal from the irradiation source. RIC and RIED effects have recently been reviewed by Zong et al. [1].

The results reported here are an extension of work reponed earlier [2, 3]. In the earlier **work** it was demonstrated that polycrystalline Al_2O_3 irradiated at elevated temperatures with high-energy spallation neutrons at the Los Alamos Spallation Radiation Effects Facility (LASREF) exhibited RIC, hut that this effect was reduced by a buildup of displacement damage that induced charge trapping and recombination [2]. On the other hand, single-crystal ac samples exhibited an apparent RIED effect [3]. This paper briefly reviews the RIC observations, and then considers possible explanations for the RED-like behavior of the ac samples.

Experimental Procedure

DC samples were in the form of 19 mm diameter, 1 to 3 mm thick disks of Wesgo 995 (99.5% pure) alumina. Electric fields of 50 kV/m and 150 kV/m were applied through a three-electrode (guard ring) configuration of Pt electrodes. These samples were encapsulated in stainless steel furnaces and held at temperatures of 395, 615, and 655°C in an atmosphere of Ar gas during irradiation. Further details of the dc study are given in ref. [2].

The single-crystal ac samples [Crystal Systems, high-purity, face orientation $(11\bar{2}0)$] were disks of dimension 12.7 mm diameter and 0.216 mm thickness, with a three-electrode configuration of Pt electrodes.

These samples were subjected to an applied voltage of 131 kV/m rms at 10 kHz, and conductivity was monitored at 100 Hz. Irradiation temperatures were the same as those for the dc study. The ac samples were also contained in stainless steel furnaces, but in this case the capsules were evacuated and sealed off. Further details of the ac study are reported in ref. [3].

The sample furnaces were irradiated at LASREF with spallation neutrons generated by the stopping of 800 MeV protons in a Cu beam stop. The resulting neutron energy spectrum is similar to that of a fast fission reactor, but with a high-energy tail. The proton beam at LASREF is pulsed, being on for 0.5 ms every 8 ms. For these experiments the neutron flux was 3×10^{16} n/m^{2}s and the fluence accumulated over a 2000 h irradiation test was 2×10^{23} n/m^2. Corresponding gamma fluxes and fluences were 300 Gy/s and 2×10^9 Gy.

Results and Discussion

DC data

An example of dc data obtained is shown in Fig. 1. Before irradiation the conductivity at 655°C was 10^{-7} (ohm-m)$^{-1}$; immediately after irradiation began, conductivity increased by an order of magnitude. This is by definition radiation-induced conductivity. As neutron damage accumulated, conductivity decreased with increase in concentration of trapping and recombination centers. This effect is seen in both the beam-off and beam-on condition. No indication of RIED (that is, an increase in conductivity with time as damage accumulates) was observed.

The beam-on data show considerable scatter as a result of fluctuations in beam intensity and in the resulting neutron and gamma fluxes [2]. RIC is a function of flux, with the flux-dependence exponent δ often being near one [4]. We fit the data of Fig. 1 with various values of δ, and found the best fit to be obtained when $\delta = 1.0$. The flux-corrected data for Fig. 1 are shown in Fig. 2.

In earlier work, in-situ dc RIC tests on single-crystal Al_2O_3 using 3 MeV protons as the irradiation source yielded resulu similar to those shown in Fig. 2 [5]. In that work it was found that the best fit to the data resulted from a double exponential relationship with two time constants, suggesting that at least two mechanisms for trapping or annihilation of the electrons or holes that cause RIC were operating.

AC data

LASREF irradiation results obtained under ac conditions are shown in Fig. 3. In may be seen that at all three test temperatures, conductivity rose dramatically starting at about 10^{22} n/m^2. This behavior resembles RIED, for example as reported by Hodgson [6] under dc conditions. However, in the work reported here we found that while post-irradiation conductivity was increased, the measured value was still orders of magnitude lower than that observed in-situ. This suggests that the apparent RIED was was not in fact due to that effect.

In bench-top laboratory work, Kennedy [7] modeled the circuitry of the samples used in the ac studies and found that a surface resistance of less than 50 ohms would be required to duplicate the in-situ results shown in Fig. 3. However, the post-irradiation surface resistance was measured and was found in every case to be higher than 1000 ohms. These findings suggest that the RIED-like in-situ results were caused by conductivity in the gas phase (a degrading capsule vacuum) surrounding the samples.

Although surface conductivity is believed not to have been responsible for the increase in current flow observed here, we are nevertheless interested in the source of the increase in surface conductivity noted

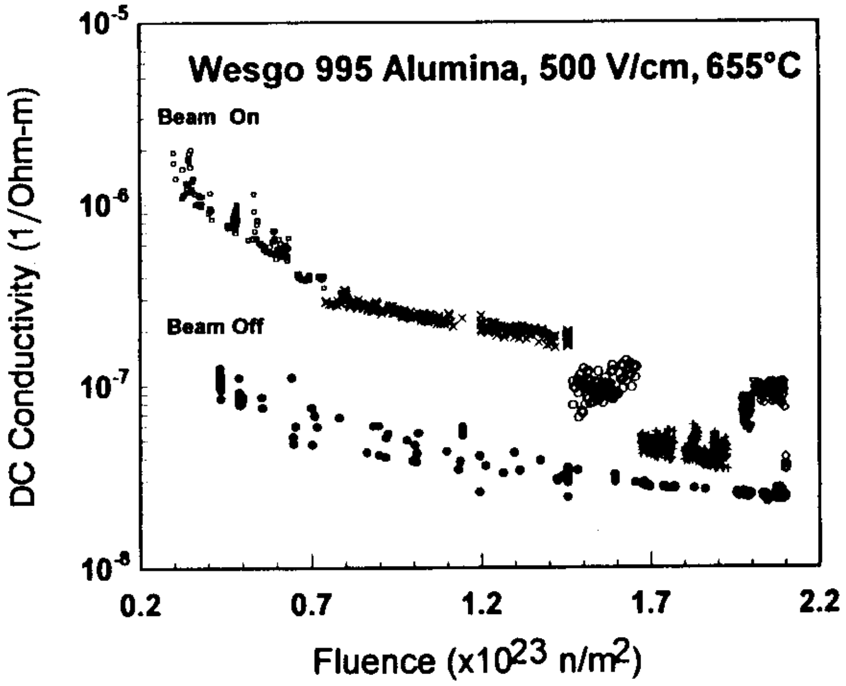

Figure 1. As-measured dc conductivity of alumina at 655°C and 50 kV/m vs. neutron fluence, before correction for flux changes [2].

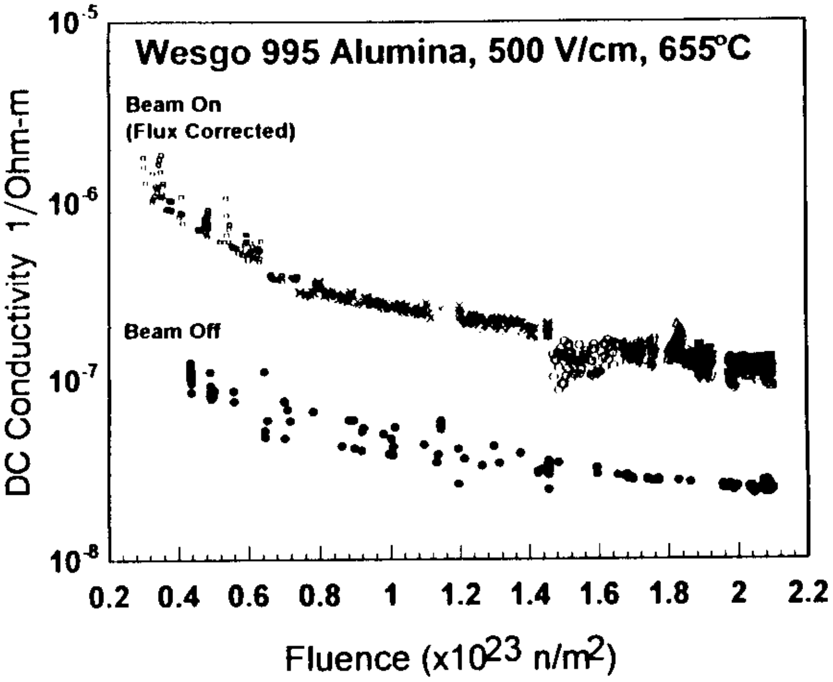

Figure 2. DC conductivity of alumina at 655°C, corrected for neutron flux changes [2].

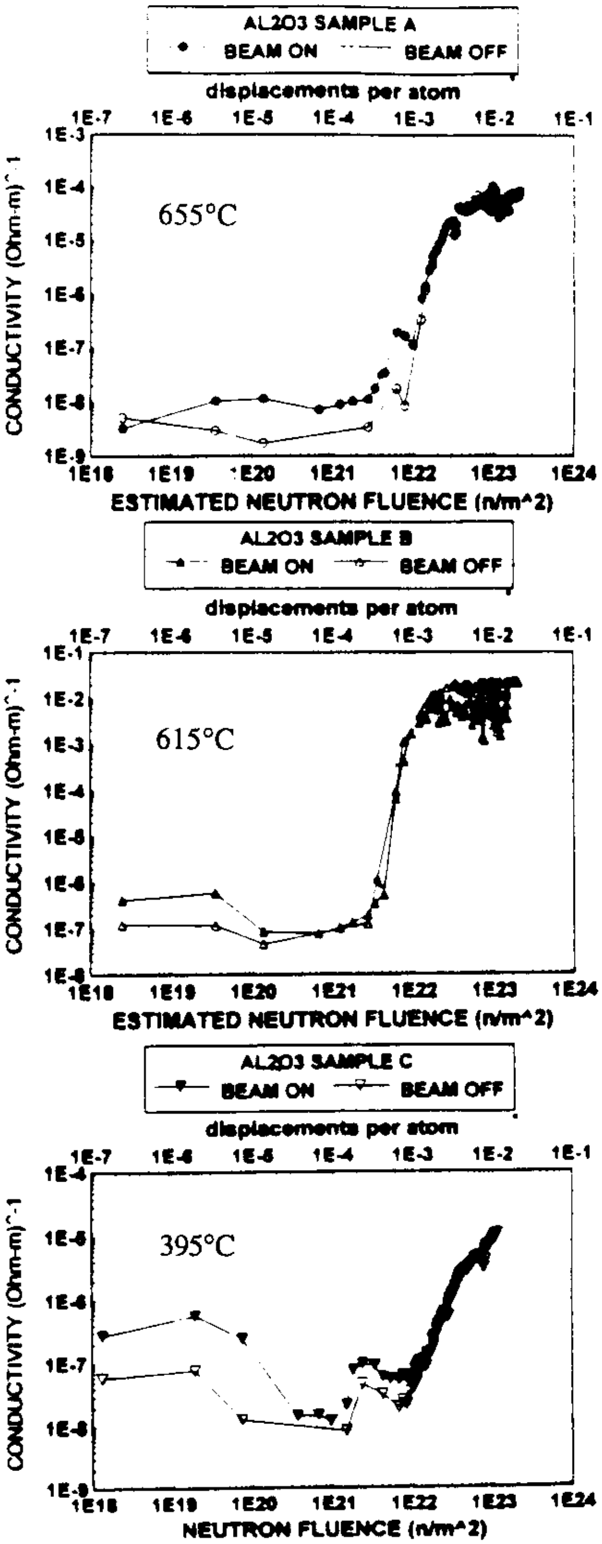

Figure 3. AC conductivity of single-crystal Al_2O_3 at the three indicated temperatures, measured at 100 Hz [3].

in post-irradiation tests. The area between the center electrode and guard electrode of the 395°C disk was subjected to surface chemical analysis by use of secondary ion mass spectrometry (SIMS) and electron microprobe analysis [8]. The SIMS data showed surface contamination from hydrocarbons, carbon, and the alkali metals Li, Na and K, while the microprobe results indicated the presence of Fe. Ni. and Cr. the constituents of 300-series stainless steels [9].

Conclusions

Results obtained under the present irradiation conditions indicate that with dc applied fields radiation-induced conductivity (RIC) is present, hut is opposed by a reduction in conductivity resulting from trapping and recombination of charge carriers at irradiation-induced lattice defects. AC experiments produced effects similar to radiation-induced electrical degradation (RIED), but those effects in fact appear to result from conductivity in the gases surrounding the samples. Surface conductivity, while not controlling in the ac studies, was nevertheless found to be a measurable contributor to overall conductivity.

It is important tn note the implications of the fact that both surface and gas phase conductivity were observed in this work. Since fusion reactor insulators must operate in less than benign environments, reactor designers should be alert to the possibility that such spurious conductivity effects can occur (for example, if insulators are exposed to the plasma or are subjected to deposition of contamination layers), and should be prepared to deal with these potential problem areas.

REFERENCES

[1] X-Fu Zong, C-Fu Shen, S. Liu, Z-Chi Wu, Yi Chen, Y. Chen, B. D. Evans, R. Gonzalez, and C. H. Sellars, Phys. Rev. B (in press 1994).

[2] E. H. Famum, F. W. Chard, Jr., W. F. Sommer, J. C. Kennedy III, and T. Shikama, J. Nucl. Mater. (in press 1994).

[3] J. C. Kennedy III, E. H. Farnum, W. F. Sommer, and F. W. Chard, Jr., Measurement of AC Electrical Conductivity of Single Crystal A1203 During Spallation-Neutron Irradiation, U. S. Department of Energy Report DOE/ER-0313/14 (1993).

[4] R. W. Klaffky, B. H. Rose, A. N. Goland and G. H. Dienes, Phys. Rev. B 21 (1980) 3610.

[5] E. H. Famum, J. C. Kennedy, F. W. Chard and H. M. Frost, J. Nucl. Mater. 191-194 (1992) 54X.

[6] E. R. Hodgson, Cryst. Lattice Defects Amorphous Material 18 (1989) 169.

[7] J. C. Kennedy III, Los Alamos National Laboratory, private communication.

[8] R. Ai, Los Alamos National Laboratory, private communication.

[9] E. H. Famum and F. W. Chard, Jr., J. Nucl. Mater. (in press).

A COMPARISON OF THE EFFECT OF RADIATION ON THE THERMAL CONDUCTIVITY OF SAPPHIRE AT LOW AND HIGH TEMPERATURE – D.P. WHITE (Oak Ridge National Laboratory)

OBJECTIVE

The effects of radiation on the thermal conductivity of sapphire have been calculated over a wide temperature range (77-400K). The phonon scattering relaxation times for various scattering mechanisms have been used in order to determine the effect each mechanism has on the lattice thermal conductivity of sapphire. The methods of calculation at low and high temperature are reviewed, and the results of these calculations are presented to compare the effect at different temperatures.

SUMMARY

It has been proposed [1-3] that sapphire be used in insulating feedthroughs and windows in radiofrequency and microwave heating systems in fusion reactors. The degradation of the thermal conductivity of sapphire with irradiation is a concern in the design of these windows [4-7]. It has been proposed [2,3] to cool microwave windows to liquid nitrogen temperatures to take advantage of the thermal conductivity peak, which occurs at approximately 30K in unirradiated sapphire, and the lower dielectric loss tangent at these temperatures. In this paper the methods used to calculate the thermal conductivity and the changes which occur with changes in point defect concentration will be reviewed and the results of the low temperature calculations will be compared to the high temperature calculations.

It is found that vacancy scattering can significantly reduce the thermal conductivity over a wide temperature range; for example, a vacancy concentration of 0.01 per atom leads to a fractional change of about 90% at 77K versus 43% at 400K. This reduction has significance for the design and placement of radio frequency and microwave windows in fusion reactors.

PROGRESS AND STATUS

Review of Methods

The calculation of the thermal conductivity degradation with vacancy concentration takes different forms at low and high temperatures. This is a result of the changes which occur in the phonon spectrum and the relaxation times of the various phonon scattering mechanisms with temperature. In both the high and low temperature cases the thermal conductivity integral has the following form;

$$K = \frac{1}{2\pi^2}\int_0^{\omega_D} \frac{\tau(\omega)}{v} C_{ph}(\omega)\omega^2 d\omega. \tag{1}$$

This expression is based on the the Debye approximation where ω_D is the Debye frequency, v is the phonon velocity, $C_{ph}(\omega)$ is the specific heat per normal mode at ω, and $\tau(\omega)$ is the effective phonon relaxation time. The evaluation of Eq. 1 at high and low temperature differ in the form of $C_{ph}(\omega)$, and $\tau(\omega)$ which are used. In the low temperature case the Callaway [8] formulation of the thermal conductivity is used. This formulation uses the low temperature form for the specific heat and an expression for the relaxation time which takes the effect of N-processes into account. In the high temperature case a formulation due to Klemens [9] is used. In this formulation the constant high temperature limit for the specific heat and a relaxation time which does not include the effect of N-processes are used. The neglect of the effect of N-processes in the high temperature case is justified [9,10]. Table 1 summarizes the low and high temperature cases. In this table τ_N is the normal process relaxation time, $1/\tau_c = 1/\tau_N + 1/\tau_r$, $1/\tau_r = \sum_j 1/\tau_j$, where τ_j are the relaxation times for resistive processes, including the umklapp scattering relaxation time τ_u. The parameter β in the low temperature relaxation time is derived by Callaway [8] and is given by;

Table 1: The forms for the specific heat and relaxation times used in Eq. 1 for the low and high temperature cases. The values of the constants b, b_u, and α, and the parameters β and B are discussed in the text. Also, $x = \hbar\omega/K_bT$ and K_b is Boltzmann's constant

Parameter	Low T	High T
$C_{ph}(\omega)$	$K_bx^2\exp(x)\{\exp(x)-1\}^{-2}$	K_b
$\tau(\omega)$	$\tau_c(1+\beta/\tau_N)$	$\tau_r(\omega)$
τ_{N1}	$b_n\omega T^4$	–
τ_u^{-1}	$b_u\omega^2T\exp(-\theta/\alpha T)$	$B\omega^2$

$$\beta = \frac{\int_0^{\theta/T} \frac{\tau_c}{\tau_N} \exp(x)\{\exp(x)-1\}^{-2}x^4dx}{\int_0^{\theta/T} \frac{\tau_c}{\tau_N\tau_r} \exp(x)\{\exp(x)-1\}^{-2}x^4dx}$$

where θ is the Debye temperature. The resistive processes considered here in the low temperature case are U-processes, point defect scattering, and boundary scattering ($1/\tau_b = v/L$, where L is a dimension on the order of the crystal). Boundary scattering will have little effect at temperatures much above the thermal conductivity maximum and is not expected to have much of an effect at 77K [11] and will not be considered here. At high temperature the resistive processes which are considered are U-processes and point defect scattering. The point defect scattering relaxation time has the form [10];

$$1/\tau_p = A\omega^4 \tag{2}$$

where A is a parameter which is proportional to the defect concentration and depends on the nature of the defect. For vacancies, $A = C_v\Omega(3\Delta M/M)^2 1/4\pi v^3$ [10,12], where C_v is the vacancy concentration per unit cell, AM is the change in mass of the unit cell due to a vacancy, M is the mass of the unit cell, and Ω is the volume ot the unit cell.

The Callaway formulation has been fitted to low temperature thermal conductivity measurements of sapphire by deGoer [13]. deGoer found that an excellent fit was found assuming the unit cell to be the formula unit, Al_2O_3, and assuming $b_n = 2.7 \times 10^{-13}K^{-4}$, $b_u = 1.7 \times 10^{-18}sK^{-1}$, and $\alpha = 2$. Using these values and varying the vacancy concentration via the parameter A in Eq. 2, Eq. 1 has been solved numerically to determine the effect of vacancies at low temperature [14].

At high temperature, using the values in Table 1, Eq. 1 may be solved analytically [9] to give;

$$K = K_0\frac{\omega_0}{\omega_D}\arctan\left(\frac{\omega_D}{\omega_0}\right) \tag{3}$$

where K_0 is the intrinsic thermal conductivity (without point defects), and ω_0 is the frequency at which U-scattering and point defect scattering have the same strength and is given by $\omega_0 = (B/A)^{1/2}$, and where B may be expressed in terms of the intrinsic thermal conductivity K_0 via Eq. 1 as $B = (K_b\omega_D)/(2\pi^2vK_0)$. Thus by varying the vacancy concentration C_v in parameter A

and given K_0 the effect of vacancy concentration on the thermal conductivity at high temperatures has been calculated. The value of $K_0(400K)$ used in this study was obtained from measured values on pure sapphire [18]. The high temperature expression for the thermal conductivity given in Eq. 3 has previously been used to model the high temperature thermal conductivity of irradiated alumina [15-17].

Results of Calculations

The results of the evaluation of Eq. 1 are shown in Figs. 1 and 2 for a range of vacancy concentrations. Fig. 1 shows the results of the thermal conductivity calculations versus vacancy concentration at 77 and 400K. Fig. 2 shows these results as the fractional change in the thermal conductivity versus vacancy concentration. The upper limit of the point defect concentration in these plots is 2%.

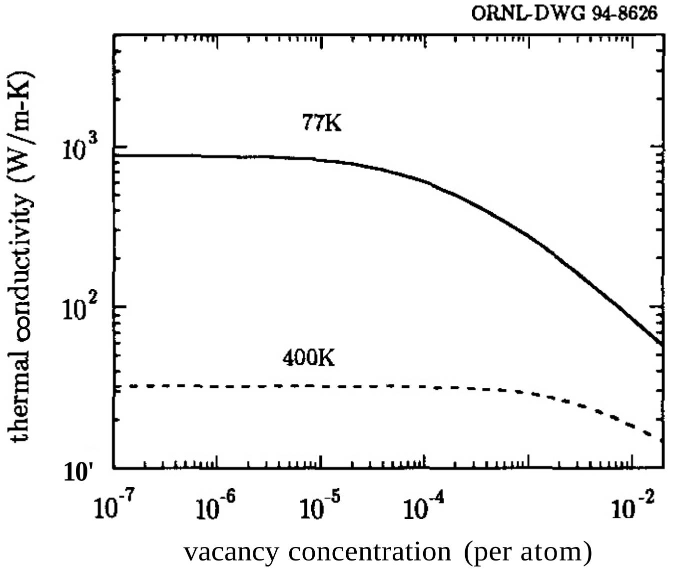

Figure 1: Plot of the thermal conductivity of sapphire versus vacancy concentration per atom at 400 and 77K.

This was chosen as the upper limit because the calculations of Rohde and Shulz [16] have estimated that vacancy concentrations up to this magnitude exist in irradiated alumina. From these plots it is seen that the low temperature thermal conductivity is much more sensitive to the vacancy concentration. The low temperature thermal conductivity is affected at much lower vacancy concentrations than the high temperature case. For example, the vacancy concentrations which will produce a 5% reduction in the thermal conductivity at 77 and 400K are 8×10^{-6} and 5×10^{-4} atom fracton respectively. Other representative values are given in Table 2. It is also seen that at 77K a fractional reduction of more than 90% is possible at the highest vacancy concentrations whereas the largest reduction at 400K is about 55%.

The results of these calculations compare favorably with measured values of the degradation of the thermal conductivity of sapphire and alumina with irradiation. For example, Berman et.al. [19] measured the low temperature thermal conductivity of neutron irradiated sapphire and Sound very large reductions compared to non-irradiated sapphire. At ≈77K a reduction of roughly 70%

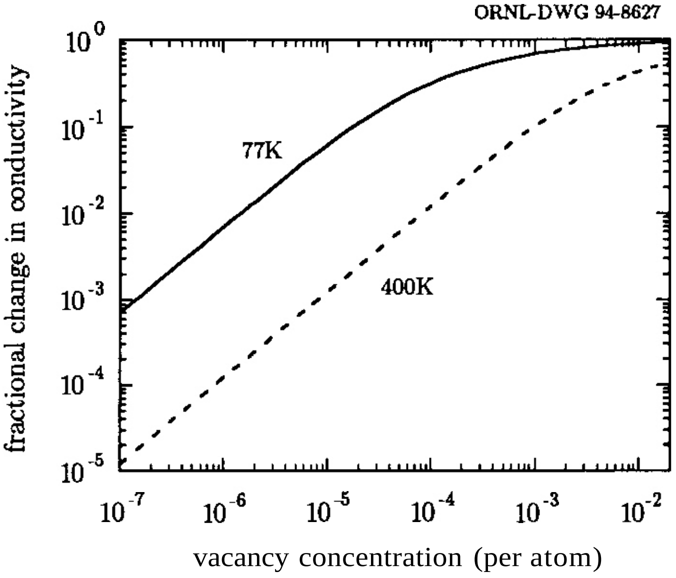

Figure 2 Plot of the fractional change in the thermal conductivity versus vacancy concentration per atom at 400 and 77K.

occurred after irradiation to a dose of —0.005 displacements per atom (dpa). From Fig. 2 it is seen that a comparable decrease occurs at a vacancy concentration of 0.001. It was also found [16] from measurements on irradiated alumina that the maximum degradation in the thermal conductivity at 400K was roughly 60% for samples neutron irradiated to a dose of 0.4 dpa at 473K, this compares the the maximum degradation of 55% calculated here for a vacancy concentration of 2%.

It should be pointed out that the damage dose and the vacancy concentration are different parameters, with the vacancy concentration being the remaining defect concentration after recombination. The relationship between these two parameters is dependent on many factors including, irradiation temperature, radiation spectrum, and post-irradiation annealing. The vacancy production rate is greater at low temperature than at high temperature. Atobe and Nakagawa [20] studied the production rate of F centers with irradiation temperature in sapphire. They found that the F center production rate was much higher in sapphire which was neutron irradiated at 15K than in sapphire neutron irradiated at 360K in the range of dose they studied, $1.6 \times 10^{16} - 3.3 \times 10^{17}$ n cm^{-2}. Agnew [21] studied the vacancy concentration produced in ion irradiated sapphire and found higher damage efficiency at 77K than at room temperature for all the ions included in the study.

CONCLUSIONS AND FUTURE WORK

The results of the calculations show that for a given point defect concentration the reduction in the thermal conductivity at low temperature is much greater than at high temperature, and that this large reduction takes away a large part of the thermal conductivity advantage gained by going to low temperature. As noted in the previous section the defect production rate is dependent on the temperature and Rohde and Shultz [16] have shown that irradiation temperature has an important

Table 2: Values of the vacany concentration per atom and corresponding fractional reduction in the thermal conductivity at 77 and 400K. Values for vacancy concentration necessary for 75% and 90% reduction at 400K are not given because these would be above the maximum expected vacancy concentration of 2%.

Reduction (%)	Vacany Concentration (per atom)	
	77K	400K
5	8.0×10^{-6}	5.0×10^{-4}
10	1.8×10^{-5}	1.0×10^{-3}
20	5.0×10^{-5}	2.5×10^{-3}
50	3.0×10^{-4}	1.5×10^{-2}
75	1.6×10^{-3}	–
90	1.0×10^{-2}	–

effect on thermal conductivity of alumina. From this data they inferred defect concentrations with a higher concentration of residual defects being present in the material irradiated at the lower temperature as compared to the material irradiated to the same fluence at a higher temperature as expected. Thus high temperature results can not be directly extrapolated to low temperature because of this difference in microstructural evolution. It is important to perform low temperature and high temperature irradiations on sapphire in order to determine the tolerable fluence level this material can withstand without an unacceptably large decrease in the thermal conductivity at a given temperature. This determination will dictate where the windows may be positioned in the reactor. Ideally the conductivity measurements would be performed in-situ. However if the measurements are to be performed post-irradiation it is important to maintain the samples at low temperature in order to guard against room temperature annealing effects which may occur, as seen by Kingery [22] in low temperature neutron irradiated sapphire.

It is also significant that the low temperature thermal conductivity is more sensitive to vacancy concentration than the high temperature thermal conductivity. Thus in order to maintain the thermal conductivity of the window within a certain percentage of its non-irradiated value a cryogenically cooled window must be positioned in a region of much lower neutron fluence than a high temperature window. From Table 2 it is seen that for a corresponding decrease in the thermal conductivity the low temperature window must have a vacancy concentration of one to two orders of magnitude less than the corresponding high temperature window, and when defect stability at low temperatures is taken into account the difference in neutron flux levels which are tolerable will be even greater than this.

Thus if cryogenically cooled windows are to be used in future fusion reactors, and the thermal conductivity advantage is to be maintained, the tolerable neutron fluence levels must be determined in order to position them properly. This determination will be more easily made if low temperature irradiations of sapphire can be made, as noted above.

ACKNOWLEDGMENTS

I would like to thank S.J. Zinkle for helpful discussions during the course of this study.

This research was performed while the author held a fellowship in the *Oak* Ridge National Laboratory Postdoctoral Research Program, administered through the *Oak* Ridge Institute for Science and Education.

REFERENCES

1. F.W. Clinard, Jr., G.F. Hurley, and R.W. Klaffky, Res. Mechanics **8** (1988), 207-235.
2. G.R. Haste, H.D. Kimrey and J.D. Proisie, Report ORNL/TM-9906 (1986).
3. R. Heidinger, J. Nucl. Mater. **174181** (1991) 64.
4. H.M. Frost and F.W. Clinard, Jr., J. Nucl. Mater. bf **155157** (1988) 315.
5. M.K. Ferber, H.D. Kimrey, and P.F. Becher, J. Mater. Sci. **19** (1984) 3767.
6. P.F. Becher and M.K. Ferber, J. Mater. Sci. **19** (1984) 3778.
7. T. Fett and D. Munz, J. Nucl. Mater. **171** (1990) 172.
8. J. Callaway, Phys. Rev. **113** (1959) 1046.
9. P.G. Klemens, Phys. Rev. **119** (1960) 507.
10. P.G. Klemens in: *Solid State Physics,* Vol. 7, Eds. F. Seitz and D. Turnbull (Academic Press, New York, 1958) p. 1.
11. D.P. White in: Fusion Reactor Materials Semiann. Prog. Report DOE/ER-0313/13, ORNL, (1992) 326.
12. C.A. Ratsifaritana in: *Phonon Scattering an Condensed Matter,* Ed. H.J. Maris (Plenum Press, New York, 1980) p. 259.
13. A.M. de Goer, J. Phys. (Paris) **30** (1969) 389.
14. D.P. White, J. Nucl. Mater. (1994) in press.
15. P.G. Klemens, Nucl. Instrum. Methods **B1** (1984) 204.
16. M. Rohde and B. Schulz, J. Nucl. Mater. **173** (1990) 289.
17. D.P. White, J. Appl. Phys. **73** (1993) 2254.
18. Y.S. Touloukian and C.Y. Ho, Eds., *Thermophysical Properties of Matter, Vol. 2* (IFI/Plenum, New York, 1970).
19. R. Berman, E.L. Foster and H.M. Rosenberg in: Report of the Conf. on Defects in Crystalline Solids, Univ. of Bristol, 1954 (The Physical Society, London, 1955) p.321.
20. K. Atobe and M. Nakagawa, Cryst. Latt. Def. and Amorph. Mat. **17** (1987) 229.
21. P. Agnew, Nucl. Instrum. Methods **B65** (1992) 305.
22. W.D. Kingery, J. Nucl. Mater. **24** (1967) 21.

NEUTRON-INDUCED CHANGES IN OPTICAL PROPERTIES OF $MgAl_2O_4$ SPINEL - A. lbarra (CIEMAT, Madrid, Spain) and F. A. Garner (Pacific Northwest Laboratory)"

OBJECTIVE

The objective of this effort is to determine the suitability of $MgAl_2O_4$ spinel as a ceramic insulator for fusion applications.

SUMMARY

High purity $MgAl_2O_4$ spinel specimens irradiated in FFTF-MOTA to very high exposure have been examined by three techniques to determine changes in their optical properties. Significant changes were observed in optical absorption, photoluminescence and radioluminescence.

PROGRESS AND STATUS

Introduction

In several earlier reports it was shown that high purity $MgAl_2O_4$ spinel irradiated in FFTF at 385° to 750°C was remarkably resistant to irradiation.'.' The single evidence that might indicate some significant degradation was that this spinel became quite dark during irradiation due to the development of color centers. This darkening may imply some degradation in the electrical insulating properties. In this report, the initial results are presented for a series of measurements on changes in optical properties, using optical absorption, photoluminescence and radioluminescence techniques.

Experimental Details

After irradiation, a thin slice (thickness between 0.2 and 0.5 mm) was cut from each of the single crystal cylinders, and then the slice was polished. Unirradiated specimens were prepared in the same manner. Optical absorption measurements between 400 and 2500 nm were made at room temperature using a Cary 17 spectrophotometer.

Luminescence measurements were performed using a 6W Ar-ion laser as the excitation source. Wavelengths at 457, 488, and 514 nm were used. Light emitted from the specimen was collected with a high diameter lens and focused on the input of a bundle of quartz optical fibers coupled to a high resolution monochrometer of 0.5 m length (with a 1200 line/mm grating blazed at 350 nm) and measured with a cooled EMI9G59QB photo multiplier (S20 response). For low temperature measurements, the specimen was installed in the cold head of a closed cycle helium gas cryostat operating between 30 and 700 K. The temperature was monitored using RhFe temperature sensors located near the specimen.

For radioluminescence measurements the excitation source was changed from a laser beam to an X-ray beam from a Siemens tube (tungsten anode) operated at SO kV and 5 to 30 mA. Irradiations

---

'Pacific Northwest Laboratory is operated for the U.S. Department of Energy by Battelle Memorial Institute under Contract DE-AC06-76RLO 1830.

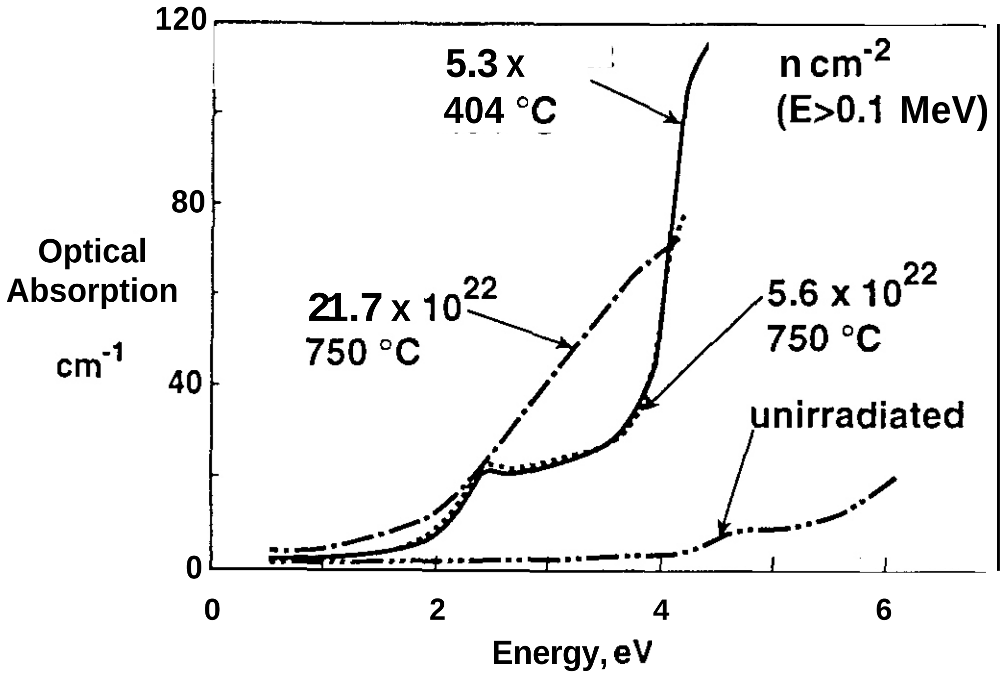

Fig. 1. Dependence of optical absoprtion on neutron dose and irradiation temperature.

were performed through a 1 mm aluminum window at a maximum dose rate of 3 x 10^3 R min^{-1}. The emission spectra presented in this report have not yet been corrected by the whole system response.

Figure 1 shows the optical absorption results obtained in both the irradiated and unirradiated specimens. A very clear irradiation-induced increase in the optical absorption occurs throughout the ultraviolet range. The samples with lower doses, independent of irradiation temperature, show a peak around 2.4 eV (510 nm), in agreement with previous qualitative results.’ This peak is not observed in the specimen at higher irradiation dose at 750°C. The unirradiated specimen shows a small peak around 4.8 eV and a constant increase in the deep ultraviolet range. This type of absorption behavior is usually ascribed to the presence of impurities like Fe^{+2} ions.

There is very little information about the effects of high dose irradiation on the optical properties of stoichiometric spinel. It is known’” that both neutron and electron irradiation induce a new absorption band around 5.27 eV (235 nm) associated with the presence of oxygen vacancies. When the dose increases (up to a maximum of 3 x 10^{17}n cm^{-2}, five orders of magnitude lower than that of this study), a few small peaks in the region between 2 to 4 eV have been observed? These peaks have been attributed to absorption of impurities. In this case, the radiation-induced increase would be due to an increased oscillator strength caused by the perturbation of the ion by a neighboring oxygen vacancy.

Figure 2 summarizes the photoluminescence results obtained at room temperature, using the 514 nm

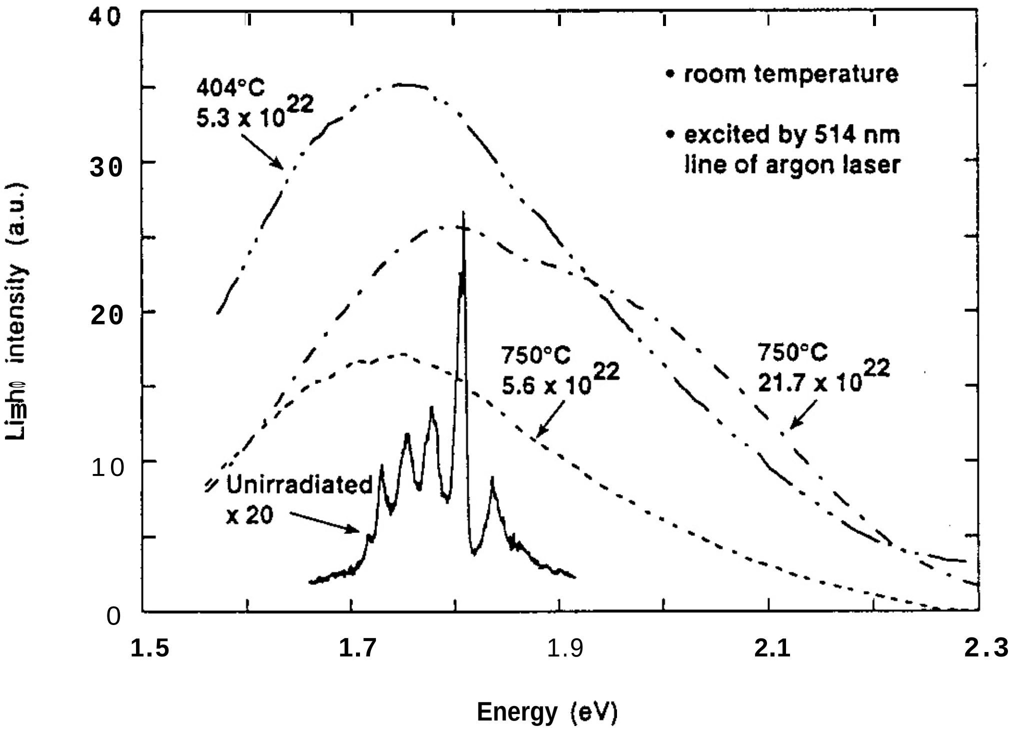

Fig. 2. Dependence of photoluminescence on neutron dose and irradiation temperature.

line of the Ar laser at the excitation source. The unirradiated sample shows several sharp peaks around 700 nm. This well-known response is related to the presence of octahedrically coordinated Cr^{3+} ions? In fact, the relative height of the central doublet at 1.8 eV and the side bands can be used to obtain information about the Al/Mg disorder: Unfortunately, in this work this information cannot be used to study the effect of irradiation on the disorder because this emission completely disappears or is overwhelmed in the irradiated samples. In fact, figure 2 shows a new emission around 1.75 eV (710 nm), much more intense than that of Cr^{3+} (more than a factor of 10 for the same excitation power). This emmission is so intense that it can be easily observed by eye. The emission seems to be composed of two Components at 1.75 and 2.1 eV, the latter proportionally more intense in specimens irradiated at higher temperature. The emission is more intense in the specimen irradiated at lower temperatures and increases with increasing dose. No temperature dependence has been observed in the shape or intensity of the hands, at least from 30 to 450K. If the excitation wavelength is 457 nm, the Cr^{3+} emission in the unirradiated samples almost disappears, in agreement with the expected excitation spectrum when the intensity of the emission of the irradiated samples is more nr less the same. The only difference is that the relative intensity of the band at 2.1 eV is higher.

This emission has not been previously observed in other studies. It is probably related to a new type of defect induced by irradiation, although Cr^{3+} as its possible origin cannot be completely dismissed. In fact, it has been observed that the Cr^{3+} emission is composed of sharp components at 700 nm together with a broad emission around 750 nm associated to the presence of Cr^{3+} in distorted surroundings?' It has been found also that the intensity of the emission around 720 nm increases in intensity and shifts the excitation spectra as a consequence of irradiation? This effect has been related to the perturbation of Cr^{3+} by nearby vacancies.

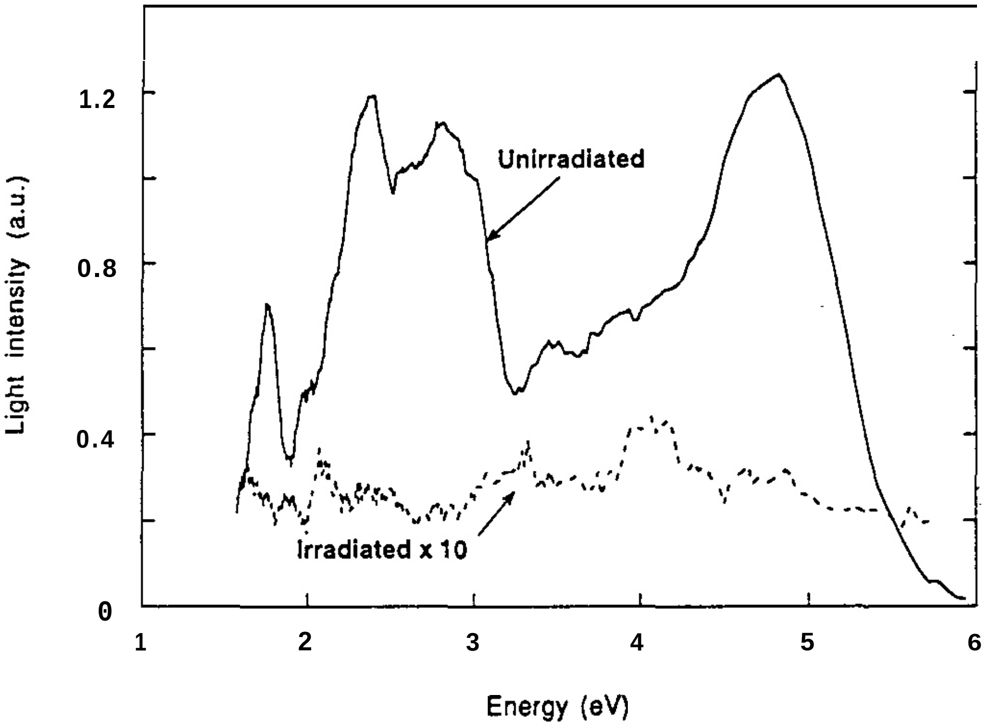

Fig. 3. Dependence of radioluminescence of $MgAl_2O_4$ spinel on neutron irradiation.

Figure 3 shows the effect of irradiation on the radioluminescence spectra. Before irradiation, the $MgAl_2O_4$ spinel undergoes x-ray induced emission in the whole visible ultraviolet range with main bands at **4.8, 3.5, 2.7, 2.4,** and **1.8** eV **(260, 350, 460, 520,** and **690** nm, respectively). Bands at **520** and 720 nm are known to be related to electron-hole recombination in Mn and Cr impurities, respectively, whereas the **5** eV emission has been ascribed to recombination at V-type centers[9] and the **2.7** eV band has been related to oxygen vacancy centers" on other unidentified impurities? The main point is that all these emissions disappear or are overwhelmed after neutron irradiation. Thus, emissions are not observed in the irradiated samples. That means that the electron-hole recombination probably takes place through non-radioactive processes.

In conclusion, high temperature, high dose neutron irradiation on stoichiometric spinel induces many changes in the full range of optical properties, contrary to the lack of significant changes in dimension, elastic, or mechanical properties. Much more work is needed to clarify the characteristics of the new emission and absorption bands observed in this study.

REFERENCES

1. F. A. Garner, G. W. Hollenherg, F. D. Hobhs, J. L. Ryan, Z. Li, C. A. Black and R. C. Bradt, *J. Nucl. Mater.,* in press.

2. C. A. Black, F. A. Garner and R. C. Bradt, *J. Nucl. Mater.,* in press.

3. L. S. Cain, G. J. Pogatshnik and Y. Chen, *Phys. Rev.* **B37** (1988) 2645.
4. G. P. Summers, G. S. White, K. H. Lee and J. H. Crawford Jr., *Phys. Rev.* **B21** (1980) 2578.
5. W. Mikenda and A. Preisinger, *J. Lumin.* 26 (1981) 53.
6. J. M. G. Tijero and A. Ibarra, *J. Phys. Chem Solids* 54 (1993) 203.
7. C. Garapou, H. Manaa and R. Moncorge, *J. Chem Phys.* 95 (1991) 5501.
8. F. Durville, B. Champagnon, E. Duval and G. Boulon, *J. Phys. Chem Solids 46* (1985) 701.
9. A. Ibarra, D. F. Mariani and M. Jimenez de Castro, *Phys. Rev.* **B44** (1991) 12158.
10. P. K. Bandynpadhyay and G. P. Summers, *Phys. Rev.* **B31** (1985) 2422.

Distribution

1-16. Argonne National Laboratory, 9700 South Cass Avenue, Argonne. IL 60439
M. C. Billone
O. K. Chopra
H. M. Chung
D. R. Diercks
R. Erck
A. K. Fisher
Y. Gohar
A. B. Hull
C. E. Johnson
F. Kassner
B. A. Loomis
R. F. Mattas
L. A. Niemark
J. H. Park
D. L. Smith
S. W. Tam
H. C. Tsai
H. Wiedersich

17-18. Argonne National Laboratory, EBR-II Division, P.O. Box 2528, Idaho Falls, ID 83403-2528
H. P. Planchon
D. L. Porter

19. Auburn University, Department of Mechanical Engineering. 201 Ross Hall, Auburn, AL 36849
B. A. Chin

20-33. Battelle-Pacific Northwest Laboratory, P.O. Box 999, Richland, WA 99352
J. L. Ethridge
F. A. Gamer (5)
D. S. Gelles
L. R. Greenwood
M. L. Hamilton
H. L. Heinisch
G. W. Hollenberg
R. H. Jones
W. W. Laity
O. D. Slagle

34. Carnegie Institute of Technology, Camegie-Mellon University. Schenley Park, Pittsburgh, PA 15213
W. M. Garrison, Jr.

35-36. EG&G Idaho, Inc., Fusion Safety Program. P.O. Box 1625, Idaho Falls, ID 83415-3523
D. F. Holland
S. J. Piet

37. GE Astrospace Division, San Jose operations, 6834 via Deloro, P.O. Box 530954, San Jose, CA 95153-5354
Mike Kangilaski

38-41. General Atomics, P.O. Box 85608, San Diego, CA 92138
T. A. Lechtenberg
D. I. Roberts
K. R. Schultz
C. Wong

42. General Dynamics Corp.. 5001 Kearny Villa Rd., San Diego, CA 92138
T. L. Cookson

43. Georgia Institute of Technology, Fusion Research Center, 0225, Atlanta. GA 30332
W. M. Stacey

44. Grand Canyon University, Department of Natural Science, 3300 W. Camelback Rd., Phoenix, AZ 85017
W. A. Coghlan

45-46. Lawrence Livermore National Laboratory, P.O. Box 808, Livermore, CA 94550
E.C.N. Dalder
J. Perkins

47-54. Los Alamos National Laboratory, P.O. Box 1663, Los Alamos, NM 87545
J. L. Anderson
F. W. Clinard
E. H. Famum
H. M. Frost
J. C. Kennedy
R. E. Siemon
W. F. Sommer
K. E. Sickafus

55. Manlabs, Inc., 231 Erie Street, Cambridge, MA 02139
D. Tognarelli

56-58. Massachusetts Institute of Technology. Department of Metallurgy and Materials Science, Cambridge, MA 02139
L. W. Hobbs
N. J. Grant
K. C. Russell

59-60. Massachusette Institute of Technology. Plasma Fusion Center Headquarters, Cambridge, MA 02139
H. D. Becker
D. B. Montgomery

61. McDonnell-Douglas Missile Systems Company, Mail Code 306 4204, P.O. Box 516, St Louis, MO 63166
J. W. Davis

62. M. J. Schiff & Associates, 1291 N. Indian Hill Blvd., Claremont, CA 91711-3897
G.E.C. Bell

63-65. National Institute of Standards and Technology, Boulder, CO 80302
F. R. Fickett
H. I. McHenry
R. P. Reed

66. National Materials Advisory Board, 2101 Constitution Avenue, Washington. DC 20418
K. M. Zwilsky

67-68. Naval Research Laboratory. Code 6506, Washington, DC 20375
D. L. Gibson
J. A. Sprague

69-109. Oak Ridge National Laboratory, P.O. Box 2008, Oak Ridge. TN 37831
Central Research Library
Document Reference Section
Laboratory Records Department (2)
Laboratory Records-RC
Patent Section
D. J. Alexander
J. Bentley
E. E. Bloom
T. D. Burchell
J. H. DeVan
G. M. Goodwin
R. H. Goulding
M. L. Grossbeck
E. A. Kenik
R. L. Klueh
E. H. Lee
A. W. Longest
L. K. Mansur
P. J. Maziasz
M. C. Osborne
J. E. Pawel
T. C. Reuther
T. K. Roche
A. F. Rowcliffe (9)
J. Sheffield
L. L. Snead
R. E. Stoller
K. R. Thoms
P. F. Tortorelli
C. A. Wang
D. P. White
S. J. Zinkle

110. Oregon Graduate Institute, Dept. of Materials Science & Engineering, 19600 N.W. Von Neumann Drive, Beaverton, OR 97006
J. M. McCarthy

111-112. Princeton University, Princeton Plasma Physics Laboratory. P.O. Box 451, Princeton, NJ 08540
H. Furth
Long-Poe Ku

113. Reactor Materials Technology, 272 Baywood Avenue, Pittsburgh. PA 15228
A. Boltax

114-115. Rensselaer Polytechnic Institute, Troy, NY 12181
D. Steiner
David Duquette

116. Rockwell International Corporation, NA02, Rocketdyne Division, 6633 Canoga Avenue. Canoga Park, CA 91304
D. W. Kneff

117-119. Sandia National Laboratories. Fusion Technology Dept., Dept. No 6531, P.O. Box 5800, Albuquerque. NM 87185-5800
M. J. Davis
W. B. Gauster
R. D. Watson

120-121. Sandia National Laboratories, Livermore Division 8316, Livermore, CA 94550
W. Bauer
W. G. Wolfer

122. San Diego State University, Mechanical Engineering Dept, San Diego, CA 92182-0191
L. D. Thompson

123. TSI Research, 225 Stevens Ave., #110, Solana Beach. CA 92075
E. T. Cheng

124. University of California at San Diego, U.S. ITER Project Office, 9500 G i Drive, Blde. 302. La Jolla. CA 92093-0035
E. C. Baker

125-126 University of California, Dept. of Mechanical, Aerospace, and Nuclear Engineering, Santa Barbara, CA 93106
G. E. Lucas
G. R. Odette

127-129. University of California, Dept. of Chemical, Nuclear, and Thermal Engineering, Los Angeles. CA 90024
M. A. Abdou
R. W. Conn
N. M. Ghoniem

130. University of California, IPFR, 405 Hilgard Avenue, Los Angeles, CA 90024-1600
S. Sharafat

131. University of Michigan, Dept. of Nuclear Engineering, Ann Arbor, MI 48109
T. Kammash

132. University of Missouri, Depamnent of Nuclear Engineering, Rolla, MO 65401
A. Kumar

133-134. University of Wisconsin, Nuclear Engineering Dept., 1500 Johnson Drive, Madison, WI 53706
J. B. Blanchard
G. L. Kulcinski

135. Washington State University-Tri-Cities, 6012 W. Ridgecrest Drive, Spokane, WA 99208
D. G. Doran

136-139. Westinghouse Hanford Company, P.O. Box 1970, Richland, WA 99352
R. E. Bauer
A. M. Ermi
F. M. Mann
R. J. Puigh

140-142. Hokkaido University, Faculty of Engineering, Kita 13, Nishi 8, Kita-ku, Sapporo 060, Japan
Heischichiro Takahashi
Somei Ohnuki
Akira okada

143-144. Japan Atomic Energy Research Institute, Tokai Research Establishment, Tokai-mura, Naka-gun. Ibaraki-ken 319-11, Japan
Tatsuo Kondo Akimichi Hishinuma

145. Kyushu University, Dept of Nuclear Engineering, Faculty of Engineering, Kyushu University 36, Hakozaki, Fukuoka 812. Japan
C. Kinoshita

146. Kyushu University, Research Institute of Applied Mechanics, 6-1, Kasuga-Koen, Kasuga-Shi, Fukuoka-Ken 816, Japan
Takeo Muroga

147-148. Muroran Institute of Technology. Dept. of Metallurgical Engineering. 27-1 Mizumoto-cho, Mororan 050, Japan
Toshihei Misawa Akihiko Kimura

149. Nagoya University. Dept. of Nuclear Engineering, Furo-Cho, Chikusa-ku, Nagoya 464-01, Japan
Michio Kiritani

150-152. National Institute for Fusion Science, Furo-cho, Chikusa-ku, Nagoya 464-01, Japan
Osamu Motojima Chusei Namba Nobuaki Noda

153-155. National Research Institute for Metals. Tsukuba Branch, Sengen, Tsukuba-shi, Ibaraki-ken, 305, Japan
Fujio Abe Josei Nagakawa Haruki Shiraishi

156. Osaka University, Dept. of Nuclear Engineering, 2-1 Yamadaoka, Suita, Osaka 565. Japan
Tetuo Tanabe

157. PNC Oarai, 4002 Narita, Oarai, Ibaraki 311-13, Japan
Itaru Shibasaki

158. Science University of Tokyo. Dept. of Materials Science & Technology, 2641 Yamazaki Noda City, Chiba Prefecture 278, Japan
Naohira Igata

159. Teikyo University. Otsuka, Hachioji, Tokyo 192-03, Japan
Akira Miyahara

160. Tohoku University, Institute for Materials Research, Katahira 2-2-1, Sendai 980, Japan
Hideki Matsui

161-162. Tohoku University, Institute for Materials Research. Oarai Branch, Oarai, Ibaraki 311-13, Japan
Tatsuo Shikama Hideo Kayono

163. Tohoku University, Dept. of Nuclear Engineering, Tohoku University, Aoba, *Aramaki.* Sendai 980, Japan
Katsunori Ahe

164-166. University of Tokyo. Dept. of Nuclear Engineering, 3-1, Hongo 7-Chome, Bunkyo-Ku, Tokyo 113, Japan
Shiori Ishino (2) Naoto Sekimura

167-168. University of Tokyo, Dept. of Materials Science, 3-1, Hongo 7-Chome, Bunkyo-ku, Tokyo 113, Japan
Akira Kohyama Yutaka Kohno

169. Commission of European Communities, Directorate-General for Research Science and
Education, Fusion Programme RUE De La Loi 200. B-1049 Brussels, Belgium
J. Darvas

70-171. Chalk River Nuclear Laboratories. Atomic Energy of Canada, Ltd., Chalk River,
Ontario KOJ 1J0, Canada
I. J. Hastings D. P. Jackson

172. Southwestern Institute of Physics, P.O. Box 432. Chenedu 610041, Sichuan, P.R. China
J. P. Qian

173. Institute of Atomic Energy, Academia Sinica, P.O. Box 275-51, Beijing. P.R. China
J. Yu

174 Riso National Laboratory, Materials Dept, P.O. Box 49, DK-4000, Roskilde, Denmark
B. N. Singh

175. Centre d'Etudes Nucleaires, Saclay, DLPC/SMCM, Commissariat a l'Energie Atomique,
91191 Gif-Sur-Yvette, Cedex. France
N. Roux

176. Commission for European Communities. Joint Research Centre, I.A.M. Ispra Establishment
21020 Ispra (Varese), Italy
P. Schiller

177. EURATOM/CIEMAT Fusion Association. Avenida Complutense 22, 28040, Madrid, Spain
E. R. Hodgson

178. Paul Scherrer Institute. CH-5232 Villigen, Wuerenlingen PSI. Switzerland
M. Victoria

179. Harwell Laboratory, B393, Radiation Damage Dept., Oxfordshire, OX11 ORA, United Kingdom
C. A. English

180. Metallurgical and Nuclear Consultant, 9A Cumnor Rise Road, Cumnor Hill, Oxford OX2 9HD,
United Kingdom
D. R. Harries

181. Culham Laboratory, U.K. Atomic Energy Authority, D5/117, Abingdon, Oxon OX14 3DB,
United Kingdom
G. J. Butterworth

182. Hahn-Mietner-Institut fur Kernforschung Berlin, Postfach 390128, Glienicker Str. 100, D-14109.

H. Wollenberger

183. Institut fur Festkorperforschung Forschungszentrum Jülich, Postfach 1913. D-52425 Jülich,
Germany
H. Ullmaier

184-185. Kernforschungszentrum Karlsruhe, Postfach 3640, 75 Karlsruhe 1, Germany
M. Dalle-Donne (INR) K. Ehrlich (IMF-II)

186. A. A. Baikov Institute of Metallurgy, USSR Academy of Sciences, Leninsky Prospect 49, Moscow, Russia
L. I. Ivanov

187. CRISM "Prometey," Naberezhnava r. Monastyrick 1, 193167, St. Petersburg, Russia
V. V. Rybin

188. D. V. Efremov Institute of Electro-Physical Apparatus, 189631, St. Petersburg, Russia
Yu. G. Prokofiev

189. Institute of Power Engineering, 218 M. Krasnosel's Kaji St., 107113 Moscow, Russia
G. M. Kalinin

190. Kharkov Institute of Physics & Technology, Radiation Damage and Materials Dept., Akademicheskaya 1, 310108 Kharkov, Ukraine
I. M. Neckludov

191. V. I. Lenin Research Institute of Atomic Reactors. 433510 Dimitrovgrad-10, Ulyanovsk Region, Russia
V. K. Shamardin

192. Department of Energy, W E *Oak* Ridge Field Office, P.O. Box 2008, *Oak* Ridge, TN 37831-6269
Assistant Manager for Energy Research and Development

193. Department of Energy, DOE *Oak* Ridge Field Office. P.O. Box 2008, *Oak* Ridge, TN 37831-6269
S. D. Frey

194. Department of Energy, Office of Basic Energy Sciences, Washington, D.C. 20585
R. J. Gottschall

195-202. Department of Energy, Office of Fusion Energy, Washington, D.C. 20585
S. E. Berk
M. M. Cohen
D. H. Crandall
N. A. Davies
W. F. Dove
T. R. James
R. E. Price
F. W. Wiffen

203. Department of Energy, Richland Operations Office, Federal Bldg.. MS-A590, Richland, WA 99352
D. Segna

204-253. Department of Energy, Office of Scientific and Technical Information, Office of Information Services, P.O. Box 62. *Oak* Ridge, TN 37831
For distribution as shown in DOFiTIC-4500, Distribution Categories UC-423 (Magnetic Fusion Reactor Materials) and UC-424 (Magnetic Fusion Energy Systems)

☆U.S. GOVERNMENT PRINTING OFFICE: 1994-550-165-00002